ISSN 1806-7662

IWT 2004 International Workshop on Telecommunications

August 23rd - 27th 2004 - Santa Rita do Sapucaí - Minas Gerais - Brazil

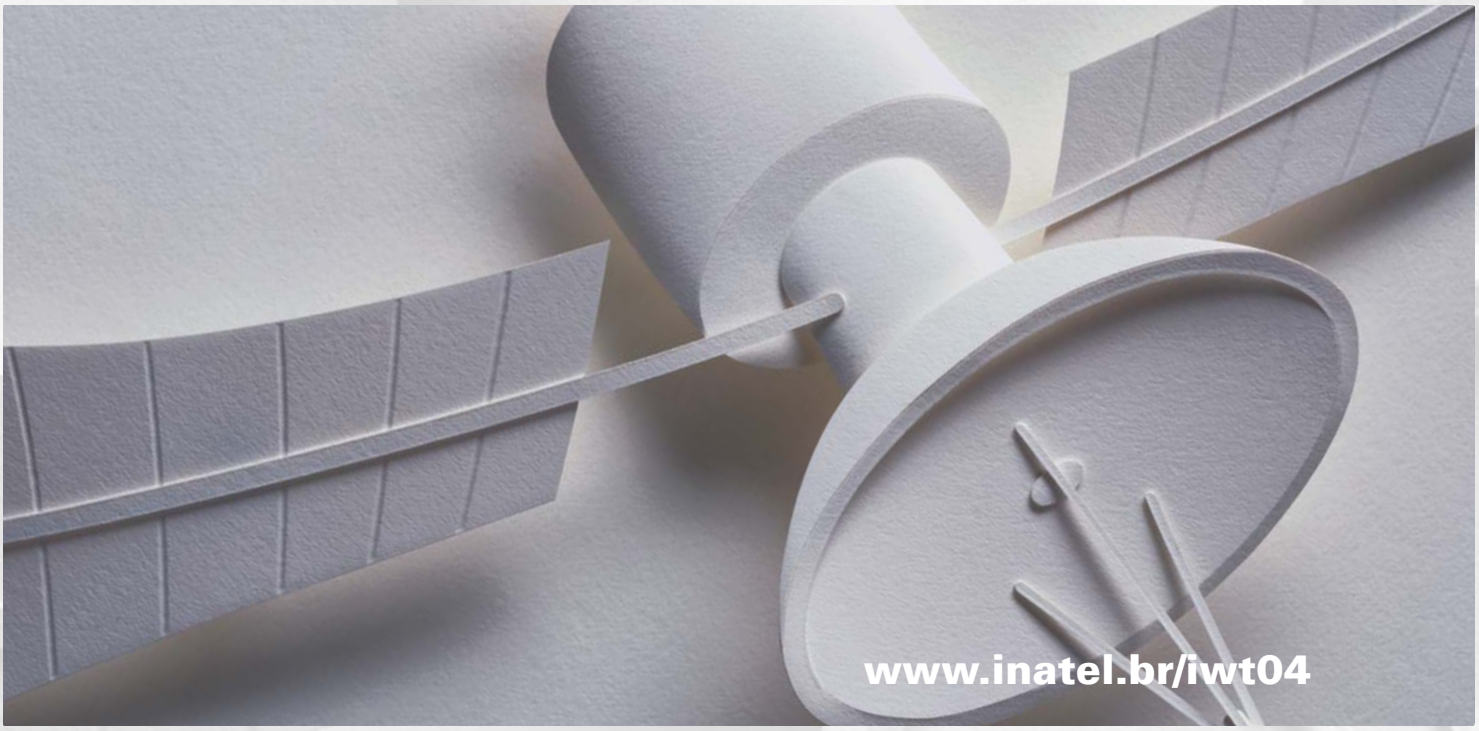

PROCEEDINGS

Realization

Inatel
Instituto Nacional de Telecomunicações

Technical Co-realization

IEEE MG SECTION
IEEE MG SECTION

FEEC UNICAMP
UNICAMP

Media Sponsor

IDG BRASIL

REDE@TELECOM www.grifotech.com.br

Support

SBrT
Sociedade Brasileira de Telecomunicações

Sponsorship

HUBER+SUHNER

Lucent Technologies
Bell Labs Innovations

Draka NK RF

Huawei Technologies

Inatel COMPETENCE CENTER

IWT 2004 International Workshop on Telecommunications
August 23rd - 27th 2004 - Santa Rita do Sapucaí - Minas Gerais - Brazil

IWT 2004
International Workshop on Telecommunications

Santa Rita do Sapucaí, MG, Brazil
August 23-27, 2004

PROCEEDINGS

REALIZATION

Inatel
Instituto Nacional de Telecomunicações

TECHNICAL CO-REALIZATION

IEEE MG SECTION
IEEE MG SECTION

FEEC UNICAMP
UNICAMP

MEDIA SPONSORS

IDG BRASIL

REDE@TELECOM
www.grifotech.com.br

LOCATION

Inatel - National Institute of Telecommunications
Avenue João de Camargo, 510
Santa Rita do Sapucaí, MG, Brazil
Phone: 55 35 3471 9200
Fax: 55 35 3471 9314
Website: http://www.inatel.br/

SUPPORT

SBrT
Sociedade Brasileira de Telecomunicações

SPONSORSHIP

Lucent Technologies
Bell Labs Innovations

HUBER+SUHNER

Draka NK RF

Huawei Technologies

Inatel
COMPETENCE CENTER

Editorial

Proceedings of the International Workshop on
Telecommunications - IWT 2004

ISSN 1806-7662

Published by
Instituto Nacional de Telecomunicações - Inatel
e-mail: ascom@inatel.br

Circulation: 350 units
Free Distribution

Instituto Nacional de Telecomunicações - Inatel
Av. João de Camargo, 510
Caixa Postal: 05
Santa Rita do Sapucaí - MG - BRASIL
CEP 37540-000
Tel: + 55 35 3471.9200 Fax: + 55 35 3471.9314
e-mail: inatel@inatel.br
http://www.inatel.br

Message from the Technical Chair

On behalf of the Organising and Technical Committees of the International Workshop on Telecommunications (IWT04), it is our great pleasure to welcome all of you at Inatel in Santa Rita do Sapucaí. We hope that IWT04 be a great opportunity for everyone to share knowledge, contact the experts in each area and get informed about the advances in telecommunications.

IWT04 has attracted high quality and world-class research works for the interest of participants from the telecommunication community. The combination of tutorial, plenary and technical sessions gives this conference a unique experience to the participants. We have attempted to schedule the technical sessions and plenary sessions to provide a broad coverage of recent advances in various fields. The technical sessions cover coding theory, digital signal processing, antennas and propagation, wireless networks, image processing, optical communications, speech processing, security, computer communications, digital television, communications theory, satellite communications, management and digital communications.

The program structure has 47 papers scheduled for Wednesday and Thursday in 10 technical sessions. Besides, four plenary sessions, addressed by great experts, will further add more values and experiences in areas that are expected to have considerable impact on our field over the next few years. In addition, three tutorials are scheduled for Tuesday.

The selection of such a comprehensive program has been an ambitious and time-consuming task. More than 70 researchers have reviewed 99 submitted papers. The technical program committee members did their best to insure the highest quality of the selected papers. We take this opportunity to thank all of them.

We would like to thank all colleagues, organisers, reviewers, speakers, session chairpersons, all members of the IWT secretariat and, of course, all participants who have made IWT04 possible. Your participation is a key to the success of the conference.

Finally, we sincerely hope that you will have a memorable stay in Santa Rita and wish you all a successful conference.

José Marcos C. Brito
Chair Technical Program Committee

ORGANIZING COMMITTEE

José Paulo Falsarella Inatel General Chair
José Marcos Câmara Brito Inatel Technical Program Co-chair
Renato Baldini Filho - FEEC UNICAMP - Technical Program Co-chair
Geraldo Gil Ramundo Gomes Inatel
Sandro Adriano Fasolo Inatel
Carlos Alberto Ynoguti Inatel
Ivanil S. Bonatti - FEEC UNICAMP
Henrique A. C. Braga - IEEE-MG Section/ UFJF

TECHNICAL PROGRAM COMMITTEE

Chair: José Marcos Câmara Brito National Institute of Telecommunications - Inatel, Brazil
Co-chair: Renato Baldini Filho State University of Campinas - UNICAMP - FEEC, Brazil

Adão Silva University of Aveiro, Portugal
Adonias Costa da Silveira National Institute of Telecommunications - Inatel, Brazil
Aggelos K. Katsaggelos NorthWestern University, USA
Alfredo Goldman University of São Paulo, Brazil
Anderson Stevens L. Gomes Federal University of Pernambuco - UFPE, Brazil
André L. Brandão Communications Research Centre, Canada
André Noll Barreto Claro, Rio de Janeiro, Brazil
Anilton Salles Garcia Federal University of Espírito Santo, Brazil
Antônio Marcos Alberti National Institute of Telecommunications - Inatel, Brazil
Carlos Alberto Ynoguti National Institute of Telecommunications - Inatel, Brazil
César Kyn d´Ávila Technological and Professional Development Center - CEDET, Brazil
Cidcley Teixeira de Souza Setember 7thCollege, Brazil
Dayan Adionel Guimarães National Institute of Telecommunications - Inatel, Brazil
Edson Moschim State University of Campinas - UNICAMP - FEEC, Brazil
Edward Brown Institute for System Level Integration, England
Emily Rozenshine Bar-Ilan University, Israel
Ernesto Luiz Andrade Neto University of Essex, England
Fábio Violaro State University of Campinas - UNICAMP - FEEC, Brazil
Francisco José Fraga da Silva National Institute of Telecommunications - Inatel, Brazil
Geraldo Gil Ramundo Gomes National Institute of Telecommunications - Inatel, Brazil
Hélio Waldman State University of Campinas - UNICAMP - FEEC, Brazil
Ian F. Akyildiz Georgia Institute of Technology, USA
Ishtiaq Ahmed Choudhry Kyoto University, Japan
Ivanil Sebastião Bonatti State University of Campinas - UNICAMP - FEEC, Brazil
Jaime Portugheis State University of Campinas - UNICAMP - FEEC, Brazil
Jerffeson Teixeira de Souza University of Ottawa, Canada
João Cesar Moura Mota Federal University of Ceará - UFCE, Brazil
Joel J. P. C. Rodrigues University of Beira Interior, Portugal
Jorge Moreira de Souza FITec , Brazil
José Antonio Apolinário Jr. Militar Institute of Engineering - IME, Brazil
José Antônio Justino Ribeiro National Institute of Telecommunications - Inatel, Brazil
José Edimar Barbosa Oliveira Technological Institute of Aeronautics - ITA, Brazil
José Ferreira de Rezende Federal University of Rio de Janeiro, Brazil
Kyandoghere Kyamakya University of Hannover, Germany
Luis Geraldo Pedroso Meloni State University of Campinas - UNICAMP - FEEC, Brazil
Marcelo Eduardo Pellenz Catholic University of Paraná - PUC-PR, Brazil
Marcelo Sampaio de Alencar Federal University of Campina Grande - UFCG, Brazil
Márcio L. Xavier dos Santos University of Taubaté - UNITAU, Brazil
Markus Endler Catholic University of Rio de Janeiro - PUC-RJ, Brazil
Maria Regina de Campos Caputo National Institute of Telecommunications - Inatel, Brazil
Marlene Sabino Pontes WiNGS Telecom, Brazil
Martin Zieher University of Applied Sciences Essligen, Germany
Masanori Kanazawa Kyoto University, Japan
Maurice Pyée PLCE - CNRS, France
Maurício Silveira National Institute of Telecommunications - Inatel, Brazil
Michel Daoud Yacoub State University of Campinas - UNICAMP - FEEC, Brazil
Miguel Arjona Ramirez University of São Paulo, Brazil
Mohammad Saleh University of Nottingham Malaysia, Malaysia
Omar Carvalho Branquinho Catholic University of Campinas - PUC-Campinas, Brazil
Pascal Lorenz University of Haute Alsace, France
Peter J. Chitamu University of fhe Witwatersrand, South Africa

Rainer Doster University of Applied Sciences Esslingen, Germany
Ralf Irmer Dresden University of Technology, Germany
Reginaldo Palazzo Júnior State University of Campinas - UNICAMP - FEEC, Brazil
Sandro Adriano Fasolo National Institute of Telecommunications - Inatel, Brazil
Shusaburo Motoyama State University of Campinas - UNICAMP - FEEC Brazil
Thomas P. Krauss Motorola Labs, USA
Valdemar C. da Rocha Jr. Federal University of Pernambuco - UFPE, Brazil
Yuzo Iano State University of Campinas - UNICAMP - FEEC, Brazil

ADDITIONAL REVIEWERS

Caterina Scoglio - Georgia Institute of Technology, USA
Francisco Madeiro - Catholic University of Pernambuco - Unicap, Brazil
Hélio Magalhães - Federal University of Pernambuco - UFPE, Brazil
Jiang Xie - Georgia Institute of Technology, USA
Luiz Carlos Kretly - State University of Campinas - UNICAMP, Brazil
Mário Minami - State University of São Paulo - USP, Brazil
Mark Thomson - Motorola Labs, USA
Ozgur Baris Akan - Georgia Institute of Technology), USA
Tricha Anjali - Georgia Institute of Technology, USA
Waslon Terllizzie Araújo Lopes - Technology and Science Faculty - AREA1, Brazil
Weilian Su - Georgia Institute of Technology, USA
Xudong Wang - Georgia Institute of Technology, USA

CONTENTS

Technical Session 1

Technical Session 2

Technical Session 3

Technical Session 4

Technical Session 5

Technical Session 6

Technical Session 7

Technical Session 8

Technical Session 9

Technical Session 10

Circuit-Switched Voice and Packet-Switched Data Wireless Link Dimensioning

Marcelo de Oliveira Marques
National Institute of Telecommunications

P.O. Box 05 – 37.540-000
Santa Rita do Sapucaí – MG – Brazil
marcelo@inatel.br

Ivanil Sebastião Bonatti
School of Electrical & Computer Engineering
University of Campinas
P.O. Box 6101 – 13.083-970
Campinas – SP – Brazil
ivanil@dt.fee.unicamp.br

***Abstract* - The wireless link dimensioning using an approximation technique that allows the decomposition of a two-dimensional Markov chain in two one-dimensional chains is improved in this paper. Instead of using several circuit-switched servers to data transmission we consider a single packet-switched server with FIFO discipline. Circuit-switched channels serve the voice-users. The total number of channels and the preemption threshold of voice-channels over the data-channels have been determined, illustrating the adequacy and efficiency of the proposed algorithm.**

***Index Terms* - GPRS, Multimedia Wireless System Dimensioning.**

I. INTRODUCTION

The introduction of the multiple access service GPRS (*General Packet Radio Service*) on GSM networks (*Global System for Mobile Communications*) increases the use efficiency of radio resource through the sharing of data and voice users on the available channels in GSM networks [1]. The GPRS uses the GSM frequency canalization, in which each carrier supports a TDMA frame (*Time Division Multiple Access*) composed of eight time-slots.

The users can share the transmission of voice, PDUs (*Protocol Data Unit*) and signaling over several frequency carriers.

The GPRS has four codification schemes. The CS1 codification scheme, with transmission rate of 9.05 kbps, is mainly used for signaling transmissions. The CS2, CS3 and CS4 codification schemes offer greater transmission rates with lesser error protection of the transmitted information.

Up to eight PDCHs (*Packet Data Channel*) are built over each carrier in the GSM system. A PDCH is formed by the recurrence of one determined time-slot in a multi-frame of 52 consecutive frames, which structure is shown in Figure 1.

This work was partially supported by CAPES - Coordenação de Aperfeiçoamento de Pessoal de Nível Superior, FAPESP - Fundação de Amparo à Pesquisa do Estado de São Paulo e CNPq - Conselho Nacional de Desenvolvimento Científico e Tecnológico.

The 52 TDMA frames forming the PDCH channel are divided in twelve radio-blocks, containing four frames each, two Idle frames destined to the interference measurement and two frames used to synchronize the mobile station and the radio-base station. The PDCH channel is allocated to the mobile stations on demand and they can share one or more PDCHs. Several PDCHs can be allocated to a single mobile station.

When a mobile station wants to transmit a PDU (*Protocol Data Unit*), it requests the creation of a TBF (*Temporary Block Flow*) through the random access channel PRACH (*Packet Random Access Channel*). The mechanism of TBF creation can be viewed as the establishment of a virtual circuit defining the connection between the mobile station and the base station. This virtual circuit is modeled as a "*circuit*" that remains connected and busy during the time necessary to the complete transmission of the PDU.

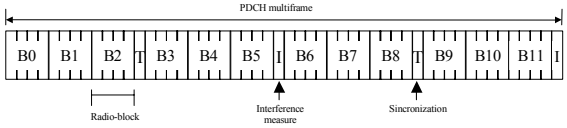

Fig. 1. PDCH multi-frame structure

The integration of voice and data users can be implemented on packet switching networks treating both in the same way, but giving priority to the voice users over the data users, in order to guarantee a maximum delay time to the voice channels [2], [3]. The multiple access protocols with reserve [4] allow the allocation of channels repeating cyclically in the appropriate cadence to synchronous users. The remaining system capacity is used to send the data signals that are sensitive to losses, but not to delays. Such integration can be implemented, for example, by the combination of the protocol TCP/IP (*Transmission Control Protocol/Internet Protocol*) for data with the protocol UDP (*User Datagram Protocol*) for voice. *Chen et al*. have investigated the voice and data sharing with priority for the voice service and buffering the preempted data packets [5]. *Meo et al*. have investigated a dynamic sharing strategy using the

information of the buffer occupation as reference for allocation of exclusive channels for data packets [6].

In this paper, an algorithm for the dimensioning of wireless links is considered using an approximation technique [7] that allows the decomposition of the two-dimensional Markov chain, in two one-dimensional Markov chains. The reference model is presented in Section 2. In Section 3, the synthesis model to determine the capacity of the wireless link is presented. Numerical results and discussions are presented in Section 4, and the Conclusions are presented in Section 5.

II. Reference Model

The channel allocation scheme for the voice packets and the PDUs is shown in Figure 2, where the random variable *Y* denotes the number of channels taken by the voice calls $0 \le y < C_v$.

Each mobile station generates PDUs having Poisson distribution with average rate λ_d / *n, n* being the number of mobile stations in the system. The lengths of the PDUs have exponential distribution with average size E{R}.

Voice calls are generated with average rate λ_v / *n* having Poisson distribution, with average service time $1/\mu_v$ and are exponentially distributed. The blocked voice calls are cleared of the system.

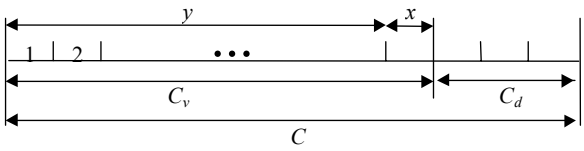

Fig. 2. Channel allocation structure

The transmission system is modeled with $C = C_v + C_d$ channels, each one having a transmission rate *r* equal to 13.4 kbps (information channels use CS2 codification scheme).

When busy due to a voice call, each channel remains unavailable during the conversation time, and is set free in the end of the communication. When busy for a PDU transmission (a mobile station is sending a PDU), the channel remains unavailable during the transmission of the PDU, unless it suffers preemption for a voice call. In that case, the remaining not transmitted bytes of the PDU are buffered and are priority sent, in a next successful access. Each station has a buffer to store the PDUs when the access is denied, being *b* the limit for the maximum number of PDUs in the system. If a PDU is generated and the buffer is full, the PDU is blocked and dropped of the system. The number of available channels for data transmissions is $m = (C_v - y) + C_d$ resulting in a overall rate of *mr*. When less than *m* data users are in the system they share the server with rate *mr* with FIFO discipline.

Both the voice calls and PDUs can access the C_v channels, from the total of *C* channels, with preemption for the voice calls over the PDUs. The $C_d = C - C_v$ channels can be exclusively taken by PDUs. The average data service time is equal to the division of the PDU length by *mr*.

The joint probability $p_{v,d}$ *(v,d)* of the number of voice and data channels can be obtained by solving the equilibrium equations of the Markovian chain of the system. The equilibrium equations for the two dimensional Markov chain model can be written as

$$\pi \cdot Q = 0 \,, \sum_{k=1}^{n} \pi_k = 1 \,, n = (b+1) \cdot (c_v + 1) \qquad (1)$$

where Q is the transition matrix. The vector elements of π are given by $\pi(d + (b+1).\ v + 1) = p_{v,d}$ (v,d) where *p* is the joint voice and data probability matrix.

III. Synthesis Model

The complexity of the Markovian chain significantly grows when the number of channels or the buffer length of the system increases, making impractical its use for dimensioning purposes.

Ghani and Schwartz had shown that the probability of the number of voice channels and the conditional probability of the number of data channels could be approximated by independent queues [8]. In general, the time to transmit a PDU is significantly lesser than the duration of a voice call, and the quality of the approximation improves as the difference between the service time of the voice and data channels increases.

The number of channels allocated to voice users, *Y,* is described by the queue $M/M/C_v/C_v$ since, due to the preemption mechanism, all C_v channels are available to the voice users.

The conditional number of data users (PDUs), *N* for a given *y*, can be approximated by the queue *M/M/1/b* which server has a rate of *mr*. Actually, in GPRS systems at most eight channels can serve one single PDU. Therefore, the approximation will provide an upper bound for the performance of the system. Considering the system composed by *n* carriers (ordered from left to right), each one with eight channels, the schedule to admit new connections in the system is:

- A voice call must be located in the first free channel found in a search running left to right starting at the first channel of the leftmost carrier.
- A PDU must be served by a TBF located in the first free carrier found in a search running from right to left starting from the rightmost carrier. If there are no free carriers, the TBF must be located in the first carrier having available channels, i.e., a carrier having less than eight busy channels.

If each PDU could use only one channel at time, i.e., the data are also circuit-switched the queue model becomes *M/M/m/b* queue [9].

The maximum current number of channels that are used by PDUs is $C_d + x$, with $x = C_v - y$, and the preempted PDUs are not considered in the buffer of the conditional queue approximation.

The traffic parameters $\rho = \lambda_d / \mu_d$ and $\rho_v = \lambda_v / \mu_v$, being $1/\mu_d$ the average time to transmit one PDU by a GPRS channel, and the structural parameters C, C_d and b are considered known when performing analysis is computed. The main purpose is to determine the service quality parameters: P_v, voice channels blocking probability; P_d, data blocking probability and T, average data transfer time (waiting time + service time).

The QoS parameters P_v, P_d and T are specified as goals to be achieved with a minimum number of channels in the system (C and the threshold for data C_d) when dimensioning the wireless link. The voice and PDU demand traffic forecasts, characterized by ρ_v and ρ parameters, are assumed to be known.

From the queue $M/M/C_v/C_v$, the voice channel probability distribution function is given by

$$p_{va}(v) = \left(\sum_{k=0}^{C_v} \frac{{\rho_v}^k}{k!} \right)^{-1} \frac{{\rho_v}^v}{v!}, v = 0,1,...,C_v \qquad (2)$$

and the voice channels blocking probability is given by the *Erlang's* Formula.

$$P_{va} = E(\rho_v, C_v) \qquad (3)$$

The number of channels available for PDU transmission is dependent of the number of channels occupied by voice users. Therefore, the conditional probability of $C_d + x$ channels available for data is given by

$$q_x = \left(\sum_{k=0}^{C_v} \frac{{\rho_v}^k}{k!} \right)^{-1} \frac{{\rho_v}^{C_v - x}}{(C_v - x)!}, x = 0,1,...,C_v \qquad (4)$$

The data channels can be modeled by a queue *M/M/1/b*, where b is the limit for the maximum number of PDUs in the system.

The probability of having k PDUs in the system is given by [10]

$$p_d(k,m) = \frac{1 - \left(\frac{\rho}{m}\right)}{\left(1 - \left(\frac{\rho}{m}\right)^{b+1}\right)} \left(\frac{\rho}{m}\right)^k \text{ for } 0 \le k \le b \qquad (5)$$

The data channel probability distribution function is given by

$$p_{da}(d) = \sum_{x=0}^{C_v} q_x \cdot p_d(d,m), \quad d = 0,1,...,b \qquad (6)$$

A new TBF requisition will be blocked if $k = b$ PDUs are in the system. Thus, the conditional blocking probability is given by $p_d(b,m)$ and the data blocking probability, P_{da}, is

$$P_{da} = \sum_{x=0}^{C_v} q_x \cdot p_d(b,m) \qquad (7)$$

The average data transfer time, T, is given by (*Little's* Theorem)

$$T = \frac{1}{\lambda_d (1 - P_{da})} \cdot \sum_{x=0}^{C_v} q_x L(m) \qquad (8)$$

where $L(m)$ is the average conditional number of PDUs given by

$$L(m) = \sum_{k=0}^{b} k \cdot p_d(k,m) \qquad (9)$$

A. Algorithm for synthesis

The proposed algorithm has two phases. First, the number of channels C_v, which are shared by the voice and data users, is determined guarantying the bound for the, P_{vspec}, voice channels blocking probability specification. Second, the number of channels, C_d, which are exclusively allocated to data users, is determined to attain the specified bounds T_{spec} (average data transfer time) and P_{dspec} (data blocking probability) values.

1) Determination of C_v

The determination of C_v implies the repetitive computation of the *Erlang's* Formula, which is computed by an iterative procedure to overcome numerical difficulties [11].

$$E(\rho_v, n+1) = \frac{\rho_v \cdot E(\rho_v, n)}{(n+1) + \rho_v \cdot E(\rho_v, n)} \qquad (10)$$

The *Erlang's* Formula $E(\rho_v,n)$ gives the blocking probability of a Poissonian traffic, with intensity ρ_v, offered to a link with capacity n. In the dimensioning process the inverse of the *Erlang's* Formula $n(\rho_v,P_v)$ is needed, which produces the minimum number of channels having blocking probability lesser than P_v.

The bisection algorithm can be used to solve the numerical inequality that produces the inverse of *Erlang's* Function $n(\rho_v,P_v)$.

The upper bound is given by [12].

$$n_s = \rho_v \cdot (1 - P_v) + \frac{1}{P_v} \tag{11}$$

The average number of occupied channels gives the lower bound

$$n_I = \rho_v \cdot (1 - P_v) \tag{12}$$

Bisection algorithm to compute C_v

$n_I \leftarrow \rho_v(1 - P_v)$
$n_S \leftarrow \rho_v(1 - P_v) + \frac{1}{P_v}$
While $n_s > n_I + 1$
$n \leftarrow \left\lceil \frac{n_s + n_I}{2} \right\rceil$
if $E(\rho_v, n) < P_{vspec}$
then $n_s \leftarrow n$
else $n_I \leftarrow n$
end while
$C_v \leftarrow n_s$

2) Determination of the threshold C_d

Bisection algorithm to compute C_d

$n_I \leftarrow \lceil C_{d\min} \rceil$
$n_S \leftarrow 2 \cdot n_I$
While $T > T_{spec}$ *ou* $P_d > P_{dspec}$
$n_I \leftarrow n_S$
$n_S \leftarrow 2 \cdot n_I$
end while
While $n_s > n_I + 1$
$n \leftarrow \left\lceil \frac{n_s + n_I}{2} \right\rceil$
If $T > T_{spec}$ *ou* $P_d > P_{dspec}$
then $n_I \leftarrow n$
else $n_S \leftarrow n$
end while
$C_d \leftarrow n_s$

IV. NUMERICAL RESULTS AND DISCUSSIONS

The number of channels C_v and C_d, $C = C_v + C_d$, are shown in Table 1 and Table 2, for several values of the traffic ρ_v and ρ with parameter values: E{R} = 1675 bytes (13400 bits), P_{vspec} = 1e-2, T_{spec} = 2 s, P_{dspec} = 1e-4 and $b = (C_v + C_d + \Delta)$. Note that the number of channels exclusively dedicated to the data users (C_d) is the minimum possible, (for $\Delta = 100$, Table 1) due to the effectiveness of sharing the channels used by the voice users. If the buffer total length is enough only to store the PDUs that are pre-empted by the voice users, $b = C_v + C_d$, i.e. ($\Delta = 0$, Table 2), then the number of channels exclusively dedicated to the data users increases. As the voice traffic ρ_v increases, the number of channels dedicated to data users C_d becomes very near of the values for Δ = 100, indicating the effectiveness of the sharing mechanism.

The number of channels C_v and the threshold C_d were also computed for buffers with $\Delta > 100$ giving pratically the same results as the Δ = 100 situation, meaning that this value of Δ is big enough when computing the number of channels.

Table 1. C_v and C_d for P_{vspec}= 1e-2; T_{spec} = 2 s; P_{dspec}= 1e-4; Δ = 100.

			$\Delta = 100$		
ρ_v	C_v	ρ	C_d	P_d/P_{dspec}	T/T_{spec}
1	5	1	1	0.29	0.22
10	18	1	1	0.60	0.29
30	42	1	1	0.52	0.32
1	5	10	10	0.26	0.15
10	18	10	10	0.55	0.10
30	42	10	10	0.48	0.08
1	5	30	30	0.29	0.14
10	18	30	30	0.51	0.09
30	42	30	30	0.44	0.07

Table 2. C_v and C_d for P_{vspec}= 1e-2; T_{spec} = 2 s; P_{dspec}= 1e-4; Δ = 0.

			$\Delta = 0$		
ρ_v	C_v	ρ	C_d	P_d/P_{dspec}	T/T_{spec}
1	5	1	2	0.23	0.11
10	18	1	2	3e-5	0.07
30	42	1	2	2e-12	0.05
1	5	10	13	0.60	0.07
10	18	10	11	0.58	0.07
30	42	10	11	0.04	0.05
1	5	30	34	0.37	0.06
10	18	30	32	0.37	0.06
30	42	30	31	0.31	0.05

In order to analyze the robustness of the values obtained for the number of channels in the synthesis process some simulations have been made. The behavior of the P_d, data blocking probability and the average data transfer time, T, as function of the normalized voice traffic is presented in Figures 3 and 4, for, C_d = 9 and C_v = 5, 18 and 42. The voice traffics taken as reference are the values 1, 10 and 30, respectively.

As shown in the Figure 3 and 4, there is a small performance degradation of the data users due to the sharing mechanism if the overload of voice traffic is smaller than 20%. The sensitivity of the P_d and of the T to the variation of the voice traffic is larger for bigger values of the nominal voice traffic. This effect can be explained by the increasing of the number of mean busy voice channels as the nominal value of the

traffic is augmented. The percentage of ocupation is 20%, 55% and 70% for ρ_v = 1, 10 and 30, respectively. Therefore, the mechanism of sharing the channels C_v can take better profity when the nominal voice traffics are small.

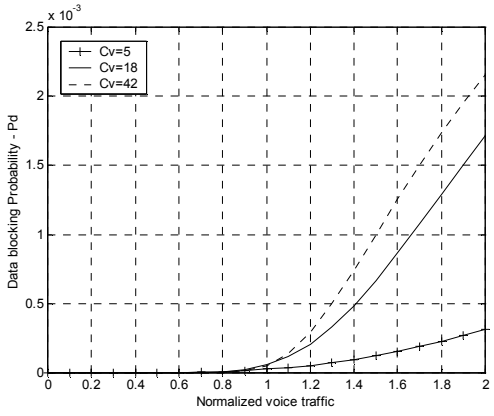

Fig. 3. Data blocking probability P_d as function of the normalized voice traffic for $C_d = 10$ and $\rho = 10$.

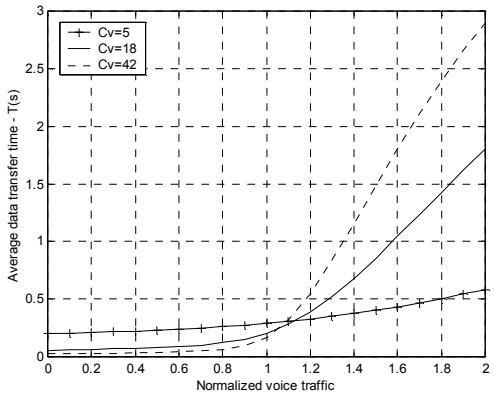

Fig. 4. Average data transfer time T as function of the normalized voice traffic for $C_d = 10$ and $\rho = 10$.

V. CONCLUSIONS

The dimensioning of wireless links sharing voice and data has been considered in this paper. The minimum number of channels that satisfies a specified blocking probability has been determined for the circuit-switched voice traffic using *Erlang's* Formula. The number of data channels that satisfies both the specified data blocking probabilities and average data transfer time for the data traffic has been obtained considering that the data users can share the voice channels, which have preemption over data users.

The dimensioning method is based on an approximation that allows decomposing the Markovian chain describing the system into two queues with analytical solutions. The proposed algorithm is computationally simple and efficient. The results obtained using only one server, with rate equals to *mr*, are better than *m* servers each one with rate *r*. The application of the proposed algorithm to GPRS links illustrates the adequacy of the method to wireless link dimensioning. Some cases of overload are analyzed demonstrating the robustness of the technique.

REFERENCES

[1] ETSI TS 101 350, (1999), "General Packet Radio Service (GPRS), Overall Description of the GPRS Radio Interface, Stage 2".

[2] Zahedi, A. and Pahlavan, K., (2000), "Capacity of a Wireless LAN with Voice and Data Services", IEEE Transactions on Communications, Vol. 48, No.7, pp.1160-1170.

[3] Kalden, R., Meirick, I. and Meyer, M., (2000), "Wireless Internet Access Based on GPRS", IEEE Personal Communications, pp.8 – 18.

[4] Kwok, Y. K. and Lau, V. K. N., (2001), "Performance Evaluation of Multiple Access Control Schemes for Wireless Multimedia Services", IEEE Proc. Commun., Vol. 148, No.2, pp.86-94.

[5] Chen, W., Wu, J.C. and Liu, H., (2002), "Performance Analysis of Radio Resource Allocation in GSM/GPRS Networks", Vehicular Technology Conference, Proceedings. VTC 2002 IEEE 56th, Vol. 3, pp.1461-1465.

[6] Meo, M., Marsan, M. A. and Batetta, C., (2002) "Resource Management Policies in GPRS Wireless Internet Access Systems", Proceedings of DNS'02.

[7] Ni, S. and Haggman, S., (1999), "GPRS performance estimation in GSM circuit switched services and GPRS shared resource systems", Proceedings of IEEE WCNC'99, Vol. 3, pp.1417-1421.

[8] Ghani, S. and Schwartz, M., (1994), "A Decomposition Approximation for the Analysis of Voice/Data Integration", IEEE Transactions on Communications, Vol. 42, No. 7, pp.2441-2452.

[9] Marques, M. O., Bonatti, I. S., (2004), "Dimensioning of Wireless Links Sharing Voice and Data", ICT International Conference on Telecommunications, LNCS 3124, pp.82-87.

[10] Gross, D. and Harris, C.M., (1998), "Queueing Theory", John Wiley & Sons, Inc.

[11] Bear, D., (1976), "Principles of Telecommunications – Traffic Engineering", Peter Peregrinus LTD.

[12] Berezner, S. A., Krzesinski, A. E. Taylor, P. G. Taylor, (1998), "On the Inverse of *Erlang's* Function" , Journal of Applied Probability, Vol. 35, pp.246-252.

Forward Link Performance Study of the 1xEV-DV System

Tania Aida Garcia Bassi
Lucent Technologies
P.O. Box 7030 – 13097-660
Campinas - SP - Brazil
tbassi@lucent.com

Shusaburo Motoyama
DT – FEEC - UNICAMP
P.O. Box 6101 – 13083-970
Campinas - SP - Brazil
motoyama@dt.fee.unicamp.br

***Abstract* – The forward link performance study of the 1xEV-DV system is presented in this paper. The system is studied through simulation that allows the analyses of the average packet delay, the throughput of the system and link utilization in function of traffic load. The performance of forward link is studied by using packet schedulers without priority, with priority of higher bit rates to lower as well as user priority. The improvement due to the code division multiplexing (CDM) technique in 1xEV-DV is also studied. The simulation results showed that the 1xEV-DV system allows transmission of high bit rates. It is also shown that the system performance can be still enhanced by introducing a priority scheduler. The estimation of how much the packet delay can be minimized and the throughput can be improved, by using CDM technique, is also presented.**

***Index Terms* – 1xEV-DV, forward link, performance, priority, packet delay.**

1. INTRODUCTION

The first wireless communication system generation was based on the analog technology and had the objective to provide mobile voice communication. This was also the main objective of the second generation (2G) system based on digital technology.

The second generation system was designed to support voice and low data rate services [6]. The 2.5G system was developed to increase the 2G system traffic capacity, improving the quality of the services and providing higher transmission data rates by using packet switching.

The main purpose of the third generation system is provide, besides the voice services, high-speed data services. This system is also based in digital technology supporting voice, data and multimedia traffic.

The IS-95A standard that defines the CDMA (Code Division Multiple Access) technology was commercially introduced in 1995 [6], supporting voice by circuit switching and data rates up to 14.4 kbps. In the next step, the IS-95B had the capability to provide transmission data rates up to 64 kbps.

The CDMA2000, defined by the IS-2000 standard in releases 0, A and B, was designed to provide data traffic through packet switching, achieving data rates up to 153.6 kbps (release 0 and A) and 307.2 kbps (release B), with backward compatibility with IS-95 systems [10].

In the IS-2000 evolution path, the 1xEV-DV, defined in IS-2000 releases C and D, is the CDMA third generation technology capable to provide packet data transmission rates up to 3.0912 Mbps in the forward link [1], and up to 1.8456 Mbps in the reverse link (release D) [7]. The 1xEV-DV standard is backward compatible with CDMA2000 and IS-95 standards.

Most of the available references describe the 1xEV-DV system standard [2], [3], [4] and [6]. Other references provide the reverse link detailed analysis relative to the aerial interface design problems [8] or relative to the data rate control scheme to optimize the link utilization [9]. In [5] it is presented a 1xEV-DV system performance study of the forward link when data and voice traffic coexist in the same carrier.

The forward link performance study of the 1xEV-DV system considering only data traffic is presented in this paper. The system is studied through simulation that allows the analyses of the average packet delay, the system throughput and the link utilization in function of traffic load. The performance of the forward link is studied by using packet schedulers without priority, with priority of higher bit rates to lower as well as user priority. Some simulation results are compared to analytical results. The simulation is performed in Matlab software tool.

The description of the 1xEV-DV system is presented in section 2. The simulation model is described in the section 3 and the simulation results are presented and analyzed in section 4. Finally, the main conclusions are presented in section 5.

2. 1XEV-DV

1xEV-DV is a third generation wireless communication system based on CDMA and developed to achieve high transmission data rates. It allows the utilization of many different data applications, including real time applications. 1xEV-DV is the CDMA2000 1X evolution defined in the IS-2000 standard releases C and D.

The IS-2000 release C concentrates most of the modifications and improvements in the forward link (from the base station to the mobile station), allowing the peak data rate up to 3.0912 Mbps in this link [1].

On the other hand, the release D of IS-2000 standard concentrates the improvements in the reverse link (from the mobile station to the base station), in

order to increase the data transmission capability of this link [7].

As in CDMA2000 1X the voice traffic in 1xEV-DV is supported by code division (CDM) dedicated channels and carried by the fundamental channel (FCH) in variable rates up to 14.4 kbps.

In CDMA2000 1X, the packet data traffic is carried by the supplemental channel (SCH) in data rates up to 307.2 kbps in forward and reverse links [10].

For the packet data traffic, the 1xEV-DV introduces the F-PDCH (forward packet data channel). The introduction of this new shared channel allows 1xEV-DV to support the data services in a flexible mode, through dedicated channels (SCH), through shared channels (F-PDCH), or in a combination of dedicated and shared channels.

Since F-PDCH is a shared channel, it cannot perform the soft-handoff, it requires forward and reverse link channels to support it, and it has short timeslot duration up to 5 ms to allow the fast link adaptation [2]. However, it is due to the F-PDCH that 1xEV-DV achieves high transmission data rates, up to 3.0912 Mbps. In the reverse link, the transmission rate specified in release C is up to 451.2 kbps. In release D the addition of new channels allowed the system to achieve 1.8456 Mbps in the reverse link [7].

In release C specification, it is defined four new channels in the physical layer: one traffic channel in the forward link (F-PDCH), one control channel in the forward link (F-PDCCH), and two control channels in the reverse link (R-CQICH and R-ACKCH).

In release D, four new channels are implemented in the reverse link, including the reverse link packet data channel (R-PDCH), and three new channels in the forward link to support the reverse link data traffic.

The main techniques implemented in 1xEV-DV to increase the data throughput include the adaptive modulation and codification (ACM), the adaptive allocation and multiplexing TDM/CDM, Hybrid ARQ, sector switch technique, and packet data control hold operation [3], [4].

In 1xEV-DV, it is introduced besides CDM the time division multiplexing (TDM) that maximizes the resource utilization, allocating the same resource to more than one mobile station for a short period of time.

The new channel R-CQIH introduced in the reverse link permits the gathering of information about the forward link channel quality. For instance, a mobile station that is experiencing fading can have the resources allocated only when the channel quality is better, avoiding the waste of resources and serving the mobile stations with higher data rates.

The channel quality information is also used in the definition of the F-PDCH optimum data rate by using the adaptive modulation and codification (AMC) techniques that change the modulation and the codification schemes according to the forward link conditions, i.e., the forward link modulation and codification vary in real time adapting themselves to the propagation conditions.

Tab. 2.1 shows the packet sizes, number of timeslots and modulation to achieve the data rates in 1xEV-DV.

TABLE 2.1
1XEV-DV MODULATION PER DATA RATE.

Subpacket data rate (kbps)	Packet size (bits)	Number of slots per subpacket	Modulation
81.6	408	4	16-QAM/QPSK
158.4	792	4	16-QAM/QPSK
163.2	408	2	16-QAM/QPSK
312	1560	4	16-QAM/8-PSK/QPSK
316.8	792	2	16-QAM/8-PSK/QPSK
326.4	408	1	16-QAM/8-PSK/QPSK
465.6	2328	4	16-QAM/8-PSK/QPSK
619.2	3096	4	16-QAM/8-PSK/QPSK
624	1560	2	16-QAM/8-PSK/QPSK
633.6	792	1	16-QAM/8-PSK/QPSK
772.8	3864	4	16-QAM/8-PSK/QPSK
931.2	2328	2	16-QAM/8-PSK/QPSK
1238.4	3096	2	16-QAM/8-PSK/QPSK
1248	1560	1	16-QAM/8-PSK/QPSK
1545.6	3864	2	16-QAM/8-PSK/QPSK
1862.4	2328	1	16-QAM/8-PSK
2476.8	3096	1	16-QAM
3091.2	3864	1	16-QAM

The F-PDCH data traffic channel allows both time division multiplexing (TDM) among different mobile stations and code division multiplexing (CDM) between two mobile stations simultaneously. This feature is very important since different applications require different packet sizes, thus for large packet transfers such as file transfers TDM is the best choice, however, for small packet sizes CDM is more efficient.

Using the TDM/CDM multiplexing, the radio base station can share the F-PDCH up to two users for one or more timeslots, allocating different Walsh codes for them.

Since the F-PDCH data traffic channel is a shared and dedicated for short periods of time (1.25, 2.5 or 5 ms), a specific control channel in the forward link is designed, the F-PDCCH – forward packet data control channel. The 1xEV-DV supports up to two F-PDCCH in the forward link (F-PDCCH0 and F-PDCCH1), that are synchronized with F-PDCH to allow the mobile to use the control information easily and correctly decode and demodulate the carried data in the F-PDCH.

The F-PDCH is designed to use a large number of Walsh codes at a spreading factor 32. The Walsh space spreading factor 32 was chosen aiming the best relationship between throughput and system complexity [2]. For a spreading factor 32, the 1xEV-DV system, without CDMA2000 1X voice and data services, has 28 available Walsh codes for the F-PDCH and the remaining available Walsh codes for the control channels. When the system supports CDMA2000 1X voice and data services, the available Walsh codes for the F-PDCH is reduced, so the maximum data transmission rate is also reduced.

Tab. 2.2 shows the number of Walsh codes required per data transmission rate defined in the releases C and D of the IS-2000 standard.

In this paper, the transmission of data packets achieving high data rates in a 1xEV-DV system, without the CDMA2000 1X voice and data services, is considered.

TABLE 2.2
NUMBER OF WALSH CODES PER MODULATION, PER DATA RATE.

Subpacket data rate (kbps)	Number of Walsh codes		
	16-QAM	8 - PSK	QPSK
81.6	1	-	4/3/2
158.4	2	-	11/6/4/3
163.2	2	-	8/5/4/3
312	4/3	5	15/9/7/6
316.8	4/3	5	19/11/8/7/6
326.4	4/3	5	19/11/8/7/6
465.6	6/5/4	8/7	20/14/11/9
619.2	6/5/4	8/7	20/16/13/11
624	6/5/4	8/7	20/15/13/11
633.6	6/5/4	8/7	19/15/13/11
772.8	9/8/7	12/11	19/16/14
931.2	11/10/9/8	15/13	23/20/17
1238.4	15/12/11	21/19/17	25/22/13
1248	15/13/12/11	21/19/17	25/22
1545.6	19/17/15/14/13	25/23/21	27
1862.4	23/20/18/16	28/25	-
2476.8	26/23/21	-	-
3091.2	26	-	-

3. SIMULATION MODEL

In this paper the 1xEV-DV F-PDCH data traffic channel performance is analyzed by simulation using Matlab tool.

The forward link model for simulation is one buffer that represents the buffer where the data packets arrive to the radio base station from core network, and are stored before the transmission in the aerial interface through the data traffic channel F-PDCH. This study is limited to the analysis of the forward link packet transmission, i.e., the situation in which the base station transmits the packets to the mobiles, considering different levels of system load.

Considering that the 1xEV-DV system allows the code division multiplexing (CDM) between two mobiles besides the time division multiplexing (TDM) among different mobile stations, the simulations are done for the case where both techniques are implemented and cases where only the time division multiplexing is available.

The 1xEV-DV standard defines eighteen different data rates (Tab. 2.1). This study considers only nine most representatives data rates. Tab. 3.1 shows the selected nine data rates and adopted probability distribution.

TABLE 3.1
PROBABILITY DISTRIBUTION PER DATA RATE.

Data rate (kbps)	Probability
3091.2	4.0%
2476.8	10.0%
1862.4	15.0%
1238.4	17.0%
931.2	22.9%
624	18.0%
312	8.0%
158.4	3.0%
81.6	2.0%

Some simulations are performed considering different priority levels among users. Tab. 3.2 shows the probability distribution considered, where P1 is the higher priority level, P2 the intermediate priority level and P3 the lower priority level.

For the simulation considering both CDM/TDM techniques, the selected number of required Walsh codes for each data rate is the best case among the options defined in the 1xEV-DV standard, i.e., the smaller number of required Walsh codes for each data rate.

TABLE 3.2
PROBABILITY DISTRIBUTION FOR DIFFERENT USER PRIORITY LEVELS.

Priority level	Probability
P1	15%
P2	35%
P3	50%

Tab. 3.3 shows the modulation, the number of timeslots and the number of Walsh codes for each data rate considered in this study.

TABLE 3.3
NUMBER OF SLOTS AND WALSH CODES PER DATA RATE.

Subpacket data rate (kbps)	Packet size (bits)	Modulation	Number of slots per subpacket	Number of Walsh codes
81.6	408	QPSK	4	2
158.4	792	QPSK	4	3
312	1560	QPSK	4	6
624	1560	8-PSK	2	9
931.2	2328	8-PSK	2	13
1238.4	3096	8-PSK	2	17
1862.4	2328	16-QAM	1	16
2476.8	3096	16-QAM	1	21
3091.2	3864	16-QAM	1	26

For the simulation considering both techniques, it is assumed the availability of 28 Walsh codes for the data traffic channel F-PDCH, which means a 1xEV-DV data-only system without CDMA2000 1X (FCH and SCH) and with dynamic allocation.

For simulation with priority, it is considered that the radio base station transmits the data packets through a server based on priority without preemption. The higher priority packets are transmitted first and when there are no more packets of the highest priority, the packets of second priority start to be transmitted and so on. The buffer size is considered to be infinite and the packets are stored in the buffer first by priority and then by arrive sequence.

It is assumed that the packets arrive according to negative exponential distribution and λ (packet arrival rate) is calculated following the probability distributions showed in Tabs. 3.1 and 3.2. The serving time per packet ($1/\mu$) is equivalent to the number of timeslots needed for transmission. Each timeslot has 1.25 ms length.

The system load ρ is defined through the relationship between the arrival rate and the packet serving time, thus, to vary the traffic load at the base station the arrival rate λ is calculated for each case, since the serving time $1/\mu$ is constant, depending on the transmission data rate only.

So, varying the 1xEV-DV system total traffic load ρ_{total}, the packet arrival rates $\lambda(i,n)$ can be calculated considering the probability distribution of each data rate (Tab. 3.1), and the probabilities of Tab. 3.2, in the cases with user priority. Thus:

$$\rho_{total} = \sum \rho(i,n) \tag{3.1}$$

$$\rho(i,n) = \frac{\lambda(i,n)}{\mu(i,n)} \tag{3.2}$$

$$Pb(i,n) = \frac{\lambda(i,n)}{\sum \lambda(i,n)} \tag{3.3}$$

Where:

$\lambda(i,n)$ = packet arrival rate for data rate *i,* and priority level *n* (for user priority cases);

$\mu(i,n)$ = packet serving rate for data rate *i,* and priority level *n* (for user priority cases);

$\rho(i,n)$ = traffic load for data rate *i* ($\lambda(i,n)/\mu(i,n)$), and priority level *n* (for user priority cases), and

$Pb(i,n)$ = probability for data rate *i,* and priority level *n* (for user priority cases).

The performance analysis parameters studied are: average packet delay, data throughput and link utilization in function of the traffic load.

Considering the data rate probability distribution in Tab. 3.1 and the user priority distribution in Tab. 3.2, the following data traffic analysis cases are considered:

1. Nine transmission data rates without priority in FIFO (first in first out) scheme.
2. Nine transmission data rates with priority from the higher data rate to the lower data rate.
3. Case 2 considering code division multiplexing.
4. Three priority user levels, each one with nine transmission data rates available, and priority for the higher data rate to the lower data rate in each priority user level.
5. Case 4 considering code division multiplexing.

All cases considered traffic load from 10% to 90%.

Analytical models based on queuing theory are used to compare the results for cases 1, 2 and 4. In the case 1 the queuing model without priority is considered and for the cases 2 and 4 the non-preemptive priority queuing model is used.

Let be:

$E\{T_0\}$ the average time to complete the current packet transmission when a packet arrives and

$E\{W\}$ the average packet delay in the queue.

For Case 1, the analytical model is given by:

$$E\{W\} = \frac{E\{T_0\}}{(1-\rho_{total})} \tag{3.4}$$

Where:

$$E\{T_0\} = \frac{1}{2}\frac{\sum \lambda(i)}{\sum \mu^2(i)}$$

The analytical model for Cases 2 and 4 is given by:

$$E\{W_1\} = \frac{E\{T_0\}}{(1-\rho_1)} \text{ (First priority)}$$

$$E\{W_k\} = \frac{E\{T_0\}}{(1-\sigma_{k-1})(1-\sigma_k)} \tag{3.5}$$

$$E\{W_r\} = \frac{E\{T_0\}}{(1-\sigma_{r-1})(1-\rho_{total})} \text{ (Last priority)}$$

Where:

$$\sigma_k = \sum_{j=1}^{j=k} \rho_j$$

In this case, $E\{W_n\}$ is calculated for each priority level and the average $E\{W_{nT}\}$ is:

$$E\{W_{nT}\} = \sum Pb(n)E\{W_n\} \tag{3.6}$$

The average throughput in both cases is calculated considering the traffic load (ρ) and the packet data rates (i):

$$\text{Throughput} = \sum i\rho(i,n) \tag{3.7}$$

4. Results Analysis

The 1xEV-DV forward link simulation with nine data rates and without priority (case 1) presents average packet delay of 0.1628 ms to 13.1144 ms depending on the traffic load. The average standard deviation is 1.5%, and the 95% confidence interval is 0.17% of the average value.

The simulation of nine data rates considering priority from the higher to the lower data rate (case 2) presents better average packet delay results, comparing to the previous simulation. This result shows that for the same traffic load, the packet delay performance is enhanced with a scheduling scheme that prioritizes the higher data rates. The average standard deviation is 1.6%, and the 95% confidence interval is 0.17% of the average value, as in the case 1.

To validate these simulations the results are compared to the analytical models using Eqs. 3.4 and 3.5. The comparison presented very close results in both cases. In case 1 the average standard deviation is 0.69% for the packet delay and 0.13% for the data throughput. In case 2 the average standard deviation is 0.54% for the packet delay and 0.12% for the data throughput.

With the same traffic distribution, nine data rates with priority for higher data rates and code division multiplexing (case 3), the packet data delay results are improved. The difference among the packet data delays becomes more evident for higher traffic load. In case 3 the average standard deviation is 0.6% and the 95% confidence interval is 0.08% of the average value. Fig. 4.1 shows the simulation results for these three cases.

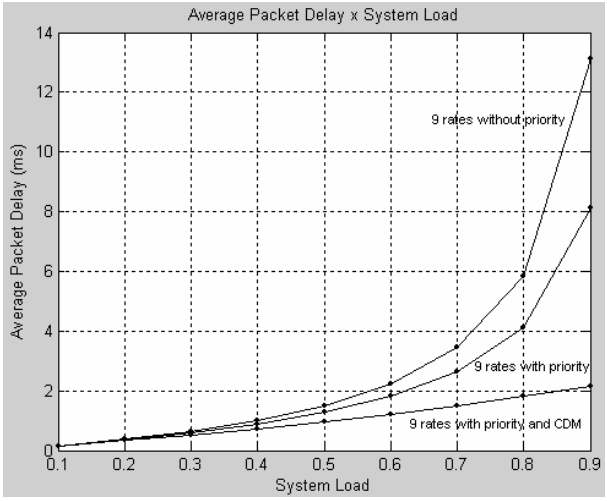

Figure 4.1 – Average packet delay in function of traffic load for cases 1, 2 and 3.

As it is shown in Fig. 4.1, for high data traffic load the code division multiplexing (CDM) implementation besides the TDM is very desirable. For a traffic load of 70%, the average delay for CDM is reduced in 43.5% compared to the case 1.

The average throughputs in function of the traffic load for the above three cases are presented in Fig. 4.2.

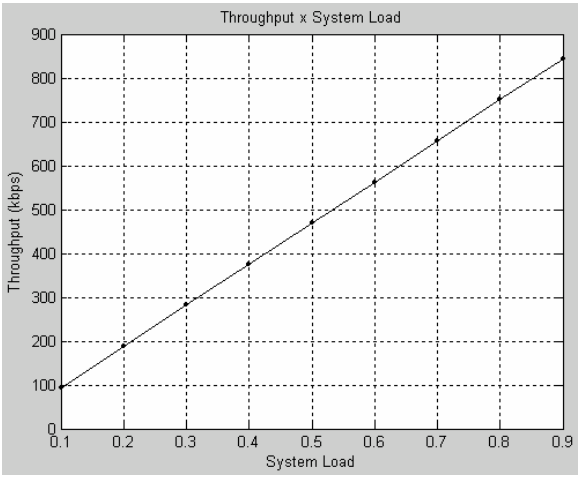

Figure 4.2 – Average throughput in function of traffic load.

When analyzed in function of the traffic load, these values are very close for the three cases as showed in Fig. 4.2, however when analyzed in function of the link utilization, it is possible to notice (Fig. 4.3) that for the same link utilization, the throughput is increased with the CDM technique, and this difference is greater as the traffic load increases.

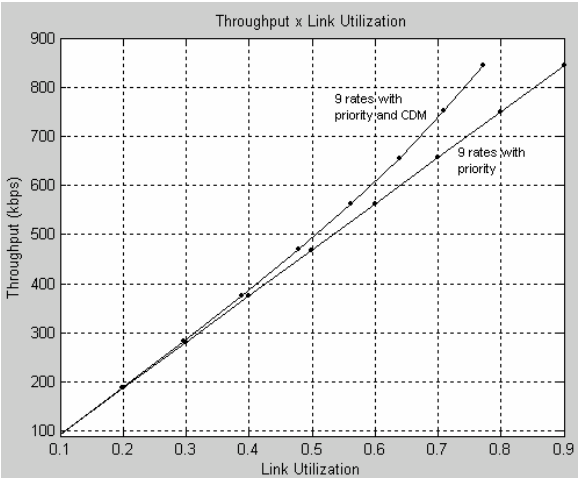

Figure 4.3 – Data throughput in function of link utilization for cases 2 and 3.

The relationship between the link utilization and traffic load is linear when CDM is not applied, however, with CDM the link utilization is lower for the same traffic load. For example, for the traffic load of 70%, without CDM the link utilization is 70%, but with CDM the link utilization is 63%.

For the simulation with nine data transmission rates, priority for higher data rates, and three different user priorities (case 4) the results presented the average packet delay for users P1 (highest priority) lower than the obtained in case 2. The average delay for users P2 is also lower than the delay obtained in case 2, however the users P3 (lowest priority) present average packet delay much higher than case 2. In case 4, in average, the simulation presents 0.66% standard deviation and the 95% confidence interval is 0.03% of the average value.

The result comparison of the simulation and the analytical model using Eq. 3.5 for this case is very close presenting the average standard deviation of only 0.04% for P1 users, 0.04% for P2 users, 0.35% for P3 users and 0.05% for the throughput.

The Fig. 4.4 shows the results obtained in case 4.

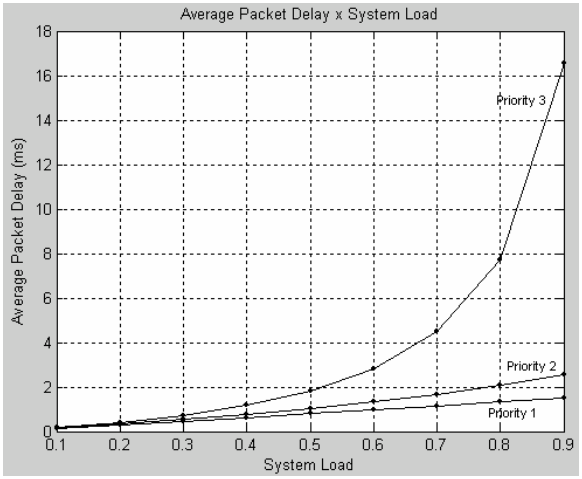

Figure 4.4 – Average packet delay in function of traffic load for case 4.

The case 5 represents the same situation of case 4 adding the code division multiplexing technique. In this case the results obtained by simulation have the average standard deviation of 0.63% and the 95% confidence interval of 0.04% of the average value. The average packet delay is much lower than case 4, presenting more significant gain for P3 users (lower priority). For these users, with 70% of traffic load, the reduction of average packet delay is 34.3%. For the same traffic load, P2 users have a reduction of 14.7%, and P1 users have a reduction of 8.2%.

Fig. 4.5 presents the results obtained in case 5.

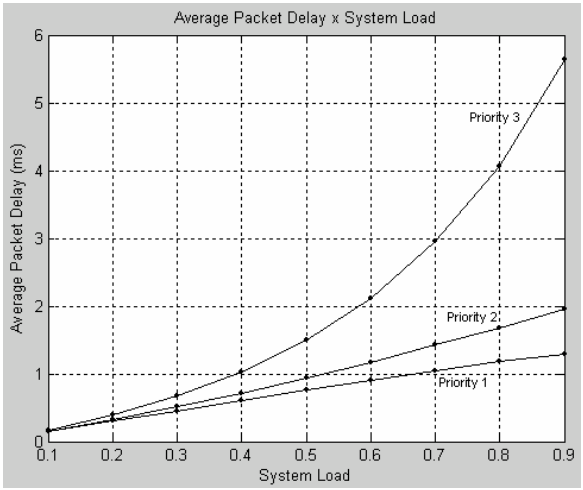

Figure 4.5 – Average packet delay in function of traffic load for case 5.

The average throughputs in function of the traffic load of 1xEV-DV system for cases 4 and 5 are the same of cases 1, 2 and 3 presented in Fig. 4.2, since

the probability distribution among data rates is the same.

Therefore, as in the first three cases, these values are very close for cases 4 and 5 when analyzed in function of the traffic load, however when analyzed in function of the link utilization, it can be noticed that for the same link utilization, the throughput is higher for the system with CDM, and the difference is greater as traffic load increases. For instance, for 70% of traffic load without CDM, the link utilization is 70%, but with CDM, the link utilization is 66.3%.

In Fig 4.6 the system throughput in function of the link utilization for cases 4 and 5 is shown.

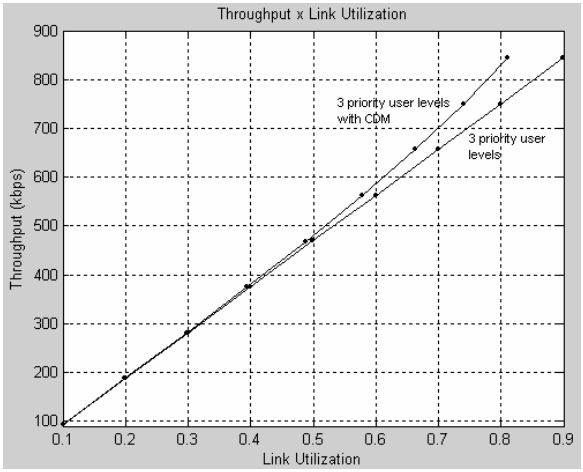

Figure 4.6 – Throughput in function of link utilization for cases 4 and 5.

5. CONCLUSIONS

The 1xEV-DV system forward link performance was analyzed through simulation in this paper. The system performance related to average packet delay and throughput were studied in function of the system traffic load.

It was possible to analyze the 1xEV-DV forward link data traffic channel behavior in situations with data rate priority, and also user priority. It was possible to verify the efficiency of the code division multiplexing (CDM) implementation, beside the time division multiplexing (TDM) in the forward link. With the CDM technique utilization, it is possible to minimize the average packet delay and in situations with user priority, the delay reduction is more expressive for users with lower priorities. Furthermore, as higher is the traffic load, higher will be the gain with the CDM implementation.

It was also possible to analyze the throughput performance in function of the link utilization, verifying that CDM implementation allows higher data throughput.

6. REFERENCES

[1] 3GPP2 C.S0002-C, Physical Layer Standard for cdma2000 Spread Spectrum Systems Release C, version 1.0, May 2002.

[2] Motorola Inc., Technical Overview of 1xEV-DV, version G1.4, 2002.

[3] L.Hsu, M. W. Cheng, I. Niva, Evolution Towards Simultaneous High-Speed Packet Data and Voice Services: An Overview of cdma2000 1xEV-DV, IEEE 10th International Conference on Telecommunications (ICT 2003), pg. 1313-1317, vol. 2, 23 Feb.-1 March 2003.

[4] A. Soong, S. Oh, A. Damnjanovic, Y. Yoon, Forward High-Speed Wireless Packet Data Service in IS-2000 – 1xEV-DV, IEEE Communications Magazine, vol. 41, issue 8, pg. 170–177, August 2003.

[5] R. T. Derryberry, Lin Ma, Z. Rong, Performance of the cdma2000 1xEV-DV System, IEEE Vehicular Technology Conference, 2003 (VTC 2003-Spring), vol. 2, pg. 1163-1167, 22-25 April 2003.

[6] S. Agrawal, I. Acharya, S. Goel, Inside 3G Wireless Systems: The 1xEV-DV

[7] 3GPP2 C.S0002-D, Physical Layer Standard for cdma2000 Spread Spectrum Systems Release D, version 1.0, February 2004.

[8] Z.Pi, R. T. Derryberry, CDMA2000 1xEV-DV Reverse Link System Design, IEEE Wireless Communications and Networking Conference 2003 (WCNC 2003), vol. 1, pg. 514-519, 16-20 March 2003.

[9] Y Chung, C. Koo, B. Bae, H. Lee, D. CHo, An Efficient Reverse Link Data Rate Control Scheme for 1xEV-DV, IEEE Vehicular Technology Conference, 2001 (VCT 2001 - Fall), vol. 2, pg. 802-823, 7-11 October 2001.

[10] 3GPP2 C.S0002-A, Physical Layer Standard for cdma2000 Spread Spectrum Systems Release A, version 6.0, Feb 2002.

A Distributed Architecture for Presence Service in UMTS IP Multimedia Subsystem

Igor Miladinovic
Telecommunication Research Center Vienna (ftw.)
Donau-City-Strasse 1, 1220 Vienna, Austria
tel. +43-1-505283054
e-mail: miladinovic@ftw.at

***Abstract*— Presence Service has gained on importance in the last several years. Basically, Presence Service distributes information about a user's willingness and ability to communicate. The Universal Mobile Telecommunication System (UMTS) will also offers this service to its subscribers. It is based on a dedicated component, the Presence Server, which is responsible for distribution of presence information. However, UMTS presence service is aimed to support not only the presence information of subscribers, but also of services. Given that some services are expected to have a large number of subscribers interested in their presence, the current centralized UMTS architecture will have scalability problems. This paper propose an architecture in which the presence information is distributed on several servers whenever the number of subscribers interested in this presence information is large. In this way, the Presence Server is able to support a large number of subscribers. The paper also includes an analytical performance estimation of the proposed architecture and compare it with the current UMTS architecture.**

***Index Terms*— IMS, SIP, Presence Service, Event Notification, UMTS.**

I. INTRODUCTION

Presence Service is already a widely spread service in the Internet today. It makes possible that a user publish presence information to other users. In this way, a user can inform other users about this user's willingness and ability to communicate. Using the Presence Service, for example, a multiparty conference can be started when all the potential participants are available. Furthermore, depending on the availability of a user, this user can be contacted over a normal call, video call, instant messaging or voice box.

After its success in the Internet, Presence Service will also be offered in the Universal Mobile Telecommunication System (UMTS) [1][2]. UMTS is a third generation mobile network that is expected to become the most popular third generation network, similarly to the Global System for Mobile communications (GSM) for the second generation networks. It has been specified by the 3^{rd} Generation Partnership Project (3GPP) and the current version is referred to as Release 6. It defines Presence Service as a service of Internet Protocol (IP) Multimedia Subsystem (IMS) [3][4]. IMS is a UMTS domain responsible for for traditional telephony services and for new multimedia services.

As the signaling protocol in IMS, 3GPP has chosen the Session Initiation Protocol (SIP) [5][6]. In its basic specification, SIP does not support Presence Service. To support it, an extension to SIP has been defined, referred to as the SIP event notification framework [7]. Together with the SIP presence event package [8], this framework provides SIP with support of Presence Service. This is also used for the Presence Service in IMS providing not only presence information of subscribers, but also of a service. For example, IMS Presence Service is able to provide presence information of a football game [9]. Subscribers interested in this presence information will get notified about the start and the end time of the game, as well as about score changes during the game. Presence information of such services are of common interest and the number of subscribers for their presence can be large.

The current IMS Presence Service architecture has a centralized character, since there is a single Presence Server on which the presence information is kept up-to-date. This Presence Server has to notify all the subscribers whenever an event occurs. This works well when the number of subscribers is relatively small, like in the case of presence information of a user. However, when the number of the subscribers is getting large, the Presence Server will not be able to handle all the notifications.

To improve scalability of the Presence Service in IMS, this paper proposes a distributed IMS Presence Service architecture. The presence information is placed on several servers, each of which is responsible for a certain group of subscribers. The presence information is kept up-to-date on each server using the SIP event notification framework between these servers and the Presence Server. In this architecture, the Presence Server can be dimensioned to support notifications to all other servers, because the number of other servers is predictable. The distributed architecture can hence support Presence Service for a large number of subscribers.

This paper is organized as follows. The next section gives an overview of the IMS, including an introduction to SIP and description of some IMS entities. Section III discussed the Presence Service in the IMS, and the current Presence Service architecture is described in Section IV. The proposed distributed architecture is presented in Section V. Section VI focuses on the performance estimation of the proposed architecture, comparing it with the current architecture. The most important findings of this work are emphasized in Section VII.

II. IP Multimedia Subsystem

The IP Multimedia Subsystem (IMS) has been introduced in the UMTS architecture by Release 5. Before introduction of IMS, UMTS architecture was composed of the following domains [10]: UMTS Terrestrial Radio Access Network (UTRAN), Circuit-Switched Core Network (CS-CN), and Packet-Switched Core Network (PS-CN). IMS has been introduced as an additional domain that is responsible for traditionally telephony services and for new multimedia services [11]. However, the idea of IMS is to take over the signaling tasks from the CS-CN reducing the need for the CS-CN until it totaly disappears from the UMTS architecture. In that case, we are speaking about an all-IP UMTS network [12] that is expected to bring advantages because the maintenance of two different networks (packet-switched and circuit-switched) is omitted. The IMS is an important step in this direction.

As mentioned in the introduction, the signaling protocol in IMS is SIP [5][6]. It is an application layer signaling protocol for IP networks. Originally, SIP was developed by the Multiparty Multimedia Session Control (MMUSIC) working group of the Internet Engineering Task Force (IETF). Today, there is a SIP working group that continues development of this protocol. In order to better understand IMS functionality, this section first gives an overview of SIP.

A. Session Initiation Protocol

SIP is a peer-to-peer, text based protocol with two types of messages, requests and responses. A request determinate the action that is to be executed, and a response informs about results of this action. For example, the REGISTER request is used for the registration of a user, and if the corresponding response is a 200 (OK), the registration was successful. The only special case is the INVITE request, used to initiate a session, since a 200 (OK) response has to be confirmed with an ACK (acknowledgment) request in order to successfully initiate a session. Therefore, SIP uses a three way handshake (INVITE, OK, ACK) for session initialization. After a successful initialization, media data are exchanged between users using the Real-Time Transmission Protocol (RTP) [13]. An active session can be terminated by sending a BYE request that has to be replied with a 200 (OK).

Messages in SIP are composed of a header and a body. The header comprises several header fields, some of which are mandatory and some optional. They contain information for routing of the messages or additional session information. The body of a SIP message is optional and it can contain any MIME [14] type content. During the initialization of a session, the body is usually used to specify media parameters of the session. They are given in the Session Description Protocol (SDP) [15] format.

Basically, there are two types of entities in SIP, User Agents (UAs) and network servers. UAs are users' terminals and they represent endpoints for a SIP communication. Network servers are responsible for registration of users and for routing of SIP messages. There are three types of network servers: proxy servers, redirect servers, and registrar servers. A proxy server is an application layer router for SIP messages. It routes both types of messages in SIP, requests and responses. Additionally, it can be enabled to apply some services, or to communicate with a service platform. A redirect server also routes SIP messages, but instead of forwarding them, it simply replies an incoming request with a redirect response. This response contains information about the next hop server towards the request's destination, so that the request can be sent there. Registrar servers are responsible for collecting users' registration information and storing them in a database, called location service. In order to be accessible, each user has to registrar at the corresponding registrar server. The registration process provides the location service with the information about user's current location. In this way, a user can be contacted using a single SIP address, called SIP Uniform Resource Identifier (URI), independently of the device that this user is currently using.

B. IMS Entities and Basic Functionality

As mentioned before, IMS uses SIP for as the signaling protocol. The functionality of a SIP UA is placed in users' terminals that are called User Equipments (UEs). The most of IMS network entities act as different SIP entities. They are called Call State Control Functions (CSCFs), and they are responsible for session and mobility management. CSCFs can act as different types of SIP network servers, or even as UAs when a session should be initiated or terminated by the network. In an IMS network there are three types of CSCFs:

- Proxy-CSCF (P-CSCF) – It is the first contact point within an IMS network for a UE. From the SIP point of view, it acts as a proxy server between a UE and the next hop CSCF.
- Interrogating-CSCF (I-CSCF) – It is the contact point within an operator's network for connection addressed to users located in this operator's service area. It can also be used to hide network configuration, capacity, and topology from the outside. Similarly to P-CSCF, I-CSCF also acts as a proxy server.
- Serving-CSCF (S-CSCF) – It accomplishes the session control functions for users. It can acts as a proxy server, as a registrar server, or as a UA. Acting as a proxy server, the S-CSCF routes SIP messages and optionally communicates with an Application Server (AS) to provide value added services, operator specific services or both [16]. In the role of a register server, the S-CSCF accepts registration requests from UEs. Finally, the S-CSCF can initiate or terminate a session and act as a UA. This is necessary to implement some services or to terminate a session when some event occurs (for example, no credits left on a user's pre paid account).

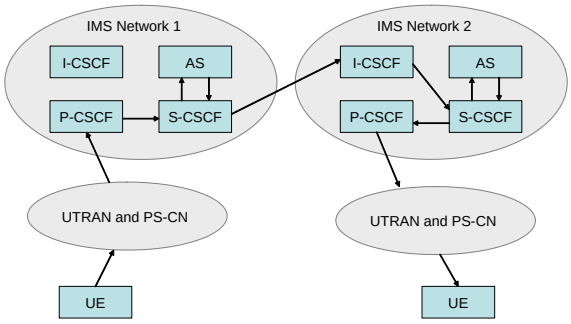

Fig. 1. Session Initialization in IMS

The initialization of a session between two users that are in the service areas of two different operators is shown in Figure 1. The figure shows the flow of the INVITE request, the corresponding response and the ACK request are not shown. Furthermore, UTRAN and PS-CN are depicted as a single network, although they are two different UMTS domains. This is because of clarity, since for this scenario these details are not as relevant. IMS network 1 is called originating network (since the call originates from this network), and IMS network 2 is called terminating network.

The originating UE sends an INVITE request over the UTRAN and PS-CN to the corresponding P-CSCF. The P-CSCF forwards this request to the S-CSCF that can interact with an AS. The AS is responsible for applying some services for the originating user on this call. Because of the destination address, S-CSCF can recognize that this request is to be routed in another network and forwards it to the I-CSCF of this network. The I-CSCF makes a lookup in the Home Subscriber Server (HSS) in order to find the responsible S-CSCF for this terminating user (this is not shown in Figure 1). After finding the address of the S-CSCF, the I-CSCF forwards the request there. The S-CSCF is now able to interact with the terminating AS that can apply some services on this call. Finally, the S-CSCF forwards the request to the terminating UE over the corresponding P-CSCF.

The terminating UE alerts the users about incoming call, or more general session. If the user accepts this call, UE replies with a 200 OK response. A response always takes the same route as the corresponding request but in the reverse order. After receiving the response, originating UE confirms the session initialization with an ACK request and completes the initialization.

III. Presence Service in IMS

The current specification of UMTS, referred to as Release 6, has introduced some new services to IMS. One of such services is the Presence Service [4]. It gives to subscribers the possibility to monitor the presence information of another subscriber or of a service. The technical realization of this service relies on the SIP event notification framework [7]. This framework provides SIP with the feature of distributing asynchronous events on subscriber's demand. It defines two new methods: SUBSCRIBE and NOTIFY. First, a subscriber has to subscribe for one or more events using the SUBSCRIBE method. After a successfully subscription, this subscriber gets notified with the NOTIFY method whenever the state of these events changes. The event notification framework is very flexible, since it does not define any specific events. Events have to be specified independently of this framework in so-called *event packages*. An example is the presence event package [8] that defines subscriptions and notifications of presence. It defines presence as the willingness and ability of a user to communicate with other users on the network. However, the Presence Service in IMS is not limited to presence information of subscribers, so that the presence information can also be related to a service. For example, with the Presence Service in IMS a subscriber can subscribe for information about a football game [9].

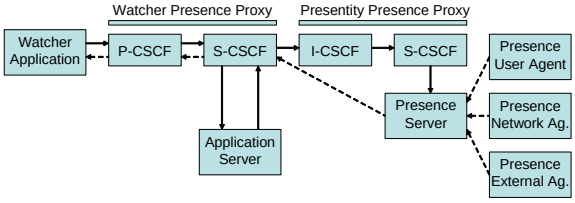

Fig. 2. IMS Presence Service architecture

Figure 2 shows the conventional IMS architecture for Presence Service. Solid arrows indicate subscriptions and dashed ones notifications. For the sake of clarity, only subscription and notification requests are shown in the figure – in fact, each request is followed by a response that provides information about request processing. Figure 2 shows that notifications do not need to traverse the Presentity Presence Proxy. However, it can require to be on path of all the notifications.

The subscriber interested in other subscriber's presence information is called *Watcher*, whereas the subscriber that publish presence information is called *Presentity*. As mentioned before, the Presentity does not necessarily need to be a subscriber – it can also be a service.. The Watcher Application, that is normally running on the Watcher's terminal, subscribes on the Presentity's presence information by sending a subscription request. This request is routed through the Watcher Presence Proxy that is composed of a P-CSCF and a S-CSCF. Before forwarding the request, S-CSCF interacts with an Application Server (AS). One of the purposes of this AS is to store *Presence Lists* for a subscriber in order to provide subscription on multiple Presentities using a single request.

After interaction with the AS, the S-CSCF forwards the subscription request to the Presentity Presence Proxy. It is composed of an I-CSCF and a S-CSCF. Finally, this S-CSCF delivers the subscription to the Presence Server. We can notice that the message flow for a subscription is very similar to the flow of an INVITE request for the session initialization (Figure 1).

Now, the Presence Server can accept or refuse this subscription. In the first case, it replies the subscrip-

tion request with a 200 (OK) response and notifies the watcher about the current state of the presentity. During the subscription time (each subscription is time limited), the Watcher will be notified immediately after any change of the Presentity's state.

The Presence Server can obtain the current state of the Presentity from several sources, including Presence User Agent, Presence Network Agent, and Presence External Agent (see Figure 2). For that purpose, several protocols and mechanisms are used and SIP is only one of them.

IV. Conventional Presence Service Architecture

The architecture shown in Figure 2 is based on the presence information placed on a central entity – the Presence Server. It is suitable for Presentities with a small number of Watchers. For Presentities with a large number of Watchers, such as football games or weather forecast, the Presence Server can easily get overloaded, since all the Watchers have to be notified whenever the state of the Presentity changes. Let us consider an example with n Watchers interested in a football game. The Presence Server has to send out n notification messages whenever the score changes. Furthermore, each of these messages is followed by a response that the Presence Server has to handle. This results in $2n$ SIP messages at the Presence Server within a short time interval.

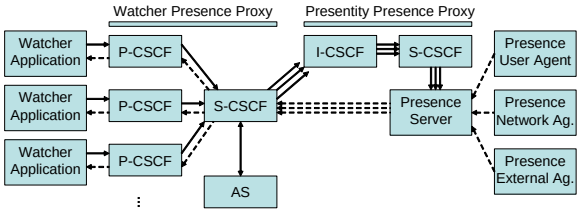

Fig. 3. Conventional IMS architecture for Presence Service

Figure 3 depicts a scenario with several Watchers. Again, subscriptions are indicated by solid arrows, whereas notifications with dashed ones. The figure shows three Watchers using the same S-CSCF in the Watcher Presence Proxy. In general, there can be a large number of Watchers that use different S-CSCFs in the Watcher Presence Proxy. Therefore, subscription requests traverse different Watcher Presence Proxies, but they all arrive at the same Presentity Presence Proxy and the Presence Server. We can notice a waste of network resources caused by multiple sending of subscriptions between S-CSCF of the Watcher Presence Proxy and the Presence Server. However this is not really critical, since subscriptions are sent asynchronously and not all at the same time. The situation is different with notifications. After any change of Presentity's state, the Presence Server has to sent notifications to all the Watchers. In Figure 3 notifications are denoted with dashed arrows between Presence Server and Watcher Applications. Similarly as in scenario from Section III, notifications do not traverse the Presentity Presence Proxy. Each notification is followed by a 200 (OK) response from the Watcher Application to the Presence Server (not shown in the figure). When the number of Watchers is large enough, the Presence Server will not be able to notify all the Watcher. Therefore, this architecture does not scale well.

V. Distributed Presence Service Architecture

The main idea of the distributed architecture is to offload the Presence Server by storing presence information at ASs of the Watcher Presence Proxies. The proposed architecture does not require any change in the IMS infrastructure, but only an extended functionality of ASs. They must be capable of storing presence information of Presentities of general interests.

There is still the question when an AS should store presence information of a Presentity. The answer is straightforward – only when this Presentity is of general interest and the number of Watchers is expected to be large. This information is placed at the Presence Server and not at the AS. Therefore, the AS will forward the first subscription for an event to the Presence Server as usual. In the case of a Presentity of general interests, the Presence Server will indicate it in the response to this subscription. This information can be placed in a new header field of the response. Thereafter, the AS will store presence information related to this Presentity. If an AS does not support this distributed architecture, it will ignore this header field and the Presence Service will work in conventional way (Figure 3).

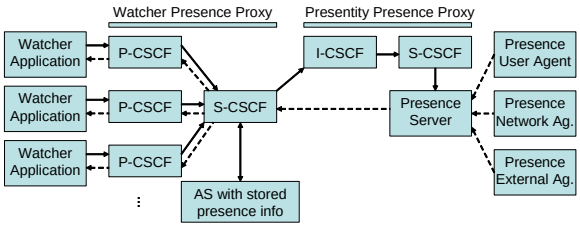

Fig. 4. Distributed IMS architecture for Presence Service

Figure 4 shows the proposed architecture. Similarly to Figure 3, this figure shows only one Watchers' S-CSCF and one AS. Normally, there would be several Watchers' S-CSCFs and ASs, each of which responsible for one or more Watchers. The AS forwards only the subscription of the first Watcher to the Presence Server. In the response to this subscription, the Presence Server indicates that the presence information should be stored at the AS. Because of this subscription, the AS will be notified after any change of the Presentity's state, so that the presence information stored at the AS will be up-to-date during all the time the subscription is valid. The AS is responsible for periodically sending of re-submissions to the Presence Server in order to stay subscribed as specified by the SIP event notification framework [7].

Because of the stored presence information, the AS need not to forward subscriptions of any further

Watcher Application to the Presence Server. These subscriptions are marked by single solid arrows between the Watchers' S-CSCF and the Presence Server in Figure 4. In contrast to Figure 3, these subscriptions are not forwarded to the Presence Server. This optimizes use of the network resources during subscriptions. But significantly more important is the situation after a Presentity's state change. In that case, the Presence Server needs to send only a single notification to each AS. As mentioned before, there is only one AS in Figure 4, and the notification is indicated by a single dashed arrow between the Presence Server and the Watchers' S-CSCF. Compared with the conventional IMS presence architecture (Figure 3), this architecture scales significantly better, since the Presence Server cannot be overloaded even if there is a large number of Watchers. This is because the number of ASs is predictable and considerably less than the number of subscribers (each of which is a potential Watcher).

The proposed architecture not only offloads the Presence Server, but also reduces the signaling traffic between ASs and the Presence Server. We can notice from Figures 3 and 4 that the number of both, subscriptions and notifications between the AS and Presence Server is reduced in the proposed architecture. The traffic reduction in IMS is important because this traffic interferes with the session signaling traffic [17].

Although the distributed architecture has significant advantages when the number of Watchers is large, the conventional architecture still has benefits when the number of Watchers is small. The AS does not need to keep any additional state, all the application logic is placed in the Presence Server. Therefore, the Presence Server has to make decision to use the distributed architecture or not. With the described mechanism, benefits of both architecture can be used. The Presence Server can require the use of the distributed architecture whenever the expected number of Watchers is large. However, if the Presence Server does not require it, the conventional architecture is used.

VI. Performance Estimation

This section considers analytically the performance of the distributed architecture. In general, there are two metrics that could be of interests: the number of messages at the Presence Server, and the number of messages between the Presence Server and ASs. The second metrics is not really expected to be critical, since all these messages are transmitted in the core network. From our experience with the IP networks came out that the equipment for the core network is relatively cheap, so that links are usually overprovisioned. The first metric, in contrast, can easily become critical, since a single component, the Presence Server, must be able to handle a large number of messages at the same time. This is especially critical in the case of notifications.

Consider we a general scenario of distribution of notifications. Some of the ASs in this scenario are able to store presence information, and some are not. Figure 5 shows this scenario. As we can see, there is a difference between ASs that are able to store presence information and conventional ASs. Watchers behind an conventional AS are notified by the Presence Server directly (lower part of the figure), and other Watchers are notified by their AS (upper part of the figure). In the ideal case, all ASs are able to store presence information, and this results in a fully distributed architecture (Figure 4). However, in this section we will consider a general scenario with some ASs that do not support the distributed architecture.

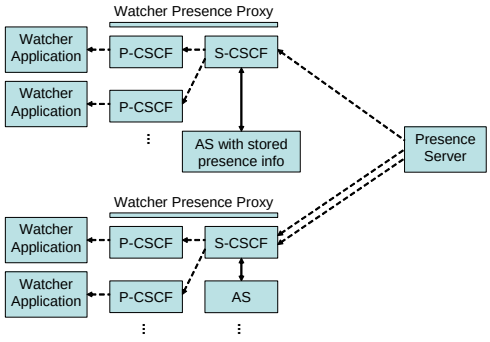

Fig. 5. Distribution of notification in a general scenario

Let us denote the number of Watchers with n, and the number of ASs that are able to store presence information with m. The number of Watchers that are placed behind these ASs is n_1, and the number of Watchers placed behind ASs that are not able to store presence information with n_2. It is clear that

$$n = n_1 + n_2. \tag{1}$$

In the case that $n_1 = 0$, we have a conventional presence architecture (Figure 3), and in the case that $n_2 = 0$, we have a fully distributed architecture (Figure 4).

Let us furthermore denote the number of messages at the Presence Server with N_{conv}, for the convectional architecture, and with N_{dist} for the distributed architecture. After a change of the state of the Presentity, the number of messages (notification requests and the corresponding responses) at the Presence Server amounts

$$N_{conv} = 2n, \tag{2}$$

or

$$N_{dist} = 2(m + n_2). \tag{3}$$

Note that $n_1 \geq m$ is always valid, and for Presentity with a large number of Watchers even $n_1 \gg m$. This is because the number of ASs is considerably less that the number of Watchers. Using this and comparing Equations 2 and 3, we can conclude that $N_{conv} \geq N_{dist}$ is always true, and even $N_{conv} \gg N_{dist}$ when the number of Watchers is large.

If we further suppose a fully distributed architecture ($n_2 = 0$), the number of messages at the Presence Server during a notification become

$$N_{dist} = 2m. \quad (4)$$

In the case of a fully distributed architecture, it is possible to optimal dimension the Presence Server. The number of ASs (m) is predictable and not really large, in contrast to the number of Watchers (n). If an Presence Server is dimensioned to cope with the number of messages given in Equation 4, it will be able to support Presence Service for any Presentity independently on the number of Watchers.

VII. Conclusion

The Presence Service is expected to become an important service in the UMTS. The standardization activities of UMTS include the specification of an Presence Service architecture. This architecture, however, is centralized, given that the presence information is stored on a single Presence Server. When the number of Watchers for a Presentity is large, the Presence Server can easily get overloaded.

This paper presented a distributed architecture for the Presence Service in IMS. In this architecture, the presence information is stored on several ASs, each of which is responsible for a group of Watchers. After a change of the Presentity's state, the Presence Server notifies only these ASs. Therefore, the number of notifications does not depend directly on the number of Watchers. This ensures that the distributed architecture can support Presentities with a large number of Watchers. The paper gave also an analytical performance estimation that had shown the benefits of the proposed architecture.

The future work will concentrate on a simulative investigation of performances in order to find the best way for dimensioning of ASs and the Presence Server. We also plan to make a prototype implementation of the distributed architecture.

References

[1] Thorsten Benkner and Christoph Stepping. *UMTS. Universal Mobile Telecommunications System*. J. Schlembach Fachverlag, 2002.

[2] 3GPP TSG SSA. Network architecture. TS 23.002 v6.5.0, 3rd Generation Partnership Project, 2004.

[3] 3GPP TSG SSA. IP Multimedia Subsystem (IMS) - Stage 2 (Release 6). TS 23.228 v 6.6.0, 3rd Generation Partnership Project, 2004.

[4] 3GPP TSG SSA. Presence Service; Architecture and Functional Description (Release 6). TS 23.141 v 6.6.0, 3rd Generation Partnership Project, 2004.

[5] Jonathan Rosenberg, Henning Schulzrinne, Gonzalo Camarillo, Alan Johnston, Jon Peterson, Robert Sparks, Mark Handley, and Eve Schooler. SIP: Session Initiation Protocol. RFC 3261, Internet Engineering Task Force, June 2002.

[6] Henning Schulzrinne and Jonathan Rosenberg. The Session Initiation Protocol: Internet-Centric Signaling. *IEEE Communications Magazine*, 38(10):134–141, 2000.

[7] Adam Roach. Session Initiation Protocol (SIP)-Specific Event Notification. RFC 3265, Internet Engineering Task Force, June 2002.

[8] Jonathan Rosenberg. A Presence Event Package for the Session Initiation Protocol (SIP). Internet draft, work in progress, Internet Engineering Task Force, January 2003.

[9] C. Faure. Presence Service in 3G Networks. In *IEE Conference on 3G Mobile Communication Technologies*, May 2002.

[10] Alexander Joseph Huber and Josef Franz Huber. *UMTS and mobile computing*. Artech House, Inc., 2002.

[11] K. Daniel Wong and Vijay K. Varma. Supporting Real-Time IP Multimedia Services in UMTS. *IEEE Communications Magazine*, 41(11):148 – 155, November 2003.

[12] Jin Yang and Ioannis Kriaras. Migration to all-IP Based UMTS Networks. In *Proceedings of the First International Conference on 3G Mobile Communication Technologies*, pages 19–23, March 2000.

[13] Henning Schulzrinne, Stephen L. Casner, Ron Frederick, and Van Jacobson. RTP: A Transport Protocol for Real-Time Applications. RFC 1889, Internet Engineering Task Force, January 1996.

[14] Ned Freed and Nathaniel S. Borenstein. Multipurpose Internet Mail Extensions (MIME) Part One: Format of Internet Message Bodies. RFC 2045, Internet Engineering Task Force, November 1996.

[15] Mark Handley and Van Jacobson. SDP: Session Description Protocol. RFC 2327, Internet Engineering Task Force, April 1998.

[16] M.L.F Grech, M. Torabi, and M.R. Unmehopa. Service control architecture in the UMTS IP multimedia core network subsystem. In *Third International Conference on 3G Mobile Communication Technologies*, pages 22– 26, May 2002.

[17] Igor Miladinovic and Klaus Umschaden. Signaling Traffic Optimization in UMTS IP Multimedia Subsystem. In *Proceedings of the 7th IEEE International Conference on High Speed Networks and Multimedia Communications HSNMC'04, Tolouse, France*, pages 556–565, July 2004.

Robust probabilistic constrained power control for 3G networks

Yusef Cáceres and Michel D. Yacoub
UNICAMP- Univ. Est. de Campinas,
Fac. de Eng. Elétrica, Depto. de Comunicações
C.P. 6101, 13081-970 Campinas, SP, Brazil.
E-mail: {yusef,michel}@decom.fee.unicamp.br

***Abstract*— This paper deals with the power control problem for wireless cellular networks. The problem is modelled by a stochastic optimization problem with probabilistic constraints considering the link gains as random vectors whose probability distribution satisfies uncertain mean and covariance constraints. Specifically, we consider that the mean vector and covariance matrix are not perfectly known, however they belong to convex hull of a fixed set. The solution is established in terms of an optimization problem over linear matrix inequalities (LMIs) and it is robust in the sense that from the set of probability distributions matching the given bounds on the mean vector and covariance matrix, we take the one that produces the lowest tail probability.**

I. INTRODUCTION

For cellular wireless networks, the control of transmitted power such that the link quality, expressed by signal-to-interference ratio (SIR), is maintained above a specified threshold, can be established mathematically as follows (cf. [1]–[5])

$$\begin{cases} \min & \sum_i p_i \\ \text{s.t. :} & \gamma_i(p, g_i) = \dfrac{g_{ii}p_i}{\sum_{j\neq i} g_{ij}p_j + \nu_i} \geq \alpha_i, \\ & 0 < p_i \leq p_{i,max}, \quad i = 1, \ldots, n, \end{cases} \tag{1}$$

where $p = [p_1, \ldots, p_n]' \in \mathbb{R}^n$ is the transmitted power vector and $p_{max} = [p_{1,max}, \ldots, p_{n,max}]' \in \mathbb{R}^n$ is the maximum allowable transmitted power vector. $g_i = [g_{i1}, \ldots, g_{in}]' \in \mathbb{R}^n$ for $i = 1, \ldots, n$ are the channel gain vectors where g_{ij} is the power gain from the transmitter of j-th link to the receiver of the i-th one and ν_i is the background noise power at the receiver of i-th link. Finally, γ_i and α_i are the received SIR[1] and the required SIR threshold for the i-th link, respectively.

In this framework, the solution of optimization problem (1) is determinate under the assumption that the channel gains g_i for $i = 1, \ldots, n$ are exactly known. In applications however, they are difficult to estimate precisely. This is due, for example, to noise corruptions. As consequence, the aforementioned power control model falls short of handling the uncertain case.

[1]It is important to point out that the γ_i model, defined in (1), is general enough to describe DS-CDMA systems with matched-filter receivers as well as one-channel TDMA/FDMA systems giving specific interpretations to their parameters (see [6]). As consequence, for theoretical studies, there is no need to distinguish between multiple access schemes.

In this paper, the power control problem is reformulated by considering the channel gains g_i for $i = 1, \ldots, n$ as random vectors. We assume that only partial information regarding the probability distributions of g_i for $i = 1, \ldots, n$ are available. In particular, this paper studies the case where they satisfies given bounds on the mean and covariance constraints. In this setting, a robust stochastic optimization problem with probabilistic constraints is used to model the power control problem. This formulation allows us achieve the specified level of link quality satisfaction (SIR reliability requirements).

We approach the problem via generalized Chebychev inequalities, i.e., optimal bounds on the probability that a certain vector random variable belongs to a given set, under moment constraints (see [7], [8]). The solution is presented in terms of a convex optimization problem with linear objective and positive definite constraints involving symmetric matrices that are affine in the decision variables, namely a LMI problem [9]. Using interior-point methods for convex optimization, the LMI problem can be solved very efficiently.

The paper is organized as follows. In Section II some notations and basic definitions are presented. Additionally, the stochastic power control problem is precisely stated. In Section III, we present the solution of proposed problem. A numerical example and some conclusions are finally presented in Sections IV and V, respectively.

II. NOTATION AND PROBLEM FORMULATION

Throughout this paper, the following notation is adopted. $\mathbb{R}^n$ denotes the n-dimensional real space and $\mathcal{M}^{r\times m}$ ($\mathcal{M}^r$) the normed linear space of all $r \times m$ ($r \times r$) real matrices. The superscript $'$ stands for the matrix transpose and the notation $U \geq 0$ ($U > 0$) for $U \in \mathcal{M}^r$, means that U is semi-definite (definite) positive. Then, the closed (opened) convex cone of all positive semi-definite (definite) positive in $\mathcal{M}^r$ is denoted by $\mathcal{M}^{r0} = \{U \in \mathcal{M}^r : U = U' \geq 0\}$ ($\mathcal{M}^{r+}$). The convex hull of the fixed set $\{U^1, \ldots, U^l\}$

is represented by

$$\mathbf{Co}\{U^1,\ldots,U^l\} = \Big\{U = \sum_{k=1}^{l}\delta_k U^k : \quad \delta_k \geq 0,\ k=1,\ldots,l, \quad \sum_{k=1}^{l}\delta_k = 1\Big\}$$

where $U^k \in \mathbb{R}^{r\times m}$ for $k = 1,\ldots,l$. Finally, for a matrix $U \in \mathcal{M}^n$, the trace operator is denoted by $tr\{U\}$ and for a vector $u \in \mathbb{R}^n$, the diagonal matrix where u is the vector of its diagonal entries is represented by $diag\{u\}$.

In [7], it was established that for a given vector $\overline{g}_i \in \mathbb{R}^n$ and matrix $\Sigma_{g_i} \in \mathcal{M}^{n0}$, there exists a random vector $g_i = [g_{i1},\ldots,g_{in}]' \in \mathbb{R}^n$, defined in the probability space $(\Omega, \mathfrak{F}, Pr)$, whose mean vector and covariance matrix are given by $\overline{g}_i$ and Σ_{g_i} respectively, i.e.,

$$E[g_i] = \overline{g}_i \quad \text{and} \quad E[(g_i-\overline{g}_i)(g_i-\overline{g}_i)'] = \Sigma_{g_i},$$

where $E[\cdot]$ stands for the mathematical expectation with respect to the basic probability space. Let $g_i \sim (\overline{g}_i, \Sigma_{g_i})$ denotes a random vector g_i which has mean $\overline{g}_i$ and covariance Σ_{g_i}.

In this scenario, we formulate the control power problem as the following robust stochastic program with probabilistic constraints

$$\begin{cases} \min & \sum_i p_i \\ \text{s.t. :} & \inf\limits_{g_i\sim(\overline{g}_i,\Sigma_{g_i})} Pr(\gamma_i(p,g_i)\geq\alpha_i) \geq \beta_i, \\ & 0 < p_i \leq p_{i,max}, \\ & \overline{g}_i \in \mathbf{Co}\{\overline{g}_i^1,\ldots,\overline{g}_i^l\},\ \overline{g}_i^k \in \mathbb{R}^n, \\ & \Sigma_{g_i} \in \mathbf{Co}\{\Sigma_{g_i}^1,\ldots,\Sigma_{g_i}^l\},\ \Sigma_{g_i}^k \in \mathcal{M}^{n+}, \\ & i=1,\ldots,m, \quad k=1,\ldots,l, \end{cases} \tag{2}$$

where $\beta = [\beta_1,\ldots,\beta_n]' \in \mathbb{R}^n$, with $\beta_i \in (0,1]$ for $i = 1,\ldots,n$, is the target reliability vector.

Remark 1: Note that the stochastic optimization problem (2) can be considered as a strategic game, where the power controller chooses a decision p while nature picks the worst possible probability distribution of g_i for $i = 1,\ldots,n$ matching the given bounds on the mean $\overline{g}_i$ and covariance Σ_{g_i}.

III. Main result

Before showing our main result, the following lemmas will be used as support.

Lemma 1: [8] Consider the vector $\overline{x} \in \mathbb{R}^n$ and the matrix $\Sigma_x \in \mathcal{M}^{n+}$. Then,

$$\sup_{x\sim(\overline{x},\Sigma_x)} Pr(a'x \geq b) = \frac{1}{1+c^2},$$

where

$$c^2 = \inf_{a'x\geq b}(x-\overline{x})'\Sigma_x^{-1}(x-\overline{x})$$

is the squared distance from $\overline{x}$ to the set $\{x \in \mathbb{R}^n : a'x \geq b\}$ under the norm induced by the matrix Σ_x^{-1}.

Lemma 2: [9] (*Schur complement*) Consider the matrices A and C symmetric. Then,

$$\begin{bmatrix} A & B \\ \star & C \end{bmatrix} > 0 \iff C > 0, \qquad A > BC^{-1}B',$$

where, for symmetric matrices, the symbol $\star$ indicates the corresponding off diagonal term.

Using matrix-vector notation, the shorthand formulation of optimization problem (2) is

$$\begin{cases} \min & tr\{P\} \\ \text{s.t. :} & 0 < P \leq P_{max}, \\ & \inf\limits_{g_i\sim(\overline{g}_i,\Sigma_{g_i})} Pr(d_i'Pg_i \geq \alpha_i\nu_i) \geq \beta_i, \\ & \overline{g}_i \in \mathbf{Co}\{\overline{g}_i^1,\ldots,\overline{g}_i^l\},\ \overline{g}_i^k \in \mathbb{R}^n, \\ & \Sigma_{g_i} \in \mathbf{Co}\{\Sigma_{g_i}^1,\ldots,\Sigma_{g_i}^l\},\ \Sigma_{g_i}^k \in \mathcal{M}^{n+}, \\ & i=1,\ldots,m, \quad k=1,\ldots,l, \end{cases} \tag{3}$$

where the matrix $P = diag\{p = [p_1,\ldots,p_n]'\} \in \mathcal{M}^{n+}$, the matrix $P_{max} = diag\{p_{max} = [p_{max,1},\ldots,p_{max,n}]'\} \in \mathcal{M}^{n+}$, and the vector $d_i = [\mathbb{1}_{\{i=1\}} - \alpha_i\mathbb{1}_{\{i\neq1\}},\ldots,\mathbb{1}_{\{i=n\}} - \alpha_i\mathbb{1}_{\{i\neq n\}}]' \in \mathbb{R}^n$ being $\mathbb{1}_{\{\cdot\}}$ the Dirac measure.

Considering that $\Delta_{g_i}^k \in \mathcal{M}^{n+}$ is the unique square root of matrix $\Sigma_{g_i}^k$ (i.e., $\Delta_{g_i}^{k\prime}\Delta_{g_i}^k = \Sigma_{g_i}^k$) and representing the identity matrix by I, the solution of proposed power control problem is determinate in the following theorem.

Theorem 1: The LMI problem

$$\begin{cases} \min & tr\{P\} \\ \text{s.t. :} & 0 < P < P_{max}, \\ & \begin{bmatrix} d_i'P\overline{g}_i^k - \alpha_i\nu_i & \left(\frac{\beta_i}{1-\beta_i}\right)d_i'P\Delta_{g_i}^k \\ \star & \left(\frac{\beta_i}{1-\beta_i}\right)(d_i'P\overline{g}_i^k - \alpha_i\nu_i)I \end{bmatrix} > 0, \\ & i=1,\ldots,n, \quad k=1,\ldots,l, \end{cases} \tag{4}$$

provides the solution for the stochastic optimization problem (3).

Proof: The inner optimization problem in (3) can be rewritten as

$$\sup_{g_i\sim(\overline{g}_i,\Sigma_{g_i})} Pr(-d_i'Pg_i \geq -\alpha_i\nu_i) < 1-\beta_i, \tag{5}$$

for $i = 1,\ldots,n$.

Applying the Lemma 1 on the optimization problem above, we have

$$\sup_{g_i\sim(\overline{g}_i,\Sigma_{g_i})} Pr(-d_i'Pg_i \geq -\alpha_i\nu_i) = \frac{1}{1+c_i^2}, \tag{6}$$

where

$$c_i^2 = \inf_{-d_i'Pg_i\geq-\alpha_i\nu_i}(g_i-\overline{g}_i)'\Sigma_{g_i}^{-1}(g_i-\overline{g}_i). \tag{7}$$

Note that the values of β_i are usually different from zero thus we have to select the matrix P such that $\overline{g}_i \notin \{g_i : -d_i'Pg_i \geq -\alpha_i\nu_i\}$.

The optimal solution for the optimization problem (7) can be obtained applying the Karush-Kuhn-Tucker conditions. To this end, define the Lagrange

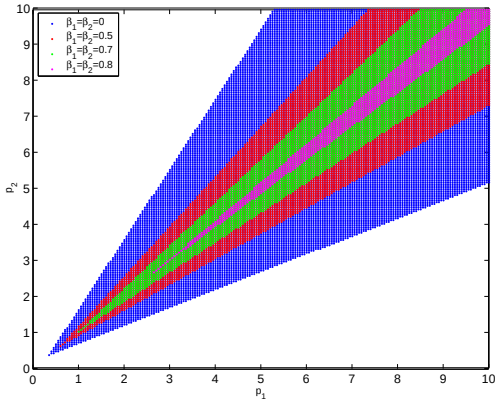

Fig. 1. Robust feasibility set.

function

$$L(g_i,\lambda_i) = (g_i-\overline{g}_i)'\Sigma_{g_i}^{-1}(g_i-\overline{g}_i)+ \lambda_i(-d_i'Pg_i+\alpha_i\nu_i),$$

for $\lambda_i \geq 0$.

The conditions for g_i to be a global minima are

$$\frac{\partial L(g_i,\lambda_i)}{\partial g_i} = 2\Sigma_{g_i}^{-1}(g_i-\overline{g}_i) - \lambda_i P d_i = 0, \qquad (8)$$

and

$$\frac{\partial L(g_i,\lambda_i)}{\partial \lambda_i} = -d_i'Pg_i+\alpha_i\nu_i = 0. \qquad (9)$$

From equations (8) and (9) we have that

$$\lambda_i = \frac{2(d_i'P\overline{g}_i-\alpha_i\nu_i)}{d_i'P\Sigma_{g_i}Pd_i}.$$

Thus,

$$c_i^2 = \frac{\lambda_i^2}{4}d_i'P\Sigma_{g_i}Pd_i = \frac{(d_i'P\overline{g}_i-\alpha_i\nu_i)^2}{d_i'P\Sigma_{g_i}Pd_i}. \qquad (10)$$

By replacing equations (6) and (10) into inequality (5), we have

$$(d_i'P\overline{g}_i-\alpha_i\nu_i)^2 > \Big(\frac{\beta_i}{1-\beta_i}\Big)d_i'P\Sigma_{g_i}Pd_i, \qquad (11)$$

Finally applying the Schur complement (see Lemma 2) in (11), the LMI problem (4) is justified. ■

Remark 2: Note that when $\beta_i = 0$ for $i = 1,\ldots,n$ and $l = 1$, the stochastic optimization problem (4) is reduced to the usual deterministic optimization problem (1) if the channel gains g_i are replaced by their mean value $\overline{g}_i$.

Remark 3: Notice that if there exist an upper bound for the transmitted power then high reliability requirements may become the optimization problem (4) infeasible. This is due to fast increase of $\sqrt{\beta_i/(1-\beta_i)}$ when β_i tends to 1.

IV. Numerical example

To illustrate the previous discussion, consider a wireless cellular network with 2 active users. The target SIR and the receiver noise are 5dB and 0.05W, respectively. Two design cases are considered:

(i) For this case, the mean vector and covariance matrix are assumed to be exactly know ($l = 1$), such that

$$\overline{g}_1 = \begin{bmatrix}0.986 & 0.160\end{bmatrix}, \quad \overline{g}_2 = \begin{bmatrix}0.150 & 0.956\end{bmatrix},$$
$$\Sigma_{g_1} = \Sigma_{g_2} = 0.004I_2 = \begin{bmatrix}0.004 & 0\\ 0 & 0.004\end{bmatrix}.$$

Figure 1 shows the feasibility set of optimization problem (4) for several reliability thresholds values. Clearly, the system reliability can be increased by allocating power in such a way that each transmitter has extra margin of SIR. As result, the system capacity is reduced.
Applying the Theorem 1, the allocation of transmitted power is $p = \begin{bmatrix}2.60 & 2.60\end{bmatrix}$ for $\beta = \begin{bmatrix}0.8 & 0.8\end{bmatrix}$.

(ii) For this case we assume that the mean vector and covariance matrix are not exactly known, but they are such that

$$\overline{g}_1 \in \mathbf{Co}\{\begin{bmatrix}1.00 & 0.18\end{bmatrix}, \begin{bmatrix}0.96 & 0.14\end{bmatrix}\},$$
$$\overline{g}_2 \in \mathbf{Co}\{\begin{bmatrix}0.17 & 0.97\end{bmatrix}, \begin{bmatrix}0.13 & 0.93\end{bmatrix}\},$$
$$\Sigma_{g_1} = \Sigma_{g_2} \in \mathbf{Co}\{0.003I_2, 0.005I_2\}.$$

The transmitted power in this case is $p = \begin{bmatrix}3.28 & 3.29\end{bmatrix}$ for $\beta = \begin{bmatrix}0.8 & 0.8\end{bmatrix}$.

V. Conclusion

We address the problem of allocating power in a wireless network considering the power gains as random vectors whose probability distribution is partially known. We assume that, it satisfies imprecise mean and covariance constraints. In this framework, the power control problem is modelled by a stochastic optimization problem with probabilistic constraints and the robust solution is established in terms of LMI problem.

A further research topic is constrain the underlying distribution to get less conservative controllers.

References

[1] F. Brock and B. Epstein, "Assignment of transmitter power control by linear programming," *IEEE Trans. Electromag. Compat.*, vol. EMC-6, pp. 36, 1964.

[2] J. Zander, "Performance of optimum transmitter power control in cellular radio systems," *IEEE Transactions on vehicular Technology*, vol. 41, no. 1, pp. 57–62, 1992.

[3] G. J. Foschini and Z. Miljanic, "A simple distributed autonomous power control algorithm and its convergence," *IEEE Transactions on Vehicular Technology*, vol. 42, no. 11, pp. 641–646, 1993.

[4] Foschini GJ and Miljanic Z, "A simple distributed autonomus power control algorithm and its convergence," *IEEE Transactions on Vehicular Technnology*, vol. 42, no. 11, pp. 641–646, 1993.

[5] J. Zander and S. Kim, *Radio resource management for wireless networks*, Artech House mobile communications series. Artech House Publishers, 2001.

[6] Q. Wu, "Optimum transmitter power control in cellular systems with heterogeneous SIR thresholds," *IEEE Transactions on Vehicular Technnology*, vol. 49, no. 4, pp. 1424–1429, 2000.

[7] I. Popescu, *Applications of Optimization to Probability, Finance and Revenue Management*, Ph.D. thesis, MIT, 1999.

[8] A. Marshal and I. Olkin, "Multivariate chebyshev inequalities," *Ann. Math. Stat.*, , no. 31, pp. 1001–1014, 1960.

[9] S. Boyd, L. El Ghaoui, E. Feron, and V. Balakrishnan, *Linear Matrix Inequalities in System and Control Theory*, vol. 15 of *SIAM Studies in Applied Mathematics*, Society for Industrial and Applied Mathematics, 1994.

A New Hybrid Scheme for Error Control in Wireless Data Networks

Prof. José Marcos C. Brito
National Institute of Telecommunications – Inatel
Santa Rita do Sapucaí – Brazil
brito@inatel.br

Prof. Ivanil S. Bonatti
State University of Campinas – Unicamp
Campinas - Brazil
ivanil@dt.fee.unicamp.br

***Abstract* – The challenge to provide a broadband wireless network with quality of service is the very noisy and time-varying environment of the radio link. To overcome this problem, several error control mechanisms have been proposed. This paper presents a new hybrid scheme for error control in wireless data networks. The performance of the proposed scheme is analysed and compared with previous schemes presented in the literature.**

Index Terms – Wireless data networks, error control schemes.

I. INTRODUCTION

Broadband and wireless are presently the two major drivers in telecommunications industry. The challenge of providing a broadband wireless network with Quality of Service (QoS) lies in the very noisy and time-varying environment of the radio link. Two important parameters related to QoS, packet error ratio and throughput, are significantly affected by the Bit Error Rate (BER) in the wireless link, making it necessary to use an additional error control mechanism. The traditional schemes for error control are Forward Error Correction (FEC) and Automatic Repeat Request (ARQ). Using FEC or ARQ in the wireless link decreases the residual bit error rate (bit error rate after the error control mechanism), increases the delay in transmitting a cell and decreases the throughput, due to overhead of the error control mechanisms.

The analyses presented in [1]–[3] show that, for non-adaptive schemes, ARQ works better than FEC, if the bit error rate in the channel is low, and worse, if the bit error rate is high, indicating that hybrid ARQ-FEC techniques can improve the performance in a non-adaptive environment.

An ARQ-FEC hybrid adaptive scheme, having multiple FEC states, is proposed for non-adaptive environment in [4]. It has been demonstrated that the hybrid scheme and an ideal adaptive FEC scheme have similar performances. Besides, the hybrid scheme does not need an estimate of the bit error rate in the channel and, consequently, has a smaller complexity. The performance of the hybrid ARQ-FEC scheme was also compared with the performance of the classical Type I Hybrid ARQ-FEC scheme in [5] and [6]. The results of this comparison are that the hybrid ARQ-FEC scheme works better than the Type I Hybrid ARQ-FEC scheme, if the bit error rate in the channel is low (BER $\leq 8.5 \times 10^{-5}$), and worse, if the bit error rate is high. Thus, a new hybrid solution embodying both hybrid schemes can improve the performance in wireless data networks.

In this paper we propose a new hybrid scheme for error control in wireless data networks that is similar to the hybrid ARQ-FEC scheme with multiple FEC states, changing the FEC states by Type I Hybrid ARQ-FEC states. The codes to achieve a given performance are defined and the throughput of the scheme is computed.

Since our goal is to compare the performances of different approaches to error control in wireless data networks, we have chosen to use bounds to define code redundancy, instead of using a particular type of code.

As a scenario for the analysis of our scheme, we consider a system composed by one wireless link and some optical wired links. The multiple access technique used in the wireless link is similar to a DAMA-TDMA (Demand Allocation Multiple Access – Time Division Multiple Access) multiple access with fixed time slots. In numerical examples, it is considered that the packet has 424 information bits (an ATM cell).

The remainder of the paper is organised as follow: in Section II, the proposed technique is detailed, the codes are defined and the throughput is computed; in Section III, the performance of the proposed scheme is compared with previous solutions; some conclusions are presented in Section IV.

II. THE NEW HYBRID ARQ-FEC SCHEME

The state diagram of the proposed technique is shown in Figure 1. The system moves from the ARQ state to the first Type-I state when a packet is received with error (and a retransmission is requested), and moves from the last Type-I hybrid state to the ARQ state after it has received y consecutive correct packets. In the ARQ-state a (n_a, k) block code is used for error detection. In the Type-I state two codes are used, a (n_f, n_{aI}) block code for error correction and a (n_{aI}, k) block code for residual error detection after the error correction code operation (if a residual error is detected a retransmission is requested). Figure 2 illustrates the packets in each state after the coding process.

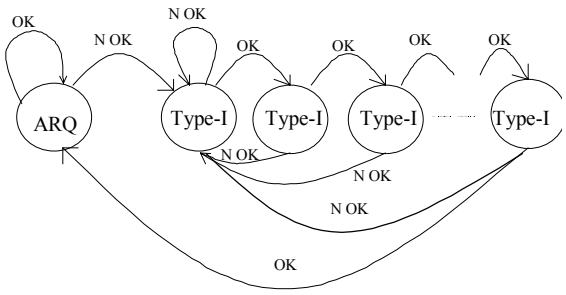

Figure 1 – State diagram for the proposed hybrid scheme.

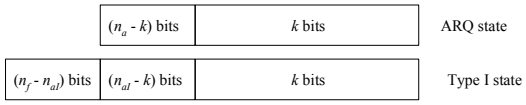

Figure 2 – Packets after the coding processes.

In the ARQ state, when a packet is received, it may contain: no errors, with probability P_c , an undetectable error, with probability P_{ue} , or a detectable error, with probability $P_e = 1 - P_c - P_{ue}$.

The probability P_c is given by

$$P_c = (1-p)^{n_a} \tag{1}$$

where p is the bit error rate in the wireless link and n_a is the total number of bits in the code of the ARQ state.

The probability P_{ue} can be computed by Korzhik's upper bound [8]

$$P_{ue} \le 2^{-(n_a-k)} \cdot \left[1-(1-p)^{n_a}\right] \tag{2}$$

In the Type I state, a received packet may contain a correctable error (including no errors), with probability P_{ccf} , or contains a not correctable error, with probability ($1 - P_{ccf}$). If the packet contains a not correctable error, the residual error (generated by the FEC decoding process) may result in an undetectable error, with probability P_{ue}, or a detectable error, with probability ($1 - P_{ue}$).

The probability P_{ccf} is computed by the Binomial distribution

$$P_{ccf} = \sum_{j=0}^{t} \binom{n_f}{j} \cdot p^j \cdot (1-p)^{n_f-j} \tag{3}$$

where n_f is the total number of bits in the FEC code of the Type I scheme and t is the error correction capacity of this code. The Plotkin bound gives a relation between n_f and t and is given by [9]

$$n_f - n_{aI} \ge 2(d_{\min} - 1) - \log_2 d_{\min} \tag{4}$$

where n_{aI} is the number of information bits from the FEC code point of view and d_{min} is the minimum distance of the code. The relation between d_{min} and t is given by

$$t = \left\lfloor \frac{d_{\min} - 1}{2} \right\rfloor \tag{5}$$

In the Type I state, the probability of the base station to accept a packet from the wireless link (and send it to the optical link) can be computed by

$$P_a = P_{ccf} + (1 - P_{ccf}) \cdot P_{ue} \tag{6}$$

where P_{ccf} is computed by expression (3) and P_{ue} is given by expression (2), changing n_a by n_{aI}.

The probability of the base station to reject a packet (requesting a retransmission) is given by

$$P_d = (1 - P_{ccf}) \cdot (1 - P_{ue}) \tag{7}$$

Finally, the probability of the wireless link to deliver a correct packet to the optical link can be computed by

$$P_{cch} = P_c P_{arq} + \frac{P_{ccf}}{1 - P_d}\left[1 - P_{arq}(1 - P_e)\right] \tag{8}$$

where P_c is the probability of receiving a correct packet in the ARQ-state (equation 1), P_e is the probability of receiving a packet containing a detectable error in the ARQ-state, P_{arq} is the stationary probability of the ARQ state (equation 9), P_{ccf} is the probability of receiving a packet containing a correctable error in the Type-I state (equation 3) and P_d is the probability of a packet being rejected (and retransmitted) in the Type-I state (equation 7).

The stationary probability of the ARQ state is computed by

$$P_{arq} = \frac{P_{cI}^{y}}{P_{cI}^{y} + P_e \cdot \sum_{j=0}^{y-1} P_{cI}^{j}} \tag{9}$$

where P_{cI}, the probability of a packet to contain no errors in the Type I state, is given by

$$P_{cI} = (1-p)^{n_f} \tag{10}$$

The three codes are computed in order to make the wireless link work as an optical link, concerning bit error characteristic. This is tantamount to saying that the probability of the wireless link to deliver a correct cell to an optical link is equal to or greater than the probability of one optical link to deliver a correct cell to the next optical link. This criterion is in agreement with the analysis presented by Cain and McGregor in [7].

The probability of an optical link to deliver a correct cell to the next optical link can be computed by

$$P_{cco} = (1 - p_o)^{424} \cdot \left[1 + 40(1 - p_o)^{39} \cdot p_o\right] \quad (11)$$

where p_o is the bit error rate in the optical link, set equal to 10^{-8} in numerical examples.

It is considered that an estimate of the bit error rate in the wireless link is not available. Thus, the ARQ code in the ARQ state and the ARQ and FEC codes in the Type I state must be defined considering the whole range of bit error rate. Several combinations of the three codes can satisfy the criterion $P_{cch} \geq P_{cco}$.

The throughput of the proposed scheme is calculated by the expression

$$\eta = \frac{k}{\left\{\left[n_a(1-P_e) + \frac{n_a P_e P_a}{1-P_d} + \frac{n_f P_e P_a}{(1-P_d)^2}\right] P_{arq} + \right.} \quad (12)$$
$$\left. + \frac{n_f P_a}{(1-P_d)^2}(1-P_{arq})\right\}$$

where k is the number of information bits in each packet, considered equal to 424 bits in numerical examples.

Computing the combination of the three codes that maximises the average throughput of the system, satisfying the criterion $P_{cch} \geq P_{cco}$ in the whole range of bit error rate considered, leads to the results presented in Table 1.

TABLE 1 – COMBINATION OF CODES THAT MAXIMISES THE THROUGHPUT.

y	t	n_{al}	n_a
1 e 2	8	438	440
3 a 5	8	438	439
6 a 10	8	438	438
11 a 16	8	438	437

Setting the codes according to Table 1, the throughput has been calculated and the results are shown on Figure 3. It can be seen that the throughput varies with the y value. Computing the average throughput in the range $10^{-2} \geq p \geq 10^{-6}$, leads to the conclusion that the average throughput it maximised when $y = 14$.

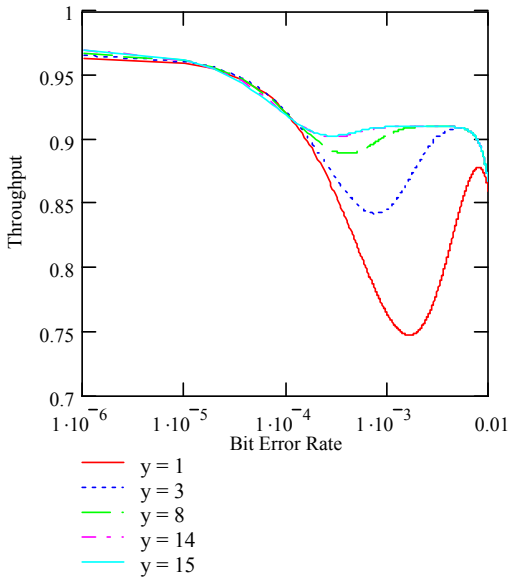

Figure 3 – Throughput for the proposed hybrid scheme.

III. COMPARING THE PERFORMANCES

This section compares the throughput of the proposed scheme, setting y = 14, with a classical hybrid Type I scheme, setting the total number of bits in the ARQ code equal to 438 and t = 8, and also with a system with multiple FEC schemes, setting y = 11, t = 17 and n_a = 437. The values used to set the parameters of the code in the hybrid Type I scheme and the parameter y and the codes in the multiple FEC scheme maximise the average throughput in these systems and were obtained from references [4] and [5].

Figure 4 compares the performances of the three schemes. It can be seen that the throughput of the new scheme is greater than the throughput of the scheme with multiple FEC states in the whole range of bit error rate considered. Furthermore, the proposed scheme performs better than or equal to the classical type I hybrid scheme for most of the bit error rate range.

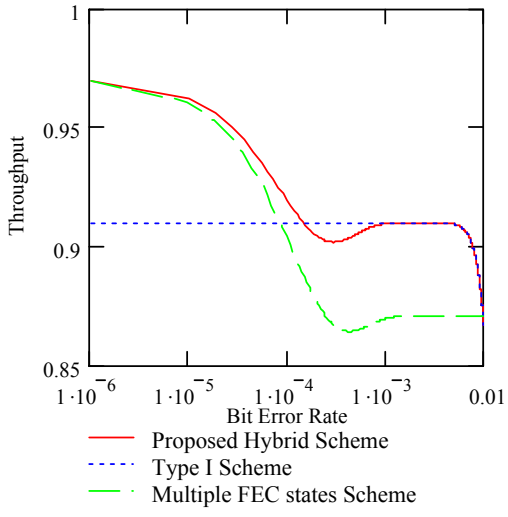

Figure 4 – Comparing the throughput.

IV. CONCLUSIONS

In this paper a new hybrid ARQ-TypeI scheme has been proposed to control errors in wireless data networks. The proposed scheme is based on two detecting-error and one correcting-error codes, which were chosen to maximise the throughput of the wireless link.

It has been shown that the proposed scheme performs better than the scheme with multiple FEC states in the whole range of the bit error rate analysed. It also performs better than the classical Type I scheme for most of the range considered.

REFERENCES

[1]. J. M. C. Brito and I. S. Bonatti, "A Comparison of End-to-End Delay in Wireless ATM Networks using FEC and Go-Back-N ARQ in the Wireless Link", 5th IEEE Malaysia International Conference on Communications (MICC 2001), pp. 84-89, Kuala Lumpur, Malaysia, 21-24 October 2001.

[2]. J. M. C. Brito and I. S. Bonatti, "A Comparison of End-to-End Delay in Wireless ATM Networks using FEC and Selective Repeat ARQ in the Wireless Link", Third IEEE Intern. Conf. on Inform., Commun. and Signal Processing (ICICS 2001), 5 pages, Singapore, 15-18 October 2001.

[3]. I. S. Bonatti e J. M. C. Brito, "A Simple Hybrid ARQ-FEC Scheme to Control Errors in the Wireless Link in Wireless ATM Networks", III Workshop de Comunicação sem Fio e Computação Móvel (WCSF 2001), pp. 63-70, Recife, Brazil, 14 e 15 de agosto de 2001.

[4]. J. M. C. Brito and I. S. Bonatti, "An Improvement in a Simple Adaptive Error Control Scheme for Wireless ATM Networks", Proceedings of the IASTED International Conference on Communication Systems and Networks, pp. 205-210, Benalmadena, Spain, September 8-10, 2003.

[5]. J. M. C. Brito and I. S. Bonatti, "Throughput in Hybrid ARQ-FEC Error Control Schemes in Wireless ATM Networks", V Workshop de Comunicação sem Fio e Computação Móvel (WCSF 2003), pp. 41-49, São Lourenço, Brazil, October 27-30, 2003.

[6]. J. M. C. Brito and I. S. Bonatti, "Time Delay in Hybrid ARQ-FEC Error Control Schemes in Wireless ATM Networks", V Workshop de Comunicação sem Fio e Computação Móvel (WCSF 2003), pp. 50-59, São Lourenço, Brazil, October 27-30, 2003.

[7]. J. B. Cain and D. N. McGregor, "A Recommended Error Control Architecture for ATM Networks with Wireless Links", IEEE Journal on Selected Areas in Communications, Vol. 15, No 1, pp. 16-28, January 1997.

[8]. Stephen G. Wilson, Digital Modulation and Coding, Prentice Hall, 1996.

[9]. J. G. Proakis, Digital Communications, second edition, McGraw-Hill, 1989.

Pre-FFT Equalization in DVB-T Systems

Luís Carlos Lorenzo Acácio
Itautec Philco S.A
Senior Electronics Engineer
R. Santa Catarina,1 - 03086-025
Tatuapé - São Paulo - SP - Brasil
luis.acacio@itautec-philco.com.br

Vítor Heloiz Nascimento
Escola Politécnica da USP
Dept. of Electronic Systems Engineering
Av. Prof. Luciano Gualberto, 158 - 05508-900
Cidade Universitária - São Paulo - SP -Brasil
vitor@lps.usp.br

***Abstract*— OFDM systems typically make use of a cyclic prefix to combat multipath fading. Although computationally cheap, this solution also reduces the channel efficiency. Time equalization is one alternative to add multipath robustness and achieve a better data rate. In this article, we introduce a time equalizer suitable for use in OFDM systems that employ pilot carriers for channel estimation, as in the case of the European DVB-T and the Japanese ISDB-T. The novelty presented is a new variant of the LMS algorithm specially adapted for OFDM systems. We show with simulations that the introduction of the pre-FFT time equalizer increases the performance of the DVB-T system. The proposed algorithm does not depend on the cyclic prefix length and can even be used in systems that do not use one. The resulting complexity of the adaptation algorithm is within the capabilities of current technology.**

***Index Terms*— DVB-T, OFDM, Pre-FFT equalization, time equalizer.**

I. Introduction

The use of orthoghonal frequency division multiplexing (OFDM) has grown vigorously in the data communications industry during the last decade. The acceptance of OFDM is partially explained by its robustness to frequency selective channels. In typical OFDM applications, robustness to fading channels is obtained through the addition of a cyclic prefix (CP) [1]. The main disadvantage of using a CP is a reduction in the total data rate of the channel. One of the methods used to aleviate the impact of this data rate reduction is the use of time equalization. In this article, we will focus in the use of a time equalizer to extend the robustness of a DVB-T (Digital Video Broadcasting - Terrestrial) system, which is based on OFDM, to channels with delays longer than the CP.

In 1998, the United Kingdom launched the DVB-T [2] as a national terrestrial digital television system. From the beginning, it has attracted the attention of researchers in search of improvements ([3] and [4]). In 1999, Armour [3] showed how a decision feedback equalizer could improve the performance of the DVB-T system. On a subsequent paper on the same topic [5], the author argued that the DFE previously suggested is far too complex to be realistically implemented in a DVB-T system, and offered as an alternative a low complexity direct adaptation algorithm based on what he calls *CSI-Channel State Information*.

In the present work, we started from a similar idea as that suggested by Armour and devised a more robust and stable version based on the LMS algorithm [6]. Although the adaptive time equalizer proposed was tested only on the DVB-T system, the idea is easily extensible to any OFDM system that uses pilot carriers for channel estimation like the more recent ISDB-T (Integrated Services Digital Broadcasting) (see [7]). As the DVB-T standard makes no provision for zero length cyclic prefix, we conducted tests limited to the minimum size allowed of 1/32 of the length of useful symbol; however, the algorithm does not rely on the size of the CP and could be used on systems without it.

The rest of this paper is organized as follows: on section II we present a quick overview of the DVB-T system focusing on the most important items for the understanding of this article; section III offers a thorough description of the channel estimation and time equalization techniques employed in our proposed implementation; section IV shows the results of our simulations as well as comments on some peculiar effects observed; on section V we draw the conclusions and add some final comments.

II. Overview of DVB-T system

The DVB-T system is the terrestrial standard for digital TV transmission used in Europe and is just one of a collection of related standards maintained by the DVB consortium. It is highly complex and we are not going to make a thorough review, on the contrary, we will focus on the most important points for the following sections of this article. This entire section is based on reference [2].

The DVB-T system is based on OFDM but builds on it adding a lot of other digital communications techniques. It has 2 modes of operation, one with 2048 carriers, usually refered to as *2k mode*, and the other with 8192 carriers, called the *8k mode*. The 8k mode is more robust to multipath fading and impulsive noise, but also requires more computational power. Since the channel bandwidth is always the same (6MHz, 7MHz or 8MHz, depending on the country), the 2k mode results in a larger spacing between carriers and is often a better choice for mobile communications in which strong doppler effect causes spreading of the carriers. Not all carriers are used for data, in both modes there are guard bands filled with null carriers on the left and right borders of the spectrum; in addition, some carriers are used for special purposes, as we will soon describe.

The standard also includes a frame structure aimed at organizing the information in a ordered fashion so that the receiver can track many of the processes going on at the same time. If, for instance, the receiver interrupts reception for some uncontrolled reason, it is the frame structure that accounts for a quick recovery of the synchronism. In the DVB-T, a *frame* is composed of 68 symbols and a *super-frame* is composed of 4 frames.

Figure 1 shows a simplified block diagram of the DVB-T signal generation process. As seen, the main blocks are:

- DVB-T coding;
- QAM mapping;
- Pilot carriers insertion;
- IFFT and Cyclic prefix insertion.

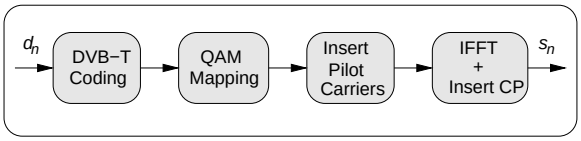

Fig. 1. Block diagram of the DVB-T signal generation.

The coding block is a necessary phase in any digital TV system. In the specific case of the *DVB-T coding*, the steps involved are:

- Generation of the MPEG2 transport stream. This step includes the creation of the program to be transmitted;
- Energy dispersal scrambling. Its main function is to garantee a minimum level of (pseudo)randomness to the data stream to be transmitted;
- Outer coding and interleaving. It is a block systematic coding based on a interleaved Reed-Solomon RS(204,188,t=8) shortened code, which offers error correcting capabilities against impulsive noise;
- Inner coding and interleaving. This is a punctured convolutional coding devised to add robustness against additive white gaussian noise.

It is common to find references to an *uncoded DVB-T system* in the technical literature, which refers to a DVB-T implementation without the coding phase. Those systems are useful, as in our case, when implementing new improvements to or studying the robustness of the DVB-T signal modulation phase. When implementing an uncoded DVB-T system, a pseudo-random byte stream with uniforme distribution should be provided as input, in order to supply a source of data similar to the original one.

The DVB-T system allows the use of 5 types of signal constellation, namely: QPSK, 16QAM, 64QAM, non-uniform 16QAM and non-uniform 64QAM; the last two are specially suited for hierarchical transmission modes. The QAM mapper divides the received byte stream in appropriate blocks of bits (2, 4 or 6bits) and maps them to the corresponding complex symbols according to the constellation type. In our simulations, we have conducted tests only with the uniform constellations which are by far the most common in practical applications.

There are 3 sorts of pilot carriers in the DVB-T system:

- *TPS Pilots*, which carry information on all the transmission parameters. Every TPS in a single symbol carries exactly the same information in a differentially encoded form. This high level of redundancy provides strong rosbustness against channel fading and is very useful on a initial synchronizing phase;
- *Continual Pilots*, which carry information known a priori and are used for channel estimation. They are called *continual* because they occur always at the same carrier number in all symbols. They are transmitted with 16/9 of the power of data carriers for extra robustness;
- *Scattered Pilots*, which are similar to the continual pilots in power and purpose, but whose position change from symbol to symbol.

Figure 2 ilustrates the typical distribution pattern of scattered and continual pilots in a sequence of DVB-T symbols. As shown in the picture: the first and last non-null carriers are continual pilots; every 4 symbols the pilot distribution pattern repeats; for every 3 carrier positions, 1 is ocupied by a pilot carrier in some symbols.

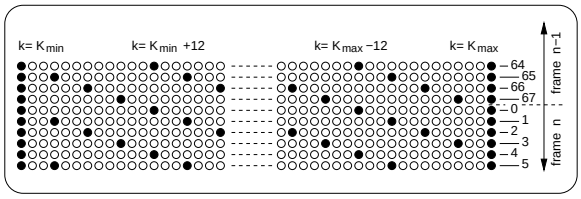

Fig. 2. Typical pilot carrier distribution pattern of DVB-T.

Continual pilots offer high temporal sampling rate of the channel response since they are available at every symbol; scattered pilots offer high frequency sampling rate of the channel response since they are available every 3 carrier positions. This bi-dimensional sampling schem results in very good channel estimation capabilities.

After inserting the pilot carriers, the next step is to execute the IFFT and obtain what is usually called in the technical literature as the *useful symbol*. The complete DVB-T symbol is obtained by the addition of the *cyclic prefix* (CP). The CP is comprised by the last samples of the useful symbol, which are repeated at the beginning. The DVB-T standard offer 4 choices for the length of the CP specified as a fraction of the length of the useful symbol: 1/4, 1/8, 1/16 and 1/32. The longer the CP, the higher the robustness to mutipath fading, but also the lower the channel efficiency since the CP carries only redundant information.

III. The Pre-FFT equalizer

A. Channel estimation

The use of a cyclic prefix (CP) in OFDM systems prevents inter symbol interference between adjacent

symbols for echo delays shorter than the CP [1], but it is still necessary to recover the complex number by which each carrier is multiplied. This step of the OFDM decoding process is known in the literature as *channel estimation* or, sometimes, *channel equalization* and is usually done in the frequency domain. To avoid confusion, in this work we will always refer to this frequency domain equalization as *channel estimation*, the terms equalizer and equalization will always be used for the *time domain equalization*.

There are many techniques used for channel estimation, among them: blind [8], trainned and pilot-assisted estimation [9]. Blind estimation is used when there is no auxiliary signal to help in the identification of the channel and typically results in the most complex method. Trainned estimation, very used in wireless [10] and ADSL systems [11], usually employs the sporadic transmission of short and previously known sequences that allow the receiver to estimate the current state of the channel. Pilot-assisted estimation is made by the use of known pilot carriers which are inserted in every symbol among the data carriers to allow the identification of the channel on distributed positions of the spectrum. The DVB-T system makes provision for many pilot carriers. So, the typical channel estimation technique employed is the pilot-assisted.

In this work, we used an LMS channel estimation method based on the distributed continual and scattered pilot carriers defined in the DVB-T standard [2]. Each carrier is assumed to be affected by a flat fading, given its narrow bandwidth, so that a one-tap LMS algorithm is enough to estimate the desired complex number. Figure 3 shows the block diagram of the algorithm employed.

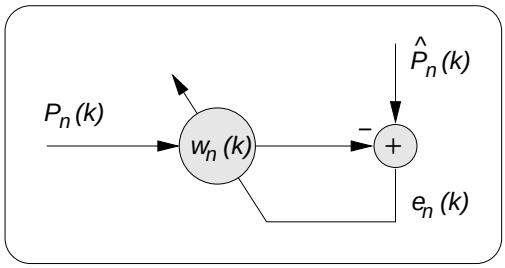

Fig. 3. Block diagram of the channel estimation LMS.

The adaptation algorithm is a traditional LMS [6] and is described in (1), where: $P_n(k)$ is the complex number transmitted in carrier n at instant k; $\hat{P}_n(k)$ is the received complex number in carrier n; $e_n(k)$ is the corresponding LMS error; μ is the LMS adaptation step; and $w_n(k)$ is an estimate of the channel response at the frequency of carrier n.

$$\begin{cases} w_0(k) = \hat{P}_0(k)/P_0(k) \\ e_n(k) = \hat{P}_n(k) - P_n(k) \cdot w_n(k) \\ w_{n+1}(k) = w_n(k) + \mu \cdot e_n(k) \cdot P_n^*(k) \end{cases} \quad (1)$$

On continual pilots the adaptation is made at every symbol; on scattered pilots the adaptation is made only once every 4 symbols, in accordance with the DVB-T standard. Once the frequency response of the channel is known on the pilot carriers, it is interpolated to provide estimates on the data carrier positions. On section IV-A we compare the efficiency of the LMS channel estimation method with a crude estimate obtained simply by: $w_n(k) = \hat{P}_n(k)/P_n(k)$, which is the most immediate and less complex technique.

B. Channel estimation plus time equalization

Channel estimation and time equalization are not mutually exclusive techniques [3]. In fact, in this article we make use of both simultaneosly taking advantage of their specific characteristics. See figure 4 for a description of the block diagram of the receiver after the inclusion of the time equalizer.

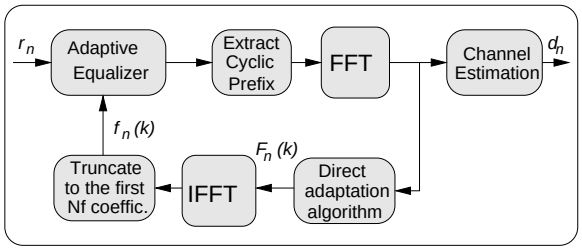

Fig. 4. Combined use of channel estimation and time equalization.

The idea of a direct adaptation algorithm based on the CSI (Channel State Information) was suggested in [5]. The authors analyze techniques of time equalization suitable for different OFDM systems and also offer estimates of the computational complexities, we recommend that article for readers interested in this subject. They conclude that equalizers based on traditional adaptation algorithms are far too complex to be implemented in OFDM systems with a large number of carriers, including the DVB-T. So, they offer as an alternative, a CSI-based direct adaptation algorithm.

Armour kept the DFE equalizing topology, but used a less complex CSI-based adaptation method on the feedback section. We used their idea as a starting point and tried a simple FIR equalizer with the direct adaptation algorithm described at (2), where: $F_n(k)$ is an estimate of the desired equalizing filter frequency response; $f_n(k)$ is an estimate of the desired equalizing filter impulse response truncated to the first N_f coefficients; $w_n(k)$ is obtained from the channel estimate step, as described in (1). Note however, that if the equalizer works correctly $w_n(k)$ will converge to unity and no longer to the channel frequency response. Unhappily, this algorithm has shown to be very unstable, it starts with reasonable equalization results, but diverges after a couple of symbols.

$$\begin{cases} F_0(l) = 1 \\ F_{n+1}(l) = F_n(l)/w_n(l) \\ f_n(k) = IFFT(F_n), \quad k = 0, 1, \ldots, N_f \end{cases} \quad (2)$$

In order to obtain a stable system and still take advantage of a direct adaptation method we devised a new variant LMS algorithm as depicted in figure 5.

The FFT block in the picture represents the FFT step of the DVB-T decoding process and was included just to ilustrate that the multiplication of $\hat{P}_n(k)$ by $F_n(k)$ is executed before the FFT while the LMS error is evaluated after the FFT. The product $\hat{P}_n(k) \cdot F_n(k)$ is only indirectly executed by the convolution of the equalizer with the received signal.

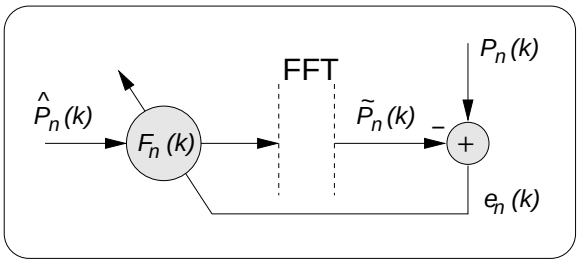

Fig. 5. Variant LMS used for estimation of the time equalizer.

With this new topology, the direct adaptation of the taps of the equalizer are evaluated according to (3), where: F_n is an estimate of the desired frequency response of the equalizer; f_n is the corresponding impulse response; $\hat{P}_n$ is the complex number received at the pilot carrier n, which is modified by the equalizer in the time domain; $\tilde{P}_n$ is the effectivelly available complex number at carrier n after the FFT evaluation; and μ is the LMS adaptation step.

$$\begin{cases} f_0 = \delta(k) \\ F_0(l) = P_0(l)/\hat{P}_0(l) \\ e_n(l) = P_n(l) - \hat{P}_n(l) \cdot F_n(l) \\ F_{n+1}(l) = F_n(l) + \mu \cdot e_n(l) \cdot \hat{P}_n^*(l) \\ f_n(k) = IFFT(F_n), \quad k = 0, 1, \ldots, N_f \end{cases} \tag{3}$$

As explained above, the product $\hat{P}_n(k) \cdot F_n(k)$ is not directly calculated because in this topology $\hat{P}_n(k)$ is not available. But $\tilde{P}_n(k)$ is available and $\tilde{P}_n(k) = \hat{P}_n(k) \cdot F_n(k)$. So, the final adaptation algorithm is as follows:

$$\begin{cases} f_0 = \delta(k) \\ F_0(l) = P_0(l)/\tilde{P}_0(l) \\ e_n(l) = P_n(l) - \tilde{P}_n(l) \\ F_{n+1}(l) = F_n(l) + \mu \cdot e_n(l) \cdot \tilde{P}_n^*(l)/F_n(l) \\ f_n(k) = IFFT(F_n), \quad k = 0, 1, \ldots, N_f \end{cases}$$

Once the frequency response F_n is estimated on the pilot carriers, it is linearly interpolated to supply an estimate also on the data carriers. This algorithm has shown to be very stable. There are, however, two problems that we had to deal with. The first is the presence of null carriers at the margins of the DVB-T spectrum which are meant to provide guard bands against interference between adjacent channels; we will return to this problem and describe the solution adopted on section IV-C when we talk about edge effects.

The second problem is that when we truncate the equalizer impulse response f_n to its first N_f coefficients, we lose control of the high rate oscilating components of F_n. If no action is taken, these components slowly diverge degrading F_n and eventually also f_n. To prevent this from happening, we sporadically re-evaluate F_n by calculating the FFT of f_n padded with the appropriate number of zeros. This is equivalent to low-pass filering F_n, eliminating high rate oscilating components. Note that this procedure does not increase the complexity of the algorithm since when we re-evaluate F_n we do not adapt the LMS, and the FFT calculated is of the same order of the IFFT used to adapt f_n. In our simulations, we re-evaluate F_n once every DVB-T super-frame (272 symbols) for safety, although we observed that once every 3 super-frames resulted in no noticeable difference.

The extra computational complexity required to adapt the equalizer taps using this algorithm is almost exactly the same as that required to decode the DVB-T signal (uncoded) with an LMS based channel estimation method. It requires one IFFT of the same order of the main FFT, and an LMS estimation stage similar to the one used to estimate the channel response.

Finally, we would like to note that:

- The new topology used has all the advantages of a one tap LMS algorithm although some of the operations are indirectly executed before the FFT and the LMS error is evaluated after it;
- The proposed algorithm does not depend on the size of the cyclic prefix and can even operate without one although we have not tested this situation yet (the DVB-T system does not include this option);
- Even though we have conducted tests only on the DVB-T system, the method is easily adaptable to any OFDM system that uses pilot carriers for channel estimation;
- The required computational power is well within current technology capability since the total complexity approximately doubles (excluding the equalizer itself).

We have not assessed the computational complexity of the equalizer itself, but it is smaller than that proposed by Armour since we use a FIR topology which is entirely based on a CSI direct adaptation algorithm. It is worthwhile mentioning that much effort have recently been devoted to new equalizing solutions for similar applications by researchers interested in the ATSC (Advanced Television Systems Committee) system [12], which is the American standard for digital TV. Our method could certainly profit from some of those pioneering techniques.

IV. Simulation results

We have run simulations comparing the performance of the following configurations:

- *Linear interpolation*: estimates the channel dividing the complex symbol received in the pilot carrier by the corresponding transmitted symbol and linearly interpolating between pilot carriers;

- *Data LMS/Linear*: estimates the channel using the LMS method described in section III-A and linearly interpolating between pilot carriers;
- *Data LMS/Cubic*: similar to *Data LMS/Linear* but using a third degree polynomial interpolation;
- *Equalizer+Data LMS*: combined use of the time equalization and channel estimation by *Data LMS/Linear*, as described in section III-B.

The setup used in the simulations is as follows:

- uncoded DVB-T 2K mode with uniform 64QAM;
- 6MHz channel bandwidth;
- FIR time equalizer with 512 taps;
- fading channel composed of a single echo of amplitude 0.3 and no noise;
- echo delay varying from 40 to 170 samples;
- simulation run for 32 DVB-T frames (2176 symbols).

In addition, some simulations were run with a cyclic prefix of length 1/16 (128 samples) of the length of the useful symbol and others with 1/32 (64 samples), this variation is indicated by an additional *CP=128* or *CP=64* respectively. Finally, see also section IV-C for further information on extrapolation of channel frequency response to the zero carriers at the margins of the DVB-T spectrum. The ploted curves show what we called $rSNIR$ which stands for *Relative Signal to Noise+Interference Ratio*. The $rSNIR$ is obtained by:

$$rSNIR = -10 \cdot log_{10}(\sigma_c^2) \quad ,$$

where σ_c^2 is the total variance of the received constellation. The $rSNIR$ is related to the $SNIR$ (or, sometimes $SINR$), usually seen in the literature, in the sense that a variation in one of them is directly reflected in the other by the same amount.

A. Channel estimation by LMS

In figure 6, we compare the performance of the configurations: *Linear Interpolation*, *Data LMS/Linear* and *Data LMS/Cubic*, some of them with *CP=64* and some with *CP=128*.

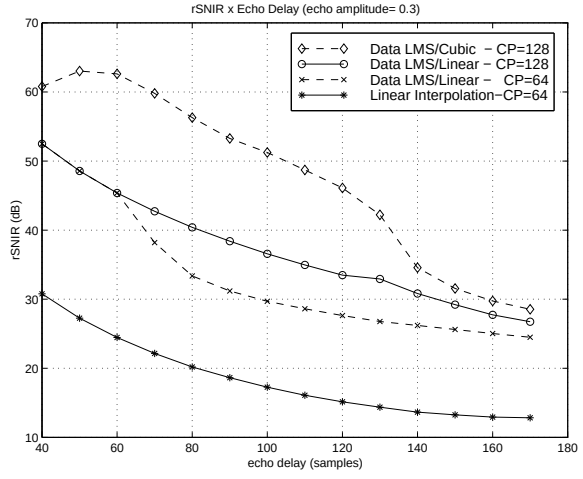

Fig. 6. Performance of channel estimation techniques.

The combinations presented are enough to show the general behaviour of each technique. Plain *Linear Interpolation-CP=64* is a poor channel estimation method that results in low $rSNIR$ even with delays smaller than the cyclic prefix (CP). *Data LMS/Linear-CP=64* shows over 20dB improvement for delays smaller than 64 samples (the size of the CP). Changing the CP to 128 samples simply extends the 20dB advantage up to the same number of samples, as can be seen in the curve *Data LMS/Linear-CP=128*. Using a more complex cubic interpolation algorithm, as in the case of *Data LMS/Cubic-CP=128*, results in more than 10dB additional improvement for delays shorter than the CP. Finally, with delays much longer than the CP, all the techniques employing LMS for data estimation converge to a $rSNIR$ approximately 10dB higher than the crude linear interpolation.

The advantages of using a *CP=128* over *CP=64* are intrinsic to the OFDM method which is used in the DVB-T system. The performance gain obtained by the use of LMS is due to its robustness in dealing with noise and/or interference. The extra improvement achieved by the cubic interpolation (at the cost of additional complexity) is a result of a better ability in tracking high rate oscillations in phase and amplitude of the channel.

B. Using the time equalizer

In figure 7, we compare the methods based on LMS of the previous section with the *Equalizer+Data LMS* using a CP of 64 samples, which is the minimum allowed by the DVB-T standard.

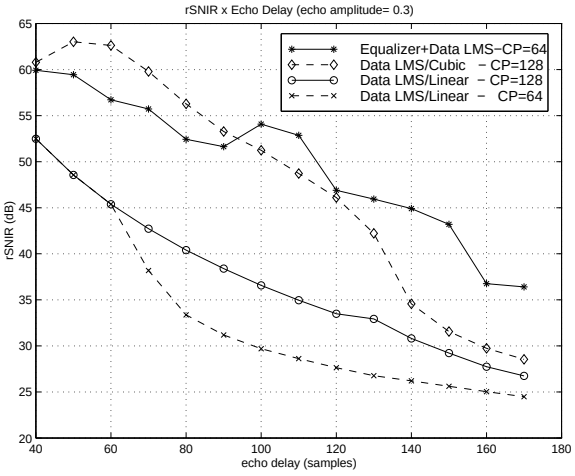

Fig. 7. Performance of the time equalizer.

As can be observed, the combination of the pre-FFT equalizer with the *Data LMS/Linear - CP=64* method improves the $rSNIR$ to a level comparable to the *Data LMS/Cubic - CP=128* for delays smaller than the CP, and even better for delays longer than the CP. In other words, the use of the pre-FFT equalizer preformed better than doubling the cyclic prefix length and using a more complex cubic interpolation. See also the next section for an explaination on the oscilating behaviour of the resulting curve.

As a matter of ilustration, compare figure 8, which is the constellation received in the last DVB-T frame of the simulation using the time equalizer, with figure 9, in which the time equalizer was turned off.

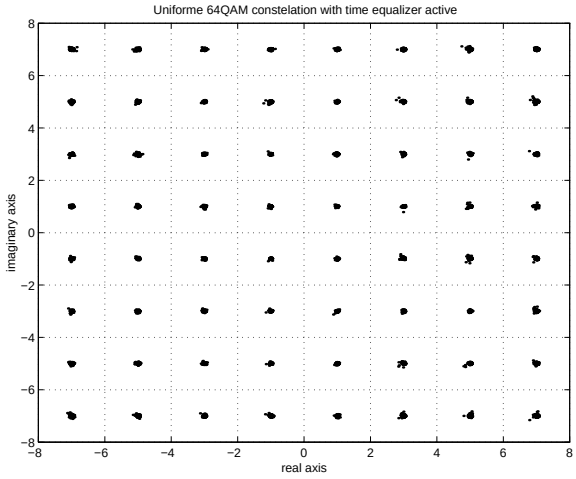

Fig. 8. Delay=100samples, amplitude=0.3: time equalizer on.

The introduction of the time equalizer strongly reduces the amplitude and phase oscilations of the channel estimated by the *Data LMS/Linear* algorithm. For low oscilations, it does not make much difference to use a linear or a cubic interpolation algotithm. In order to confirm this, we also run the *Equalizer+Data LMS* using a third order polynomial interpolation with almost no improvement in the $rSNIR$ (not plotted in this article).

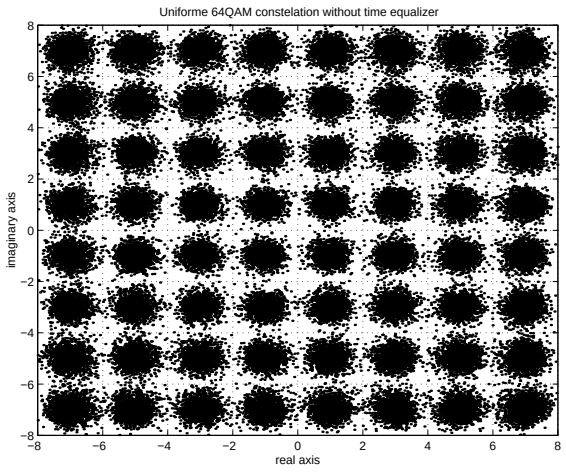

Fig. 9. Delay=100samples, amplitude=0.3: time equalizer off.

C. Edge effects

An effect rarely mentioned on the literature but that affects time equalization performance, and also some blind channel estimation techniques, is the presence of null carriers at the margins of the spectrum. This is standard procedure in most OFDM systems to provide guard bands and prevent interference between adjacent channels, and is used in the DVB-T system.

The presence of the null carriers impossibilitates the estimation of the desired frequency response for the equalizer since they provide no information on the channel response itself. Unhappily, when obtaining the equalizer coefficients by the use of the IFFT, we need a full-channel frequency response. We tested 2 possible solutions for this problem:

- *Average Response*: set the entire margins of the spectrum to the average of the estimated spectrum at the non-null pilot carriers;
- *Repeat Last Estimate*: set the left margin of the spectrum to the estimate obtained at the leftmost pilot carrier and the right margin to the estimate of the rightmost pilot carrier.

Figure 10 shows the results of simulations for both cases. As seen, the *Average Response* method gives the worst results, adding a ground noise that prevents the $rSNIR$ from getting better than 50dB.

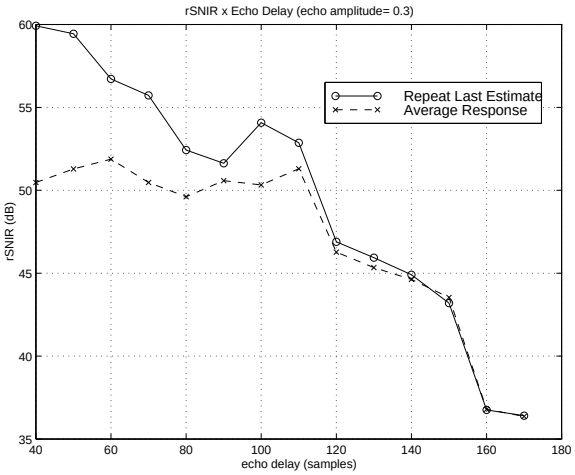

Fig. 10. Effect of the extrapolation algorithm used for null carriers.

This behaviour can be explained by the fact that the higher the order of the first discontinuous derivative of the impulse response of a signal, the faster its spectrum decreases [13]. The same is valid when going from the frequency response to the impulse response. By setting the margins to the average of the estimated spectrum, we introduce a discontinuity at the zeroth order derivative; by repeating the last estimate we set the first discontinuity at the first order derivative. So, in the *Repeat Last Estimate* algorithm, we get smaller lateral lobes on the impulse response of the equalizer and a better performance. This suggests that a more adequate transition algorithm that delays the first discontinuity beyond the second derivative may offer even better results.

The oscilations observed in the $rSNIR$ curve are a result of better and worse transition conditions at the left and right boundaries. Since a high amplitude single echo, as we used in the simulations, results in a channel with high amplitude and phase oscilations, depending on the delay chosen sometimes the last pilot carrier used for estimation (on left and right margins of the spectrum) falls in a better or worse boundary condition.

V. Conclusion and final comments

The main contribution of this work is to devise a new adaptation algorithm for a FIR pre-FFT equalizer to be used in OFDM systems, whose complexity is well within the capabilities of current technology. We started from an unstable version and introduced a new LMS algorithm, specially suited for OFDM systems, that proved to be very stable and reliable. We also tested different channel estimation techniques to be used in combination with the time equalizer, taking advantage of the specific characteristics of each method.

We present simulation results that show that the introduction of the pre-FFT equalizer in an uncoded DVB-T receiver with a 1/32 cyclic prefix (CP) resulted in much better performance than doubling the CP. In fact, for echo delays longer than the CP the performance was even better than simultaneosly doubling the CP and changing the interpolating algorithm at the channel estimation stage from linear to cubic (third order interpolating polynomial).

The current work is just at the beginning and opens space for a lot of future studies such as:

- We have limited the number of taps of the equalizer to 512 to keep its complexity under reasonable terms. However, the pre-FFT equalizer could profit from changing to a better topology than a simple FIR. The challenge here is to find a creative low complexity solution to go from the frequency response estimated by the modified LMS algorithm to the equalizer parameters;
- Since the DVB-T system does not allow the use of a zero length CP, we limited the initial tests to the shortest possible alternative (1/32) for consistency. On the other hand, there is nothing in the proposed algorithm that requires the use of a CP. The variant of the LMS algorithm used is based on the minimization of the frequency response error on the pilot carrier positions, no matter if that error is due to a short CP or to a long echo delay;
- The simulations were conducted using a single echo of high amplitude (0.3) and long delays. Although this is a very unfavorable condition due to the high amplitude and phase oscilations of the channel response, it would be very interesting to make tests with more realistic channels, including time variant ones;
- It was pointed-out on section IV-C, when we described edge effects, that further improvements may be obtained if a better algorithm is used to extrapolate the channel response to the null carriers at the left and right borders of the spectrum.

We will soon start tests on these directions.

References

[1] R. van Nee and R. Prasad, *OFDM for Wireless Multimedia Communications*. 46 Gilligham Street, London SW1V 1AH: Artech House, 2000.

[2] ETSI, “Digital Video Broadcasting (DVB); Framing structure, channel coding and modulation for digital terrestrial television.” Padrão ETSI EN 300 744 v1.4.1, publicado pelo European Telecommunications Standards Institute, Janeiro 2001.

[3] S. Armour, A. Nix, and D. Bull, “Performance analysis of a pre-FFT equalizer design for dvb-t,” *IEEE Transactions on Consumer Electronics*, pp. 544–552, Agosto 1999.

[4] R. S. Sherrat and S. L. Linfoot, “Deterministic equalization and results of a DVB-T multipath equalizer for both 16-qam and 64-qam operation,” *IEEE Transactions on Consumer Electronics*, vol. 49, pp. 21–26, Fevereiro 2003.

[5] S. Armour, A. Nix, and D. Bull, “Complexity evaluation for the implementation of a pre-FFT equalizer in an ofdm receiver,” *IEEE Transactions on Consumer Electronics*, pp. 428–437, Agosto 2000.

[6] P. S. R. Diniz, *Adaptive Filtering - Algorithms and Practical Implementation*. Kluwer Academic Publishers, 1st ed., 1997.

[7] ARIB, “Transmission System for Digital Terrestrial Television Broadcasting.” Padrão ARIB STD-B31 Version 1.0, publicado pela Association of Radio Industries and Businesses, Maio 2001.

[8] B. Muquet, M. de Courville, and P. Duhamel, “Subspace-based blind and semi-blind channel estimation for OFDM systems,” *IEEE Transactions on Signal Processing*, vol. 50, pp. 1699–1712, Julho 2002.

[9] F. Sanzi and J. Speidel, “An adaptive two-dimensional channel estimator for wireless OFDM with application to mobile DVB-T,” *IEEE Transactions on Broadcasting*, vol. 46, pp. 128–133, Junho 2000.

[10] ETSI, “Broadband Radio Access Networks (BRAN); hiperlan type 2; physical (PHY) layer.” Padrão ETSI TS 101 475 v1.3.1, publicado pelo European Telecommunications Standards Institute, Dezembro 2001.

[11] ANSI, “Network and Customer Installation Interfaces - Asymetric Digital Subscriber Line (ADSL) metallic interface.” Padrão ANSI T1.413-1998, revisão do ANSI T1.413-1995, publicado pelo American National Standards Institute, Inc., 1998.

[12] ATSC, “ATSC Digital Television Standard - Doc. A/53b.” Revisão B do padrão Doc.A/53, publicado pelo Advanced Television Systems Committee, Agosto 2001.

[13] R. W. Hamming, *Digital Filters*. Dover Publications, 3rd ed., 1998.

A simulation tool: analysis of ISBD-T

Luís Eduardo Antunes de Resende
CETUC - PUC Rio
Rua Marquês de São Vicente 225
Ala K - 7° Andar
Rio de Janeiro - RJ - Brazil
luisres@cetuc.puc-rio.br

Weiler Alves Finamore
CETUC - PUC Rio
Rua Marquês de São Vicente 225
Ala K - 7° Andar
Rio de Janeiro - RJ - Brazil
weiler@cetuc.puc-rio.br

***Abstract*— A computer program developed to analyze the performance of DTTB (Digital Terrestrial Television Broadcasting) data transmission is here discussed and presented. All configurations proposed by the ISDB-T (Integrated Services Digital Broadcasting - Terrestrial) standard have been examined with this tool — although discussion was primarily based on this standard, the tool is adequate, with minor changes, for other standards as well. Results illustrating the transmission over AWGN channels and AWGN plus multipath are included.**

***Index Terms*— Digital TV, Channel coding, Bit Error Rate (BER).**

I. Introduction

A tool which has been developed to assess the quality of DTTB systems trough simulation will be presented and discussed in this paper, together with some preliminary analysis results. DTTB systems are replacing the conventional TV systems, bringing high quality video and audio plus many other new services. HDTV (High Digital Television) is one of the new services, and probably the most important one. The other services are SDTV (Standard Digital Television), hierarchical transmission, program interactivity, e-commerce, internet access and so on. In such a scenario, ISDB-T which is one of the three developed standards currently proposed, plays an important role.

To accommodate all these new services, the transmission method has able to be sufficiently flexible and extendible. The DTTB system must also be resistant to multipath and fading interference that portable and mobile reception are possible, be extendible enough to ensure that future needs are met, use frequency effectively and be compatible with existing analogue services and other digital services.

The three standards proposed have very similar structures, composed basically by a concatenated coding (outer code followed by an interleaver and by an inner code). A Reed-Solomon coding scheme was a choice common to all standards as the outer code because of its excellent performance in correcting burst errors. Also the interleaver is a common solution adopted by each standard (each one with its own proposal). Finally the inner code goes from Trellis Coding used by the American standard (ATSC - Advanced Television System Committee) to Punctured Convolutional Coding used by DVB-T (Digital Video Broadcasting Terrestrial) and ISDB-T [1], [2].

The computer program that has been developed currently simulates the ISDB-T procedure but with minor changes it can be adapted to simulate the other procedures as well.

The paramount difference between the standards resides in the modulation technique. ATSC uses a single carrier modulation scheme to achieve high video and audio performance while DVB-T and ISDB-T use multiple carrier modulation technique. The American system uses 8-VSB: bits driven to 8-PSK modulators generate the digital modulated signal to be carried by a Vestigial Side Band signal. DVB-T and ISDB-T bit stream have a choice of three different digital modulators (QPSK, 16-QAM and 64-QAM) — discrete time digital modulated signal is then carried by the multiple carrier technique known as OFDM (Orthogonal Frequency Division Multiplex). In brief a vector with complex components entering an IFFT (Inverse Fast Fourier Transform) module followed by an digital/analog conversion constitutes the OFDM procedure. In order to lessen the ISI (Inter Symbol Interference) problem the frame that enters the IFFT section of the OFDM module is composed by the aforementioned complex vector augmented by guard interval samples.

II. ISDB-T

The japanese DTTB standard [1], [2] was developed to achieve all services listed. ISDB-T is composed by 13 segments, which can be grouped in up to 3 layer. Each layer accommodates one MPEG2 program and can be differently configured. Taking advantage of the commonality with other media, the transport signal of ISDB-T utilizes the MPEG2 Transport Stream (TS). The TS has a frame structure called multiplex frame, so that a single TS can be applied to hierarchical transmission. The number of TS packets constituting a multiplex frame depends on the configuration chosen on the layer. The multiplex frame is synchronous with the OFDM frame. Although the number of TSPs transmitted by an OFDM signal varies according to properties of OFDM segments, the TS can connect a Reed-Solomon (RS) decoder to a TS decoder at a single constant clock by inserting an adequate number of null packets. The transmission clock of TS is four times faster than that used for FFT sampling in wide band ISDB-T and 2 times faster than that used in

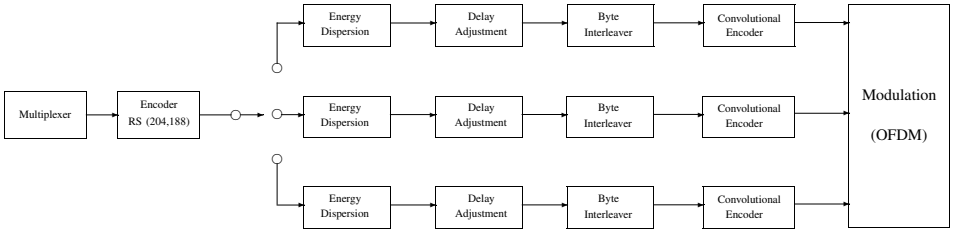

Fig. 1. Channel coding block diagram

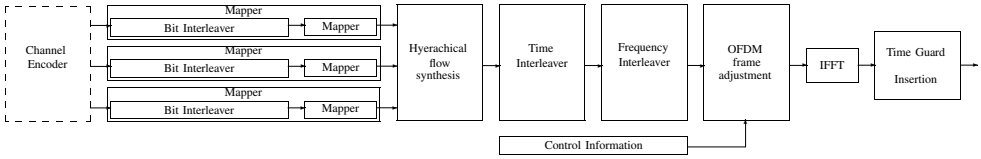

Fig. 2. Modulation block diagram

narrow band receivers. Therefore receivers can use one common clock for OFDM signal and transport signal.

The outer code is a shortened RS(204,188) which is responsible to introduce parity bytes on TSPs, to avoid channel interferences. The energy dispersal and byte interleaver then randomizes data for robustness against burst errors. Following, the inner code introduces more parity information. A convolutional coding scheme allows 5 different coding rate (1/2, 2/3, 3/4, 5/6 and 7/8). The channel coding block is presented in Fig. 1.

ISDB-T allows to set one different carrier modulation schemes (DBPSK, QPSK, 16QAM and 64QAM) in each layer. This feature provides the flexibility needed by DTTB systems. The modulation block is followed by time and frequency interleaver, which randomizes the symbol position inside the frame. Control information, which is composed by TMCC, auxiliary channels (AC1 and AC2) and reference carriers, are then inserted on the OFDM frame. IFFT is a mathematical tool responsible for OFDM and to finish the modulation process an interval guard (IG) is then inserted in front of the frame. IG is composed by a piece of copy of the same frame. The receptor have to do the inverse process in order to restore the transmitted MPEG2 program. The modulation coding block is presented in Fig. 2.

TMCC carrier carries the information of modulation schemes and MPEG2-TS ID, which is assigned to the slots. The system can deal flexibility with various requests on these transmission schemes by means of TMCC signals. The configuration for receivers is automatically changed to demodulate the appropriate signal format.

III. Simulation

The simulation tool was developed according to the ISDB-T documentation [1], [2], and MATLAB is the language chosen. This tool is composed by blocks, which eases changes and modifications on the standard. The results are BER $versus$ $E_B/N0$ graphs which shows the performance of each possible system configuration working on an AWGN channel, characterized by variance $^2_n = N_0/2$.

Multipath is one of most disturbing channel interference, and was considered and implemented on the simulation tool. The 2 ray model was chosen according to [5], which specifies attenuation and delay model. This model is an outdoor scenario where the second ray has 9dB attenuation and 110nS delay.

This tool randomly generates the input data systems, simulating a MPEG2 program and compares with the received data. The results of this comparison is expressed by BER curves, according to Figs. 4-9 in the end of this paper.

All possible different parameters of the system can be tested, in order to compare each choice. These parameters are: transmission mode, modulation scheme, convolutional coding rate, time interleaving parameter and IG. The transmission mode parameter selects the number of carries that system must work. Mode 1 configures 2048 carries, Mode 2, 4096 and Mode 3, 8192 carries. The possible modulation schemes were lately presented (DBPSK, QPSK 16QAM and 64QAM), in the same manner with the possible convolutional coding rates. According to the channel behavior, a convolutional coding and modulation scheme is select. The trade-off is protection or throughput, because as long as the configurations adopted inserts more protections on data, the throughput is reduced and vice versa. The time interleaver is responsible to spread the symbols, in order to promote a randomization effect on data. This technique minimizes bursts errors, but increases data latency.

IV. Results

A sample of the results obtained with the simulation tool are shown on Figs. 4, 5, 6, 7 and 8. Each curve displays the bit error probability (BER) observed on the points A, B and C of the ISDB-T structure selected as shown on Fig. 3. Observation on point A will render the BER between bits which were transported from the channel input and the correspondent output bit. On point B the BER between bits at the input and the corresponding bits at the output can be assessed. Point C allows to observe the final system performance. Graphs with performance over AWGN as well as

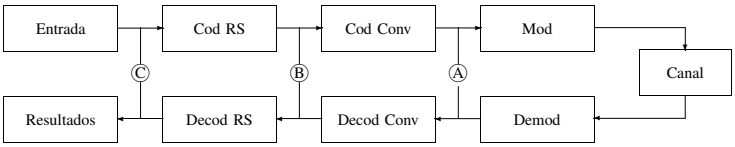

Fig. 3. Points on ISDB-T where the results are collected

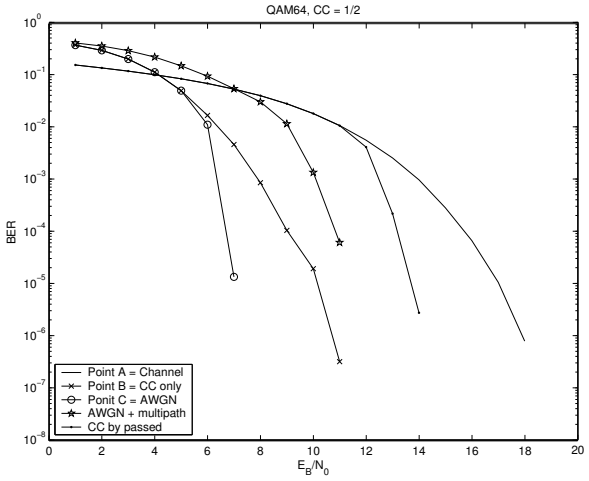

Fig. 4. BER x E_B/N_0 Mode 3, QAM64, R_C = 1/2

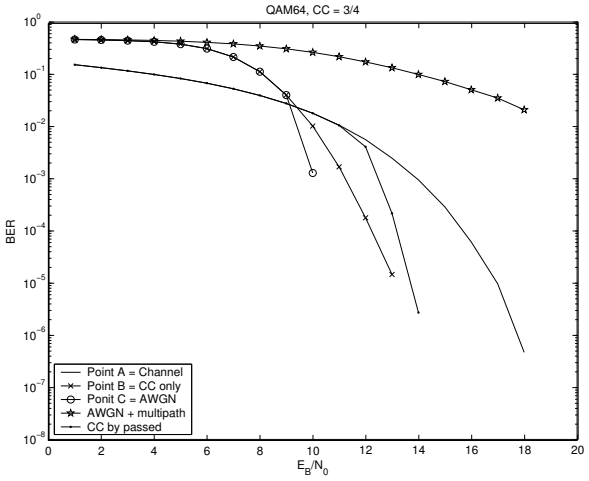

Fig. 6. BER x E_B/N_0 Mode 3, QAM64, R_C = 3/4

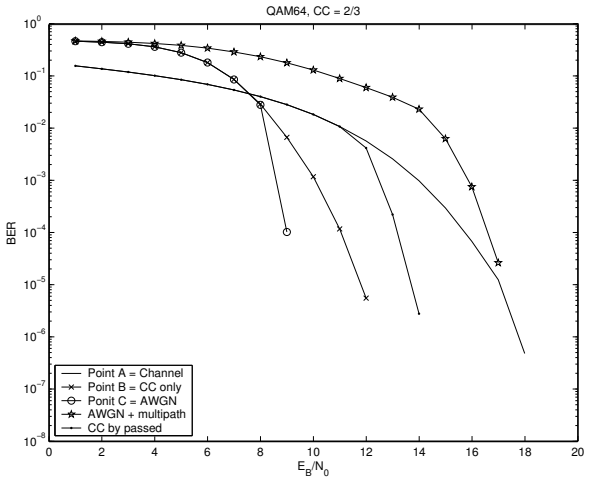

Fig. 5. BER x E_B/N_0 Mode 3, QAM64, R_C = 2/3

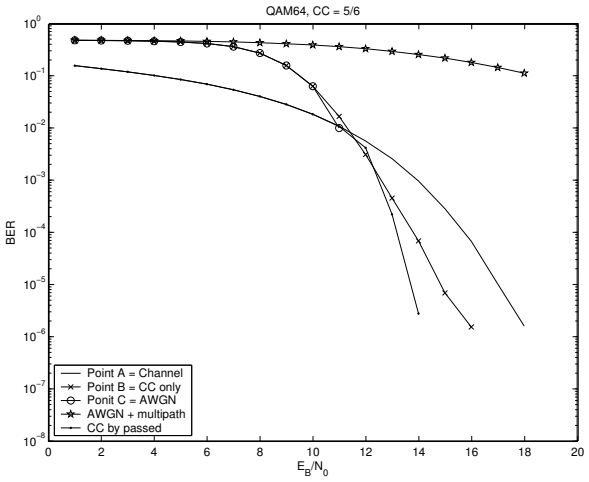

Fig. 7. BER x E_B/N_0 Mode 3, QAM64, R_C = 5/6

over AWGN and multipath are also presented on this figures.

One more scenario was tested, which punctures the convolutional coding. Comparing the result of this scenario with the result of the default scenario, is possible to mensure the effects promoted by the convolutional coding. This effects dependes on the $\frac{E_b}{N_0}$, and can provide a BER improvement or a BER degradation.

Simulation results displaying the performance of ISBD-T configured on Mode 3 with a rate $R_c = \frac{1}{2}$ convolutional code and 64-QAM modulation is exhibited on Fig. 4. Similar results are displayed on Fig. 5 trough Fig. 8. Figure 9 presents a BER curve comparison among all possible convolutional coding rates. It can be observed that BER performance gets worse as long as a greater convolutional coding rate is used.

These graphs shows the BER performance improvement that can be achieved by the convolutional coding and by the RS as well, when $\frac{E_b}{N_0}$ is high. Simulation shows the enormous performance degradation in the presence of multipath distortion.

It is worth mentioning that our simulation incorporates the use of the control channels TMCC (Transmission and Multiplexing Configuration Control). Also the auxiliary channels AC1 e AC2 are incorporated in the simulation model. One should notice that, if TMCC information is corrupted by the channel disturbances, the system will lose configuration information and it might not be able to retrieve the information

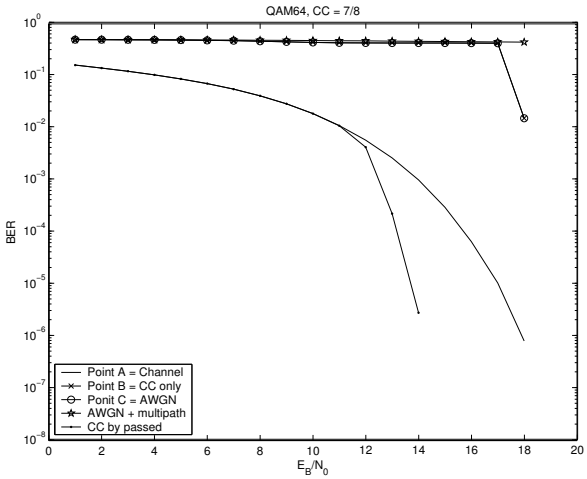

Fig. 8. BER x E_B/N_0 Mode 3, QAM64, R_C = 7/8

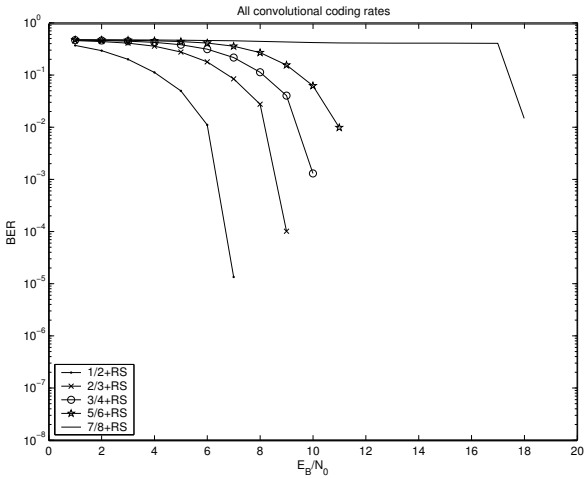

Fig. 9. BER x E_B/N_0 Mode 3, QAM64, all CC rate.

transmitted by the source (a "black screen" may take place if the last configuration were not used). Also notice that auxiliary channel data are transmitted with no protection against channel impairments — if the protection is needed, the standard assumes it has to be provided by the application layer.

V. Conclusion

A simulation tool has been developed and used to analyze the performance of ISDB-T — with minor modifications, other well established standards can also be handled by the simulation program.

The current article exhibits the importance and usefulness the tool by examining the system performance in simple scenarios. It can be also helpful in the development of new standards or as an aid for system management and operation.

References

[1] Association of Radio Industries and Businesses, *Transmission System for Digital Terrestrial Television Broadcasting*, ARIB, 2001, May.

[2] ITU - Radio Communication Study Groups, *Channel coding, frame structure and modulation scheme for ISDB-T*, International Telecommunication Union, 1999.

[3] Simon Haykin, *Communication Systems*, John Wiley and Sons.

[4] Harada Prasad, *Simulation and Software Radio for Mobile Communications*. August 2002.

[5] Fakhrul Alam, *Simulation of Third Generation CDMA Systems*. Virginia Polytechnic Institute and State University, December 1999.

A Multimedia Framework for Mixed Reality TV Shows

Milena Radenkovic, Steve Benford
School of Computer Science and IT
Jubilee Campus
University of Nottingham
Wollaton Road NG81BB
Nottingham, UK
mvr@cs.nott.ac.uk

***Abstract*—This paper is concerned with multimedia architectues for supporting produciton and post-production of mixed reality TV shows. Such shows introduce a set of novel and challanging requirements that cannot be supported by currnet multimedia srevices. This paper proposes a prototype service-oriented intergarted multimedia middleware that is semanticlaly rich and driven by both network and user requirements.**

***Index Terms*—Mixed Reality, Multimedia Networks, Multimedia-Content analysis.**

I. Introduction

Mixed reality TV shows are based on Mixed Reality games and Inhabited TV that combine fixed and wireless networking in new and unconventional ways that stretch existing views of multimedia to provide support for broader set of users that reach out to the real world. Mixed Reality Games are new games that mix street and online players. Goals of our research have been to develop distribution and interface technologies, demonstrate applications and understand user experience. Inhabited television sees the combination of collaborative virtual environments (CVEs) and broadcast TV to create a new medium for entertainment and social communication (Benford, 2000). The defining feature of this medium is that an online audience can socially participate in a show that is staged within a shared virtual world. The producer defines a framework, but it is the audience interaction and participation that brings it to life. A broadcast stream is then mixed from the action within the virtual world and transmitted to a conventional viewing audience, either as a live event or as a post-produced and rendered broadcast stream. Inhabited TV has been a topic of research since 1996 through projects such as *TheMirror* (Illuminations Television/BT/BBC) and *Heaven and Hell Live!* (Illuminations Television/BT/Channel 4). At the time of writing, we are seeing the first commercial examples of inhabited TV beginning to appear on mainstream television, for example the current show *Fightbox* from Richochet/BBC. Our own research into inhabited TV has unfolded through a series of collaborative projects that explored different aspects of the user experience and production technologies. In 1998 we staged a live inhabited TV show called *Out of This World* (University of Nottingham/Illuminations TV/BT) that demonstrated how dedicated virtual camera and participant management technologies could be used to create a relatively fast-paced and coherent gameshow within a CVE (Greenhalgh, 1999). In 2000, in a follow-on project called *Avatar Farm*, we attempted to create a more complex show which took the form of an online drama in which members of the public and professional actors collaborated as part of a non-linear drama of four chapters that roamed across four virtual worlds (Craven,2001). A key feature of Avatar Farm was that we made use of a 3D record and replay mechanism for collaborative virtual environments that was implemented in the MASSIVE-3 system (Greenhalgh 2002) to enhance the experience in several ways:

- Our actors improvised and recorded several scenes in the virtual world on the day before the show. These pre-recorded scenes were then replayed during themain show as, enabling the live participants to move among a series of ghostly flashbacks as shown in figure 1 down.
- We saved the whole of Avatar Farm as a series of 3D recordings and subsequently created a series of interfaces to support observers in exploring the story, moving through the action and following different characters such as the table interface.
- We demonstrated the possibility of exporting selected parts of these 3D recordings into conventional animation tools so that offline rendered animations of the action could be made as shown in figure 1 right.

One of the potential problems with inhabited TV is the visual quality of the material produced from CVEs. Certainly our early discussions with broadcasters consistently raised the concern that the quality of the real-time computer graphics was insufficiently rich to provide a compelling viewing experience, for example that avatars were insufficiently expressive for viewers to be able to empathise with them. The current approach taken by the currnet inhabited TV shows is to mix the computer graphics with conventional video

footage of real actors and players. These shows are typically set within a studio environment, providing the possibility of mixing footage of the human players and a studio audience with computer graphics. Postproduction of the computer graphics to create offline rendered animations that can match the quality of current cartoons and animated films. The tools and techniques that we introduce in this paper are intended to support both approaches.

We illustrate this paper with an example of a possible inhabited television show –making a television show from the mixed reality game Can You See Me Now (CYSMN). CYSMN is a chase game. Up to fifteen *online players* at a time, logged in over the Internet, are chased through a virtual model of a city by three *runners*, professional performers, who are running through the actual city streets equipped with handheld computers, wireless network connections (using 802.11b) and GPS receivers. The online players can move through the model with a fixed maximum speed, can access a map view of the city, can see the positions of the other players and the runners, and can exchange text messages with them. The runners move through the streets, can see the positions of the online players and other runners on a handheld map, can see the players' text messages and can communicate with one another using walkie-talkies. A key feature of the game is that the runners' walkie-talkie communication is streamed to the players over the Internet, providing them with ongoing description of the runners' actions, tactics and experience of the city streets, including reports of traffic conditions, descriptions of local topology and the sound of the physical exertion involved in catching a player. If a runner gets to within five virtual meters of an online player, the player is 'seen' and is out of the game (their score is the time elapsed since joining the game). Runners also carry digital cameras so that they can take a picture of the physical location where each player was caught and these pictures appeared on an archive web site after the event.

II. Motivation

We are interested in adopting CYSMN as the basis for an inhabited TV show – as are other bodies such as the Arts Council who have provided funding for creating a pilot in collaboration with a broadcaster – believing that it offers a rich way of engaging real-world participants with a virtual environment.

This paper considers the production process for creating an inhabited TV show based upon CYSMN and identifies technical challenges. Our starting assumption here is that in order for online players to be real viewers- members of the public – the game needs to be initially played live and a TV broadcast then created from the material that is recorded, rather than pre-scripting all of the action and then shooting the show scene by scene. In other words, the process is essentially one of creating a TV show of a live event (this is not to say that the TV show itself has to be live – but the event does): Key activities in the production process are as follows.

- Designing and staging a (revised) live experience.
- Recording the live experience:System-state recording of online action. Video recording of street action using (instrumented) fixed, steerable and mobile cameras
- Reviewing, selecting and overdubbing the material: Select key scenes (e.g., chases), Review them – repeatedly watch and compare online and video material side by side, Overdub selected online or video action
- Animating and rendering

Figure 1 Mixed Reality games and TV shows

III. Prototype Architecture

The paper proposes a prototype service based infrastructure that provides access to very large scale multimedia resources, computing and visualising tools to multidisciplinary teams. The middleware architecture exposes pool of multimedia resources as services to allow rich real-time interaction with the resources and to keep rich provenance data about heterogeneous types of recordings. The infrastructure is shown in figure 2. At one end of the architecture is the Mixed Reality (MR) Show production team, game developers and network providers who require access to large scale multimedia and computing resources, high performance visualisation back end and network logs. At the other end are actual physical and virtual players, a number of sensors, GPSs, cameras, IPAQs

that generate the data that are stored in the MR Recordings Repository. Distributed Mixed Reality Multimedia Recordings Repository lies in the heart of the proposed architecture and consists of rich data and metadata of heterogeneous recordings. We have identified the following types of recordings (streaming log files): video and audio recordings in various formats including proprietary (such as MASSIVE 3), non-proprietary and RTP dumps, sensors logs, Massive 3 recordings consisting of checkpoints and event logs, EQUIP recordings consisting of checkpoints and event logs, console logs and TCP dumps. The recordings are associated with related resources such as: Geometries, Texture, Software components and Types. Note that a recording can be *compound* i.e. include multiple overlayed recordings. Each recording (simple of compound) describes what the file is, where it came from, what we can do with the recordings (i.e. this includes which tools, applications and/or components that we can associate with them), specify how the recordings relate to both the external/nominal references and to each other (i.e there is a number of dimensions according to which these relationships can exists including: time, physical space, information, subject, genre) and finally describe what is in the file and the structure of the file (i.e. allow for multiple substreams within the current stream with sequential or random access). The paper introduces the structural description scheme of the recordings. Service Repository and Service type Service include a number of instances and types of proprietary and non-proprietary tools that we aim to expose as services for interoperability reasons. These tools include tools for extracting interesting scenes, visualising them, cross indexing and synchronising the recordings. Due to high complexity of the architecture design, at the moment, the workflow engine and workflow repository target to currently support only limited number of workflows.

To cope with volatilioty of the environment legacy services, we adopt two layers of abstraction: a gateway and component model. A gateway provides optinal unified single point of programmatic access to the whoel system, for easy of user, especially from diverecse laguages and legacy applications. This isolates the end user (and the client software) from the detailed operation and interaction of the core architecture and “add value” to the architecture with respect to the personalisation, provenenace and collaboration. Gateway deals with single sign on and certification managed by the application. A component model abstracts over many service delivery mechnisams used by the community in order to allow service developers and providers to separate concerns in their buisness logic from on-the-wire protocol specifications, and service providers to configure service behaviour, such as fault tolerance and security. Client interact with services in protocol independent manner. For example, when a user interacts with a service, it may appear that the service exposes metadata when in fact this is being added in transit through the gateway.

Synchronisation engine is of key relevance when condiering replay multiple recordings. Synchronisation can happen in time and also otehr aspectssuch as overlap space. Till now we have experimented with replaying a recording within a
live environment (Figure 1 down). This requires that environments are linked to themselves in the past.

Simplest workflow enabled by the workflow engine involves user replaying recordigns/log files through their preferred standalone viewing client. The tasks within this workflow might comprise displaying canonical view of events (e.g., as seen by a central server); choosing appropriate viewpoint manually (by the user) or automatically (transparently from the user where the user specifies the rules in advance or chooses from a set of offered rules); showing participants what happened during the show after the show has finished and promting them to annotate parts. More complex workflows would involve multiple simultaneous clients viewing the same replay, collaborative analysis or synchronised viewpoints. An example of highly configurable workflow is when at some stage a workflow involves replaying selected parts of recordings e.g by participant, object type, event type, location, time. Besides requiring facility to directly jump to a specified time (e.g., ‘checkpointing’), this also requires rich semantic descriptionsthat can allow transparent cross-indexing and cross-referencing of the recordings.

IV. Semantic Discovery and Metadata Management

Our basic object can be definedas any idnetifyable entity that plays role in a MR show production and post-production. Thus, a data entry in a database, a workflow specification, a concrete workflow, a servicer, an annotatoin, a link between a concrete workflow and the dta collection. A show producer ned knoweldge to fin data collections nd use these objects, and form workflows or form queries effectivley and efficienlty.

A key feature of the proposed architcure is the incorporation of the specialist knowledge into semanticlaly rich description of services and the objects they exchange and act upon them. This knowledge is used thoughout: for example to linktogther components or find links, to find workflows or validate them etc. Our services and objects carry a range of descriptions: “operational” metadata detailing their origins, quality of service and so on; structural descriptions detailing their types (audio, video, image, string, sequence, measurement data, collections etc) or signatyures (input, output, portType); and semantic description that cover what they mean (a scene, a leading character, a shadow).

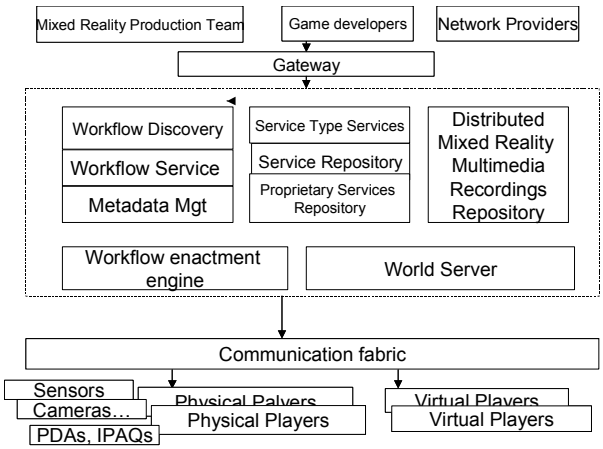

Figure 2 Prorotype Architecture for MR Shows

We have been experimenting with metadata attched to objects, so that it becomes possibel to determine what can be done with an object regardless of how it was produced. Metadata is also attached to services to determine the types of objects being cinsumed and produced.

Providers publish their services, and consumers find and match services and obejcts, by a range of mechanisms such as name, words, signatures, types and in praticular ontological descriptions. For semantic service and object discovery we use techniques form the Semantic Web. B oth data and services are semanticaly annotated usign ontologies represented in RDF/XML based semantic web ontology languages DAML+OIL [Hendler J, 2003] and OWL (http://www.w3.org/TR/owl-ref/). Using automatd classification-based reasoning over concept descriptons it is possible to classify and match services (with degrees of imprescision), negotiate service substitutions and relate database entries to service inputs and outputs based on their semantics. It is possibel that services (am for that matter obejcts) may be descibed using (mulitple) ontologies, and descriptions by third parties for users who wish to personalise their choice of services, including those they do not own themselves.

Service registration uses a multi-level service model distingushing between "classes" os services and "insatnces" of services. The latter are real services/tools that may have many copies distributed across the Internet, whereas the former are abstract notions of services.

V. RECORDINGS

A. *Types of Recordings*

Apart from DV, VHS or DAT tapes that have been used in some projects, we identified the following types of file recordings:

- Video recordings in various formats including mpeg, avi, QT or proprietary such as Massive 3, RTP dumps
- Audio recordings in various formats including mp3, proprietary such as Massive 3, RTP dumps
- Sensor logs
- Massive 3 recordings consisting of checkpoints and event logs
- EQUIP recordings consisting of checkpoints and event logs
- Console logs
- Tcp dumps

The recordings are associated with related resources such as:

- Geometries
- Texture
- Software components
- Types

A. High level Overview of the Requirements for Modelling the Recordings

We found that at least the following data, metadata and relationship need to be defined and modelled:

- We need to describe what the file is. This includes paths and URLs of the files.
- We need to describe where the file came from. This refers for example whether a human recordings a video or the recordings comes form a particular sensor or tcpdump.
- It is very important to model what we can do with the recordings. This includes which tools, applications and/or components that we can associate with them. We propose to use different MIME types for this.
- We need to specify how the recordings relate to both the external/nominal references and to each other. There is a number o fdimenstion sacccording to which these relationshsips can exists including: time, physical space, information, subject, genre
- We need to describe what is in the file.
- We also want to describe the structure of the file and allow for multiple substreams in it with sequential or random access.

C STREAMING RECORDING DESCRIPTION SCHEME

The structural description scheme of the recordings should at the very least include the following:

Overall Structure:

RecordingID -- unique ID for the recording
RecordingName -- human readable name of the recrding
RecrodingType -- as described in the first section of the document
RecordingLocation (where it is stored) -- URL/path of the recroding
RecordingLocalTimecode -- local timecode
RecordingStartTimecode -- calibrated timecode
RecordingStopTimecode -- calibrated timecode
TimecodeReferencePoint -- endpoint used to calibrate
TimeOfSynchronisation -- local time of last callibration

CalibrationAlgorithm --- algorithm /method tool used to do time calibration
PointerToListOfSubstreams -- pointer to Ids of the substreams that are part of the structure e.g. in case of video having multiple audio streams
Annotations -- space to allow annotations about he structure

Media Information:

RecordingBitrate -- bitrate of the recording
RecordingFramerate --- framerate of the recording
RecordingSize -- size of the recording
RecordingDuration -- duration of the recording
RecordingMediatype -- e.g. audio, video,animation
MIMEtype -- MIME type of the media
MediaFormat -- (e.g., RealMedia, Windows Media, QuickTime)

Creation/annotationInformation:

RecordingAuthorID -- who recorded the recording
RecordingAccessRights -- e.g. read-only, write-only, read-write
RecordingContectOwner e.g.school, BlastTheory, Hospital

Classification:

RecordingCategory -- root nodes of our taxonomy
RecordingGenre -- can represent a path from the root using our controlled vocabularies (to be developed)

Related Material: Referring page URL(s), title, anchor text, HTML meta tags (e.g., description, keywords)

PointerToExternalReferences -- ((MIME)type of the reference, URL of the reference, dimension(s) (e.g. time physical space, subject..))
PointerToRecordings (URL of the reference, dimension(s) (e.g. time physical space, subject..))

VI. Basic User Requirements

The proposed architecture draws its inspiration from the vision of grid that aims to create an infrastructure that enables flexible coordinated resource sharing among multiple interdisciplinary teams. This section describes the requirements identified by the MR team production. The basic reuirment is the disovery of a workflow that match design goals of the producers. This is based on enabling matching input to the workflows. In MR show productin and pos-productin input data are often colletions and the user may well need to select only a subset of those input data for the input to the workflow.For example, the user might want to match a particular character description to existing scenes or contexts of similar characters and situations. This means that all of these must be recorder and tracable by the users.The architecture must also be able to assist the user when they beginthe process and during the process of a wokflow. This is done by offering a set of semantically similar tools from which the user will choose which ones they would use in order to do a particular operation. In our scenarios. Users will also need to interact with thrid party tools , particulalry the user interfaces of these toolsduring workflow enactment. Having completed the workflow, the user will wish to view results. There is a grand challenge in this requirement because all data are itnerlinked and the user will need to be assisted in viewing and managing this data. As new dta arrives in the reportory, tools change, new workflows of those already existing are modified, the user will wish to be notified. Having looked at the type of change, the user can make decision about repeating or performing a workflow. The user will also wish to make free textual annotations/commentary of data used, tools and services used that record their thoughts. More fundamantal to this is recording user's method, decisions, results and conclusions. This is refered to *proveennance* data about the workflow. We believe that all the data stored by the user has provenence: the workflows, the enactment of the workflows, the input and output data and the users themeselves.

VII. Network Layer

Given that in a production of MR games and shows there will be a large number of dynamically deployable heterogenious devices (camers and GPSs), an infrastructure is needed that will allow dynamic discovery of these devices over heterogenious netowrk conenctions. Fro example, we can not reply on all devices being eaqaly capable when storing, manipulating and transfering data to nearby servers. A peer-to-peer self-organised model is needed in order to accommodate wide network and end system hetereogneity and high pace dynamics. Our current implementation, described in [Radenkovic, 2004], is mainly network-driven with static pre-set application requirements. Our immediate future work will be directed towards extending this model to be semanticlaly aware.

VIII. Conclusion

The major motivation for this paper is increasing interest in mixed reality TV shows (based on location-based games). With recent advances in Grid technologies and multimedia applications we identifed the importance of state, resource, rich provenance, rich context in the face of transient services. Multiple projects that deal with record and reuse of large numbers of heterogeneous types of recordings e.g. sensor logs, audio, video, tcpdumps, rtp logs, console logs, M3 system state logs, EQUIP system state logs.

ese recordings need to be indexed, annotated, synchronised and replayed. This raises complex infrastructure challenges concerning event store, media synchronisation, calibrated camera set-up, indexing and annotation (human and/or automated), metadata (templates for specifying and verifying recorded data). The key controbution of the paper is the introduction of the new concept to cover heterogenious straming data called *Recording* and proposal for their common format. The paper prpoposed high middleware layered infrastrcuture that supports production and post-producition of Mixed Relity TV shows based on rich semantic descriptions of workflows

REFERENCES

[1] B enford S, Greenhalgh c, Craven M, Regan T, Morphett J, and Wyver j, *Inhabited Television: broadcasting interaction from within collaborative virtual environments,* ACM Transactions on CHI, December 2000, ACM Press

[2] Greenhalgh C, Flintham M, Purbrick J, Benford S, *Applications of Temporal Links: Recording and Replaying Virtual Environments*, Proceedings of IEEE Virtual Reality VR 2002, Orlando, Florida, 2002

[3] Radenkovic, M, *Framework for Scaleable and Adoptable Audio to Support* CVEs, PRESENCE, MIT Press, 2004

[4] Goble C., Wroe C, Stevens R., and the myGrid Consortium. *The myGrid project: Services, Architetcure and Demonstrator,* in Proceedings UK e-Sicne programmer All Hands Conference, 2-4 2003, Nottingham, UK, 2003

[5] Hendler J., *Scienc and The Semantic Web*, Science, page 24, Jan 2003

A New Fast Stopping Rule for Iterative Decoders

Massimo Rovini
European Space Agency, ESA-ESTEC,
Keplerlaan 1, 2200AG Noordwijk ZH,
The Netherlands
massimo.rovini@iet.unipi.it

Alfonso Martinez
Technische Universiteit Eindhoven, TU/e
Den Dolegh 2, 5600MB Eindhoven,
The Netherlands
P.O. Box 513 - tel: +31 40 245742
a.martinez@tue.nl

***Abstract*— This paper presents a new stopping rule for iterative decoders, with application to turbo-like codes. Based on an extended MAP algorithm that also outputs extrinsic estimates on the channel codeword, and on re-encoding of the hard decisions, the rule checks the consistency between the channel codeword and the hard decisions (IOC, Input–Output Consistency check). When used in Serial or Parallel Concatenation of Convolutional Codes, IOC closely approaches the ideal 'Genie' behaviour, in terms of both frame (bit) error rate and convergence speed.**

***Index Terms*— Stopping rule, Iterative decoding, MAP algorithm, Serial and Parallel Concatenation of Convolutional codes.**

I. Introduction

Turbo [1] and turbo-like codes [2] achieve error rates very close to the Shannon limit through iterative decoding. In practical implementation decoders usually run a fixed number of iterations, determined on the basis of a worst-case analysis, even though only a few frames need the full number of iterations. An early stopping criterion would not only save unnecessary computations and decoding delay, but also increase the decoder throughput or dually reduce the chip complexity thanks to architectures based on statistical multiplexing [3].

Several stopping rules have been proposed and studied in the past [4], some working with soft, extrinsic information, others with hard bits, some suitable only to parallel concatenation of convolutional codes (PCCC), others for both PCCC and serial concatenations of convolutional codes (SCCC). Among these, the Cross-Entropy (CE) criterion [5] considers the soft outputs of a PCCC scheme, whilst its simpler versions Sign Change Ratio (SCR) and Hard Decision Aided (HDA) make use of the hard decisions. The first one halts the decoding when the number of sign changes in the estimated sequence between two consecutive iterations, $C(i)$, normalized to the info bits frame size K, is less than a certain threshold δ, $C(i) \leq \delta \cdot K$. Similarly, HDA terminates the iterative process when the hard-bit estimates output by the decoder agree between two consecutive iterations over the entire block.

In this letter we present a new versatile stopping rule working with hard decision bits and suitable for any iterative decoder. Crucial to this rule is the availability at the decoder of a Maximum a Posteriori (MAP) estimate of the channel code bits, that must be computed as well.

II. Extended Soft Input Soft Output Decoder

The basic component of the iterative decoders for PCCC and SCCC is a MAP decoder [6]. Using the channel soft observations $\mathbf{r}$, the MAP algorithm computes the log-likelihood ratio (LLR) $L(u) \doteq \log\big(\mathrm{P}(u=+1|\mathbf{r})/\,\mathrm{P}(u=-1|\mathbf{r})\big)$ of each information bit u. In a (k_c, n_c) convolutional code, focusing on the trellis transition $s' \rightarrow s$ from the state $s_{k-1} = s'$ at time $k-1$ to the new state $s_k = s$ at time k, the information (input) bits $u_{k,i}$, $i = 0, ..., k_c - 1$ are encoded into the coded (output) bits $c_{k,j}$, $j = 0, ..., n_c - 1$. With a notation derived from [7], the LLRs of the info bits are computed as:

$$L(u_{k,i}) = \log \frac{\sum_{U_i^+} p(k, s, s')}{\sum_{U_i^-} p(k, s, s')} \tag{1}$$

where, for the sake of compactness of the notation, we defined $p(k, s, s') \doteq \mathrm{P}_\alpha(s_{k-1}{=}s') \cdot \gamma_k(s', s) \cdot \mathrm{P}_\beta(s_k{=}s)$, and U_i^+, U_i^- being the sets of valid pairs (s', s) related to $\hat{u}_{k,i} = +1$ and $\hat{u}_{k,i} = -1$, respectively.

The state probabilities $\mathrm{P}_\alpha(s_{k-1} = s')$ and $\mathrm{P}_\beta(s_k = s)$, also referred to as α and β metrics, are computed via the so-called 'forward' and 'backward' recursion, respectively:

$$\begin{cases} \mathrm{P}_\alpha(s_k{=}s) = \sum\limits_{s' \text{valid}} \mathrm{P}_\alpha(s_{k-1}{=}s') \cdot \gamma_k(s', s) \\ \mathrm{P}_\beta(s_{k-1}{=}s') = \sum\limits_{s \text{valid}} \mathrm{P}_\beta(s_k{=}s) \cdot \gamma_k(s', s) \end{cases} \tag{2}$$

In (1) and (2), $\gamma_k(s', s)$ is the transition probability:

$$\gamma_k(s', s) = \prod_{i=0}^{k_c-1} \mathrm{P}_\beta(u_{k,i}) \cdot \prod_{j=0}^{n_c-1} \mathrm{P}_\alpha\big(c_{k,j}\big) \tag{3}$$

$\mathrm{P}_\beta(u_{k,i})$ being the *a priori* probability[1] of the information bit $u_{k,i}$, and $\mathrm{P}_\alpha\big(c_{k,j}\big)$ the one of the coded bit $c_{k,j}$. Depending on the concatenation scheme, the former may be either the *a priori* 'extrinsic' probability computed by the companion decoder (PCCC and inner code of SCCC) or a constant denoting equal likelihood

[1]With a notation borrowed from [7], we will also refer to P_α and P_β as 'up' and 'down' probability, respectively.

(outer code of SCCC); the latter may be either the channel reliability[2] (PCCC and inner code of SCCC) or the *a priori* 'extrinsic' information (outer code of SCCC). The notation introduced so far is summarized in Fig. 1 with the factor graph of a section of the trellis [7].

Besides (1), the decoder must also calculate the *a posteriori* 'down' LLR of the coded bits, denoted with $L_\beta(c_{k,j})$; these are independent of the 'up' *a priori* probabilities $\mathrm{P}_\alpha(c_{k,j})$ of the same bits. In analogy with (1),

$$L_\beta(c_{k,j}) = \log \frac{\sum_{C_i^+} f_j(k,s,s')}{\sum_{C_i^-} f_j(k,s,s')} \tag{4}$$

where, again, we defined $f_j(k,s,s') \doteq \mathrm{P}_\alpha(s_{k-1}=s')\cdot\gamma_k^{(j)}(s',s)\cdot\mathrm{P}_\beta(s_k{=}s)$ and the sums are computed over the sets C_i^+ and C_i^- of trellis transitions corresponding to $\hat{c}_{k,j}=+1$ and $\hat{c}_{k,j}=-1$, respectively. In (4), $\gamma_k^{(j)}(s',s)$ is the extrinsic piece of the transition probability $\gamma_k(s',s)$, and for its computation, the 'up' probability of bit $c_{k,j}$ is excluded:

$$\begin{aligned}\gamma_k^{(j)}(s',s) &\doteq \prod_{i=0}^{k_c-1}\mathrm{P}_\beta(u_{k,i})\cdot\prod_{l=0,l\neq j}^{n_c-1}\mathrm{P}_\alpha(c_{k,l}) = \\ &= \frac{\gamma_k(s',s)}{\mathrm{P}_\alpha(c_{k,j})}\end{aligned} \tag{5}$$

Finally, merging (4) and (5) the following relation between the LLRs of the coded bits $c_{k,j}$ holds:

$$L(c_{k,j}) = L_\beta(c_{k,j}) + L_\alpha(c_{k,j}) \tag{6}$$

However, the decoder does not implement (6), rather it carries out the 'extrinsic' LLRs defined in (4), as they represent the true 'added value' of the BCJR algorithm.

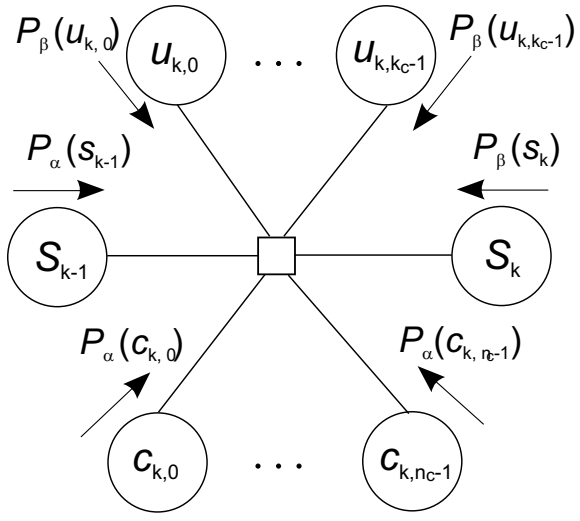

Fig. 1. Trellis section of a (k_c, n_c) convolutional code.

[2]Given the channel observation r_n of the coded bit $c_{k,j}=c_n$, the channel reliability $\mathrm{P}_\alpha(c_n)$ is proportional to the probability distribution $p(r_n|c_n)$.

III. Early Stopping of the Iterative Decoding

An efficient stopping rule for iterative decoders may be conceived as a generalization of the one used with low-density parity-check (LDPC) codes, where decoders cease iterating when all the messages computed by the bit node processors satisfy the (even) parity check at every check node of the code [8]; this condition assures that not only the current decoded word is a valid codeword, but also that the internal status of the decoder has reached a 'steady state' configuration, fully compatible with the set of parity check constraints defining the code. The idea underlying the new criterion is to perform a consistency check between input and output of the decoder, and use this check as a proxy for the 'steady state' regime.

A. Input Output Consistency Stopping Rule

Fig. 2 shows the block diagram of an iterative decoder equipped with the new Input Output Consistency (IOC) check.

Basically, the hard-decision bits $\hat{u}_k$, $k=0,...,K-1$, output by the decoder are first re-encoded into the coded sequence c'_n and then compared with the sequence $\hat{c}_n$, $n=0,...,N-1$ also output by the decoder. These are the hard-decision bits (sign) taken on the 'down' LLR $L_\beta(c_n)$ of the channel code sequence c_n, computed according to (4). If all the bits c'_n equal $\hat{c}_n$, then the decoder is in a consistent state, and early convergence is declared.

As far as the complexity overhead arising with the implementation of the IOC check is concerned, we only have to take the encoder and two buffers storing the coded sequences $\hat{c}_n$ and c'_n into account. The former is mainly composed by the interleaving memory, whose management (address generation) can be shared with the decoder, with no complexity overhead. On the other hand, the buffers contain N hard-bit locations each. Note that these memories (interleaving and buffers) are clearly negligible compared to the decoder memories for the received soft bits and extrinsic info.

Additional complexity is added to the decoder to compute the 'down' LLRs $L_\beta(c_n)$. However, as suggested by (5), an efficient implementation may re-use some of the temporary results for the computation of (1), with a small impact in the overall decoder complexity.

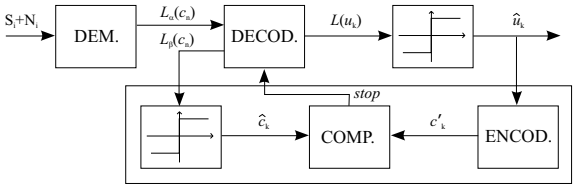

Fig. 2. Input Output Consistency check principle.

B. Iterative Decoding Performance for SCCC and PCCC

1) SCCC: We considered the serial concatenation of a recursive systematic convolutional (RSC) code

with rate $1/2$, 16 states and generator $[1, 35/31]_{oct}$ as outer code, (optimally) punctured for higher rates, an S-random interleaver, and a simple convolutional code with rate 1 and 2 states (accumulator) as inner code.

Each decoding iteration of a SCCC is composed of two successive half iterations, namely the decoding of the inner code (DI), followed by the outer one (DO). As new updates for $\hat{c}_n$ and $\hat{u}_k$ are available after DI and DO respectively, the IOC check is performed every half iteration to possibly reduce the decoder latency. Note that to perform IOC check, only the inner decoder has to be extended with (4) (whose complexity is rather small, the code being very simple), while it is already normally implemented in the outer one.

Fig. 3 reports the FER performance and the convergence speed of the IOC compared with HDA, SCR and the Genie-aided stopping rule for a SCCC code on AWGN channel, information block size equal to 1 MPEG packet, $K = 1504$, rate $R = 2/3$ and 8PSK modulation. For the SCR rule, two different thresholds have been used, namely $\delta_1 = 0.3\%$ and $\delta_2 = 0.1\%$. Fig. 3(a) shows that IOC follows the Genie's behavior with no loss in performance even at low FER (up to 10^{-6}). On the contrary, all other rules show a flattening caused by undetected errors [4]; particularly, SCR with δ_1 perform the worst as many packets meet the rule before being completely reliable (error-free). As a result, its average convergence speed is faster than that with δ_2 and HDA, but still slower than IOC, which is only 0.4 iterations far from the Genie, on average.

As the IOC rule might be affected by the puncturing operation, we extend our analysis to the case of high-rate codes. Accordingly, Fig. 4 summarizes the results carried out with the SCCC code with information block size $K = 1504$ bits, rates $1/2$, $2/3$, $4/5$, $7/8$ and 8PSK modulation. As expected, puncturing at high rates makes the IOC rule less robust, and a slight loss in performance may be observed below 10^{-5} for rates $4/5$ and especially for $7/8$.

The convergence speed of these codes is also reported in Fig. 4: for all of them, the IOC rule takes roughly half an iteration more than the Genie to declare convergence. Particularly, we registered 4.03 iterations for IOC against 3.61 for the code rate $1/2$ at 3.9 dB, and 1.75 against 1.42 for the code rate $7/8$ at 8.60 dB.

Interestingly, given a certain error rate, increasing the code rate results in reducing the average number of iterations, but the absolute gap from the Genie stopping rule remains almost unchanged.

2) PCCC: We considered the parallel concatenation scheme standardized for UMTS [9], where the constituent codes are two identical RSC codes with rate $1/2$, 8 states and generators $[1, 15/13]_{oct}$. The systematic output of the second encoder (the one working on interleaved input sequence) is always pruned off, thus the resulting code rate is $1/3$.

Decoding of PCCC is performed with two companion decoders which iteratively update and exchange 'extrinsic' information [1]. Both decoders are complemented with the computation of (4)[3]. Unlike SCCC, early convergence check is performed only after the completion of a whole iteration, as both decoders concur to the estimate of the coded bits.

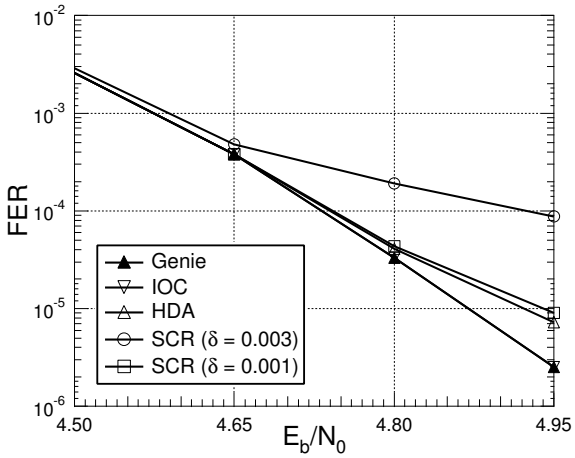

(a) FER performance.

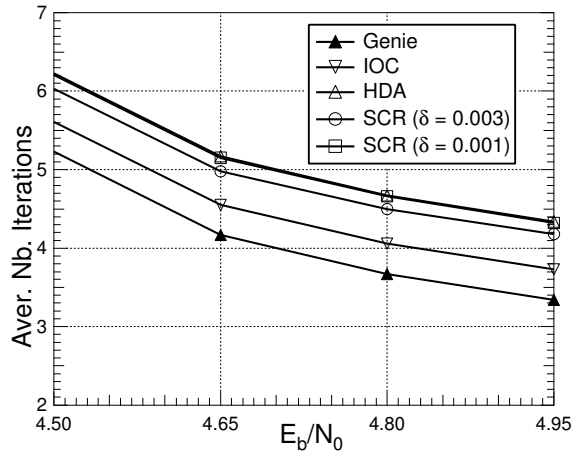

(b) Average number of iterations.

Fig. 3. Performance comparison of IOC check.

Fig. 5 compares the FER and the average number of iterations for both the Genie-aided and the IOC check stopping rule applied to the UMTS turbo-code with rate $1/3$ and block size $K = 1504$. The new IOC rule performs exactly the same of the reference Genie criterion in term of performance (no undetected errors are introduced) and convergence speed.

IV. Conclusion

In this paper we have presented the new Input-Output Consistency (IOC) check. This criterion allows the early stop of the decoding operations when the estimates of the info bits output by the decoder match, after a preliminary re-encoding, the MAP estimations of the channel (coded) bits. To adequately support the IOC, the constituent decoders have been extended with the additional computation of the 'extrinsic' APPs of the coded bits; however, no significant penalties are

[3]Actually, it is not evaluated anew for the systematic bits, as it may be derived by multiplying – adding in the log domain – the 'extrinsic' APP of the information bits by the *a priori* APP coming from the other decoder

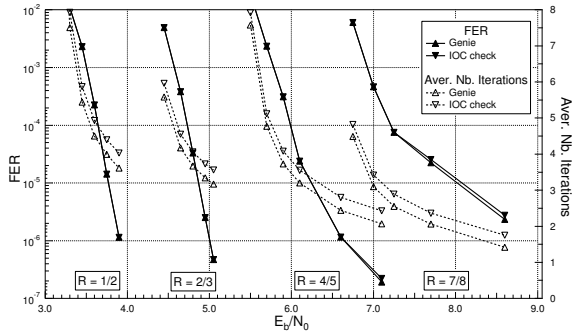

Fig. 4. FER performance analysis at high-rate.

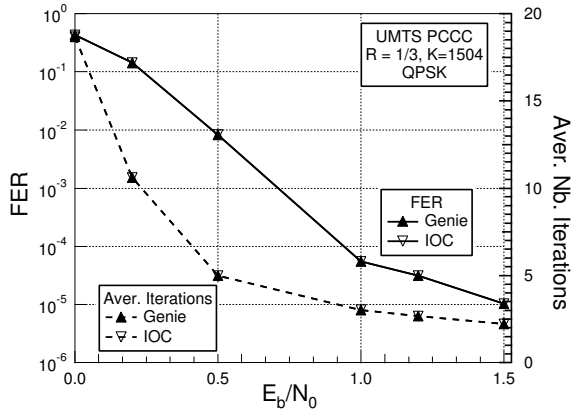

Fig. 5. Performance of the IOC check with the UMTS PCCC scheme.

envisaged in the overall complexity, as their implementation largely re-uses the resources to compute the APPs of the info bits.

Computer simulations showed that the IOC check outperforms other stopping rule such as HDA or SCR, as no undetected errors are introduced even at very low FER rate and that its convergence speed is higher. A slight performance loss has only been measured in a SCCC scheme with high rate of puncturing. Astonishingly, for PCCC schemes, the IOC rule even reveals to be the 'best' stopping criterion, its average number of iterations and frame/bit error rate performance being exactly the same as the ones of the Genie.

ACKNOWLEDGMENT

The authors would like to thank Dr. Jossy Sayir from the Telecommunications Research Centre Vienna (FTW) for the fruitful talk that inspired this work.

REFERENCES

[1] C. Berrou, A. Glavieux, and P. Thitimajshima, "Near shannon limit error-correcting coding and decoding: Turbo-codes," *Proc. IEEE ICC 93*, pp. 1064–1070, 1993, Geneva.

[2] S. Benedetto *et al.*, "Serial concatenation of interleaved codes: Performance analysis, design, and iterative decoding," *IEEE Trans. Inform. Theory*, vol. 44, no. 3, pp. 909–926, May 1998.

[3] A. Martinez and M. Rovini, "Iterative decoders based on statistical multiplexing," *Proc. 3^{rd}; International Symposium on Turbo Codes and Related Topics*, pp. 423–426, Sept. 2003, brest, France.

[4] A. Matache, S. Dolinar, and F. Pollara, "Stopping rules for turbo decoders," TMO Progress Report, Tech. Rep. 42-142, Aug. 2000.

[5] J. Hagenuaer, E. Offer, and L. Papke, "Iterative decoding of binary block and convolutional codes," *IEEE Trans. Inform. Theory*, vol. 42, no. 2, pp. 429–445, Mar. 1996.

[6] L. Bahl, J. Cocke, F. Jelinek, and J. Raviv, "Optimal decoding of linear codes for minimizing symbol rate," *IEEE Trans. Inform. Theory*, vol. 20, no. 2, pp. 284–287, Mar. 1974.

[7] G. D. Forney Jr., "Codes on graphs: Normal realizations," *IEEE Trans. Inform. Theory*, vol. 47, no. 2, pp. 520–548, Feb. 2001.

[8] R. Gallager, "Low-density parity-check codes," Ph.D. dissertation, Massachusetts Institute of Technology, 1963.

[9] European Telecommunications Standards Institute, "Universal Mobile Telecommunications System (UMTS); Multiplexing and channel coding (FDD)," vol. ETSI TS 125 212 (v3.3.0), June 2000.

Single Parity Check Turbo Product Codes for the DVB-RCT Standard

Angelo Pinelli Martins Samia
National Institute of Telecommunications - Inatel
P.O. Box 05 - 37540-000
Santa Rita do Sapucaí - MG – Brazil
angelo.pinelli@inatel.br

Dayan Adionel Guimarães
National Institute of Telecommunications - Inatel
P.O. Box 05 - 37540-000
Santa Rita do Sapucaí - MG – Brazil
dayan@inatel.br

***Abstract*—This article suggests some modifications in conventional single-parity check turbo product code structures to fulfill the specifications of the DVB-RCT standard proposed for the return channel of DVB-T based Digital TV systems. The resultant codes are two and three-dimensional array codes, in which diagonal parity equations are applied. Simulation results are presented for the AWGN and Rayleigh fading channels and reveal a good trade-off between performance and complexity for the suggested channel coding schemes.**

***Index Terms*—Array codes, Single Parity Check Product Codes, Block Turbo Codes, DVB-RCT, DVB-T.**

I. Introduction

Two-way communications are essential to provide real-time interactivity between the subscriber and the digital television content provider. The so-called DVB-RCT (Return Channel-Terrestrial) standard [1] defines a wireless interface that can be shared by a large number of terminals, enabling them to send "return" signals to a base station, at the same time and through the same antenna that it receives IP data on the "forward" link, which are carried using the DVB-T [2] broadcast channel.

A discussion on the utilization of Single Parity Check Turbo Product Codes (SPC-TPC) [5] for the requirements of DVB-RCT is in order. Conventional two and three-dimensional (2D and 3D) SPC are modified through the use of different component codes in each dimension, diagonal parity equations and zero padding, in order to match the specifications of the DVB-RCT standard, concerning block sizes and code rates. The key feature of the channel-coding scheme suggested here is the low complexity of the coding and the decoding processes.

The remainder of this paper is organized as follows. Section II presents the channel-coding requirements according to the DVB-RCT standard, i.e. block sizes and code rates associated to each modulation scheme. In Section III, details about the code construction are presented, in order to fulfill the specifications listed in Section II. Section IV is devoted to the turbo-decoding algorithm, while Section V presents simulation results for the channel-coding schemes suggested here, for the AWGN and the Rayleigh fading channels. Finally, Section VI concludes the paper, highlighting some open questions to be addressed in future work.

II. Code Requirements

According to the DVB-RCT, one of the following methods of channel-coding is used in a given RF channel: turbo codes or concatenated Reed-Solomon plus convolutional codes. The turbo code adopted for the standard uses parallel concatenation of Circular Recursive Systematic Convolutional (CRSC) codes [3] [9] and its performance is evaluated in [4] for a variety of input block sizes

No matter the channel-coding method used in the DVB-RCT standard, the data bursts produced after the coding and modulation process have a fixed length of 144 modulated symbols. Table 1 lists the original sizes of the useful data payloads to be encoded, given the selected modulation and code rate [1].

TABLE I
Useful data payload of a burst (DVB-RCT standard) [1]

Modulation	Rate = 1/2	Rate = 3/4
QPSK	144 bits	216 bits
16-QAM	288 bits	432 bits
64-QAM	432 bits	648 bits

In order to match the code structure with the requirements given by Table 1, the number of dimensions of a single parity check (SPC) product code and the length of the component codes proposed here are varied. In addition to the conventional multi-dimensional parity equations, diagonal parity [5] equations are also considered as a means to achieving these requirements. The resultant structure can be viewed as a form of Array Codes [12].

III. Code Construction

The channel code can be constructed as shown in Figure 1, for the case where the input block size is 144 bits. First, the parity is calculated column-wise using a $(n,k) = (7,6)$ single parity check component code, which will make the original input block grow by 24 bits. The parity of the rows is then calculated using the same (7,6) component code used in the first dimension. After that, the 49 parity bits corresponding to the encoding in the third dimension are calculated

using a (5,4) SPC code. Diagonal parity is applied to the resulting (7×7×5, 6×6×4) code by computing 7 parity bits for each of the 5 planes, successively towards the "depth" of the structure. The final output block has 280 bits, which results in an overall code rate $r = 0.51$. Zero-padding the output with 8 symbols brings the code rate down to ½ in this case, as required.

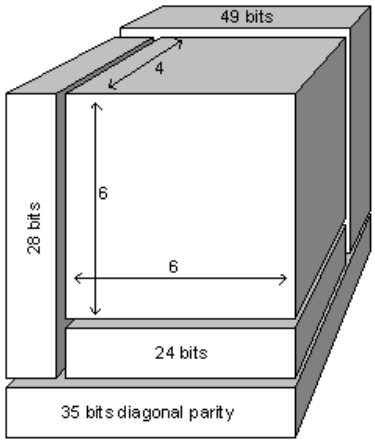

Fig. 1. Block shape matched to the specifications of DVB-RCT for QPSK (R = ½).

An example of the procedure used to compute the diagonal parity on each plane is shown in Figure 2. The block formed with the information bits plus the symbols corresponding to the horizontal and vertical parities is first re-arranged to form a new 5×5 array, the columns of which corresponding to the left diagonals of the original block. One way to accomplish this is to do circular shifts on the lines of the structure in Figure 2(a). The first line is not shifted; the second line is shifted to the left by one bit and the l^{th} line of the original block is shifted by $l - 1$ bits. The left diagonal parity bits are then calculated by computing the parity bits along the columns of the array shown in Figure 2(b).

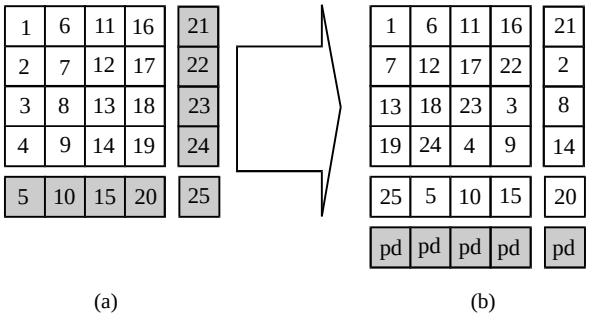

Fig. 2. Computation of the left diagonal parity for a 2D $(5,4)^2 = (5\times5, 4\times4)$ product code. (a) Array with information bits, horizontal and vertical parity bits; (b) Modification in (a) for left diagonal parity calculation.

The influence of diagonal parity is analyzed with more details in [8], where the best results were obtained with the restriction that the component codes in each dimension being equal and having an odd number of bits. An independent initiative to compute the diagonal parity is proposed in [5] and, in this case, it is enough that the component codes have the same length. Because the requirements in terms of code rate and block length are defined by DVB-RCT, the structures suggested in this article were built so as to optimize these parameters, following the guidelines given in [5].

When the required code rate is ¾, a two-dimensional product code is used, as illustrated in Figure 3, for a 432-bit input block. Note that the last 9 positions of the array has to be filled with zeros so that the input bits are arranged as a perfect square and diagonal parity can be applied [5] [8]. Two rows of 16 bits are generated based on the calculation of the diagonal parity bits to the left and to the right of the array formed by the information bits plus vertical and horizontal parity bits.

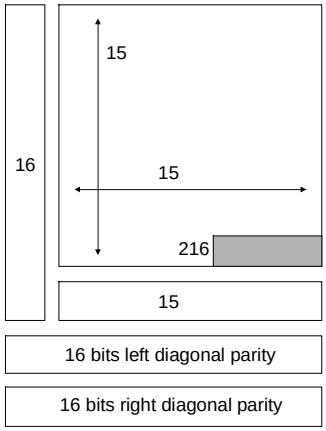

Fig. 3. Block shape matched to the specifications of DVB-RCT for QPSK (R = ¾).

The structures designed for operation with 16-QAM (*Quadrature Amplitude Modulation*) and 64-QAM follow the same aforementioned principle. For each case, the number of dimensions and the size of the component codes had to be adjusted. The codes ere designed so that the resulting code rate is equal or exceeds the one specified by the DVB-RCT standard.

It was found that 3D codes are viable only when the required code rate is R = ½. When R = ¾ it is not possible to use more than two dimensions in the product code. As in QPSK mode, diagonal parity is applied to both 3D and 2D structures, but while in the first case the diagonal parity can only be applied left *or* right-wise due to rate restrictions, the latter case implements both left and right diagonal parity. In some configurations, both the input and output blocks had to be zero-padded. Figure 4 and 5 show the suggested structures for ½ and ¾ code rates, respectively, when using 16-QAM modulation. For the 3D case, the resulting codeword has 288 + 48 + 56 + 49 + 63 = 504 bits, and it has to be appended with 72 null symbols to comply with the R = ½ specification.

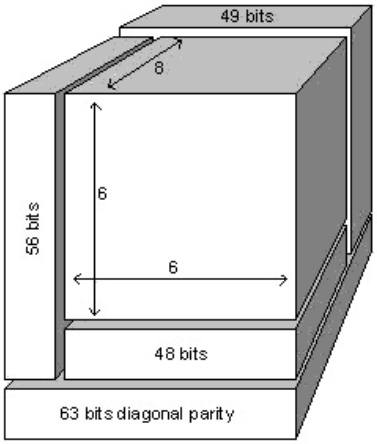

Fig. 4. Block shape matched to the specifications of DVB-RCT for 16-QAM (R = ½).

The required input block for 16-QAM mode and R = ¾ has 432 bits and the 2D product code with diagonal parity suggested for this case is shown in Figure 5. Here the resulting codeword has 528 bits and it is zero-padded with 43 symbols at the output to bring the code rate down to ¾.

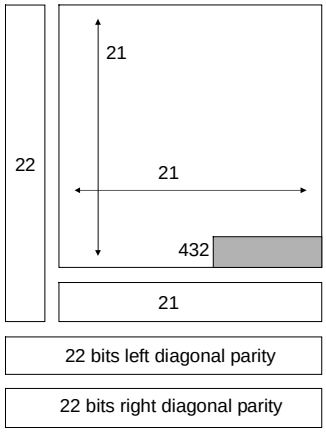

Fig. 5. Block shape matched to the specifications of DVB-RCT for 16-QAM (R = ¾).

The structure designed for ½ code rate and 64-QAM modulation is depicted in Figure 6. Concerning this 3D case, it was necessary to pad the input block with 16 zeros in order for the diagonal parity of the eight successive planes to be properly calculated from perfect 8 × 8 squares.

For the same 64-QAM modulation scheme, and when the required code rate is ¾, a 2D structure like the one shown in Figure 7 is suggested. This time, 28 bits were appended to the input block for the diagonal parity computation.

IV. Turbo Decoding

A turbo decoding process was used to decode the channel-coding schemes described in Section III. For simplicity, such schemes were evaluated using BPSK (*Binary Phase Shift Keying*) modulation over AWGN (*Additive White Gaussian Noise*) and Rayleigh fading channels, for the specified block lengths and rates listed on Table 1, Section II. Simulation of these schemes strictly in accordance with DVB-RCT is beyond the scope of this work. Similar approaches have been adopted in [4] [7] to evaluate the Circular Recursive Convolutional Code (CRSC) performance, which is specified by DVB-RCT as an alternative to the serial concatenation of Reed-Solomon with non-recursive convolutional codes, as mentioned in Section II.

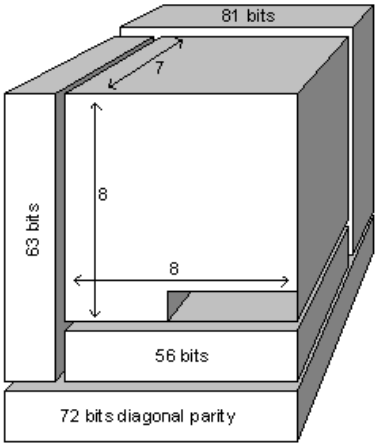

Fig. 6. Block shape matched to the specifications of DVB-RCT for 64-QAM (R = ½).

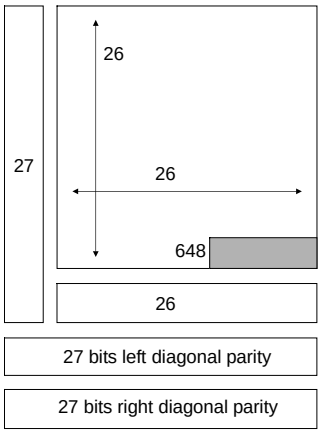

Fig. 7. Block shape matched to the specifications of DVB-RCT for 64-QAM (R = ¾).

A symbol-by-symbol MAP algorithm was used for turbo-decoding of the SPC product code, as in [13, pp. 57-60], in which the extrinsic information is factored out and passed between decoders in each dimension, referred to as a SISO (soft-input, soft-output) decoding process. A simple extension of this algorithm is done here for the case where diagonal parity is used. In this case, the diagonal encoding can be considered as a form of a new "dimension" of the code. The decoding steps are as follows:

(i) Calculate the channel log-likelihood ratios (LLR) for all received symbols and set the extrinsic information to zero for all bits in the code;

(ii) Calculate the extrinsic information for all bits and each dimension. The *a priori* information for each bit in a given dimension is the sum of the extrinsic information from the other dimensions in the code;

(iii) The decoding of all dimensions one time is called iteration. Repeat this process for as long as required.

The *a posteriori Log-Likelihood Ratio* (LLR) of the symbol at the output of the detector (soft-input of the SISO decoder) can be expressed as [6]:

$$L(\hat{x}) = L(x \mid y) = \ln\left[\frac{P\left(x = +\sqrt{E_c} \mid y, g\right)}{P\left(x = -\sqrt{E_c} \mid y, g\right)}\right] \quad (1)$$

where g accounts for the fading and is called *channel gain*. Using the Bayes Theorem, from Equation (1) it is obtained:

$$L(\hat{x}) = \ln\left[\frac{P\left(y \mid x = +\sqrt{E_c}, g\right)}{P\left(y \mid x = -\sqrt{E_c}, g\right)}\right] + \ln\left[\frac{P\left(x = +\sqrt{E_c}\right)}{P\left(x = -\sqrt{E_c}\right)}\right] \quad (2)$$

where the first term on the right of Equation (2), which will henceforth be designated as $Lc(y)$, corresponds to the channel measurement or channel state information at the detector output, given the alternate conditions that a 1 or a 0 may have been transmitted. The second term on the right of Equation (2) will be called $L(x)$ and is the *a priori* value of the input symbol, whose value is not known until the first decoding iteration is completed. That is why, in general, the *a priori* values of the input symbols are initially set to zero.

Substituting the numerator and the denominator of $Lc(y)$ by the equations that describe the Gaussian distribution, considering the expected values in each case, according to (1), yields:

$$Lc(y) = \ln\left[\frac{\exp\left[-\frac{1}{2}\left(\frac{y - g\sqrt{E_c}}{\sigma}\right)^2\right]}{\exp\left[-\frac{1}{2}\left(\frac{y + g\sqrt{E_c}}{\sigma}\right)^2\right]}\right] = 4g\frac{\sqrt{E_c}}{N_0}y \quad (3)$$

where $\sigma^2 = N_0/2$ is the average noise power at the matched filter output and $g = 1$ if the channel is purely AWGN.

From the LLR at the output of the detector expressed in Equation (2), it can be shown that, for systematic codes, the log-likelihood ratio at the output of the decoder (soft output), at a given dimension q, can be written as [10]:

$$L_q\left(\hat{\vec{x}}\right) = Lc\left(\vec{y}\right) + L_q\left(\vec{x}\right) + Le_q\left(\hat{\vec{x}}\right) \quad (4)$$

where $L_q\left(\vec{x}\right)$ is the vector or array that bear the *a priori* information that feeds the input of the decoder at the q^{th} dimension, and $Le_q(\hat{\vec{x}})$ is the *extrinsic information*, or additional information due to parity, that is obtained after the decoding process at the q^{th} dimension. The extrinsic information represents the amount of information added to the soft value at the input of the decoder to form the soft output. The extrinsic information for the i^{th} bit ($i = 1, 2, \ldots, n_q$) of a received codeword is given by [5] [13]:

$$Le_q\left(\hat{x}_i\right) = (-1)^{n_q}\, 2\text{atanh}\left[\prod_{\substack{j=1 \\ j \neq i}}^{n_q} \tanh\left(\frac{L_q\left(x_j\right) + Lc\left(y_j\right)}{2}\right)\right] \quad (5)$$

where n_q is the number of coded bits in the q^{th} dimension, $Lc(y_j)$ is the channel state information (CSI) at bit position j and $L_q(x_j)$ is the input LLR of bit j at the q^{th} dimension. Equation (5) differs from the one shown in [13] by the term $(-1)^{n_q}$, which is necessary when the logical element "0" is represented by symbol $-\sqrt{E_c}$, as it is the case of this article and of the example given in [14, p. 483-488]. When the bit "0" is represented by the symbol $+\sqrt{E_c}$, the term $(-1)^{n_q}$ is not used [11] [13]. The vector that holds the *a priori* values at the input of the decoder, according to step (ii) of the algorithm described above, can be expressed as:

$$L_q\left(\vec{x}\right) = \sum_{\substack{i=1 \\ i \neq q}}^{D} Le_i\left(\hat{\vec{x}}\right) \quad (6)$$

where D is the number of dimensions of the code. Note that diagonal parity vectors or arrays are considered as additional dimensions in the schemes proposed here. The total LLR at the output of decoder is then calculated through:

$$L_T\left(\hat{\vec{x}}\right) = Lc\left(\vec{y}\right) + \sum_{i=1}^{D} Le_i\left(\hat{\vec{x}}\right) \quad (7)$$

where $L_T(\hat{\vec{x}})$ is a vector with real numbers whose sign of each element yields a hard decision about the corresponding transmitted symbol and whose magnitude reveals the reliability of that decision. Practical aspects require the total values of the extrinsic information to be limited to avoid numerical problems during implementation. According to what has been suggested in [13], the results of the calculations to find the extrinsic information, at each dimension, were limited within the range $-100 \leq L_T\left(\hat{x}\right) \leq +100$. An estimation on the

transmitted codeword, $\hat{\hat{x}}$, can be carried out by using the following decision criteria:

$$\hat{x} = \begin{cases} 1 & L_T(\hat{x}) \geq 0 \\ 0 & L_T(\hat{x}) < 0 \end{cases} \quad (8)$$

V. Simulation Results

The performance as a function of the number of iterations is shown in Figure 8 for the (10×9×8, 8×8×7) code depicted in Figure 6. Each decoding cycle improves the performance, with decreasing returns, but after a number of iterations equivalent to the number of dimensions of the code, this improvement, as expected [13], becomes only marginal.

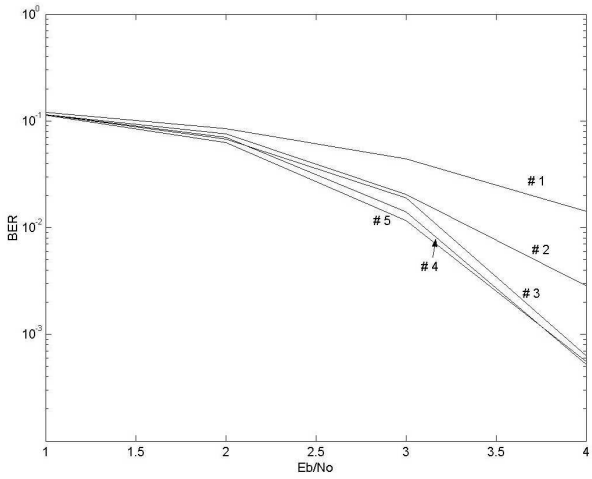

Fig. 8. BER as a function of the number of iterations for the 54-bytes input block 3D product codes with diagonal parity.

The distribution of $L_T(\hat{\hat{x}})$, the total LLR out of the turbo decoder after one to five iterations is shown in Figures 9(a) to 9(e), for equally likely input symbols and for E_b/N_0 = 4 dB.

The center of the horizontal axis of the histograms in Figure 9 is the decision threshold, on the right of which the decision is favorable to bit "1". Otherwise, bit "0" will be chosen. The soft values of the LLR have greater magnitude the more distant they are from the threshold. It can be seen the similarity between the amplitude distribution after four and five iterations, which is in agreement with the convergence observed in Figure 8. This is the reason why the simulation results presented here for BER estimation were obtained using a fixed number of five iterations. Figure 9 also reveals that the soft values of the LLR are concentrated at regular intervals. This behavior is similar to what happens for all codes mentioned in this work, and represents an opportunity for future investigation.

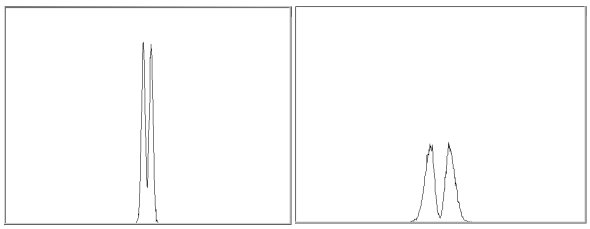

(a) 54-byte input, E_b/N_0 = 4 dB, 1 iteration.

(b) 54-byte input, E_b/N_0 = 4 dB, 2 iterations.

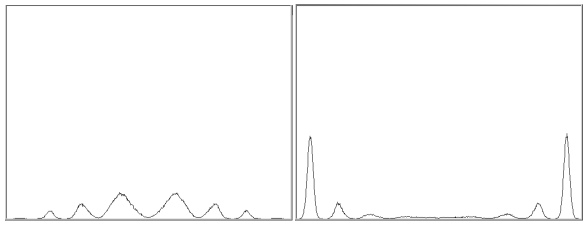

(c) 54-byte input, E_b/N_0 = 4 dB, 3 iterations.

(d) 54-byte input, E_b/N_0 = 4 dB, 4 iterations.

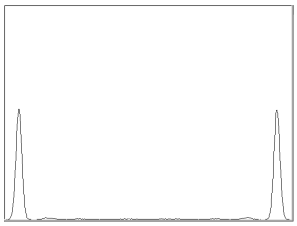

(e) 54-byte input, E_b/N_0 = 4 dB, 5 iterations.

Fig. 9. Normalized histograms resulting from the measurements of LLR soft values at the output of the turbo decoder for the code (10×9×8, 8×8×7) @ E_b/N_0 = 4 dB.

A. Performance in AWGN channel

The performance results from the simulation of the 3D product codes with diagonal parity over AWGN channel are shown in Figure 10.

The number of bytes in the legend of Figure 10 corresponds to the input block size. Coding gain is approximately 4.8 dB for the 54-byte input block size code and its distance from capacity (≅0,2 dB for R = ½ and BPSK modulation [6]) is around 4.6 dB, both results considering a BER = 10^{-5}. This is a quite good result, given the low complexity of the coding and the decoding processes and the relatively short codeword length.

When the required code rate is ¾, 2D product codes with diagonal parity are used. The performance for the corresponding codes is shown in Figure 11. If compared to the 3D case, the 2D code that operates with 54 bytes at the input requires an additional 0.6 dB of normalized signal-to-noise ratio to yield the same bit error rate of 10^{-5}.

Still referring to Figures 10 and 11, it is worthy noting that the shorter codes outperforms the longer ones for low signal to noise ratios, a fact that can be attributed to the longer sequences of zero-padding used in the longer codes. However, the asymptotic gain of the longer codes seems to make the

corresponding curves steeper, probably leading to lower BER for higher values of signal-to-noise ratios, when compared to the shorter codes.

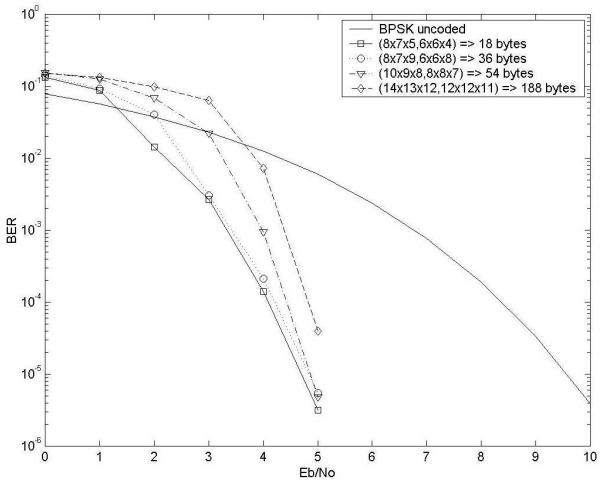

Fig. 10. Simulation results for rate ½ 3D product codes with diagonal parity, after 5 decoding iterations: AWGN channel.

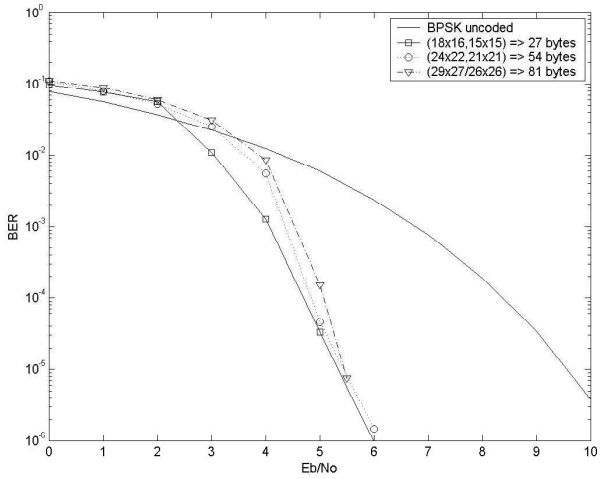

Fig. 11. Simulation results for rate ¾ 2D product codes with diagonal parity, after 5 decoding iterations: AWGN channel.

B. Performance over the Rayleigh channel

The performance of the 3D product codes *without* diagonal parity, after 5 decoding iterations, and over the *Rayleigh* channel is illustrated in Figure 12. The curves show the simulation results when the channel state information (CSI) is not available to the decoder. In this case, the bit error rate seems to be affected by an error floor after a certain value of E_b/N_0 and this behavior was also observed for codes that implement diagonal parity. The code that operates with 18 bytes at its input needs a signal-to-noise ratio of about 11 dB to yield BER = 10^{-5}.

For the case when the receiver is implemented with some sort of mechanism that allows the CSI to be estimated and fed to the decoder input, the performance of the 3D product codes with diagonal parity is like the one shown in Figure 13. In this case, there seems to be no error floor, at least for the signal-to-noise ratios under consideration, and the (7×7×5, 6×6×4) code now requires only 10 dB to operate with BER = 10^{-5}. This improvement is due to both the diagonal parity and the availability of the CSI. Because of the error floor, a larger difference on the required E_b/N_0 should be expected if the analysis is carried out at a lower BER.

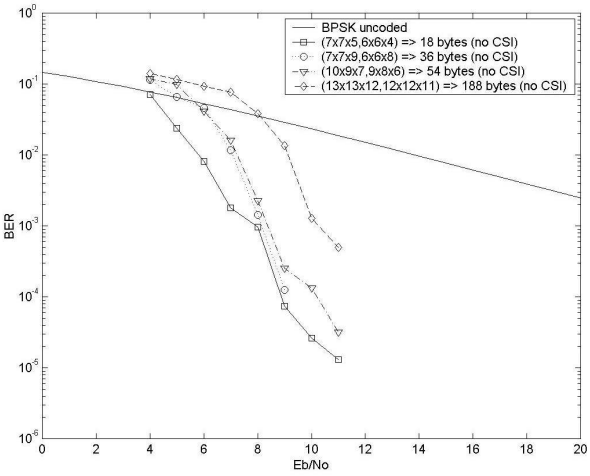

Fig. 12. Simulation results for rate ½ 3D product codes with diagonal parity, after 5 decoding iterations: Rayleigh channel, no CSI available for the decoder.

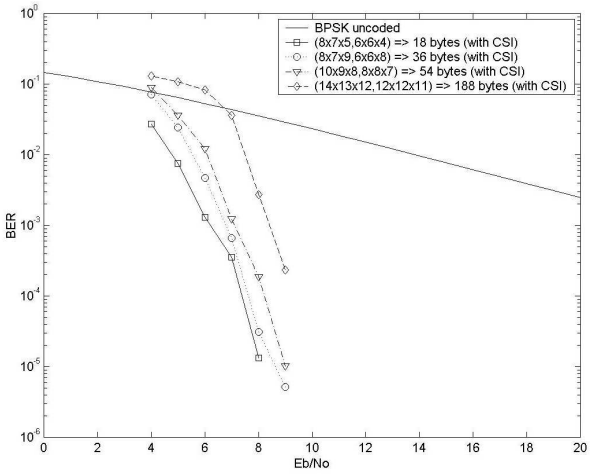

Fig. 13. Simulation results for rate ½ 3D product codes with diagonal parity, after 5 decoding iterations: Rayleigh channel, with CSI available for the decoder.

According to Figure 13, coding gains greater than 14 dB for the 18-byte input block size code can be achieved (and greater than 11 dB for all block sizes) for bit error rates less than 10^{-3}. A distance of approximately 6.5 dB from capacity (≅1.5 dB for R = ½ and BPSK modulation [6]) is obtained for the 18-byte input block size code, for a BER equal to 10^{-5}.

The simulation results presented herein for the fading channel were obtained under the ideal condition in which a sufficiently large interleaver is employed, in a manner that the fading that takes place in a given symbol is uncorrelated with the fading that affects the other symbols in the same codeword. Therefore, the

simulated fading was generated as independent and identically distributed random variables for each symbol transmitted through the channel.

Figure 14 shows the performance results for the case where the required code rate is ¾ and 2D product codes with diagonal parity are used. An E_b/N_0 around 10.5 dB is needed for the 54-byte input block size product code to operate with a 10^{-3} bit error rate.

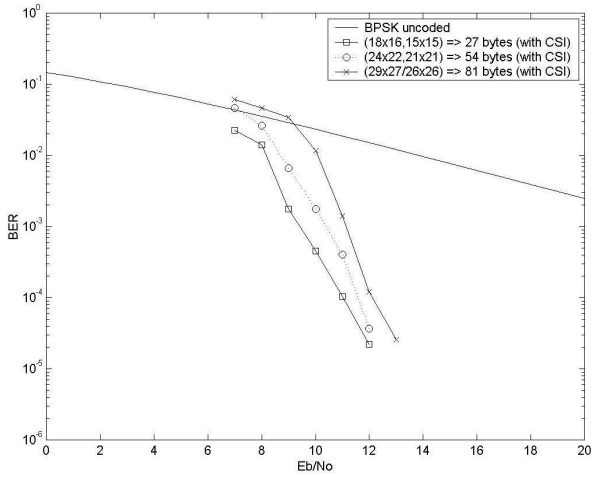

Fig. 14. Simulation results for rate ¾ 2D product codes with diagonal parity, after 5 decoding iterations: Rayleigh channel, with CSI available for the decoder.

VI. Concluding Remarks

It was found through simulation that, for low signal-to-noise ratios, the performance of the product codes is better the shorter is the block length. When E_b/N_0 increases, codes that operate with larger blocks tend to perform better. Therefore, it is expected that there is a crossing point in the curve, from which longer codes will have better performance.

The behavior for low E_b/N_0 seems to be aggravated when zeros are inserted at the output. To make matters worse, the suggested structures that have more null symbols at the output are exactly those with the larger block length. The inconveniences brought by zero-padding were partially overcome by replacing the null symbols with new parity equations, computed towards the left and right diagonal of the 2D product code and only towards the left diagonal of the several planes that compose the 3D product codes. One of the reasons why right diagonal parity has not been applied to the 3D product codes is because one of the structures (with 18 bytes at the input) does not support the additional parity bits while keeping the specified code rate at ½.

A comparison between BER performances between the product codes presented in this article and the turbo code defined in DVB-RCT standard indicates that the latter has better performance. Although the decoding complexity of the product codes is clearly low, more investigation is needed for this complexity/performance trade-off to be exactly quantified.

Among the future work that would explore further what was covered so far could be to investigate the performance of these codes using higher order modulation schemes, specifically 16-QAM and 64-QAM. It would also be worth investigating why the LLR's have such a concentration of amplitudes at regular intervals, according to what was seen in Figure 9. Another suggestion for future work is to confirm and investigate the reasons for the error floor, observed in a Rayleigh channel when no CSI is available for the decoder. Finally, an investigation using bounds on bit error probabilities would be useful to validate (or not) the conjecture stating that the longer codes considered here will outperform the short codes for high values of the signal-to-noise ratio.

References

[1] ETSI EN 301 958 V1.1.1, *Digital Video Broadcasting (DVB); Interaction channel for Digital Terrestrial Television (RCT) incorporating Multiple Access OFDM*, European Standard (Telecommunications series), December, 2001.

[2] ETSI EN 300 744 V1.4.1, *Digital Video Broadcasting (DVB); Framing structure, channel coding and modulation for digital terrestrial television*, European Standard (Telecommunications series), January 2001.

[3] Berrou, C., Douillard, C. and Jézéquel, M. *Multiple parallel concatenation of circular recursive convolutional (CRSC) codes*, Annals of Telecommunications, Vol. 54, Nº3-4, pp. 166-172, March-April 1999.

[4] Berrou, C., Jézéquel, M., Douillard, C., Brengarth, N., Tousch, J. and Pham, N., *The Turbo Code Standard for DVB-RCS*. 2nd Int'l Symposium on Turbo Codes & Related Topics: September 2000. pp. 535-538.

[5] Guimarães, D. A., Turbo Decoding of Single-Parity Check Product Codes, *Revista Telecomunicações - Inatel*, June 2002 (original title in Portuguese: Decodificação Turbo de Código Produto de Paridade Simples).

[6] Guimarães, D. A., *A Class of Product Codes and its Turbo Decoding Applied to a Multicarrier CDMA System.* Ph.D. Thesis, Universidade Estadual de Campinas, SP, Brazil, June 2003. (original title in Portuguese: Uma Classe de Códigos Produto e sua Decodificação Turbo Aplicada em um Sistema CDMA Multiportadora).

[7] Guinand, Paul; Kabal, Peter; Ould-Cheikh-mouhamedou, Youssoulf. *Enhanced Max-Log-APP and Enhanced Log-APP Decoding for DVB-RCS*. Proc. Int. Symp. Turbo Codes, Brest: September 2003. pp. 259-263.

[8] Hunt, Andrew W., Hyper-codes: *High-performance Low-complexity Error-correcting Codes*, Master's Thesis, Ottawa-Carleton Institute of Electrical Engineering, May 1998.

[9] Berrou, C., Douillard, C., Jézéquel, M. *Designing turbo codes for low error rates. IEE Colloquium on Turbo Codes in Digital Broadcasting – Could It Double Capacity?* Electronics Letters, v.35 n.1. January 1999. p. 39-40.

[10] Berrou, C., Glavieux, A., Thitimajshima, P., Near Shannon limit error-correcting coding and decoding: Turbo-codes. *IEEE International Conference on Communications*, v.2 pp.1064-1070. ICC 1993.

[11] Hagenauer, J.; Offer, E., Papke, L. *Iterative Decoding of Binary Block and Convolutional Codes*. IEEE Transactions on Information Theory, v. 42, n. 2, March 1996. pp. 429-445.

[12] Honary, B. and Markarian, G., *Trellis Decoding of Block Codes: A practical approach*, Kluwer, 1997.

[13] Rankin, David M., *Single Parity Check Product Codes and Iterative Decoding*, Ph.D. Thesis, University of Canterbury, Australia, May 2001.

[14] Sklar, Bernard. *Digital Communications – Fundamentals and Applications*. 2nd. ed. Upper Saddle River: Prentice Hall, 2001.

Mixed Phase-Precoding Method with Turbo Codes for Wireless-ISI Channel Applications

D. Chumchewkul
Faculty of Engineering,
King Mongkut's Institute of Technology Ladkrabang (KMITL),
Bangkok, Thailand.

K. Sripimanwat
National Electronics and Computer Technology Center (NECTEC),
NSTDA, Bangkok, Thailand.
E-mail: ksripima@ieee.org

A. Lasakul
Faculty of Engineering,
King Mongkut's Institute of Technology Ladkrabang (KMITL),
Bangkok, Thailand.

***Abstract*-This paper presents a novel precoding method for BPSK signals through multipath fading channel. It is named as "*mixed* phase-precoding method". This technique is developed mixing on the principle of spiral curve phase precoding and with a dimension partitioning technique. In order to apply this method for applications with turbo code, a specific detector is also proposed. Simulation results show that concatenation of turbo codes and *mixed* phase-precoding achieves a better gain compared to that of the ruled precoder method of spiral curve with the same turbo coding schemes.**

***Index Terms- Pre*-Equalization, Turbo code, ISI**

I. INTRODUCTION

In wireless communications, intersymbol interference (ISI) is one of the major impairments that reduces system efficiency dramatically. Thus, powerful *pre*-equalization techniques have been devised to decrease ISI effect. The first well-known version of those precoding techniques is Tomlinson-Harashima (TH) precoding which is used to precode amplitude modulated signals only [1][2]. Thus, Spiral curve-phase precoding [3] has been developed to avoid the disadvantage of TH-precoding. This was done by proposing *Spiral*-based phase precoding method. In addition, another precoding technique, *Dimension Partitioning* [4], has been published with the same purpose.

In previous works [5][6], a proposed wireless-transmission model by concatenation of turbo code [7] and a "modified" version of Spiral curve precoding on BPSK and QPSK signal through multipath fading channel, was introduced. That was also included the use of another interesting precoding technique of Dimension Partitioning. Simulation results show that concatenation of "modified" Spiral curve phase precoding with turbo codes is a successful method to combat ISI effect for signal transmission through the multipath fading channel. However, this previous model was noted that it still performs poor at low signal to noise ratio (SNR) region. It, therefore, should be re-designed with a better approach to achieve the optimal system performance.

This paper presents a novel version of phase precoding that developed on the principle of spiral curve phase precoding with dimension partitioning technique. It is named as "*mixed* phase-precoding method". Moreover, a specific detector designed for turbo codes is also proposed. In section II, the proposed transmission model is presented. Next, The precoding and detection algorithm for *mixed* phase-precoding are shown in section III and section IV respectively. In section V, a specific detection for turbo decoder is proposed. Finally, their simulation results are discussed in section VI.

II. THE PROPOSED TRANSMISSION MODEL

Figure 1 shows the proposed transmission model with two-duplex two signal links which the forward link direction receives digital input sequence d_i. Each input sequence is encoded by using binary turbo encoder at the rate 1/2 and gives the code word $(c_{p,i}^0, c_{p,i}^1)$ as an output. This code word is passed to the signal mapper to provide appropriate format of signal for precoding method. As a result, a complex coded symbol $\vec{S}_i = Ae^{j\beta_i}$ is obtained, where A is a constant amplitude and β_i is phase of the i^{th} information signal. After that, this signal sequence is interleaved and passed to the precoder in order to create the precoded signal $\vec{P}_i = Ae^{j\theta_i}$ (where θ_i is the precoding phase). Due to the channel for this system fades slowly, the channel-estimated parameter $\vec{I}_i$ which is used for this operation can be investigated from the process of the reverse link in the same data frame of TDD multiplexing systems. That is the channel fades so slowly such that it is assumed to be the time invariant over two adjacent frames of the forward and reverse link. In addition, the channel impulse response can be modeled as a linear and time-invariant over two adjacent data frames so that the radiation patterns are reciprocal in both forward and reverse links. Moreover, channel parameters are estimated perfectly on the reverse link. Due to the limitation of size and power consumption of the mobile unit, precoding is used only at the transmitter of base station.

At the receiver, signal $\vec{R}_i'$ that passed from the multipath Rayleigh fading channel, is detected and computed by the Logarithm of Likelihood Ratio

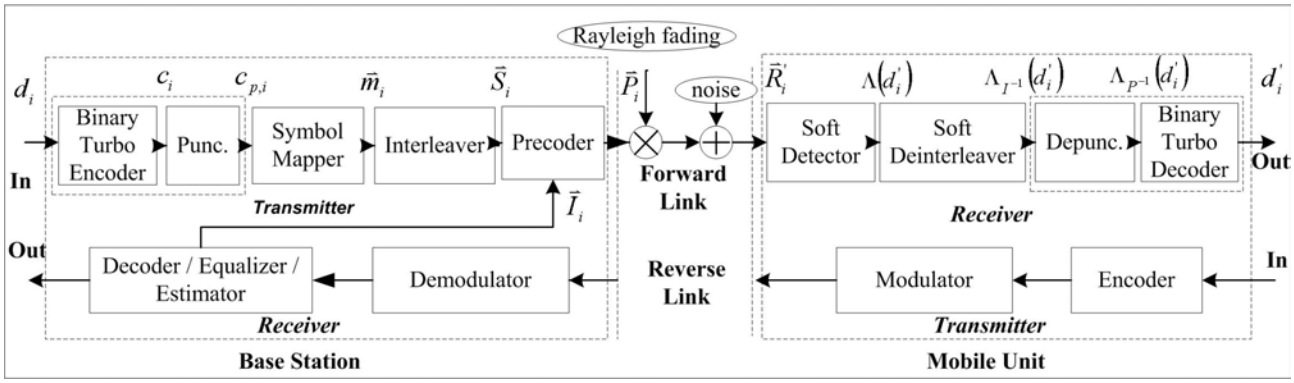

Fig. 1 Proposed Wireless Transmission Model

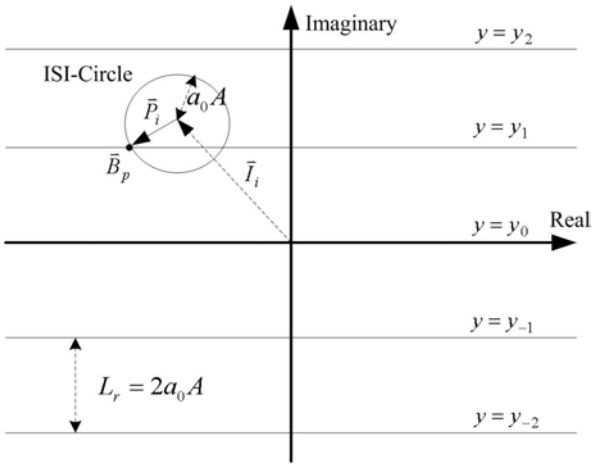

Fig. 2 *Mixed* Phase-Precoding Structure

(LLR); $\Lambda(d_i')$, defined as

$$\Lambda(d_i') = \log\left[\frac{P(d_i = 1 \mid \vec{R}_i')}{P(d_i = 0 \mid \vec{R}_i')}\right] \quad (1)$$

Subsequently, the sequence of this parameter is deinterleaved and passed to the turbo decoder to recover information data d_i'.

III. *MIXED* PHASE-PRECODING

If spiral curve precoding [3] is used in this system, the received signal $\vec{R}_i' = r_i' e^{j\phi_i'}$ at time t_i will be computed by using spiral curve equation to obtain

$$\beta_i' = \phi_i' + \left(\frac{r_i'}{A} - 1\right) C\pi \quad (2)$$

However, when $\vec{R}_i'$ is very close to the center of spiral curve, effect of noise becomes larger. Thus, their operations should be modified to avoid from this case. An approach method could be done by changing the precoding algorithm to have the suitable results for all of ISI cases, such as using of the concept of Dimension Partitioning [4]. This paper presents an alternative precoding method called "*mixed* phase - precoding".

The operations of *mixed* phase-precoding is based on a function of a group of lines, paralleled to the real-axis in the signal space, as shown in Figure 2. Each line is separated equally by L_r and their imaginary part y_z is

$$y_z = zL_r + \frac{\beta_i L_r}{2\pi} \quad ; z = ...,-2,-1,0,1,2,... \quad (3)$$

where β_i is phase of the information signal and z is an integer number referred to a line of y is y_z. Due to each line of this function will be used for the decision at the detector, they are called "the decision line". Basically, the precoded signal for this schemes is calculated by determine roots of equation (3) and the ISI-circle, centered at $\vec{I}_i$ and with radius $a_0 A$, denoted by

$$(a_0 A)^2 = (\mathrm{Re}(\vec{I}_i) - x)^2 + (\mathrm{Im}(\vec{I}_i) - y)^2 \quad (4)$$

where (x, y) is the position of a point on the signal space. Respectively, a_0 and φ_0 is amplitude and phase distortion of the first path fading, $\mathrm{Re}(\vec{I}_i)$ and $\mathrm{Im}(\vec{I}_i)$ is a number of real and imaginary of $\vec{I}_i$. Consequently, only one root $\vec{B}_p$ will be selected. It is the desired received signal which is subtracted by $\vec{I}_i$ to be the precoded signal or

$$\vec{P}_i = Ae^{j\theta_i} = \vec{B}_p - \vec{I}_i \quad (5)$$

Finally, phase of this precoded signal is subtracted by φ_0 to compensate from phase distortion of the first path fading. The value of L_r plays an important role. In this paper, L_r is set to $2a_0 A$ to prevent from the case that there is no existing root of equation (3) and (4).

IV. PHASE DETECTING ALGORITHM

From precoding algorithm described in section III, the precoded signal is generated by using relationship between the desired received signal's imaginary part and β_i as in (3). Therefore, at the detector, the received information carrying phase $\beta_i^{'}$ can be calculated by.

$$\beta_i^{'} = (\mathrm{Im}(\vec{R}_i^{'}) \bmod (L_r)) \frac{2\pi}{L_r} \tag{6}$$

where $\mathrm{Im}(\vec{R}_i^{'})$ is a number of imaginary of $\vec{R}_i^{'}$ and $\mathrm{mod}(x)$ is a function of modulo operation. In order to use this precoding method with turbo decoder, another kind of detecting algorithm is also developed. This algorithm for application with BPSK-signal is presented in the next section.

V. APPLICATIONS WITH TURBO CODES

The detected data from the detector in the form of LLR can be done by computing condition probabilities $P(\vec{S}_i = Ae^{j\beta_{d_i=0}} \mid \vec{R}_i^{'})$ and $P(\vec{S}_i = Ae^{j\beta_{d_i=1}} \mid \vec{R}_i^{'})$ from $\vec{R}_i^{'}$ at each time. They are probabilities of $\vec{S}_i$ which their phase are $\beta_{d_i=0}$ and $\beta_{d_i=1}$ respectively. When error distribution of the received signal is assumed as *Gaussian* distribution with zero mean and variance σ_N^2, this condition probability can be calculated by

$$P(\vec{S}_i = Ae^{j\beta_{d_i=x}} \mid \vec{R}_i^{'}) = \frac{1}{\sqrt{2\pi\sigma_N^2}} \exp\left(\frac{-\left(\mathrm{Im}(\vec{R}_i^{'}) - \left(z' L_r + \frac{\beta_{d_i=x} L_r}{2\pi} \right) \right)^2}{2\sigma_N^2} \right) \tag{7}$$

where $z^{'}$ is an integer number of the selected decision line which can be computed by

$$\left| \mathrm{Im}(\vec{R}_i^{'}) - \left(z' L_r + \frac{\beta_i L_r}{2\pi} \right) \right| \le L_r / 2 \tag{8}$$

Finally, $\Lambda(d_i^{'})$ is then calculated from

$$\Lambda(d_i^{'}) = \log\left[\frac{P(\vec{S}_i = Ae^{j\beta_{d_i=1}} \mid \vec{R}_i^{'})}{P(\vec{S}_i = Ae^{j\beta_{d_i=0}} \mid \vec{R}_i^{'})} \right] \tag{9}$$

VI. SIMULATION RESULTS

In this paper, simulation is carried out to investigate performance of the proposed model. ISI channel is modeled by two equal strength rays of Rayleigh fading on the τ - spaced discrete-time model

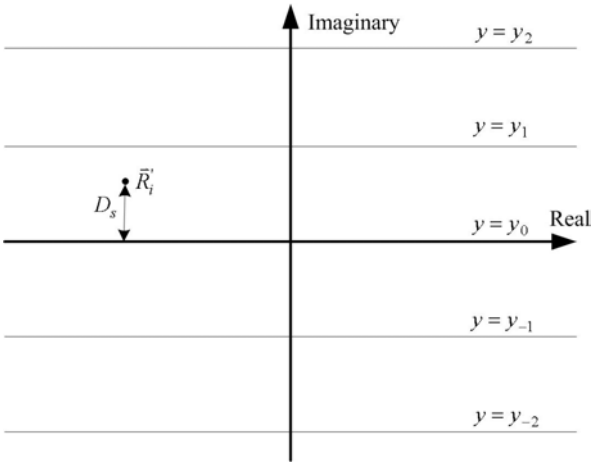

Fig. 3 Phase detection

where the delay $\tau = |\tau_1(t) - \tau_0(t)|$ is one symbol period *T*. Doppler effect is not taken into account. In Figure 4, performance comparison of Spiral curve and *mixed* phase-precoding on uncoded-BPSK signal is presented. Amplitude of the transmitted signal is set to unity, Spiral curve constant C for Spiral curve precoding is $1/a_0$, and L_r of *mixed* phase-precoding is $2a_0A$. From simulation result, it is obvious that *mixed* phase-precoding has the better performance compared to that of Spiral curve.

The performances of the concatenation of turbo codes with modified Spiral curve and *mixed* phase-precoding on BPSK signal are shown in Figure 5. Turbo code for this simulation is $[23_8, 35_8]$, rate 1/2 (throughput 1 bit/sec/Hz) with 1024 bit per block and the internal interleaver is a pseudo-random interleaver. The external interleaver works in block style and decoder for this simulation is the Log-MAP turbo decoder. Parameters for each precoding are as used in the previous case. Their results at iteration 1, 3 and 18 show that performance of turbo code with *mixed* phase-precoding achieves the better gain compared to that of Spiral curve with the same turbo coding scheme.

VII. CONCLUSION

This paper presents a novel precoding method that developed on the principle of Spiral curve phase precoding and Dimension Partitioning. It's called *mixed* phase-precoding and designed to use with phase modulated signal. For applications with turbo codes, an another kind of detecting algorithm that generates soft-decision data in the format of LLR is also proposed. Their simulation results on BPSK signal show that it is a suitable precoding algorithm for using of both with and without turbo coding schemes. Evidently, this work shows the successful invention of new phase precoding method. Its application for wireless ISI channel by concatenation with turbo code achieves dramatically performance improvement.

In the future, improvement on performance of this schemes at low SNR region, and under other channel condition such as Nakagami will be studied.

ACKNOWLEDGEMENT

For the author, *D. Chumchewkul*, his work is supported with a scholarship granted by the Thailand Graduate Institute of Science and Technology (TGIST), National Science and Technology Development Agency (NSTDA), Thailand.

REFERENCES

[1] M. Tomlinson, "New Automatic Equalizer Employing Modulo Arithmetic", *IEEE Electronics Letters*, Vol. 7, pp. 138-139, Mar 1971.

[2] H. Harashima, H. Miyakawa, "Match-Transmission Technique for Channels with Intersymbol Interference", *IEEE Trans. on Commun.*, Vol. Com-20, August, 1972, pp.774-780.

[3] W. Zhuang, V. Huang, "Phase precoding for frequency-selective Rayleigh and Rician slowly fading channels", *IEEE Trans. Veh. Tech*., Vol. 46, pp. 129-142, Feb 1997.

[4] Y. Chan, W. Zhuang, "Channel Precoding for Indoor radio Communications Using Dimension Partitioning", *IEEE Transactions on Vehicular Technology*, Vol. 48, No. 1, January 1999.

[5] D. Chumchewkul, K. Sripimanwat, A. Lasakul, I. Fair, P. Thitimajshima, *"Pre*-Equalized QPSK-Signal with Turbo Codes for Wireless-ISI Channel", *3rd International Symposium on Turbo Codes & Related topics*, Breast, France, September, 2003.

[6] A. Pradabphon, D. Chumchewkul, K. Sripimanwat, A. Lasakul, "BPSK-Turbo Codes with Spiral curve phase precoding for Wireless-ISI Channel", *WPMC '03*, Yokosuka, Kanagawa, Japan, October, 2003.

[7] C. Berrou, A. Glavieux and P. Thitimajshima, "Near Shannon Limit Error-correcting Coding and Decoding: Turbo-Codes", *Proc. ICC'93*, pp. 1064-1070, May 1993.

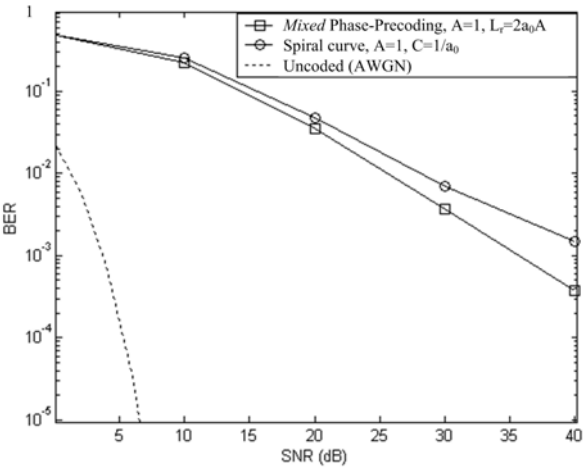

Fig. 4. Performance Comparison for Uncoded-BPSK Signal

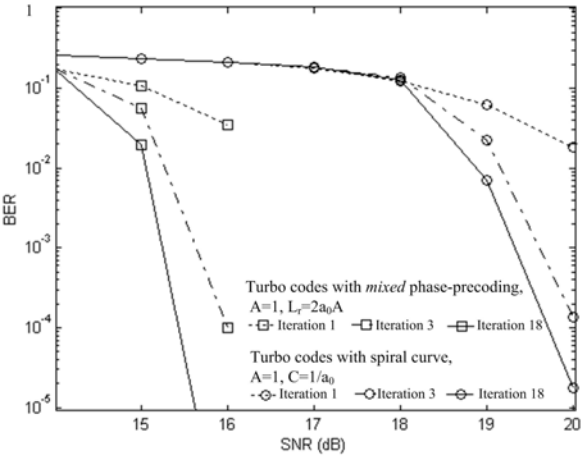

Fig. 5. Performance of Concatenation of Turbo Codes with Two Types of Precoding

Low-Complexity Block Coded Multicarrier Modulation for Non-Square M-QAM to line-of-sight Microwave Systems

Leandro Coimbra da Fonseca
National Institute of Telecommunications - Inatel
Av. João de Camargo, 510 - 37540-000
Santa Rita do Sapucaí - MG – Brazil
Phone: ++55 24 3322 0271
leandrocoimbra@bol.com.br

Geraldo Gil R. Gomes
National Institute of Telecommunications - Inatel
Av. João de Camargo, 510 - 37540-000
Santa Rita do Sapucaí - MG – Brazil
Phone: ++55 35 3471 9322
ge@inatel.br

***Abstract*— One of the main factors that cause the quality degradation of the long-range digital systems to line-of-sight with transmission rates in the order of some ten Mb/s is the frequency-selective fading. One of the alternatives to decrease the effect caused by the frequency-selective fading is the use of a coded modulation on multiple carriers [3, 11]. This article aims to analyze the performance of low complexity block coded multicarrier modulation for non-square M-QAM constellations, more suitable to the canalizations with bandwidth next to 29MHz. A BCMCM (*Block Coded Multicarrier Modulation*) 128-QAM scheme, using a simple code array is compared to the BCMCM 64-QAM scheme presented in [3, 11], when it is noted besides the reduction of the used bandwidth, a reduction of the system signature area.**

***Index Terms* — multicarrier modulation, frequency-selective fading, coded modulation, signature area.**

I. INTRODUCTION

The OFDM (*Orthogonal Frequency Division Multiplexing*) is a MCM (*Muticarrier Modulation*) time-limited and has been used in lots of applications. This technique consists of the parallel data transmission in several subcarriers with QAM or PSK modulation. With this technique use, the digital transmissions systems become more efficient in the combat to frequency-selective fading than the systems that use the conventional transmission, i.e., in a single carrier modulation. Using this technique, the effects of the frequency-selective fading presented by a channel for the single carrier transmission, can be analyzed as being in a nature of flat fading or almost flat in the MCMs schemes. Therefore, the equalization need in this system is practically null or significantly reduced [1].

The digital radio systems to line-of-sight are limited systems in bandwidth, whose traffic can impose transmissions rates of hundreds of Mb/s, therefore, orthogonal MCMs schemes with limitation in band are necessary for this application.

As the OFDM has a power spectrum that decreases softly out of Nyquist bandwidth, its use is inadequate for this application, i.e., if the OFDM is transmitted through frequency-limited channels, a significant part of the OFDM spectrum flanks should be attenuated, resulting in an ICI (*Inter-Channel Interference*) and IFI (*Inter-Frame Interference*) increase, by orthogonality loss [2].

Then, an improved scheme of multicarrier modulation, time-limited, called ITLO-MCM (*Improved Time Limited Orthogonal – Multicarrier Modulation*) and that also presents a frequency-limited through its properties, has been proposed for digital radio systems to line-of-sight [3, 12].

II. MULTICARRIER MODULATION FOR MICROWAVE DIGITAL RADIO

The MCM performance presents better performance than a SCM (*Single Carrier Modulation*) according to the frequency-selective fading, however, the MCM is subject to the burst-errors. Then, in digital transmission systems that use the MCM is common the use of coded channel scheme associated with an interleaving.

The interleaving can be made basically of two forms: by block or in the convolution form [4]. In this work is used the block interleaving.

In the MCM the total bit error probability is calculated considering the bit error probability by carrier, whose values depend on notch depth and the localization of it inside the band. It is evident that only the carriers next to the most directly reached carrier by notch contribute of significant form for total system bit error rate [3]. The interleaving function in the MCM is making the symbols to be transmitted are rearranged in the way that the burst-errors produced by a notch are not concentrated on an single word code.

With the interleaving, the capacity burst-error correction, becomes to be m times the correction capacity C, gotten with the use of systematic linear block code, (n,k), where n is the word code length and

k is the information bit number, i.e.,

$$C \le \left\lfloor \frac{1}{2}(n-k) \right\rfloor \tag{1}$$

Therefore, an l burst can be corrected since

$$l = m.C \le m\left\lfloor \frac{1}{2}(n-k) \right\rfloor \tag{2}$$

The block interleaving can be gotten from a rectangular array, with m rows and n columns, as shown in Figure 1. The interleaving length is defined by number m array row and the code n length to be used, defines the number n array column. Then, each array row is composed by a word code.

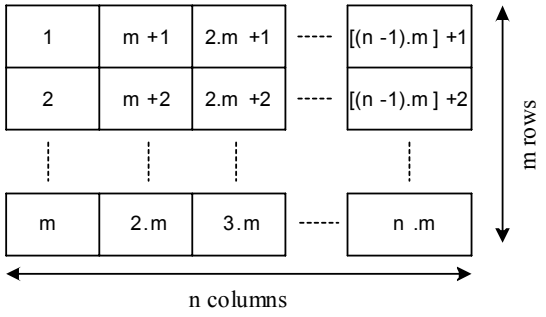

Fig. 1. Interleaving for correction burst-error.

The array shown in Figure 1 is such as: the N symbols, one by one of N carriers, are placed in the array sequentially from top to bottom and from left to the right until the cell below and more to the right to be filled by the number symbol $m.n=N$.

III. BCMCM TO NON-SQUARE M-QAM CONSTELLATION

The non-square constellation, constellation with 2^N points, where N is odd, can be constructed by several forms [5]. A construction form of non-square constellation, which will be used in this work, is presented in Figure 2. It can be observed that such constellation is constituted by the two square M-QAM constellation interlacement.

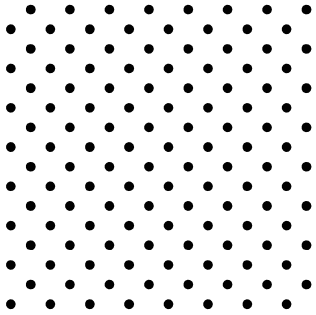

Fig. 2. Constellation of a 128-QAM.

In this way, it is possible to reduce the non-square M-QAM constellation dimension as presented in [6], reducing thus, and the complexity of BCM schemes decoding process.

In the block coding scheme, generalized by Sayegh [7], which can be used in multicarriers modulation, the coding process consists on codes array mounting. For the case of an M-QAM constellation, where M is an odd power of two, the array can be mounted as shown in Figure 3.

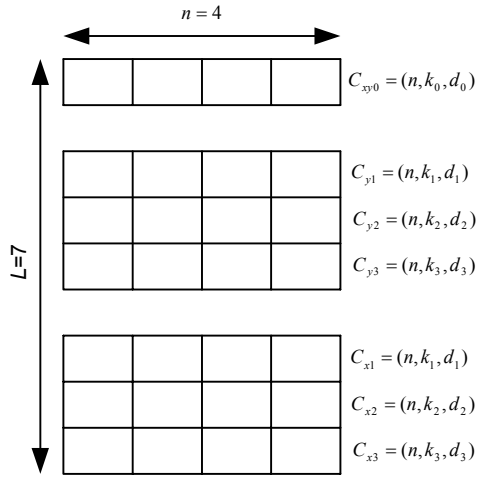

Fig. 3. Codes array for a 128-QAM constellation.

In Figure 3 array, each column corresponds to one of the symbols that compose the 128-QAM constellation. The existing codes in each array row are called linear block code $C=(n,k,d)$, where n corresponds to the code length, k is the information bits amount and the d represents the minimum Hamming distance of the used code.

For a system with multiple carriers, this array is associated with the interleaving presented in Figure 1, as shown in Figure 4.

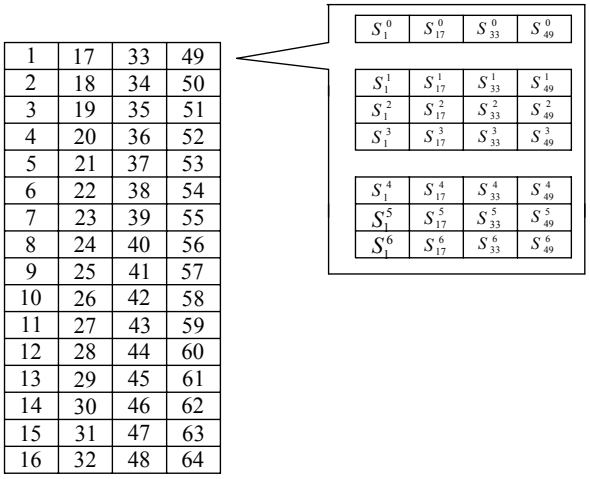

Fig. 4. Sayegh's array for a 128-QAM constellation inserted in an interleaving for 64 carriers.

The codification rate, R_c, can be calculated through the Equation (3).

$$R_c = \frac{\sum_{i=1}^{L_x} K_{xl} + \sum_{i=1}^{L_y} K_{yl}}{n.(L_x + L_y)} \tag{3}$$

Table I presents the codification rates used in the BCMCM 64-QAM schemes presented in [3, 11] and in BCMCM 128-QAM scheme presented in this work.

TABLE I
CODING RATE FOR BCMCM 64-QAM AND 128-QAM SYSTEMS.

Constellations	Coded levels	Code arrays	Coding rate
64-QAM	1	(4,3,2) (4,4,1) (4,4,1)	11/12
128-QAM	2	(4,1,4) 2x (4,3,2) 2x (4,4,1) 2x (4,4,1)	23/28

IV. BCMCM PERFORMANCE ANALYSES FOR NON-SQUARE M-QAM CONSTELLATION IN RUMMLER'S CHANNEL MODEL.

Selective fading are caused by multipath propagation. Basically, because of wave front, traveling different paths, it reaches the reception antenna in different times. These signal combination in the receiver can modify the characteristics of the transmitted signal, becoming its frequency response non-linear, inside the bandwidth interest [8]. For systems with high transmission rates, those attenuations have the behavior of a reject-band filter, presenting a cut (notch) in the frequency response of the transmitted signal.

The produced distortions by the selective fading can be evaluated by the amplitude distortions analysis and phase obtained since the transfer function that describes the channel behavior. In this work, the Rummler's channel is used in digital radio systems to line-of-sight [2, 9].

The Equation (4) describes the transfer function for the Rummler's channel model.

$$H(w) = a.\{1 - b.\exp[-j(w - w_0)\tau]\} \tag{4}$$

The magnitude module and the transfer function phase, H(w) e φ(w), are described in the Equations (5) e (6), respectively, i.e.,

$$|H(w)| = a.\sqrt{[1 + b^2 - 2b\cos(w - w_0)\tau]} \tag{5}$$

$$\varphi(w) = -\arctan\left\{\frac{[b.\mathrm{sen}(w - w_0)\tau]}{[1 - b.\cos(w - w_0)\tau]}\right\} \tag{6}$$

where, a is the variable that represents the flat fading, in general, associated to multipath, b represents the relative amplitude between main rays (direct) and secondary, whose value is understood between zero and one, w is the angular frequency, w_0 is the angular frequency where notch happens, i.e., minimum function value, and τ is the time delay between the direct and secondary rays.

The amplitude distortion of the transfer function is evaluated through its relative slope, α(w), in s/rad, as follows:

$$\alpha(w) = \frac{1}{|H(w)|}\frac{d|H(w)|}{dw} \tag{7}$$

The transfer function phase distortion is evaluated through the group delay, β(w), in seconds, given by Equation (8).

$$\beta(w) = \frac{-d\varphi(w)}{dw} \tag{8}$$

In this work the a value, flat fading, will always be equal to the unit, i.e., we will only consider the effects caused by the frequency-selective fading. The needed condition so that it happens is determined by [2]

$$C_\alpha = 2\pi.\alpha_p.B_p << 1 \tag{9}$$

$$C_\beta = \frac{\beta_p}{T} << 1 \tag{10}$$

where, α_p and β_p are α(w) e β(w) values for w=wp, being w_p the angular frequency value for the carrier p, and B_p is the bandwidth of each BCMCM carrier p, in Hz.

Table II presents C_α e C_β values for the MCM system with 64, 128 e 256 carriers, with bandwidth

for carrier of 347.2 KHz, 173.6 KHz and 86.8 KHz, respectively, for different notch depth. These systems support a transmission rate of 155.52 Mb/s with a 128-QAM. It can be checked through Table II that the conditions imposed by the Equations (9) and (10) depend on the notch depth and the carriers number.

TABLE II
RELATIVE SLOPE(α_p) AND GROUP DELAY (β_p) MAXIMUM VALUES, FOR 64, 128 AND 256 SUBCARRIERS(N) AS FUNCTION NOTCH DEPTH(D).

Notch Depth	Number of subcarriers					
	64		128		256	
	C_α	C_β	C_α	C_β	C_α	C_β
20 dB	0,009	0,02	0,002	0,010	0,0005	0,005
25 dB	0,029	0,037	0,007	0,018	0,002	0,009
30 dB	0,092	0,066	0,023	0,033	0,006	0,017
35 dB	0,269	0,107	0,071	0,058	0,018	0,03
40 dB	0,662	0,149	0,209	0,097	0,057	0,053
45 dB	1,222	0,154	0,541	0,141	0,17	0,088

Through the Table II, it is observed that, the conditions imposed by the Equations (9) and (10) so that *a* is equal to the unit, to be accepted, therefore, we will only analyze the degradation imposed by the selective fading, considering only the ISI. This degradation, for the proposed MCMs schemes, can be evaluated under the point of view of relationship signal/noise interference – SIR (*Signal to interference Ratio*) in each modulated carrier that composes the MCM frame. A good SIR estimate can be made by (11), obtained from simulation data [9], i.e.,

$$\chi_p = \left(\frac{T_s.N.\left|H\left(w_p\right)\right|}{\pi.\tau.a.b} \right)^2 \qquad (11)$$

Where $\left|H\left(w_p\right)\right|$ is equal the $\left|H\left(w\right)\right|$ for the angular frequency of a private *p* carrier and the other variables were already defined for the Equations (5) and (6). Considering that the interference acts as a noise white addictive gaussian, the symbol rate caused by the interference can be calculated by the Equation (12) [10], i.e.,

$$Ps_p = \frac{4M - 4\sqrt{2M} + 2}{M} Q\left(\sqrt{\frac{24}{2M-1}\chi} \right) \qquad (12)$$

where Ps_p is function of the relationship carrier/interference, χ, and, therefore, this is the symbol error probability for a private carrier, with the angular frequency w_p. The Equation (12) is worth for M-QAM constellation, since M is an odd power of two and the constellation has the format equal to the shown in Figure 2, according presented in [10]. This Equation (12) can only be used for the symbol error probability calculation, because, the M-QAM constellations where *M* is an odd power of two, don't admit the Gray code mapping. Therefore, the relationship adopted between the bit error probability and the symbol error probability, presented by (13), for the approximated calculation of bit error probability in systems that use square M-QAM constellation mapped with the Gray code is not valued for non-square M-QAM constellations, i.e., where Gray mapping is possible, the following relationship is valid

$$Pb_p = \frac{Ps_p}{\log_2 M}, \qquad (13)$$

where Pb_p is the bit error probability for a private carrier in function of Ps_p and M is symbols amount of the used QAM constellation.

For a better analysis of BCMCM x 128-QAM systems performances were accomplished some computing simulations.

The performance of BCMCM 128-QAM systems is presented through the Figures 5, 6 and 7.

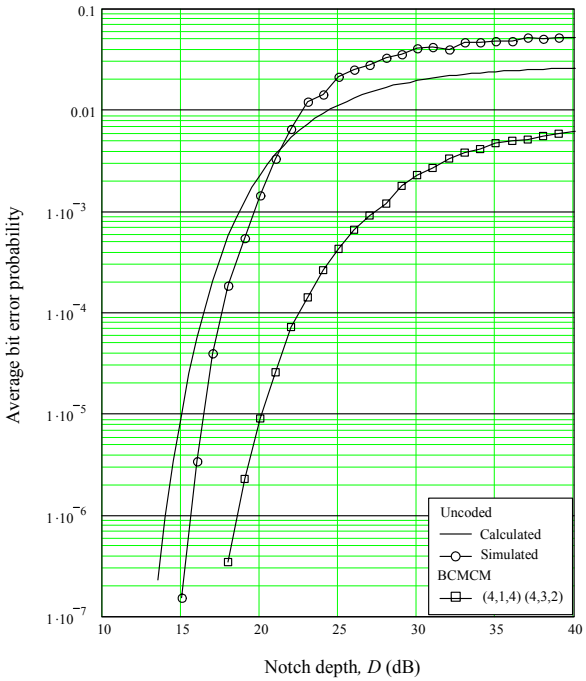

Fig. 5. Performance of BCMCM 64 x 128-QAM (155,52Mb/s).

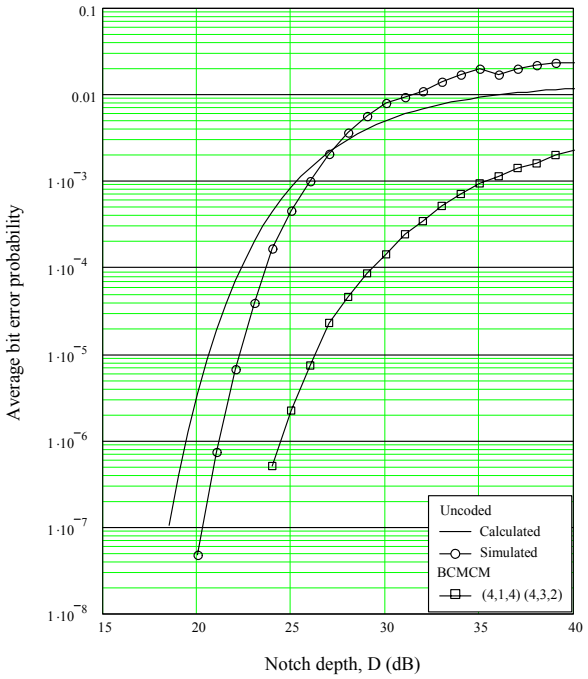

Fig. 6. Performance of BCMCM 128 x 128-QAM (155,52Mb/s).

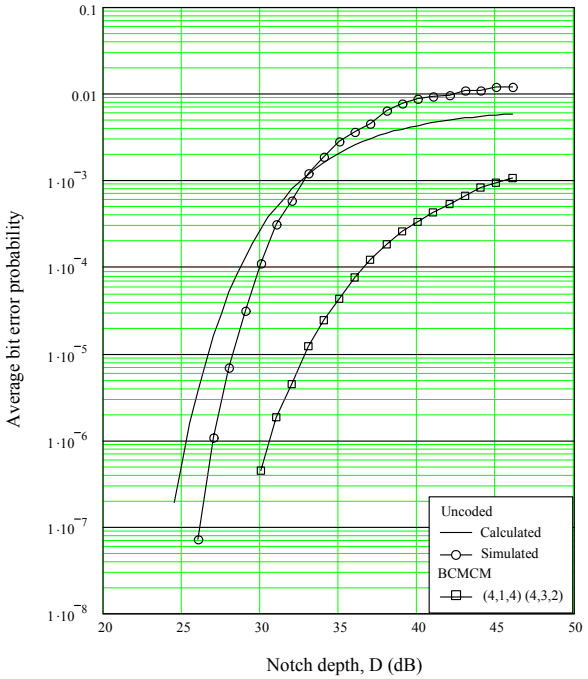

Fig. 7. Performance of BCMCM 256 x 128-QAM (155,52Mb/s).

Through the Figures 5, 6 and 7, it is noticed that, for the same BCMCM 128-QAM scheme, as larger the number of carriers, minor is the total bit error probability, i.e., for the same error rate, the schemes with a larger number of carriers support larger notch depths.

It is important to emphasize that the theoretical curve was plotted from the Equation (12). As it was said before, this Equation can only be used for the symbols error probability calculation, but it was made an approximation, i.e., the Equations (12) and (13) were used considering the Gray mapping for the 128-QAM constellation, so that it could have a reference for the results obtained from the computing made simulation. Therefore, this is the only aim of this theoretical curve, because, we can not compare it with the curve without plotting codification from a computing simulation that describes the BCMCM 128-QAM system behavior.

V. SIGNATURE AREA

The signature area is the one under signature curve, that itself, presents the notch depth geometric places on the modulated signal frequency spectrum where a threshold error rate is considered constant [11].

From this curve, we can know if the system operating in a channel with selective fading is outage or not. Because, if the notch generated by the frequency-selective fading, touches or invades the area under this curve, the system is taken to the outage situation. Therefore, this curve supplies the maximum value of attenuation allowed by the system.

We can obtain the system signature area through two methods, using the rectangular approximation process. Through simulation as presented in [3] or through the method, used in this work, that consists on using notch depth value in the center of band as being medium depth of the signature curve along the band and adopt as the signature bandwidth the MCM scheme bandwidth.

Through the used method in this work and the with the help of the curves in Figures 5, 6 and 7, obtained from computing simulations, it is possible to calculate the systems signature areas in study. These calculations can be accomplished through the Equations (14) and (15) [3, 8]

$$\lambda_a = 10^{\frac{-D}{20}} \tag{14}$$

$$S = \frac{\lambda_a \times w}{\tau_r} \tag{15}$$

where D is the notch depth, in dB; λ_a is the average notch depth, in linear scale, w is the signature bandwidth, in GHz, τ_r is the reference delay, i.e., time delay between the arrival main ray and the secondary in the receiver, using for the plotted curves in Figures 5, 6 and 7, in *ns,* and *S* is the signature area, in ns^{-2}.

The Table III presents the BCMCM 128-QAM system signature areas with 64, 128 and 256 carriers for an 10^{-3} error rate.

TABLE III
SIGNATURE AREAS, IN FUNCTION OF 10^{-3} ERROR RATE, OBTAINED FROM SIMULATIONS RESULTS PRESENTS IN THE FIGURES 5, 6 AND 7.

Code arrays	Number of carriers	Signature area (BER=10^{-3})
Uncoded	64	366 x 10^{-6} ns^{-2}
	128	175 x 10^{-6} ns^{-2}
	256	80 x 10^{-6} ns^{-2}
(4,1,4)	64	185 x 10^{-6} ns^{-2}
2x (4,3,2)	128	73 x 10^{-6} ns^{-2}
2x (4,4,1) 2x (4,4,1)	256	23 x 10^{-6} ns^{-2}

VI. CONCLUSION

A BCMCM 128-QAM scheme using a simple code array is compared with the BCMCM 64-QAM presented in [3, 11], when it is noted besides the reduction of the used bandwidth, a reduction of the system signature area, i.e., from the data presented in Table IV we can better verify the results obtained in the comparison accomplished between BCMCM 128-QAM and BCMCM 64-QAM systems.

TABLE IV
COMPARISON BETWEEN A BCMCM X 64-QAM AND BCMCM X 128-QAM SCHEME.

	BCMCM x 64-QAM	BCMCM x 128-QAM
Code Arrays	(4,3,2) (4,4,1) (4,4,1)	(4,1,4) 2x (4,3,2) 2x (4,4,1) 2x (4,4,1)
Coding Rate	11/12	23/28
Total Bit Rate (Mb/s)	169.658	189.329
BW (MHz)	28.276	27.05
Signature Area, (BER=10^{-3}), to 64, 128 and 256 subcarriers, respectively	250 x 10^{-6} ns^{-2}	185 x 10^{-6} ns^{-2}
	95 x 10^{-6} ns^{-2}	73 x 10^{-6} ns^{-2}
	35 x 10^{-6} ns^{-2}	23 x 10^{-6} ns^{-2}

REFERENCES

[1] E. L. Pinto & C. P. Albuquerque, *A Técnica de Transmissão OFDM*, Revista do Instituto Nacional de Telecomunicações, Vol 5, N° 01, Junho 2002.

[2] R. LI, *Multicarrier modulation and the application of SAW chirp Fourier Transform*, Ph.D Dessertation, Department of Telecommunications, Norwegian Institute of Technology, University of Trondheim, Norway, November 1994.

[3] G. G. R. Gomes, *Modulação Multiportadora Codificada por Bloco para Radioenlaces Digitais em Microondas com Linha de Visada*, Tese de Doutorado, DECOM, FEEC, UNICAMP, Campinas, Dezembro 2002.

[4] J. D. Proakis, *Digital Communications*, 3.ed, New York, McGraw Hill, 1995.

[5] E. A. Lee & D.G. Messerschimitt, *Digital Communication,* 2 ed, Boston, Massachusetts, Kluwer Academic Publisher, 1994.

[6] G. G. R. Gomes, *Modulação codificada por blocos para constelações M-QAM não-quadradas,* Tese de Mestrado, DECOM, FEEC, UNICAM, Campinas, Junho 1997.

[7] S. I. Sayegh, *A class of optimum block codes in signal space,* IEEE Transactions on Communications, COM – 34(10) : 1043-45, October 1996.

[8] T. Manning, *Microwave radio transmission – design guide,* Norwood, MA, Artech House, 1999.

[9] R. Li & G. Stette, *Waveform shaped MCM for digital microwave radio,* IEEE, ISSN 0-7803-2486, February 1995.

[10] L. L. Mendes & A. C. Silveira, *A New Approach to Analyse the Performance of Non-Square M-QAM Systems in AWGN Channels,* In 14th Virginia Tech/MPRG Wirelles Personal Communication Symposium, Blacksburg – VA Proceedings of the symposium, v.1, n, p. 165-171, 2004.

[11] G. G. R. Gomes & R. Baldini Filho, *On Line-of-Sight Microwave Block Coded Multicarrier Modulation Performance in Rummler´s Frequency Selective Channel Model,* In 7th International OFDM - Workshop, at the Hotel Hafen Hamburg, Hamburg, Germany, 10-11 September 2002.

[12] R. Li & G. Stette, *Time-limited orthogonal multicarrier modulation schemes,* IEEE Transaction on Communications, 43 (4) : 1269-1272, April 1995.

Performance Enhancements in OFDM-WLAN Systems Using MIMO Access Techniques

Eduardo R. de Lima, Santiago J. Flores, Vicenç Almenar
Departamento de Comunicaciones
Universidad Politécnica de Valencia - UPV
phone: +34 962849345, fax: +34 962849313
Cta. Nazaret-Oliva s/n, 46730 - Gandia - Spain
edrodde@doctor.upv.es, {sflores, valmenar}@dcom.upv.es

Maria José Canet
Departamento de Ingienería Electrónica
Universidad Politécnica de Valencia - UPV
phone: +34 962849345, fax: +34 962849313
Cta. Nazaret-Oliva s/n, 46730 - Gandia - Spain
macasu@doctor.upv.es

***Abstract*—In this paper we examine the improvements in the performance of a broadband OFDM-based system using MIMO techniques. The MIMO techniques evaluated are VBLAST, SFBC, STBC and Subcarrier by Subcarrier Selection. Performance results are presented for coded/uncoded OFDM, for a typical indoor scenario.**

***Index Terms*—IEEE802.11a, Hiperlan/2, Performance, MIMO-OFDM, SFBC, STBC, Subcarrier Selection, WLAN.**

I. Introduction

The demand for high data rate wireless systems is pushing the wireless technologies to the Shannon's frontier. This demand is a reality already, especially due the recent deployment of third generation networks in several places around the world and the dissemination of the wireless local area networks (WLAN) as well. Nevertheless, concomitantly to the increase of the data rate, the symbol period decreases and the systems usually are disturbed by intersymbol interference (ISI) from multipath propagation and its inherent delay spreading. Orthogonal Frequency Division Multiplexing (OFDM) with cyclic prefix (CP) is a multicarrier technique capable of mitigate ISI and improve the spectral efficiency of wireless systems. On the other hand, MIMO systems promise the increase of the capacity with acceptable bit error rate (BER). These two techniques are rising in importance in wireless communications, particularly in wireless systems focused in high spectral efficiency, for high data rate delivery. The combination of both of them seems to be a choice for future and emergent wireless systems.

This work is part of a research regarding spatial diversity techniques, space time coding (STC) and spatial multiplexing (SM) with the aim of improving the performance and throughput of OFDM-based wireless local area networks [9]. In that work we made comparisons of the performance of STC and spatial diversity techniques applied either to transmitter or receiver with the aim of improving the performance of the WLAN standards IEEE802.11a and Hiperlan/2 when working over a multipath fading scenario. Nevertheless, that first phase is based on SIMO and MISO cases and is mainly focused in performance enhancement by means of diversity gain.

In this new work we are focused in MIMO cases, so that, we extend the Subcarrier by Subcarrier Selection, STBC and SFBC to MIMO case (2Tx,2Rx). In addition we evaluate Spatial Multiplex, by means of Zero Forcing VBLAST (ZF-VBLAST) using several configurations of Tx and Rx Antennas. The main idea in this case is in this case is to observe a throughput enhancement but keeping the overall performance in acceptable levels in relation to those techniques focused in diversity gain and the SISO case (1Tx,1Rx).

II. System Overview

An OFDM system, based on the physical layer of the IEEE802.11a and Hiperlan/2 standards is assumed. The sample rate at the receiver and transmitter is 20 MHz. The code rate is 3/4 and is obtained by puncturing the 1/2 rate encoded data. The block diagram of those standards is presented in Fig.1.

Notations used are as follow

$\overline{(\cdot)}$	Complement of $(\cdot)$
$(\cdot)^{-1}$	Inverse of $(\cdot)$
$(\cdot)^{T}$	Transpose of $(\cdot)$
$(\cdot)^{\dagger}$	Pseudo-inverse of $(\cdot)$
$\left\|(\cdot)\right\|$	Euclidian norm of $(\cdot)$
$\left\|(\cdot)\right\|$	Module of $(\cdot)$
$\mathbf{T}_{CP}$	Insertion matrix of cyclic prefix
$\mathbf{F}$	FFT
$\mathbf{F}^{-1}$	IFFT
$\underline{(\mathbf{G})_i}$	i-th row of matrix
$(\mathbf{G})_j$	j-th column of matrix

Assuming, initially, a SISO OFDM system, the ith block of data [6], $\tilde{\mathbf{u}}_i$ (i-th OFDM symbol with cyclic prefix) is given by $\tilde{\mathbf{u}}_i = \mathbf{T}_{CP}\mathbf{F}^{-1}\mathbf{u}_i$. The data vector $\tilde{\mathbf{u}}_i$ is of length K, the size of the cyclic prefix insertion matrix ($\mathbf{T}_{CP}$) is P×K, where P=C+K, and C is the length of the cyclic prefix, $\mathbf{F}$ is of size K×K. At the receiver, the actual transmitted block $\tilde{\mathbf{u}}_i$, in addition to a fraction of the previous block $\tilde{\mathbf{u}}_{i-1}$, is received.

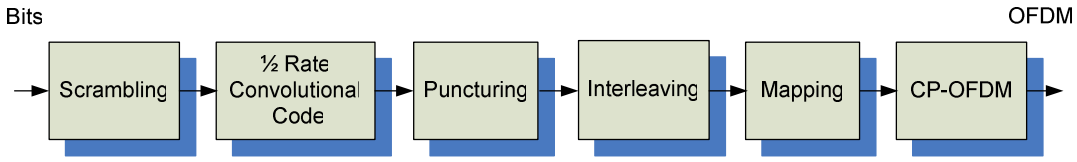

Fig. 1: IEEE802.11a/Hiperlan/2 Physical Layer.

This is described by Toeplitz channel matrices $\mathbf{H_0}$ and $\mathbf{H_1}$. The i-th received block $\tilde{\mathbf{x}}_\mathbf{i}$, is described by

$$\tilde{\mathbf{x}}_\mathbf{i} = \mathbf{H_0}\tilde{\mathbf{u}}_i + \mathbf{H}_1\tilde{\mathbf{u}}_{i-1} + \tilde{n}_i \qquad (1)$$

It is assumed that the length of the channel L-1 ≤ C and that the receiver removes the first C samples of $\tilde{\mathbf{x}}_\mathbf{i}$ by a matrix $\mathbf{T}_R$. Hence, the input-output relationship of a SISO OFDM with cyclic prefix [6] can be expressed as

$$\tilde{\mathbf{x}}_\mathbf{i} = \mathbf{F}\mathbf{T}_R\mathbf{H_0}\mathbf{T}_{CP}\mathbf{F}^{-1}\mathbf{u}_i + \mathbf{F}n_i \qquad (2)$$

A specific construction of guarantees that $\mathbf{T}_R\mathbf{H_0}\mathbf{T}_{CP}$ is circulant, and thus is diagonalised by $\mathbf{F}$. Hence

$$\mathbf{F}\mathbf{T}_R\mathbf{H_0}\mathbf{T}_{CP}\mathbf{F}^{-1} = \tilde{\mathbf{H}} \qquad (3)$$

Therefore, the channel matrix $\tilde{\mathbf{H}}$ for a MIMO channel with *N* transmit and *M* receive antennas can be expressed as

$$\tilde{\mathbf{H}}_{N,M} = \begin{bmatrix} h(\omega^0) & 0 & 0 & 0 & 0 & \cdots & 0 \\ 0 & h(\omega^1) & 0 & 0 & 0 & \cdots & 0 \\ 0 & 0 & h(\omega^2) & 0 & 0 & \cdots & 0 \\ 0 & 0 & 0 & h(\omega^3) & 0 & \cdots & 0 \\ 0 & 0 & 0 & 0 & h(\omega^4) & \cdots & 0 \\ \vdots & \vdots & \vdots & \vdots & \vdots & \ddots & \vdots \\ 0 & 0 & 0 & 0 & 0 & \cdots & h(\omega^{K-1}) \end{bmatrix} \qquad (4)$$

And the overall channel matrix is given by

$$\mathbf{H} = \begin{bmatrix} \tilde{\mathbf{H}}_{1,1} & \tilde{\mathbf{H}}_{1,2} & \cdots & \tilde{\mathbf{H}}_{1,N} \\ \tilde{\mathbf{H}}_{2,1} & \tilde{\mathbf{H}}_{2,2} & \cdots & \tilde{\mathbf{H}}_{2,N} \\ \vdots & \vdots & \cdots & \vdots \\ \tilde{\mathbf{H}}_{M,1} & \tilde{\mathbf{H}}_{M,2} & \cdots & \tilde{\mathbf{H}}_{M,N} \end{bmatrix} \qquad (5)$$

In this work the channel impulse response (CIR) is considered invariant during all OFDM symbols and known at all receivers as well as at the transmitter that uses selection of subcarrier at the transmitter side. The assumed CIR is based on the channel Model A, defined by ETSI in [12], that corresponds to a typical office environment for NLOS conditions and 50 ns average rms delay spread. It is generated a total of 1e3 realizations of the channel matrix **H** for each evaluated C/N ratio. Hard decision is assumed for all techniques as well. IEEE802.11a/Hiperlan/2 physical layer simulations are based on Mode 6, i.e: 16QAM, Code Rate ¾ , 36 Mbits/s. Furthermore we consider simulations without coding.

III. ZF-VBLAST ALGORITHM

In [3] [4] the authors present a low complexity sub-optimal algorithm ZF-VBLAST. At each symbol time, it first detects the "strongest" layer (transmitted signal), then cancels the effects of this strongest layer from each of the received signals, and then proceeds to detect the "strongest" of the remaining layers, and so on.

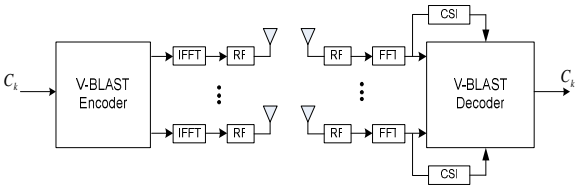

Fig. 2: MIMO-OFDM System With VBLAST.

Assuming that the receiver has perfect knowledge of the channels matrix **H,** the algorithm consists of four steps we will present subsequently:

1. **Ordering:** Determine the optimal detection order corresponds to choosing the row of the Moore-Penrose pseudo inverse **H†** with minimum Euclidian norm.

   $\mathbf{G} = \mathbf{H}^{\dagger} = (\mathbf{H}^{*}\mathbf{H})^{-1}\mathbf{H}^{*}$, is the nulling matrix

   $$k = \arg\left\{ \min_{i} \left\| (\mathbf{G})_i \right\|^2 \right\}$$

2. **Nulling:** Choose the row $\underline{(G)_k}$ as the nulling vector $\mathbf{w}_k$ and use it to null out all the "weaker" transmit signals and obtain the "strongest" transmit signal $y_k = \mathbf{w}_k^T\mathbf{r}$

3. **Slicing:** The estimated value of the strongest transmit signal is detected by slicing to the nearest values in the signal constellation Ω.

   $$\hat{s}_k = \arg\left\{ \min_{\hat{s}\in\Omega} \left\| \hat{s} - y_k \right\|^2 \right\}$$

4. **Cancellation:** Since the strongest transmitted signals has been detected, its effect must be cancelled from the received signal vector to reduce the detection complexity for remaining transmit signals:

   $$\mathbf{r} \leftarrow \mathbf{r} - \hat{s}_k (\mathbf{H})_k$$

Likewise, the k-th column $(H)_k$ of the channel matrix should be zeroed,

$$\mathbf{H} \leftarrow (\mathbf{H})_{\bar{k}}$$

The process above corresponds to detecting one layer, after which the algorithm return to step 1 and detect the next layer.

Assuming a coded OFDM with CP and a total of 64 subcarriers, as well as we can express (3) like (4), it is possible to construct 64 subchannel matrices that will allow creating 64 independent ZF-VBLAST decoders. Furthermore, in IEEE802.11a/Hiperlan/2 systems just 48 out of 64 sub-carriers are used to transport data. Therefore just 48 ZF-VBLAST are implemented i.e. we do not consider the pilot subcarriers in this work.

Given M transmit and N receive antennas, $N \geq M$, and k=1:64 subcarriers, the k-th independent matrix is described by

$$\mathbf{H}_k = \begin{bmatrix} \tilde{\mathbf{H}}_{1,1}[k,k] & \cdots & \tilde{\mathbf{H}}_{M,1}[k,k] \\ \vdots & \ddots & \vdots \\ \tilde{\mathbf{H}}_{1,N}[k,k] & \cdots & \tilde{\mathbf{H}}_{M,N}[k,k] \end{bmatrix} \quad (6)$$

Given M=2 transmit and N=2 receive antennas and k=3 we have

$$\mathbf{H}_3 = \begin{bmatrix} \tilde{\mathbf{H}}_{1,1}[3,3] & \tilde{\mathbf{H}}_{2,1}[3,3] \\ \tilde{\mathbf{H}}_{1,2}[3,3] & \tilde{\mathbf{H}}_{2,2}[3,3] \end{bmatrix} \quad (7)$$

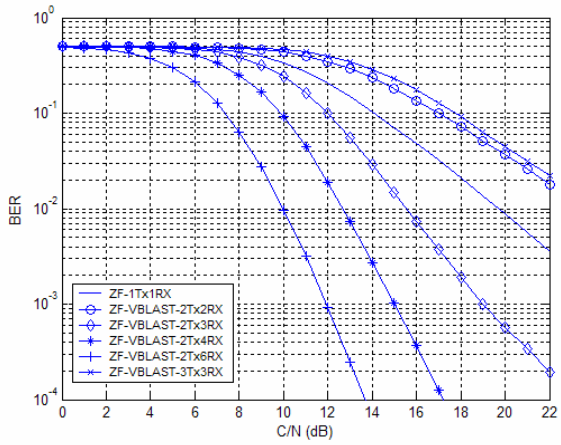

Fig. 3: Performance of ZF-VBLAST, for Coded OFDM, Code Rate3/4.

IV. STBC, SFBC USING ALAMOUTI'S SCHEME

Space-Time Codes were introduced as a method of providing diversity in wireless fading channels using multiple transmit antennas. Previously, multipath fading in multiple antennas wireless system was mostly dealt by time, frequency, Rx and Tx antenna diversities. Receive antenna diversity is the most common applied technique. For cost reasons multiple antennas are preferred at base station (BS) but transmit diversity schemes are increasing in popularity.

STC could be divided in two classes - space time trellis code (STTC) and Space-Time Block Coded (STBC). The first need more complex receivers than the second one. Alamouti's scheme [5] is a particular case of STBC that minimizes the receiver complexity and reaches a diversity gain similar to maximal ratio combining Maximal Ratio Combining (MRC), but using diversity at transmitter side instead at the receiver. The scheme does not require bandwidth expansion, any feedback from the receiver to transmitter and its complexity is similar to MRC. Nevertheless this scheme makes the assumption of no channel variation within the two symbols used for codification.

Given 2 Tx and 2 Rx antennas and $h_{T,R}$ representing the channel response between Tx antenna T and Rx antenna R, the received symbols y_1 and y_2, after pass trough the encoder, at the transmitter ,and the channel can be represented as:

$$x_1 = \sqrt{\frac{Es}{2}} \begin{bmatrix} h_{1,1} & h_{1,2} \\ h_{2,1} & h_{2,2} \end{bmatrix} \begin{bmatrix} s_1 \\ s_2 \end{bmatrix} + \begin{bmatrix} n_1 \\ n_2 \end{bmatrix}$$
$$x_2 = \sqrt{\frac{Es}{2}} \begin{bmatrix} h_{1,1} & h_{1,2} \\ h_{2,1} & h_{2,2} \end{bmatrix} \begin{bmatrix} -s_2^* \\ s_1^* \end{bmatrix} + \begin{bmatrix} n_3 \\ n_4 \end{bmatrix} \quad (8)$$

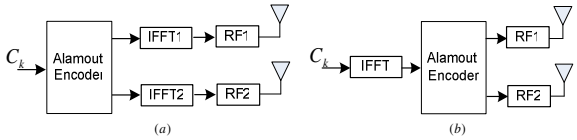

Fig. 4: Alamouti's Encoder in Frequency (a) and Time Domain(b).

The receiver will form a signal vector x according to

$$\mathbf{x} = \sqrt{\frac{Es}{2}} \begin{bmatrix} h_{1,1} & h_{1,2} \\ h_{2,1} & h_{2,2} \\ h_{1,2}^* & -h_{1,1}^* \\ h_{2,2}^* & -h_{2,1}^* \end{bmatrix} \begin{bmatrix} s_1 \\ s_2 \end{bmatrix} + \begin{bmatrix} n_1 \\ n_2 \\ n_3^* \\ n_4^* \end{bmatrix}. \quad (9)$$

Assuming a generic receiver (MISO/MIMO) with M receive antennas, the receiver combiner performs the following operations

$$\tilde{x}_1 = \sum_{i=1}^{M} \left[\left(|h_{i,1}|^2 + |h_{i,2}|^2 \right) x_1 + h_{i,1}^* n_{i,1} + h_{i,2} n_{i,2}^* \right]$$
$$\tilde{x}_2 = \sum_{i=1}^{M} \left[\left(|h_{i,1}|^2 + |h_{i,2}|^2 \right) x_2 + h_{i,2}^* n_{i,1} - h_{i,1} n_{i,2}^* \right] \quad (10)$$

Developing (10) for MISO (2Tx,1Rx) case we have

$$\tilde{x}_1 = \left(|h_{1,1}|^2 + |h_{1,2}|^2 \right) x_1 + h_{1,1}^* n_{1,1} + h_{1,2} n_{1,2}^*$$
$$\tilde{x}_2 = \left(|h_{1,1}|^2 + |h_{1,2}|^2 \right) x_2 + h_{1,2}^* n_{1,1} - h_{1,1} n_{1,2}^* \quad (11)$$

That can be equalized in frequency domain by zero

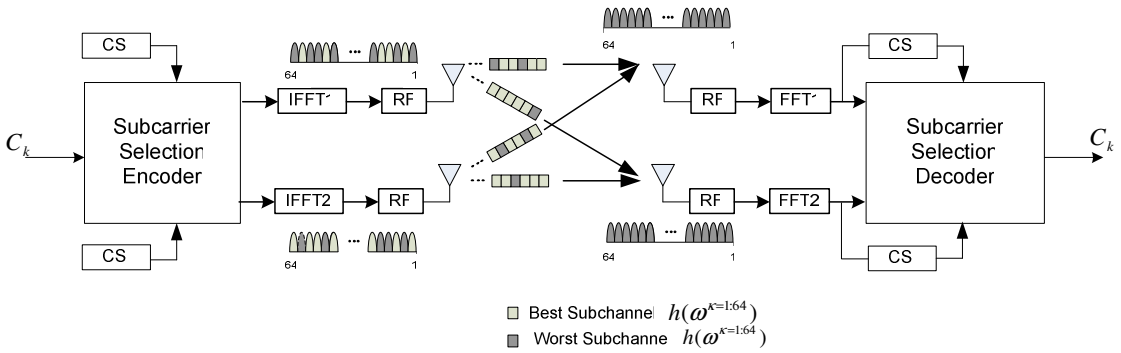

Fig. 5: Transmit and Receive Antenna Selection for MIMO case.

forcing (ZF) the term

$$|h_{1,1}|^2 + |h_{1,2}|^2 \tag{12}$$

Additionally, developing (10) to MIMO case with 2TX and 2Rx antennas we have

$$\begin{aligned}\tilde{x}_1 &= \left(|h_{1,1}|^2 + |h_{1,2}|^2 + |h_{2,1}|^2 + |h_{2,2}|^2\right)x_1 \\ &+ h_{1,1}^* n_{1,1} + h_{1,2} n_{1,2}^* + h_{2,1}^* n_{2,1} + h_{2,2} n_{2,2}^* \\ \tilde{x}_2 &= \left(|h_{1,1}|^2 + |h_{1,2}|^2 + |h_{2,1}|^2 + |h_{2,2}|^2\right)x_2 \\ &+ h_{1,2}^* n_{1,1} - h_{1,1} n_{1,2}^* + h_{2,2}^* n_{2,1} + h_{2,1} n_{2,2}^*\end{aligned} \tag{13}$$

Once more we have an independent term to equalize in frequency domain

$$|h_{1,1}|^2 + |h_{1,2}|^2 + |h_{2,1}|^2 + |h_{2,2}|^2 \tag{12}$$

Subsequently, the data $\tilde{x}_i$ could be detected using any desired detection criteria.

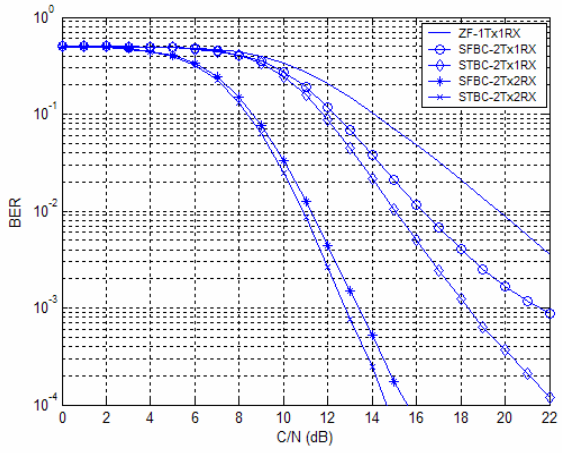

Fig. 6: Performance of Alamouti's scheme, for Coded OFDM , Code Rate =3/4.

In this work we apply the Alamouti's scheme in two cases: time domain (STBC) - figure 4 (b) - and frequency domain (SFBC) - figure 4 (a). The first one is applied to the OFDM symbols, whereas the second to the mapped symbols, in frequency domain, just before the IFFT operation that will send them to time domain. The data $\tilde{x}_i$ is equalized in frequency domain.

V. Transmit and Receive Antenna Selection (TRSS)

In this section, and adaptive subcarrier-by-subcarrier basis antenna selection scheme is discussed, for a joint selection at the transmitter and receiver (See Fig. 6).

Consider a (M_T, M_R) MIMO systems i.e., there are M_T available transmit antennas and M_R available receive antennas. In this case the k-th subchannel matrix **H**[k] is a $(M_T \times M_R)$ matrix that can be written as

$$\mathbf{H}[k] = \begin{bmatrix} h_{1,1}[k] & h_{1,2}[k] & \cdots & h_{1,M_T}[k] \\ h_{2,1}[k] & h_{2,2}[k] & \cdots & h_{3,M_T}[k] \\ \vdots & \vdots & & \vdots \\ h_{M_R,1}[k] & h_{M_R,2}[k] & \cdots & h_{M_R,M_T}[k] \end{bmatrix} \tag{15}$$

In this scheme N_R antennas can be selected out of M_R antennas and N_T antennas are selected out of M_T transmit antennas. Therefore, there is a total of

$$\binom{M_T}{N_T}\binom{M_R}{N_R} \tag{16}$$

possible selections of transmit/receive antennas. The optimal selection is to select $(N_T \times N_R)$ sub-matrix of the $(M_T \times M_R)$ subchannels with the highest magnitude response.

In general, the SNR gain obtained from the antenna selection can be defined by:

$$Gain_{SNR} = \frac{E\left\{\sum_{i=1}^{N_R}\sum_{j=1}^{N_T}\left|H'_{i,j}[k]\right|^2\right\}}{N_T N_R} \tag{17}$$

In this work we evaluate the single case M_T=M_R=2, in other words N_T=N_R=1.

VI. Results

Despite the evident performance or throughput gains offered by the techniques presented in this work, the complexity of the system is increased substantially as the number of antennas increases.

The simplest technique is the subcarrier selection.

Nevertheless for implementing this technique, the transmitter needs to have the estimation of the channel or the information about the subcarriers that must be active (see Fig. 6) at the transmitter side. This technique does not have any array gain but only diversity gain.

The two techniques based in the Alamouti's Scheme have as a good advantage the fact that there is no need of channel information at the transmitter side. But, the assumption that the channel does not vary – or vary a little – in the two subcarriers (SFBC) or two OFDM symbols (STBC) used for coding, at the transmission side, may not be true for some scenarios.

Among those evaluated techniques, ZF-VBLAST is the more complex. On the other hand it is the one that offer the most impressive gain. The initial throughput of the Mode 6 of Hiperlan/2 and IEEE802.11a working according to the standards is 36 (coded) and 48 Mbit/s (uncoded). After applying spatial multiplex and ZF-VBLAST decoding, this throughput is 72 (coded) and 96 Mbit/s (uncoded) for 2TxNRx and 108 (coded) and 146 Mbit/s (uncoded) for 3Tx3Rx.

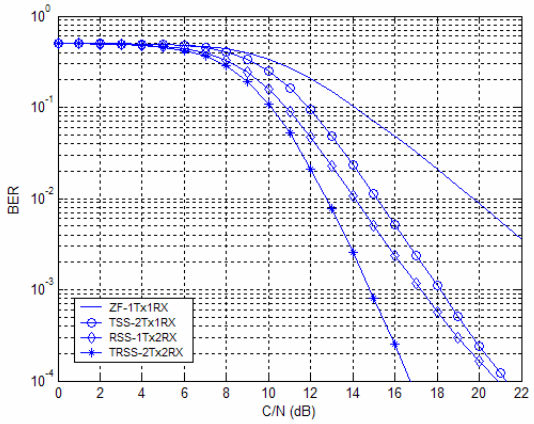

Fig. 7: Performance of Subcarriers Selection Schemes, or Coded OFDM, Code Rate =3/4.

VII. CONCLUSION

In this paper, we show that the considered MIMO techniques enhance significantly the performance of the OFDM-based system under evaluation. The increase is more evidently observed when using coded-OFDM. The performance of ZF-VBLAST-2Tx4Rx is similar to STBC and SFBC-2Tx2Rx as well as TRSS -2Tx2Rx. Nevertheless, ZF-VBLAST-2Tx4Rx achieves 72 Mbit/s for coded and 96 Mbit/s for uncoded-OFDM, contrasted to 36 and 48 Mbit/s of the other two techniques.

REFERENCES

[1] G. J. Foschini. "Layered Space-Time Architecture for Wireless Communications in a Fading Environment When Using Multielement Antennas," Bell Labs Technical Journal, Vol. 1, No. 2, pp 41-59, Autumn 1996.

[2] N.Sehadri and J.H. Winters, "Two Schemes for Improving the Performance of Frequency-division Duplex (FDD) Transmission Systems Using Transmitter antenna Diversity," Int. J. Wireless Info. Network, vol.1 pp 49-60, Jan. 1994.

[3] P. W. Wolniansky, G. J. Foschini, G. D. Golden, and R. A. Valenzuela, "V-Blast: An Architecture for Achieving Very High data Rates Over the Rich-Scattering Wireless Channel," in Proc. ISSSE-98, Pisa, Italy, Oct. 1998, pp. 295-300.

[4] G. J. Foschini, G. D. Golden, P. W. Wolniansky, and R. A. Valenzuela, "Simplified Processing for Wireless Communication at High Spectral Efficiency," IEEE Journal of Selected Areas in Communications – Wireless Communications Series, Vol. 17, pp.1841-1852, 1999.

[5] S. M. Alamouti, "A simple Transmit Diversity Technique for Wireless Communications," IEEE Journal on Select Areas in Communications, Vol. 16 Number 8, October 199, pp. 1451-1458.

[6] R.J.Piechoki, P.N. Fletcher, A.R. Nix, C.N. Canagarajah, J.P. McGeehan. "Performance Evaluation of BLAST-OFDM Enhanced Hiperlan/2 Using Simulated and Measured Channel Data," Electronic Letters,Vol.37 No.18, August 2001.

[7] D. Gesbert, M. Shafi, Da-shan, P. J.Smith and A. Naguib. "From Theory to Practice: An Overview of MIMO Space-Time Coded Wireless Systems". IEEE Journal on Selected Areas in Communications, Vol.21 No.3, April 2003.

[8] A. Paulraj, R. Nabar, D.Gore "Introduction to Space-Time Wireless Communications" . Cambridge University Press, Cambridge,U.K.,1st edition 2003.

[9] E. R. Lima, S. J. Flores, V. Almenar, M. J. Canet, "Analysis and Contrast Between STC and Spatial Diversity Techniques for OFDM WLAN Using Channel Estimation", in 11st International Conference on Telecommunications, Fortaleza, Brasil, Aug. 2004 , in press.

[10] L. Giagaspero, L. Agarossi, G. Paltengui, S. Okamura, M. Okada, S. Komazi, "Co-Channel Interference Cancellation Based on MIMO OFDM Systems", IEEE Wireless Communications, pp 8-17Dec. 2002.

[11] R.J. Kopmeiners, P.Wijk, "Criteria for Comparison" ETSI EP BRAN#9, Sophia Antipolis, France,Jul. 1998.

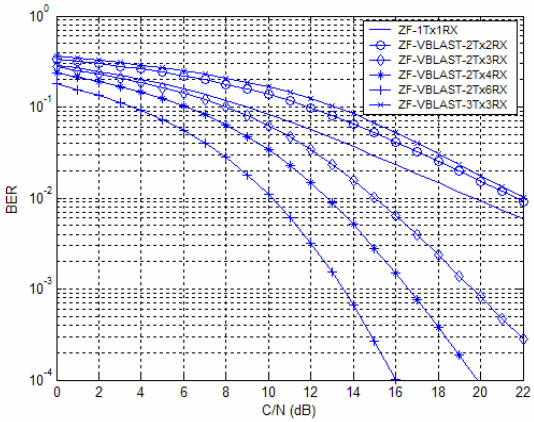

Fig. 8: Performance of ZF-VBLAST – Without Coding.

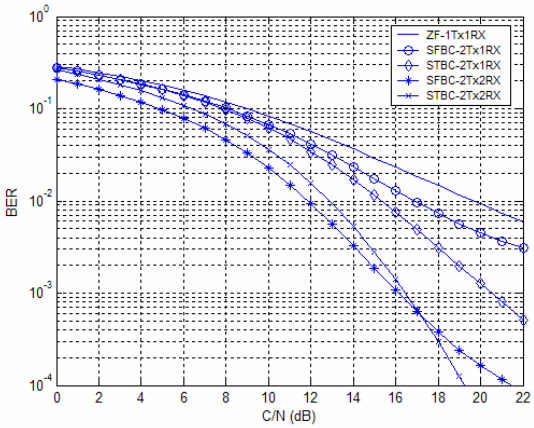

Fig. 9: Performance of the Alamouti's Scheme MISO/MIMO, Without Coding.

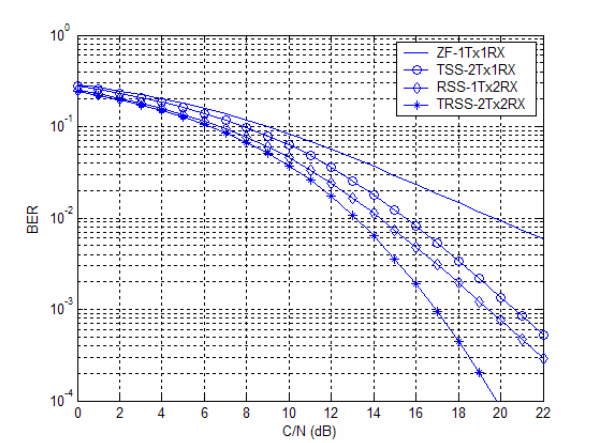

Figure 10: Performance of the Subcarrier Selection Schemes MISO/MIMO - Without Coding.

ACKNOWLEDGMENT

This work was supported by Ministerio de Ciencia y Tecnología under Research Project TIC2001-26-88-C03-01 and in part by the Universitat Politècnica de València.

GEOLOCAL: New Space Telecommunication Concept for Remote Positioning and Navigation

Pierre Kaufmann
Mackenzie Presbyterian University
CRAAM, Graduate Program on Electrical Engineering,
Rua Consolação 896, 01302-907 São Paulo - SP
Part-time researcher at CCS-Unicamp
013983-970 Campinas - SP – Brazil
kaufmann@craam.mackenzie.br

Adonias Costa da Silveira
National Institute of Telecommunications - Inatel
P.O. Box 05 - 37540-000
Santa Rita do Sapucaí - MG - Brazil
adonias@inatel.br

***Abstract*— A new concept for remote positioning and navigation is described. It is based in a telecommunication network consisting in transmitters and receivers placed at well-known geodetic ground-based reference locations and a signal repeater in space. Time generated at the receivers, at the reference locations and at the targets, which positions are to be determined, is compared to time transmitted from the ground, retransmitted by the repeater space. The new system requires just a simple passive or active transponder in space that might be carried by a nanosatellite in low earth orbit. It is considerably simpler in comparison to existing spatial geolocation systems using satellites carrying complex on-board instrumentation, based on multiple space beacons´ triangulation (GPS for example) and Doppler effect on multiple ground-based transmissions (Transit for example).**

***Index Terms*—geolocation, remote positioning, navigation, space supported location.**

I. Introduction

Various conceptual techniques use electromagnetic transmissions for remote position determination of a site, a target or a vehicle, located on or above the Earth surface, described by well known geodetic coordinate equations [1]. They may use from natural celestial light sources eye-observed by sextants to sophisticated Navstar satellites radio beacons of the Global Positioning System (GPS) constellation.

Low frequency (LF) and very low frequency (VLF) radio transmitters were installed in the 50´s at well-determined geographic locations to serve as references for positioning and navigation of vehicles, derived from signal phase measurements of signals from different sources. This system remain being used to these days. The better known are Loran-C at LF, covering up to 2000 km, and the worldwide VLF Omega network, providing accuracies of the order of few hundred meters [2][3].

II. Doppler positioning concept

Soon after the launching of the first artificial satellites the concept of position location derived from Doppler effect was successfully developed [Refs. 4-6]. Target position is deduced from frequency drifts due to the satellite low orbit movement with respect to the target and a large number of auxiliary reference sites placed at well-known locations on the Earth surface.

The concept was largely explored using Transit satellites until recently, as well in other position and navigation systems such as Argos [7] and Doris [8], reaching accuracies of tens of meters, that might be reduced to tens of centimeters after full processing of multiple measurements (see Fig. 1).

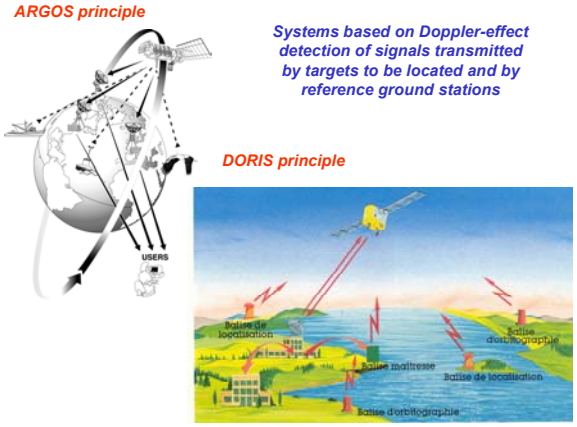

Fig. 1. The ARGOS and DORIS positioning systems are based on Doppler effect on radio signals transmitted by reference beacons on the ground, by the target which position is to be determined, received by a low orbit satellite.

III. The GPS concept

The GPS second generation of space location and navigation system was developed in the 80´s, and became operational in 1994 [Refs. 9-11]. It uses a constellation of 21 active Navstar (plus a number of spares) slow moving satellites in high altitude orbits. The GPS receivers triangulate data transmitted from

multiple satellites above the horizon to obtain the position. Accuracies go from tens to few meters, depending transmitting codes and frequencies, and may be further reduced with the processing of multiple measurements and accurate orbital ephemeris updates.

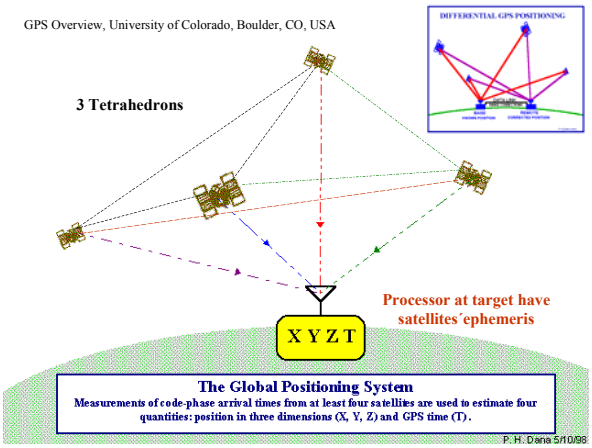

Fig. 2. A simplified illustration of 4 Navstar satellites of the GPS constellation above the horizon for the site, which position is to be determined. The satellites are also used for timing dissemination. The small box above, at right, illustrates the GPS differential navigation.

Fig. 2 illustrate four GPS satellites transmissions received by a target which position is to be determined. Three redundant tetrahedrons are formed for accurate position determination. Absolute timing can be obtained from the satellites signals. The differential GPS navigation, illustrated in the upper right corner of Fig. 2, adds a radio connection to a fixed transmitter at a very well known geographic location.

Fig.3. The GPS constellation of satellites for geopositioning.

The GPS Navstar satellite constellation is shown I n Fig. 3. The same concept was also used for the Russian (ex-soviet) GLONASS [12] positioning system and will be adopted for the new European GALILEO [13]. Although the GPS and GLONASS systems were initially conceived for military purposes, they are widely used in commercial applications. The three systems (GPS, GLONASS and GALIEO) will be, in principle operated jointly, at least for non-military or commercial applications.

III. THE NEW GEOLOCAL CONCEPT

The GEOLOCAL is a new concept proposed to determine target geographic position referred to ground-based sites with well-known geodetic locations and a signal repeater in space. It was developed starting from a conceptual system and process patented in Brazil, filed in 1991, awarded in 1997 [14] and one Patent Addition Certificate filed in 2002 [15]. More recently the geolocation system and process concepts were considerably modified and improved, producing another Patent Deposit, filed in October 2003 [16].

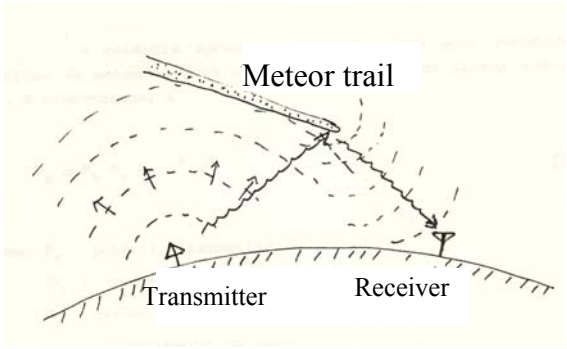

Fig. 4. A plasma tube formed in the upper terrestrial atmosphere is an efficient reflector of radiowaves in the VHF-UHF range

The first concept approach required a signal repeater in the sky. The space device might be, for example, a transponder in a balloon, aircraft of spacecraft. Natural sporadic signal scattering phenomena, such as ionized meteor trails in the upper terrestrial atmosphere, might also act as repeaters in the sky (Fig. 4).

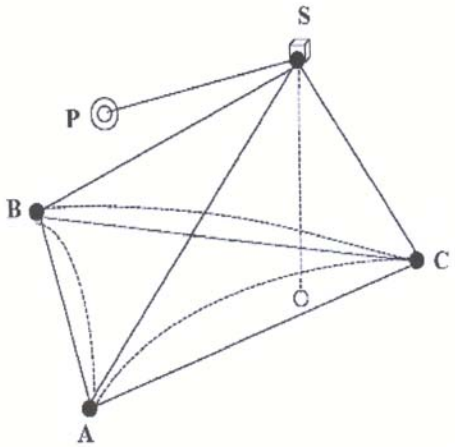

Fig. 5. Schematic diagram showing the ground-based reference network, a repeater in space, and the target P, which position is to be determined.

A simplified diagram of the GEOLOCAL system is shown in Fig. 5. The reference bases transmit time-encoded signals that are received by the bases and the target P which location is to be determined, after being retransmitted by some kind of transponder sufficiently high above the ground or in space. Time differences of the received signals solve the tetrahedron ABCS; determine the repeater position in the sky and the target location the sky (Fig.5).

Preliminary position accuracy estimates for the GEOLOCAL system and process are for tens of meters for single initial determinations, that can be improved considerably by averaging several measurements and after determining carefully the space-borne repeater path or orbital parameters, adding regular and frequent ephemeris updates.

The GEOLOCAL is not intended to compete in quality of position determination with existing systems. It provides an alternative system and process, offering multiple technical options in different applications. It brings new attractive possibilities , presenting advantages compared to the other existing systems, mentioned before, on the following aspects:

•Reduced technical requirements for the space (satellite) segment. A simple repeater is required, using an antenna (or antenna array) with field of view defined by the area of coverage.

•Satellite attitude control not critical.

•Possibility to use small mass nanosatellites (< 10 kg) to carry the telecommunications repeater, with low costs in construction, launch and overall mission operations.

•Possible use of communication channels available on existing low earth orbit satellites.

•Ground-based reference sites in small number and presenting low technical complexity.

•Options for position determination: at a control center, or at the target.

•Target technical hardware installation requirements less complex compared to other systems.

•Optional use of the same space transponder to return messages from target, making the system self-sufficient. Otherwise, one can use the usual multiple communications between the targets and the control center (via other satellites; other links by microwaves, mobile phones, radio-ionosphere, etc.).

•Reduced costs for a number of geolocation and navigation services compared to other systems and processes.

IV. THE PROPOSED DEVELOPMENT

The GEOLOCAL project proposes the development of detailed studies, defining hardware and software designs, of particularly critical aspects of the system, process and a number of applications, with emphasis on:

•orbitography and navigation;

• selection telecommunication systems;

• modulation options;

•design options for hardware to be used on targets;

•options for space repeaters;

•options for specific dedicated nanosatellite platform;

•set up and operation of a system using available telecommunication satellite channels for tests and proofs of concepts;

•studies of costs involved for large scale applications
•evaluation of markets of potential users.

The main support of the GEOLOCAL project development will be provided by Brazilian funding agencies, with partial support from private companies. The project development is being proposed by the Fundação Instituto Nacional de Telecomunicações, FINATEL, with the co-participation of scientists and engineers in partnership from the following organizations:

•National Institute for Telecommunications, INATEL, Santa Rita do Sapucaí, Minas Gerais
•Center of Radio Astronomy and Astrophysics, CRAAM of the Graduate Program on Electrical Engineering from Mackenzie Presbyterian University, in São Paulo; SP
•Department of Orbitography and Planetology of the Engineering School of the State of São Paulo University, UNESP-FEG, in Guaratinguetá, SP
•Center of Semiconductor Components, CCS, of Campinas State University, Campinas, SP
•Institute of Aerospace Research, IAE-CTA, São José dos Campos, SP
•Polytechnic School of University of São Paulo, São Paulo, SP; and from
• Brazilian and international consulting specialists

V. CONCLUSIONS

A new space telecommunication concept used for remote geographic location, and applications for navigation, has been proposed and was briefly described. It is based on an original concept using time differences of propagation times of a coded-signal transmitted by one of three ground based reference stations, re-transmitted by a transponder in

the sky, and received by the three stations, allowing the determination of a tetrahedron and the altitude of the signal transponder. The position of targets receiving the same signal is accomplished at the same time.

The system is not intended to compete in accuracy and practical uses of existing well-established positioning systems such as triangulations based on Doppler-effect on signals transmitted by beacons on targets, detected by low altitude satellites (like the Transit, Argos and Doris systems), or using triangulations of multiple transmitting slow-orbiting satellites which signals are received at the targets which positions are to be determined (GPS, GLONASS and GALILEO.

The GEOLOCAL original concept may present a number of attractive and cost-effective alternatives for remote location in a number of applications requiring moderate accuracies – which might be largely improved as the system development takes place.

REFERENCES

[1] Ewing, C.E. and Mitchell, M. M., "Geodetic Astronomy", Ch. 5 in *Introduction to Geodesy*, Elsevier Science Publ. Co. Inc., New York, USA, pp. 55-90, 1970.

[2] Watt, A.D., *VLF Radio Engineering*, Pergamon Press, Oxford, UK, 1967.

[3]] Kayton, M., " Introduction to Ship Navigation", Part 4 in *Navigation Land, Sea, Air & Space*, ed. by M. Kayton, IEEE Press Selected Reprint Series, IEEE Aerospace and Electronic System Society, New York, USA, pp. 147-160, 1990.

[4] Guier, W.H. and Weiffenbach, G.C., "Theoretical analysis of Doppler radio signals from Earth satellites", *Nature*, vol. 181, 1525-1526, 1958.

[5] McClure, F.T., "Method of navigation", U.S. Patent 3,172,108, 1965 (filed May 12, 1958).

[6] Kouba, J., "A review of geodetic and geodynamic satellite Doppler positioning", Rev. Geophys. Space Phys., vol. 21, 27-40, 1983.

[7] ARGOS User´s Manual, Service Argos Inc., www.argosinc.com, 2003.

[8] DORIS website, http://www-aviso.cls.fr/html/faq/doris_uk.html, 2003.

[9] Wells, D. (editor), "Guide to GPS Positioning", Canadian GPS Association, N. Brunswick, Canada, 1987.

[10]] Cariveau, B.K. and Therkelsen, K.L., "Satellite data management in DoD NAVSTAR GPS receivers", 1988 Proc.IEEE Position Location and Navigation Symp., 1988, reprinted in *"Navigation: Land, Sea, Air & Space"*, ed. by M. Kayton, IEEE Press, Selected Reprint Series, IEEE Aerospace and Electronic System Society, New York, USA, pp. 120-130, 1990.

[11] Strang, G. and Borre, K., *Linear Algebra, Geodesy, and GPS* , Wellesley-Cambridge Press, Wellesley, MA, USA, 1997.

[12] Börjesson, J, Darin, F., Jarlemark, P. and Johansson, J. *Incorporating GLONASS in a nation-wide RTK positioning service* , GNSS-99, Genoa, Italy, October 5-8, 1999

[13] GALILEO website http://www.esa.int/export/esaSA/GGGMX650NDC_navigation_0.html

[14] Universidade de São Paulo and Kaufmann, P., "Sistema e processo de posicionamento geográfico", Brazil Patent PI 9101270-8, September 30, 1997 (filed March 25, 1991).

[15] Universidade de São Paulo and Kaufmann, P., Addition Certificate CI 9101270-8, Brazil INPI Protocol # 002174, filed May 17, 2002.

[16] Kaufmann, P., "Sistema e processo de posicionamento geográfico e espacial", Brazil Patent Deposit PI03003968-4, filed October 8, 2003.

Implementation of Multi-Mode Modem ASIC for Ka Band COMS Satellite Communications

Dae-Ig Chang
Communications Satellite Research Group
Electronics and Telecommunications Research Institute
161 Gajeong-dong, Yuseong-gu, Daejeon 305-350, KOREA, dchang@etri.re.kr

Young-Wan Kim, Deock-Gil Oh, and Ho-Jin Lee
Communications Satellite Research Group Electronics and Telecommunications Research Institute
161 Gajeong-dong, Yuseong-gu, Daejeon 305-350, KOREA, ywkim@etri.re.kr

Abstract— To transmitting the high data rate such as ATM, high-speed internet, and 3D-HDTV using satellite communication link, Ka-band broadband transponder is need. Korea has a plan to lunch multi-purpose satellite(COMS) including high speed satellite communication services. However, the use of this ka-band is seriously affected to the received data performance by rain fading and atmospheric propagation at the Ka-band satellite communication link. In this paper, we will present the design and implementation of the 155Mbps adaptive satellite Modem adaptively compensated against rain attenuation level. In order to compensate the rain attenuation over high-speed satellite link, the adaptive coding schemes with variable coding rates and the multiple modulation schemes such as trellis coded eight PSK(TC-8PSK), QPSK, and BPSK are adopted. The blind demodulation scheme is proposed to demodulate without information of modulation mode at the multi-mode demodulator, and the fast phase ambiguity resolving scheme is proposed by directly detecting the phase ambiguity information from receive signal. The computer simulated results of detecting the modulation mode by SPW model are provided. This 155Mbps adaptive MODEM was designed and implemented by single ASIC chip with the CMOS standard cell technology. Now, the Adaptive modulator and demodulator (MODEM) system is being implemented in one MODEM box by ETRI.

I. INTRODUCTION

Owing to the prospects of a heavy spectrum congestion of Ku-band and lower frequency then Ku-band in near future, we will soon need to be implemented at the higher Ka-band (20/30GHz).[1] On the other hand, we require Ka-band broadband transponder to transmit high speed data rate such as multimedia, high-speed internet, 3D-HDTV, and broadband-ATM. The operation at Ka-band has attractive features; broadband service and low density frequency spectrum. So, Korea has a plan to launch the Communication, Ocean, and Meteorological Satellite(COMS) for super high speed internet via satellite, remote medicine, distance learning, recovery and prediction service for natural disaster, and emergency communication and relief service. However, the use of this ka-band is seriously a ffected to the received data performance by rain fading and atmospheric propagation at the Ka-band satellite communication link.

Satellite systems with highly nonlinear transponders require a constant envelope modulation such as BPSK, QPSK, 8PSK, 16PSK, OQPSK, MSK, etc. Increasing the level of modulation with number of symbols allowed, increases amount of information per symbol. So, multi-level phase modulation(large M) is required to increase the spectral efficiency.[2] So to speak, higher level modem can process higher speed data under same symbol clock and effectively transmit the high speed data. But, greater energy is needed to maintain the same performance (BER) as Fig. 1

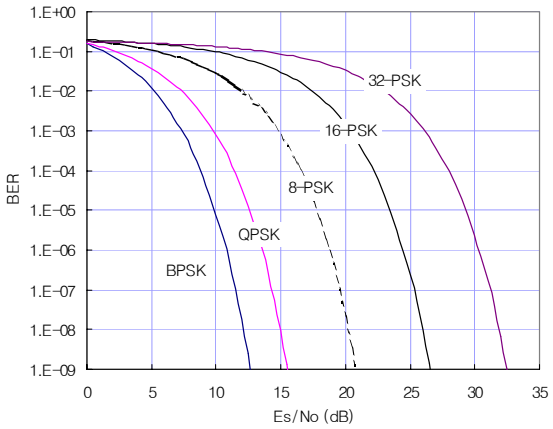

Fig. 1. Relationship between SNR and BER over M-PSK MODEM

Due to rain fading and other channel impairments such as atmospheric propagation in high frequency satellite communication channel, especially Ka-band application of error correcting code scheme and modulation scheme is necessary. Furthermore, the trend of satellite communication is transformed from narrow-band service to broadband multimedia service. To compensate the reduction of receive signal performance TCM(Trellis Coded Modulation) [3,4] code is adopted, but adaptive modulation scheme is needed to adaptively cope with heavy rain attenuation. [1] Therefore during poor channel conditions, QPSK or BPSK with (n,k,m) convolutional code is employed in order to maintain the performance. As channel conditions are improved, higher rate schemes such as TC-8PSK(Trellis Coded 8PSK) are used for satellite communications. So to speak, multi-level modem, TC-8PSK guarantees high speed data rate during clear sky, and BPSK guarantees signal performance during

rain attenuation

In this paper, we designed and implemented the 155Mbps adaptive Modem for the broadband satellite communications. Adaptive channel coding schemes are defined as European standard[6] which is DVB(Digital Video Broadcasting) specification. The transmission frame is synchronous with the MPEG-2 transport stream(TS). The Modem was implemented the BPSK, QPSK and 8PSK modulations, and the concatenation of convolutional and Reed-Solomon codes. For 8PSK, "Pragmatic" trellis convolutional code is able to be configured flexibly, allowing the optimization of the system performance for a given satellite transponder bandwidth. Satellite systems can be affected by power limitations, therefore ruggedness against noise and interference has been one of the design objectives of the system. On the other hand, when larger power margins are available, spectrum efficiency can be increased to reduce the cost of the space segment. Therefore our adaptive Modem offers many transmission modes(variable coding and modulations), giving different trade-offs between power and spectrum efficiency. All the modes are appropriated for operation in quasi-linear satellite channels.

II. SPEC & STRUCTURE OF ADAPTIVE MODEM

The adaptive Modem scheme which is selected modulation schemes according to the satellite link channel condition is BPSK/QPSK/TC-8PSK, and the specifications of adaptive Modem is table 1. Fig. 2 is configuration of adaptive satellite Modem and implemented in single ship.

TABLE I. SPECIFICATIONS OF ADAPTIVE MODEM

Items	Specifications
Modulation scheme	BPSK, QPSK, TC-8PSK, Continuous
Encoding/Decoding	Inner Code : Convolutional(1/2,2/3,3/4,5/6,7/8) Trellis Codes(R=2/3,5/6,8/9) Interleaver : Convolutional Interleaver Outer Code : RS(204,188)
Shaping/Matched	SQRC(α=0.25, 0.35)
Demodulation	Blind Demodulation
Information Rate	155.52Mbps(Max. 72Msps)
Scrambling	V.35 scrambler

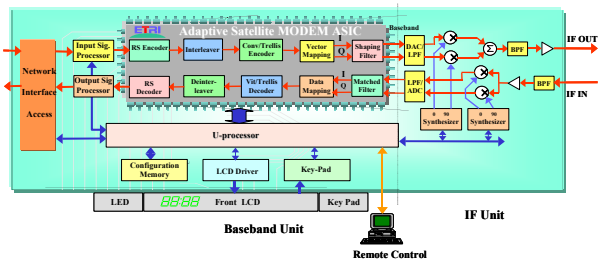

Fig. 2. Configuration of adaptive satellite Modem

Adaptive Modem ASIC chip consists of PRBS (Pseudo Random Bit Stream generator), Frame Sync. Generator/Detector, Scrambler/Descrambler, RS En-coder/Decoder, Interleaver/Deinterleaver, Convolution -al/Trellis Encoder/decoder, and BPSK/QPSK/TC-8PSK modulator/demodulator.

A. Adaptive Modulator

This adaptive modulator consists of 3 Symbol mappers, Pulse shaping filter(Square Root Raised Cosine), and DAC. And the input symbol data encoded by FEC are complexly mapped as Fig. 3 and 4 according to modulation scheme. The block diagram of adaptive modulator is Fig 3.

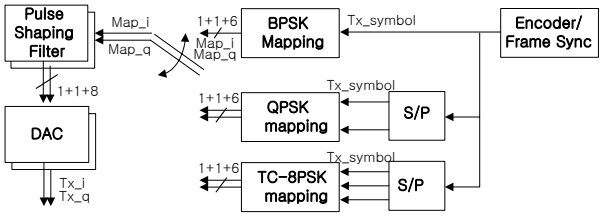

Fig. 3. Block diagram of adaptive modulator

1. Modulation Signal Mapper

The Symbol mapper converts the input symbol sent from FEC to complex signal such as BPSK, QPSK, and 8PSK, and the mapped constellations are Fig. 4 and 5.

TC-8PSK modulator can have 8 constellations such as 8 phase information from 3 bits data as Table 2.

$$S(t) = \sqrt{2} \cdot e^{j(2\pi f_o t + \theta_i)} \quad (1)$$

TABLE 2. MAPPING OF TC-8PSK MODULATOR

Coded data		Mapping degree	Mapping Point	
			I	Q
Y_0	000	22.5 (0)	1.307 (1.414)	0.541 (0)
Y_1	001	67.5 (45)	0.541 (1)	1.307 (1)
Y_3	011	112.5 (90)	-0.541 (0)	1.307 (1.414)
Y_2	010	157.5 (135)	-1.307 (-1)	0.541 (1)
Y_4	100	205.5 (180)	-1.307 (-1.414)	-0.541 (0)
Y_5	101	247.5 (225)	-0.541 (-1)	-1.307 (-1)
Y_7	111	292.5 (270)	0.541 (0)	-1.307 (-1.414)
Y_6	110	337.5 (315)	1.307 (1)	-0.541 (-1)

* ( ) : mapping starts from 0 degree constellation

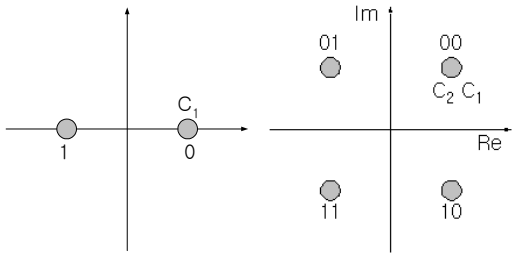

(a) BPSK constellation (b) QPSK constellation

Fig. 4 BPSK and QPSK constellation

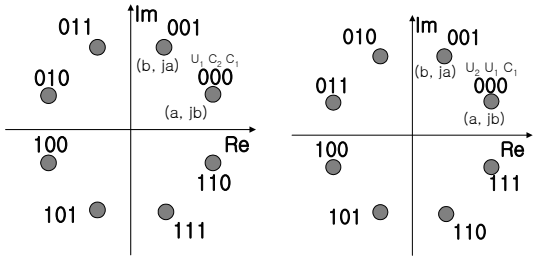

(a) R=2/3 constellation (b) R=5/6 and 8/9 constellation

Fig. 5 TC-8PSK constellation

2. *Shaping Filter*

The shaping filter is SQRC(Squire Root raised Cosine). This SQRC filter limits pulse bandwidth of transmitted digital data and prevents ISI (Inter Symbol Interference).

$$h(t)=\frac{4\alpha}{\pi\sqrt{T}}\cdot\frac{\cos\left((1+\alpha)\pi t/T\right)+T\sin\left((1-\alpha)\pi t/T\right)/(4\alpha t)}{1-(4\alpha t/T)^2} \quad (2)$$

The bandwidth is determined by roll-off factor α and we decided the roll-off factor α to 0.25 for utilizing 72MHz satellite transponder to transmit 155Mbps ATM data.

B. *Adaptive Demodulator*

This adaptive demodulator consists of ADC, Matched Filter, AGC, Timing Recovery, Carrier Recovery, Modulation Type Detector, Frame Sync Detector, Phase Ambiguity resolve, and Soft Decision Logic etc. The block diagram of adaptive demodulator is Fig 6.

1. *Structure of adaptive demodulator*

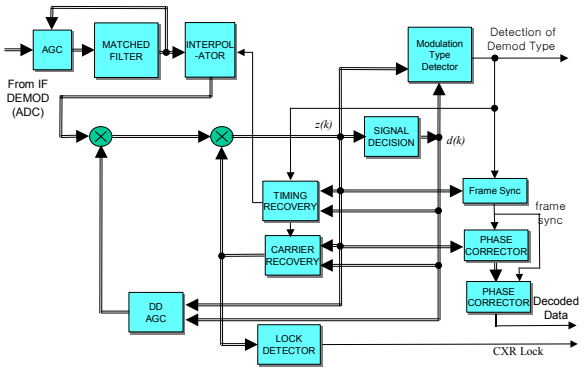

Fig. 6 Block diagram of adaptive demodulator

- Matched Filter → same with Shaping Filter(SQRC Filter) of modulator, reduces noise of wireless channel, passes correspond signal with TX signal, and increases received S/N ratio
- Symbol Timing Recovery → detects the timing error and adjusts sampling time for recovering the receiving clock by interpolator
- Carrier recovery → compensates phase and frequency offset included in receiving signal using DD method.
- Phase Ambiguity Resolve → detects phase ambiguity information using frame sync pattern and resolves phase ambiguity occurred from M-ary PSK demodulator
- Modulation Mode Detector → automatically detects modulation mode without modulation information in adaptive MODEM

III. DESIGN AND IMPLEMENTATION OF DEMODULATOR

The adaptive Modem is designed and simulated by SPW(Signal Processing Worksystem) tool. This adaptive Modem SPW model consists of adaptive modulator block, satellite channel block(AWGN noise, phase and frequency offset generator, timing offset generator), and adaptive demodulator block which includes AGC, symbol timing recovery, carrier recovery, frame sync detector, modulation mode type detector, phase ambiguity resolve, and BER check block. Adaptive Modem algorithm is verified by this SPW model.

A. *Symbol Timing Recovery*

Symbol timing recovery scheme employs DD(Decision Directed) Gardner timing error estimation algorithm[7]. The estimated timing error is given equation (3). The results from equation (3) involve noise components, and we can remove the noise components using low pass filter. This low pass filter acts the averaging the input signal and removes the AWGN noise. The simple low pass filter is AR(Auto Regressive) loop filter as shown in equation (4). According to the estimated timing error, the interpolation filter coefficients are changed for corrected symbol sampling position and interpolation[7]. If the accumulated timing error is above threshold, the reference symbol time is shifted one sampling time by interpolator and new recovered symbol timing is achieved.

Interpolator adjusts the symbol timing according to the estimated timing error. Fig. 7 shows the block diagram of symbol timing recovery for timing recovery.

$$e_\tau(k)=\mathrm{Re}\left\{y_{k-1/2}\{\hat{d}_k^{\,*}-\hat{d}_{k-1}^{\,*}\}\right\} \quad (3)$$

where, $e(r)$: symbol timing estimate at t=rT

$y(r)$: sample value at t = rT

$d(r)$: decided symbol at t =rT

$$\hat{\Omega}_{AR,k}=\beta\hat{\Omega}_{AR,k-1}+(1-\beta)\hat{e}_{\tau,k} \quad (4)$$

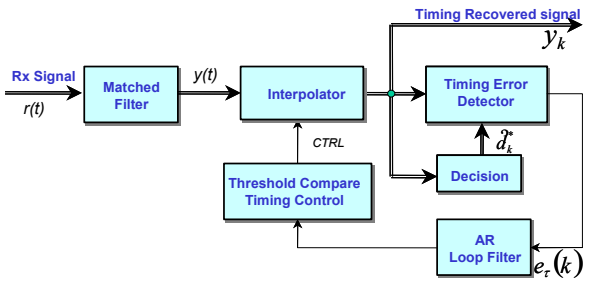

Fig. 7 Block diagram of symbol timing recovery

B. *Carrier Recovery*

The carrier recovery compensates reference signal unstability of ground station equipment and satellite transponder, and frequency and phase offset of

received signal accused doppler shift. The carrier recovery scheme employs decision directed scheme using low pass filters for high speed satellite communication and fast acquisition. This structure consists of two loops; one compensates the frequency offset as a frequency tracking loop(FTL), the other compensates the phase offset as a phase tracking loop(PTL). The low pass filters are used in suppressing the noise within FTL and PTL.

The received signal for MPSK signal can be represented as equation (5)

$$x_k = e^{j(\omega_0 k+\theta_0)} d_k + n_k \tag{5}$$

where, $d_k \in \left\{ e^{j2\pi l/M} \middle| l = 0,1,\cdots,M-1 \right\}$ is data symbol, n_k is AWGN(Adaptive White Gaussian Noise) with a double-sided power spectral density of $N_0/2$, ω_o is angle frequency offset, and θ_o is the unknown phase offset .

The estimated value of angle frequency offset is given in equation (6). This frequency offset detector requires only one sample. The estimator of equation (6) is taken place of AR filter to suppress the Gaussian noise components. And the frequency and phase offset are determined by products of input signal and conjugation of decision signal.

$$\hat{\Omega}_k = E\left\{ x_k \hat{d}_k^{\,*} \right\} = e^{j(\omega_0 k+\theta_0)} \tag{6}$$

In order to compensate the phase offset θ_o, we can obtain the phase estimation value by taking the detected angle frequency offset by equation (6). The estimation of phase offset exp(jwo) is estimated by equation (7).

$$\hat{\Phi}_k = E\left\{ y_k \hat{d}_k^{\,*} \right\} = E\left\{ x_k \hat{d}_k^{\,*} \hat{\Omega}_{k-1}^{\,*} \right\} = e^{j\omega_0} \tag{7}$$

where, $y_k = x_k \hat{\Omega}_{k-1}^{\,*}$

Fig. 8 shows the block diagram of carrier recovery according to equation (6) and (7).

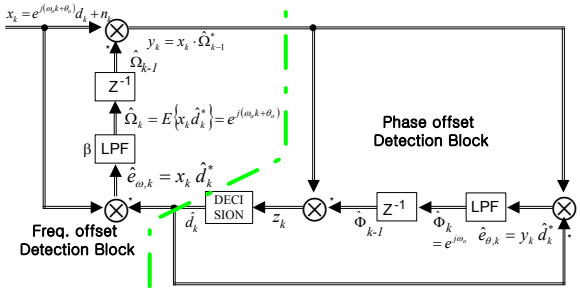

Fig. 8 Block diagram of carrier recovery

C. Modulation Mode Detector

The modulation mode detector is very important part at the adaptive demodulator. It decides demodulation mode by detecting the modulation mode at demodulator without modulation mode information from adaptive modulator.

The capable modulation schemes by demodulator are shown in Table 3. 8PSK demodulator can demodulate the BPSK, QPSK, and 8PSK. QPSK demodulator can demodulate the BPSK and QPSK, but can not demodulate the 8PSK. BPSK demodulator can demodulate the BPSK only, but can not demodulate the QPSK and 8PSK. So we can use these characteristics to detect the modulation mode at the demodulator.

TABLE 3. DEMODULATOR STATE ACCORDING TO MODULATION MODE

Demod. / Mod. mode	BPSK	QPSK	8PSK
BPSK	O	O	O
QPSK	X	O	O
8PSK	X	X	O

O : be possible demodulate, X : be not possible demodulate

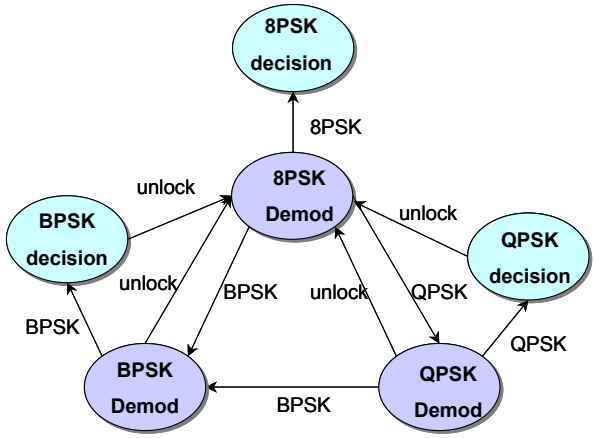

Fig. 9 Modulation Type Detection Scheme

The modulation mode type detector consists of modulation mode type search block, modulation mode type detector block, and error power estimation block.

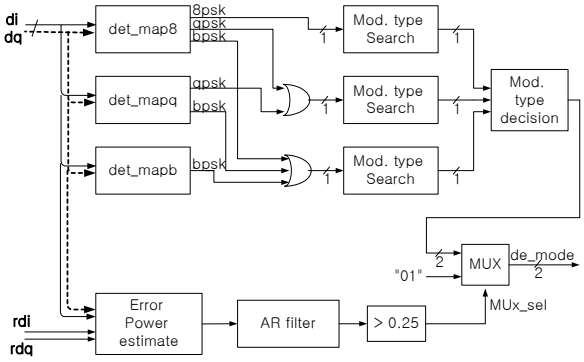

Fig. 10 Block Diagram of Modulation Mode Detector

The Fig. 11 is simulation results of modulation type detector by SPW tool, and it detects modulation types after 330 symbols (5.16us) at demodulator.

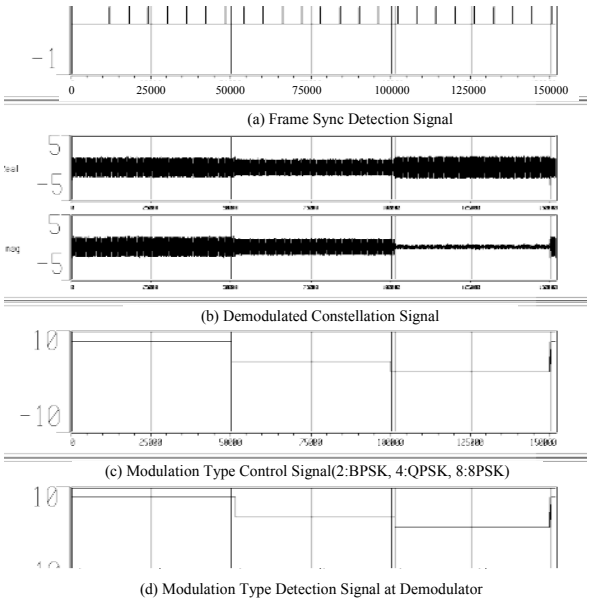

Fig. 11 Results of Modulation Mode Detection

D. *Fabricated Adaptive MODEM ASIC Chip*

The adaptive Modem includes FEC encoder/decoder and modulator/demodulator, and has the simplified interface circuits among the many functional blocks and the parallel processing architecture to achieve the high speed data rate such as 155Mbps. This adaptive Modem was designed and implemented by single ASIC chip for simplifying the MODEM box. The features of fabricated ASIC chip are as follow;

- Includes FEC and Modulator/Demodulator in a single chip
- 240pins PQFP(Plastic Quad Flat Package) Type
- ASIC Technology : COMS Standard-Cell, 980k gates
- Power Consumption : 1.2W
- Die Size : 7.80678 x 7.79788mm

Fig 12 shows the fabricated 155Mbps adaptive Modem ASIC by ETRI.

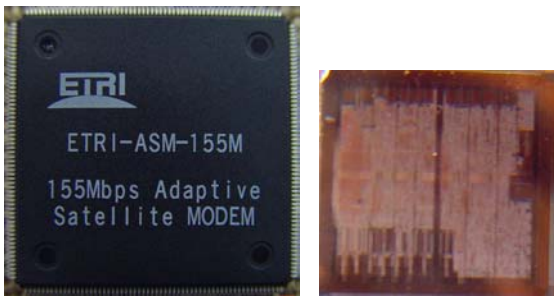

(a) ASIC Package (b) MODEM ASIC DIE

Fig. 12 Implemented 155Mbps Adaptive MODEM ASIC

E. *Adaptive MODEM box*

The adaptive modem box was manufactured by ETRI using 155Mbps adaptive Modem ASIC. The features are as follow;

- Data Transmission Rates : 6 to 155.52Mbps, Variable data rate
- Interface: STM-1, DS-3, MPEG-2 ASI
- IF Frequency: 140MHz (BW: 80MHz)
- BER: ≤ 10-10(QEF) @Eb/No=9.2dB(TC-8PSK)
- ASM-155M Chassis: 2RU(h)x19”(w)x14.5”(d)

Fig. 13 shows a manufactured 155Mbps adaptive Modem which can simultaneously transmit and receive broadband signal in single chassis.

Fig. 13. Single Chassis 155Mbps Adaptive MODEM box

F. *Simulation and Test Results*

In this paper, we designed the adaptive modem including modulator, demodulator, and satellite channel environment using SPW. And we executed the simulation of the modem performance before ASIC fabrication. The BER performance results of computer simulation are shown in Table 4. For BER performance test of manufactured Modem box hardware, we executed PER test under the IF loopback condition. We assume that 10^{-7} PER is equal to 10^{-10} BER in case of 188byte MPEG-2 TS. The test results are shown in Table 4. Also, the data sheets of BER performance of COMTECH SDM-2020D are involved for comparing. According to Table 4, we can see that our Modem performance is better than the COMTECH SDM-2020D.

TABLE 4
PERFORMANCE COMPARISON BETWEEN OUR MANUFACTURED MODEM AND COMMERCIAL MODEM[8]

MODUL	Code Rate	Simulation	TEST	COMTECH SDM-2020
BPSK	1/2	0.8	1.5	
	2/3	1.3	1.9	
	3/4	1.8	2.4	
	5/6	2.5	3.1	
	7/8	2.8	3.4	
QPSK	1/2	3.8	4.3	4.3
	2/3	4.3	4.9	4.9
	3/4	4.8	5.4	5.6
	5/6	5.4	6.0	6.2
	7/8	6.4	6.4	6.7
8PSK	2/3	6.2	6.8	6.9
	5/6	8.1	8.7	8.8
	8/9	8.6	9.2	9.8

IV. CONCLUSION

In this paper, we designed adaptive modem algorithm for channel adaptive transmission and implemented 155Mbps adaptive Modem ASIC and modem box. Especially, to overcome the rain impairment factor in Ka-band satellite communications,

we implemented blind demodulation algorithm to makes simplify the receive system structure for multi-mode adaptive modem such as BPSK/QPSK/8PSK.

According to the computer simulation, the adaptive demodulator detected the modulation scheme within 330 symbols (5.16us) after change of modulation scheme at modulator. But the 155Mbps adaptive modem box implemented by us misses 500 to 2500 symbols.

Our Modem performance is better than the COMTECH SDM-2020D as shown in Table 4.

We have remaining open homework that is modulation scheme change according to channel environment. So, we will study the accurate channel detect scheme at receiver and the determination criterion of modulation scheme changing point at transmitter.

REFERENCES

[1] M.Flip and E.Vilar, *"Adaptive Modulation as Fade Countermeasure. An Olympus Experiment"*, Int. Journal of Sat. Comm. Vol.8, 99.31-41, 1990.

[2] Ezio Bigieri, "*High-level modulation and coding for nonlinear satellite channels*," IEEE Trans. Commun., vol. COM-32, no. 5, pp. 616-626, May. 1984

[3] Ungerboeck and Gottfried, "*Trellis Coded Modulation with Redundant Signal Sets, Part I & II"* IEEE Comm. Magazine, Vol. 25, No.2, pp5~21, Feb. 1987.

[4] S.Nakajima, *"Adaptive Coding Rate Trellis-Coded 8PSK System"*, IEICE Trans. Vol.E80-A, No.7, July 1997.

[5] M. S. Kim, J. H. Kim, Y. J. Song, J. W. Jung, J. S. Chae, H. S. Lee, *"Design and analysis of decision-directed carrier recovery for high-speed satellite communications,"* IEICE Trans. Commun., vol. E81-B, No, 12 December 1998

[6] ETSI, *"Digital Video Broadcasting(DVB): Framing Structure, Channel Coding and Modulation for Digital Satellite News Gathering(DSNG) and Other Contribution Applications by Satellite"*, ETSI EN 301 210 :European Standard

[7] Floyd M. Gardner, *"A BPSK/QPSK Timing-Error Detector for Sampled Receivers,"* IEEE Trans. On Comm. Vol., Com-34, No.5, pp. 423-429, May 1986.

[8] SDM-2020D, "Digital Video Demodulator High Speed Data Demodulator", http://comtechefdata.com, Comtech DFDATA, Nov. 2001.

Magnetic storm effects on the GPS signal

N. Reggiani[1], O. C. Branquinho[2], T. A. Xastre[3], T. C. Nascimento[4]

Pontifícia Universidade Católica de Campinas
Centro de Ciências Exatas, Ambientais e de Tecnologias
13086-900 Campinas - SP - Brazil
[1]nreggiani@puc-campinas.edu.br
[2]branquinho@puc-campinas.edu.br
[3]txastre@hotmail.com
[4]timcabral@hotmail.com

E.R. de Paula[5], I.J. Kantor[6], M. Fedrizzi[7], L.F.C. Rezende[8]

National Institute for Space Research-INPE
Caixa Postal: 515
12227-010 São José dos Campos - SP - Brazil

[5] eurico@dae.inpe.br
[6] kantor@dae.inpe.br
[7] fedrizzi@dae.inpe.br
[8] lfelipe@dae.inpe.br

Abstract— **The Global Positioning System has been largely used to indicate the position of a receiver. The GPS stability in time is important when it is used to indicate the position of an aircraft landing or of the location of a petroleum platform. This stability depends on the ionosphere conditions. In the present work we study the relation between the magnetic storm and the variations of the amplitude of the GPS signal, measured with the S_4 index.**

Index Terms— **Magnetic Storm, GPS, S_4**

I. INTRODUCTION

The purpose of this work is to establish a correlation between the magnetic storms, identified by the indices Dst and Kp, and the amplitude variation of the Global Positioning System (GPS) signal, characterized by the parameter S_4. The variations of the amplitude of the GPS signal can be very intense and in some cases the lock of the GPS signal is lost. It means a disaster when the system considered needs the information of the precision position all the time as is the case of a landing aircraft. It is also the case of a petroleum platform which position cannot be fixed by an anchor due to the ocean depth and must be adjusted all the time with the information obtained by transponders and by the GPS. A failure in this adjustment can imply in rupture in the pipes with ecological and financial damages. A relation of the quality of the GPS signal with quantities associated with the ray path environment that are continuously measured can help to indicate the level of confidence of the system. More than this, if these relations are well understood, the environment data can be used to correct the GPS signal.

II. MAGNETIC STORMS

The magnetic storm can be characterized by several magnetic indices [1]. In the present work we consider the Dst and Kp indices and also the profile of the southward component (Bz) of the Interplanetary Magnetic Field (IMF).

The Dst is a geomagnetic index, which monitors the worldwide magnetic storm level [1,2,3]. It is calculated by averaging the horizontal component of the geomagnetic field from mid-latitude and equatorial magnetograms from all over the world. Negative Dst values larger than 30 nT indicate a magnetic storm is in progress, the more negative Dst is the more intense the magnetic storm. For –30 > Dst > -50 nT the storm is weak, for –50 > Dst > -100 nT the storm is moderate, for –100 > DsT > -250 nT the storm is intense and for Dst < -250 nT we have a very intense one.

The other index Kp that is related to the maximum fluctuations of horizontal components observed on a magnetometer relative to a quiet day, during a three-hour interval. The official planetary Kp index is derived by calculating a weighted average of K-indices from a network of geomagnetic observatories [1,2,3]. Also in this case the value of Kp indicates the level of the storm and values greater than 4 indicates an intense magnetic activity and a possible magnetic storm.

The behavior of the Bz component of the IMF can also characterize a magnetic storm, because during a magnetic storm it presents north to south inversion.

These magnetic indices values are measured in several observatories and are available in some sites, for instance, the sites indicated in references [2] , [3] and [4].

III. S4 PARAMETER

The scintillation index S_4 has being largely used to describe the amplitude variations of the signal of the Global Positioning Systems (GPS), characterizing the stability of the communication link and navigation by satellites. [5,6]. The scintillation of a radio wave is due to its propagation through regions of the ionosphere with irregularities in the electronic density.

The data of scintillation presented in this work were obtained by a Scintillation Monitor (SCINTMON) receiver [7]. The SCINTMON data analysis uses a low frequency filter with cut frequency of 0.1 Hz, in such a way that medium local values of the large band power channel P_k and of the noise channel N_k are obtained, where k is the number of the sample . These values are indicated by $<P>_k$ and $<N>_k$, respectively. The variance of the intensity of a signal for a 1 minute interval is defined by

$$\hat{\sigma}^2 = \frac{1}{M}\sum_{k=1}^{M}\left(P_k - <P>_k\right)\left(P_{k-1} - <P>_{k-1}\right) \quad (1)$$

where M = 3000 is the number of samples per minute, and P_0 and $<P>_0$ are defined as the final values of potency and medium potency of the previous 1 minute interval. Furthermore, the medium power for the same time interval is defined as

$$\hat{S} = \frac{1}{M}\sum_{k=1}^{M}\left(<P>_k - <N>_k\right) \quad (2)$$

The scintillation index is defined as [6]:

$$S_4 = \frac{\sqrt{\hat{\sigma}^2}}{\hat{S}} \quad (3)$$

The index S_4 can be interpreted as the rate of the standard deviation of the signal normalized by the average power of the signal [7]. Note that the average value of the signal in the equation above is the average value of the signal for the time interval considered. In this way, the standard deviation calculated is related with the distribution of the signal values with relation to a local average and allow us to characterize better the deviations.

IV. RESULTS

The effect of strong magnetic storms on the GPS amplitude scintillations over the Brazilian territory was analyzed using data from 1998 to 2003. These scintillations are due to the ionospheric irregularities, and they can affect satellite based navigation and communication systems. During this period many magnetic storms occurred and in the present work we present the data related to the storm of April 2000.

In Figure 1 we present the values of the Dst and Kp magnetic indices and the Bz component provided by the ACE spacecraft for the period of April 5 to 11, 2000. Around midnight from April 6 to 7, 2000, the Dst index reached below –250 nT, at the same time that the Kp index reached the value of 9 and the Bz presented an inversion. All these information indicate that there was a strong magnetic storm in the period of April 5 to 11, 2000.

This work analyses if the occurrence of a magnetic storm leads to scintillations in the GPS signal. In the Figures 2a, 2b and 2c we present the GPS signal obtained from the satellites number 05, 09 and 24. In Figure 3 we present the scintillations observed in three stations in Brazil, São Luís, Cuiabá and São José dos Campos.

The signals from the satellites 05, 09 and 24 were from around 2200 UT to around 0400 UT next day (Universal Time – this is the time scale from all the figures presented) and presented large scintillations. The same happened to the signal of other satellites that were recorded during this period. We can observe that the signal of the satellite 09 presented scintillations also around midnight from April 5 to 6, 2000, when no magnetic storm was occurring. This can be explained remembering that magnetic storm is not the unique cause of the scintillation of a GPS signal.

The data presented in this work indicate us that a magnetic storm can lead to GPS scintillations, however GPS scintillations can be observed during magnetically quiet time periods.

REFERENCES

[1] M. Fedrizzi, “Estudo do Efeito das Tempestades Magnéticas Sobre a Ionosfera da Região Sul-Americana Utilizando Dados do GPS”, PhD Thesis, INPE (2004)
[2] www.sel.noaa.gov
[3] http://spidr.ngdc.noaa.gov/spidr/index.html
[4] http://cdaweb.gsfc.nasa.gov/
[5] F. S. Rodrigues, “Estudo das Irregularidades Ionosféricas Equatoriais Utilizando Sinais GPS”, MsC. Thesis, INPE (2003)
[6] K.C. Yeh and C.H.Liu, “Radio Wave Scintillations in the Ionosphere”, Proceedings IEEE vol. 70, n. 4, pag 324 – 360, April (1982)
[7] T.L. Beach, “Global Positioning System Studies of Equatorial Scintillations”, PhD Thesis, Cornell, May(1998).

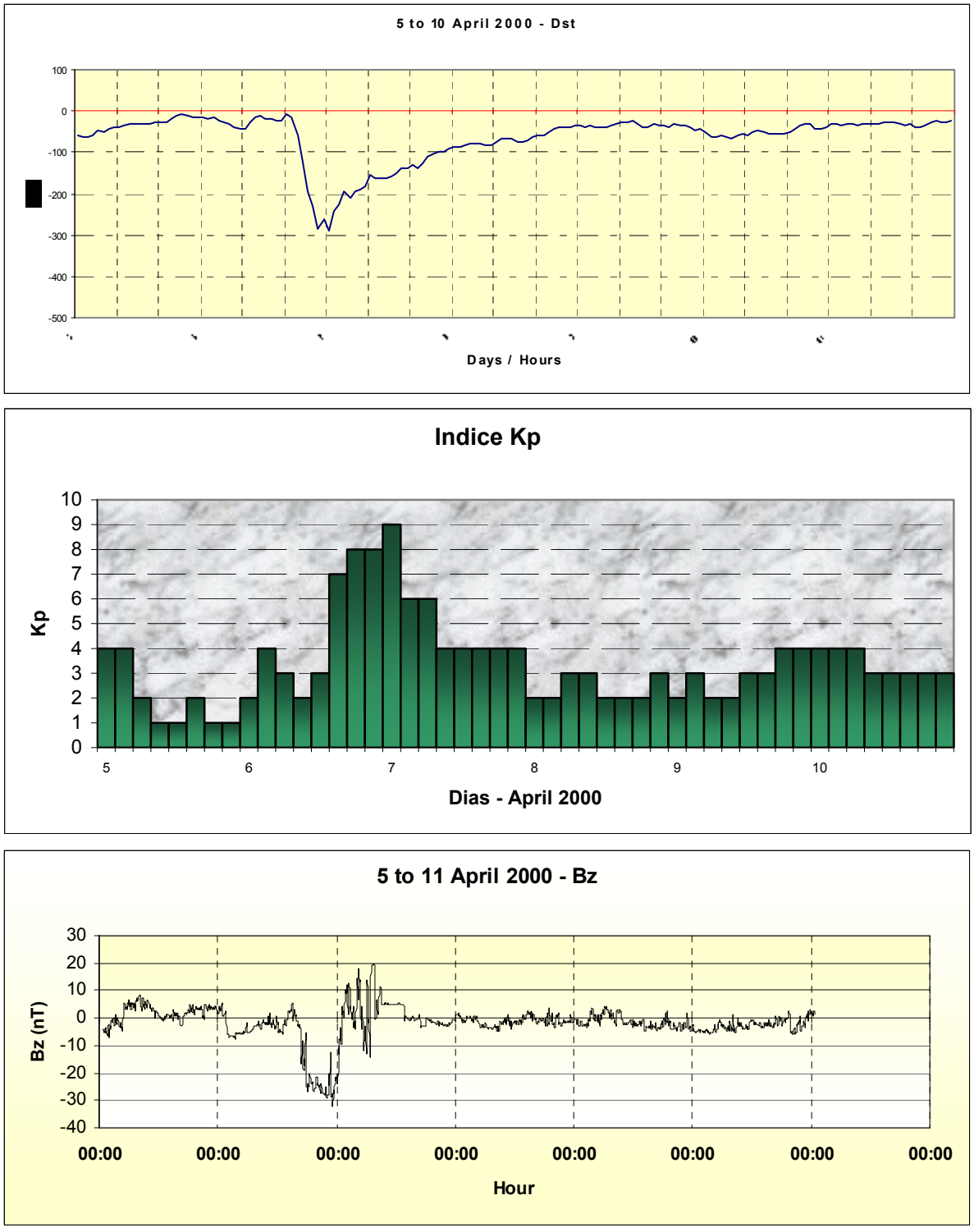

Figure 1: The values of the Dst and Kp magnetic indices and Bz obtained from the ACE satellite for the period from April 5 to 11 2000

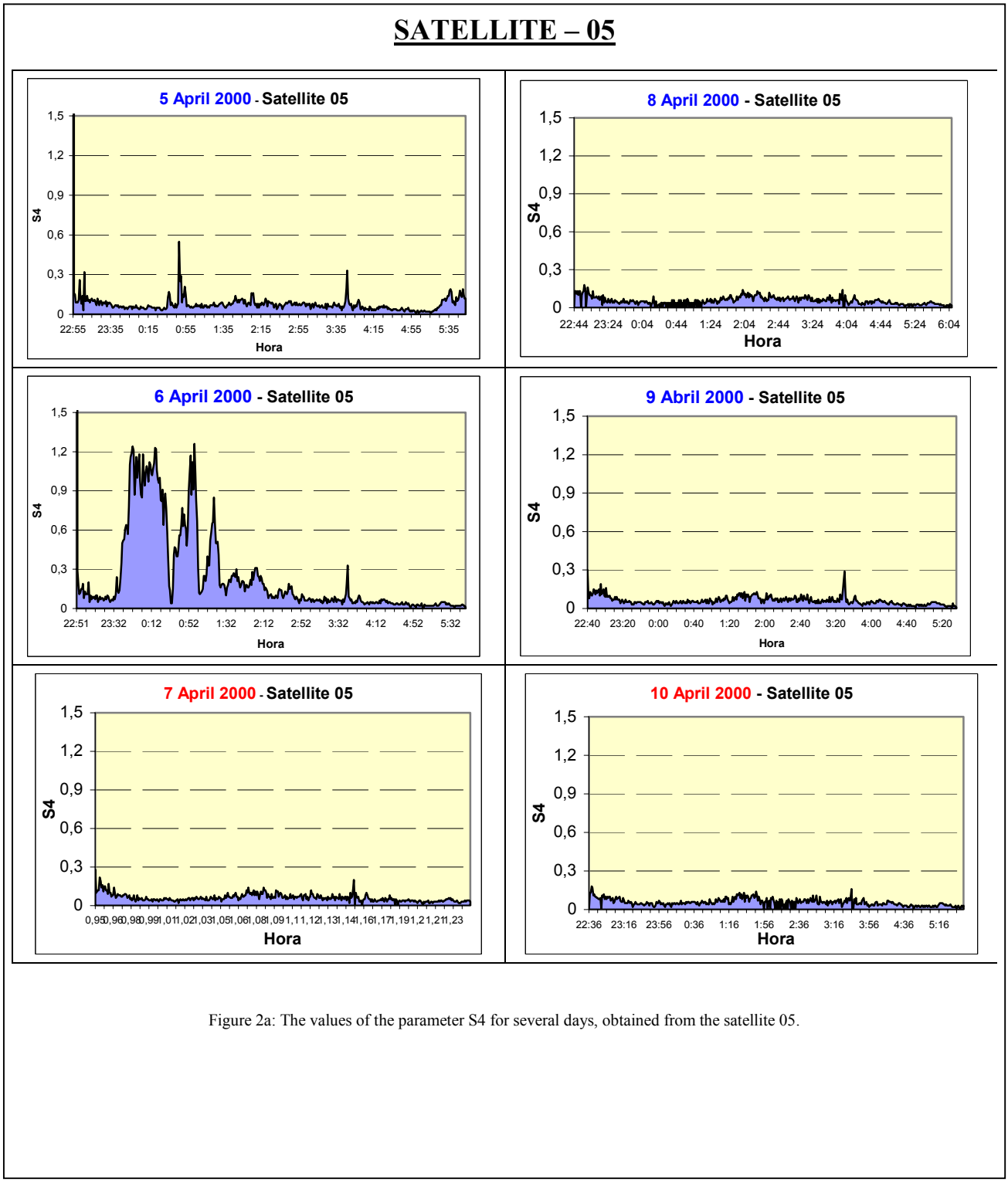

Figure 2a: The values of the parameter S4 for several days, obtained from the satellite 05.

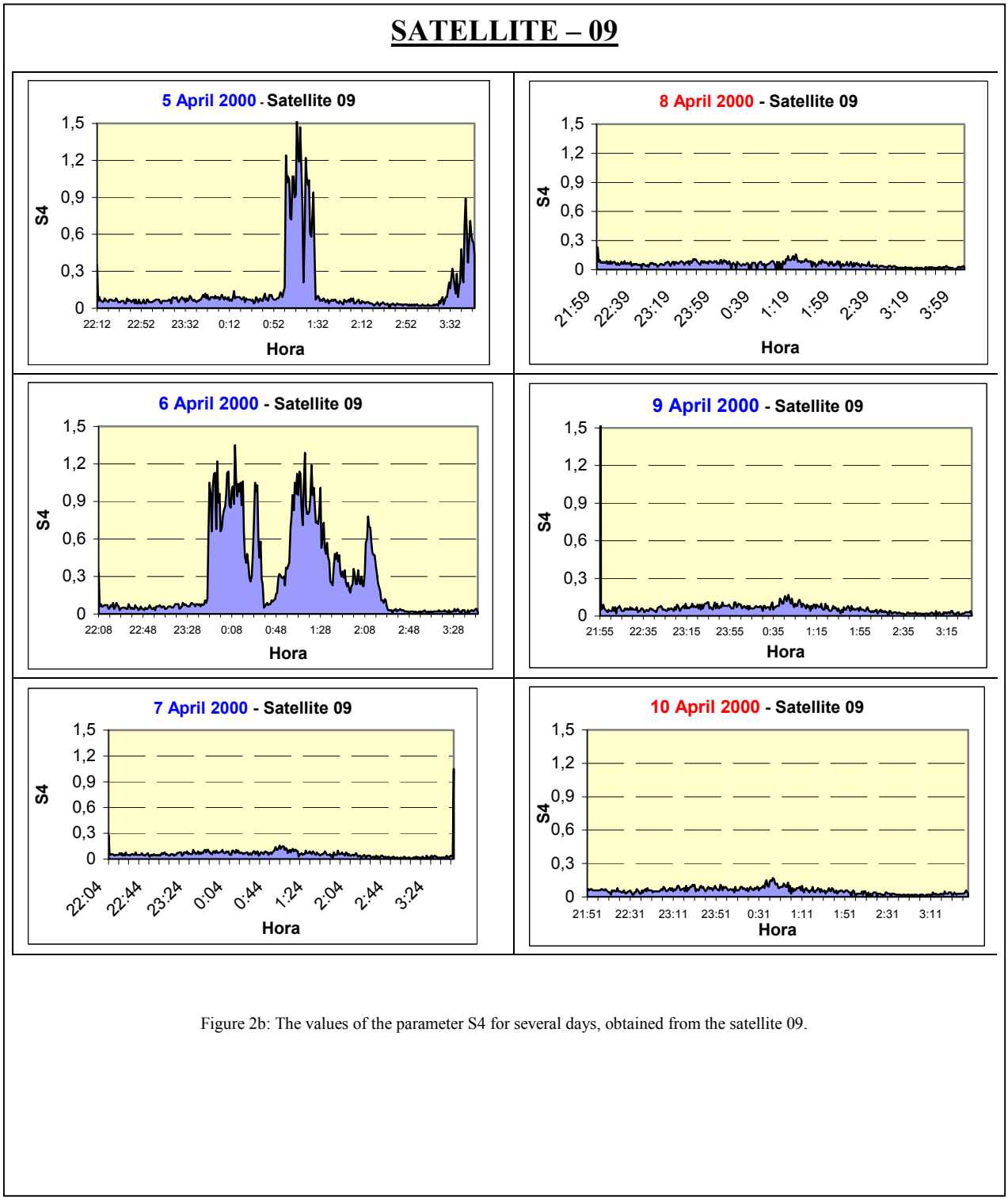

Figure 2b: The values of the parameter S4 for several days, obtained from the satellite 09.

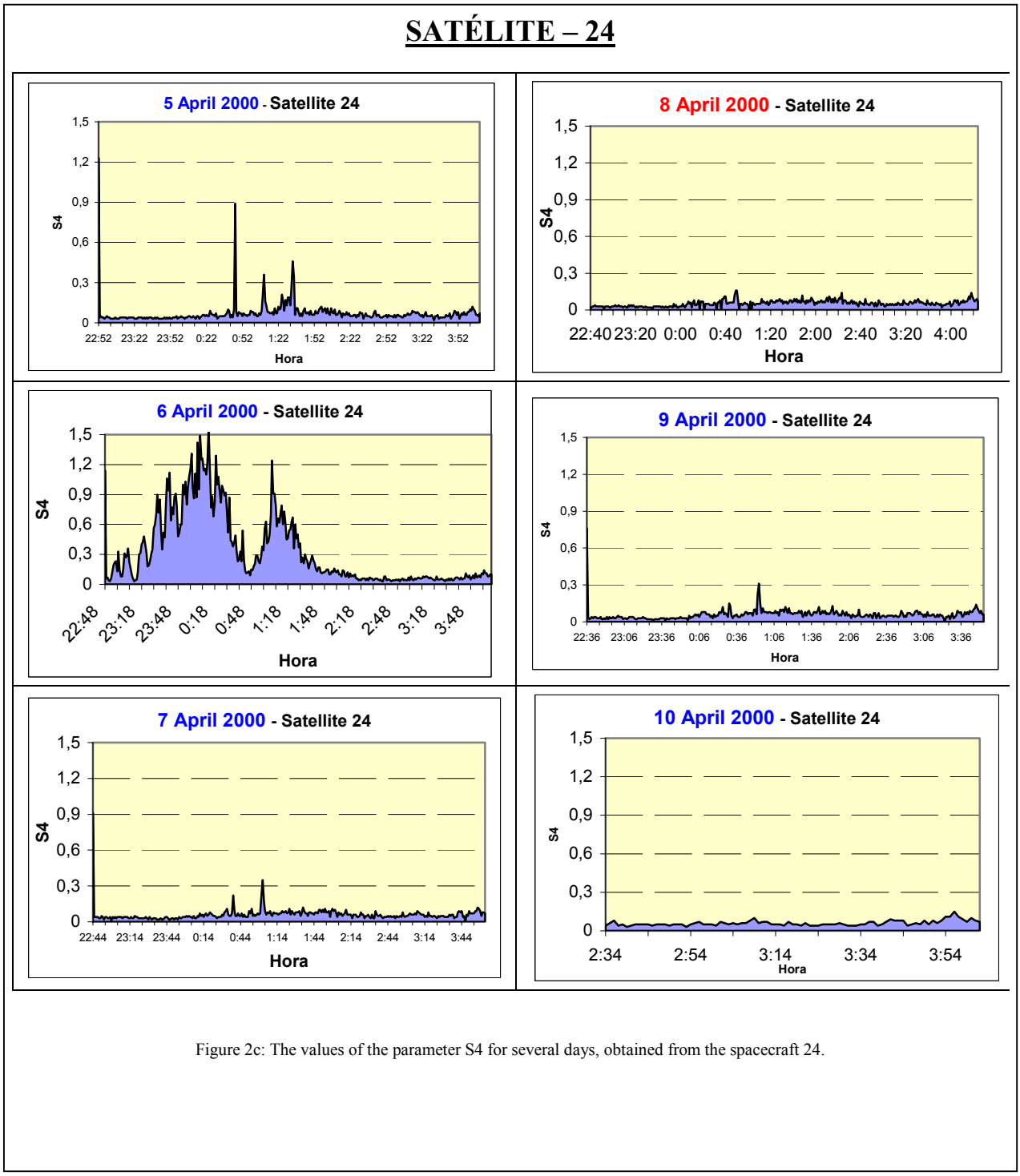

Figure 2c: The values of the parameter S4 for several days, obtained from the spacecraft 24.

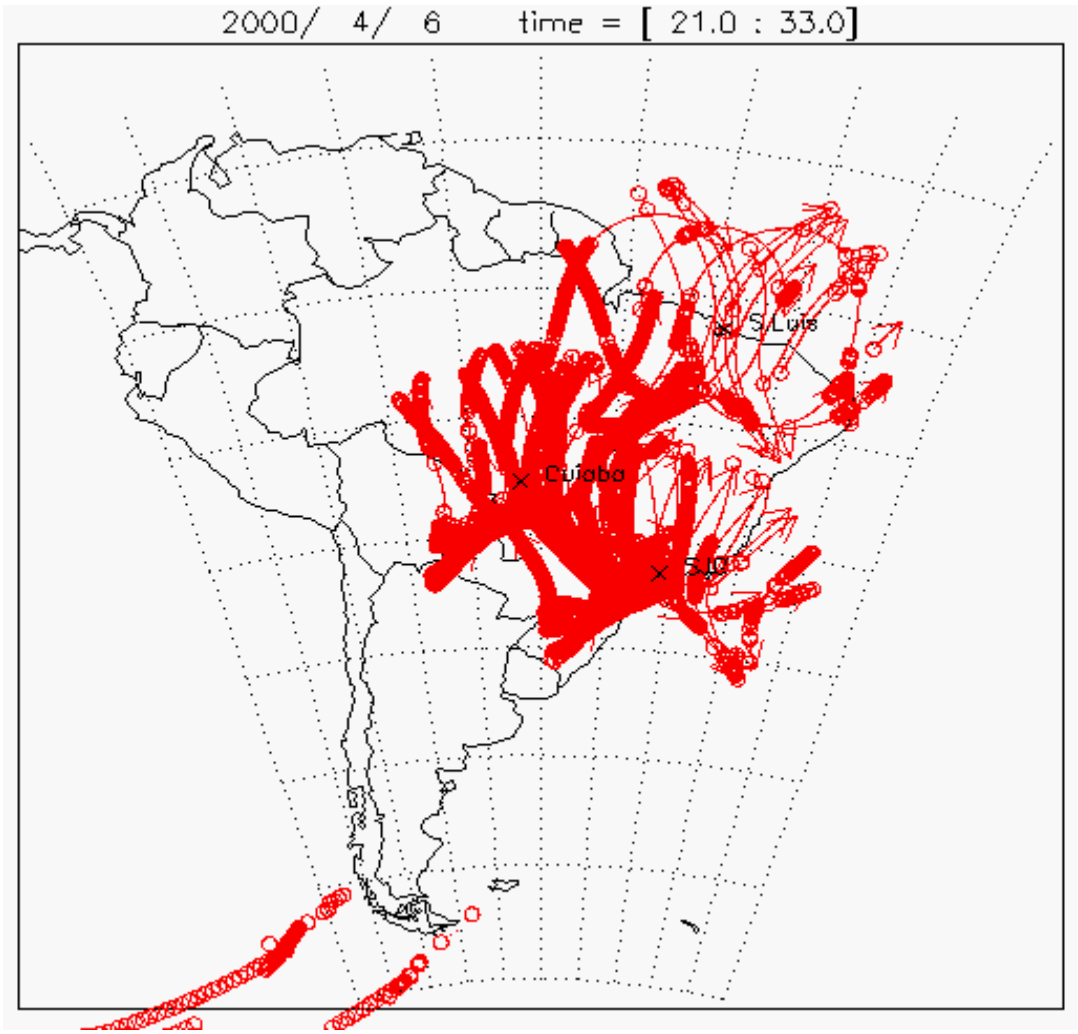

Figure 3: The scintillation observed in the stations of São Luís, Cuiabá and São José dos Campos

Parameter S4 to Analyze the WLAN Variability

O. C. Branquinho[1], N. Reggiani[2], L. F. da Silva[3]

Pontifícia Universidade Católica de Campinas
Centro de Ciências Exatas, Ambientais e de Tecnologias
13086-900 Campinas - SP - Brazil

[1]branquinho@puc-campinas.edu.br
[2]nreggiani@puc-campinas.edu.br
[3] lufas@terra.com.br

***Abstract* – The WLAN networks are being largely implemented and their performance depends strongly on the propagation conditions. We present a parameter to analyze the quality of transmission in a WLAN network for different conditions of signal propagation. As this parameter is associated with the WLAN network performance it can be used as a guide to improve these networks.**

***Index terms:* WLAN, 802.11, propagation, S_4.**

I INTRODUCTION

The Internet has become the most used way of data communication. Traditionally the users access the Internet with LAN (Local Area Network) using wires. Complementing these networks the WLAN (Wireless Local Area Network) has been developed. The version that predominates is the IEEE 802.11, mainly the 11b, also known as WiFi, with transmission rates of 1, 2, 5.5 and 11 Mbps.

Due to these transmission rates, the WLAN becomes attractive to multimedia services, being used as a cellular network complement [1]. Furthermore, the WLAN extends the LAN networks to public environments, denominated PWLAN (Public WLAN), allowing mainly mobility [2]. In these cases the variation in the propagation conditions represents a great challenge [3] because these variability changes the signal strength, leading to data rate modification [4,5] through fallback mechanism that change data rate between the four possible rates. To obtain the results we used the software DumboManager, developed in PUC-Campinas.

This work introduces a new parameter, named S4, to be considered together with others parameters to optimize WLAN. The S4 evaluates the environment variability.

II – S4 PARAMETER

To evaluate WLAN variability in different sceneries we used the scintillation index S4, that has being largely used to describe the magnitude of amplitude variations of the Global Positioning Systems (GPS) signal strength, that characterize the stability of enlacement of communication and navigation by satellites. [6,7]. This index is defined as the rate of the standard deviation of the signal normalized by the average power of the signal [8]:

$$S_4 = \frac{\sqrt{\hat{\sigma}^2}}{\hat{S}} \tag{1}$$

where the standard deviation is given by the expression

$$\hat{\sigma}^2 = \frac{1}{M}\sum_{k=1}^{M}\left(P_k - < P >\right)^2 \tag{2}$$

where

$$< P >= \frac{1}{M}\sum_{k=1}^{M} P_k \tag{3}$$

and the average power of the signal is given by

$$\hat{S} = \frac{1}{M}\sum_{k=1}^{M}\left(P_k - N_k\right) \tag{4}$$

where P_k and N_k are the values of the signal and noise for each sample measured, k is the number of the sample and M is the number of samples in each time interval considered. Note that the average value of the signal given by equation (3) is the average value of the signal for the time interval considered. In this way, the

standard deviation calculated is related with the distribution of the signal values with relation to a local average and allows characterizing better the deviations.
The purpose of using the parameter S4 is to deal direct with the experimental data in order to manage the network, our main goal. This calculation could be refined using a certain distribution to describe the signal, for instance, the Rayleigh distribution and this will be done in the future.

III – RESULTS

In the present work the signals were measured in a period of some hours each 3 seconds. The S4 index was calculated in intervals of 12 seconds.
To evaluate the technique proposed in this work four sceneries were investigated, where one AP (Access Point) and two wireless stations (EW1 and EW2) were used. The station EW1 stayed in the same place for the four sceneries, being a reference to evaluate possible anomalies. The EW2 changed place, being in four different situations, as presented in Table I. During the night, there was nobody in the environment, and during class there were many students moving in the room. So the conditions of propagation were very different.

Table I - Test Sceneries

Scenery	Condition	Distance[m]	Characteristics of the environment
1	Favorable	5	1 wall of wood, night period
2	Less favorable	10	2 walls of wood, night period
3	Unfavorable	15	2 walls of wood and 1 wall of brick, night period
4	Favorable	5	1 wall of wood, data obtained during class

To choose the places of the EW2 we considered the variability conditions of the environment, without caring for the obstacles attenuation. We tried to create four distinct sceneries to obtain a data set with enough variability in order to check the technique proposed.
Although the experiment does not have the purpose of covering all possible sceneries, it was note the asymmetry between the uplink (from the wireless station to the AP) and the downlink (from AP to the wireless station). In the Figure 1 we present the parameter S4 to the downlink for the sceneries 1, 3 and 4. We can observe that the parameter S4 characterizes the different conditions of transmission.

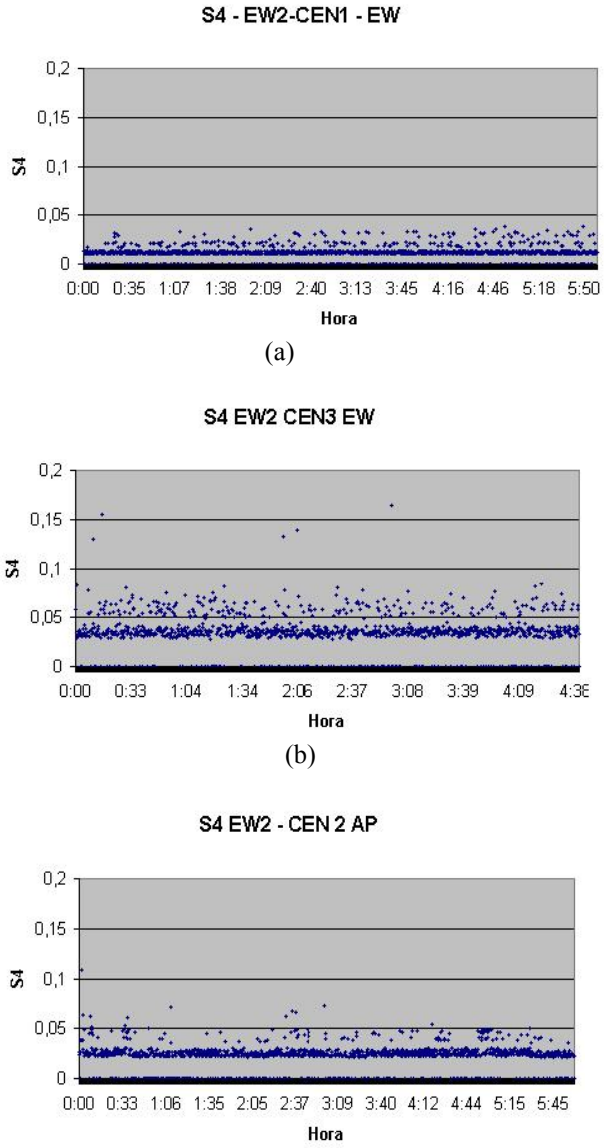

Figure 1: Values of S4 to the sceneries 1 (a) , 3 (b) e 4 (c), all downlink.

Figure 2 shows the power variation in function of time. Until point 401 its possible to see the variation of power. After the point 401 this variation is small. This behavior affect the WLAN performance.

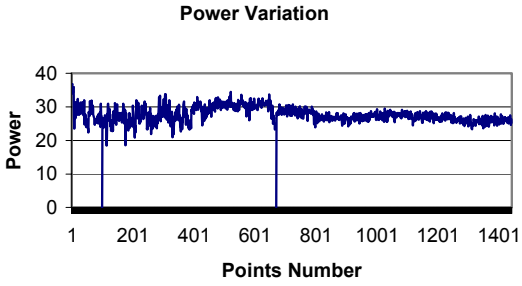

Figure 2 – Power Variation

Figure 3 shows WLAN variability. The number of points is related with time. Each point represents 3 seconds. Between 0 and 400 the variability is grater than the period between 400 and 1400. So, with S4 is

possible to evaluate the variability and correlate with performance. Comparing Figure 2 and 3 is possible to see that the factor S4 represents the power variability and is a very powerful instrument to prevent degradation, acting in the WLAN parameters, like power, to correct the variability. So, S4 is a parameter to be monitored all time.

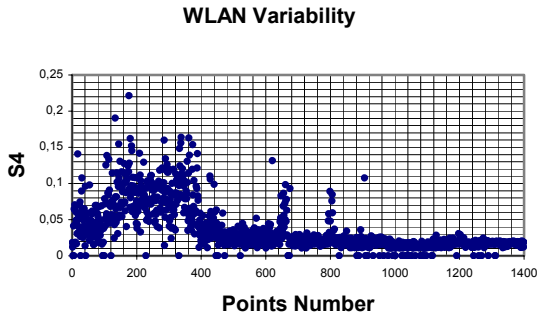

Figure 3 – WLAN Variability

The Figure 4 presents the transmission rate variation with the time. In the point 703 there is a strong change in the environment and de fallback reduce the rate from 11 Mbps to 5 Mbps. The WLAN transmits 11 Mbps in 15.4% of time and 5 Mbps in 84.6% of time. This kind of result associated with the parameter S4 will be of great utility to the analysis the influence of the variability of the transmission on the network performance.

VI – CONCLUSION

This work presented a technique that uses the parameter S4 to evaluate the WLAN variability. The results showed that this parameter allows a refinement in the analysis of performance of WLAN networks. This parameter will be used to evaluate the performance of WLAN networks and will guide optimization actions.

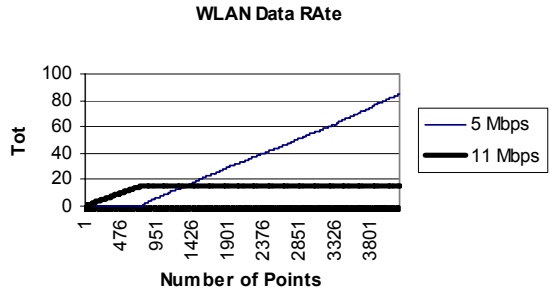

Figure 4 – Rate variation

The software DumboManager presents this type of results to evaluate the WLAN performance in real time.

REFERENCES

[1] R. Bresil, O. C. Branquinho and Nelson L. S. da Fonseca, "*Uma Análise Comparativa entre Formas de Interconexão de Redes Móveis com Redes Locais Sem Fio 802.11"*, Available in the site http://docente.puc-campinas.edu.br/CEATEC/branquinho after August 2004.

[2] J. S. Kurose and K. W. Ross, *Computer Networking – A Top Down Approach Featuring the Internet*, Addison Wesley, 2003.

[3] C. Correa, O. C. Branquinho and Nelson L. S. da Fonseca, "*Avaliação de Redes WLAN 802.11b com Arquiteturas Fat e Thin"*, accepted to the 21º Simpósio Brasileiro de Telecomunicações (SBrT). Available in the site http://docente.puc-campinas.edu.br/CEATEC/branquinho after August 2004.

[4] IEEE Std 802.11 *Wireless LAN Medium Access Control (MAC) and Physical Layer (PHY) Specifications*. ANSI/IEEE Std 802.11, Information technology , 1999 Edition.

[5] O. C. Branquinho, N. Reggiani and L. F. Silva, "Avaliação de Desempenho em Redes PWLAN 802.11 em Ambientes com Alta Variabilidade", accepted to the 21º Simpósio Brasileiro de Telecomunicações (SBrT). Available in the site http://docente.puc-campinas.edu.br/CEATEC/branquinho after August 2004.

[6] K.C. Yeh and C.H. Liu, "Radio Wave Scintillations in the Ionosphere", Proceedings IEEE Vol. 70, n. 4, pag 324-360, April (1982).

[7] F. S. Rodrigues, "Estudo das Irregularidades Ionosféricas Equatoriais Utilizando Sinais GPS", Master Thesis, INPE, Instituto Espacial de Pesquisas Espaciais (2003).

[8] T.L. Beach, "Global Positioning System Studies of Equatorial Scintillations", PhD Thesis, Cornell University (1998).

The Asymmetrical $\eta - \kappa$ Distribution

Michel Daoud Yacoub[1], Gustavo Fraidenraich, Hermano B. Tercius, and Fábio C. Martins
[1] DECOM/FEEC/Unicamp, CP. 6101, 13083-852, Campinas, SP, Brazil, michel@decom.fee.unicamp.br

***Abstract*— This paper specializes and parameterizes the general result presented elsewhere in the literature in order to propose, fully characterize, and investigate the Asymmetrical $\eta - \kappa$ Distribution. It yields estimators for the involved parameters and uses field measurements to validate the distribution. The Asymmetrical $\eta - \kappa$ Distribution includes, as special cases, important distributions such as Rayleigh, Rice, Hoyt, Nakagami-q, and One-Sided Gaussian. The fact that the Asymmetrical $\eta - \kappa$ Distribution has one more parameter than the well-known distributions renders it more flexible. Of course, in situations in which those distributions included in it give good results a better fitting is given by the Asymmetrical $\eta - \kappa$ Distribution. In addition, in many other situations in which these distributions give poor results a good fitting may be found through the Asymmetrical $\eta - \kappa$ Distribution. More specifically, its non-monomodal feature finds applications in several circumstances, examples of which are given in this paper.**

***Index Terms*— Fading distributions, Rayleigh distribution, Rice distribution, One-sided Gaussian distribution, Hoyt distribution.**

I. Introduction

THE propagation of energy in a mobile radio environment is characterized by incident waves interacting with surface irregularities via diffraction, scattering, reflection, and absorption. The interaction of the wave with the physical structures generates a continuous distribution of partial waves, with these waves showing amplitudes and phases varying according to the physical properties of the surface. A great number of distributions exist that well describe the statistics of the mobile radio signal. Among those describing the short term signal variation, Rayleigh, Rice, Hoyt, Nakagami-q, and Nakagami-m are the well-known distributions. It has been found that the different distributions yield different fittings in different situations. Finding general fading distributions is indeed an old problem that still attracts the attention of the communications researchers [1]–[6]. In [3], a general result is presented in which the in-phase and quadrature components of the fading envelope are *dependent* Gaussian variables with *different non-zero means* and *unequal variances*. The classical Rayleigh, Rice, Hoyt, Nakagami-q, and One-Sided Gaussian density functions are special cases of this general result.

This paper specializes and parameterizes the general result presented in [3] in order to propose, fully characterize, and investigate the Asymmetrical $\eta - \kappa$ Distribution. It yields estimators for the involved parameters and uses field measurements to validate the distribution. The Asymmetrical $\eta - \kappa$ Distribution includes, as special cases, important distributions such as Rayleigh, Rice, Hoyt, Nakagami-q, and One-Sided Gaussian. The fact that the Asymmetrical $\eta - \kappa$ Distribution has one more parameter than the well-known distributions renders it more flexible. Of course, in situations in which those distributions included in it give good results a better fitting is given by the Asymmetrical $\eta - \kappa$ Distribution. In addition, in many other situations in which these distributions give poor results a good fitting may be found through the Asymmetrical $\eta - \kappa$ Distribution. More specifically, its non-monomodal feature finds applications in several circumstances, examples of which are given in this paper.

II. The General Result

In his classical paper [1], Nakagami departs from a very general fading model and carries out a series of simplifications, considered to be "sufficiently good enough for engineering problems [1]", in order to arrive at the well-known Nakagami-m distribution. In the very general model, i.e. without laying hold of the mentioned simplifications, the signal intensity at any observing point is assumed to be composed of a sum of independent random phasors, subject that the in-phase and quadrature components of the sum are normal, i.e., their terms satisfy the conditions of the Central Limit Theorem. These components, therefore, are *dependent* Gaussian variables with different non-zero means and unequal variances. By choosing the in-phase and quadrature axes parallel to the axes of the equiprobability ellipses (i.e., by performing a convenient change of reference phase), the covariance between the Gaussian terms vanishes. The distribution can then be written in terms of *independent* Gaussian variables with different non-zero means and unequal variances. The derivation of the distribution in its very general form is presented in [3], where it is shown in terms of the means and variances of the Gaussian components.

It seems that very little attention has been given to this distribution, maybe because of its rather intricate form of presentation, or for lack of estimators, or, in general, for lack of full characterization. In a work from which the present paper is extracted [7], this general fading distribution is parameterized in terms of the envelope rms value and three power ratios: 1) in-phase dominant component and in-phase scattered wave; 2) quadrature dominant component and quadrature scattered wave; and 3) in-phase term and quadrature term [7]. By taking some specific, but still wide-ranging conditions, simpler forms of the general case can be achieved. In particular, for the power ratios

of 1) and 2) assumed to be identical the Symmetrical $\eta - \kappa$ Distribution is attained [7]. For either one the ratios of 1) or 2) assumed to be nil, the Asymmetrical $\eta - \kappa$ Distribution is accomplished. The concept of symmetry shall be clarified in the text. This paper explores the Asymmetrical $\eta - \kappa$ Distribution.

III. The Asymmetrical $\eta - \kappa$ Distribution

The Asymmetrical $\eta - \kappa$ Distribution is a general fading distribution that can be used to represent the small-scale variation of the fading signal. For a fading signal with envelope r, phase θ, and normalized envelope $\rho = r/\hat{r}$, in which $\hat{r} = \sqrt{E(r^2)}$ is the rms value of r, the Asymmetrical $\eta - \kappa$ joint probability density function $p(\rho, \theta)$ is written as

$$p(\rho,\theta) = \frac{\sqrt{h}\ (1+\kappa)\ \rho e^{2(h+H)\sqrt{\kappa(1+\kappa)}\,\rho\,\cos(\theta)}}{\pi e^{(h+H)\kappa}} \times e^{-(1+\kappa)\,\rho^2\,(h+H\cos(2\theta))} \quad (1)$$

where $h = \frac{2+\eta+\eta^{-1}}{4}$, $H = \frac{\eta^{-1}-\eta}{4}$, $\kappa \geq 0$ is the ratio between the total power of the dominant components and the total power of the scattered waves, and $\eta \geq 0$ is the ratio between the powers of the in-phase term and quadrature term. The normalized envelope probability density function is obtained as

$$p(\rho) = \frac{2\sqrt{h}\ (1+\kappa)}{e^{(h+H)\kappa}} \rho\, e^{-h\,(1+\kappa)\,\rho^2}\ \mathrm{M}(u,v,0) \quad (2)$$

where the $M(.,.,.)$ function, as defined here, is given by

$$M(u,v,\phi) = \frac{1}{2\pi}\int_0^{2\pi} e^{u\cos(\theta)+v\cos(2(\theta+\phi))}d\theta \quad (3)$$

with $u = 2\,(h+H)\,\sqrt{\kappa\,(1+\kappa)}\,\rho$ and $v = -\left(H\,(1+\kappa)\,\rho^2\right)$. The phase distribution is obtained here in a closed-form manner as

$$p(\theta) = \frac{e^{-(h+H)\,\kappa}\sqrt{h}}{2\,\pi\,(h+H\,\cos(2\,\theta))^{\frac{3}{2}}}\left(\sqrt{h+H\,\cos(2\,\theta)}\right. + e^{\frac{(h+H)^2\,\kappa\,\cos(\theta)^2}{h+H\,\cos(2\,\theta)}}\ (h+H)\,\sqrt{\pi\kappa}\,\cos(\theta) \times \left.\left(1+\mathrm{erf}(\frac{(h+H)\,\sqrt{\kappa}\,\cos(\theta)}{\sqrt{h+H\,\cos(2\,\theta)}})\right)\right) \quad (4)$$

where $\mathrm{erf}(.)$ is the Gaussian error function. The $n-th$ moment $E[\rho^n]$ of ρ can be attained in the usual integral manner or in a series expansion given by [7] where ${}_2F_1(.,.;.;.)$ is the Gauss hypergeometric function, $\Gamma(.)$ is the Gamma function. Of course, $E[r^n] = \hat{r}^n E[\rho^n]$. The $M(.,.,.)$ function presents some interesting properties related to the Bessel functions. In particular $M(u,0,\phi) = I_0(u)$ and $M(0,v,\phi) = I_0(v)$, where $I_0(.)$ is the modified Bessel function of the first kind and order zero. It can be written in terms of the Bessel functions as For the particular case of the Asymmetrical $\eta - \kappa$ Distribution, in which $\phi = 0$,

$$M(u,v,0) = I_0(u)I_0(v) + 2\sum_{k=1}^{\infty}(-1)^k\, I_k(v)I_{2k}(u) \quad (7)$$

Figure 1, for a fixed η ($\eta = 0$) and varying κ, Figure 2, for a fixed η ($\eta = 0.5$) and varying κ, and Figure 3, for a fixed κ ($\kappa = 1$) and varying η, show the various shapes of the Asymmetrical $\eta - \kappa$ probability density function $p(\rho)$.

IV. Outline of the Derivation of the Asymmetrical $\eta - \kappa$ Distribution

The fading model for the Asymmetrical $\eta - \kappa$ Distribution considers a signal composed of multipath waves propagating in an non-homogeneous environment. The powers of the in-phase and quadrature scattered waves are assumed to be arbitrary. In the same way, the power of the in-phase component is also assumed to be arbitrary but the power of the quadrature dominant component is assumed to be nil, which explain the reason to be called asymmetrical distribution. Let x and y be independent Gaussian wide sense stationary processes of the in-phase and quadrature components of the propagated wave, respectively. Assume that $\mathrm{E}(x) = \mu_x$, $\mathrm{E}(y) = 0$, $\mathrm{Var}(x^2) = \sigma_x^2$, and $\mathrm{Var}(y^2) = \sigma_y^2$, where $E(.)$ and $Var(.)$ are the mean and variance operators, respectively. The joint distribution $p(x,y)$ of x and y is found in the usual manner. The envelope r can be written in terms of the in-phase and quadrature components of the fading signal as $r^2 = x^2 + y^2$ with $x = r\cos(\theta)$, $y = r\sin(\theta)$, and $\theta = \arctan\left(\frac{y}{x}\right)$. Then the joint density $p(r,\theta)$ of r and θ is obtained by the well-known procedure of transformation of variables. Given the physical model of the distribution, $\eta = \frac{\sigma_x^2}{\sigma_y^2}$ and $\kappa = \frac{\mu_x^2}{\sigma_x^2+\sigma_y^2}$. For the Asymmetrical case then $E\left(r^2\right) = r_{rms}^2 = \left(1+\eta^{-1}\right)(1+\kappa)\ {\sigma_x}^2$. By carrying out the appropriate substitutions and after long algebraic manipulations the densities as presented in Section III follow.

V. Estimators for the Parameters η and κ

Estimators for the parameters η and κ can be obtained in terms of the moments of the envelope. In particular, $E[\rho^4]$ and $E\left[\rho^6\right]$ can be expressed in a radical form as functions of η and κ. These equations are then manipulated to give (8). Given $E[\rho^4]$ and $E\left[\rho^6\right]$ (8) yields six possible solutions for κ, but only one will be non-negative and real. Using this value for κ, (9) can be solved to obtain two possible values for η. Therefore, two possible pairs of solutions, (η_1, κ) and (η_2, κ), are attained. Such an ambiguity can be resolved by comparing the two corresponding Asymmetrical $\eta - \kappa$ curves to the one obtained experimentally and choosing the one that best fits. Such a procedure has been extensively and successfully followed for both simulated as well as experimental data. There are other forms of solving this ambiguity, though. One of them involves the estimation of the phase, which is certainly a task more complicated than that of detecting the envelope. Another form of

$$E\left[\rho^n\right] = \sum_{j=0}^{\infty}\sum_{t=0}^{\infty}\sum_{i=0}^{t}\left(\begin{array}{c} t \\ i \end{array}\right)\frac{(-1)^{-i+2\,j+t}\,4^t\,e^{\frac{h\,\kappa}{-h+H}}\,h^{-1+i-2\,j-t-n}\,(h-H)^{\frac{1-2\,t+n}{2}}\,H^{-i+2\,j+t}}{\sqrt{\pi}\,(1+\kappa)^{\frac{n}{2}}\,\Gamma(1+j)\,\Gamma(1+2\,t)\,\Gamma(1-i+2\,j+2\,t)}$$
$$\times\,(h+H)^{\frac{1}{2}-2\,i+4\,j+3\,t-2\,(-i+2\,j+t)+\frac{n}{2}}\,\kappa^t\,\Gamma(\frac{1}{2}+j+t)\,\Gamma(1-i+2\,j+2\,t+\frac{n}{2}) \tag{5}$$

$$M\left(u,v,\phi\right) = \sum_{k=-\infty}^{\infty}\sum_{n=-\infty}^{\infty}(j)^n\,(-1)^k\,I_k(-v\,\cos(2\phi))I_n(v\,\sin(2\phi))I_{2(k+n)}(u) \tag{6}$$

$$144-216\,\mathrm{E}\left[\rho^4\right]+81\,\mathrm{E}\left[\rho^4\right]^2+24\,\mathrm{E}\left[\rho^6\right]-18\,\mathrm{E}\left[\rho^4\right]\,\mathrm{E}\left[\rho^6\right]+\mathrm{E}\left[\rho^6\right]^2+$$
$$\left(864-1296\,\mathrm{E}\left[\rho^4\right]+486\,\mathrm{E}\left[\rho^4\right]^2+144\,\mathrm{E}\left[\rho^6\right]-108\,\mathrm{E}\left[\rho^4\right]\,\mathrm{E}\left[\rho^6\right]+6\,\mathrm{E}\left[\rho^6\right]^2\right)\kappa+$$
$$\left(2160-3240\,\mathrm{E}\left[\rho^4\right]+1215\,\mathrm{E}\left[\rho^4\right]^2+360\,\mathrm{E}\left[\rho^6\right]-270\,\mathrm{E}\left[\rho^4\right]\,\mathrm{E}\left[\rho^6\right]+15\,\mathrm{E}\left[\rho^6\right]^2\right)\kappa^2+$$
$$\left(2496-4032\,\mathrm{E}\left[\rho^4\right]+1620\,\mathrm{E}\left[\rho^4\right]^2+448\,\mathrm{E}\left[\rho^6\right]-360\,\mathrm{E}\left[\rho^4\right]\,\mathrm{E}\left[\rho^6\right]+20\,\mathrm{E}\left[\rho^6\right]^2\right)\kappa^3+$$
$$\left(1296-2520\,\mathrm{E}\left[\rho^4\right]+1215\,\mathrm{E}\left[\rho^4\right]^2+264\,\mathrm{E}\left[\rho^6\right]-270\,\mathrm{E}\left[\rho^4\right]\,\mathrm{E}\left[\rho^6\right]+15\,\mathrm{E}\left[\rho^6\right]^2\right)\kappa^4+$$
$$\left(288-720\,\mathrm{E}\left[\rho^4\right]+486\,\mathrm{E}\left[\rho^4\right]^2+48\,\mathrm{E}\left[\rho^6\right]-108\,\mathrm{E}\left[\rho^4\right]\,\mathrm{E}\left[\rho^6\right]+6\,\mathrm{E}\left[\rho^6\right]^2\right)\kappa^5+$$
$$\left(16-72\,\mathrm{E}\left[\rho^4\right]+81\,\mathrm{E}\left[\rho^4\right]^2-8\,\mathrm{E}\left[\rho^6\right]-18\,\mathrm{E}\left[\rho^4\right]\,\mathrm{E}\left[\rho^6\right]+\mathrm{E}\left[\rho^6\right]^2\right)\kappa^6=0 \tag{8}$$

$$\eta = \frac{1-\kappa\pm\sqrt{-2+\mathrm{E}\left[\rho^4\right]-4\,\kappa+2\,\mathrm{E}\left[\rho^4\right]\,\kappa+\mathrm{E}\left[\rho^4\right]\,\kappa^2}}{1+\kappa\mp\sqrt{-2+\mathrm{E}\left[\rho^4\right]-4\,\kappa+2\,\mathrm{E}\left[\rho^4\right]\,\kappa+\mathrm{E}\left[\rho^4\right]\,\kappa^2}} \tag{9}$$

estimating η is by means of (11) (see Section VII), which makes use of κ and the Nakagami parameter m. Alternatively, the Asymmetrical $\eta-\kappa$ Distribution can be applied by estimating m, choosing κ within an appropriate range of m, and calculating η as a function of m and of the chosen κ, as detailed in Section VII.

VI. The Asymmetrical $\eta-\kappa$ Distribution and the Other Fading Distributions

The Asymmetrical $\eta-\kappa$ Distribution is a general fading distribution that includes the Rayleigh, Rice, Hoyt, Nakagami-q, and One-Sided Gaussian distributions as special cases. It may also approximate the Nakagami-m distribution.

A. Rayleigh, Rice, Hoyt, Nakagami-q, and One-Side Gaussian

The Hoyt distribution can be obtained from the Asymmetrical $\eta-\kappa$ Distribution in an exact manner by setting $\kappa=0$ and using the relation $b=\frac{\eta-1}{\eta+1}$, where b is the Hoyt parameter. From the Hoyt distribution the One-Sided Gaussian is obtained for $b\rightarrow\mp1$ ($\eta\rightarrow0$ or $\eta\rightarrow\infty$). In the same way, from the Hoyt distribution the Rayleigh distribution is obtained in an exact manner for $b=0$ ($\eta=1$). The Nakagami-q distribution can be obtained from Asymmetrical $\eta-\kappa$ Distribution in an exact manner by setting $\kappa=0$ and using $q=\eta$, where q is the respective parameter. From the Nakagami-q the One-Sided Gaussian can be obtained for $q\rightarrow0$ or $q\rightarrow\infty$ ($\eta\rightarrow0$ or $\eta\rightarrow\infty$). In the same way, from the Nakagami-q the Rayleigh distribution can be obtained by setting $q=1$ ($\eta=1$). The Rice Distribution can be obtained from the Asymmetrical $\eta-\kappa$ Distribution in an exact manner by setting $\eta=1$ and using $k=\kappa$, where k is the Rice parameter. From the Rice distribution the Rayleigh can be obtained for $k=0$ ($\kappa=0$).

B. Nakagami-m

The Nakagami parameter m can be written in terms of η and κ by recognizing that m is the inverse of the normalized variance of the squared envelope, i.e. $m=Var^{-1}\left(\rho^2\right)$. Using such a definition for the Asymmetrical $\eta-\kappa$ Distribution, it can be shown that

$$m=\frac{\left(1+\eta^{-1}\right)^2\left(1+\kappa\right)^2}{2\,\left(1+\eta^{-2}+2\,\left(1+\eta^{-1}\right)\,\kappa\right)} \tag{10}$$

From (10) it can be seen that, apart from the case $m=0.5$, for which $(\eta,\kappa)=(0,0)$ is the only possible solution, an infinite number of Asymmetrical $\eta-\kappa$ curves can be found for the same m parameter. An appropriate choice of $(\eta,\,\kappa)$ pairs may be found that leads to the best Nagakami-m approximation. Interestingly, it can be observed that the minimum of (10) is obtained for $(\eta,\kappa)=(0,0)$, for which $m=0.5$. In this case, the Asymmetrical $\eta-\kappa$ Distribution specializes into the One-Sided Gaussian, as does Nakagami-m.

VII. Application of the $\eta-\kappa$ Distribution

The application of the Asymmetrical $\eta-\kappa$ Distribution implies the estimation of its parameters η and κ (see Section V). On the other hand, it may be possible to use the Asymmetrical $\eta-\kappa$ Distribution by estimating the parameter m and choosing the appropriate $(\eta,\,\kappa)$ pair satisfying (10) that leads to the best

fit. In particular, for a given m and κ the remaining parameter η can be chosen as

$$\eta = \frac{1}{-1+2\,m-2\,\kappa+4\,m\,\kappa-\kappa^2}\left(1+2\,\kappa-2\,m\,\kappa+\kappa^2 \pm 2\,\sqrt{m\,(1-m+2\,\kappa-2\,m\,\kappa+\kappa^2+m\,\kappa^2)}\right) \quad (11)$$

with the usual physical constraint $\eta \geq 0$ and *real*. Figure 4 depicts a sample of the various shapes of the Asymmetrical $\eta-\kappa$ probability distribution function $P(\rho)$ as a function of the normalized envelope ρ for the same Nakagami parameter $m = 1.25$. It can be seen that, although the normalized variance (parameter m) is kept constant, the curves are substantially different from each other. Note that the lower tail of the distribution may yield differences in the probability of some orders of magnitude. Note also that the Asymmetrical $\eta-\kappa$ curves can be above or below the Nakagami curve.

VIII. Validation Through Field Measurements

A series of field trials was conducted at the University of Campinas (Unicamp), Brazil, in order to investigate the short term statistics of the fading signal at 1.8GHz [8]. In particular, transmitter and receiver were placed within buildings (*indoor propagation*), and the procedure used is that of the already widely reported in the literature [9].

Through our measurements, it has been observed that the Asymmetrical $\eta-\kappa$ Distribution finds its applications for the cases in which the Rice Distribution is also applicable ($m \geq 1$). In the same way, it has found its applicability in those (less frequent) cases in which Hoyt is also applicable ($0 \leq m \leq 1$). On the other hand, because of its versatility it yields excellent fitting for the cases in which the fitting provided by these respective distributions is only moderate. Figure 5 shows some sample plots illustrating the adjustment by the Asymmetrical $\eta-\kappa$ Distribution as compared to the Rice one. Note, in Figure 5, that the Rice distribution provides good fitting in both cases, although the Asymmetrical $\eta-\kappa$ Distribution gives a better adjustment. Also in Figure 5 note how the Asymmetrical $\eta-\kappa$ Distribution tends to reproduce or very closely follow the trends (concavity and/or convexity) of the true curve.

IX. Conclusions

This paper has presented the Asymmetrical $\eta-\kappa$ Distribution, a general fading distribution that includes Rayleigh, Rice, Hoyt, Nakagami-q, and One-Sided Gaussian as special cases. Simulation and field trials have been conducted in order to better characterize this distribution. It has been found that Asymmetrical $\eta-\kappa$ Distribution finds its applications for the cases in which Hoyt as well as Rice distributions are also applicable. Because of its versatility it yields excellent fitting for the cases in which the fitting provided by these respective distributions is only moderate. It has been observed that the Asymmetrical $\eta-\kappa$ Distribution tends to closely follow the shapes of the true distribution which, sometimes, does not comply with the monomodal behavior of the well-known distributions.

References

[1] M. Nakagami. *The M-Distribution - A General Formula of Intensity Distribution of Rapid Fading*. Statistical Methods in Radio Wave Propagation. W. C. Hoffman, Ed. Elmsford, NY: Pergamon, 1960.

[2] R. S. Hoyt. Probability Functions for the Modulus and Angle of the Normal Complex Variate. *Bell System Technical Journal*, vol. 26:pp. 318–359, April 1947.

[3] P. Beckmann. *Probability in Communication Engineering*. Harcourt Brace and World, New York, 1967.

[4] E. W. Stacy. A generalization of the gamma distribution. *Ann. Math Stat.*, vol. 33(no. 3):pp. 1187–1192, 1962.

[5] D. S. Polydorou, Christos N. Capsalis. A New Theorical Model for the Prediction of Rapid Fading Variations in an Indoor Environment. *IEEE Trans. Veh. Technol.*, vol. 46(no. 3):pp. 748–754, August 1997.

[6] Ali Abdi. Comments on "a new theorical model for the prediction of rapid fading variations in an indoor environment". *IEEE Trans. Veh. Technol.*, vol. 50(no. 1):pp. 331–334, January 2001.

[7] M. D. Yacoub, G. Fraidenraich. Generalized $\eta-\kappa$ distribution. Technical report, School of Electrical and Computer Engineering - Unicamp, January 2000.

[8] Hermano B. Tercius, Fábio C. Martins, et. al. Modular spacially controlled data aquisition equipment (in Portuguese). In *Congresso Brasileiro de Ensino de Engenharia - COBENGE-Rio de Janeiro*, 14-18 September 2003.

[9] A. F. Abouraddy, S. M. Elnoubi. Statistical Modeling of the Indoor Radio Channel at 10 GHz Through Propagation Measurements - Part I: Narrow-Band Measurements and Modeling. *IEEE Trans. Veh. Technol.*, vol. 49(no. 5):pp. 1491–1507, September 2000.

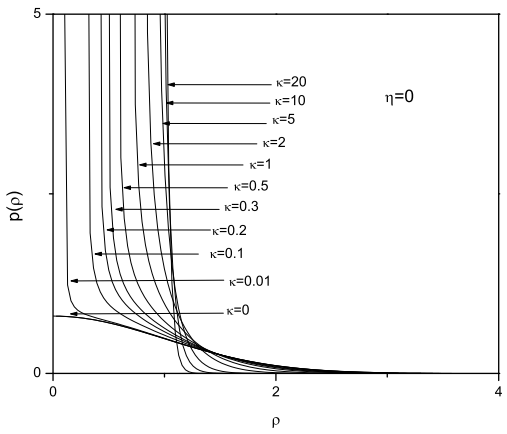

Fig. 1. The Asymmetrical $\eta-\kappa$ probability density function for a fixed η ($\eta = 0$).

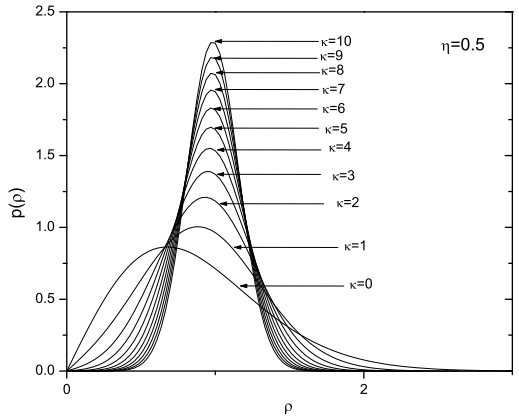

Fig. 2. The Asymmetrical $\eta - \kappa$ probability density function for a fixed η ($\eta = 0.5$).

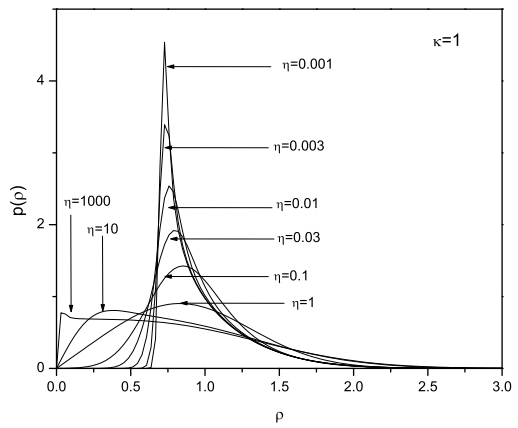

Fig. 3. The Asymmetrical $\eta - \kappa$ probability density function for a fixed κ ($\kappa = 1$).

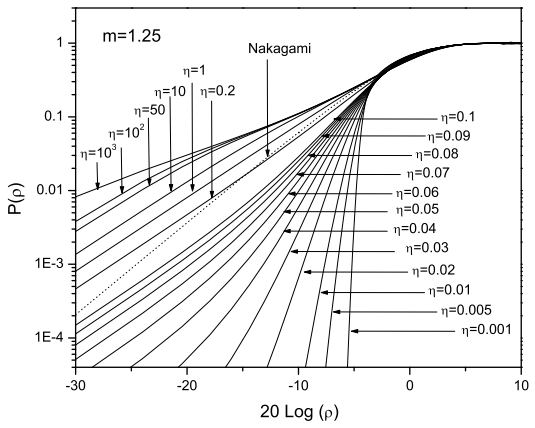

Fig. 4. The Asymmetrical $\eta - \kappa$ probability distribution function for the same Nakagami parameter m (m=1.25).

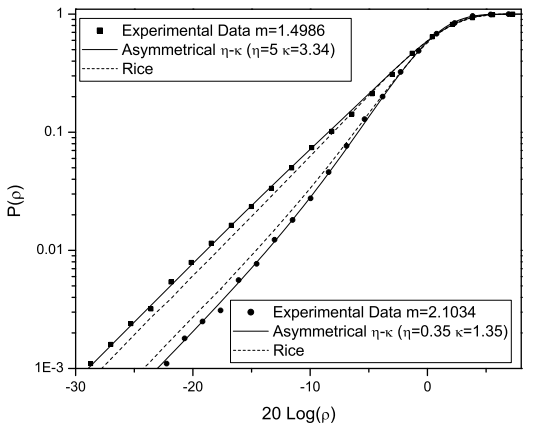

Fig. 5. The Asymmetrical $\eta - \kappa$ distribution function adjusted to data of an indoor propagation measurement at 1.8 GHz conducted at Unicamp.

Validating the $\kappa - \mu$ Distribution and the $\eta - \mu$ Distribution

Fábio Cézar Martins*, Hermano Barros Tercius† and Michel Daoud Yacoub†
*State University of Londrina - UEL
P.O. Box 05 - 86051-990
Londrina - PR - Brazil
fabio@uel.br
†State University of Campinas - UNICAMP
P.O. Box 05 - 13083-970
Campinas - SP - Brazil
hermanob@decom.fee.unicamp.br, michel@decom.fee.unicamp.br

***Abstract*— This article validates two new fading distributions, namely $\kappa-\mu$ Distribution and $\eta-\mu$ Distribution. The analysis have been carried out over a set of substantial amount of data collected at the campus of the State University of Campinas - UNICAMP. The experiments have been performed with propagation into and within buildings at 1.8 GHz.**

***Index Terms*— Measurements, data acquisition, fading, fading distributions, Distribution $\kappa-\mu$, Distribution $\eta-\mu$.**

I. Introduction

A great number of distributions exist that well describe the statistics of the mobile radio signal. Extensive field trials have been used to validate these distributions and the results show a very good agreement between measurements and theoretical formulas. The long term signal variation is well characterized by the Lognormal Distribution whereas the short term signal variation is described by several other distributions such as Rayleigh, Rice, Nakagami-m, and Weibull, though to the latter, originally derived for reliability study purposes, little attention has been paid.

Among these, the Nakagami-m Distribution has been given a special attention for its ease of manipulation and wide range of applicability. Although, in general, it has been found that the fading statistics of the mobile radio channel may well be characterized by the Nakagami-m, situations are easily found for which other distributions such as Rice and even Weibull yield better results [1]. More importantly, situations are encountered for which no distributions seem to adequately fit experimental data, though one or another may yield a moderate fitting. Some researches [2] even question the use of the Nakagami-m Distribution because its tail does not seem to yield a good fitting to experimental data, better fitting being found around the mean or median.

The well-known fading distributions have been derived assuming a homogeneous diffuse scattering field, resulting from randomly distributed point scatterers. With such an assumption, the central limit theorem leads to complex Gaussian processes with in-phase and quadrature Gaussian distributed variables x and y having zero means and equal standard deviations. In case one cluster of multipath wave is considered then the Rayleigh Distribution can be obtained. If a specular component predominates over the scattered waves, then the Rice Distribution is accomplished. The Nakagami signal can be understood as composed of clusters of multipath waves so that within any one cluster the phases of scattered waves are random and have similar delay times with delay-time spreads of different clusters being relatively large. The assumption of a homogeneous diffuse scattering field is certainly an approximation because the surfaces are spatially correlated characterizing a non-homogeneous environment [3].

More recently [4], [5], two new fading distributions have been proposed that include or closely approximate the most common fading distributions. The $\eta - \mu$ Distribution [4] includes the Hoyt and the Nakagami-m distributions as special cases. The $\kappa - \mu$ Distribution [5] includes the Rice and the Nakagami-m distributions as special cases. Therefore, in both fading distributions, the One-Sided Gaussian and the Rayleigh distributions also constitute special cases and the Lognormal Distribution may be well-approximated by these distributions. The fading model of the $\eta - \mu$ Distribution considers a signal composed of clusters of multipath waves propagating in a non-homogeneous environment. Within any one cluster, the phases of the scattered waves are random and have similar delay times with delay-time spreads of different clusters being relatively large. The in-phase and quadrature components of the fading signal within each cluster are assumed to have different powers. The fading model of the $\kappa - \mu$ Distribution considers a signal composed of clusters of multipath waves propagating in an non-homogeneous environment. Within any one cluster, the phases of the scattered waves are random and have similar delay times with delay-time spreads of different clusters being relatively large. The clusters of multipath waves are assumed to have the scattered waves with identical powers but within each cluster a dominant component is found that presents an arbitrary power.

To validate these new distributions *into and within building measurements campaigns* have been carried

out at the UNICAMP campus. The analysis of the data have demonstrated that these new distributions yield excellent adjustments in all of the cases.

This article is organized as follows: Section II details the experiment; Section III briefly describes the two new fading distributions, namely $\kappa - \mu$ and $\eta - \mu$. Section IV shows some sample of the results. Section V draws some conclusions.

II. The Experiment

A. Transmitter

The into building measurement campaigns (transmitter and receiver located in separate buildings) used a transmitter tuned at 1.8 GHz and an 11 dBi monopole antenna. The transmitting apparatus was set up in a room at the top floor of the School of Electrical and Computer Engineering with the antenna mounted at its rooftop, as shown in Figure 1. The within building measurement campaigns (transmitter and receiver located in the same building) used approximately the same transmitter differing only on the antenna, which in this case was substantially smaller.

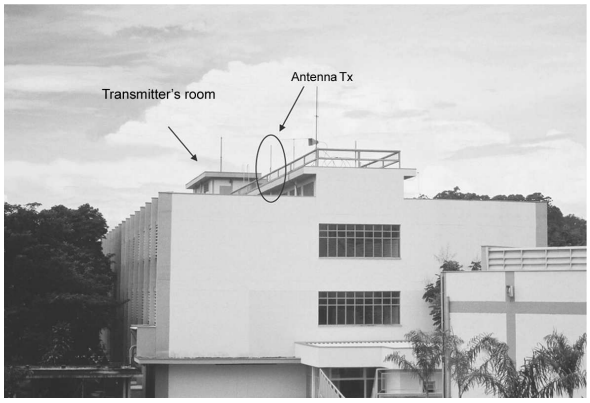

Fig. 1. View of the top floor of the FEEC E building.

B. Data Acquisition Equipment

A modular data acquisition instrument, named EADMEC, was specially designed and built to perform the narrowband measurements. EADMEC is basically composed of four modules: the spatial sampler, the data collector, the signal processor, and the power supplier. The spatial sampler is a slotted wheel (the fifth wheel) used to determine the appropriate instant to sample the receiving signal. The data collector is an off-the-shell microcontroller that acquires and stores the sampled signal. The control software has been developed in LabVIEW ®6.1 and provides for real time signal monitoring. Figure 3 presents the user/software interface. The signal processor performs the signal receiving function. It is composed of antenna, amplifier, variable attenuator, and spectrum analyzer. The purpose of the power supply module is to provide for an adequate autonomy for field measurements. It is composed of two 12 volts automotive batteries and a DC/AC converter. Figure 2 shows the EADMEC.

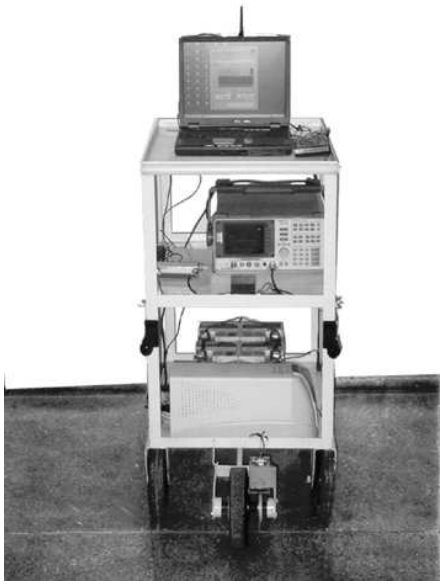

Fig. 2. Front view of EADMEC.

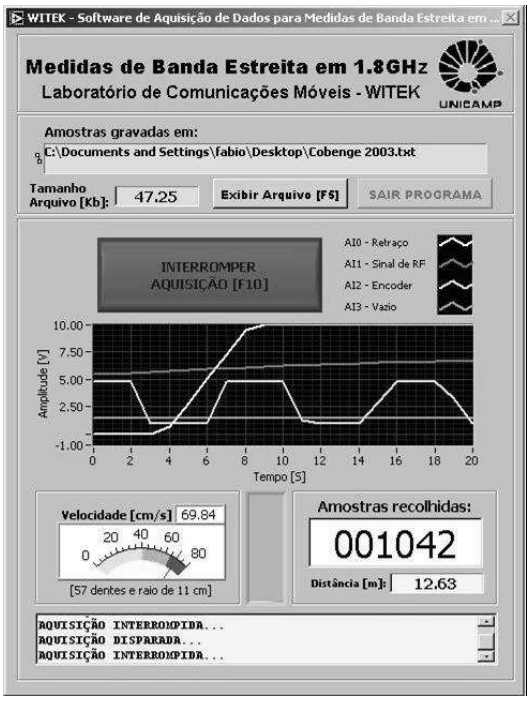

Fig. 3. Software/User Interface.

C. Buildings and Data

The into and within building measurements have been carried out at UNICAMP campus. The distance of the buildings from the transmitter varied from some meters to several hundreds of meters. The buildings presented similar constructive and architectural characteristics presenting one to three floors. Figure 4 illustrates the type of building used. For each data file at least 10.000 samples were collected. In particular, for the sports gymnasium of (Figure 5) 10 files of 100.000 samples each were collected. The validation of the measurements were made *in loco*, as provided

Fig. 4. FEC Building of classrooms.

Fig. 5. FEF Sports Gymnasium.

by the data acquisition equipment. In case, the data were found inappropriate, a new set of measurements was carried out. By the end of the experiment, the into building measurements generated a data bank of 307 MBytes whereas the within building measurements generated 153 files and a data bank of 108 MBytes.

III. The $\kappa - \mu$ Distribution and the $\eta - \mu$ Distribution

A brief description of the $\kappa - \mu$ Distribution and the $\eta - \mu$ Distribution is carried out in this section. For a fading signal with envelope r and normalized envelope $\rho = r/\hat{r}$, $\hat{r} = \sqrt{E(r^2)}$ being the rms value of r, the $\kappa - \mu$ probability density function $p(\rho)$ is written as

$$p(\rho) = \frac{2\mu(1+\kappa)^{\frac{\mu+1}{2}}}{\kappa^{\frac{\mu-1}{2}} exp(\mu\kappa)} p^{\mu} exp(-\mu(1+\kappa)\rho^2) \times I_{\mu-1}(2\mu\sqrt{\kappa(1+\kappa)}\rho)$$

where $\kappa \geq 0$ is the ratio between the total power of the dominant components and the total power of the scattered waves, $\mu \geq 0$ is given by $\mu = \frac{E^2(r^2)}{Var(r^2)} \times \frac{1+2\kappa}{(1+\kappa)^2}$ (or equivalently, $\mu = \frac{1}{Var(\rho^2)} \times \frac{1+2\kappa}{(1+\kappa)^2}$), and $I_v(.)$ is the modified Bessel function of the first kind and arbitrary order ν (ν real).

For a fading signal with envelope r and normalized envelope $\rho = r/\hat{r}$, $\hat{r} = \sqrt{E(r^2)}$ being the rms value of r, the $\eta - \mu$ probability density function $p(\rho)$ is written as

$$p(\rho) = \frac{4\sqrt{\pi}\mu^{\mu+\frac{1}{2}} h^{\mu}}{\Gamma(\mu) H^{\mu-\frac{1}{2}}} \rho^{2\mu} exp(-2\mu h\rho^2) \times I_{\mu-\frac{1}{2}}(2\mu H\rho^2)$$

where $h = \frac{2+\eta^{-1}+\eta}{4}$, $H = \frac{\eta^{-1}-\eta}{4}$, $\mu = \frac{E^2(r^2)}{Var(r^2)} \times \frac{1+\eta^2}{(1+\eta)^2}$ (or equivalently, $\mu = \frac{1}{Var(\rho^2)} \times \frac{1+\eta^2}{(1+\eta)^2}$), $\Gamma(.)$ is the Gamma function, $I_\nu(.)$ is the modified Bessel function of the first kind and arbitrary order ν (ν real), $\mu \geq 0$ and $0 \leq \eta \leq 1$.

The Nakagami-m Distribution is included in both distributions and it defines a "border" between the two distributions in the fading plane. Generally speaking, Nakagami-m can be thought of as a mean distribution with respect to the $\kappa - \mu$ Distribution and the $\eta - \mu$ Distribution (see Fig. 6). Because these distributions are more flexible than the other fading distributions they yield better fitting to experimental data.

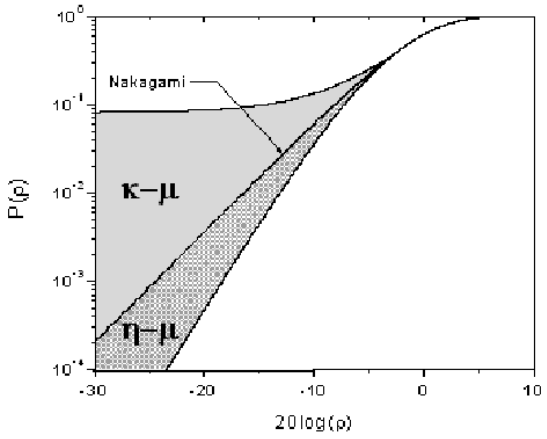

Fig. 6. Nakagami-m, $\eta - \mu$ and $\kappa - \mu$ Distributions.

IV. Results

To illustrate some of the results, two cases are presented. The first case concerns data acquired in a classroom located on the first floor of the School of Mechanical Engineering. The $\eta - \mu$ Distribution is used to adjust the data with $\eta = 0.003$ and $\mu = 0.994$, as shown in Figure 7. It can be the $\eta - \mu$ Distribution makes a better adjustment of the data than the Rayleigh, Rice, and Nakagami distributions. The second case concerns data collected in a corridor located on the first floor of the School of Chemical Engineering. The $\kappa - \mu$ Distribution is used to adjust the data with $\kappa = 0.5$ and $\mu = 1.102$ (Figure 8). It can be observed that the $\kappa - \mu$ Distribution adjusts the data very well. As a rule of thumb, if the data are below the Nakagami-m curve, then the $\eta - \mu$ Distribution can be used. If the data are above, then the $\kappa - u$ Distribution can be used. In practice, it has been observed that it is always possible to adjust the data by either the $\kappa - u$ Distribution or by the $\eta - \mu$ Distribution.

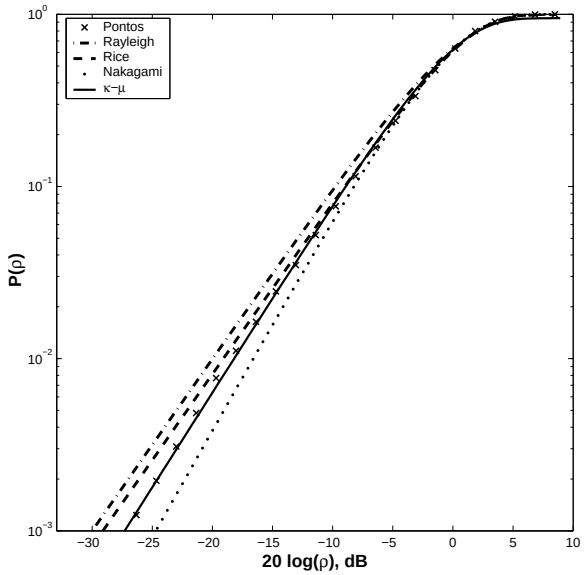

Fig. 7. $\kappa - \mu$ Distribution adjustment.

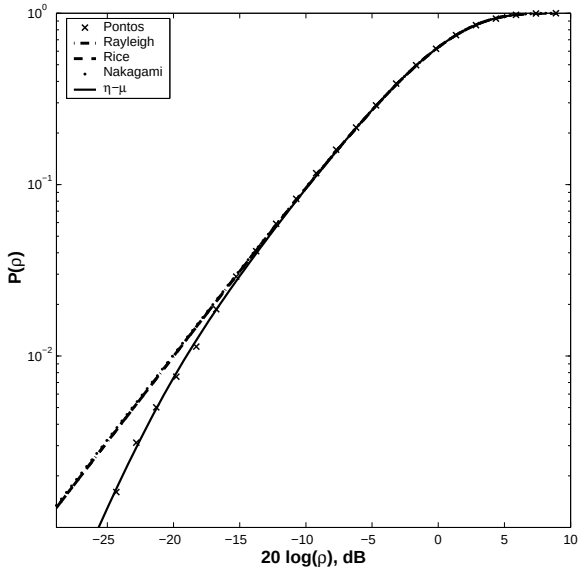

Fig. 8. $\eta - \mu$ Distribution adjustment.

V. Final Comments

Into and within building measurement campaigns have been carried out at UNICAMP campus to validate two new probability distributions, namely $\kappa - \mu$ Distribution and $\eta - \mu$ Distribution. The experiments have been carried out at 1.8 GHz and has been observed that these distribution always fit the data adequately.

References

[1] J. D. “Parsons, The Mobile Radio Channel,” 2nd Edition, John Wiley & Sons, Chichester, 1, 2000.

[2] S. Stein, “Fading Channel Issues in System Engineering,” IEEE J. Selected Areas in Commun., vol. 5, no. 2 , pp. 68-89, Feb. 1987.

[3] W. R. Braun and U. Dersch, “A physical mobile radio channel model,” IEEE Trans. Veh. Technol. vol. 40, no. 2, pp. 472-482, May 1991.

[4] M. D. Yacoub, “The $\eta - \mu$ Distribution: A general fading Distribution”, IEEE Vehicular Technology Conference - Fall 2000, Boston, 2000.

[5] M. D. Yacoub, “The $\kappa - \mu$ Distribution: A general fading Distribution”, IEEE Vehicular Technology Conference - Fall 2001, Atlantic City, 2001.

On Fractional Fourier Transforms for Fading Mitigation in High Mobility Wireless Environments

Carlos A. R. Behaine, Claudio J. Bordin Jr. and Luiz A. Baccalá
Escola Politécnica - Universidade de São Paulo
Av. Prof. Luciano Gualberto, trav. 3, 158
CEP 05508-900 - São Paulo - Brazil
{behaine,bordin,baccala}@lcs.poli.usp.br

***Abstract*— In this work we evaluate the performance of a generalized OFDM communication system that employs fractional Fourier transforms in lieu of the usual Fourier transform. We verify through numerical simulations that the fractional Fourier transforms provide a more efficient set of modulation/demodulation bases that can improve the multicarrier system performance under certain time-frequency selective channel scenarios.**

***Index Terms*— OFDM, fractional Fourier transform, fast fading.**

I. Introduction

Traditional multicarrier-based modulation techniques like OFDM offer advantages as efficient spectral use and robustness to multipath propagation channels, properties that follow directly from the fact that the circular convolution operation, resulting from the transmission of cyclic prefixed signals through time-invariant linear channels, is mapped onto a multiplication by the discrete Fourier transform (DFT), thereby eliminating intersymbol interference (ISI). Under high mobility conditions, however, rapid channel variations violate this principle leading in general to unacceptable performance.

In this work, we evaluate the performance of OFDM-like communication systems that employ fractional Fourier transforms [1] - generalizations of the usual Fourier transform suitable for the treatment of nonstationary signals - under high mobility scenarios, i.e., scenarios in which the Doppler spread is of the same order of the symbol transmission rate. We extend the work presented in [2] by considering the use of the discrete Fourier fractional transform [3] as well as a new equalization criterion.

This paper is organized as follows: Sections II and III review the continuous and discrete time fractional Fourier transforms that are used in Sec. IV to construct a generalized OFDM system, whose performance we assess via numerical simulations in Sec. V.

II. The Fractional Fourier Transform

The $a-$order fractional Fourier transform (FRFT) $F^a_{[f]}(\omega)$ of the continuous-time signal $f(t)$ was defined in [1] as:

$$F^a_{[f]}(\omega) \triangleq \int_{-\infty}^{+\infty} B^a(\omega,t)\, f(t)\, dt \quad (1)$$

$$B^a(\omega,t) \triangleq A_\phi e^{\left[j\pi\left(\omega^2\cot\phi - 2\omega t\csc\phi + t^2\cot\phi\right)\right]} \quad (2)$$

$$A_\phi \triangleq \frac{e^{(-j\pi\,\mathrm{sgn}(\sin\phi)/4 + j\phi/2)}}{|\sin\phi|^{1/2}} \quad (3)$$

where $\phi \triangleq a\pi/2$, j is the imaginary unit, and $0 < |a| < 2$.

Note that when $a = 0$ the fractional Fourier transform reduces to the identity operator, and that when $a = \pm 1$ it is equivalent to the usual Fourier (anti)transform. As pointed out in [1], the definition of the FRFT can be extended for $|a| > 2$, by noticing that $F^{4k}_{[f]}(\omega) = F^0_{[f]}(\omega)$, for all integers k, and that the transform is index additive.

The evaluation of the integral in (1) is in general a difficult task, requiring the use of sophisticated numerical methods to cope with the transform kernel rapid oscillations. In this work, we consider the approximated method for evaluating (1) derived in [1], which assumes that the Wigner distribution of the energy of $f(t)$ is zero outside a circle of radius Δ. Under this assumption, the vector $\mathbf{F}^a_c$ that collects N samples of $F^a_{[f]}(\omega)$ can be obtained as

$$\mathbf{F}^a_c \approx \mathbf{D}\mathbf{K}_a\mathbf{J}\mathbf{f}_c \triangleq \mathbf{F}^a\mathbf{f}_c, \quad (4)$$

where $[\mathbf{F}^a_c]_m = F^a_{[f]}(m/\Delta)$, $\mathbf{f}_c$ is a vector whose entries are defined as $[\mathbf{f}_c]_n \triangleq f(n/\Delta)$, for $n, m \leq |N|$, $\mathbf{J}$ and $\mathbf{D}$ are respectively interpolation and decimation by 2 matrices [1], and

$$\mathbf{K}_a = \frac{A_\phi}{2\Delta} e^{j\pi\left(\alpha(m/2\Delta)^2 - 2\beta\left(mn/(2\Delta)^2\right) + \alpha(n/2\Delta)^2\right)} \quad (5)$$

with $\alpha = \cot\phi$ and $\beta = \csc\phi$.

It was shown in [1] that (4) can be evaluated in $\mathcal{O}(N\log N)$ operations, the same order of complexity of the fast Fourier transform (FFT). The resulting approximate transformation matrix $\mathbf{F}^a$, however, is not unitary and precludes perfect reconstruction.

III. The Discrete Fractional Fourier Transform

The definition of a discrete version of the fractional Fourier transform (DFRFT) consistent with the continuous transform challenged researchers for a long time. As remarked in [3], such transform would have to satisfy the following properties:

1) unitarity;
2) index additivity;
3) reduction to the DFT when the order $a = 1$;
4) approximation of the continuous FRFT.

After some algebra, it is easy to see that the matrix transform $\mathbf{F}^a_{[\mathbf{f}]} = \mathbf{F}^a\mathbf{f}$, where $\mathbf{F}$ is the DFT matrix, satisfy these properties. Unfortunately, this definition is ambiguous because the eigenvector set of $\mathbf{F}$ is not unique, problem which was solved in [3] by defining $\mathbf{F}^a$ as:

$$[\mathbf{F}^a]_{m,n} \triangleq \sum_{k=0}^{N-1} u_k[m] e^{-j\frac{\pi}{2}ka} u_k[n] \ , \qquad (6)$$

where u_k is a set of discrete Hermite-Gaussian functions, that can be evaluated by the algorithm described in [3], p. 1334.

Differently from the FRFT, the evaluation of the DFRFT involves multiplication by an unstructured matrix, requiring thus $\mathcal{O}(N^2)$ operations.

IV. The Generalized OFDM System

Let t_k denote the symbols to be transmitted by the proposed OFDM system. The transmitted signal Z_k is generated by applying the fractional Fourier anti-transform (either FRFT or DFRFT) on each block of B symbols $\mathbf{t}_n \triangleq [\ t_{(n-1)B+1}\ \ldots\ t_{nB}\ ]^T$ as

$$\mathbf{T}_n \triangleq \mathbf{F}^{-a}\mathbf{t}_n \ , \qquad (7)$$

and appending a $P-$length cyclic prefix according to

$$\begin{aligned}\mathbf{Z}_n &\triangleq [\ Z_{(n-1)(P+B)+1}\ \ldots\ Z_{n(P+B)}\ ]^T \\ &\triangleq [\ T_{nB-P+1}\ \ldots\ T_{nB}\ T_{(n-1)B+1}\ \ldots\ T_{nB}\ ]^T \ . \end{aligned} \qquad (8)$$

We assume that the received signal Y_k is related to Z_k by

$$Y_k = \sum_{l=0}^{L} Z_{k-l} h_l^k + V_k \ , \qquad (9)$$

where h_l^k is the transmission channel impulse response at instant k, assumed to be of length $L \leq P$, and V_k is the additive noise, assumed to be of zero mean and variance σ_v^2.

Transmitted symbol estimates $\hat{t}_k$ are then obtained at the receiver by discarding the cyclic prefix and applying proper weighting to the fractional Fourier transform of the remaining samples as

$$\hat{\mathbf{t}}_n^a \triangleq \mathbf{\Lambda}_n^a \mathbf{F}^a \mathbf{Y}_n \ , \qquad (10)$$

where $\mathbf{\Lambda}_n^a$ is a diagonal matrix and

$$\mathbf{Y}_n \triangleq [\ Y_{n(B+P)-B+1}\ \ldots\ Y_{n(B+P)}\ ]^T \ . \qquad (11)$$

The overall structure of the proposed receiver is summarized in Fig. 1. In order to determine the equalizing matrix $\mathbf{\Lambda}_n^a$, first notice that (10) can be rewritten in the absence of additive noise as

$$\hat{\mathbf{t}}_n^a = \mathbf{\Lambda}_n^a \mathbf{W}_n^a \mathbf{t}_n \ , \qquad (12)$$

where

$$\mathbf{W}_n^a \triangleq \mathbf{F}^a \mathbf{H}_{n(P+B)} \mathbf{F}^{-a} \ . \qquad (13)$$

and $\mathbf{H}_k$ is defined as

$$\mathbf{H}_k = \begin{bmatrix} h_0^{k-P+1} & h_1^{k-P+1} & \ldots & h_{L-1}^{k-P+1} \\ h_1^{k-P+2} & h_2^{k-P+2} & \ldots & h_0^{k-P+2} \\ \vdots & \vdots & & \vdots \\ h_{L-1}^k & h_0^k & \ldots & h_{L-2}^k \end{bmatrix} . \qquad (14)$$

It can be shown that if the channel impulse response is time-invariant, $\mathbf{H}_{n(P+B)}$ will be a circulant Toeplitz matrix, and therefore will be diagonalized by the ordinary Fourier transform. However, if the channel impulse response is rapidly time-varying, the Toeplitz structure of $\mathbf{H}_{n(P+B)}$ is destroyed and consequently $\mathbf{W}_n^a$ will have no structure in general. Thus, in order to make the multiplicative equalizer $\mathbf{\Lambda}_n^a$ effective, the block transform index $\hat{a}_n$ must be chosen so that $\mathbf{W}_n^a$ is as diagonal as possible, i.e.

$$\hat{a}_n = \arg\min_a \frac{\mathrm{tr}\left\{\mathbf{W}_a^n (\mathbf{W}_a^n)^H\right\}}{\mathrm{tr}\left\{\mathbf{W}_a^n \odot (\mathbf{W}_a^n)^*\right\}} \qquad (15)$$

where $\odot$ denotes the Hadamard (pointwise) matrix product.

Once the optimal transform index is determined, the optimal equalizer that minimizes the mean square estimation error can be obtained as

$$[\mathbf{\Lambda}_n]_k = \frac{\sigma_t^2 [\mathbf{W}_n^{\hat{a}_n}]_{k,k}^*}{\sigma_v^2 + \sigma_t^2 \sum_{k=1}^{B} \left|[\mathbf{W}_n^{\hat{a}_n}]_{k,k}\right|^2} \ . \qquad (16)$$

where σ_t^2 is the variance of the transmitted symbol sequence.

V. Numerical Simulations

In order to evaluate performance of the proposed algorithms, we performed Monte Carlo simulations in which we measured the resulting bit error rate (BER) as function of the signal-to-noise ratio (SNR) over 100 independent realizations, in each of which 100 (binary) symbol blocks were transmitted.

In Fig. 2 we show the results obtained for the algorithm described in Sec. IV employing the usual (FFT) and the fractional (FRFT and DFRFT) Fourier transforms. In the upper graph, we show the performance obtained for a static channel with $L = 2$ taps[1], using $B = 4$ and $P = 1$. As one may notice, the FFT and DFRFT-based algorithms exhibited, as expected, the same performance. The FRFT-based algorithm, on the other hand, performed poorly, mainly due to the fact that the algorithm described in Sec. II for the evaluation of the transform is not equivalent to the DFT when $a = 1$.

In the bottom graph of Fig. 2 we repeat the experiment for a time-varying channel ($L = 2$), in which

[1]Each channel tap was obtained as a draw from a circular gaussian random variable with zero mean and unitary variance.

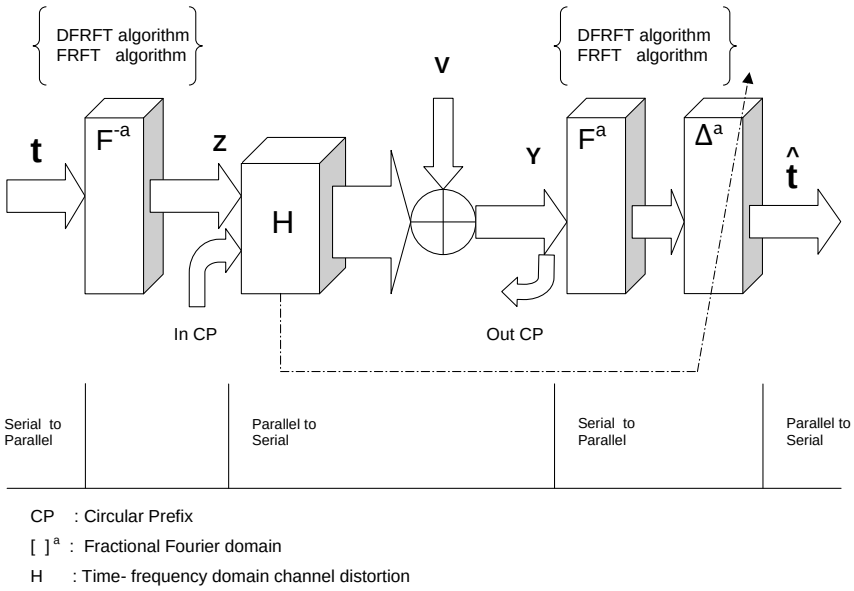

Fig. 1. Block diagram of the proposed FRFT - DFRFT based multicarrier system

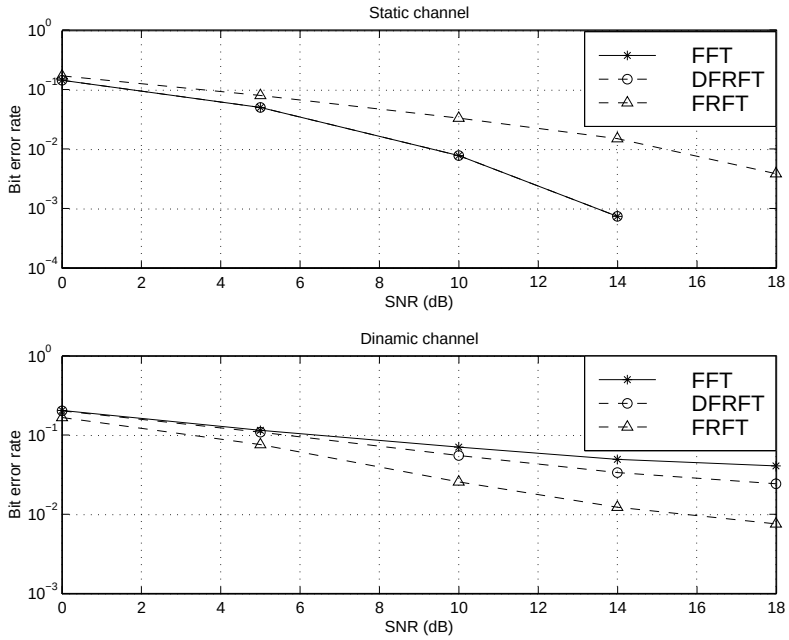

Fig. 2. Mean performance of the generalized OFDM system as a function of the signal-to-noise ratio (SNR) employing the FRFT, DFRFT and the usual Fourier transform (FFT), for static channels (top) and time-varying channels (bottom).

each channel tap h_k^l was modeled as a first order autoregressive complex gaussian process of zero mean, unit variance and $3-$dB bandwidth (Doppler spread) equal to 9.2% of the sample rate. In this situation, the FRFT performs best, confirming the results presented in [2]. The DFRFT-based algorithm, on the other hand, performed only slightly better than the DFT-based algorithm, an unexpected result that deserves further research.

VI. Conclusion

In this work we evaluated the performance of a generalized OFDM communication system employing the fractional Fourier transform. Numerical simulations showed that the use of the fractional Fourier transform does not enhance the OFDM system's BER performance if the communication channel impulse response is static. On the other hand, if the channel impulse response is rapidly time-varying, it is in general possible to find transform indexes $a \neq 1$ that minimize the measured square estimation error on a block-by-block basis.

References

[1] M. Alper Kutay, H. M. Ozaktas, O. Arikan e G. Bozdagi,"Digital computation of the fractional fourier transform",*IEEE Transactions on Signal Processing*, vol. 44, no. 6, pp. 2141-2150. September 1996.

[2] M. Martone,"A multicarrier system based on the fractional Fourier Transform for time-frequency-selective channels",*IEEE transactions on communications*, vol. 49, no. 6, pp. 1011-1020. June 2001.

[3] M. Alper Kutay, H. M. Ozaktas, O. Arikan e . Candan,"The discrete fractional fourier transform",*IEEE Transactions on Signal Processing*, vol. 48, no. 5, pp. 1329-1337. May 2000.

Path-loss determination model at urban environments in the VHF and UHF bands

Anderson Escudero
National Institute of Telecommunications - Inatel
P.O. Box 05 - 37540-000
Santa Rita do Sapucaí - MG - Brazil
aescudero@inatel.br

José Antonio Justino Ribeiro
National Institute of Telecommunications - Inatel
P.O. Box 05 - 37540-000
Santa Rita do Sapucaí - MG - Brazil
justino@inatel.br

***Abstract*—This article presents a theoretical model to estimate the average path loss of electromagnetic waves propagation in urban environments. It was assumed fixed communications systems at VHF and UHF bands. The method is an extension of the model developed by Chung, Walfisch and Bertoni and is useful for frequencies from 30MHz to 3GHz. The obstacles, in this case the building, are replaced by screens with appropriated electromagnetic characteristics. The propagation must occur above and through these structures and the field crossing each screen is obtained with the aid of physical optics approaches. The reflections in the ground are included and it was assumed that the signal propagates from a transmission antenna, installed in raised heights, to a reception one, installed in the average buildings heights, to get the waves incidence angle in the reception point. The description of the building heights variation is gotten with the uniform probability distribution. From the random signal obtained through simulations at several frequencies and building distances, the average field strength and the path loss are acquired. The computer simulations are carried out in MATLAB® platform and the results are in agreement with prediction models and field strength measurements data published.**

***Index Terms*—Large-scale attenuation, urban path-loss model.**

I. INTRODUCTION

The radio wave propagation at urban environments is an important information for modern wireless communications systems design [1]. The transmitter antennas are usually installed in high places and the receivers are fixed or moving among the buildings or inside them. The systems implementation requires accuracy of propagation prediction at VHF and UHF bands, because the growth of the mobile cellular communications systems [2]. Usually, the messages in urban environments travel through different media, the spaces among buildings or inside them, and it results especially critical problems for modern digital communications systems involved [3].

The theoretical model path-loss prediction at urban areas shown is applicable to frequency between 30MHz to 3GHz. The original model was proposed by Chung and Bertoni [1] and is a generalization of approach used to predict loss for shade areas in cellular systems [2]. It assumes that the constructions are organized in lines together the streets. There is high attenuation in signals crossing the individual constructions at high frequencies and the propagation between the constructions occurs with multiple diffractions. In order to calculate the attenuation and phase-shift associated with the penetration through the constructions, consistent with the optic physics (PO) approach, each row of constructions is replaced by a screen that cause an equivalent attenuation and phase displacement. The resulting propagation in several rows of constructions is then simulated by repeated numerical evaluations of the physical optic integral over the area of each screen and the plan above it. The Green function for integral is chosen to include the reflection of the ground.

The integral can be executed in two dimensions, by considering the building heights and gaps variations along a row. Such kind of integration would consume to much time to allow its application for more than few rows. For that, the constructions along the row are assumed to be continuous and of uniform height. Assuming the rows to be parallel, the integration in one dimension can be obtained analytically. It is then practical to execute the repeated integration in the other dimension using numerical methods.

We calculate the physical optic integral for an incident plane wave at an angle θ_{in} referenced to the horizontal plane. After the propagation through enough screens, the results give the final reduction due to diffraction by the rows of constructions. To take in account the ground effect, it must be obtained the field reflection coefficient Γ_g, according the plane wave polarization.

II. OBSTACLE MODELING

In general, the urban constructions are organized in rows nearly parallel, as in Fig. 1. The propagation between a transmitting and a reception antenna, installed on the top of a tower, building or in a mobile telephone, can be analyzed with this modeling. The wave propagates through and above different obstacles and the effects concerning the power losses and phase displacement must be computed.

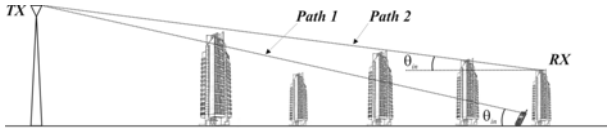

Fig. 1. Side view of radio wave propagation between a transmitter and a receiver antenna, in an urban environment.

The procedure follows Fig. 2 representation, where part (a) represents the building with its internal and external walls. The integral structure can be compressed to a simple equivalent layer, as shown in Fig. 2 (b), with W_e equivalent layer thickness, according the model by Chung and Bertoni [1]. If T represents the module of the transmission coefficient of the signal that crosses obstacle and $\Delta\Phi$ the corresponding phase shift, it is possible to substitute the layer for a screen of null thickness, as in Fig. 2(c), with the same transference characteristics. The normal plane to the boundary between the obstacle and the external medium, that contains the incidence wave direction, is the incidence plane and will be the reference to define the incident wave polarization.

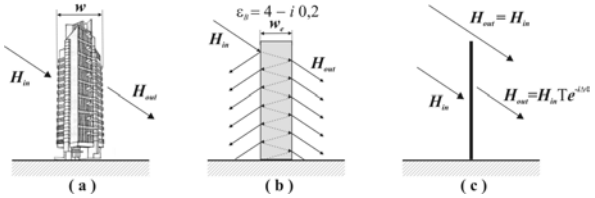

Fig. 2. Building modeling for attenuation and phase shift calculations on an electromagnetic field.

With the electric field parallel to the incidence plane, the magnetic field will be normal, indicating a transversal magnetic wave (TM). For this polarization, it is easier to determine its transference coefficient by relating the amplitudes of incident, reflected and refracted magnetic field components, by applying the magnetic field boundary conditions on the separation surface. At the other side of the equivalent obstacle screen the amplitude of that field is:

$$H_{out} = H_{in}\, \mathrm{T}\, e^{-i\,\Delta\Phi} \tag{1}$$

where H_{in} is the amplitude of the incident wave. From this, it is possible to calculate the resultant field and repeat it for successive screens. In this way, the propagation factor for a specified path is gotten.

It will be obtained T and $\Delta\Phi$ from the absolute value and argument of following equation [4]

$$\mathrm{T} = \frac{\tau_{12}\tau_{23}e^{i\delta/2}}{1+\Gamma_{12}\Gamma_{23}e^{i\delta}} \tag{2}$$

where Γ_{ij} and τ_{ij} are the reflection and transmission coefficient between the i and j media. The δ factor at angular frequency $\omega = 2\pi f$ is obtained through

$$\delta = 2W_e \frac{\omega}{c}\sqrt{\varepsilon_r - i\frac{\sigma}{\omega\varepsilon_0}}\cos\theta_t \tag{3}$$

with c the electromagnetic wave propagation velocity in the medium (3×10^8 m/s for the air). The term ε_r is the real part of the complex dielectric constant (ε_B) and σ is the conductivity of the obstacle material.

III. Propagation Through Obstacle Sequence

A. Numerical analysis

To evaluate the field at the reception antenna, the constructions rows are replaced by sequences of screens with attenuation and phase shift, as described in last section, having random heights and uniform separations d. It was assumed the screens heights are uniformly distributed between the limits h_{max} and h_{min}, with average value h_{avg}.

The physical optics approach is used, a consistent method for the attenuation and phase shift of the electromagnetic wave propagation through obstacles. For a $n^{th.}$ screen known output field, the incident field in the plan of $(n+1)^{th}$ screen can be obtained through the integration that includes the ground reflection as in Fig. 3. The physical optics procedure allows calculate the field by using the equivalent magnetic current model on the aperture of n^{th} plan, as proposed by Xia and Bertoni [5], [6]. It was assumed a plane and uniform wave incidence, with variations only in the resultant propagation direction. With the inclusion of the ground reflection, is obtained a general expression [1]. The incident field in $(n+1)^{th}$, with no variation in the parallel direction to screen, is

$$H_{in}(y_{n+1}) = \frac{e^{j\pi/4}}{\sqrt{\lambda}}\int_0^{\infty} H_{out}(y_n)\left[\frac{e^{-jkR_1}}{\sqrt{R_1}} + \Gamma_g(\theta)\frac{e^{-jkR_2}}{\sqrt{R_2}}\right]dy_n \tag{4}$$

where y_n show the height variation in the plane of n^{th} screen and y_{n+1} is the value in the plane of $(n+1)^{th}$ screen [6]. The factor λ is the wavelength in the free space and $k = 2\pi/\lambda$ is the phase factor. The path distance between two consecutive screens is calculated by

$$R_1 = \sqrt{d^2 + (y_{n+1} - y_n)^2} \quad \text{(a)}$$
$$R_2 = \sqrt{d^2 + (y_{n+1} + y_n)^2} \quad \text{(b)} \tag{5}$$

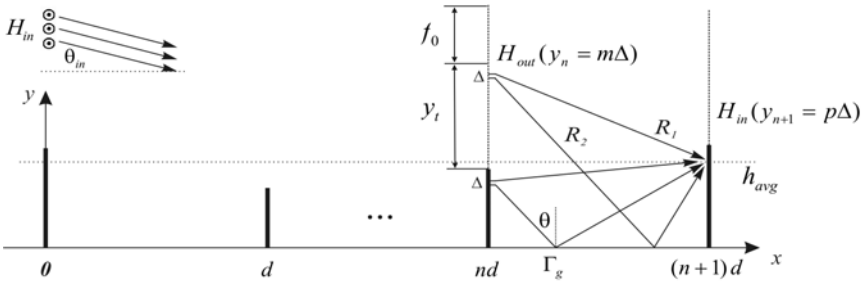

Fig. 3. Incident field in the $(n+1)^{th}$ screen is gotten by numerical integration of the transmitted field that through the n^{th} screen.

In (4) $\Gamma_g(\theta)$ is the ground reflection coefficient for TM polarization, for an angle of incidence in relation to the normal, calculated by

$$\theta = cos^{-1}\left[\left(y_{n+1} + y_n\right) / R_2\right] \tag{6}$$

whose value depends on the local ground properties. Equation (4) represents screen field recursive relationship, beginning with incident wave in first one.

The integration in (4) requires a finite upper limit. To execute it by using numerical techniques, it will be converted to a discrete summation. The region that offers the main field contribution at far way point is identified from Fresnel first zone radius. Spurious contributions, resulted of a finite value of integration limit, can be prevented with multiplying the integrand equation by a window function that softly reduces the integral to zero for great values of y_n. The discretization process is made by linear interpolation of amplitude and phase over intervals Δ, which must be less than half wavelength (λ/2). The integration will be made of continuous form between $m\Delta$ and $(m+1)\Delta$, with superposition of partial results. The final expression is

$$H_{in}(y_{n+1}) = \frac{e^{j\pi/4}}{\sqrt{\lambda}} \sum_{m=0}^{\infty} \int_{m\Delta}^{(m+1)\Delta} \left[A_1(y_n) e^{-j\phi_1(y_n)} + \Gamma(\theta) A_2(y_n) e^{-j\phi_2(y_n)}\right] dy_n \tag{7}$$

with the following factors

$$A_1(y_n) = \frac{H_{out}(y_n)}{\sqrt{R_1}} W(y_n) \quad \text{(a)}$$

$$A_2(y_n) = \frac{H_{out}(y_n)}{\sqrt{R_2}} W(y_n) \quad \text{(b)} \tag{8}$$

$$\phi_1(y_n) = kR_1 \quad \text{(a)}$$

$$\phi_2(y_n) = kR_2. \quad \text{(b)} \tag{9}$$

and the Kaiser-Bessel window function $W(y_n)$ [7]. Assuming linear variation of the amplitude and phase in a interval $m\Delta < y_n < (m+1)\Delta$, Eq. (7) can be rewrite as

$$H_{in}(y_{n+1}) = \frac{e^{j\pi/4}}{\sqrt{\lambda}} \sum_{m=0}^{\infty} \int_{m\Delta}^{(m+1)\Delta} \left\{ \left[A_{1,m} + \left(A_{1,m+1} - A_{1,m}\right)\left(\frac{y - m\Delta}{\Delta}\right)\right] exp\left\{-j\left[\phi_{1,m} + \left(\phi_{1,m+1} - \phi_{1,m}\right)\left(\frac{y - m\Delta}{\Delta}\right)\right]\right\} + \Gamma_g(\theta)\left[A_{2,m} + \left(A_{2,m+1} - A_{2,m}\right)\left(\frac{y - m\Delta}{\Delta}\right)\right] exp\left\{-j\left[\phi_{2,m} + \left(\phi_{2,m+1} - \phi_{2,m}\right)\left(\frac{y - m\Delta}{\Delta}\right)\right]\right\}\right\} dy \tag{10}$$

Solving the integration and define a finite upper limit to the sum [8], we have

$$H(y_{n+1} = p\Delta) = \frac{e^{j\pi/4}}{\sqrt{\lambda}} \Delta \sum_{m=0}^{M} \left\{ j \frac{A_1[(m+1)\Delta] exp\{-j\phi_1[(m+1)\Delta]\} - A_1(m\Delta) exp[-j\phi_1(m\Delta)]}{k\left(R_{1,m+1,p} - R_{1,m,p}\right)} + \frac{A_1[(m+1)\Delta] - A_1(m\Delta)}{k^2\left(R_{1,m+1,p} - R_{1,m,p}\right)^2} \{exp\{-j\phi_1[(m+1)\Delta]\} - exp[-j\Phi_1(m\Delta)]\} + j\Gamma_g(\theta_m) \frac{A_2[(m+1)\Delta] exp\{-j\phi_2[(m+1)\Delta]\} - A_2(m\Delta) exp[-j\phi_2(m\Delta)]}{k\left(R_{2,m+1,p} - R_{2,m,p}\right)} + \Gamma_g(\theta_m) \frac{A_2[(m+1)\Delta] - A_2(m\Delta)}{k^2\left(R_{2,m+1,p} - R_{2,m,p}\right)^2} \{exp\{-j\phi_2[(m+1)\Delta]\} - exp[-j\Phi_2(m\Delta)]\} \right\} \tag{11}$$

where $M = \left(h_{avg} + y_t + f_0\right)/\Delta$ with $y_t = 3\sqrt{\lambda N d}$ and $f_o = 15\sqrt{\lambda d}$. General Eq.(11) was used to developing a routine on Matlab® platform and the results are in Fig. 4. The obstacle heights were random distributed between 6 and 14 meters, and neighbors centers separation is 50 meters. The incidence angle is $\theta_{in} = 1.4°$ and the operation frequency is 100MHz. Fig. 4 shows the magnetic field strength at average height (h_{avg}) of the obstacle, based on an initial magnetic field of unitary amplitude. After a serious initial variation, the field amplitude presents a random fluctuation around an average value H_{avg}. Previous studies show that this initial variation occur until the obstacle $N_o = \lambda/\left(2sin^2\theta_{in} d\right)$ [2].

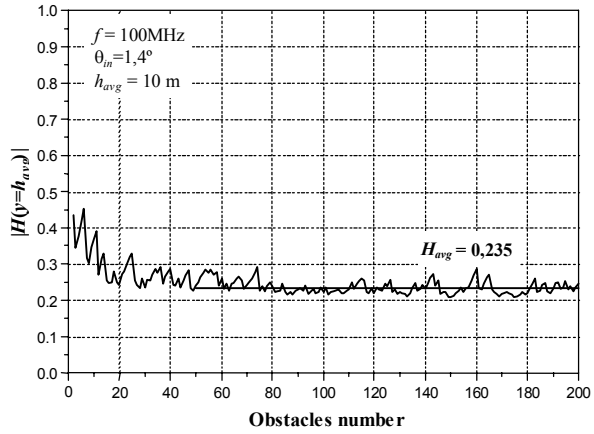

Fig. 4. Module of the relative intensity of the magnetic filed at average high of the obstacles.

Assuming plane wave propagation over the buildings with uniform height in VHF and UHF bands, the dependence of stabilized field with value H_{avg}, the frequency (f), the incidence angle(θ_{in}) and gaps between obstacles (d) can be represented by a parameter g_p [2], [6]. This parameter is represented by

$$g_p = sin\,\theta_{in} \sqrt{\frac{d}{\lambda}} \tag{12}$$

and the stabilized field will be represented by factor Q. This is a relative value to a unitary field and it defines the link attenuation factor, its value is always lesser than the unit. Computer simulations for different incidence angles and frequencies of 100, 300, 900 and 1800MHz are plotted versus the parameter g_p in Fig. 5. It is shown that the different frequencies points present a curve behavior. By making the polynomial fit of these values it is obtained the expression

$$Q(g_p) = 2.592\,g_p - 2.283\,g_p^2 + 0.607\,g_p^3 \tag{13}$$

This polynomial was plotted together the points to verify its validity. Eq. (13), which can be used to get the attenuation factor for different g_p values, will permit to create the path loss model.

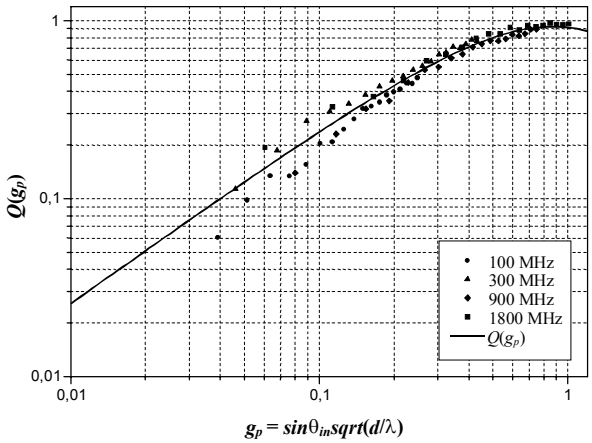

Fig. 5. Resultant curve of the polynomial adjust of the simulations results for frequencies of 100, 300, 900 and 1800MHz.

B. Path-loss equations

To elaborate a prediction model to calculate the average path loss between the transmitter and receiving antennas is necessary to know the influence factors on the signal propagation. At urban areas, the free space loss between antennas, the field attenuation in the top of the constructions $Q(g_p)$ and the effect of diffraction due to the propagation from the rooftop to the ground level are the most relevant factors. The developed model is applied to fixed systems of communications, where the electromagnetic wave propagates from a transmitter antenna to a receiving installed in the rooftop, and for this it will be taken in account just the two first factors.

By assuming isotropic antennas with unity gains, the decibel relationship between received and transmitted powers in the free space is [9]

$$L_0 = 32.44 + 20\log f + 20\log R \qquad (14)$$

For actual situation, it is necessary include factor Q in (14), concerning to urban obstacles attenuation. As the Q factor refers to electromagnetic field loss, its squared value indicates to the corresponding power attenuation. Therefore, Eq. (14) can be rewrite as

$$L = 32.44 + 20\log f + 20\log R - 10\log Q^2 \qquad (15)$$

or, by including the transmitter and receiver antennas gains over isotropic one, it will be obtained the equation to calculate the large scale path loss at urban environments:

$$L = 32.44 + 20\log f + 20\log R - \\ -20\log Q - G_{tx}(dB) - G_{rx}(dB) \qquad (16)$$

IV. Comparison With Measurements

In the previous section, a path loss model in urban environments was developed. To show the method reliability, some comparisons with other criteria will be presented. The first one is the Okumura-Hata method [10],[11], widely used at this environment analysis[12]. The theoretical development will be compared also with other published measurements.

A. Okumura-Hata Model

The Okumura-Hata propagation model is based on field strength measurements curves carried through by Okumura in the region of Tokyo[10], for different ground types and transmission and reception antennas heights. In search to automate the Okumura method, Hata developed empirical equations representing the measurements plots with accuracy. The Okumura-Hata equations are ITU recommendations[13], used to compare with the developed prediction method. The following figures present simulations results to $h_{tx} = 150\,\text{m}$ and equivalent isotropic radiated power (EIRP) of 1kW for distances between 1 to 50km. The calculations are made for frequency of 100, 450, 900 and 1800 MHz. and corrections due different antennas gain are considered.

The developed model presents a good agreement with Okumura-Hata method. The maximum difference is less than 10dB, a standard deviation common value for that kind of method [12].

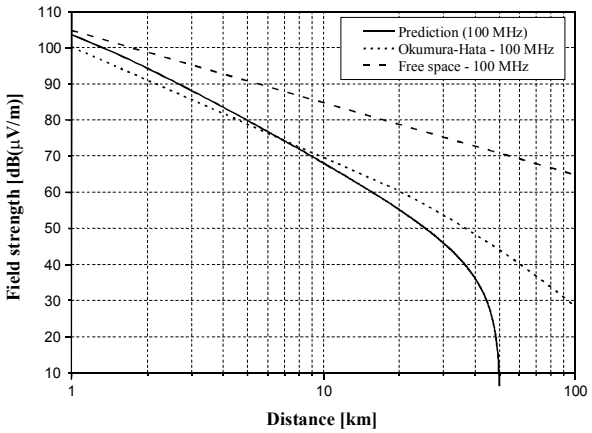

Fig. 6. Comparison between the prediction, the Okumura-Hata model and propagation in free space, for 100MHz.

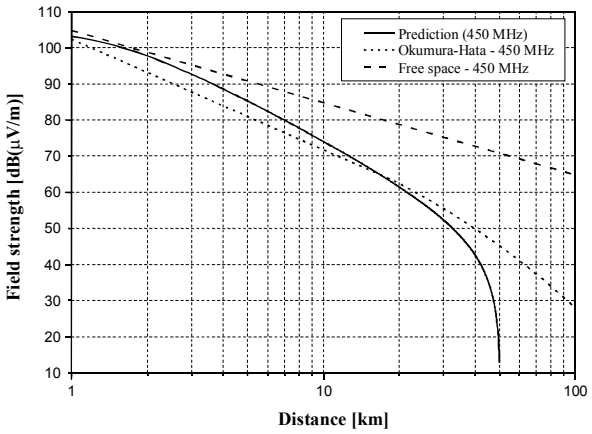

Fig. 7. Comparison between the prediction, the Okumura-Hata model and propagation in free space, for 450MHz.

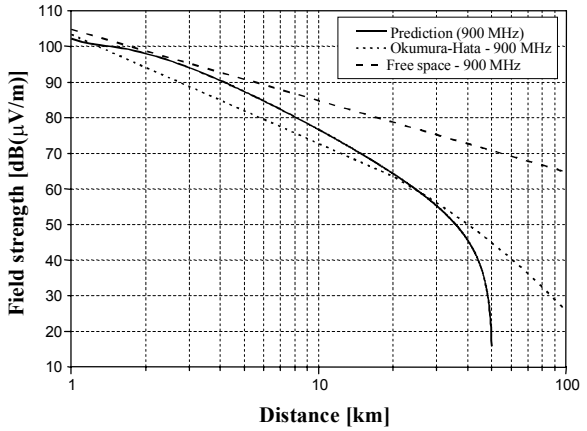

Fig. 8. Comparison between the prediction, the Okumura-Hata model and propagation in free space, for 900MHz.

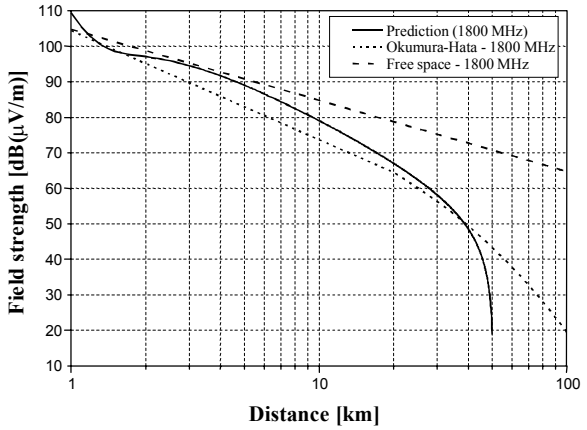

Fig. 9. Comparison between the prediction, the Okumura-Hata model and propagation in free space, for 1800MHz.

B. *Ott e Plitkins Measurements*

Average reception power measurements had been carried out by Ott and Plitkins[14], at Philadelphia city in the United States. The transmissions had been made with a six antennas array, installed between 14 and 78 meters above the ground level. The received signal was by 1.5m mobile antennas height. The measurements had been carried out at 820MHz frequency, with transmission power of 16W (42dBm). In the transmission side it was used a horizontal omnidirectional collinear array with 8.15dBi gain. The reception antenna was vertical antenna of ¾ wavelengths with 3.15dBi gain.

The average height of the constructions in that region is between 9 and 12 meters and distances between its centers are 35 meters, approximately. For the attenuation factor (Q) calculation it was assumed frequency and incidence angle varying with the distance between the transmission and reception points. To generate the graph, Eq. (12), (13) and (16) had been used, considering the effect terrestrial curvature and the transmission and reception antennas gains. An additive precaution reefers to reception antenna height. In present model its height is fixed 10m, however the measures were made at 1.5 meter. The correction was made by using the ITU recommendation[13]. Fig. 10 presents the comparison between the prediction and Ott e Plitkins measurements, the continuous line represents the estimation and the dots refer to published results.

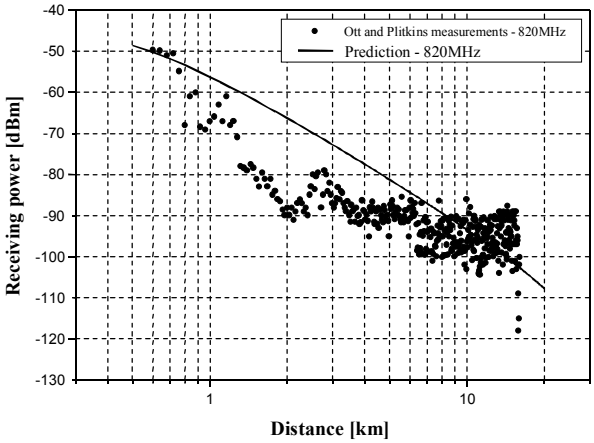

Fig. 10. Comparison between the prediction and measures made at urban area by Ott and Plitkins.

C. *Young Measurements*

Experimental results are carried out by Young [15] at urban region of New York and are presented in terms of the field intensity, for 150MHz and 900MHz frequencies. The transmission antenna was at 150m height and the received signal was through a mobile unit with a 2m antenna height. The transmission power was 1kW in EIRP value. Both in transmission and reception sides were used half-wavelength antennas with 2.15dBi gain. A space around 50 meters between building centers was assumed, a usual urban constructions value. To verify the measurements to developed model matching, due the difference in the reception antenna height, it was used ITU recommendation again [13]. The relative correction is of 14dB for VHF and 18.6dB for UHF bands. With these adjustments, Fig. 11 and 12 give the results for 150MHz and 900MHz frequencies, respectively. Using (12) and (13), the field strength for some distances between transmitter and receiver are shown. The continuous line refers to the model argued in this work and the resultant line of the points union represents measurements by Young. It can be observed the estimated results are come close sufficiently to the measured values, for both frequency values.

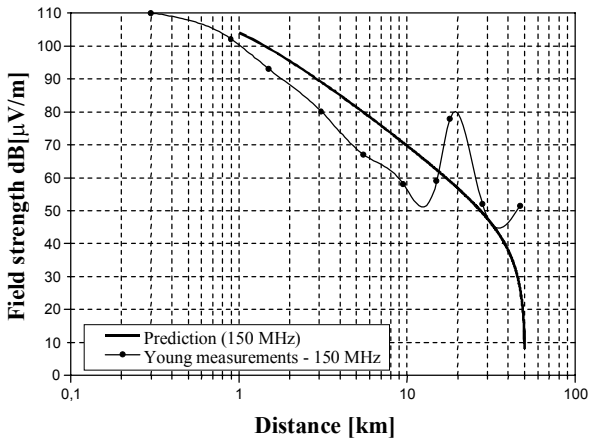

Fig. 11. Comparison between the prediction and measures made at urban area by Young, for 150 MHz.

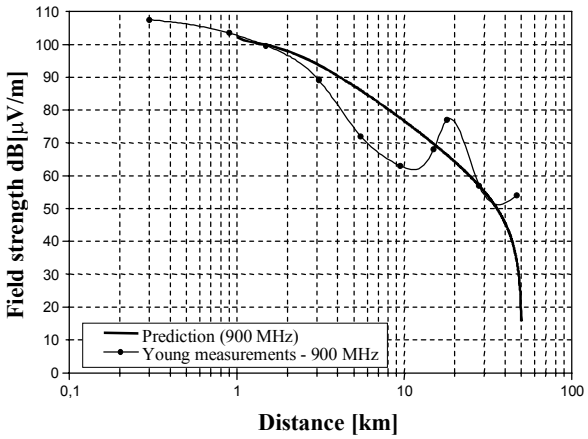

Fig. 12. Comparison between the prediction and measures made at urban area by Young, for 900 MHz.

V. CONCLUSIONS

A theoretical model to calculate the average path loss of electromagnetic waves at urban environments was demonstrated. The model utilizes physical optics approaches to find propagation resultant field through an obstacles sequence. The prediction presents good accuracy at VHF and UHF bands. The results are obtained for frequency, spacing between building and incidence angle variations of analyzed signal. Computer simulations are carried out in MATLAB® platform and it was showed that are in good agreement with other prediction models and field strength measurements data published.

REFERENCES

[1] CHUNG, H. K.; BERTONI, H. L. Range-Dependent Path-Loss Model in Areas for the VHF and UHF Bands. *IEEE Trans. Antennas Propagation*, v. 50, n. 1, p.1-11, Jan. 2002.

[2] WALFISCH, J.; BERTONI, H. L. A Theoretical Model of UHF Propagation in Urban Environments. *IEEE Trans. Antennas Propagation*, v. 36, n. 12, p.1788-1796, Dec. 1998.

[3] RAPPAPORT, T. S. *Wireless Communications – Principles and Practice*. Upper Saddle River: Prentice Hall, 1996.

[4] ESCUDERO, A.; RIBEIRO, J. A. J. Modeling for Calculation of the Propagation Loss of Electromagnetic Waves in Obstacles at Urban Environments, *World Congress on Engineering and Technology Education,* Guarujá / Santos - Brasil, 2004.

[5] COLLIN, R. E. *Field theory of guided waves*, New York: McGraw-Hill, 1960.

[6] XIA, H. H.; BERTONI, H. L. Diffractions of cylindrical an plane waves by and array of absorbing half-screens. *IEEE Trans. Antennas Propagation*, v. 40, n. 2, p. 170-177, Feb., 1992.

[7] PIAZZI, L.; BERTONI, H. L. Effect of Terrain on Path Loss in Urban Environments for Wireless Applications. IEEE Trans. Antennas Propagation, v. 46, n. 8, p.1138-1147, Aug. 1998.

[8] ESCUDERO A. Modelagem para o cálculo da perda no percurso de propagação em áreas residenciais nas faixas de VHF e UHF, M.S. dissertation, Dept. of Telecommunication and Electronic, National Institute of Telecommunications - Inatel, Santa Rita do Sapucaí, Brazil, 2004.

[9] YACOUB, M. D., *Foundations of mobile radio engineering*. Boca Raton: CRC Press, 1993.

[10] OKUMURA, Y. *et al*, Field Strength and Its Variability in VHF and UHF Land-Mobile Radio Service, *Review of the Electrical Communications Laboratory*, vol. 16, n. 9-10, p. 825-873, Sep./Oct. 1968.

[11] HATA, M. Empirical Formula for Propagation Loss in Land Mobile Radio Services, *IEEE Trans. on Veh. Technol.*, vol. VT-29, n.03, p. 317-325, Aug 1980.

[12] RAPPAPORT, T. S. *Wireless Communications – Principles and Practice*. Upper Saddle River: Prentice Hall, 1996.

[13] INTERNATIONAL TELECOMMUNICATIONS UNION. *Prediction methods for the terrestrial land mobile service in the VHF and UHF bands,* ITU-R P.529-3, 1999.

[14] OTT, G. D.; PLITKINS, A. Urban path-loss characteristics at 820MHz, *IEEE Trans. Veh. Technol.*, vol. VT-27, n.04, p.188-197, Nov.1978.

[15] YOUNG, Jr. W. R. Comparison of mobile radio transmission at 150, 450, 900, and 3700 Mc., *Bell Syst. Tech. J.*, vol. 31, no. 6, pp. 1068–1085, Apr. 1952.

Concurrent Blind Decision Feedback Equalizer

Magno T. M. Silva,
Universidade de São Paulo - EPUSP - PTC
Av. Prof. Luciano Gualberto, 158, trav. 3
05508-900 - São Paulo - SP - Brazil
magno@lcs.poli.usp.br

Maria D. Miranda, and Rita Soares
Universidade Presbiteriana Mackenzie - PPGEE
Rua da Consolação, 869
01302-907 - São Paulo - SP - Brazil
mdm@mackenzie.com.br
rita.soares@iqaratelecom.com.br

***Abstract*— Decision Feedback Equalizers (DFEs) play an important role in digital communication systems. They reduce the effect of intersymbol interference, holding a favorable compromise between computational complexity and efficient behavior. When blind adaptation of DFEs is required, algorithms based on the constant modulus criterion may converge to so-called degenerative solutions. Among different algorithms which avoid these undesirable solutions, the one proposed by Szczecinski and Gei is the most efficient. However, in many practical situations, as for example time-variant channels, its good behavior is not always assured. In this paper, it is proposed an improvement of that algorithm based on a concurrent blind deconvolution method. At the cost of a moderate increase in computational complexity, the resulting algorithm presents faster convergence and lower symbol error rate than the previous one. Illustrative simulations considering M-QAM signaling and high definition television (HDTV) channels are presented.**

***Index Terms*— Decision Feedback Equalizer (DFE), Constant Modulus Algorithm (CMA), Concurrent Algorithms.**

I. Introduction

Decision Feedback Equalizers (DFEs) have been widely used to remove intersymbol interference from the data received through communication channels [1]. They present good performance in difficult environments as, for example, channels with long and sparse impulse response, non-minimum phase, spectral nulls or non-linearities [2]. This behavior can be justified by the interpretation of DFEs as fractionally spaced equalizers which, under certain conditions, are able to achieve the zero-forcing solution [3].

In many practical applications, DFEs must be blindly adapted. In this case, algorithms based on the constant modulus criterion [4] for joint updating of the feedforward and feedback filters may converge to so-called degenerative solutions. This occurs when the signal at the equalizer output is independent of its input [3], [2]. To avoid this problem, many authors consider a decoupled adaptation of the feedforward and feedback filters [5]-[8]. Nevertheless, this adaptation form is less efficient than the joint adaptation, mainly if the channel is time-variant [2].

This work was supported by Fapesp (00/12350-6), CNPq, and Mackpesquisa.

In this scenery, Szczecinski and Gei proposed a new criterion for reliable detection of degenerative solutions [2]. This criterion is based on the Godard cost function with constraint on the feedforward and feedback filters and is minimized by a stochastic algorithm called DFE-CMA-FB (DFE Constant Modulus Algorithm with Feedback). It was shown in [2] that this algorithm avoids degenerative solutions, being more efficient than the previous algorithms proposed in the literature, which impose constraint only on the feedforward filter [3].

In the context of blind adaptation of Linear Transversal Equalizers (LTEs), Castro *et al.* [9] proposed to operate a Decision-Direct (DD) algorithm concurrently with CMA (Constant Modulus Algorithm) for M-QAM (M-Quadrature Amplitude Modulation) signaling. At the cost of a moderate increase in computational complexity, CMA+DD presents a great improvement in equalization performance over CMA. After that, inspired by this idea, Chen [10] proposed a modification on this scheme based on a novel soft decision-direct (SDD) adaptation. The CMA+SDD, also called bootstrap maximum *a posteriori* probability (bootstrap MAP) [11], has lower computational complexity and faster convergence rate than CMA+DD. Furthermore, these concurrent algorithms have capability of correcting the phase rotation for M-QAM signaling.

Since concurrent algorithms outperform non-concurrent algorithms for linear equalization, one expects that they can improve the performance of DFEs. Thus, we consider the combination of DFE-CMA-FB with SDD for joint blind adaptation of the feedforward and feedback filters and M-QAM signaling. The algorithm, called NDEG-CMA-SDD (Non-Degenerative Constant Modulus Algorithm with Soft Decision-Direct), beyond avoiding degenerative solutions, should outperform DFE-CMA-FB.

The paper is organized as follows. The blind DFE and Chen's concurrent algorithm are revisited in sections 2 and 3 respectively. The proposed NDEG-CMA-SDD is introduced in Section 4. Thereafter, some simulation results are presented and a conclusion section closes the paper.

II. The blind DFE

A communication system with a typical DFE model is depicted in Figure 1 [12]. The signal $a(n)$, assumed independent, identically distributed, and non Gaussian, is transmitted through an unknown channel whose model is constituted by an FIR (Finite Impulse Response) filter $H(z)$ and additive white Gaussian noise $\eta(n)$. The received signal $u(n)$ is filtered by an FIR feedforward filter $F(z)$ with M_f taps. The past decisions are fed back and filtered by an FIR feedback filter $B(z)$ with M_b taps. Then, a linear combination of the filters' outputs enters to the decision device. The blind DFE must mitigate the channel effects and recover the signal $a(n)$ for some delay τ_d.

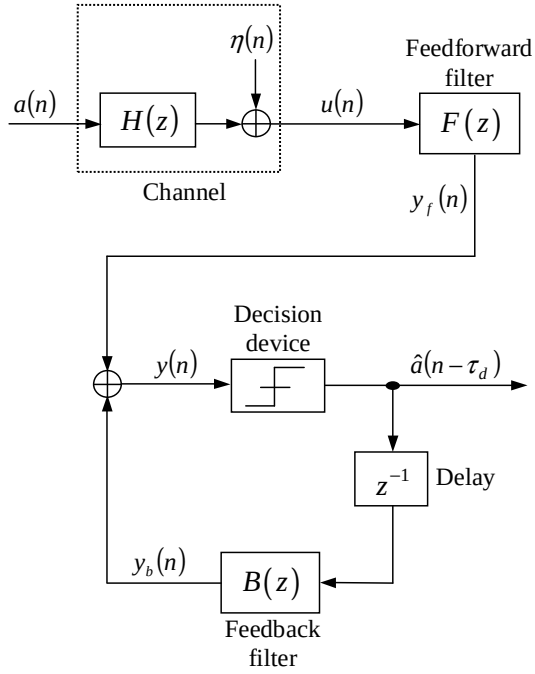

Fig. 1. A typical DFE model.

The summary of DFE-CMA-FB is shown in Table I. Its detailed derivation can be found in [2]. This algorithm avoids degenerative solutions and provides a joint blind adaptation of $F(z)$ and $B(z)$. The following notation and definitions are used: $(\cdot)^T$ and $(\cdot)^H$ stands respectively for transpose and complex-conjugate transpose of a vector and $(\cdot)^*$ for complex-conjugate; $\mathbf{f}$ and $\mathbf{b}$ are the coefficients of the feedforward and feedback filters respectively. The vectors $\mathbf{u}(n)$ and $\hat{\mathbf{a}}(n)$ are defined by

$$\mathbf{u}(n) = [u(n)\ u(n-1)\ \cdots\ u(n-M_f+1)]^T, \quad (1)$$

$$\hat{\mathbf{a}}(n) = [\hat{a}(n-\tau_d-1)\ \cdots\ \hat{a}(n-\tau_d-M_b)]^T, \quad (2)$$

$\lambda(n)$ is the Lagrange multiplier, $\lambda = \lambda_o > 0$ if $c(n) > 0$, $v(x) = \{1$ if $x \geq 0;\ 0$ if $x < 0\}$ is the step function, α is a forgetting factor, μ the step-size, and $R_2^a \triangleq \mathrm{E}\{|a(n)|^4\}/\mathrm{E}\{|a(n)|^2\}$ the expected modulus, being $\mathrm{E}\{\cdot\}$ the expectation operator [2], [4]. It is usual to assume $\lambda_o = 2$ and $\alpha = 0.95$.

TABLE I
Summary of DFE-CMA-FB.

Initialize the algorithm by setting:
$\mathbf{f}(0) = [0 \cdots 0\,1\,0 \cdots 0]$
$\mathbf{b}(0) = \mathbf{0}, \quad \mathbf{g}(0) = \mathbf{0}, \quad E_{y_f}(0) = 0$
For $n = 1, 2, \cdots$, compute:
$y_f(n) = \mathbf{f}^H(n-1)\mathbf{u}(n)$
$y_b(n) = \mathbf{b}^H(n-1)\hat{\mathbf{a}}(n)$
$y(n) = y_f(n) + y_b(n)$
$e(n) = (R_2^a - \lvert y(n)\rvert^2)y(n)$
$E_{y_f}(n) = \alpha E_{y_f}(n-1) + (1-\alpha)\lvert y_f(n)\rvert^2$
$\mathbf{g}(n) = \alpha\mathbf{g}(n-1) + (1-\alpha)\mathbf{u}(n)y_f^*(n)$
$c(n) = \lVert\mathbf{b}(n-1)\rVert^2 - E_{y_f}(n)$
$\lambda(n) = \lambda_o v(c(n))$
$\mathbf{f}(n) = \mathbf{f}(n-1) + \mu[e^*(n)\mathbf{u}(n) + \lambda(n)\mathbf{g}(n)]$
$\mathbf{b}(n) = [1-\mu\lambda(n)]\mathbf{b}(n-1) + \mu e^*(n)\hat{\mathbf{a}}(n)$

A common problem of blind equalization based on the constant modulus criterion is the random phase rotation [13]. In general, the output of the equalizer is given by $y(n) = e^{j\varphi}a(n-\tau_d)+\nu(n)$, with $\varphi \in [0,\ 2\pi[$ and complex noise sample $\nu(n)$. The phase rotation must be compensated before the decision device. The literature contains several blind phase recovery algorithms [13], but for simplicity we assume in this paper the modified Phase Tracking Algorithm (PTA) [2], [12], which provides the following phase update

$$\varphi(n+1) = \varphi(n) + \mu_\varphi \mathrm{Im}(y'(n)\hat{a}^*(n-\tau_d))$$

being $y'(n) = y(n)e^{-j\varphi(n)}$, μ_φ the step-size, and $\mathrm{Im}(v)$ the imaginary part of v.

III. Chen's concurrent algorithm

In the concurrent scheme for blind adaptation of LTEs, proposed by Castro *et al.* [9], to avoid error propagation due to incorrect decisions, the updating of the Decision-Direct coefficients is executed after that of CMA. Its adjustment is made only if the CMA adaptation has achieved a successful updating with high probability [9], [10].

In the Chen's concurrent scheme [10], this adaptation form is also considered but with a Soft Decision-Direct (SDD). The use of SDD instead of Decision-Direct makes Chen's concurrent algorithm more efficient than the original one proposed in [9]. Moreover, the adaptation of the CMA and SDD coefficients occurs simultaneously. In the sequence, this algorithm is revisited.

Assume that the LTE coefficient vector is

$$\mathbf{w}(n) = \mathbf{w}_c(n) + \mathbf{w}_d(n), \quad (3)$$

being $\mathbf{w}_c$ and $\mathbf{w}_d$ coefficient vectors updated by CMA and SDD algorithm respectively and that the equalizer output is $y(n) = \mathbf{w}^H(n-1)\mathbf{u}(n)$.

After successful convergence, the equalizer output can be modelled by

$$y(n) \approx a(n-\tau_d) + \nu(n) \tag{4}$$

where $\nu(n) = \nu_R(n) + j\nu_I(n)$ is approximately a complex Additive White Gaussian Noise (AWGN) with $\mathrm{E}\{\nu_R(n)\nu_I(n)\} = 0$ and $\mathrm{E}\{\nu_R^2(n)\} = \mathrm{E}\{\nu_I^2(n)\} = \rho$. Thus, the *a posteriori* probability density function (p.d.f.) of $y(n)$ can be approximated by

$$p(y(n)) \approx \sum_{k=1}^{K}\sum_{l=1}^{K} \frac{P_{kl}}{2\pi\rho} \exp\left[-\frac{|y(n)-a_{kl}|^2}{2\rho}\right] \tag{5}$$

where a_{kl} takes the value from the M-QAM symbol set defined by

$$A = \{a_{kl} = (2k-K-1) + j(2l-K-1), 1 \le k,l \le K\}$$

with $K = \sqrt{M}$ and P_{kl} the *a priori* probability of a_{kl}. For equiprobable symbol transmission $P_{kl} = 1/M, \quad 1 \le k,l \le K$.

Let the complex plan be divided into $M/4$ regular regions. As indicated in Figure 2, each region A_i contains four symbols, that is

$$A_i = \{a_{im},\ m = 1,2,3,4\},$$

being $i = 1,2,\ldots,M/4$. If the equalizer output is within the region A_i, a local approximation to the *a posteriori* p.d.f. of $y(n)$ is

$$\hat{p}_i(y(n)) \approx \sum_{m=1}^{4} \frac{1}{8\pi\rho} \exp\left[-\frac{|\varepsilon_{im}(n)|^2}{2\rho}\right] \tag{6}$$

where $\varepsilon_{im}(n) = a_{im} - y(n)$ and the *a priori* probability has been set to 1/4.

The SDD algorithm maximizes log of the local *a posteriori* p.d.f criterion given by

$$J_{MAP} = \mathrm{E}\{\rho \log[\hat{p}_i(y(n))]\}. \tag{7}$$

Using a stochastic gradient algorithm to adjust $\mathbf{w}_d(n)$, we arrive at

$$\mathbf{w}_d(n) = \mathbf{w}_d(n-1) + \mu_d \xi^*(n)\mathbf{u}(n) \tag{8}$$

where

$$\xi(n) = \frac{\displaystyle\sum_{m=1}^{4} \exp\left[-\frac{|\varepsilon_{im}(n)|^2}{2\rho}\right]\varepsilon_{im}(n)}{\displaystyle\sum_{m=1}^{4} \exp\left[-\frac{|\varepsilon_{im}(n)|^2}{2\rho}\right]}. \tag{9}$$

To ensure a proper separation of the clusters, the parameter ρ should be lower than the half of the minimum distance between two neighbouring symbol points [10].

As indicated in (9) the SDD adaptation needs to compute only 4 $\exp(\cdot)$ at each iteration, which can be implemented through a table. The task of M-QAM equalization, where $M = 2^{2L}$, is achieved with L-stage process. The identification of the region A_i does not cause a significant increase in computational complexity since it requires only $2(L-1)$ comparisons. Thus, the algorithm's complexity is always equivalent to the minimum complexity of the 4-QAM case [11]. Considering for example 64-QAM, the complex plan is divided in $64/4 = 16$ regions. Each region must contain 4 symbols as shown in Figure 2. Suppose that the equalizer output is $5.3 + j5.7$. The first stage consists in classifying the output into the 4 quadrants of the complex plan. In the example the output is in the first quadrant because its real and imaginary parts are positive. At the second stage, the output must be classified into other 4 regions and at the last stage $\xi(n)$ can be calculated using the four symbols $a_{im},\ m = 1,2,3,4$ of the final region A_i.

The concurrent CMA+SDD has a computational complexity that lies between those of CMA and the concurrent CMA+DD [10]. Due to soft-decision direct nature, the step-size range which ensures the convergence of CMA+SDD is larger than that of CMA. Moreover, as shown in [11], CMA+SDD does not suffer from a serious phase rotation as CMA does.

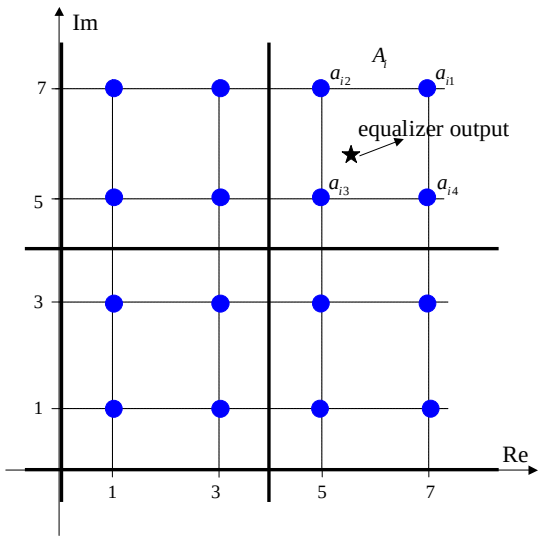

Fig. 2. Illustration of local regions for SDD adaptation and 64-QAM (first quadrant of the complex plan).

IV. The Proposed Algorithm

Motivated by the good behavior of Chen's concurrent algorithm for blind adaptation of LTEs and M-QAM signaling, we propose a concurrent algorithm for blind adaptation of DFEs. The algorithm, named NDEG-CMA-SDD (Non-Degenerative CMA-SDD), operates concurrently the SDD algorithm with DFE-CMA-FB. Thus, one expects that it avoids degenerative solutions as DFE-CMA-FB and acquires the good behavior of concurrent algorithms. Its operations consist basically of those shown in Table I added to SDD operations.

The algorithm is summarized in Table II. Note that $\mathbf{w}_f$ and $\mathbf{w}_b$ are respectively the feedforward and feed-

back coefficient vectors updated by the SDD algorithm (Equation (8)) and $\mathbf{f}$ and $\mathbf{b}$ the coefficient vectors updated by DFE-CMA-FB (Table I).

Table III shows the computational complexity of the algorithms. The complexity of NEG-CMA-SDD is compared to those of DFE-CMA+PTA and DFE-CMA-FB+PTA. Although the conventional CMA for blind adaptation of DFEs, called DFE-CMA [2], does not avoid degenerative solutions, it is considered here for comparison. The NDEG-CMA-SDD complexity shown in Table III was evaluated for 4-QAM signaling. In the case of M-QAM signaling, to identify the region A_i, it is necessary to add $2(L-1)$ comparisons. It is relevant to note that the computational complexity of the proposed algorithm is moderately higher than that of DFE-CMA-FB.

TABLE II
SUMMARY OF NDEG-CMA-SDD.

Initialize the algorithm by setting:

$$\mathbf{f}(0) = [0 \cdots 0\,1\,0 \cdots 0], \quad E_{y_f}(0) = 0$$

$$\mathbf{w}_f(0) = \mathbf{g}(0) = \mathbf{0}, \quad \mathbf{b}(0) = \mathbf{w}_b(0) = \mathbf{0}$$

For $n = 1, 2, \cdots$, compute:

$$y_f(n) = \left[\mathbf{f}(n-1) + \mathbf{w}_f(n-1)\right]^H \mathbf{u}(n)$$

$$y_b(n) = [\mathbf{b}(n-1) + \mathbf{w}_b(n-1)]^H \hat{\mathbf{a}}(n)$$

$$y(n) = y_f(n) + y_b(n)$$

$$e(n) = (R_2^a - |y(n)|^2) y(n)$$

$$E_{y_f}(n) = \alpha E_{y_f}(n-1) + (1-\alpha)|y_f(n)|^2$$

$$\mathbf{g}(n) = \alpha \mathbf{g}(n-1) + (1-\alpha)\mathbf{u}(n) y_f^*(n)$$

$$c(n) = \|\mathbf{b}(n-1)\|^2 - E_{y_f}(n)$$

$$\lambda(n) = \lambda_o \upsilon(c(n))$$

$$\mathbf{f}(n) = \mathbf{f}(n-1) + \mu[e^*(n)\mathbf{u}(n) + \lambda(n)\mathbf{g}(n)]$$

$$\mathbf{b}(n) = [1 - \mu\lambda(n)]\mathbf{b}(n-1) + \mu e^*(n)\hat{\mathbf{a}}(n)$$

Identify the region A_i making $2(L-1)$ comparisons and compute:

$$\xi(n) = \frac{\sum_{m=1}^{4} \exp\left[-\frac{|\varepsilon_{im}(n)|^2}{2\rho}\right] \varepsilon_{im}(n)}{\sum_{m=1}^{4} \exp\left[-\frac{|\varepsilon_{im}(n)|^2}{2\rho}\right]}$$

$$\mathbf{w}_f(n) = \mathbf{w}_f(n-1) + \mu_d \xi^*(n)\mathbf{u}_f(n)$$

$$\mathbf{w}_b(n) = \mathbf{w}_b(n-1) + \mu_d \xi^*(n)\hat{\mathbf{a}}(n)$$

V. SIMULATION RESULTS

A channel of high definition television (HDTV) terrestrial metropolitan transmission is assumed [1]. In this case, the channel presents large echoes fairly close to the main path. Such a scenario is common where large buildings are close to the receiver, e.g. in New York [1]. The coefficients and frequency response of the channel are depicted in Figure 3. In the simulations, the transmitted signal and the equalizer input signal are normalized to have unit power, i.e. $\sigma_a^2 = \sigma_u^2 = 1$.

TABLE III
COMPUTATIONAL COMPLEXITY OF THE ALGORITHMS PER WEIGHT UPDATE.

Op.	DFE-CMA +PTA	DFE-CMA-FB +PTA	NDEG-CMA-SDD
$\times$	$8M_f+8M_b$ $+19$	$16M_f+12M_b$ $+28$	$20M_f+16M_b$ $+36$
$+$	$8M_f+8M_b$ $+7$	$14M_f+10M_b$ $+11$	$20M_f+16M_b$ $+25$
$\div$	–	–	1
exp	–	–	4

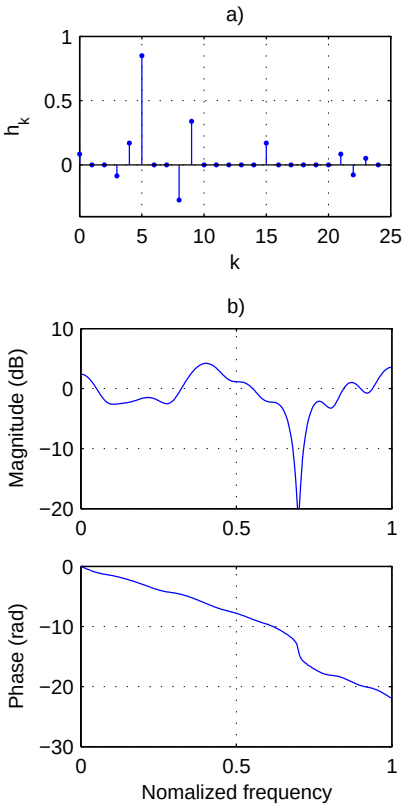

Fig. 3. a) Impulse response and b) frequency response of the HDTV channel used in simulations.

The performance of NDEG-CMA-SDD is compared to those of DFE-CMA-FB+PTA and DFE-LMS (DFE-Least Mean Square) for the DFE training with $M_f = 11$, $M_b = 17$ and 16-QAM signaling. Figure 4 shows the measurement of the symbol error rates (SER). As expected, the supervised DFE-LMS algorithm without error propagation (WEP) has the best performance. NDEG-CMA-SDD presents a performance close to DFE-CMA-FB+PTA for signal-to-noise ratio (SNR) below 19 dB but outperforms it for $\mathrm{SNR} > 19$ dB becoming close to DFE-LMS for $\mathrm{SNR} > 22$ dB. Thus, the proposed algorithm presents a behavior close to DFE-CMA-FB+PTA for lower SNR and outperforms it for higher SNR.

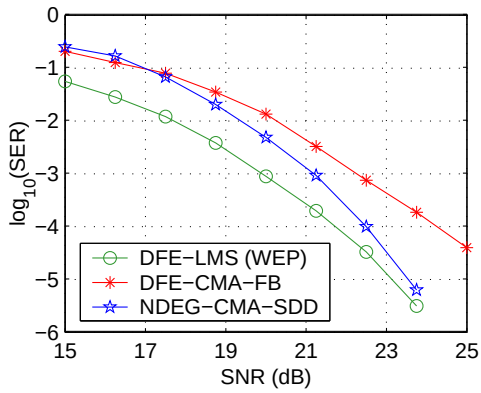

Fig. 4. Plot of decimal logarithm of SER for $M_f = 11$, $M_b = 17$, 16-QAM, channel of Figure 3, $\sigma_d = 10$, $\mu = 10^{-3}$, $\mu_d = 10^{-2}$, $\mu_\varphi = 10^{-2}$, $\rho = 0.06$, $\lambda_o = 1$, and $\alpha = 0.95$.

Figure 5 shows the decision based Mean Square Error $\mathrm{MSE} = \mathrm{E}\{|y(n) - \hat{a}(n-\tau_d)|^2\}$ of NDEG-CMA-SDD and DFE-CMA-FB+PTA for $\mathrm{SNR} = 22.5$ dB and 16-QAM signaling. To facilitate the visualization, the MSE signals were filtered by a moving-average filter with 32 coefficients. In this case, the algorithms were experimentally adjusted to reach the same steady-state MSE. Note that NDEG-CMA-SDD has faster convergence rate than DFE-CMA-FB+PTA.

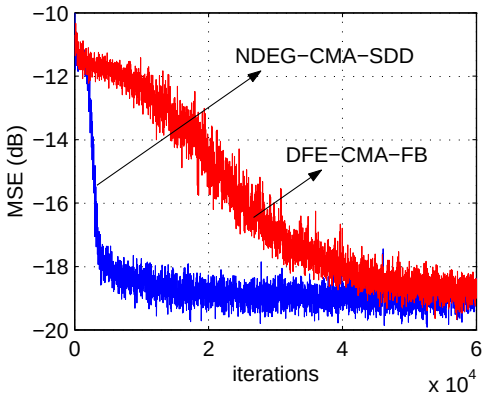

Fig. 5. Decision based MSE for DFE-CMA-FB+PTA ($\mu = 2.5 \times 10^{-4}$, $\rho = 0.06$, $\lambda_o = 1$, $\alpha = 0.95$, $\mu_\varphi = 2.5 \times 10^{-3}$) and NDEG-CMA-SDD ($\mu = 10^{-3}$, $\mu_d = 10^{-2}$, $\rho = 0.06$, $\lambda_o = 1$, $\alpha = 0.95$), $M_f = 11$, $M_b = 17$, $\mathrm{SNR} = 22.5$ dB, 16-QAM, and channel of Figure 3; average over 50 experiments.

In order to investigate the efficacy of the algorithms in tracking dynamic multipath we consider a channel whose coefficients are given by $[1\,0\,0\,0\,0\,0\,0\,0\,0\,0\,0\,0.5\sin(2\pi f n T)]$, where $f = 5$ Hz, $T = 0.0929$ ms, and n is the time index [1]. Figure 6 shows errors at the output of decision devices by considering 16-QAM signaling, $M_f = 11$, and $M_b = 17$. The SNR was set to 20 dB and the step-size of each algorithm was experimentally adjusted to obtain the best tracking performance. The absolute values of the channel roots are shown if Figure 6-d. The channel has 11 zeros homogeneously distributed in a circle. Thus, all the zeros have the same absolute values. The channel becomes more difficult to equalize when the zeros are close to the unit circle. In this case, DFE-CMA-FB+PTA presents error bursts (Figure 6-c) while DFE-LMS (WEP) (Figure 6-a) and NDEG-CMA-SDD (Figure 6-b) have faster recuperation.

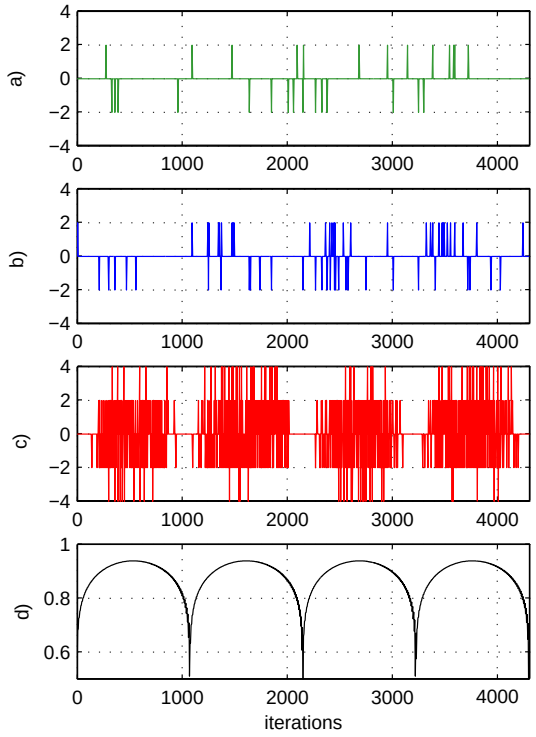

Fig. 6. Output errors, 16-QAM, SNR=20 dB, $M_f = 11$, $M_b = 17$ a) DFE-LMS ($\mu = 10^{-2}$, $\sigma_d = 5$), b) NDEG-CMA-SDD ($\mu = 2 \times 10^{-3}$, $\mu_d = 2 \times 10^{-2}$, $\rho = 0.06$, $\lambda_o = 1$, $\alpha = 0.95$) c) DFE-CMA-FB+PTA ($\mu = 5 \times 10^{-4}$, $\rho = 0.06$, $\lambda_o = 1$, $\alpha = 0.95$, $\mu_\varphi = 5 \times 10^{-3}$), d) Absolute root values of the dynamic multipath channel.

Figure 7 shows the measurement of the symbol error rates for the dynamic multipath channel. Due to error bursts DFE-CMA-FB+PTA presents high values of SER. The DFE-LMS algorithm shows the best performance followed by NDEG-CMA-SDD. However, the latter suffers with low values of SNR. For $\mathrm{SNR} < 17.5$ dB its performance becomes worse than that of DFE-CMA-FB+PTA. As previously observed, the good behavior of the proposed algorithm is obtained for high values of SNR.

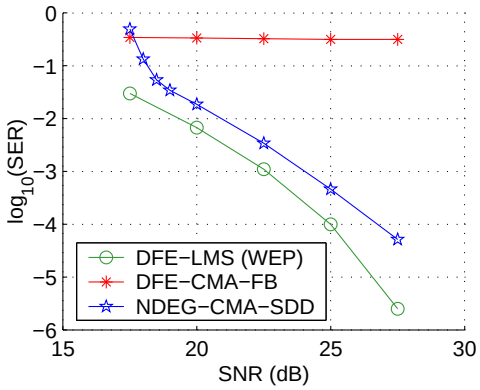

Fig. 7. Plot of decimal logarithm of SER for $M_f = 11$, $M_b = 17$, 16-QAM, and dynamic multipath channel.

VI. Conclusion

We have proposed an improvement of DFE-CMA-FB for blind adaptation of DFEs and M-QAM signaling based on a concurrent method which uses a Soft-Decision Direct algorithm. At the cost of a moderate increase in computational complexity, we showed by means of simulations that the resulting algorithm presents good tracking performance and lower symbol error rate than DFE-CMA-FB for high values of SNR.

References

[1] M. Ghosh, "Blind decision feedback equalization for terrestrial television receivers," *Proceedings of the IEEE*, vol. 86, pp. 2070-2081, Oct. 1998.

[2] L. L. Szczecinski and A. Gei, "Blind decision feedback equalisers, how to avoid degenerative solutions," *Signal Processing*, vol. 82, pp. 1675-1693, 2002.

[3] C. B. Papadias and A. Paulraj, "Decision-feedback equalization and identification of linear channels using blind algorithms of the bussgang type," *Proceedings of ASILOMAR-29*, pp. 335-340, Pacific Grove, Oct. 1995.

[4] D. N. Godard, "Self-recovering equalization and carrier tracking in two dimensional data communication system," *IEEE Transactions on Communications*, pp. 1867-1875, Nov. 1980.

[5] R. A. Casas *et al.*, "Blind adaptation decision feedback equalizers based on constant modulus algorithm," *Proceedings of ASILOMAR-29*, vol. 1, pp. 698-702, Pacific Grove, Oct. 1995.

[6] L. Tong and D. Liu, "Blind predictive decision-feedback equalization via the constant modulus algorithm," *Proccedings of ICASSP'97*, pp. 3901-3904, Munich, Apr. 1997.

[7] J. Labat, O. Macchi, and C. Laout, "Adaptive decision feedback equalization: can you skip the trainning period?," *IEEE Transactions on Communications*, v. 46, pp. 921-930, July 1998.

[8] R. A. Casas *et al.*, "On initialization strategies for blind adaptive DFEs," *Proceedings of WCNC'99*, vol. 2, pp. 792-796, New Orleans, Sept. 1999.

[9] F. C. C Castro, M. C. F. Castro, and D. S. Arantes, "Concurrent blind deconvolution for channel equalization," *Proceedings of ICC'2001*, vol. 2, pp. 366-371, Helsink, 2001.

[10] S. Chen, "Low complexity concurrent contant modulus algorithm and soft directed scheme for blind equalization," *IEE Proceedings - Vision, Image, and Signal Processing*, v. 150, pp. 312-320, Oct. 2003.

[11] S. Chen, T. B. Cook, and L. C. Anderson, "A comparative study of two blind FIR equalizers," *Signal Processing*, v.14, pp.18-36, 2004.

[12] J. Proakis, *Digital Communications*, McGraw-Hill, New York, 1995.

[13] A. Haidary and M. Nasiri-Kenari, "A family of simple blind phase recorevy algorithms," *Proc. of ISPACS'2000*, vol. 1, pp. 24-28, Honolulu, 2000.

On the Performance for MMSE Detection of Direct Sequence CDMA Signals with Random Spreading in Multipath Rayleigh Fading Channels

Gustavo Fraidenraich[1], Renato Baldini Filho and Celso de Almeida
[1] DECOM/FEEC/Unicamp, CP. 6101, 13083-852, Campinas, SP, Brazil, gf@decom.fee.unicamp.br

***Abstract*— In this paper simplified expressions to evaluate the performance of multiuser MMSE detector in CDMA systems using random spreading sequence on multipath Rayleigh fading channel are obtained. The expressions were validated through simulation.**

***Index Terms*— CDMA, direct-sequence, multiuser detection, random signatures sequence, spread spectrum.**

I. Introduction

The mean bit error probability of CDMA systems using the matched filter depends on the instantaneous crosscorrelation of the spreading sequences of all users. Random spreading sequences and the Gaussian approximation for the multiple access interference [1] are considered, therefore the mean bit error probability can be expressed as a function of the load, i.e., processing gain and the number of users. Using similar approach it is possible to obtain expressions for the MMSE detector in the presence of multipath Rayleigh fading channel as a function of the load.

II. Bit Error Probability of the MMSE detector in AWGN channel

A mean bit error probability of the MMSE detector on a AWGN channel using random spreading sequences in a synchronous CDMA system with perfect power control is given by [2]:

$$P_b^s = \mathrm{Q}\left(\sqrt{2\frac{E_b}{N_0} - \frac{1}{4}F\left(2\frac{E_b}{N_0}, \frac{N-1}{G}\right)}\right) \quad (1)$$

where

$$F(x,y) = \left[\sqrt{x\left(1+\sqrt{y}\right)^2+1} - \sqrt{x\left(1-\sqrt{y}\right)^2+1}\right]^2 \quad (2)$$

and G is the processing gain, $\frac{E_b}{N_0}$ is the signal-to-noise ratio, N is the number of users of the system and Q(.) is the complementary Gaussian error function. For the asynchronous CDMA systems, the mean bit error probability can be evaluated by the following expression:

$$P_b^a = \mathrm{Q}\left(\sqrt{2\frac{E_b}{N_0} - \frac{1}{4}F\left(2\frac{E_b}{N_0}, \frac{2(N-1)}{3G}\right)}\right) \quad (3)$$

III. Performance in multipath Rayleigh fading channel

On the multipath Rayleigh fading channel with equal strengh L paths, P_b in the synchronous case is given by:

$$P_b^s(\alpha) = \mathrm{Q}\left(\sqrt{\sum_{i=1}^{L}\alpha_i^2\left[2\frac{E_b}{N_0} - \frac{1}{4}F\left(2\frac{E_b}{N_0}, \frac{N-1}{G}\right)\right]}\right), \quad (4)$$

and in the asynchronous case:

$$P_b^a(\alpha) = \mathrm{Q}\left(\sqrt{\sum_{i=1}^{L}\alpha_i^2\left[2\frac{E_b}{N_0} - \frac{1}{4}F\left(2\frac{E_b}{N_0}, \frac{2(N-1)}{3G}\right)\right]}\right) \quad (5)$$

where α is the Rayleigh fading amplitude. The mean bit error probability is then given by averaging Eq. (5) over the Rayleigh fading [3]:

$$\overline{P}_b = \left[\frac{1}{2}\left(1-\sqrt{\frac{\overline{\gamma}_b}{\overline{\gamma}_b+L}}\right)\right]^L \times \sum_{i=0}^{L-1}\binom{L-1+i}{i}\left[\frac{1}{2}\left(1+\sqrt{\frac{\overline{\gamma}_b}{\overline{\gamma}_b+L}}\right)\right]^i \quad (6)$$

in the synchronous case $\overline{\gamma}_b$, the mean signal-to-interference ratio is given by:

$$\overline{\gamma}_b = L\overline{\alpha^2}\left[\frac{E_b}{N_0} - \frac{1}{8}F\left(2\frac{E_b}{N_0}, \frac{N-1}{G}\right)\right] \quad (7)$$

and in the asynchronous case $\overline{\gamma}_b$ is given by:

$$\overline{\gamma}_b = L\overline{\alpha^2}\left[\frac{E_b}{N_0} - \frac{1}{8}F\left(2\frac{E_b}{N_0}, \frac{2(N-1)}{3G}\right)\right] \quad (8)$$

The accuracy of the expression of $\overline{P}_b$ can be verified using some first order approximation on the F function. For low signal-to-noise ratio, the MMSE detector should achieve similar performance of the matched filter and for high signal-to-noise ratio it should achieve similar performance of the decorrelator detector.

Then for x $\gg$ 1, which means a high signal-to-noise ratio, $F(x,y)$ can be approximated by:

$$F(x,y) \approx 4xy \quad (9)$$

Substituting the expression above in Eq. (7), the mean signal-to-noise ratio in the synchronous case will be

given by:

$$\overline{\gamma}_b = \frac{E_b}{N_0}\left(1 - \frac{N-1}{G}\right) \tag{10}$$

which is the Gaussian approximation for the multiple access interference for the decorrelator detector [4].

For low signal-to-noise ratio, that is, for x$\ll$1, a variable transformation z = x.y associated to Taylor series in relation to the x variable at point x=0 can be used to obtain:

$$F(x,y) \approx \frac{4x^2 y}{1+xy} \tag{11}$$

Substituting Eq. (11) in Eq. (7), the mean signal-to-noise ratio in the synchronous case can be evaluated by:

$$\overline{\gamma_b} = \frac{1}{2\left(\frac{1}{2\frac{E_b}{N_0}} + \frac{N-1}{G}\right)} \tag{12}$$

As expected the expression in Eq. (12) is the mean signal-to-interference ratio to the matched filter detector.

Using the same approach, asynchronous expressions can be devised to the high and low mean signal-to-noise ratio. For the high signal-to-noise ratio, $\overline{\gamma_b}$ can be evaluated by:

$$\overline{\gamma}_b = \frac{E_b}{N_0}\left(1 - \frac{2(N-1)}{3G}\right) \tag{13}$$

and for the low signal-to-noise ratio, $\overline{\gamma_b}$ is given by:

$$\overline{\gamma_b} = \frac{1}{2\left(\frac{1}{2\frac{E_b}{N_0}} + \frac{K-1}{3G_p}\right)} \tag{14}$$

IV. Numerical Results and Comparisons

Simulations were carried out in order to validated the mean bit error probability expressions. It is considered in the asynchronous and synchronous cases the AWGN and multipath Rayleigh fading channel with 1,2 and 4 paths.

The results are presented in Fig. 1-4. The analytic expressions and simulations results present very similar performance.

V. Conclusions

Simplified expressions to evaluate the performance of MMSE detector in CDMA systems using random spreading sequence on multipath Rayleigh fading channels were obtained. Those expressions are function of the processing gain, the number of users and the signal-to-noise ratio $\frac{E_b}{N_0}$.

References

[1] M. B. Pursley, D. V. Sarwate, and W. E. Stark, Error Probability for Direct-Sequence Spread Spectrum Multiple-Access communications Part II: Code Sequence Analysis, IEEE Trans. On Comm., Vol. Com-25, No. 8 Aug, 1977

[2] S. Verdu Multiuser Detection Cambridge Press 1998

[3] J. G. Proakis, Digital Communications, 2nd ed. New York: McGraw-Hill, 1995.

[4] Celso de Almeida and Gabriel M. da Silva On the performance of CDMA Systems with multiuser Decorrelating Detectors for Random Sequences on AWGN channels. Submitted to Electronic Letters, Nov 2003.

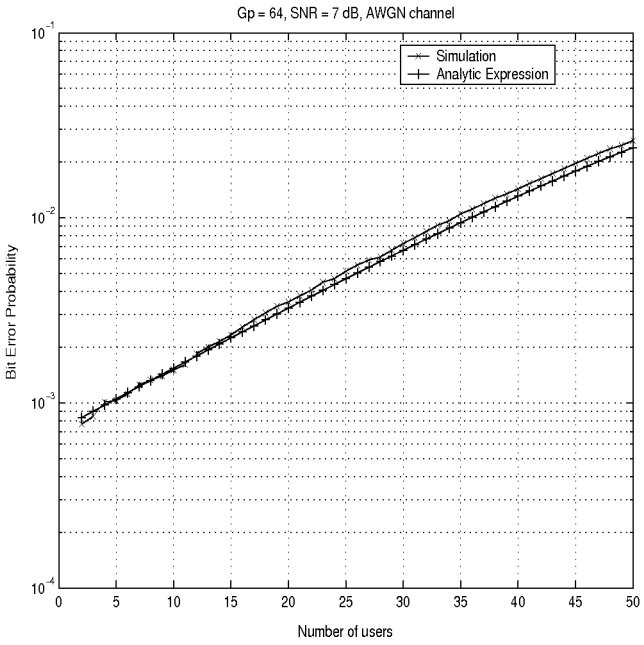

Fig. 1. MMSE Synchronous, Gp=64 and SNR = 7 dB, AWGN channel

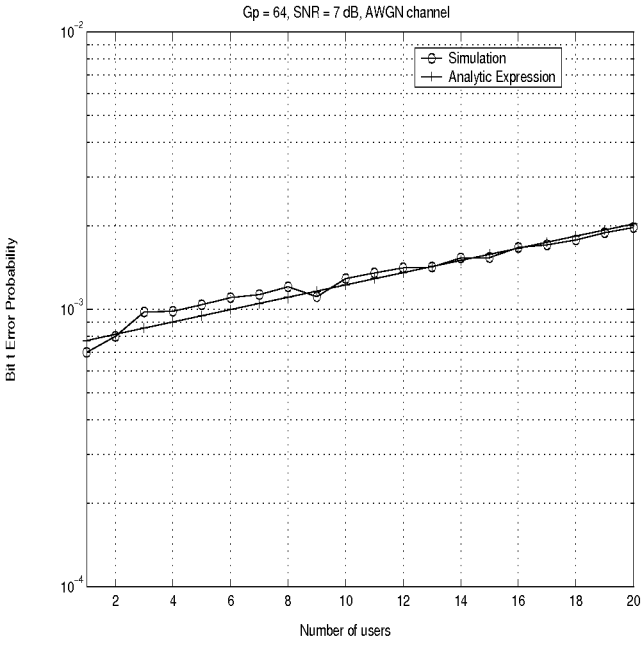

Fig. 2. MMSE Asynchronous, Gp=64 and SNR = 7 dB, AWGN channel

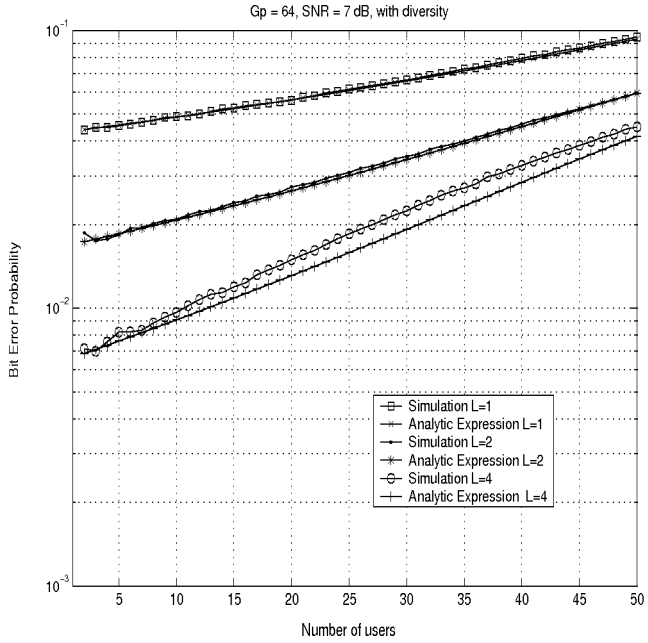

Fig. 3. MMSE Synchronous, Gp=64 and SNR = 7 dB, selective Rayleigh fading channel

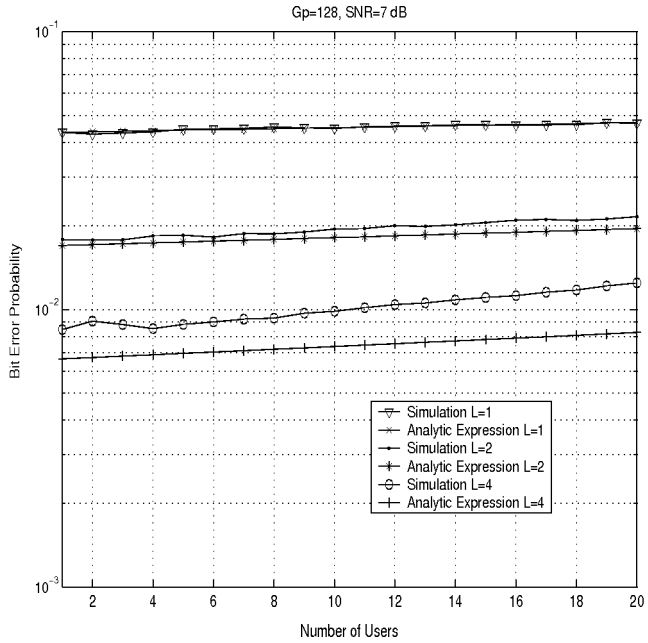

Fig. 4. MMSE Asynchronous, Gp=64 and SNR = 7 dB, selective Rayleigh fading channel

Implementation of a Synchronizer for Hiperlan/2 on FPGA

MªJosé Canet
Dpto. Ing. Electrónica
U.P.Valencia
Spain
macasu@doctor.upv.es

Felip Vicedo
Dpto. Física y Arquitectura de Computadores
U. Miguel Hernández, Elche, Spain
felip@umh.es

Vicenç Almenar
Dpto. Comunicaciones
U.P.Valencia
Spain
valmenar@dcom.upv.es

Javier Valls
Dpto. Ing. Electrónica
U.P.Valencia
Spain
jvalls@eln.upv.es

Eduardo R. de Lima
Dpto. Comunicaciones
U.P.Valencia
Spain
edrodde@doctor.upv.es

***Abstract*—This paper deals with the design and implementation of a frame, time and frequency synchronizer for Hiperlan/2 WLAN standard on FPGA. Fixed-point realization of the synchronization algorithm is evaluated and some simplifications are introduced to reduce the cost in area. The implementation is optimized for the FPGA structure, for example, using embedded multipliers. Finally, the performance of the implemented synchronizer is analysed and compared with the performance of the floating-point realization.**

***Index Terms*—OFDM, carrier frequency offset, synchronizer, Hiperlan, FPGA.**

I. Introduction

Hiperlan/2 is a Wireless LAN (WLAN) standard from ETSI BRAN [1,2] which works in the 5 GHz band and achieves data rates up to 54 Mbps. For the physical layer, Orthogonal Frequency Division Multiplexing (OFDM) is used, since it allows getting high bit rates in highly dispersive fading environments.

In Hiperlan/2 systems data is transmitted in bursts, always preceded by a preamble. So, the acquisition stage at the receiver must be quick enough to get all the data in the burst.

Most of the practical solutions for frame and time synchronization based on a pilot preamble that can be found in the literature are based on the autocorrelation of the received signal, as it was proposed by Schmild and Cox [3]. For example, in [4] a hardware architecture of a time OFDM synchronizer is presented. This is similar to [3] but some simplifications have been carried out on the algorithm. First, in [4] the branch that calculates the energy of the received signal is removed. We have checked that if the signal amplitude varies and the input signal energy is not calculated, the synchronizer performance is drastically reduced. Besides the autocorrelation scheme, it is possible to perform the time and frame synchronization using the cross-correlation between the received and the known preamble, but this solution has smaller performance [5] and bigger hardware cost [6].

This paper describes in detail the hardware implementation of a frame, time and frequency synchronizer for Hiperlan /2. This paper is organized as follows. Section 2 presents an overview of the physical layer. Section 3 deals with frame detection, Section 4 with symbol time estimation and Section 5 with Carrier Frequency Offset (CFO) estimation and CFO compensation. In Section 6 complete synchronizer is commented and in Section 7 hardware results are summarized. Lastly, in Section 8 some conclusions are presented.

II. Physical Layer

The physical layer is based on OFDM baseband modulation. The baseband signal is built using a 64-point IFFT. Then a cyclic prefix of 16 samples is added to make the system robust to multipath, prevent inter-symbol interference and to have some tolerance for symbol timing errors.

Each symbol is 80 samples long, that gives a duration of 4μs with a sampling frequency of 20 MHz. In order to facilitate implementation of filters and to achieve sufficient adjacent channel suppression, only 52 subcarriers are used: 48 data carriers and 4 pilots for phase tracking. This allows uncoded data rates from 12 to 72 Mbps using variable modulation types from BPSK to 64-QAM. Convolutional coding is used with the rate 1/2, this rate may be increased to 2/3 or 9/16 by puncturing the coded output bits. As a result, seven data bit rates are specified: 6, 9, 12, 18, 24, 36, 48 and 54 Mbps.

The air interface of Hiperlan/2 is based on time-division duplex (TDD) and dynamic time-division multiple access (TDMA). There is a basic MAC frame with a fixed length of 2 ms, which comprises five phases for broadcast and frame control, downlink,

direct link (optional), uplink and random access.

The medium access is controlled by an Access Point (AP) which informs the Mobile Terminals (MT) at which point in time during the MAC frame they must listen to the transmitted data or they are allowed to transmit their data. These time slots are allowed dynamically depending on the need for transmission resources. During the broadcast phase, the AP transmits a preamble that is used by MT's to perform frame synchronization, time synchronization, automatic gain control (AGC), frequency synchronization and channel estimation. The preamble transmitted by the AP during the downlink phase is designed for channel estimation only. The preambles transmitted by the MT´s during the uplink phase and the random phase have to allow the AP to perform time synchronization, frequency synchronization, and channel estimation.

Therefore, the synchronization phase in an MT can be divided in three parts: detection of the broadcast preamble; time synchronization, that consists in estimating the sample when the OFDM symbol starts; and carrier frequency offset (CFO) estimation. These tasks should be done using the broadcast preamble structure (Fig. 1). In this structure we can distinguish 3 sections: A, B, and C. A and B sections are intended for frame detection, time synchronization, AGC and coarse CFO estimation; section C can be used for fine CFO estimation and channel estimation. The frame detection task must be done only the first time, after that, a MT must track the MAC frame structure every 2ms. In an AP the synchronization phase is easier because it knows where the uplink preamble is, thanks to the TDMA structure of the MAC frame which is scheduled by the AP.

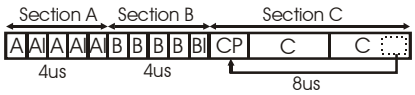

Fig. 1. Broadcast preamble

III. Frame Detection

Frame detection is the first phase of the whole synchronization process, and the most important, since a false detection could cause that an MT transmission begins at a wrong instant [5].

A. Detection Algorithm

We will work with one of the algorithms proposed in [5], this makes use of the autocorrelation of the received signal in a similar way as in [3]. In Fig. 2 it is shown the block diagram of this algorithm. The received signal (r_{cx}) is correlated with a delayed (16 samples) version of itself. Then, the obtained signal is averaged over 48 samples giving the autocorrelation signal R and scaled by the mean power (signal P) of the input signal:

$$R(m) = \sum_{k=m}^{m+47} r_{cx}(k) r_{cx}^{*}(k-16) \qquad (1)$$

$$P(m) = \sum_{k=m}^{m+47} |r_{cx}(k)|^2$$

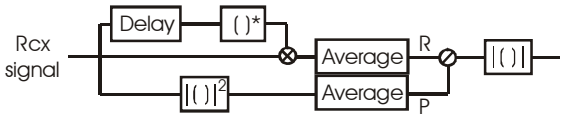

Fig. 2. Block diagram of the autocorrelation scheme

Fig. 3 shows the output, without any channel distortion, of the autocorrelation scheme (magnitude, and phase scaled by π) for Hiperlan/2 broadcast preamble. This result is compared with the output obtained when an uplink long preamble is introduced, since the frame detection algorithm must distinguish between both kinds of preambles. On the one hand, the broadcast preamble has two peaks in the magnitude plot, one in section A (sample 64) and another in section B (sample 144). Also, the phase is ±π during section A and 0 during section B. On the other hand, the uplink preamble has a magnitude of 1 between samples 64 and 144 and has a phase of 0.

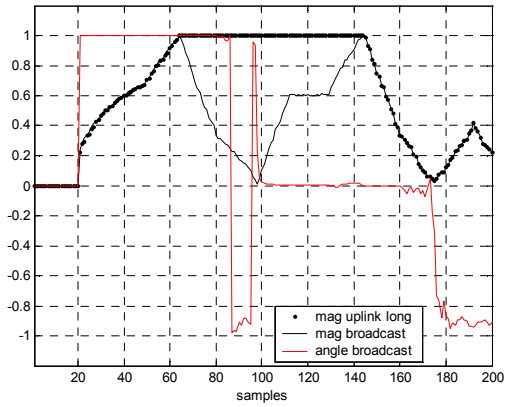

Fig. 3. Output of the autocorrelation scheme for Hiperlan/2 broadcast and uplink preambles.

The detection algorithm sets a magnitude threshold THR_{MAG} and a phase checking. After threshold is exceeded, the phase of the 30 previous samples is checked. If they are greater (in magnitude) than π/2, the algorithm assumes that a broadcast preamble is present. In order to detect the phase condition it is enough to look at the sign of the real part of the autocorrelation scheme output (it should be negative).

To evaluate the performance of this algorithm we have measured the probability of detection failure (DF) and of false alarm (FA) under these conditions:

- Channel model A (*delay spread* of 50 ns), since it represents a typical indoor office environment [7].
- Number of test frames: 10.000
- Signal clipping (preamble): 5 dB below the rms, 5 dB above the rms and no clipping (10 dB above the rms).

- SNR: 10 dB. This is a worst case since to achieve an acceptable packet error rate (10^{-2}), the SNR should be at least 12 dB, for a 6 Mbit/s bit rate [8].

The implementation of the scheme presented above would require one complex multiplier (3 real multipliers and 5 adders) to calculate the autocorrelation, two real multipliers to obtain the input signal energy, two dividers to scale the real an imaginary autocorrelation output, and a CORDIC [9] to estimate output magnitude. All this operators would require a lot of hardware resources in the FPGA. In this paper we propose to modify the synchronization algorithm, insofar as possible, in order to reduce the hardware cost, but without reducing the performance (without increasing probability of DF or FA).

Some simplifications of the initial algorithm have been studied. For this algorithm, the threshold magnitude condition [3] is modified as follows:

$$\left|\frac{R}{P}\right| > THR_{MAG} \rightarrow |R|^2 > THR_{MAG}^2 \cdot |P|^2 \quad (2)$$

The main purpose of this modification is to eliminate the dividers, since their hardware design is complicated and their cost is high. We have replaced two divisors by two multipliers, one to calculate the squared energy and another to multiply it by the squared threshold. Also we obtain the squared modulus of the averaged and scaled signal instead of the modulus: the use of a CORDIC, which has a high hardware cost, is avoided. This is replaced by two multipliers and one adder.

The performance of this modification has been compared with the one of the original algorithm. Fig. 4 illustrates the obtained results in Hiperlan/2 for a signal clipping of 5 dB below the rms. Floating-point data has been considered, and magnitude thresholds between 0.1 and 0.9 have been evaluated. In the original algorithm, which works with THR_{MAG}, DF probability is very small for thresholds below 0.75. Simplified algorithm works with THR^2_{MAG}, for this reason the magnitude threshold is lower than before. The DF probability is lower than 10^{-3} for thresholds under 0.55 and FA probability is lower than 10^{-3} for thresholds over 0.4. Finally, we have decided to use a threshold of 0.5 because it provides a good performance and avoids the use of one multiplier (multiply by 0.5 is performed as a hardwired shift).

B. Finite Precision Analysis and Hardware Implementation

A Matlab finite precision model of the whole synchronizer has been performed. The quantization has been applied to each block of the system, meanwhile the rest of the blocks keep the ideal behavior. The aim has been to reduce the precision maintaining the same performance as in the floating-point solution. This study has been carried out with a signal clipping of 5 dB under the preamble rms and without signal clipping (10 dB above the preamble rms).

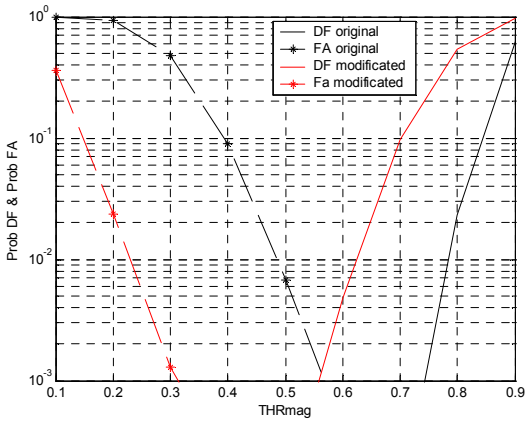

Fig. 4. DF and FA probability in Hiperlan/2

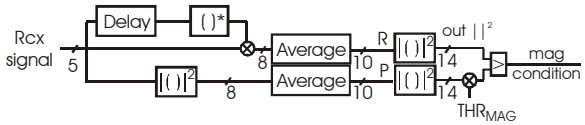

Fig. 5. Implemented synchronizer

The average circuit has been implemented with an accumulator and a subtractor. In each cycle, the accumulator adds a new sample and the subtractor eliminates the sample 48th. Phase condition is fulfilled if the real part of the autocorrelation output is negative during 30 cycles. Their most significant bit (MSB) is registered with 29 flip-flops, and then multiplied (with an AND gate) with the MSB of the last sample. Only one comparator is needed to check the magnitude condition. It is assumed that a broadcast preamble is present if phase and magnitude conditions are met (another AND gate is used). Finally, a low cost circuit has been implemented to reduce FA probability: magnitude and phase condition must meet during more than 8 cycles. With these circuits we have obtained DF and FA probability (in %) of the implemented synchronizer, for 10000 test frames, 10dB SNR and channel model A. Table I summarizes the obtained results.

TABLE I
IMPLEMENTED SYNCHRONIZER PERFORMANCE

Clipping	10dB rms	5dB rms	-5dB rms
DF	0.05%	0.03%	0.64%
FA	0.20%	0.14%	0.08%

IV. TIME SYNCHRONIZATION

After frame detection is accomplished, it is necessary to estimate the first sample of the broadcast preamble. This estimation must be as accurate as possible to avoid ISI with previous or later symbols when the FFT window is taken. Multipath channel, analog filters required in transmitter and receiver, and interpolate and decimate filters distort between 6 and 7

samples of the cyclic prefix [10]. So, there is a window of 9 samples where the FFT can begin without introducing ISI.

In Hiperlan/2, after detection of the maximum magnitude value in section A, section B peak is searched in order to perform time synchronization. An average of the autocorrelation scheme output has been made and a low cost maxima detection is used: actual and previous samples are compared. If actual sample is smaller than previous sample during 2 cycles, we assume that there is a maximum.

Fig. 6 illustrates the deviation between the symbol timing estimator and the ideal initial sample using the implemented synchronizer when there is not signal clipping (we assume that AGC has finished during A phase). It can be seen that 95% of the estimated initial samples fall in the range between 0 and 4, and that the maximum deviation is lower than 9, which was the maximum width of the valid window. So, this solution is valid and would not degrade the performance of the receiver due to ISI.

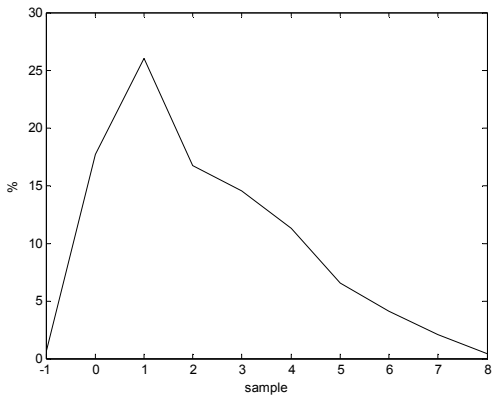

Fig. 6. Deviation from initial sample

V. CFO ESTIMATION AND CFO COMPENSATION

One of the main drawbacks of OFDM is its sensitivity to CFO. In Hiperlan/2, section B peak is used for coarse CFO estimation. If received signal has carrier frequency offset and noise is ignored, it can be expressed by:

$$r_{cx}(k) = s_{tx}(k) \cdot e^{j2\pi(f_{tx}-f_{rx})kT} = s_{tx}(k) \cdot e^{j2\pi f_o kT} \qquad (3)$$

where s_{tx} is the transmitted signal, $f_o = f_{tx} - f_{rx}$ is the carrier frequency error, f_{tx} is the transmitter carrier frequency, f_{rx} the receiver carrier frequency and T is the sampling period. In this case, the autocorrelation output will be:

$$R(k) = \sum_{k=m}^{L-1} s_{tx}(k) \cdot e^{j2\pi f_o kT} \cdot \left(s_{tx}(k-D) \cdot e^{j2\pi f_o (k-D)T}\right)^* \qquad (4)$$

$$R(k) = e^{-j2\pi f_o DT} \cdot \sum_{k=m}^{L-1} s_{tx}(k) \cdot s_{tx}{}^*(k-D)$$

where D is the delay in the autocorrelation scheme and L the moving average length. So, the estimated frequency offset ($\hat{f}_o$) can be calculated by [3]:

$$\hat{f}_o = -\frac{\angle(R)}{2 \cdot \pi \cdot D \cdot T}, \qquad (5)$$

The angle of correlator output ($\angle(R)$) is calculated with a circular vectoring mode CORDIC. Next, the estimated frequency will be used to remove this CFO from de signal, by using the same CORDIC processor, configured as circular rotation mode.

The maximum frequency error that can be estimated depends on the delay (D) in the autocorrelation scheme [11]:

$$\hat{f}_{o\max} = \frac{1}{2 \cdot D \cdot T} \qquad (6)$$

The autocorrelation scheme used to detect B peak has D=16, so $\hat{f}_{o\max}$ =625kHz. This frequency offset is higher than 212kHz (20ppm) frequency offset allowed in [1].

The effect of carrier frequency error on the performance can be measured with the SNR loss. For relatively small frequency errors, it can be calculated by [11]:

$$SNR_{Loss} = \frac{10}{3\ln 10}(\pi T f_\Delta)^2 \frac{E_S}{N_0} dB \qquad (7)$$

where f_Δ is the frequency error as a fraction of the subcarrier spacing (SSP) and T is the sampling period. The performance varies strongly with the modulation used. For example, 64-QAM can not tolerate more than 1% error in the carrier frequency for a SNR loss of 0.5dB, while QPSK can tolerate up to 5% for the same SNR loss. On the other hand, 64-QAM needs at least 30dB SNR to achieve an acceptable packet error rate (10^{-2}), whereas BPSK only needs 12dB [8]. A higher SNR improves the performance of the CFO estimator [11].

The next frequency offsets have been considered: 62.5kHz (0.2·SSP), 125kHz (0.4·SSP), 187.5kHz (0.6·SSP) and 250kHz (0.8·SSP). Higher frequency offsets are not allowed in Hiperlan/2 [1].

First, a floating point analysis has been made. It can be supposed that in section B there is not clipping. Multipath channel model A is used. In Table II, standard deviation can be seen for 10dB SNR (BPSK) and 30dB SNR (64-QAM). It has been obtained that the worst case is 64-QAM (30 dB SNR). An error less than 1.6% can not be reached. For this error we have an SNR loss of 1.6dB. If less SNR loss is desired, a fine frequency offset technique must be also used. In BPSK (10dB SNR) there are not problems: the error is less than 5% and, therefore, the SNR loss is less then 0.5dB.

TABLE II
CFO STANDARD DEVIATION IN FLOATING POINT ANALYSIS

SNR	62.5kHz	125kHz	187.5kHz	250kHz
10dB	2.533%	2.579%	2.535%	2.525%
30dB	1.58%	1.58%	1.565%	1.579%

In order to reduce errors in CFO estimation, section C of the broadcast preamble is used. First, the estimated coarse CFO must be compensated from samples of Section C. To do this we reuse the same CORDIC that was employed for coarse CFO estimation. Next, corrected Section C is autocorrelated using a delay of 64 samples and an average of 96 samples. Then, the obtained peak is used to calculate fine CFO with the same CORDIC as before. The autocorrelation can be performed with the same structure used in A, B sections. Only some multiplexers in the delay block and in the average block must be included (Fig. 7). In this case:

$$R(m)=\sum_{k=m}^{m+95} r_{cx}(k)\,r_{cx}^{*}(k-64) \qquad (8)$$

$$P(m)=\sum_{k=m}^{m+95} |r_{cx}(k)|^{2}$$

The autocorrelation scheme used to detect C peak has D=64, so $\hat{f}_{o\max}$ =156,25kHz. This frequency offset is lower than the worst case of 212kHz. For this reason, first it is necessary to perform a coarse CFO estimation and, after compensation, a fine CFO estimation. In this, standard deviation for 30dB SNR (64-QAM) is less than 0.3% in a floating point analysis.

Now, a fixed point analysis has been made. Our frame and time synchronizer only needs 5 bits in the input. We have checked that this input precision is not sufficient for the coarse and fine CFO estimator. At least 6 input bits are needed as can be seen in Fig.7. Moreover, the output of the multipliers and the output of the average must have complete precision. The inputs of the CORDIC need 8 bits precision and the output must have also 8 bits. In Fig. 8 final synchronizer is shown. The CORDIC used in the CFO estimation can be reused in CFO correction, so the required hardware is reduced. A standard deviation of 0.35% is reached with the implemented fine CFO estimator, so SNR loss is less than 0.5dB, as shown in Fig. 9.

Once fine CFO is calculated, Section C must be corrected before being used for channel estimation. The received OFDM symbols must be corrected with a combination of the coarse and fine CFO estimation.

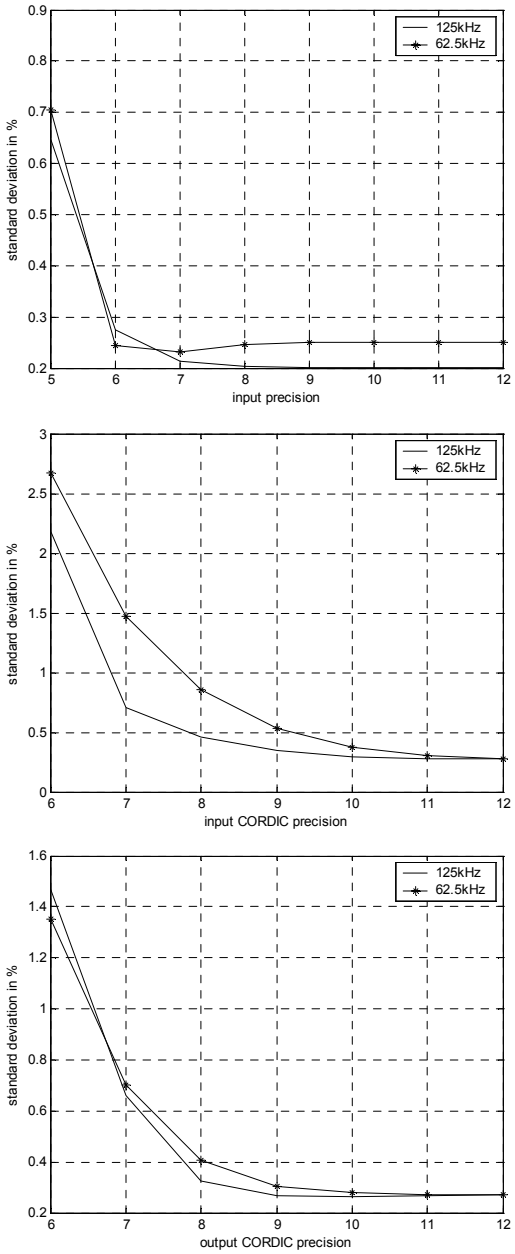

Fig. 7. Finite-precision analysis: (a) input quantified and the other blocks in floating point; (b) 6 bits input, multipliers with complete precision -12 bits- and input CORDIC quantified; (c) complete synchronizer quantified

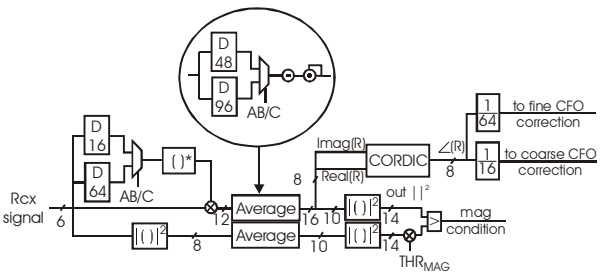

Fig. 8. Final synchronizer

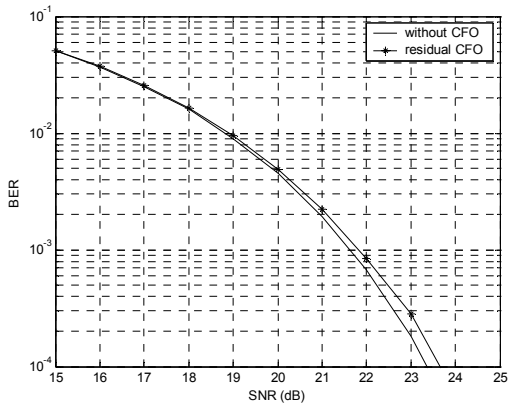

Fig. 9. Measurement of SNR loss due to residual CFO for 64-QAM

A. CORDIC

CORDIC is an iterative algorithm for the calculation of the rotation of a two-dimensional vector, in linear, circular and hyperbolic coordinate systems, using only add and shift operations. It consists of two operating modes, the rotation mode (RM) and the vectoring mode (VM). In the rotation mode a vector (X,Y) is rotated by an angle θ to obtain a new vector (X',Y'). In every micro-rotation i, fixed angles of the value $\arctan(2^{-i})$ which are stored in a ROM are subtracted or added from/to the remainder angle θ_i, so that the remainder angle approaches to zero (Fig. 10). In the vectoring mode, the length R and the angle α towards the x-axis of a vector (X,Y) are computed. For this purpose, the vector is rotated towards the x-axis so that the y-component approaches to zero. The sum of all angle rotations is equal to the value of α, while the value of the x-component corresponds to the length R of the vector (X,Y). Hence, the mathematical relations to be iterated are shown in (9). By selecting the appropriated value for the parameter m in (9) a different coordinate system can be achieved (m=0,1,-1 corresponds to linear, circular, and hyperbolic coordinate system, respectively).

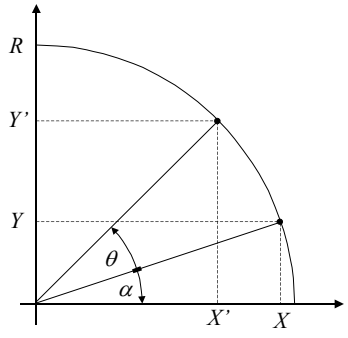

Fig. 10. The rotation and vectoring mode of the CORDIC algorithm

$$\begin{aligned} X_{i+1} &= X_i - \sigma_i \cdot 2^{-i \cdot m} \cdot Y_i \\ Y_{i+1} &= Y_i + \sigma_i \cdot 2^{-i \cdot m} \cdot X_i \\ Z_{i+1} &= Z_i - \sigma_i \cdot \theta_i \end{aligned} \tag{9}$$

To satisfy an M-bit precision CORDIC operation, M+1 iterations are needed. Furthermore the length of the data-path to compute the X and Y variables has to be $N=M+2+\log_2(M)$ and for the computation of Z only a precision of M+1 is needed in the operations [9].

VI. Complete Synchronizer

Figure 11 shows complete synchronizer. It is composed of three blocks: frame detection, time synchronization and CFO estimation & compensation. Frame detection block is based on an autocorrelator and a circuit that finds Section A peak of the broadcast preamble. With this information, frame detection block generates an output (final_cond) that indicates where Section B peak can be found (±20 samples). Time synchronization block searches Section B peak of the autocorrelator output when final condition is accomplished. This peak is used to enable CFO estimation. Once coarse CFO is estimated, CFO in Section C is compensated using this information and, next, fine CFO is estimated (autocorrelation of Section C is done using the autocorrelation circuit of the frame detection block, and then Section C peak is found with time synchronization block). Finally, input OFDM symbols are compensated with coarse and fine CFO estimation.

VII. Hardware Results

The design of all necessary circuits has been done using the tool System Generator from Xilinx [12], this tool is integrated in the Matlab-Simulink environment and allows rapid prototyping. The synchronizer has been implemented on a Spartan-3 Xilinx FPGA. These devices have slices composed by look-up tables to implement logic, arithmetic resources to propagate carries, and embedded multipliers that can be used to simplify our design. In table III are summarized the resources that are required by each block.

So, the whole synchronizer requires 827 slices and 10 embedded multipliers and runs at 20MHz. The design fits in a XC3S400-4 Spartan-3 device (4775 slices, 16 BRAM and 16 embedded multipliers).

TABLE III
HARDWARE RESOURCES

	Slices	**Mults**
Frame Detection	411	8
Time Synchronization	64	0
CFO Estimation & Compensation	310	2
Control Logic	42	0

VIII. Conclusions

In this paper we have presented a hardware design of a frame, time and frequency synchronizer for Hiperlan/2. We have taken one of the algorithms proposed in [5] and have introduced some simplifications to reduce the area cost of the final circuit. Finally, we have implemented all the necessary circuits in a low cost Xilinx FPGA to validate the

process.

As it is shown is Table I, DF and FA probability is low enough in the studied case (10dB SNR, channel model A and signal clipping), so frame synchronization is accomplished. Time synchronization is achieved in channel model A, but in other multipath channels, with higher delay spread, we have to study other techniques in order to reduce the timing offset, for example, by using channel impulse response estimation. Frequency synchronization applied gets a SNR loss less than 0.5dB, for the worst case 64-QAM. Residual frequency offset must be corrected with carrier phase tracking. Our future work will be centered in fine timing offset estimation and carrier phase traking.

ACKNOWLEDGEMENTS

This work was supported by the *Ministerio de Cicencia y Tecnología* under Research Project TIC2001-2688-C03, by *Generalitat Valenciana* research grant CTBPRB/2002/225, and in part by the *Universitat Politècnica de València*.

REFERENCES

[1] ETSI TS 101 475 v1.2.2 BRAN ; HIPERLAN Type 2 ; Physical (PHY)layer.

[2] R. Van Nee and R. Prasad. *OFDM for Wireless Multimedia communications.*Archech House, 2000.

[3] T. Schmidl, and D. Cox. "*Robust Frequency and Timing Synchronization for OFDM".* IEEE Trans. On Comm. Vol 45, No. 12, December 1997.

[4] S. Johansson, M. Nilsson, P. Nilsson. "*An OFDM Timing Synchronization ASIC".*ICECS2000. Jounieh,Lebanon, 2000.

[5] V. Almenar, S. Abedi, Rahim Tafazolli. "*Synchronization Techniques for HIPERLAN/2".* VTC 2000 (Fall), Atlantic City, USA, 2002.

[6] A. Fort, J. Weijers, V. Derudder,W. Eberle, A. Bourdoux. "A performance and complexity comparison of auto-correlation and cross-correlation for OFDM burst synchronization". ICASSP 2003. Hong Kong, 2003.

[7] BRAN WG3 PHY Subgroup. *Criteria for Comparison*. ETSI/BRAN document no. 30701F, 1998.

[8] J. Khun-Jush,G. Malogren, P.Schramm and J. Torsner. *HIPERLAN type 2 for broadband wireless communication.* Ericsson Review No.2, P108-120, 2000.

[9] J. Valls, M. Kuhlmann, K.K. Parhi, "Evaluation of CORDIC Algorithms for FPGA design", Journal of VLSI Signal Processing, Vol. 32, No. 3. pp. 207-222, Nov 2002.

[10] M.J. Canet, F. Vicedo, J. Valls, V. Almenar. "*Design of a digital front-end transmitter for OFDM-WLAN systems using FPGA".* ISCCSP 2004, Hammamet, Tunisia, 2004.

[11] J. Heiskala, J. Terry. *OFDM Wireless LANs: A theoretical and practical guide.* SAMS Publishing, 2001

[12] Xilinx System Generator for DSP v2.2 Reference Guide.

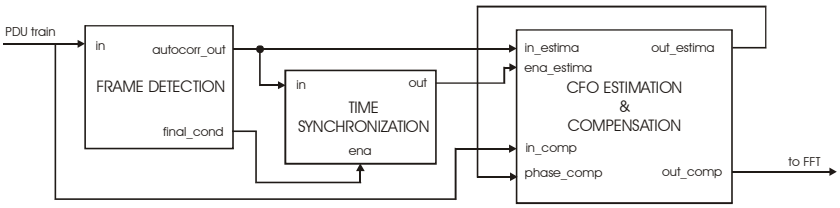

Fig. 11. Complete synchronizer

Development of a Software Defined Radio UWB Prototype Based on COTS Devices

André Gustavo M. Lima
IESB
Brasília - DF - Brazil
agmlima@brturbo.com

Erlison O. Santos
IESB
Brasília - DF - Brazil
erlison@eos.com.br

Francisco Carlos P. Dias
IESB
Brasília - DF - Brazil
dias.francisco@brturbo.com

***Abstract*— The future of mobile communication in an environment with heterogeneous network, implies the need of simpler interfaces for users, so they can use all the technological advances available in those nets. To enable the development of these interfaces, the use of techniques, like Software Defined by Radio (SDR) and Ultra Wideband (UWB), which provides a real mobility between the nets is important, with the use of Commercial Off The Shelf (COTS) devices, allowing the solution to be economically viable.**

In this article are presented the characteristics of a SDR architecture, with the use of UWB technique, based on COTS devices.

***Index Terms*— UWB, SDR, COTS, wireless communication, IWT2004.**

I. Introduction

SDR is a technology that will allow the use of different waves and standards, based on the reuse of the minimum hardware base for its functions and self-reconfiguration. The SDR objective is to manipulate the parameters, presently determined by hardware, by means of software. Its basic function consists in the conversion of the received signal directly into a digital signal, allowing its treatment through digital processing of the radio signal. This processing must be based on digital processors of signals (DSP), Field Programmable Gate Array (FPGA) or Application Specific Integrated Circuits (ASIC's). With the exception of ASIC, these devices make the radio flexible, allowing for the configuration of the equipment by a simple substitution of the program, permitting itself to substitute, modify or alternate protocols, modules of codification of the channel and the source, diverse keys of authentication, archives for reconfiguration of the device, among others.

The multifunctional equipment flexibility and possibility of communications observed in the SDR associated with the UWB will be able to offer benefits in systems of communications used currently. This union of technologies could become a market standard and be used in Wireless Personal Area Network (WPAN), in which Bluetooth technology is more use currently.

Some undesired limitations in the use of the Bluetooth, like the bit rate of 1 Mb/s, allows only the substitution of the handles of mice, keyboards and printers. The substitution of the cables of monitors, linking with DVD devices could be supplied through UWB, making possible even the connection of cellular telephones with external cameras, because of the 500 Mbps transmission rates available.

With a scattering wider than the current standardized systems and with a power of transmission of about 75nW per MHz, UWB still allows communication, used in the free band, which is more immune to interferences. Among the challenges for the implementation of this technique, are those related to the blocks of transmitters directly influenced by the wide band of this technique, as is the case of amplifiers of low noise and mixers.

II. Convergence

The concept of a communication system integration requires two different characteristics. The first is a global extension which reaches all geographic areas, called Roaming. The second is an interface with different systems and service standards, regarding location. An example would be the multimode handsets, which can work in different standards, like IS-95 and GSM.

Others standards for wireless communication are developed in the world, indicating the presence in several systems with high transmission capacity of data between the mobile devices, like Wireless Local Area Network (WLAN), Wireless Metropolitan Area Network (WMAN) and Wireless Personal Area Network (WPAN). The use of those nets has increased in recent years, especially in corporations, public environments with access points and even in residences.

The standard of the next mobile devices, that will contain all those technologies, will need elevated flexibility to attend to each of those standards, allowing for wireless communication regardless of the interface, protocol or net available in the environment. Systems and devices that use the concept of reconfigured radios are radios that can alternate to different communication protocols by moving among the many environments. An example of that, could be the handover from standard 802.11b to 802.11a and then to Wideband Code Division Multiple Access (W-CDMA). These systems could support simultaneously many radio protocols in several bands of frequency through multiple operation environment in wireless. Through the more intelligent implementation of radio devices, there will be a convergence of several services in a single terminal, which will allow, for example, access to a wireless LAN, digital TV, cellular service, etc.

Thus, it is possible to use the concept of software defined radio to attend the necessary flexibility, reaching the major objectives and problems that can occur in the development of a device in the way of 4G.

III. Software Defined Radio

With the growing advance in telecommunication, it becomes necessary to implement equipment that can interact simultaneously with many technologies. The digital signal processors are a positive factor, because they allow work with digital data, through the use of software, make new implementations more flexible.

The first SDR prototype was developed by the American Defense Department, and only one radio had capacity to communicate simultaneously with four other communication systems. Several other projects were developed by DoD and, in function of the need of creating a standard, a group was created with the objective to stimulate, standardize and develop applications and integration with existing services for SDR. This group was known as the SDR Forum, which has the support for more than 100 companies.

A. Architecture

The SDR architecture is divided in four basic units: antenna, analogical/digital converters (ADC), digital/analogical converters (DAC), digital signal processors (DSP) and the software.

The antenna is responsible for the transmission and reception of the electromagnetic waves. In the SDR, antennas need to be able to work with a large band, adequate to attend to many systems of wireless communication.

Another important factor in the SDR implementation is the digitization of the RF signal, currently executed by ADC and DAC. The digitalized signal allows the processors to execute functions through the software, previously executed by hardware. Application Specific Integrated Circuits (ASIC), Digital Signal Processors (DSP), and Field Programmable Gate Arrays (FPGA) allow the filters, equalizers, wave shapes etc. to be packages of programs executed by one chip. With this, less energy is consumed, less space is occupied at a low cost if it is compared to analogical equipment.

Software can be divided in three layers. The first layer, physical, is implemented in the digital processors, enabled the use C language and VHDL, for development. The software of this layer is responsible for frequency selection, channel separation and the output power. The intermediate layer is responsible for the modulation project, transference rate, Quality of Service (QoS), authentication and management of the equipment. In the third layer, applications are the programs used to interface with users of mobile terminals, such as games, electronic commerce, video, voice, etc.

IV. Ultra Wideband

With the growth of the use of wireless communication and the need for large volume of data transmission in WPAN nets, has become a large capacity of transmission in communication channels necessary. This demand for high transmission rate implies in a use of larger frequency band by communication channels. The Ultra Wideband (UWB) is a novel term to determine a technology that was already known by the researchers of electromagnetic and mobile communication areas. The UWB uses old concepts, from the years between 1870 to 1950, developed to provide wireless transmission, awaited and well accepted by the users in the new millennium.

The UWB was first used in military mobile communication applications. A UWB signal is characterized by an spectrum that occupies a band larger or equal to 20% of the central frequency, measured considering the 10dB attenuations or bandwidth greater than 500MHz. An UWB transmitter sends billions of pulses through an large spectrum of frequency around many GHz, without remaining in the same frequency for more than some fractions of a second. Only the two parts involved know the frequency standard used, which helps to maintain the data security [5].

One of the greatest advantages of UWB technology is the possibility of UWB transmitters not jamming with other radio transmission handsets not among them selves. It is because the short space of time in which two handsets can operate in the same frequency would not confuse the transmission. Another advantage is the low spectral density of power (figure 1) which helps to solve coexistence problems, because to transmit in UWB only 75nW per MHz, is needed or about 0.26mW. By the comparison with others technologies, like Bluetooth stays between 1mW to 1W, or the radios 802.11b that stays between 30 to 100mW, the UWB devices keep lower levels.

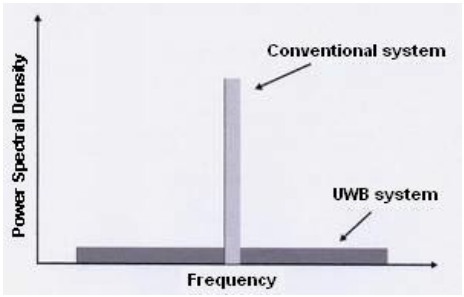

Fig. 1. Power Spectral Density

Another aspect very important for WPAN is the high transmission rate that the UWB devices can reach over short distances, being able to reach a 500 Mbps within 5 meters distance, or close to 250Mbps when the distance is increased to 10 meters. The typical rate of transmission in a WLAN are respectively 11Mbps and 54Mbps for standards IEEE 802.11b and IEEE 802.11g. Thus, in a 10 meter distance UWB is 4.6 times faster than the standard “g” and 22.7 times faster than the standard “b”.

The UWB technology is being studied by the work group TG3 from IEEE, which is verifying the possibility of creating a standard IEEE 802.15.3a for WPAN with multimedia applications. These group is

studying two proposals, the first uses the multiplex OFDM technology with QPSK modulation; and the second works with spread spectrum technology, Direct Sequence (DS) and BPSK modulation.

A. Proposal 1

An Orthogonal Frequency Division Multiplex (OFDM) is a multi carrier transmission technique that divides the spectrum in to many bands. This multiplex technique becomes similar to Frequency Division Multiple Access (FDMA), considering the division of the spectrum in many frequency bands with many carriers. The main difference between OFDM technique and FDMA is the space between the carriers, which is minor in OFDM, because the carriers are orthogonal. Thus, these orthogonal characteristics is a great advantage of the systems that use OFDM, allowing for transmission of large amounts of information with the same range of band, figure (2).

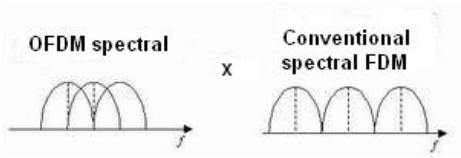

Fig. 2. OFDM spectral

Some concerns need to be considered in order to maintain this advantage:

- perfect synchronism between the receiver and the transmitter;
- analogical components of receivers and transmitters need to have a good quality;
- attention should be given to possible problems in multipath channels.

A great part of transmissions using UWB, are carried through multipath channels, and it is necessary to use a insertion of cyclical prefix (figure 3) where the last part of the OFDM symbol is inserted in the beginning of it.

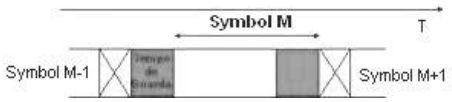

Fig. 3. Insertion of Cyclical Prefix

This procedure allows the periodic signal to help avoid the Inter Symbolic Interference and the interference between carriers. If the interval of the prefix is bigger than the maximum delay of the channel, the reflections of the previous signals will disappear before the real signal begins to be analyzed. The cyclical prefix is removed in the receiver, eliminating any form of interference. However, this part of the signal does not carry information, reducing the signal/noise rate.

B. Proposal 2

In the technique of Direct Sequence Spread Spectrum, the information signal is multiplied by a pseudo noise code, known as ”chip sequence”. The signal coder is a generated binary signal in a much large frequency than of that the rate of the information signal. It is used to modulate the carrier in order to expand the bandwidth. In the receiver the information signal is restored through a complementary process using a similar generator and synchronized local code with the code generated in the transmission.

In order to use a large width of band for transmission, the systems in direct sequence make use of a few channels inside of the band. These channels are totaly separate so as not to generate interference among them. The advantages of this technique are: the tuner is simpler, therefore it does not need to change frequency constantly. The spread process is simple; therefore, it is carried through the multiplication of the signal of information for a code and greater transmission capacity.

The disadvantages of this technique are: difficulty to keep the synchronism between the generated signal and the received signal; difficulty in solving problems of interferences and the cost of the equipment.

C. The future

The UWB uses radio controls of low energy in the form of short pulses. With the generation of millions of pulses for second, devices UWB can transmit great amounts of data. The potential applications of the technology include local wireless, domestic multimedia nets, direct communication between mobile devices, radars and sensors that help in the control of collisions.

In WPAN, gradually the Bluetooth chips will be substituted by technology UWB, that will be able to pass through until 500Mbps of data between devices within residences and offices, with range of up to 30 meters. The first UWB chipsets are already being produced and UWB devices will arrive at the market until the end off 2005. From 2010 the UWB will be part of our daily life and by 2020, it will be used in the whole world. With it, we will be able to distribute points of video through the home, that will have access to a central server of media, similar to set-top box, capable of distributing different channels to the diverse receivers [4].

V. SDR WITH UWB

The major UWB projects are based on implementations using hardware, like sample circuits and match filters. A disadvantage of the sample circuits is the reduction of the data rate, because received pulses are used as sample, by catching series of snapshots to produce a final wave shape. Thus, multiple pulses per bit are necessary to transmit data, limiting the maximum data rate. In order to demodulate data using match filters, it is necessary to estimate the received pulses in the receiver and correlate it with the wave form received. A system with this architecture needs to have a stable oscillator and a high precision time.

Another component, the sweeping receiver, is needed in multipath problems. It is hard to implement a hardware capable of creating a signal with enough energy. Multiple correlator are needed to determine

each multipath of the channel which detects the time each correlator needs to be activated and determine the channel polarity. A perfect synchronism is necessary where the pulse rate is high, because the time of processing the data and the delay in the propagation of the signal become a problem.

There are other disadvantages like extra hardware and a limited number of sweepings because of the fixed number of correlators.

Some of those disadvantages are solved by using SDR concepts, which provide a better flexibility compared to hardware implementation. The capacity of auto reconfiguration allows the use of various modulation schemes in a transmission using UWB.

The device can be adapted to the different transmission rate available in the environment. So, for a lower bit error rate (BER), in multipath, multiple pulses per bit can be sent after the match filters have already been formed. An algorithm of digital match filter is needed for the demodulation of data using a match filter model pilot based, which is generated in software. Another possibility is the increase of the data rate in indoor environment without obstacles. In this case, the software needs to process the data more quickly. All those different situations can be controlled more easily by using software, which makes the SDR with UWB a system that more easily adapts to different environments existing today. But, there are some limitations in the conception of these devices, using COTS elements.

A. Limitations

Two of the main components of the receiver, the ADC and the DSP, together with the clock distribution hardware are commercially available to adjust to the requirements of the system. However, those components have some significant restrictions in the system project, although some of those components offer favorable specifications [3].

1) Analogical to Digital Converter: The basic limitation of an ADC is the analogical bandwidth received, in other words, the frequency band of the converter can provide a sample of a signal without great losses in relation to the original. Most of the ADC available in the market, like the ones from Texas Instruments and Analog Devices, have a bandwidth of 500MHz. The ADC with high performance available in the market, manufactured by Atmel or by Maxim, can operate with a bandwidth from 2 to 3GHz. These highly specialized converters are available, however they represent a high cost for the system project. Thus, using ADC available in the market, the communication system using UWB will be restricted to using one pulse in base band below of 2 or 3GHz, or one that has a duration time greater that 333 or 500ps, depending on the chosen converter.

Another practical limitation of an ADC is the variation of delay. The delay is a time between the ADC increasing edge of the signal of clock and the point where the ADC really begins to show the received signal. For a system using just an ADC, the opening delay is not so serious. For a technique of parallel sampling in the domain of time, the receiver performance is based in each ADC sampling of the received signal in intervals of time equally spaced. If the delay of opening in each ADC is constant, the time between the samples remains constant, so the variation of the delay will be equal to zero. However, if the delay modify significantly in ADC, the received signals will be distorted, because the spaces will be different. The typical ADC with 100MSamples/sec or greater, has a variation of the opening delay between 50ps to 1ns. The performance of a digital receiver will be severely degraded if the variation of the opening delay is bigger than the sample rate, making the samples in the time overlap.

2) Digital Processing: The heart of the receiver is the hardware that does the digital processing. It has to be capable of treating multiple streams of data from the ADC and treating the data in real time. With the objective of attending to the specifications of the project, the DSP must be capable of self reconfiguration to provide the demanded flexibility of the SDR project. Considering those limitations, it is necessary to choose a FPGA for the block of digital processing of the receiver. The best FPGAs available nowadays are capable of manipulating multiple streams of data at a high rate, have some central processors inlaid for any necessary operations of DSP, and can easily be reconfigured for many modulation and demodulation projects. The practical FPGAs are limited by the rate at which they can enter with the data; and the maximum data rate realizable in a wireless link is limited by the necessary time for the processing and demodulation of each received pulse. A Xilinx, however, produces many FPGAS capable of maintaining data entry at a rate of 100Mbps.

3) Clock Distribution: As discussed before, the performance of the technique of parallel sampling in the domain of time is highly dependent at the sample received signal to be equally spaced in time. This way, a net of distribution of clock with low inclination is necessary. These restrictions of the signals of clock in the printed circuit must be used to assure that all the sets of tracks are synchronized. Eventually, this will complicate in the assembly of the plate, consequently causing the need to organize the components and the tracks.

VI. Final Comments

The future of the mobile communication presents many transmission techniques, with different rates, protocols and modulation projects together with some topologies of mobile nets that will dominate our homes, offices and public environment. Because of that, it will be necessary to develop a device or communicator capable of connecting or communicating with any electronic device existing at home or in offices, like refrigerators, fans, monitors of video, printers, and others. Besides, that it needs to maintain this connection during the movement of the user. That is because the majority of users would not like to carry

with them a set of electronic equipment they could use in the existing mobile nets.

Thus, the concept of the universal device must be created, an equipment that will allow total flexibility in an environment as mentioned above. This device will have to be fast in its decision regarding which net is offering the best service at a determined moment, monitoring continuously the level of the signal, to have agility in a possible change or reconfiguration to another air interface. It will need to offer to the user a form to maintain its data connection.

There are several challenges that the engineers will have to face in the conception of a universal device. However, concepts like Software Defined by Radio implemented in the COTS devices, will help to develop a system capable of reconfiguring itself thus enabling for instance, two transmission techniques in UWB, without the need to standardize such technology.

ACKNOWLEDGEMENTS

The authors are grateful to Dr. Eurice de Souza and Teacher William Vitelli for reading and making many constructive suggestions for the writing of this paper.

REFERENCES

[1] Roger Hurwitz and Bryan Peebler, *The Universal Communicator Handset Prototype*. Intel Research and Development, 2003.
[2] Patrick Mannion, *Ultrawideband radio set to redefine wireless signaling*. EE Times, 2002.
[3] Aaron Michael Orndorff, *Transceiver Design for Ultra-Wideband Communications*. Virginia Polytechnic Institute, 2004.
[4] J. Gerry Purdy, *The Next 50 Years in Mobile and Wireless*. Mobile Trax, 2003.
[5] Federal Communications Commission, *Authorization of Ultrawideband Technology, First Report and Order,*. Federal Communications Commission, 2002.
[6] Jeff Foerster, *Channel Modeling Sub-committee Report Final*. IEEE P802.15 Working Group for Wireless Personal Area Networks, 2003.
[7] MBOA Aliance, *Multi-band OFDM Physical Layer Proposal*. Multi-band OFDM proposal for IEEE 802.15 TG3a, 2003.
[8] C. R. Anderson, *Ultrawideband Communication System Design Issues and Tradeoffs*. Virginia Polytechnic Institute and State University, 2003.
[9] S. Srikanteswara, *Design and Implementation of a Soft Radio Architecture for Reconfigurable Plataform*. Virginia Polytechnic Institute and State University, 2001.
[10] Paul Burns, *Software Defined Radio for 3G*. Artch House, 2002.
[11] Antti V. Raisanen and Arto Lehto, *Radio engineering for wireless communication and sensor applications*. Artech House,2003.
[12] George Lawton, *Flexible Future*. 2001.
[13] Lars Godell and Matthew M. Nordan and Thaís Lapolla and Manuel Ángel Méndez, *WLAN and Bluetooth Update: Beyond the Hype*. Forrester Research, 2003.

Robust System for Generation of Clock Signals

Ricardo Bressan Pinheiro
Escola Politécnica of Universidade of São Paulo
Av. Prof.Luciano Gualberto, travessa 3, 158 – 05508-900
São Paulo - SP, Brazil
ricardo.pinheiro@poli.usp.br

José Roberto Castilho Piqueira
Escola Politécnica of Universidade of São Paulo
Av. Prof.Luciano Gualberto, travessa 3, 158 – 05508-900
São Paulo - SP, Brazil
piqueira@lac.usp.br

José Jaime da Cruz
Escola Politécnica of Universidade of São Paulo
Av.Prof.Luciano Gualberto, travessa 3, 158 – 05508-900
São Paulo - SP, Brazil
jaime.cruz@poli.usp.br

***Abstract*—In this paper, the generation of time signals in a network node, based on the weighting of phases from two master signals, is studied. A discussion about the stability of such system is conducted, using techniques of multivariable robust control.**

***Index Terms*—Synchronization signals; stability; multivariable robust control; LQG/LTR procedure.**

I. INTRODUCTION

The digitalization of telecommunication networks brought in the need to synchronize the nodes that are part of such networks. In other words,each network node must receive one or more clock signals, generated by devices called *master clock generators*, located at strategic points of networks.

The last ten years have seen the dissemination, in the telecommunication networks around the world, of the so-called *Synchronous Digital Hierarchy* (SDH) defined by several international standards organizations [1]. With the widespread adoption of this standard, optical fiber transmission media with high reliability became available, thus simplifying the task of sending clock signals to all network nodes.

As a consequence of the availability of such reliable and relatively cheap transmission media, the simultaneous existence of several reference signals at the network nodes has become a common ocurrence. In such cases, each of the clock signals reach a node after passing, in general, through different transmission paths.

The availability of several reference signals at the network nodes has made possible the use of the timing information present in all such signals, in the process of generating all the clock references that are to be emitted from the node being considered to other nodes.

In this work, the central idea is to use the device denominated *Phase Weighting Matrix*, or PWM for short, whose function is to assign *weights*, or coefficients, to the several reference signals available in one network node. The criterion for such weighting is to assign highest values of coefficients to the clock signals with smallest degree of impairments (for instance, smaller jitter amplitudes).

The working of the PWM must be such that, even in the event of failure of any reference signal applied to the device, the generation of the output signals is uninterrupted. This state of things is maintained while at least one of the input clock signals continues to arrive at the network node where is located the PWM.

In the situation of vanishing of all reference signals received by the node, it is necessary to use a local signal source of high stability. When there are clock signals arriving at the node, this signal source must be synchronized by such signals, probably by use of an arrangement similar to that used in the PWM. Obviously, in the situation of failure of all input reference signals of the node, the generated output clock signals will be out of synchronization with the rest of the network.

In the proposed generation scheme, the output reference signals will have characteristics that are, approximately, equal to averages of the corresponding characteristics of the input clock signals. This fact is a consequence of the proposed structure for the PWM, to be discussed later. The characteristics of the more impaired input signals can be attenuated through the choice of weights, as explained before.

The main objetive of this work is, first, to propose a topology for the WPF. After this, in view of the high reliability that must characterize such structure, an evaluation is made of the stability of the proposed topology. This study is made using techniques of the theory of Multivariable Robust Control [2].

For the sake of simplicity, the proposed topology is considered in the situation corresponding to two input reference signals, whose effects result in the generation of two output clock signals. The extension to a greater number of input and output signals may be done following the same reasoning.

II. PROPOSED STRUCTURE FOR THE PWM

In order to understand the topology suggested for the PWM, it is necessary to discuss briefly the method normally used for transmission of reference signals from one node of a network to another., as depicted in Fig.1.

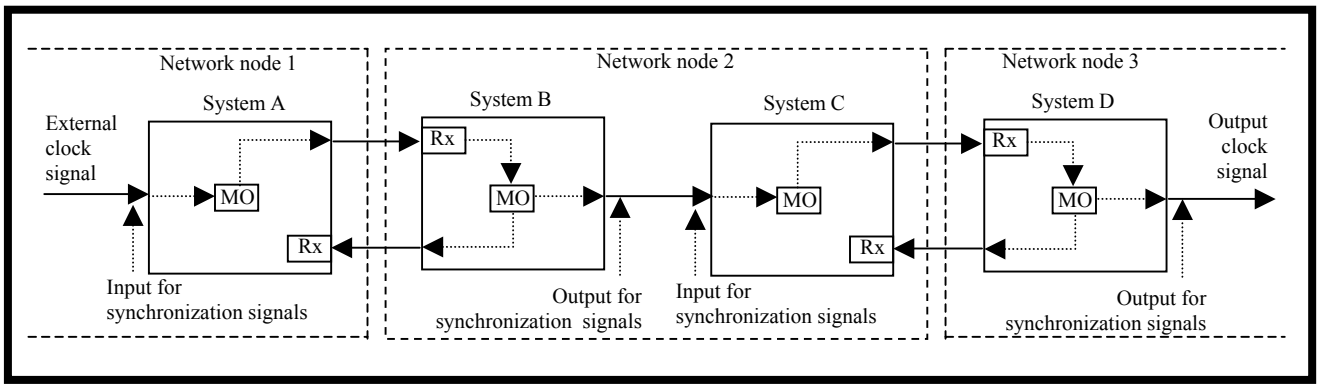

Figure 1 – Scheme for distribution of reference signals

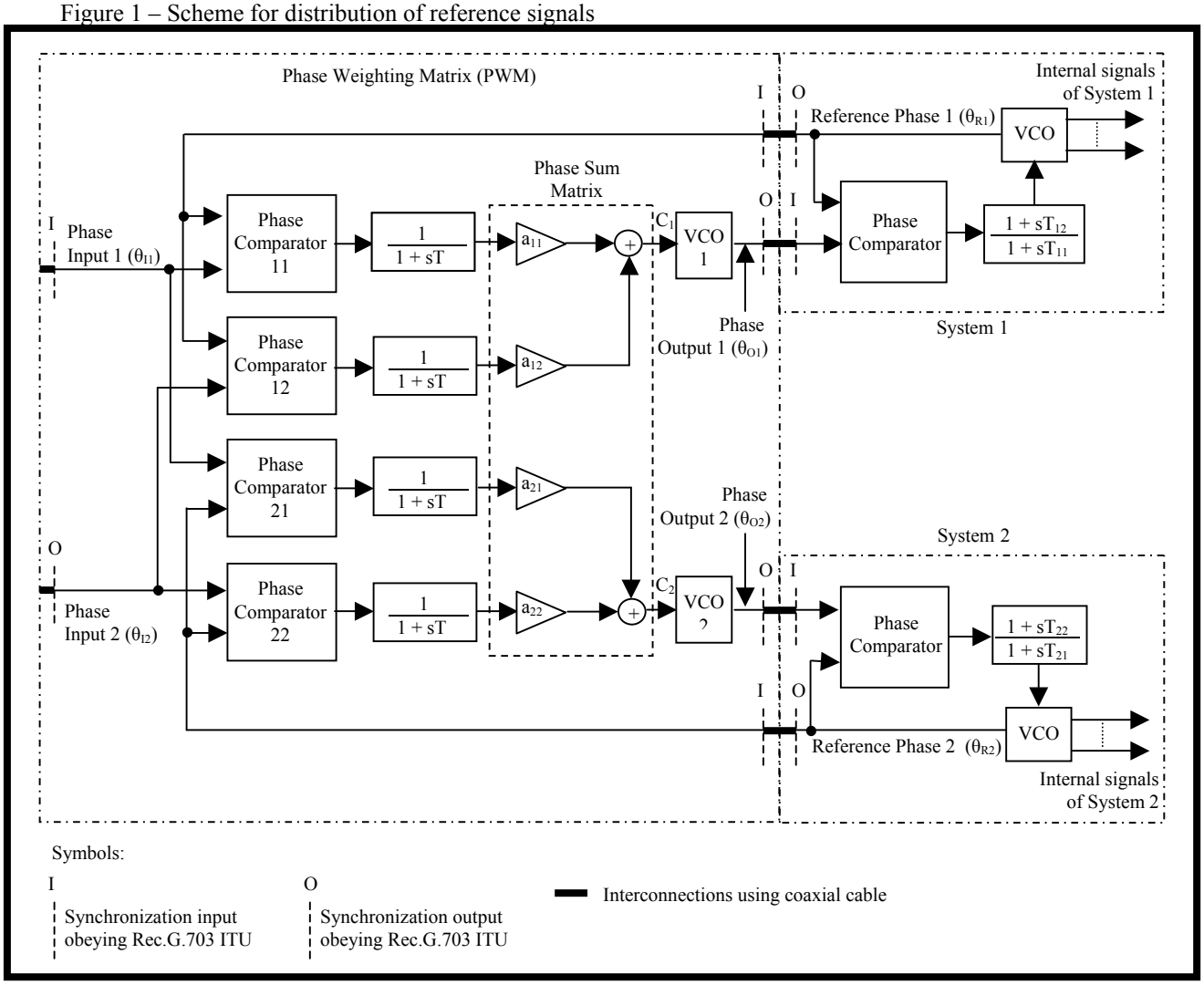

Figure 2 – Structure of the PWM

As can be seen from the figure, the inputs and outputs for synchronization signals are key elements in the scheme of transmission of reference signals between nodes. Such inputs and outputs are defined by international standards [3], which define the frequency of 2048 kHz for such signals, as well as electrical characteristics for these interfaces.

In the situation shown in Fig.1, a clock signal available at node 1, probably received in some way from other node of the same network, is applied to the synchronizing input of system A, so that the *Master Oscillator* (MO) of the latter becomes synchronized to that signal. All frequencies of system A are generated by the MO, and therefore are also synchronized with the clock supplied to the synchronization input of A.

System A generates a digital signal that is sent to system B, situated in node 2. This signal is

characterized by a clock signal, which is extracted in system B and further used to synchronize the MO of B. The digital signal transmitted by B back to A, and also the reference signal applied to the synchronization output of B, will be thus locked to the signal applied to the synchronization input of A.

The situation just described is repeated for the systems C and D, respectively situated in nodes 2 and 3. The final result is that the signal present at the synchronization output of system D, in node 3, is locked with the signal injected at the synchronization input of system A, in node 1.

Using the scheme just described, the master oscillators of all digital systems situated at the several network nodes can be synchronized with the high stability clock sources of the network.

The PWM was conceived to be introduced, in the scheme shown in Fig.1, in the position between the synchronization output of system B and the synchronization input of system C. Since the PWM is assumed to have two inputs, one of them must come from system B, and the other could be provided by the synchronization output of another system. Similarly, since the PWM is assumed with two outputs, one of them goes to the synchronization input of system C, while the other could be applied to the input of another system. This situation is general and could be found in any network node that receives, through different paths, more than one reference signal. The arrangement so described could be extended to a PWM with more inputs and outputs in an obvious way.

The main motivation for the introduction of the PWM in the nodes of a network is that the generation of output signals continues to be done while there is at at least one reference signal applied to one of its inputs. The main disadvantage is the additional hardware and the cabling needed to interconnect the inputs and outputs of the PWM to the associated systems.

The structure of the PWM is shown in Fig.2. This figure shows that the device receives two input reference signals that come from other systems in the same node. Such signals are combined, in phase comparators, with signals with reference phases (θ_{R1} and θ_{R2} in Fig.2), provenient from synchronization outputs of the systems associated with the PWM, indicated in the figure as systems *1 and 2*. Such systems also receive, from the PWM, signals with output phases (θ_{O1} and θ_{O2} in Fig.2), whose function is to control the PLLs that receive the synchronization inputs in these systems.

In this figure, it can be seen that each of the two reference input signals, with its corresponding phase input (θ_{I1} and θ_{I2} in Fig.2), is applied to two phase comparators. Each one of these comparators also receives, in its other input, one of the two signals that contains a reference phase, and that comes from the synchronizing output of a system associated with the PWM.

After each phase comparator, there exists a Low Pass Filter (LPF), characterized by just one finite pole, with associated time constant T, as shown in Fig.2. The function of each of these LPFs is to supress high frequency components that can be generated by the phase comparators, and is similar to the role of LPFs used in phase locked loops ([4],[5]). In the output of each LPF there is available an electrical signal proportional to the phase of the input signal applied to the comparator associated to that LPF. The phase of such input signal is measured relative to the reference phase contained in the signal applied to the other input of the comparator. In other words, the reference phases transported in the signals generated in the systems associated with the PWM are used to measure the phases transported by the input signals applied to the PWM.

Each output of a LPF is then applied to an input of the phase sum matrix, characterized by the coefficients a_{11}, a_{12}, a_{21} and a_{22}. These coefficients are such that $a_{11}+a_{12}=1$and $a_{21}+a_{22}=1$, in order to satisfy certain requirements, to be discussed later. The matrix outputs contain electrical signals, whose values are proportional to the weighted sum of the phases of the input signals of the PWM.

Each sum matrix output is applied to a crystal stabilized *Voltage Controlled Oscillator* (VCO), whose function is to generate a signal characterized by a phase that corresponds to the information contained in the respective signal applied to its input.

The signals produced by the VCOs are applied to the synchronizing inputs of the transmission systems included in the PWM. In each system, there is a *Phase Locked Loop* (PLL) which becomes synchronized by the respective input signal. In consequence, the MO of the same system and the clock signal present in the synchronizing output become locked to the same signal.

Through the action of the MO, all internal signals of the systems included in the PWM, in particular the signals that are transmitted to another network nodes, become locked to the signals present in the respective synchronizing inputs.

Finally, in each system associated to the PWM, the signals that transport the phase reference information are applied to the respective synchronizing outputs, and then return to the input of the PWM, where they are connected to phase comparators inputs.

From what has been said, the use of the PWM is strongly dependent on the existence of the synchronizing inputs and outputs in telecommunication equipment. This fact is not really a problem, since these types of interfaces are present in virtually all transmission equipment, and even in some switching equipment.

As can be seen in Fig.2, the two systems that are part fo the PWM are each represented by a PLL structure. The reason for such representation is that, in the present state of technology, all telecommunication equipment that includes synchronizing inputs and outputs uses a PLL to lock all the internal signals to the signals coming from the synchronizing inputs, and also uses the outputs from such PLL to generate the signals sent to the synchronizing outputs. Thus, from

the point of view of the PWM, the effects of the associated systems can be modeled by two PLLs, which are shown in Fig.2.

Since the two systems included in the PWM can possibly be distinct, the following hypotheses, relative to the PLLs of Fig.2, have been made:

i. The two PLLs are assumed distinct, representing different equipment, and implemented by analog-digital (mixed) realizations. These PLLs cannot be altered in any way, since they are part of the systems associated with the PWM;
ii. The LPFs included in these PLLs are assumed to be passive and characterized by one finite zero and one finite pole, with distinct associated time constants;
iii. The LPFs included in the PLLs are such that the jitter transfer characteristics defined by ITU [6] are satisfied;
iv. The VCOs of these PLLs have distinct *gain* constants K_V, and can have the so-called *parasitic poles*.

Such hypotheses have been made with the objective of reproduce common values and configurations used to implement PLLs. Newer implementations of these devices are in use, for instance all-digital PLLs, *software* PLLs [4],and so on. However, the dynamic behavior of such realizations is very similar to that of the implementations considered in this paper.

The reason for the choice of the passive type of lag type LPF is that it is a very well known topology, capable of satisfying most of the typical specifications for PLLs. Other LPF structures, for instance, the integrator with zero, will have effects over the dynamics of the PWM that are similar to those found with the chosen structure.

The other hypothesis made relative to the LPFs of the representative PLLs is that such LPFs are designed so the jitter transfer characteristics of the PLLs satisfy the specifications described in [6]. The reason is that these specifications have as main objective to limit the growing of jitter amplitudes as reference signals are distributed in a network following the scheme of Fig.1. Since such specifications are relatively restrictive, it is of interest to see how they can be introduced in the structure of the PWM.

The specified jitter transfer characteristic, and the jitter transfer curve for the PLL1, representative of system 1 of Fig.2, are both shown in Fig.3. It is not necessary to show the jitter transfer curve for the PLL of system 2, since it is very similar to that of PLL1.

It remains to discuss the hypothesis of parasitic poles that were assumed as occurring in the representative PLLs. Such poles have been reported in the literature ([5], [7], [8]) with values that cover a range going from 10 Hz to frequencies above 10 kHz, in the newest VCOs. The effect of such poles is to transform the transfer function of a VCO, ideally the same as that of a pure integrator, to the form

$$F_{VCO} = \frac{K_V}{s\left(1 + s/p\right)}$$

where K_V is the constant, or *gain* of the VCO, in rad/s/V;

p is the angular frequency of the parasitic pole, in rad/s.

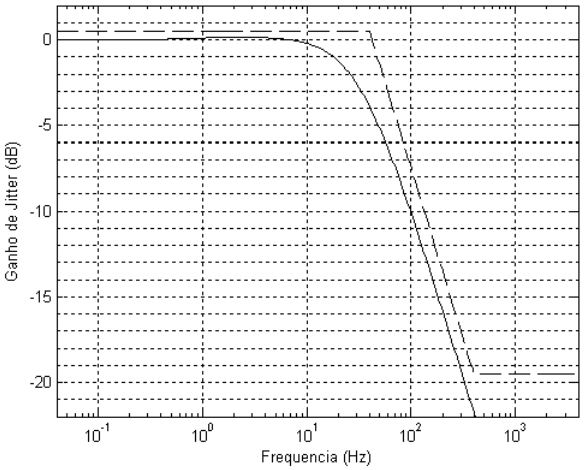

Fig.3. Limits for Jitter Transfer (dashed line) and Jitter Transfer Curve of PLL1 (continuous line).

The presence of parasitic poles can be verified by applying, to a VCO input, a pure sinusoidal signal with constant amplitude and variable frequency. As the input frequency is increased, a value is eventually reached where the frequency deviation of the output signal begins to reduce progressively, even though the input amplitude is constant. Such value is the frequency of the parasitic pole.

If a PLL is designed assuming ideal VCOs, and is implemented with components that can have parasitic poles, its behavior can differ markedly from that expected. For instance, the jitter transfer curve for PLL1 of Fig.2, assuming a parasitic pole at 10 Hz, is shown in Fig.5. It can be seen that the limits for jitter transfer are not satisfied anymore.

III. ASSUMED VALUES FOR THE PROPOSED STRUCTURE

Before we discuss the assumed values for parameters of the blocks shown in Fig.2, it is important to observe that the topology presented in that figure may be described by the mathematical model presented in Fig.4. It is important to observe that this model is based on the so-called *baseband model* of a PLL ([9], [10]), in which attention is focused on the phase errors θ_{Ii}-θ_{Ri}, i=1,2, independently of the value of quiescent frequency. Incidentally, the value of the latter frequency for all the phase signals θ_{Ii}, θ_{Oi} and θ_{Ri}, indicated in Fig.2, is 2048 kHz, since this is the frequency defined by ITU [3] for use in synchronizing inputs and outputs.

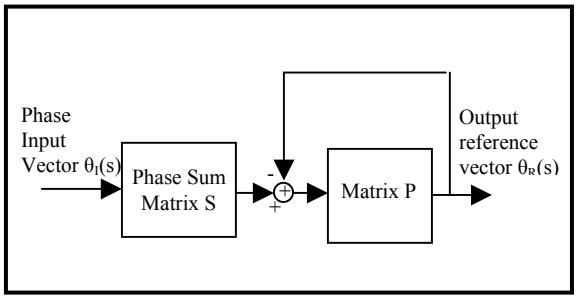

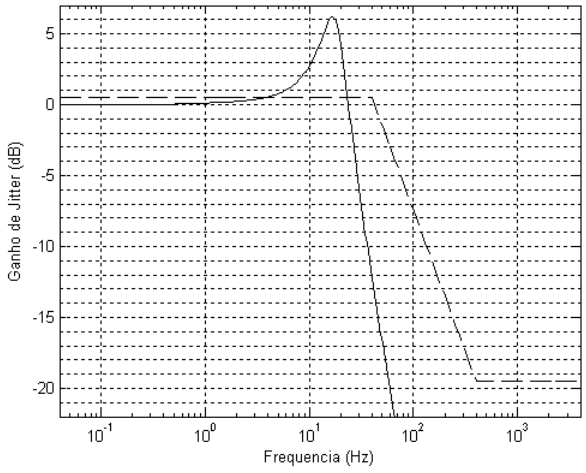

Fig.4. Mathematical model for the structure of Fig.2
Fig.5. Limits (dashed line) and Jitter Transfer Curve (solid line) for PLL1 assuming that itsVCO has a parasitic pole at 10 Hz.

In this figure, the indicated vectors and matrices are:

$\theta_I(s)$=vector of Laplace transforms of phase inputs, considered as baseband variables;

$\theta_R(s)$=vector of Laplace transforms of reference phases, considered as baseband variables;

S=phase sum matrix, discussed later;

P(s)=Nominal System open-loop transfer function matrix, which includes the phase comparators, the LPFs, the VCOs and the PLLs that represent the systems associated with the PWM. The reason for the name *Nominal System* will be explained later.

The mathematical model of Fig.4 is obtained through manipulations of the baseband variables associated with the structure of the PWM. It is important to observe that the signals θ_{Oi}, i=1,2, are considered as internal signals, and for this reason are not shown in Fig.4.

The vector $\theta_I(s)$ contains the phase information carried by signals provenient from synchronization outputs of systems situated in the network node. This phase information constitutes the real input to the PWM. On the other hand, the vector $\theta_R(s)$ is composed of phase signals that can be considered as the outputs of the PWM, since such signals reflect the phase information that is passed to the rest of the network, through the action of the signals transmitted by the systems included in the PWM.

Turning now to the phase sum matrix S, we observe that its elements are the coefficients attributed to the input phase signals, reflecting the degree of impairments presented by such signals. The matrix S is given by:

$$S = \begin{bmatrix} a_1 & 1-a_1 \\ a_2 & 1-a_2 \end{bmatrix}$$

where a_1 and a_2 are constants such that S is nonsingular, so that it is possible to use the techniques of robust multivariable systems. In the nomenclature of Fig.2, we have $a_{11}=a_1$, $a_{11}=1-a_1$, $a_{21}=a_2$, and $a_{22}=1-a_2$. As has been said, the choice of the elements of S must reflect the fact that one of the input signals of the PWM may have a degree of impairments greater than that of the other input. For the numerical evaluation of the behavior of the PWM, it was assumed that a_1 =0,80 and a_2 =0,70, thus indicating that input signal 1 has smaller levels of degradation than input signal 2.

Finally, the matrix P(s) is given by

$$P(s) = \begin{bmatrix} \frac{K_d K_V}{s(1+sT)} H_{PLL\,1}(s) & 0 \\ 0 & \frac{K_d K_V}{s(1+sT)} H_{PLL\,2}(s) \end{bmatrix}$$

where

K_V/s is the transfer function of the VCOs that are part of the PWM;

$1/(1+sT)$ is the transfer function of all LPFs of the PWM;

$H_{PLL1}(s)$ and $H_{PLL2}(s)$ are the transfer functions that represent the systems associated with the PWM.

The parameters associated with the matrix P received the following values, never losing sight of the need to use realistic figures:

i. The time constant T, that characterizes the LPFs of the PWM, was chosen as T=1,592 ms;
ii. The VCOs of the PWM have identical gain constants, equal to 1286,80 rad/s/V, and are assumed to have parasitic poles situated above 10 kHz, therefore causing little effects;
iii. The PLLs representative of the transmission systems included in the PWM have transfer functions of second order, with PLL1 characterized by ξ=3, ω_n=11π and constant of its VCO equal to 643,40 rad/s/V, and PLL2 characterized by ξ=2,5, ω_n=8π and constant of its VCO equal to 1286,80 rad/s/V.

The matrix P(s), with the values assigned as described, constitutes the open loop transfer function matrix of the part of the PWM that must operate inside a feedback loop. It is this part of the PWM that can cause instabilities, in view of the feedback loop, and will be analyzed later, to determine the necessary precautions to avoid instabilities. This part of the PWM will be called *Nominal System*, from now on,

since the possible sources of instability come from deviations with respect to this *nominal* model, for instance the existence of parasitic poles in the representative PLLs.

In terms of the matrices shown in Fig.4, the transfer function of the PWM is given by

$$G_{PWM}(s) = \frac{\theta_R(s)}{\theta_I(s)} = [I + P(s)]^{-1} \cdot P(s) \cdot S$$

where I is the identity matrix of same dimensions as P(s). It can be seen that the transfer function matrix $[I+P(s)]^{-1} \cdot P(s)$ corresponds to the Nominal System in the condition of closed loop.

IV. STABILITY OF THE PWM

Before the beginning of the study of stability of the PWM, it is important to emphasize that all the concepts and techniques here used, relative to the Multivariable Robust Control field, are based on references [2], [11] and [12].

The PWM is implemented, as Fig.2 shows, by a multivariable plant with two inputs and two outputs. For this kind of plant, the frequency response is given in terms of the so-called *singular values* [2] of the transfer function matrix that describes the plant. The singular values of a NxN matrix A are defined by

$$\sigma_i(A) = \sqrt{\lambda_i(A^H \cdot A)}, \text{ i=1,2…N,}$$

where

A^H is the transpose conjugate matrix of A;

λ_i is the i^{th} eigenvalue of matrix A.

Since the matrix P(s) is 2x2, it has two singular values, denoted respectively by $\sigma_M[P(s)]$ and $\sigma_m[P(s)]$, where *M* stands for *maximum*, and *m* stands for *minimum*. The frequency response of P(s) consists of the values of $\sigma_M[P(j\omega)]$ and $\sigma_m[P(j\omega)]$, calculated for all values of ω that constitute the band of angular frequencies of interest.

As it has been said, the part of this plant denominated *Nominal System*, situated inside the feedback loop of Fig.5, is the part of the PWM that will be studied with respect to instabilities. This Nominal System has P(s) as its open-loop transfer function matrix, and the singular values of such matrix, that is, its frequency response, are shown in Fig.6.

The stability analysis of a multivariable plant is done by the determination of the so-called *stability barrier* of this plant. This barrier is a function of ω that must be situated, for each ω, above the maximum singular values of the open-loop transfer matrix of the plant being studied.

For a generic plant with nominal open-loop transfer function $G_N(s)$, departures from such *nominal* model could result in plants characterized by several "real" open loop-transfer function matrices $G_R(s)$. For each real plant, a measure of the departure with relation to the *nominal* plant is given by the so-called *error matrix* ε(jω), defined by

$$\varepsilon(j\omega) = [G_R(j\omega) - G_N(j\omega)] \cdot G_N^{-1}(j\omega)$$

where

$G_R(j\omega)$=one of the possible open-loop transfer function matrices that could be obtained by departures from the nominal plant;

$G_N(j\omega)$=open-loop transfer function matrix corresponding to the *nominal* plant;

ω=angular frequency where the error matrix is evaluated.

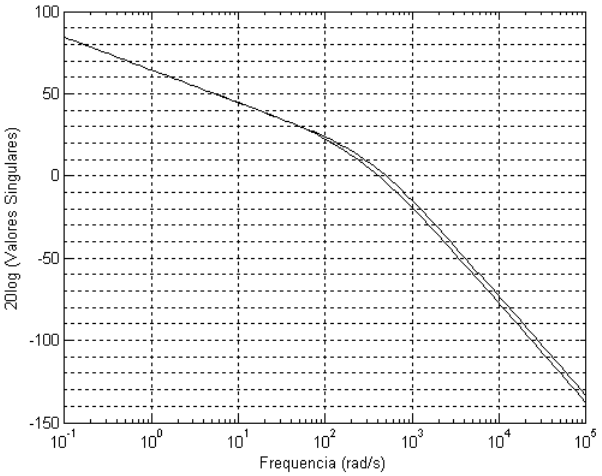

Fig.6. Singular values of the open-loop transfer function matrix P(s).

To determine the stability barrier, first a function e(ω) is defined such that the value of this function, at a particular value of ω, is equal to the maximum value of $\sigma_M[\varepsilon(j\omega)]$, found when all possible error matrices are evaluated at this value of ω. In other words, one has

$$e(\omega) = \{\sigma_M[\varepsilon(j\omega)]\}_{greatest\ among\ all\ \sigma_M[\varepsilon(j\omega)]}$$

The value of e(ω) at a particular value of ω is then a measure of the greatest modeling error. The corresponding value of the stability barrier b(ω) at this value of ω is defined as b(ω)=1/ e(ω), reflecting the fact that greater modeling errors impose greater restrictions over the behavior of a plant, for instance greater limitations over the values of frequency responses.

Once defined the function e(ω), the following relations must be satisfied [2]

$$\sigma_M[G_N(j\omega)] < b(\omega) \qquad (1)$$

and

$$\sigma_M\{[I + G_N(j\omega)]^{-1} \cdot G_N(j\omega)\} \qquad (2)$$

It can be seen that the stability barrier imposes restrictions over both the open-loop and closed-loop transfer function matrices.

For the case of the PWM, the unique possible departure from the Nominal System is the effect of the parasitic poles of the VCOs of the equipments. Such hypothesis is reasonable, since the phase comparators and LPFs are implemented with components with fairly close tolerances, and the VCOs of the PWM may be chosen as having parasitic poles at high frequencies. The gain constants K_V of all VCOs may also be assumed as having close tolerances.

The function e(ω) is then evaluated by calculating, for 101 values of ω covering the band of interest, the maximum singular values of the error matrices that result when all combinations of parasitic poles are used to calculate the possible matrices $G_R(j\omega)$. Of course, a finite number of parasitic poles is used for each of the two VCOs, but with a spacing between values small enough to give reliable results for the calculations. The parasitic poles have been assumed as located in the band of frequencies that extends from 10 Hz to 100 Hz, with 11 values considered in this band for each VCO, corresponding to a spacing between adjacent values of 9 Hz. It has been found that parasitic poles above 100 Hz have little effect upon the Nominal System, in view of the small bandwidths of the PLLs representative of the equipments.

With the assumptions made, the maximum singular values of the open-loop transfer function matrix P(s) and the stability barrier are plotted as functions of angular frequency in Fig.7. On the other hand, Fig.8 shows the maximum singular values of the closed-loop transfer function matrix of the feedback loop of the Nominal System, compared with the stability barrier.

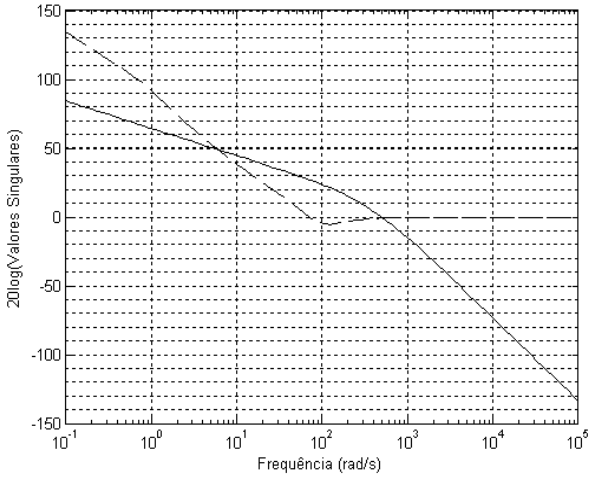

Fig.7. Maximum singular values (continuos line) of open-loop transfer function matrix of Nominal System and stability barrier (dashed line).

The figures show that neither of the relations (1) and (2) are satisfied, and so it will be necessary to introduce a multivariable compensator, characterized by transfer function matrix K(s), in series with the Nominal System. Thus the feedback loop of Fig.5 will include such series combination, whose open-loop transfer function matrix is now $P(s)\cdot K(s)$.

The determination of the compensator matrix K(s) is done according to the so-called *LQG/LTR* procedure [2], where *LQG* stands for *Linear Quadratic Gaussian* and *LTR* stands for *Loop Transfer Recovery*. This procedure yields a structure that is essentially composed of a state feedback regulator combined with a state observer. With K(s) defined by such procedure, the matrix $P(s)\cdot K(s)$ will be such that relations (1) and (2) will be satisfied, thus assuring the stability of the combination compensator-Nominal System. Fig.9 presents the singular values of the closed-loop transfer function $[I+P(j\omega)\cdot K(j\omega)]^{-1}\cdot P(j\omega)\cdot K(j\omega)$ compared with the stability barrier, and it can be seen that relation (2) is indeed satisfied.

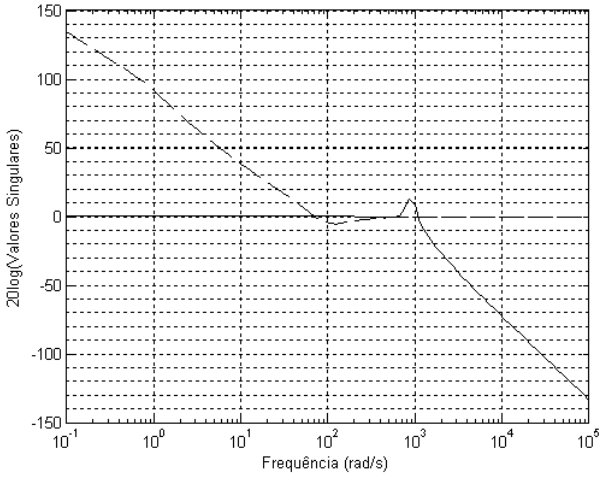

Fig.8. Maximum singular values (continous line) of closed-loop transfer matrix of Nominal System and stability barrier (dashed line).

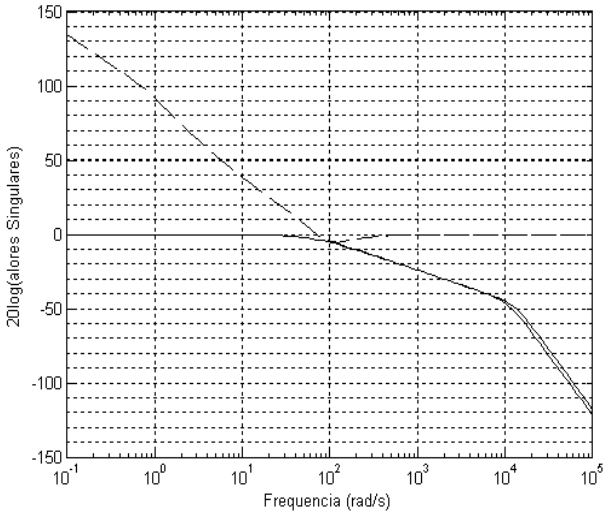

Fig.9. Singular values (continuous lines) of new closed-loop transfer function of Fig.5, and stability barrier (dashed line).

V. PERFORMANCE OF PWM WITH COMPENSATOR

The complete transfer function matrix of the PWM, including the compensator, is given by

$$G_{PWM}(s) = \frac{\theta_R(s)}{\theta_I(s)} = [I + P(s)\cdot K(s)]^{-1}\cdot P(s)\cdot K(s)\cdot S$$

The singular values of matrix $G_{PWM}(s)$ are shown in Fig.10.

After the characterization of the PWM in the frequency domain, Figs 11 and 12 show the time responses observed at PWM outputs for phase steps applied respectively to inputs 1 and 2. Fig.13 shows the time responses to phase ramps of amplitude $2\text{x}10^{-3}$ rad/s applied simultaneously to the two inputs of PWM.

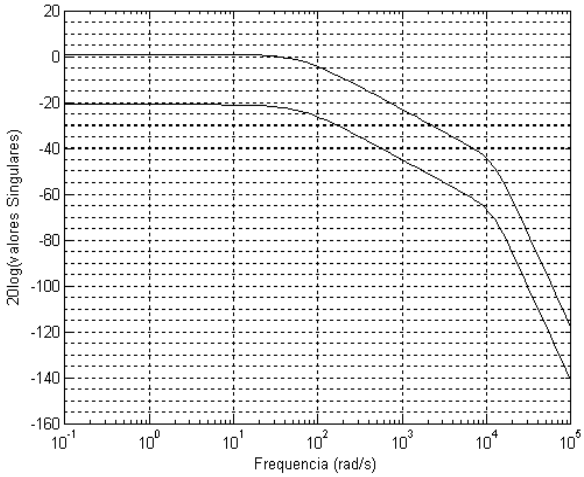

Fig.10. Singular values of complete structure of PWM, including compensator.

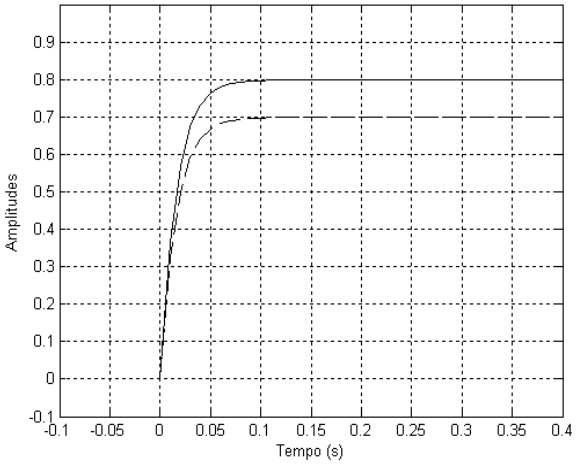

Fig.11.Responses at output 1 (continuous line) and 2 (dashed line) to unitary phase step applied at input 1.

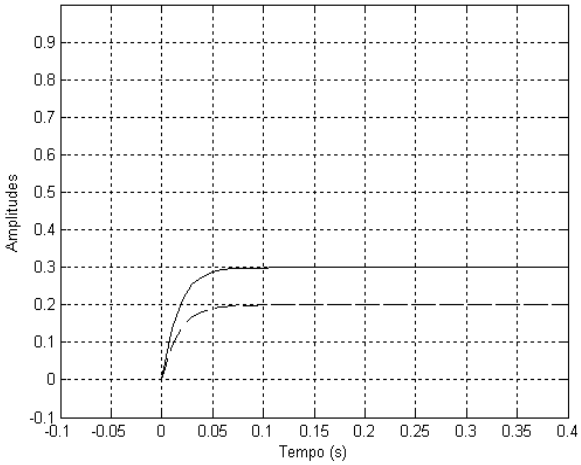

Fig.12.Responses at output 1 (dashed line) and 2 (continuous line) to unitary phase step applied at input 2.

Figs.11 and 12 show the effect of the weighting of the phase inputs. The responses observed at the outputs when the phase step is applied to input 1 have greater amplitudes than in the situation in which the phase step is applied to input 2. Fig.13 shows that ramps of phase are observed in the two outputs.

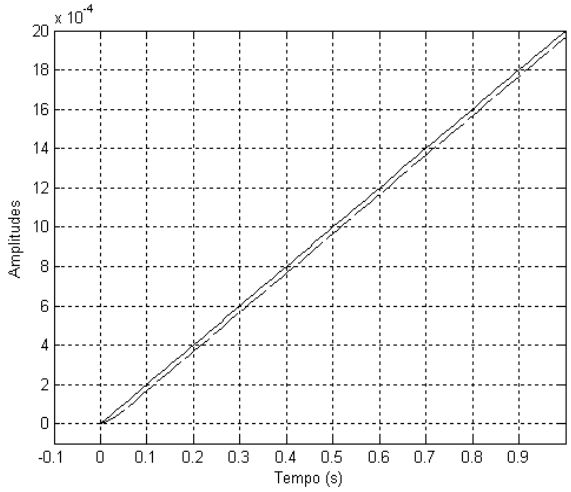

Fig.13.responses at output 1 (continuous upper line) and output 2 (dashed lower line) to phase ramp inputs of amplitude $2x10^{-3}$ rad/s applied to the two inputs of PWM.

VI. CONCLUSIONS

A structure (PWM) was proposed to generate reference signals that are to be sent from one network node to other nodes. Typical values for such structure were discussed, as well as possible limitations of the component blocks. The techniques of multivariable robust control were used to discuss and also to guarantee the stability of the PWM. Finally, the time response of the latter was simulated when phase step and ramp signals were apllied to its inputs.

The results of the simulations show that the PWM can effectively generate clock signals, using the information present in all its input reference signals. It can also be seen that the influence of each input can be controlled through its assigned weight.

VII. REFERENCES

[1] ITU-T, *Rec.G.707 - Network Node Interface for the Synchronous Digital Hierarchy,* ITU, 1996.

[2] J.J. da Cruz, *Controle Robusto Multivariável,* EDUSP, 1996.

[3] ITU-T, *Rec.G.703 - Physical/Electrical Characteristics of Hierarchical Digital Interfaces,*ITU, 1998.

[4] R.E.Best, *Phase Locked Loops - Theory and Implementation,* McGraw-Hill, 1999.

[5] W.F.Egan, *Phase-Lock Basics.* Wiley, 1998.

[6] ITU-T, *Rec.G.742 – Second Order Digital Multiplex Equipment Operating at 8448 kbit/s and Using Positive Justification,* ITU, 1988.

[7] R.S.Saunders, "PLACE 2.0 – An Interactive Program for PLL Analysis and Design"*, AT&T Technical Journal,* vol. 64, nº5, May-June 1985.

[8] CTS-Reeves, "Datasheet for Model 324 SM VCXO", CTS-Reeves, 2001.

[9] H. Meyr and G. Ascheid, *Syncronization in Digital Communications, vol.1 - Phase-, Frequency-Locked Loops and Amplitude Control,,* Wiley, 1990.

[10] S.Bregni, *Synchronization of Digital Telecommunications Networks,* Wiley, 2002.

[11] J.C.Doyle and G.Stein, "Robustness with Observers", *IEEE Transactions on Automatic Control,* vol. AC-24, nº4, August 1979.

[12] J.C.Doyle and G.Stein, "Multivariable Feedback Design: Concepts for a Classical/Modern Synthesis", *IEEE Transactions on Automatic Control,* vol. AC-26, February 1981.

Development and Production of Fiber Based Optical Components for Telecommunications in Brasil

F.M.Smolka
Optolink, Ind e Com. Ltda, Campinas, SP, Brasil
smolka@optolink.com.br

Abstract — **The intent of this presentation is to show the actual work being done in the field of optical fiber based components and its results, focused preferentially on the necessity of the optical communication industry in Brasil.**

***Index Terms*— Optical fiber coupler, optical passive device.**

I-INTRODUCTION

Research work on optical fiber based components, for optical communication, started in Brasil, in the early 80's by the pionering efforts done by the Telebrás Research Center (presently Fundação CPqD) [1]. By the end of the 90's, the use of commercial bidirectional optical links increased the interest for local industrial production, specially of 3dB optical couplers for operation at the 1.31 micron wavelength region. Since then, the use of this type of components has been expanded to applications in Erbium doped optical amplifiers (EDFA), passsive optical network (PON) wavelength division multiplexing (WDM, CWDM) systems as well as in CATV, LAN and for optical fiber sensors technology. A compreensive status of the state the art of this type of technology, one can find in [2].

The intent of this presentation is to show the actual work being done in the field of optical fiber based components and its results, focused on the necessity of the optical communication industry in Brasil.

II-BASICS

A Theory

When two singlemode optical fibers are fused together and then streched, guided light that is originally concentrated in the core of one of the fibers, expands to the whole fused section and two guided modes are excited and beating between them occurs. The coupling coefficient of this beating process depends on the shape and overall dimensions of the fused section as well as in the wavelength and the external index of refraction. So, by controlling the geometry of the taper and fused region, various types of ligtht transmission characteristcs in the output fibers can be achieved.

The theoretical basis has been established many years ago [3-5], with great sucess in explaining what is observed and providing the theoretical mainframe for the development of new devices. The power output in the coupled fiber is given by [5]:

$$P_{out} = P_{in}.\ F^2.\ \sin^2\{(C_{12}.C_{21})^{1/2}.\ z/\ F\} \quad (1)$$

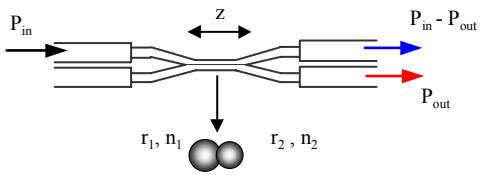

Fused+streched

Where $F = \{1- (\beta_1-\beta_2)^2 / 4C_{12}C_{21}\}^{-1/2}$ and $C_{ij}$are the cross coupling coefficients given by:

$Cij = k\ (n1\text{-}nj) \int \Psi i \Psi_j\ dA$, where$\Psi_i$ is the intensity field of fiber i. This equation represents the interaction of the field of one fiber in the other fiber. Finally, the β_i's are the propagation constants of the modes in each fiber, while z is the effective couper length, which is a function of the fused+streched region dimension and shape.

From (1) and F, one can see that, if the fibers are equal, that is $\beta_1=\beta_2$, then F=1. In this situation there can be complete power transfer between the fibers in the coupler. Since the C's are function of wavelength there is the possibility of manufacturing coupler where the power transfer depends on the wavelength, so Wavelength Divison Multiplexers/Demultiplexers (WDM) can be made, for instance.

If the fibers geometries in the fused region are not equal, one can make components that are less dependent on the wavelength, and since F is smaller than one, the modulation is lower than 100%. In this situation there is never a complete power transfer between the fibers. So, by controlling the fibers differences, plus some fabrication process parameters, a diversity of components are possible.

III-FABRICATION TECHNOLOGY

Based in Eq 1, plus the particular fibers used and the production equipment configuration, a simulation software was developed, to determine the basic process parameters to obtain a given component characteristcs. With it, the coupler transmission as a function of the drawing length as well as wavelength can be determined. A parametric adjustment with the real values can be made to do fine adjustment. This software as proven of great utility, specialy for the production of custom made components with transmission characteristcs that are not the ones used for the more common couplers, where there is already a stablished process.

The production process involves the use of a computer controlled equipment that has very precise fiber moving stages, a heating element small but that can reach temperatures above 1500ºC and a set of optical sources and detectors, to monitor in real time the power coupling between the fibers. A schematic of the equipment, is shown in Figure 2, see below.

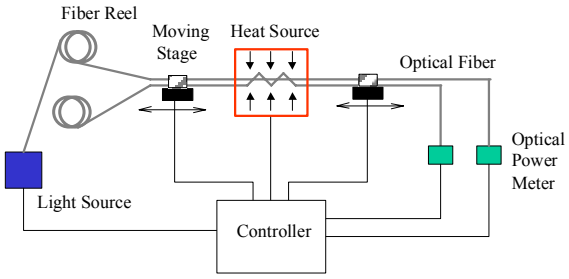

After the fibers are joined together, they are packaged in a structure as shown in Figure 3, composed of a silica glass substrate and a polimeric shield tube, all placed inside a stainless steel tube for mechanical protection . Depending on the final application of the component, the end fibers can be just with its secondary acrylate coating or protected with polimeric tubes, both of them, shown in Figure 3.

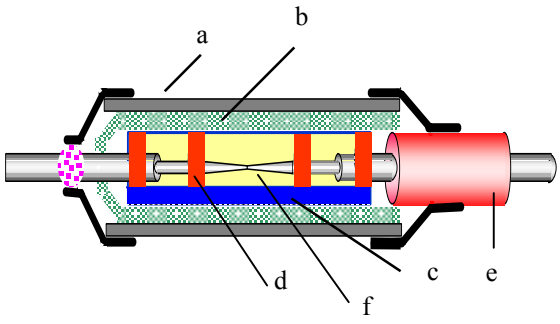

Finally the components go thru a complete set of mechanical, environmental tests and optical measurements, based on Tellcordia GR 1221 Requirements, as given in Table1.

Tabel 1 - Standard Characterization Routine

Test/Measurement **Mechanical/Environmental**	**Condition**
Mechanical Vibration	5 cycles, 50-130Hz (5-12G) 6 minutes each cycle
Fiber pulling	0.5 kgf for time > 1 minute
Temperature "burn-in"	-40ºC to 80ºC Five cycles of 6 hours each
Temperature performance	-40ºC to 80ºC for outdoor. 0ºC to 70ºC for indor use
Optical Parameters	
Insertion loss	As a function of wavelength
Loss spectra	As a function of wavelength
Excess Loss	As a function of wavelength Normally <0.5 dB
Optical bandwidth	For < 0.5 dB uniformity
Channel Isolation	Out of band power For WDM couplers
Directivity	Return loss from one fiber to the other in the same side >50 dB
Polarization Dependent Loss	< 0.2 dB

IV-RESULTS

Production has been carried out at Optolink, in an industrial basis, since the second half of 2001. From a single client, single product situation, the company component portfolio has evolved to a larger base, and at the present time, more that 20 customers, are consuming at least 15 different types of couplers. In the last 2 years, a few ten of thousands of components have been produced.

In order to show the flexibility of the technology used, the most important characteristcs of some of the devices, that are produced on a routine basis, will be commented as follow:

A-TYPES OF COMPONENTS

a – 3dB couplers operating at 1310 or 1550nm are the ones consumed in large quantities and used primarily in optical modem for bi-directional links. In Figure 4, the basic schematic for this type of transmission on a single wavelength is shown. This solution is in widespread use in Brazil, specially for E1/E16 tributaries in SDH/PDH transmission systems. A key parameter for this type of application is a large direcivity, above 50 dB, so to isolate the Rx from the Tx on the same side of the link. A figure of merit of the components made, is the distribution of the excess loss (the total power loss), obtained out of a production batch, as shown in Figure 5. One can see that most of the devices are below 0.2 dB, value comparable with other commercial products.

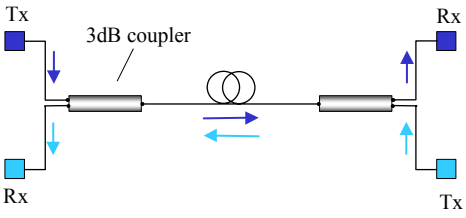

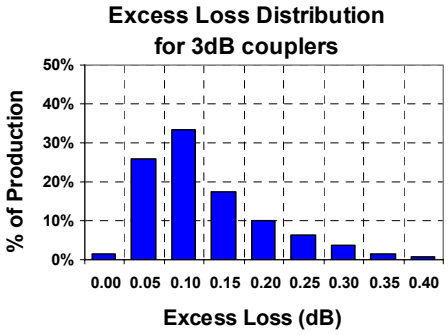

Figure 5 – Typical production distribution

b – A device that is used mostly for monitoring purpose, inside an EDFA (Erbium Doped Fiber Amplifier), for instance, is the tap coupler, as shown in Figure 6. From Figure 7, one can see that the output, stays well within +/- 2 % over the whole range of the S, C and L band.

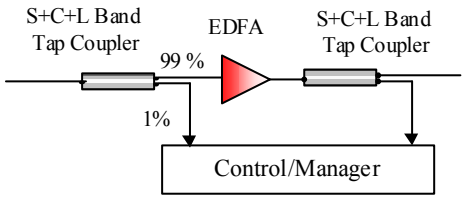

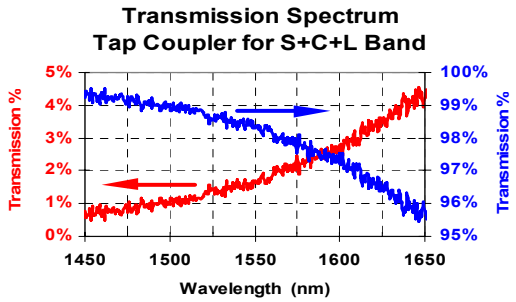

Figure 7 - Transmission spectrum of a tap coupler, for each arm,

c – For application in Wavelength Division Multiplexing systems as the one shown in Figure 8, the technology used, can produce multiplex/demultiplex for 1.31µm/1.55µm operation , with low insertion loss as well as good isolation as the one shown in Figure 9, where the transmission for each one of the ouput fibers is plotted.

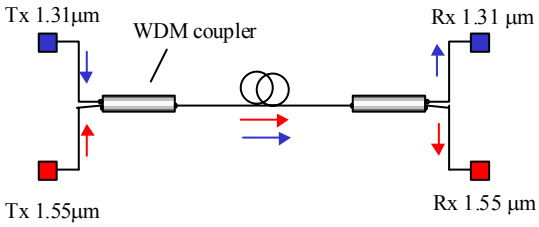

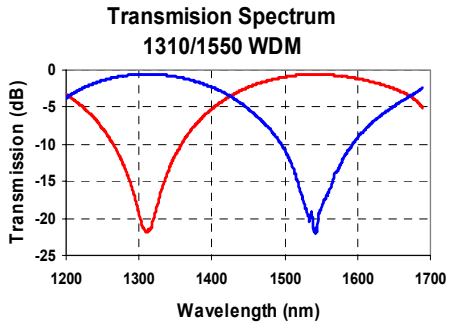

Figure 9 – WDM coupler for 1.31/1.55 operation, The above spectrum was measured with a resolution of 10 nm, for each output arm.

d –For applications such as the bidirectional two wavelength transmission, as shown in Figure 10, for example a wideband or double window coupler is necessary. The so called doublewindow coupler can be produced with the same technology. The transmission spectrum is shown in Figure 11. Over the whole band, from 1250nm to 1650 nm the splitting ratio is within +/-5%

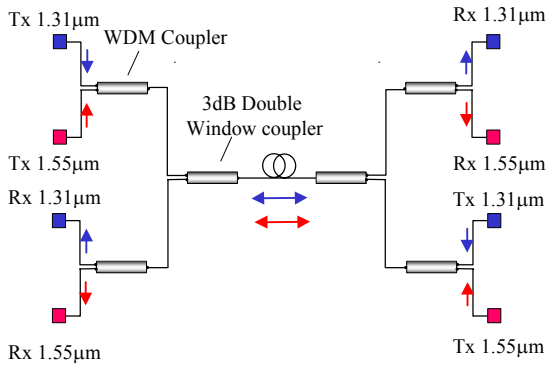

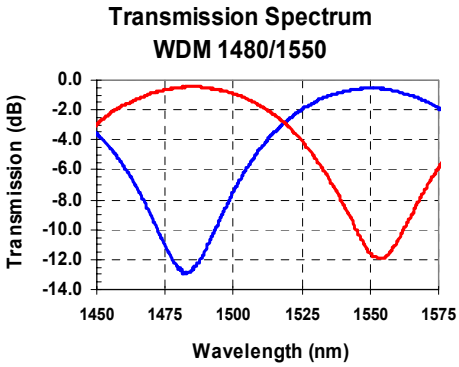

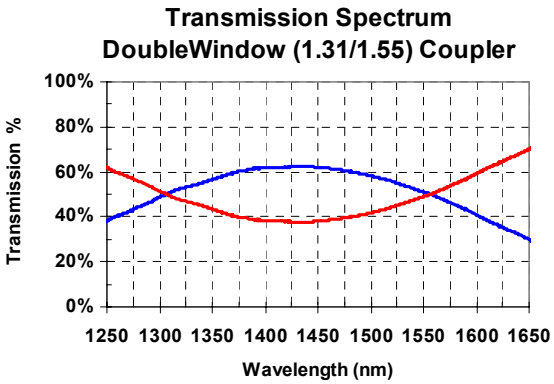

Figure 11 – A double window, coupler, with equal transmission at 1.31 and 1.55 µm

e – For use in Erbium Doped Fiber Amplifier, or Raman amplifier, WDM couplers for the pump wavelength are needed, as shown in Figure 12. Figure 13, show the transmision spectrum for a device of this type. Thanks to the all fiber construction, this component can withstand high power, well above 25 dBm

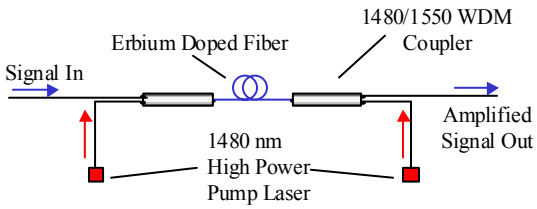

B-Temperature Dependence

Finally, just to show the robustness of these type of fiber based components, in Figure 14, the insertion loss variation from –40°C to 80°C , for the 3dB couplers both at 1.31µm and 1.55µm are given. In Figure 15, the insertion loss a function of temperature for a typical 1%/99% tap coupler is shown. It can be appreciated, in both cases, that even at very low temperatures, the transmission stays constant, within the measurement error.

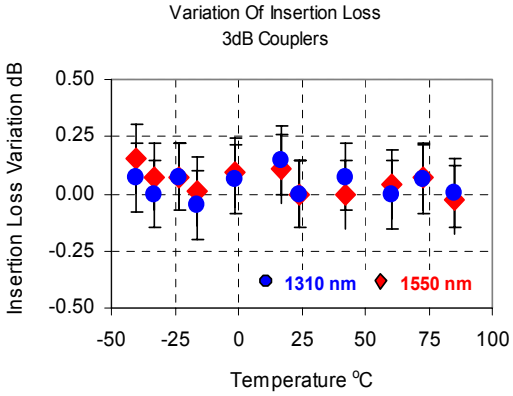

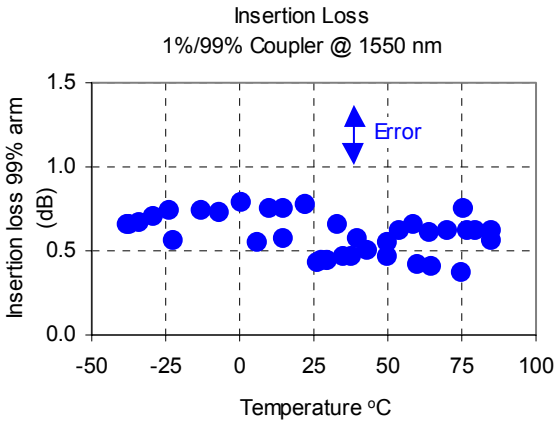

V-CONCLUSION

The objective os this paper, is to show the current status of the production technology of fiber based components in Brasil. The theoretical background for fiber couplers was already well stablished many years ago, in the international literatur and serves very nicely to design and fabricate the main types of components. The results for some types of components presently being used in Brasil were shown. In resume, it is a mature technology and is one that is very flexible, for the manufacturing of different components that are needed for optical communication systems, including the network as well as equipments**.** Some characteristics of the components being manufactured was shown to illustrate the current status of the production at Optolink.

References

[1] - S.Celaschi and F.M.Smolka, Revista Telebrás, página 3, Dezembro 1985
[2] - T.A.Birks et al, Proceedings of the Optical Fiber Communication Conference 2004, on CD-ROM, Los Angeles, USA, Paper ThK2,
[3] – A.W.Snyder, J.Optical Society of America, Volume 62, 1267, 1972.
[4] – A.Ankiewicz et al, J.Lightwave Tech, LT-4, 1317, 1986
[5] – A.W.Snyder, and A.Ankiewicz, J.Lightwave Tech, LT-6, 463, 1988

Comparative Performance of the Standard and NZD-Normal Fibers, with Directly Modulated Laser, in Transparent Metropolitan Networks

ANDRÉ LUIZ AGUIAR DA COSTA
National Institute of Telecommunications- Inatel
Avenida João de Camargo, 510 –
Santa Rita do Sapucaí – MG - BRAZIL - 37540-000
andre-aguiar@inatel.br

MARIA REGINA CAMPOS CAPUTO
National Institute of Telecommunications- Inatel
Avenida João de Camargo, 510
Santa Rita do Sapucaí – MG - BRAZIL - 37540-000
mreginacaputo@inatel.br

***Abstract*- In this work the performance of two different optical fibers, on a transparent metropolitan network, is compared by numerical simulations based on non linear Schrödinger equation. One of the fibers studied is the *Standard fiber*; it mitigates the penalty of the chromatic dispersion through the use of Dispersion Compensate Fibers. The other fiber studied works on normal regime *It* mitigates the penalty of the chromatic dispersion through the *"pre-chirp"* of the directly modulated laser On transparent networks, where different lightpaths accumulate different values of dispersion, the efficient management of this parameter is complex with use of Dispersion Compensate Fiber.**

Index Terms– Transparent Optical Network, Lightpath, Chromatic Dispersion Management.

I- Introduction

There is a gap between the fiber transmission capacity and the nodes processing capacity on today's optical networks based on DWDM [1,2]. This gap caused a "bottleneck" and the use of optical technology at the nodes has contributed to mitigate this effect. The networks nowadays consist basically of three segments:

- the *access network,* which is responsible to aggregate the final users traffic; it is tens of miles long.

- the *metropolitan network,* which connects several access networks and make the interface with a *backbone wide area network*; with some hundreds of the miles long; in these networks several technologies, such as Ethernet, IP, ATM, are transported trough SDH over CWDM over fiber rings [1]. Its traffic can suffer a large fluctuation with the time, for example, an intense diurnal traffic in business place, in beaches during the summer, etc. This causes a large variation in the bandwidth demand of circuits and virtual paths

- the *backbone wide area network* which connects metropolitan networks and has hundreds of thousands of miles makes use of the SDH technology transport over DWDM [1,2].

The nodes process the signal with variable "granularity", through Add/ Drop Multiplexers (ADMs) and Digital Cross Connects (DCSs). ATM Switches process the signals at cell level. The ATM and SDH signals are electronically processed at the nodes. Many times it is not necessary to access the signal in its electronic form and in this case the same can travel, from the origin node to the destination node, in the optical domain trough Optical Cross Connects (OXCs) and Optical Add/ Drop Multiplexers (OADMs). These devices commute the several wavelengths, which compound the WDM signal. Nowadays there is an intense research on switches with granularity at level of optical packets. Its implementation will give to the future networks a major flexibility and scalability[3].

Portions of the network where the signal is in optical domain are assigned "transparent islands". The best optical path between origin and destination of a specific signal is selected from the *virtual topology of the network* [4], which is the group of all possible lightpaths between the origin and destination. The Figure 1 shows two different light paths on the optical network.

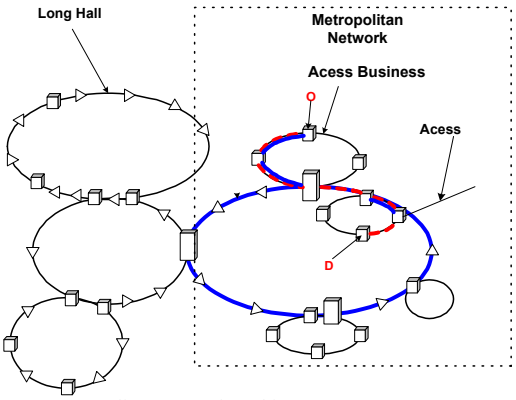

Figura-1 – Metropolitan network architecture

The virtual topology design depends on the physical topology of the fiber network, as the complexity of the management of the parameters as losses, dispersion, non linear effects, as the number of wavelengths disposable and as the traffic process capability of each node.

II- Mathematical Model and Fibers Parameters

In this article the performance of two different optical fibers, on a transparent metropolitan network, is compared by numerical simulations based on non linear Schrödinger equation [5]. This equation includes the loss effect, first and second orders of the chromatic dispersion and the self phase modulation (SPM). One the fibers studied is the *Standard fiber* [6], which is predominant on the installed networks. Its performance, with *chromatic dispersion compensate fibers* (DCF) [7], is very good on point to point links. On transparent networks, where different lightpaths accumulate different values of dispersion, the efficient manangement of this parameter is very dificculty. The second fiber studied works on normal regime of dispersion and it is here designed by *NZD-Normal fiber. It* mitigates the penalty of the chromatic dispersion through the *"pre-chirp"* of the directly modulated laser [8-11]. The Tables I and II list the parameters of the *Standard, NZD- Normal* and *dispersion compensations fiber* used in this article [6,7,8]**.** The *NZD-Normal fiber* here considered it is a *Metrocor*® manufactured by *CorningInc***.**

TABLE I - PARAMETERS OF THE STANDARD FIBER AND DCF AT λ=1560NM [6,7,8]

Parameters	Standard Fiber	DCF
D(ps/nm km)	17,901	105,49
$A_{eff}(\mu m^2)$	80	19
$S_0(ps/nm^2\ km)$	0,092	-0,35
$n_2(x10^{-20}m^2/W)$	2,6	2,69
α(dB/km)	0,2	0,5

TABLE II – PARAMETERS OF THE *S*TANDARD FfIBER AND NZD-NORMAL FIBER, AT 1550NM

Parameters	Standard Fiber	NZD-Normal Fiber
$A_{eff}(\mu m^2)$	80	55
$S_0(ps/nm^2\ km)$	0,092	0,07
$n_2(x10^{-20}m^2/W)$	2,6	2,3
α(dB/km)	0,2	0,25

The Figure 2 shows how a DCF 16.93 km long, perfectly compensates the dispersion on a lightpath, built on *Standard fiber* 100km long. The Figure 3 considers an alternative lightpath, built on *Standard fiber* 120km long, making use of the same DCF preceding. The results show that the perfect cancel of the dispersion has not occurred in this case. On metropolitans networks the lightpaths lengths can vary in a band larger than the one considered here (100km to 120km) and temporal enlargement ratio of the pulse, caused by the accumulated dispersion, can cause impairment through of the increase the final Bit Error Rate of Distance in Km y difficult to implement an effective DCF modules in transparent networks.

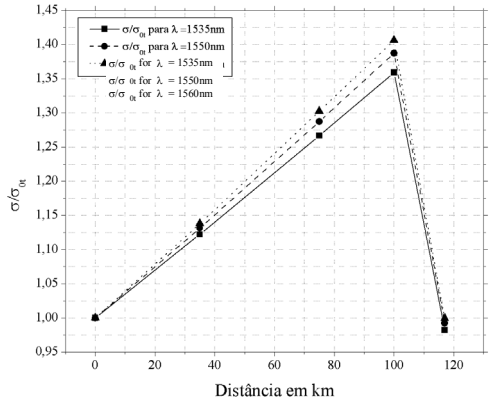

Figure2- Results of simulation with the Standard Fiber 100km long more DCF 16,93km long.

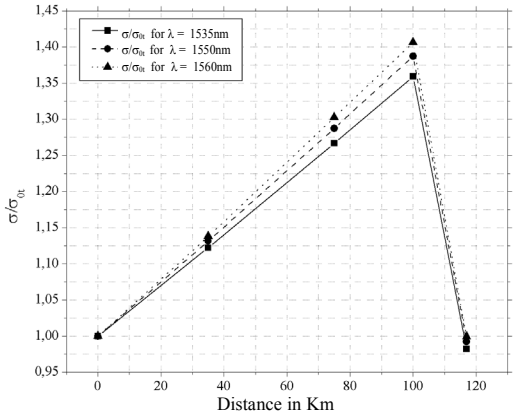

Figure 3 – Results of simulation for an alternative lightpath with Standard fiber 120km long, utilizing the same DCF of the figure 2.

III- Simulations and Results

On the numerical simulations in this work optical pulses were taken input with super Gaussian format, second order, 200ps large, previously chirped by directly modulated laser, with chirp factor *C*= -4,4 [10]. It was also considered for comparison the chirp factor C=0 (ideal laser). The input optical pulses were investigated with three different central wavelengths: λ=1535nm, λ=1550nm and λ=1560nm. The Figures 4, 5 and 6 show the results of the simulations for these channels. For the 1535nm case can be observed that for C=-4.4, the *NZD-Normal fiber* presents better performance than the *Standard fiber*.

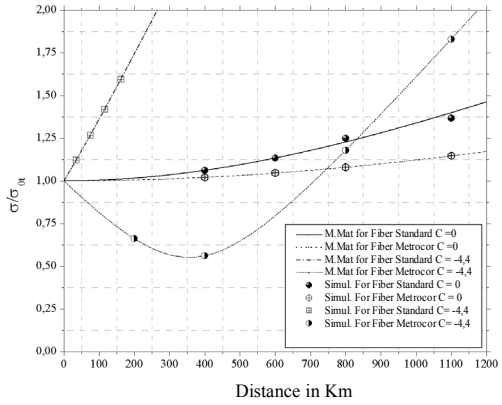

Figure 4- Result of simulatıon showıng the temporal enlargement for the channel with λ=1535nm

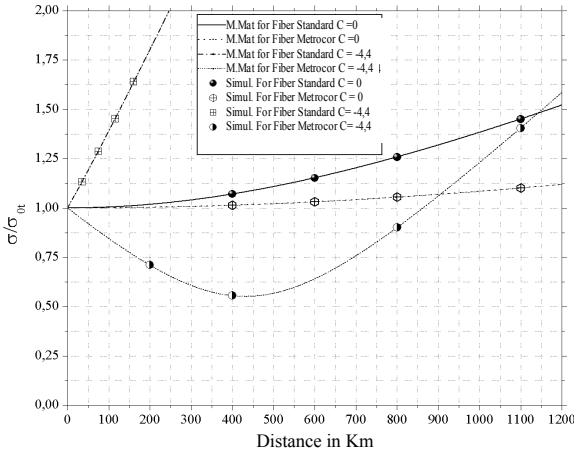

Figure 5- Result of simulation showing the temporal enlargement for the channel with λ=1550nm.

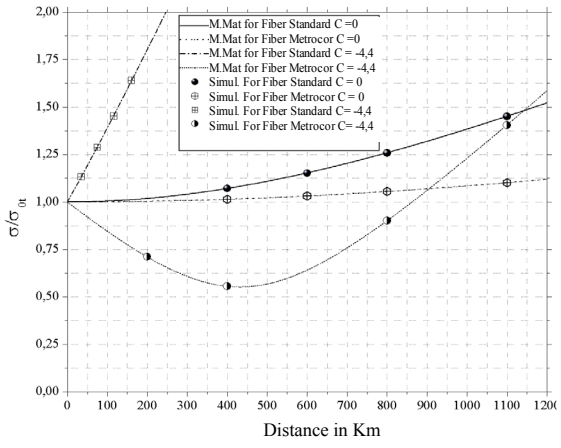

Figure 6- Result of simulatıon showıng the temporal enlargement for the channel with λ=1560nm.

On the *Standard* fiber, the temporal enlargement of the temporal rms (root mean square) of the pulse was about 62%, at 162km. On the *NZD-Normal* fiber the temporal rms value of the pulse was compressed about 30%, at 200km, due to the counter characteristics of the chirp imposed to the signal by the directly modulated laser and to the fiber working at normal regime. The result of the simulation shows better performance of the *NZD-Normal fiber* over the typical band of extension between nodes in transparent metropolitan networks.

The results for the three carriers are summarized on Figure 7, which shows that the Power Penalty [1] imposed to the signal, for C = -4.4 with the *Standard* fiber at 100km, is about 1.4dB and at 160km is about 1.6dB. The *NZD-Normal* fiber presents minor value of Power Penalty.

These results were analyzed by eye-diagram, too. The Figure 8 shows the eye-diagram on the input of the both fibers. The Figures 9 and 10 show the eye-diagram after 100 km of propagation, on the *Standard* and *NZD-Normal* fibers respectively. It is easy to see than the worst closure of the eye-diagram occurs in the standard fiber case. The Figures 11 and 12 show the eye- diagram after 200 km of propagation, on the *Standard* and *NZD-Normal* fibers respectively. It is very interesting to note the better performance of the *NZD-Normal* fiber relative to the case of 100 km, the same fiber, because the pulse was more compressed.

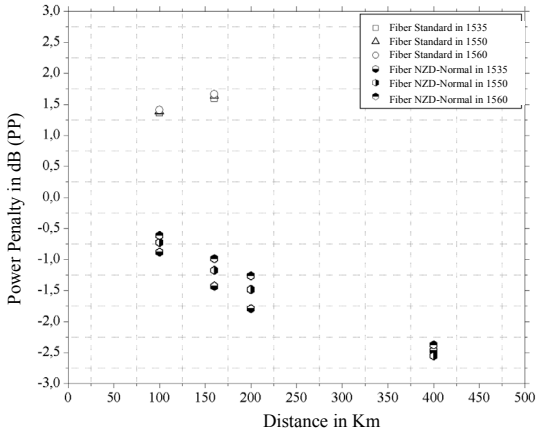

Figure 7- Result of simulations showing the Power Penalty imposed to the system, by the Standard and NZD-Normal fibers

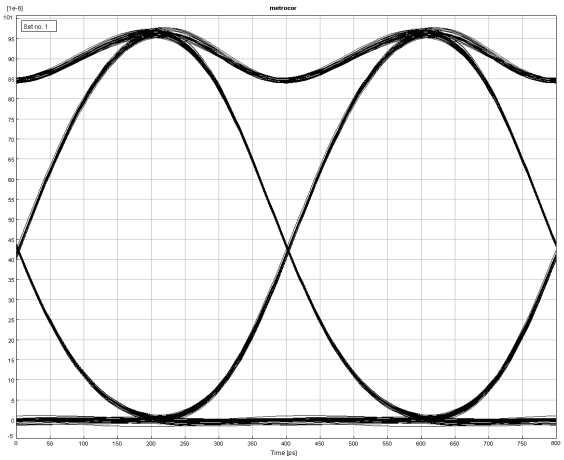

Figure 8- Eye–diagram on the input of the Standard and NZD-Normal fibers.

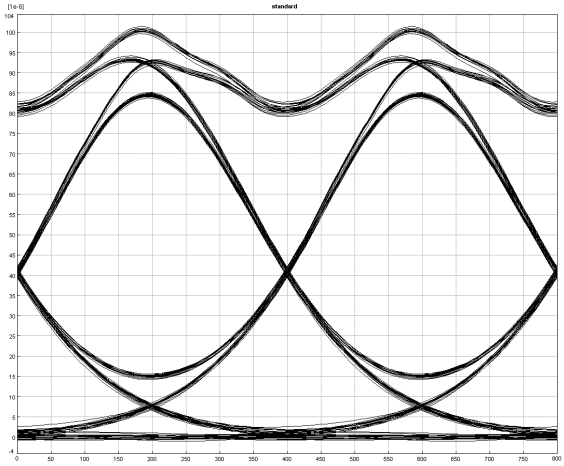

Figure 9- Eye–diagram on the output of the Standard fibers, after 100km

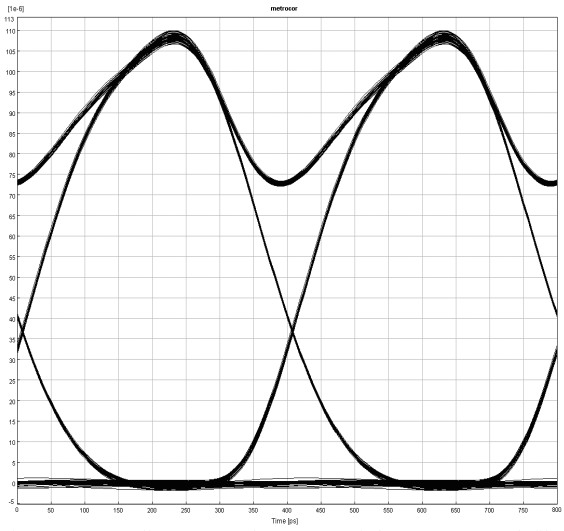

Figure10- Eye–diagram on the output of the NZD-Normal fibers, after 100km

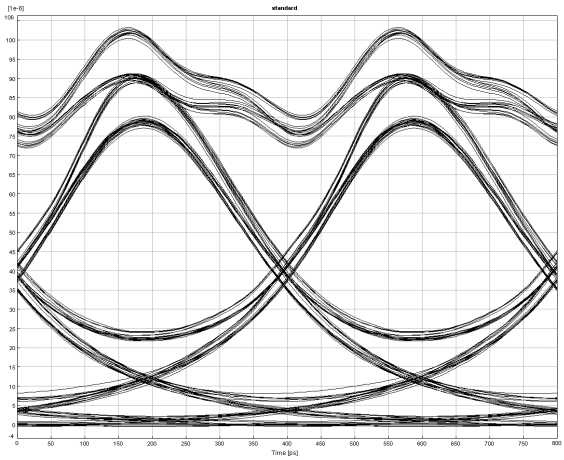

Figure 11- Eye–diagram on the output of the Standard fibers, after 200km

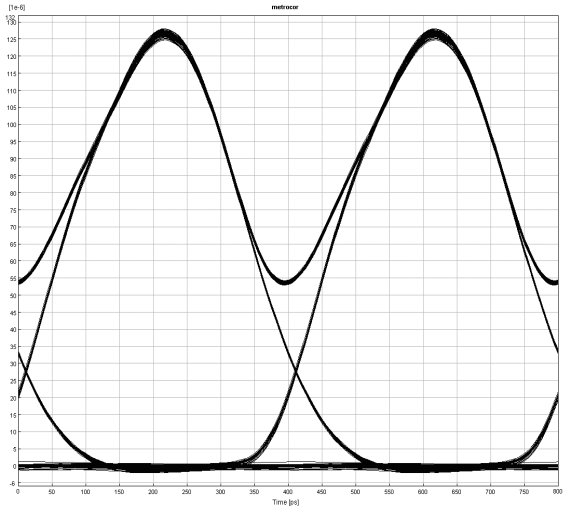

Figure12- Eye–diagram on the output of the NZD-Normal fibers, after 200km

In another simulation the performance of the fibers for several levels of power of the input pulse has been compared. Figure 13 shows that the *Standard fiber* has compressed the temporal rms width of the pulse, due the chirp caused by the SPM which has reverse effect of the chirp caused by the laser and by the *Standard fiber* working at anomalous regime.

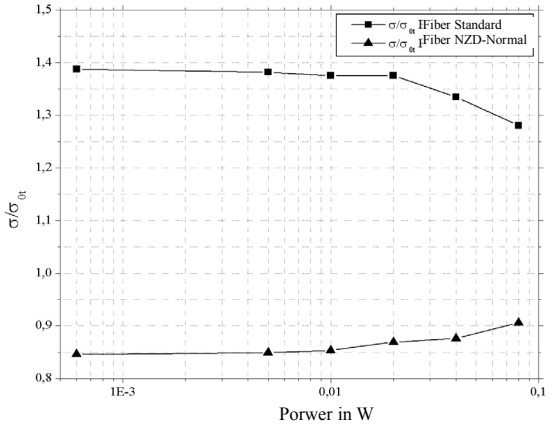

Figure13-Results of simulation showing the temporal enlargement factor for the Standard and NZD- Normal fiber, after 100km, for several power values.

This effect is aggravated when the level of the power is increased, due the higher efficiency of the SPM. With the *NZD-Normal fiber*, the temporal rms width of the pulse increases in the proportion as the power of the input pulse is increased. It happens because of the effect of the chirp caused by the SPM, which is the same of that caused by the fiber working on the normal regime, notwithstanding the effect of the laser chirp is reverse. Although the *NZD-Normal fiber* presents major enlargement (due to the increased power), the penalty imposed to the system is still negative for this fiber and positive for the *Standard fiber*.

IV- Conclusions

In this work it has been seen the difficulty to manage the dispersion on *Standard fiber* when it is used with *dispersion compensating fiber*, in transparent metropolitan optical networks. As an alternative for this the performance of the *NZD-Normal fiber* was studied. The results showed that *NZD-Normal fiber* presents better performance than the *Standard fiber*, due to the interaction between the effect caused by the frequency chirp imposed by the directly modulated laser and the effect imposed by the fiber operating in the normal dispersion regime.

References

[1] YOO MYUNGSIK et al, IEEE Communications Magazine, pp. 98-104, February 2001.

[2]- RAMASWAMI, R., SIVARAJAN, N. K. – *Optical Networks* – 2nd. Edition, New York, Morgan Kaufmann Publishers, 2002; KARTALPOULOS,V. S. – *Introduction to DWDM Technology* 1st. Edition, New York, A Publication of the International Society for Optical Engineering, 2000.

[3]- CHEN B, IEEE Journal Selected Areas in Communications, vol21, No 7, pp1071, September 2003.

[4]- S J BEN YOO et al, IEEE Journal Selected Areas in Communications, vol21, No 7,pp 1041 September 2003.

[5]- AGRAVAL, P. G. – *NonLinear Fiber Optics* – 3rd. Edition, New York, Academic Press, 2001.

[6] G.652 Recommendation (10/98)-Generic Characteristics of optical fiber amplifier and subsystems.

[7] MOLLENAUER, L. F. et al, Optics Letters, Volume 24, Number 4, p.220-222, February 1999.

[8] G.655 Recommendation (10/00) - Characteristics of non-zero dispersion –shift single-mode optical fiber.

[9] CULVERHOUSE, D. et al. – *Corning Metrocor Fiber and Its Application in Metropolitan Networks*. Cornig White Paper, New York, 2000. Number 5078. Available at: http://www.corning.com; CORNING INCORPORATED – C*orning Metrocor Fiber Value Proposition*. Cornig White Paper, New York, 2000. Available at: <http://www.corning.com>.

[10] DAS, S.; EICHENBAUM, B. and FILIOS, A. – *Building Metro Fiber Networks that Last*. Light wave, New York, September 2001. Available at: http://lw.pennnet.com/Articles/Article_Display.cfm?Section ves&Subsection=Display&ARTICLE_ID=115589> Access on 1st January2002.

[11] OSINSKI, M. and BUSS, J. – *Linewidth Broadening Factor in Semiconductor Lasers-An Overview.* IEEE Journal Quantum Electronics, Volume 3, Number 1, p.9–29, January 1987.

On the performance of new and classical approaches to AOA estimation for near-field acoustic waves

Maurício Henrique Costa Dias
Military Institute of Engineering – IME
Pc Gen. Tiburcio, 80 – Urca – 22290270
Rio de Janeiro – RJ – Brazil
mhcdias@ime.eb.br

Roberto Mouzinho de Castro
Military Institute of Engineering – IME
Pc Gen. Tiburcio, 80 – Urca – 22290270
Rio de Janeiro – RJ – Brazil
mouzinho@ime.eb.br

José Antônio Apolinário Jr.
Military Institute of Engineering – IME
Pc Gen. Tiburcio, 80 – Urca – 22290270
Rio de Janeiro – RJ – Brazil
apolin@ime.eb.br

***Abstract*—Classical AOA estimation methods usually rely on some simplifying assumptions that do not hold in many practical situations, like the far-field condition, for instance. The present work assesses three widely known methods (beamforming, Capon and MUSIC) under the near-field condition. In order to improve such analysis, a simple adaptation to the classical models is proposed and tested for that condition. The analysis comprises also a recently released approach, based on TDOA estimation.**

***Index Terms*—AOA, acoustic waves, beamforming, Capon, MUSIC, TDOA-based AOA estimation.**

I. INTRODUCTION

Angle-of arrival (AOA) estimation is a prominent application field of space-time signal processing. Its basic theory applies to harmonic signals in general, comprising physical nature wave phenomena as distinct as electromagnetic fields, acoustic waves, and oceanic waves, among others. Regarding telecommunications applications, for instance, AOA estimation is widely used for location-based services and smart antennas systems [1]-[2]. In the acoustics field, highly directive microphone synthesis and indoor speaker tracking can be picked as applications examples [3]-[4].

There are several AOA estimation methods available in the literature. They can be seen as specializations of the generic spectral estimation problem in which the searched "frequency" is a parameter associated to a spatial information sampling, measured with properly arranged multiple sensors [5]. The simplest algorithms are the Fourier based ones, like the "classical" beamforming [5]. More elaborated approaches are the Capon [6] and the MUSIC (MUltiple SIgnal Classification) [7] methods. All those procedures assume a complex envelope signal arriving at the sensors. On the other hand, a new class of algorithms referred to as TDOA-based [4], [8] does not require complex signals. Such methods try to exploit the correlation between sensor pairs in order to better estimate the time difference of arrival (TDOA) between the wave fronts and, consequently, the corresponding AOA.

In general, all AOA estimation algorithms rely on a number of simplifying assumptions concerning the source signal (or signals) and the array surroundings. Far-field condition is one of those, as well as phase information availability of the signal's envelope. Actually, such is the case for many situations, especially outdoor sensors for communication systems. Conversely, for applications like acoustic signals indoor AOA estimation, those basic assumptions are actually not likely to be fulfilled.

Although the above-mentioned situation is not quite unusual, it is hard to find AOA estimation methods specially tailored for that specific scenario or, at least, any references assessing typical estimation algorithms performance when basic hypotheses break down. The present work tried to contribute to "fill that gap" on this matter, proposing simple realistic changes on classical AOA estimation approaches. Simulations of the near-field-real signal problem were carried out, in order to analyze the proposed methods and also to assess its performance in comparison to some classical methods and to a modern TDOA-based approach.

The organization of this paper is as follows. Section II states the main simplifying assumptions typically accepted for AOA estimation. Some widely used estimation methods are briefly reviewed in Section III, which also proposes near-field adapted versions of the classical methods and presents a simple TDOA-based AOA estimation method. The following section comprises a comparative analysis of the previously reviewed approaches under near-field condition, based on simulations. Finally, some concluding remarks are discussed in section V.

II. TYPICAL SIMPLIFYING ASSUMPTIONS

An almost ubiquitous hypothesis assumed for the AOA estimation problem is the far-field condition, where the wave fronts are plane, and the array is "far enough" from the source. More specifically, such condition may be analytically described as [9]:

$$\begin{cases} r >> \frac{2D^2}{\lambda} \\ r > \lambda \end{cases} \quad (1)$$

where r is the separation between the array and the source, D is the maximum dimension of the array (width or height), and λ is the signal wavelength.

Fig. 1 illustrates a single signal impinging a uniform linear array (ULA) of sensors under the far-field condition.

For outdoor applications, the far-field condition is usually respected with great confidence. On the other hand, in indoor environments the far-field condition may not be respected within a considerable range. As an example, for a 1 kHz tone (λ = 0.34m) and a 4-sensors ULA with a $\lambda/2$ separation between consecutive sensors, the far-field condition corresponds to $r >>$ 1.53 m; this is barely achievable within a typical room. In this case, a near-field representation would be more suitable, with spherical wave fronts, as illustrated in Fig. 2.

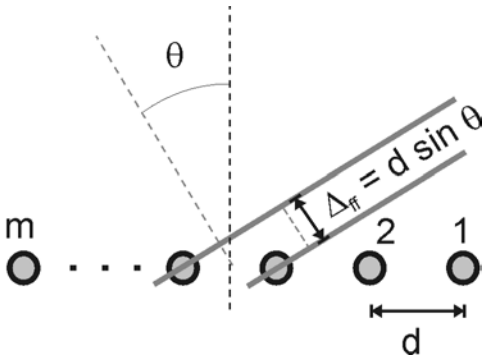

Fig. 1. Uniform linear array under far-field condition.

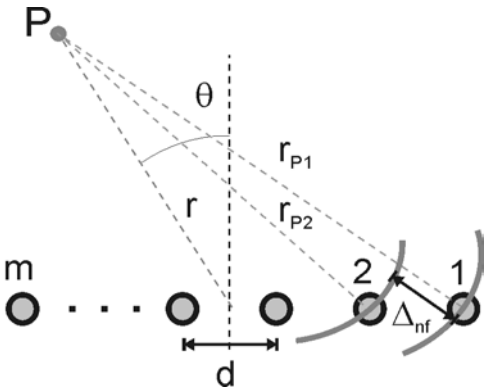

Fig. 2. Uniform linear array under near-field condition.

Another usual assumption when dealing with AOA estimation methods is that both amplitude and phase information of the transmitted signal are available. In other words, a complex envelope signal is assumed impinging the array of sensors. If the problem regards communication systems, this is usually true. But, when acoustic waves are considered, the signal is actually real. Nevertheless, most of the classical estimation methods rely on the complex envelope hypothesis. Thus, when real signals are considered, those methods no longer provide optimum spatial spectrum estimates.

Narrowband signals are usually assumed for most of the classical AOA estimation methods. Though such hypothesis is fairly reasonable for many communication systems problems, for acoustic signal AOA estimation the wideband model occurs more frequently.

III. Estimation Methods

A. Classical Methods

The classical AOA methods are simply "spatial" versions of some frequently referred spectral estimation methods. Beamforming and Capon are among the simplest and widest used non-parametric algorithms. On the other hand, MUSIC is perhaps the most popular among the parametric methods [5]. The advantage of these two non-parametric methods is that they do not assume anything about the signals statistical properties. On the other hand, in the cases where such information is available, or at least when it is likely that those properties may be partially assumed, parametric methods may present better performances than the non-parametric ones.

In general, classical methods rely on the *array model*, which can be briefly stated as follows [5]. Taking Fig. 1 as reference, if a signal $s(t)$ impinges a m-sensors ULA at an AOA θ, a vector $\mathbf{y}(t)$ is formed on the sensors outputs, such that:

$$\mathbf{y}(t) = \mathbf{a}(\theta)\cdot s(t) + \mathbf{n}(t) \quad (2)$$

$$\mathbf{y}(t) = [\, y_1(t) \cdots \; y_m(t) \,]^{\mathrm{T}} \quad (3)$$

$$\mathbf{n}(t) = [\, n_1(t) \cdots \; n_m(t) \,]^{\mathrm{T}} \quad (4)$$

where symbol $\{^{\mathrm{T}}\}$ represents the transposition of a vector or matrix, $y_i(t)$ is the signal at the i^{th} sensor, and $n_i(t)$ is the i^{th} sensor noise, usually considered as white Gaussian distributed. Vector $\mathbf{a}(\theta)$ is frequently known as *steering vector*, and is given by:

$$\mathbf{a}(\theta) = [\, 1 \; \exp(-j\omega_c\tau_2) \; \cdots \; \exp(-j\omega_c\tau_m) \,]^{\mathrm{T}} \quad (5)$$

$$\tau_k = (k-1)\frac{d\cdot\sin(\theta)}{v} = (k-1)\frac{\Delta_{ff}}{v} \quad (6)$$

where ω_c is the signal frequency (a narrowband signal is assumed), τ_k is the far-field time delay of arrival (TDOA) between the k^{th} sensor and the first sensor, and v is the phase velocity of the impinging signal.

As it can be noticed in eqs. (5) and (6), the steering vector indeed contains the desired AOA information. How such information is "extracted" depends on the specific formulation of each estimation method. It is also worth mentioning that the array model may also be extended to the multipath case. If the impinging signal arrives at the array from n different AOAs, then there will be a steering vector for each direction. If the n $m \times 1$ steering vectors are put together, a $m \times n$

matrix is formed, which is commonly referred as *array manifold*. Thus, the basic array model equation for the multipath case may still be represented by eq. (2) if we just replace the steering vector for the array manifold $\mathbf{A}(\theta)$.

Beamforming is an array model based estimation method that may be seen as a bank of filters, where each sensor is attributed a weight. An optimization criterion is chosen to calculate the filter weights, such that the filter output maximizes only a specified AOA θ, equally minimizing all other directions [5]. This principle is very simple and fast to compute, providing a spatial spectral estimate given by:

$$P(\theta) = \mathbf{a}^H(\theta) \cdot \hat{\mathbf{R}} \cdot \mathbf{a}(\theta) \tag{7}$$

where the symbol $\{^{\mathrm{H}}\}$ represents the hermitian of a vector or matrix, and $\hat{\mathbf{R}}$ is an estimate of the signal covariance matrix **R**, usually taken as:

$$\hat{\mathbf{R}} = \frac{1}{N}\sum_{t=1}^{N} \mathbf{y}(t)\mathbf{y}^H(t) \tag{8}$$

where N is the number of (time) snapshots of the signal available.

The beamforming method presents resolution limitation as a function of the number of sensors. The least the number of sensors, the worst the capability to distinguish two or more multipath signals arriving at AOAs very close to each other. However, if such situation is unlikely to happen, or if precision is not an issue, this method is adequate enough.

Capon's AOA estimation has the same basic idea of beamforming. The goal of Capon's filter is to maximize a certain direction θ, while attenuating any other signals *actually* impinging the array from AOAs $\neq \theta$ [6]. The beamforming filter, on the other hand, pays uniform attention to all AOAs $\neq \theta$, even when there might be no incoming signal at those AOAs, as previously stated. Capon's method is expected to present superior performance compared to beamforming, what is usually confirmed empirically. Capon's spatial spectral estimate is given by:

$$P(\theta) = \left\{\mathbf{a}^H(\theta) \cdot \hat{\mathbf{R}}^{-1} \cdot \mathbf{a}(\theta)\right\}^{-1} \tag{9}$$

The MUSIC method is a relatively simple and efficient eigenstructure method of AOA estimation [7]. It has many variations and it is perhaps the most studied method in its class. In its standard form, also known as spectral MUSIC, the method estimates the noise subspace from the available samples. This can be done by either eigenvalue or singular value decomposition of the estimated data covariance matrix. Once the noise subspace has been estimated, a search for some directions has to be carried out, looking for steering vectors that are as orthogonal to the noise subspace as possible. More specifically, if **R** is the signal covariance matrix, it can be eigen-decomposed such that:

$$\mathbf{R} = \begin{bmatrix}\mathbf{S} & \mathbf{G}\end{bmatrix}\begin{bmatrix}\lambda_1 & & \\ & \ddots & \\ & & \lambda_m\end{bmatrix}\begin{bmatrix}\mathbf{S}^H \\ \mathbf{G}^H\end{bmatrix} \tag{10}$$

$$\begin{aligned}\mathbf{S} &= \begin{bmatrix}\mathbf{s_1} & \cdots & \mathbf{s_n}\end{bmatrix} \\ \mathbf{G} &= \begin{bmatrix}\mathbf{g_1} & \cdots & \mathbf{g_{m-n}}\end{bmatrix}\end{aligned} \tag{11}$$

where λ_i is an eigenvalue of a **R** matrix of rank m, $\mathbf{s_i}$ is a $m \times 1$ vector representing the actual signal subspace, and $\mathbf{g_i}$ is a $m \times 1$ vector representing the noise subspace, with both subspaces orthogonal to each other. Based on such orthogonality, the AOAs may be interpreted as the n sharpest peaks of the following function:

$$P(\theta) = \left\{\mathbf{a}^H(\theta) \cdot \hat{\mathbf{G}} \cdot \hat{\mathbf{G}}^H \cdot \mathbf{a}(\theta)\right\}^{-1} \tag{12}$$

where $\hat{\mathbf{G}}$ is an estimate of the noise subspace matrix **G**.

MUSIC usually presents high accuracy and resolution when the actual signal properties are close to the ones assumed *a priori* in the method. For such reason, it is frequently referred to as a "super-resolution" method. On the other hand, a major drawback of this parametric approach is that it assumes the number of the sources (n) as a known parameter, when in fact, knowing that number is an additional estimation problem.

B. TDOA-based approach

A simple TDOA-based estimation method was addressed in [4], and consists on computing the time delay estimates between sensor pairs of microphones, and then processing those estimates in order to extract the inherent AOA information, which is also function of the site and of the array geometry. This approach is applicable either to wideband or narrowband signals, which is a major advantage compared to the classical methods. However, the TDOA-based methods assume a single path impinging the array. Thus, its application to multipath problems is limited. Computation of time delays between signals from any pair of sensors can be performed by first computing the cross-correlation of the signals at each possible sensors pair. The cross-correlation for the i^{th} and j^{th} sensors is a $N \times 1$ vector represented here by $\boldsymbol{\phi}_{\mathbf{ij}}$, and given by:

$$\boldsymbol{\phi}_{\mathbf{ij}} = y_i(t) * y_j(t) \tag{13}$$

where N is the number of time lags of the resulting convolution. Since a binomial combination gives the number of possible pairs np, that is:

$$np = \binom{m}{2} = \frac{m!}{2!(m-2)!} \tag{14}$$

a $N \times np$ cross-correlation matrix $\boldsymbol{\phi}$ may be computed for the entire array. The cross-correlation may be easily calculated if its corresponding cross-power spectral density (XPSD) is first estimated, since in the spectral domain a single multiplication is needed, rather than a convolution.

The number of time delay lags that maximize $\boldsymbol{\phi}$ for each pair of sensors corresponds to the TDOA $\hat{\tau}_{ij}$ between the considered sensors. In other words:

$$\hat{\tau}_{ij} = \arg\max \{\boldsymbol{\phi}_{ij}\}/f_s \tag{15}$$

where f_s is the sampling frequency applied to the signal.

Assuming the single-path far-field condition, the AOA estimation is straightforward. Recalling eq. (6), $np \times 1$ vectors $\mathbf{d}$ and $\boldsymbol{\tau}$ may be composed, such that:

$$d_{ij} \sin(\theta) = v\ \hat{\tau}_{ij} \tag{16}$$

$$\mathbf{d} \sin(\theta) = v\ \hat{\boldsymbol{\tau}} \tag{17}$$

Finally, the AOA θ may be calculated from [4]:

$$\theta = \sin^{-1}\left\{\left(\mathbf{d}^{\mathbf{T}}\mathbf{d}\right)^{-1}\mathbf{d}^{\mathbf{T}}\left(v\hat{\boldsymbol{\tau}}\right)\right\} \tag{18}$$

C. Adapted Classical Methods

The present work tried to assess some AOA estimation methods for ULA under near-field condition, typical of indoor applications. In order to do that, classical complex-envelope waves algorithms have been adapted to incorporate spherical wave fronts separations, rather than plane wave ones. Regarding the first two sensors of the arrays represented in Figs. 1 and 2, the wave fronts displacements for the near-field and far-field cases are, respectively:

$$\Delta_{nf} = r_{P1} - r_{P2} = \tag{19}$$

$$= \sqrt{\left[\left(\frac{m-1}{2}\right)\cdot d\right]^2 + r^2 + 2\left(\frac{m-1}{2}\right)\cdot d \cdot r \cdot \sin\theta} -$$

$$- \sqrt{\left[\left(\frac{m-1}{2}-1\right)\cdot d\right]^2 + r^2 + 2\left(\frac{m-1}{2}-1\right)\cdot d \cdot r \cdot \sin\theta}$$

$$\Delta_{ff} = d \cdot \sin\theta \tag{20}$$

Thus, a near-field equivalent of the steering vector given by eq. (5) could be proposed simply replacing Δ_{ff} by Δ_{nf} in eq. (6). Actually, the near-field model should also comprise an amplitude correction, since the spherical wave front amplitude is proportional to $1/r$. However, since phase variation is much more critical than amplitude variation, for small array apertures (small m), this spherical amplitude variation has not been considered for the adapted model proposed.

At last, another adaptation is due to the real domain nature of signals such as audio recorded from each sensor (as in a microphone array): the complex-envelope AOA estimation algorithms do not work properly when real signals are available. In this work, a simple procedure has been adopted in order to transform the original real signal into its complex domain equivalent. Basically, the upper band (mirror from π to 2π of the left part 0 to π) of the signal Fast Fourier Transform (FFT) was nulled, and the result was then inverse transformed (IFFT). The overall result was a good estimate of the desired corresponding complex signal. In other words, with this procedure, a single cosine became a complex exponential.

IV. Near-field Comparative Performance Analysis

The near-field performance analysis comprised the classical beamforming, Capon and MUSIC methods, as well as the TDOA-based approach described in the previous section. Both the original far-field versions and the proposed near-field adaptations have been assessed. Simulations have been carried out for an additive white noise corrupted narrowband signal (1 kHz tone), arriving at a 4-sensors ULA from several directions. The 4 sensors choice concerns future tests with a practical electrets array that is being assembled.

Still concerning future measurements, the simulations tried to reproduce the near-field main conditions of a small acoustic chamber available in our signal processing lab: source to array separation r around 0.5 to 2 m, signal-to-noise ratio (SNR) varying from 0 to 40 dB, and distance between consecutive sensors d = 10 cm (less than the $\lambda/2$ Nyquist limit [5]). A sample rate f_s = 180 kHz were assumed instead of a more realistic 44 kHz frequency ("wav" files acquisition rate), in order to focus the assessment on the estimation methods. Lower rates result in higher quantization errors, what could mask some minor differences between the estimation approaches. The total sampling time for each simulation was 0.1 s.

The simulation results indicated an unexpected robustness of the original far-field classical algorithms to the near-field condition, as observed in Figs. 3 and 4. Actually, only for distances smaller than 0.5 m the far-field methods errors were noticeable, as exemplified in Figs. 5 and 6. Regarding SNR influence, beamforming and Capon were more susceptible than MUSIC, as Figs. 7 and 8 suggest. The lower the SNR, the broader the peak "skirt" width, though the AOA estimation error remained as small as for the higher SNR case. In general, the MUSIC algorithm presented the best results among the classical methods, while beamforming presented the worst (though also with relatively small errors).

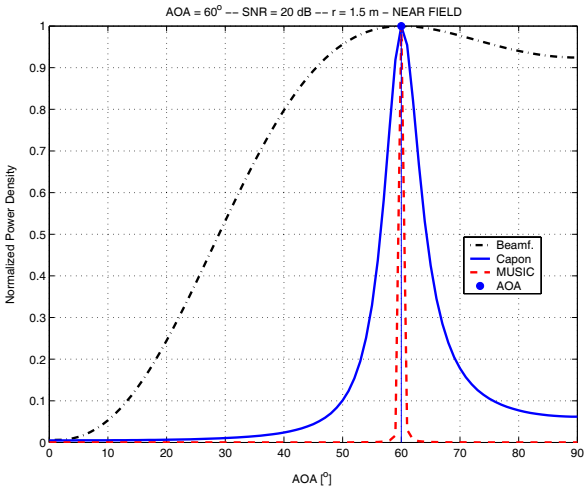

Fig. 3. Simulation results using near-field methods for AOA = 60°, r=1.5 m and SNR = 20 dB.

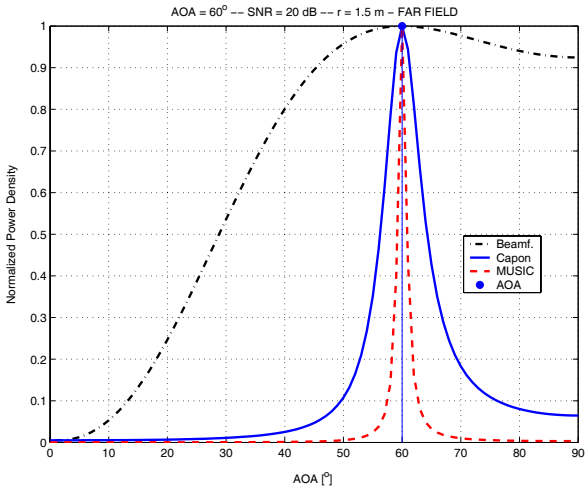

Fig. 4. Simulation results using far-field methods for AOA = 60°, r=1.5 m and SNR = 20 dB.

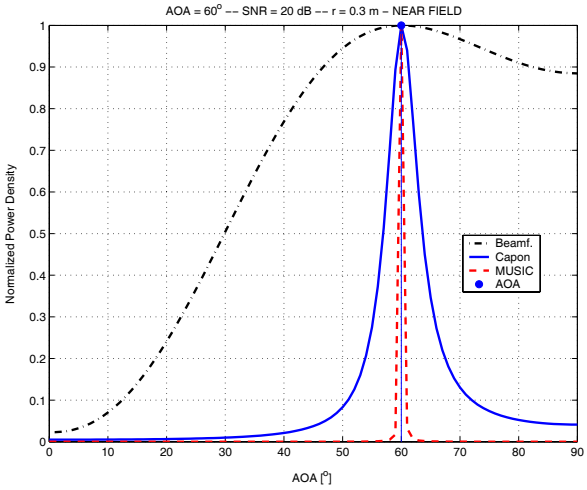

Fig. 5. Simulation results using near-field methods for AOA = 60°, r=0.3 m and SNR = 20 dB.

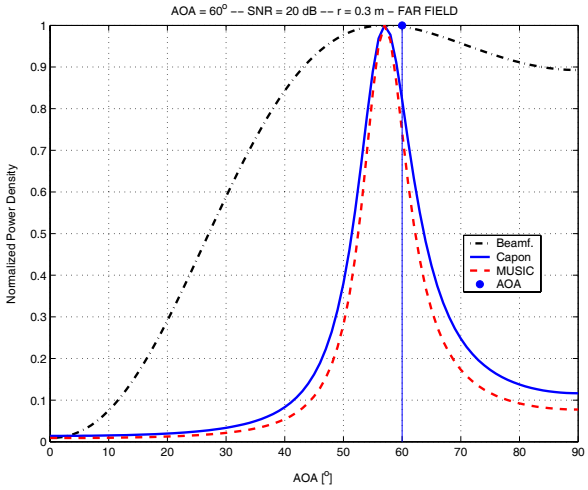

Fig. 6. Simulation results using far-field methods for AOA = 60°, r=0.3 m and SNR = 20 dB.

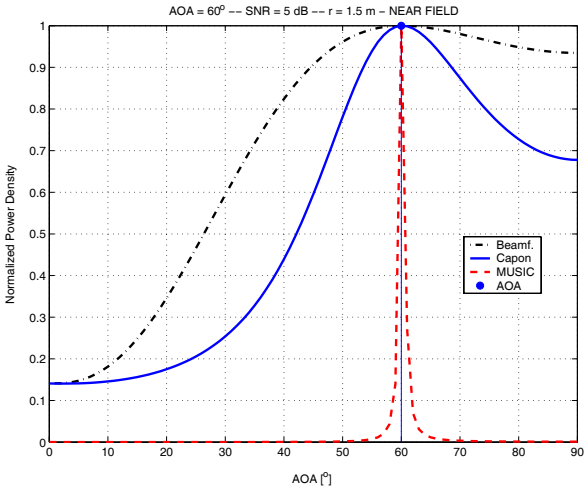

Fig. 7. Simulation results using near-field methods for AOA = 60°, r=1.5 m and SNR = 5 dB.

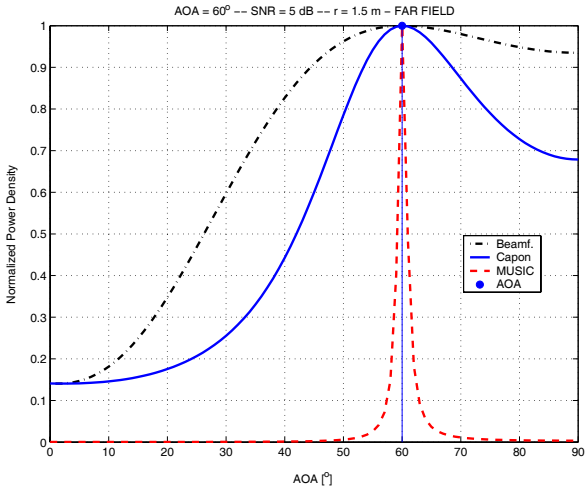

Fig. 8. Simulation results using far-field methods for AOA = 60°, r=1.5 m and SNR = 5 dB.

Besides the previously mentioned classical methods, the simple version of the new TDOA-based approaches described in Section III [4] has also been assessed for the same indoor scenario. Unlike those

methods, rather than spatial spectra, the TDOA-based approach provided directly an AOA estimate. Thus, in order to compare the performances of all the simulated algorithms, a maximum peak search was applied to the classical methods to extract their respective AOA estimates. Tables I and II present absolute error comparisons for the situations partially depicted in Figs. 5-6 and 7-8 (for SNR = 20 dB, r = 0.3 m and for SNR = 5 dB, r = 1.5 m, respectively), comprising 10 distinct angles of arrival (AOAs) from 0^o to 90^o.

In both Tables I and II, the previously referred behavior of the classical methods is more explicit. It is also noticeable that the TDOA-based approach from [4] presented the worst performance of all the simulated algorithms.

TABLE I
ABSOLUTE ERRORS [$\theta - \hat{\theta}$ IN ^{O}], SNR = 20 DB, R = 0.3 M

θ [in ^{o}]	FF Beam	FF Cap	FF MUS	NF Beam	NF Cap	NF MUS	TDOA
0	-1.00	-1.00	-1.00	-1.00	-1.00	-1.00	-30.66
10	1.00	1.00	1.00	0.00	0.00	0.00	-9.19
20	1.00	1.00	1.00	0.00	0.00	0.00	1.84
30	2.00	2.00	2.00	0.00	0.00	0.00	2.43
40	3.00	3.00	3.00	0.00	0.00	0.00	3.15
50	3.00	3.00	3.00	0.00	0.00	0.00	3.19
60	3.00	3.00	3.00	0.00	0.00	0.00	3.00
70	2.00	2.00	2.00	0.00	0.00	0.00	2.67
80	1.00	1.00	1.00	0.00	0.00	0.00	0.82
90	1.00	1.00	1.00	1.00	1.00	1.00	0.00

TABLE 2
ABSOLUTE ERRORS [$\theta - \hat{\theta}$ IN ^{O}], SNR = 5 DB, R = 1.5 M

θ [in ^{o}]	FF Beam	FF Cap	FF MUS	NF Beam	NF Cap	NF MUS	TDOA
0	-1,00	-1,00	-1,00	-1,00	-1,00	-1,00	-30,66
10	0,00	0,00	0,00	0,00	0,00	0,00	-0,12
20	0,00	0,00	0,00	0,00	0,00	0,00	0,01
30	0,00	0,00	0,00	0,00	0,00	0,00	0,21
40	0,00	0,00	0,00	0,00	0,00	0,00	0,04
50	0,00	0,00	0,00	0,00	0,00	0,00	0,09
60	0,00	0,00	0,00	0,00	0,00	0,00	0,53
70	0,00	0,00	0,00	0,00	0,00	0,00	0,46
80	0,00	0,00	0,00	0,00	0,00	0,00	-0,08
90	4,00	4,00	4,00	4,00	4,00	4,00	6,01

V. FINAL COMMENTS

The present work analyzed some typical AOA estimation methods, and also a new TDOA-based approach, under near-field conditions, especially for acoustic signals propagation. Besides the geometric implications of that condition, the impact of the real nature of acoustic signals to the frequently referred AOA estimation approaches has also been discussed.

A simple near-field adaptation has been proposed to be used in AOA estimation techniques based on classical methods such as beamforming, Capon, and MUSIC. The new proposal has been assessed with the help of simulations of a narrowband single arriving path signal impinging a small aperture array of sensors, under near-field conditions. Although the proposed method represented more accurately the near-field scenario, typical of indoor environments, the far-field original approaches presented an unexpected robustness. The small error increase observed only for situations where the source is extremely close to the array was an indication that even for near-field conditions, the far-field approaches provide accurate AOA estimates.

A simple version of a new TDOA-based approach has also been simulated, in order to compare its performance with the classical methods. Though such methods are claimed to present superior performance [8], specially for wideband signals, the narrowband single-path simulations led to a slightly different conclusion. Anyway, except for the poor estimation behavior at the spatial spectrum edges (0^o and 90^o), the TDOA-based approach performed quite as well as the far-field classical methods.

A multipath analysis has also been carried out with the same algorithms described in this work. However, since the real-to-complex domain signal transformation described in Section III does not apply to a sum of cosines, the expected performance was poor, what has been confirmed for 2 or 3 paths simultaneously arriving at the array. Different approaches still have to be tested in order to incorporate the multipath effect to the AOA estimation methods analysis for the case of real signals. The other major issue still to be considered for the next stage of this work is wideband signal analysis.

Despite the limitations above, the main simulated results presented in this paper have been recently corroborated experimentally. Preliminary tests with a 4-microphones ULA in a small acoustic chamber provided fairly accurate results, though obviously not as accurate as those from the theoretical simulations.

REFERENCES

[1] J. C. Liberti Jr, T. S. Rappapport, *Smart antennas for wireless communications*. Prentice Hall, 1999.

[2] L. C. Godara, "Applications of antenna arrays to mobile communications, part I: performance improvement, feasibility, and system considerations," *Proceedings of the IEEE*, vol. 85, n. 2, pp. 1029-1060, Jul 1997.

[3] S. L. Gray, J. Benesty, *Acoustic Signal Processing for Telecommunication*. Kluwer, 2001.

[4] K. Varma, T. Ikuma, and A. A. Beex, "Robust TDE-based DOA estimation for compact audio arrays," in *Proceedings of the Second IEEE Sensor Array and Multichannel Signal Processing Workshop (SAM 2002)*, pp. 214-218, 2002.

[5] P. Stoica, R. Moses, *Introduction to Spectral Analysis. Prentice Hall*, 1997.

[6] J. Capon, "High resolution frequency-wave number spectrum analysis," *Proceedings of the IEEE*, vol. 57, pp. 1408-1418, 1969.

[7] R. O. Schmidt, "Multiple Emitter Location and Signal Parameter Estimation," *IEEE Transactions on Antennas and Propagation*, vol. AP-34, n. 3, Mar 1986.

[8] Y. Rui and D. Florencio, "New direct approaches to robust sound source localization," in *Proc. International Conference on Multimedia & Expo (ICME 2003)*, Baltimore, MA, USA, pp. 737-740, 2003.

[9] C. A. Balanis, *Advanced Engineering Electromagnetics*. Wiley, 1989.

Circularly Polarized Microstrip Phased Array With Reduced Side Lobe Level

Guilherme A. M. Rodrigues, Ricardo Schildberg, J. C. da S. Lacava

Divisão de Eletrônica, IEET – LAP, ITA
CEP: 12228-900, São José dos Campos, SP
guilherm, schild,lacava@ele.ita.br

Lucio Cividanes

Divisão de Eletrônica Aeroespacial, DEA - INPE
CP: 515, CEP: 12001-970, São José dos Campos, SP
lucio@dea.inpe.br

Abstract — **This paper presents a useful method to design microstrip phased arrays with reduced aside lobe level. First, a truncated corner patch electromagnetic coupled fed microstrip antenna was designed. The element was constructed and the measured results were compared to the numerical predictions, and very good agreement were obtained. Second, an algorithm synthesis was implemented to give the correct input port excitations for the array main lobe to point to a specified scan angle and to keep the side lobes under a required level. Finally, scan arrays were designed and an eight-element phased array performance was analyzed by numerical simulation, when it was fed by currents whose weights and phases were given by the algorithm.**

Index Terms — **Linear phased arrays, microstrip antennas, phased array pattern synthesis.**

I. INTRODUCTION

Although antenna arrays have many decades of development and history, the last two have experienced great maturation, both in understanding and designing of arrays, and in the use of large sophisticated ones [1,2]. For many applications, like the tracking function in low Earth orbiting satellites, it is interesting to have antenna arrays with highest directivity at a desired direction and low sidelobe levels at the other directions.

For the particular case of linear arrays, this paper presents an useful method to design circularly polarized microstrip phased array whose main lobe can be squinted to a desired scan angle and, at the same time, the magnitudes of all side lobes shall be under a specified level. The microstrip antenna technology was chosen because it is lightweight, low profile and can easily be integrated to a microstrip beam forming circuit.

II. METHOD DESCRIPTION

The method consists, first, in a preliminary element design in which the most important antenna parameters were analyzed in order to adjust the antenna to the specified requirements. The second step is the implementation of the *Remez* optimization algorithm [3]. This technique is able to find out the amplitude and the phase of the current in each one of the array elements in order to achieve desired patterns for a linear array. The last step is the computation of the designed array by commercial CAD packages.

III. MICROSTRIP ELEMENT DESIGN

The element, a trimmed opposite corner square patch electromagnetic coupled fed microstrip antenna, is shown in Fig. 1. The substrate material used in the simulations was *CuClad*®-250 *GX*, with thickness $h_1 = h_2 = 1.524$ mm, a relative dielectric constant $\varepsilon_{r1} = \varepsilon_{r2} = 2.55$, and loss tangent $tg\delta = 0.0022$. The element was designed to operate centered at 1.616 GHz and to produce right hand circularly polarized (*RHCP*) waves, since it is the polarization requirement for the most satellite systems.

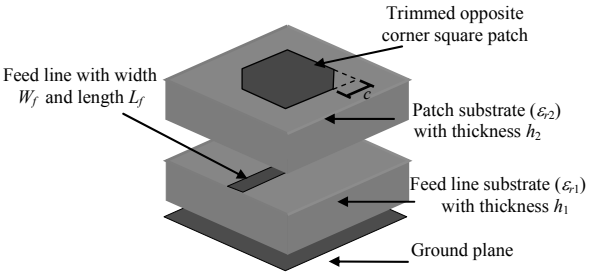

Fig. 1. Trimmed opposite corner square patch electromagnetic coupled fed microstrip antenna.

In the initial approximation, square patch dimensions and the cut-out triangle length were evaluated by using *CPPATCH* software [4]. The feed line width for a 50 Ω characteristic impedance was $W_f = 3.95$ mm. The final dimensions of the antenna and the feed line relative position with regard to the patch was adjusted using *Ensemble*® 8.0 [5] and were depicted in Fig. 2. The impedance measurements have carried out at the reference plane *R* (see Fig. 2) by using an HP8714C vector network analyzer. The element performance can be seen through the Figs. 3, 4, 5 and 6. The antenna prototype was shown in Fig. 7.

The measured results for the 10 dB return loss bandwidth (*RLBW*) was approximately 56 MHz whereas the 3 dB axial ratio bandwidth (*ARBW*) was 14 MHz. As it can be noted, the *RLBW* is four times greater than *ARBW*, what is a well-known characteristic of this particular circularly polarized microstrip radiator.

The directivity and gain of the single element were

computed using *IE3D*™ [6] and are illustrated in Fig. 6. The antenna directivity was approximately 7.2 dBi, and gain was 6.35 dBi, a typical value for microstrip patch radiators with a thin substrate, which leads to an efficiency of 82 %.

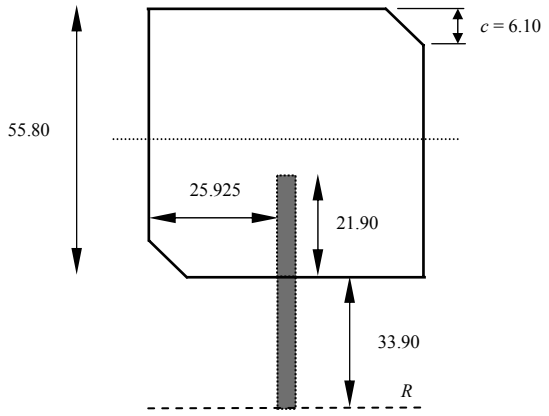

Fig. 2. Adjusted dimensions (mm) for the patch element.

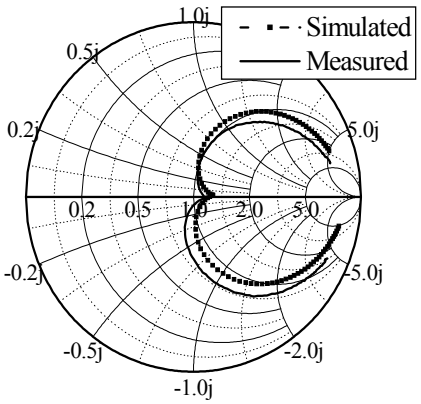

Fig. 3. Smith chart plots of input impedance. Dashed line (----) for simulated results and solid line (—) for measured results.

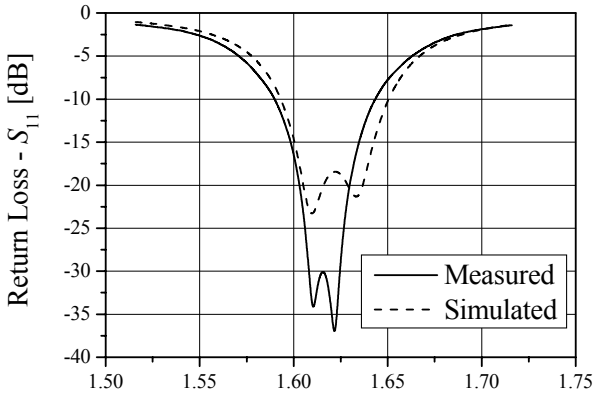

Fig. 4. Return loss of a trimmed opposite corner square patch microstrip antenna: (——) measured, and (-----) simulated.

According to the algorithm synthesis, it is necessary to calculate the element pattern function, $\boldsymbol{g}(\theta, \phi)$ (vectors are represented by boldface letters), and it was done, in a first approximation, by means of the cavity model of an equivalent circularly polarized near-square patch element. In this case, $\boldsymbol{g}(\theta, \phi)$ must be computed considering the two fundamentals TM_{01} and TM_{10} antenna modes.

If a and b are the lengths of the approximately square patch sides, m and n are the cavity resonant modes, ε_r is the substrate relative dielectric constant, it can be found that a = 56.3 mm and b = 53.8 mm, for the near-square element, operating at 1.616 GHz, using a 3.048 mm thickness substrate with ε_r = 2.55.

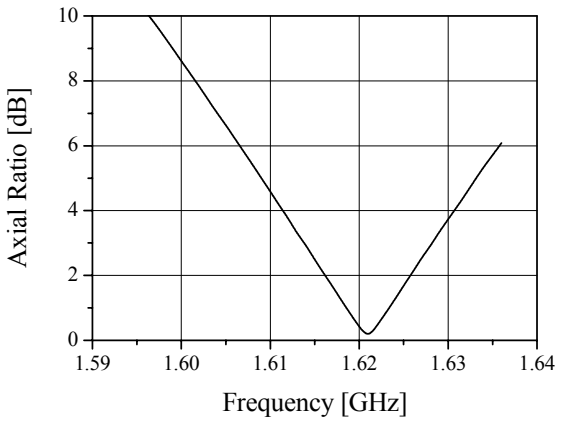

Fig. 5. Axial ratio of a trimmed opposite corner square patch microstrip antenna.

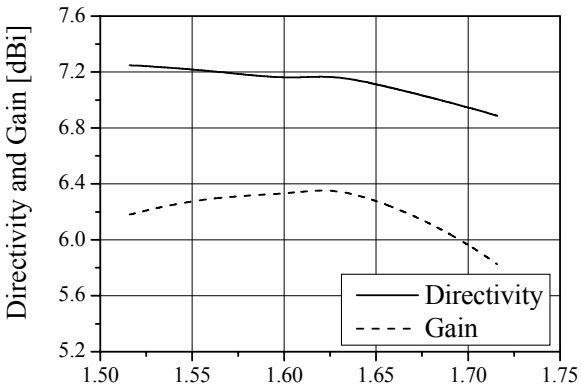

Fig. 6. Directivity and gain of the trimmed opposite corner square patch microstrip antenna.

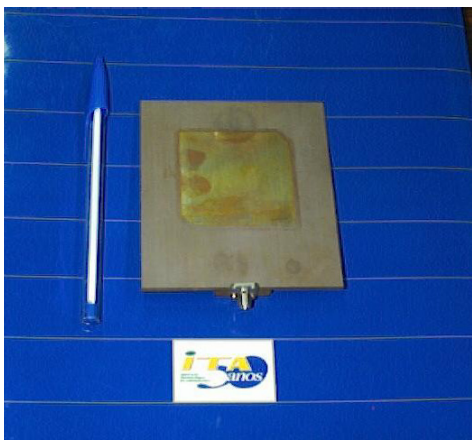

Fig. 7. Photo of the trimmed opposite corner square patch microstrip antenna prototype.

In this way, normalized components of the electric far field can be expressed as [7]:

$$\begin{aligned} e_\theta &= 2k_0^2 \sin\theta \sin\phi \cos\phi \\ &\times [\cos^2(\frac{m\pi}{2}) \sin(\frac{k_0 a}{2} \sin\theta\cos\phi) \\ &+ i \sin^2(\frac{m\pi}{2}) \cos(\frac{k_0 a}{2} \sin\theta\cos\phi)] \\ &\times [\cos^2(\frac{n\pi}{2}) \sin(\frac{k_0 b}{2} \sin\theta\sin\phi) \\ &+ i \sin^2(\frac{n\pi}{2}) \cos(\frac{k_0 b}{2} \sin\theta\sin\phi)] \\ &\times \left[\left(k_0^2 \sin^2\theta\cos^2\phi - (m\pi/a)^2\right)^{-1} \right. \\ &\left. + \left(k_0^2 \sin^2\theta\sin^2\phi - (n\pi/b)^2\right)^{-1} \right] \end{aligned} \quad (1)$$

$$\begin{aligned} e_\varphi &= 2k_0^2 \sin\theta \cos\phi \\ &\times [\cos^2(\frac{m\pi}{2}) \sin(\frac{k_0 a}{2} \sin\theta\cos\phi) \\ &+ i \sin^2(\frac{m\pi}{2}) \cos(\frac{k_0 a}{2} \sin\theta\cos\phi)] \\ &\times [\cos^2(\frac{n\pi}{2}) \sin(\frac{k_0 b}{2} \sin\theta\sin\phi) \\ &+ i \sin^2(\frac{n\pi}{2}) \cos(\frac{k_0 b}{2} \sin\theta\sin\phi)] \\ &\times \left[\cos^2\phi \left(k_0^2 \sin^2\theta\cos^2\phi - (m\pi/a)^2\right)^{-1} \right. \\ &\left. - \sin^2\phi \left(k_0^2 \sin^2\theta\sin^2\phi - (n\pi/b)^2\right)^{-1} \right] \end{aligned} \quad (2)$$

where

$$k_0 = \omega \sqrt{\mu_0 \varepsilon_0} \quad (3)$$

and ω is the operating angular frequency.

IV. Linear Array Pattern Synthesis

The array pattern synthesis problem is to find out the weight vector $\boldsymbol{w}$ which produces the magnitude of the response to closely match the desired side lobe specification, while guarantees maximum of the pattern function in the scan angle γ_s, with the input specification parameters, like the side lobe regions, the distance between the elements, d, and the desired side lobe level, σ.

The most common way to squint the main lobe to a desired direction is to establish a constant phase difference, δ, among the array elements, given by $\delta = -k_0 d \cos\gamma_s$ (for an linear array along x-axis, $\cos\gamma_s = \sin\theta\cos\phi$). This procedure takes into account an ideally isotropic radiated element. On the other hand, the *Dolph-Tschebyscheff's* synthesis can be used to control the side lobe level, but it is not suitable for large scan angles, as the *Dolph-Tschebyscheff's* synthesis is more adequate for broadside arrays [8].

When it is facing a problem of designing weights that achieve specified patterns for arrays with non-isotropic elements, it is necessary to consider a more general method [9-11]. The chosen algorithm and its array weights initialization are well explained in [9]. Taking a set of complex weights $\boldsymbol{w}$ to the input ports and summing the result so that the spatial response can be expressed as formed an input for the array

$$\boldsymbol{s}(\theta) = \boldsymbol{w}^t \cdot \boldsymbol{v}(\theta) \quad (4)$$

where $\boldsymbol{v}(\theta)$ is the steering vector of the array in the direction θ, and ^{t} denotes the Hermitian transpose.

If all the patch elements are equal, and if it is assumed that they have the same spatial response (radiation pattern) given by the cavity model of an equivalent circularly polarized near-square patch element, the steering vector $\boldsymbol{v}(\theta)$ can be expressed as [12]:

$$\boldsymbol{v}(\theta) = \begin{bmatrix} \boldsymbol{g}(\theta) \cdot e^{-i\omega\tau_1(\theta)} \\ \boldsymbol{g}(\theta) \cdot e^{-i\omega\tau_2(\theta)} \\ \cdots \\ \boldsymbol{g}(\theta) \cdot e^{-i\omega\tau_8(\theta)} \end{bmatrix} \quad (5)$$

where $\tau_l(\theta)$ is the time delay for a leaving signal from the array which makes a θ angle with the z-axis. The elevation angle, α, is given by: $\alpha = 90° - \theta$.

These weights are found as the solution to a specific constrained least-square problem

$$\min_{w} \quad \boldsymbol{w}^t \boldsymbol{A}\, \boldsymbol{w} \quad (6)$$

subject to two linear constraints,

$$\begin{aligned} &\boldsymbol{v}_s^t\, \boldsymbol{w} = 1 \\ &\mathrm{Re}[\boldsymbol{v}_d^t\, \boldsymbol{w}] = 0 \end{aligned} \quad (7)$$

where, in this expression, the vectors $\boldsymbol{v}_s$ and $\boldsymbol{v}_d$ are the steering vector and its derivative (regard to θ) at the squint angle, θ_s . With the matrix $\boldsymbol{A}$ denoting the covariance matrix of the steering vector, we have [9]:

$$\boldsymbol{A} = \frac{1}{2} \sum_{l=1}^{L} \boldsymbol{v}(\theta_l)\, \boldsymbol{v}^t(\theta_l) \quad (8)$$

in the side-lobe regions.

To illustrate the method, it is now considered an equidistant eight-element linear array with half-wavelength spacing. The array element was designed in Section III. Scan angle and desired side lobe level were set to be 45° and –20 dB, respectively. In the optimization algorithm, it is important to discuss that it is not necessary to use both the components of the vector $\boldsymbol{v}(\theta)$ to compute the matrix $\boldsymbol{A}$. Thus, it was used only the theta-component of the function $\boldsymbol{v}(\theta)$ in the matrix $\boldsymbol{A}$ evaluation. This procedure is suitable when the two orthogonal modes in the patch are excited with a 90° time-phase difference between them. Table I shows the current amplitudes and phases after optimization process.

TABLE I

CURRENT WEIGHT AND PHASE RESULTS FOR AN 8-ELEMENT MICROSTRIP PHASED ARRAY. INTER-ELEMENT SPACING IS $0.5\lambda_0$; $\gamma_S = 45°$ ($\phi = 0$, $\theta_S = 45°$ AND $\sigma = -20$ dB). THIS TABLE SHOWS THE COMPARISION OF THE EFFECT ON THE ALGORITHM BY USING TWO DIFFERENT PATTERN FUNCTIONS.

	$\boldsymbol{g}(\theta, \phi)$ = cavity model		$\boldsymbol{g}(\theta, \phi) = 1^*$	
	Weight	Phase	Weight	Phase
w_1	1.00(-7.75 dB)	0.0°	1.00(-9.5 dB)	0.0°
w_2	1.39(-4.9 dB)	-143.7°	1.16(-8.2 dB)	-155.5°
w_3	2.00(-1.7 dB)	83.8°	2.16(-2.8 dB)	72.3°
w_4	2.44(0.0 dB)	-44.5°	2.99(0.0 dB)	-47.7°
w_5	2.44(0.0 dB)	-171.6°	2.99(0.0 dB)	-164.4°
w_6	2.00(-1.7 dB)	60.1°	2.16(-2.8 dB)	75.6°
w_7	1.39(-4.9 dB)	-72.4°	1.16(-8.2 dB)	-56.6°
w_8	1.00(-7.75 dB)	143.9°	1.00(-9.5 dB)	147.9°

* considered only in the half space z > 0.

In the second and third columns, the vector $\boldsymbol{w}$ was computed with the complex pattern function $\boldsymbol{g}(\theta, \phi)$ given by the cavity model, whereas, in the fourth and fifth columns, $\boldsymbol{w}$ was computed with function $\boldsymbol{g}(\theta, \phi)$ given by an ideal isotropic radiator, considered, as a first approximation, only in the half space $z > 0$. In Table II, it was shown the comparison between the algorithm synthesis and the current weight and phase calculated by means of a constant phase difference, δ, among the array elements (fifth column), and the *Dolph-Tschebyscheff's* synthesis to control the side lobe level (forth column), as it has been done in the standard antenna textbooks [8]. It can be noted that a constant phase difference, δ, between the elements was not suitable for reaching the desired scan angle.

TABLE II

CURRENT WEIGHT AND PHASE RESULTS FOR AN 8-ELEMENT MICROSTRIP PHASED ARRAY. INTER-ELEMENT SPACING IS $0.5\lambda_0$; $\gamma_S = 45°$ ($\phi = 0$, $\theta_S = 45°$ AND $\sigma = -20$ dB) THIS TABLE SHOWS THE COMPARISON BETWEEN THE ALGORITHM SYNTHESIS RESULTS AND THE DOLPH-TSCHEBYSCHEFF'S METHOD.

	$\boldsymbol{g}(\theta, \phi)$ = cavity model		$\boldsymbol{g}(\theta, \phi) = \mathbf{1}$	
	Weight	Phase	Weight	Phase
w_1	1.00(-7.75 dB)	0.0°	1.00(-5.5 dB)	0.0°
w_2	1.39(-4.9 dB)	-143.7°	1.22(-3.8 dB)	-127.3°
w_3	2.00(-1.7 dB)	83.8°	1.64(-1.2 dB)	105.4°
w_4	2.44(0.0 dB)	-44.5°	1.89(0.0 dB)	-21.9°
w_5	2.44(0.0 dB)	-171.6°	1.89(0.0 dB)	-149.2°
w_6	2.00(-1.7 dB)	60.1°	1.64(-1.2 dB)	83.5°
w_7	1.39(-4.9 dB)	-72.4°	1.22(-3.8 dB)	-43.8°
w_8	1.00(-7.75 dB)	143.9°	1.00(-5.5 dB))	-171.1°

Another important capability of the implemented algorithm is to predict the minimum required number of elements that are able to reach the desired scan angle. It is almost intuitive to see that, for a given inter-element spacing, d, and a given side lobe level, σ, the greater scan angle is wanted, the larger number of elements is required, particularly for wide scan angle, since e_φ given by the cavity method goes fast to zero close to the ground plane. This behavior is shown in Table III for a scan angle of 20°, 60° and 70°. In the above examples, peaks within the side lobe regions were determined to an accuracy of 0.1°.

TABLE III

MINIMUM NUMBER OF ELEMENTS OF A MICROSTRIP PHASED ARRAY FOR REACHING THE DESIRED SCAN ANGLE AS A FUNCTION OF THE PARAMETERS d, σ AND θ_s.

d(wavelength)	$\sigma(dB)$	θ_s (°)	Required Minimum **No**. of elements (N)
0.50	-30	20	5
0.50	-20	60	16
0.50	-20	70	36

It is very important to emphasize that this algorithm may encounter numerical difficulties if the set of linear constraints are nearly dependent, as described in [9].

Figs. 8 - 11 show the computed algorithm radiation pattern for different scan angle cases (0°, 10°, 20° and 40°). In the first one, it was illustrated the broadside synthesis, i.e., $\theta_s = 0°$ ($\alpha = 90°$). It should be emphasized that, for the broadside case and $\boldsymbol{g}(\theta, \phi) = 1$, the excitation currents calculated by the present algorithm are exactly the same as the *Dolph-Tschebyscheff's* method [8].

In the second case ($\theta_s = 10$), the phase difference, δ, between the elements calculated by the algorithm were not constant. However, instead of these results, if the expression $\delta = -k_0 d \sin\theta_s$ is used the main lobe can reach the desired scan angle on the *Dolph-Tschebyscheff's* synthesis. In the third synthesis, the same situation happens. On the other hand, in the last synthesis, ($\theta_s = 40$) the current amplitudes given by *Dolph-Tschebyscheff's* method were quite different to that calculated by using the algorithm synthesis, and the main lobe can not reach the desired scan angle if the expression $\delta = -k_0 d \sin\theta_s$ is used. These results show the *Dolph-Tschebyscheff's* synthesis is more adequate for broadside arrays, in according to the previous statement [8].

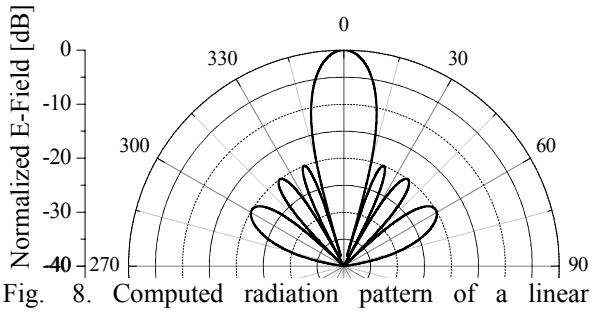

Fig. 8. Computed radiation pattern of a linear 8–element microstrip phased array squinted to $\theta_s = 0°$, at $\phi = 0$ plane.

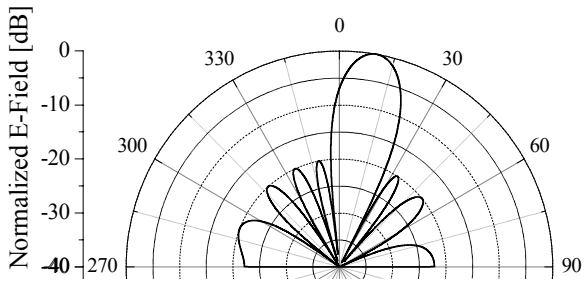

Fig. 9. Computed radiation pattern of a linear 8–element microstrip phased array squinted to $\theta_s = 10°$, at $\phi = 0$ plane.

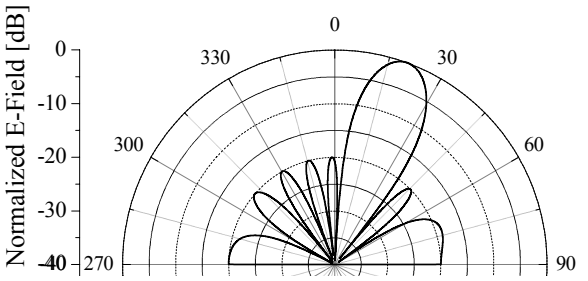

Fig. 10. Computed radiation pattern of a linear 8–element microstrip phased array squinted to $\theta_s = 20°$, at $\phi = 0$ plane.

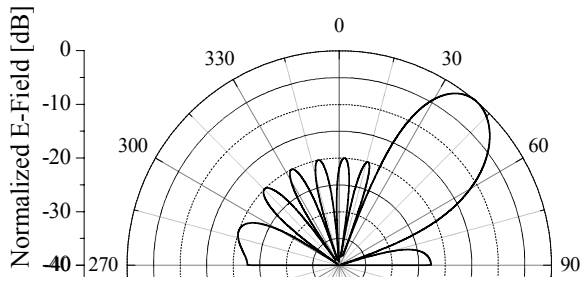

Fig. 11. Computed radiation pattern of a linear 8–element microstrip phased array squinted to $\theta_s = 40°$, at $\phi = 0$ plane.

V. PHASED ARRAY SIMULATED RESULTS

The radiation patterns of the eight elements microstrip phased array designed in Section IV with inter-element spacing, d , equals to 0.5 λ_0 (see Table I for the array characteristics) were computed by *Ensemble*® and *IE3D*™ packages at the operation frequency. In this calculation, the eight input ports were fed with the current amplitudes and phases encountered in the last Section. In the initial simulations, it was necessary to adjust the truncated corner patch so as to set the minimum axial ratio value at the operation frequency. After this, c was set to 5.4 mm. This procedure indicates that the array axial ratio varies with changing the scan angle. Fig. 12 shows the array geometry and the coordinate system for the radiation pattern calculation.

Fig. 13 shows the phased array axial ratio bandwidth, which remains close to the single element axial ratio. For the array case, the 3 dB axial ratio bandwidth (*ARBW*) was 15 MHz.

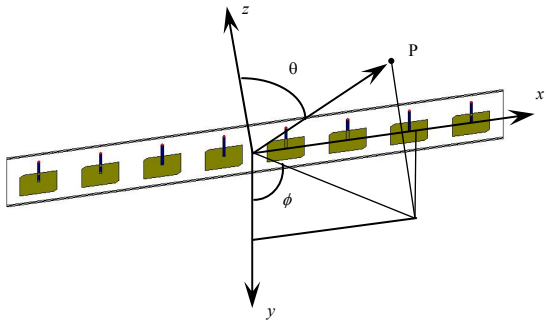

Fig. 12. Coordinate system for the 8-element microstrip phased array radiation pattern calculation.

In Fig. 14 we have the simulated axial ratio as a function of the theta angle, and it can be seen that at the scan angle direction (45°), the *ARBW* is excellent.

Regarding to array directivity and gain, it has been shown in Fig. 15 that, at the operation frequency, directivity was 13.8 dBi and gain was 12.6 dBi, which lead to an array efficiency of 76 %.

Radiation pattern for the 8-element microstrip phased array calculated at the operation frequency (H-plane), is depicted in Fig. 16. Very good agreement between algorithm synthesis and *Ensemble*® evaluation is obtained.

In Fig. 17 it is shown the radiation pattern calculated by the algorithm in comparison with *IE3D*™ simulation. The two results are in very good agreement.

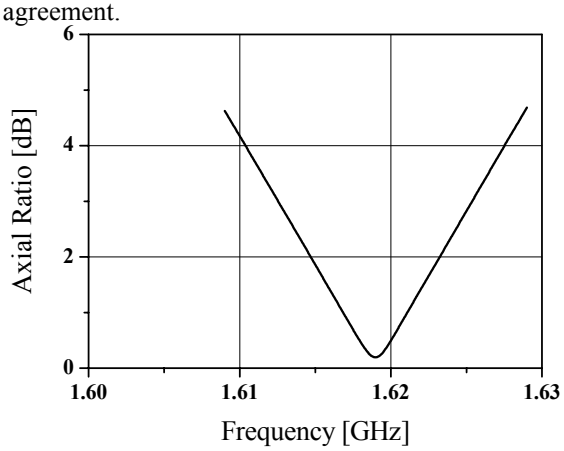

Fig. 13. Computed phased array axial ratio.

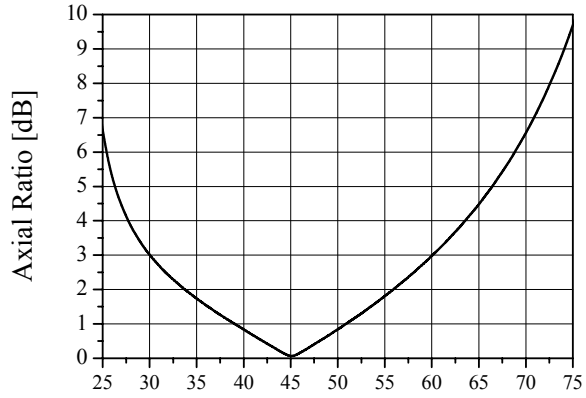

Fig. 14. Computed axial ratio as a function of the scan angle.

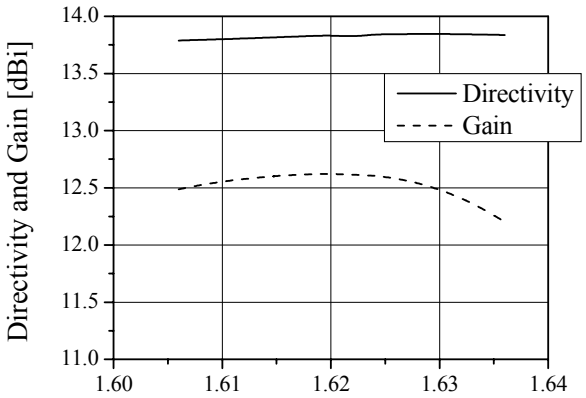

Fig. 15. Directivity and gain of the 8–element phased array microstrip antenna with $\theta_s = 45°$.

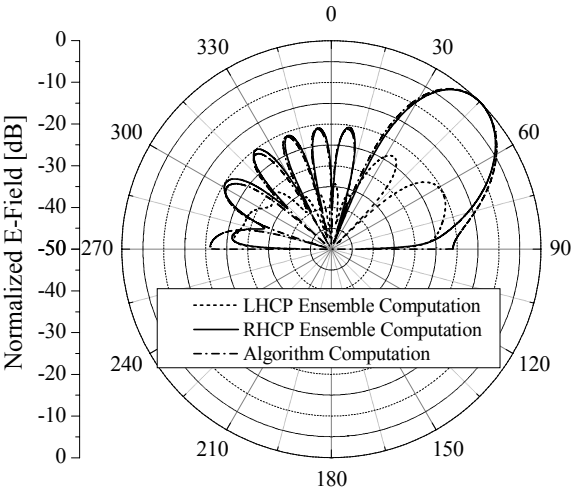

Fig 16. Algorithm *vs*. *Ensemble*® computed phased array radiation pattern at H-plane.

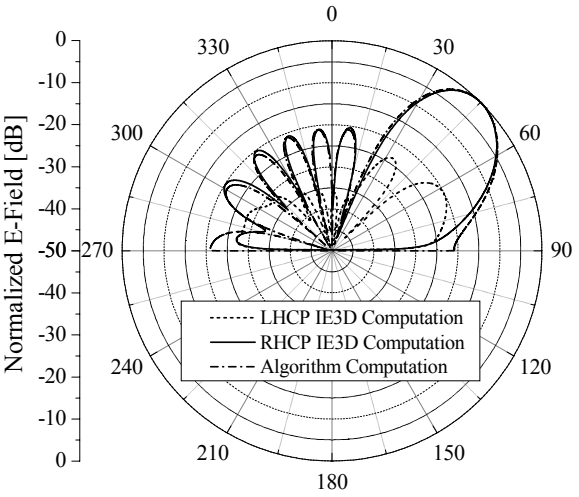

Fig 17. Algorithm *vs*. *IE3D*™ computed phased array radiation pattern at H-plane.

In Fig. 18, it is depicted the algorithm radiation pattern by using the currents found in the synthesis with the function $\boldsymbol{g}(\theta, \phi)$ given by an ideal isotropic radiator, or $\boldsymbol{g}(\theta, \phi) = 1$, for z ≥ 0 and the *Ensemble*® radiation pattern simulated with the element input ports fed by these same currents. The input array parameters were set to the same values: $d = 0.5\ \lambda_0$, number of elements equals to eight, side lobe level, $\sigma = -20\ dB$ and $\theta_s = 45°$. *Ensemble*® results showed an array radiation pattern somewhat different from the algorithm pattern. Besides, it can be seen a broader main lobe pointed to a scan angle of 43.5°, 1.5° different from the synthesis.

Another result obtained with the developed algorithm synthesis can be seen in Fig. 19. In this particular example the phased array parameters were $d = 0.5\lambda_0$, $\gamma_s = 50°$ ($\phi = 0°$, $\theta_s = 50°$), $\sigma = -20$ dB and $N = 16$-*RHCP* microstrip elements. This figure clearly shows the 50° beam scan angle and side lobes below –20 dB.

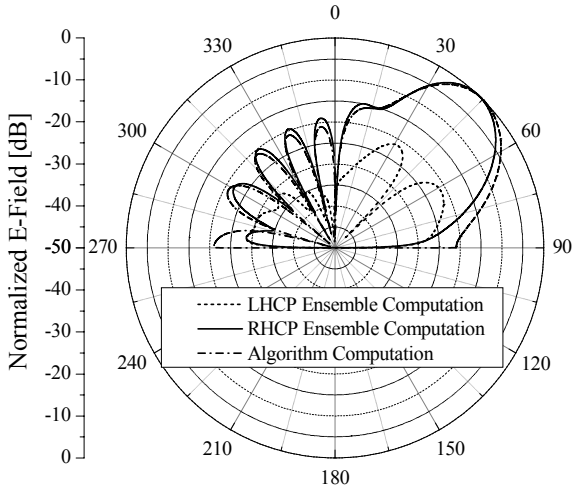

Fig. 18. *Ensemble*® computed phased array radiation pattern at H-plane using $\boldsymbol{g}(\theta, \phi) = 1$ in algorithm computation.

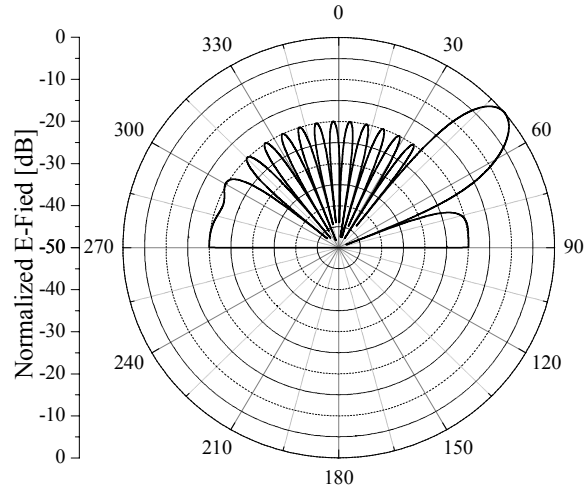

Fig. 19. Phased array radiation pattern for 16-*RHCP* microstrip elements, computed with the developed algorithm synthesis, at $\phi = 0$ plane.

VI. CONCLUSION

A useful method to design microstrip phased arrays with reduced side lobe level was presented. The microstrip antenna technology was chosen because it is lightweight, low profile and can easily be integrated to a microstrip beam forming circuit. The microstrip element, a truncated corner patch electromagnetic coupled fed antenna was designed and manufctured. Very good

agreement between numerical predictions and measured results were obtained. Then, an algorithm synthesis was implemented to design circularly polarized microstrip phased array whose main lobe can be squinted to a desired scan angle and, at the same time, the magnitudes of all side lobes shall be under a specified level. A linear array of eight microstrip elements was designed and analyzed by numerical simulations. It could be seen that the use of an isotropic radiator model in phased array synthesis was not suitable for a good accuracy, especially at low elevation angle. This technique can be used to design more complex structures, like 2D and 3D arrays, and can also be employed as an efficient tool for education purpose in microstrip antenna courses.

REFERENCES

[1] R. J. Mailloux, *Phased array antenna handbook*. Norwood: Artech House, 1994.

[2] R. C. Hansen, *Phased array antennas*. New York: John Wiley & Sons, 1998.

[3] E. W. Cheney, *Introduction to approximation theory*. Chelsea: Amer. Mathematical Society, pp. 57-100, 1982.

[4] R. A. Sainati, *CAD of microstrip antennas for wireless applications*, Chapter 5, Norwood: Artech House, 1996.

[5] *Ensemble® planar EM simulation*, Ansoft Corporation, Feb., 2001.

[6] *IE3D™ User's manual*, Release 5, Zeland Software, 1999.

[7] F. Lumini, L. Cividanes and J. C. S. Lacava, Computer aided design algorithm for singly fed circularly polarized rectangular microstrip patch antennas, *Int. J. RF and Microwave CAE*, No. 9, pp. 32-41, 1999.

[8] C. A Balanis, *Antenna theory: analysis and design*. 2nd edition. New York: John Wiley & Sons, 1997.

[9] C. Y. Tseng and L. J. Griffiths, A simple algorithm to achieve desired patterns for arbitrary arrays, *IEEE Trans. Signal Processing*, vol. 40, pp. 2737-2746, Nov. 1992.

[10] C. A. Olen and R. T. Compton, A numerical pattern synthesis algorithm for arrays, *IEEE Trans. Antennas Propagat.*, vol. 38, pp. 1666-1676, Oct. 1990.

[11] B. P. Ng, M. H. Er and C. Kot, A flexible array synthesis method using quadratic programming, *IEEE Trans. Antennas Propagat.*, vol. 41, pp. 1541-1550, Nov. 1993.

[12] R. T. Compton Jr., *Adaptive antennas*. Englewood Cliffs: Prentice-Hall, 1988.

Determination of the Resonant Frequencies of a Rectangular Patch Antenna by the Application of the Modified Transverse Resonance Technique

Jefferson Costa e Silva, Joabson N. de Carvalho,Rafael Marrocos Magalhães, Paulo Farias Braga, Alfrêdo Gomes Neto
Federal Center of Technological Education of Paraíba – CEFET-PB
Av. 1 de maio, 720 João Pessoa - CEP:58.015-430
alfredogomes@ieee.org

Adaildo Gomes D'Assunção
Federal University of Rio Grande do Norte UFRN
P. O. Box 1655 - Natal, RN CEP: 59.072-970
adaildo@ct.ufrn.br

***Abstract*—This article presents the determination of the resonant frequencies of a patch antenna by the application of the Modified Transverse Resonance Technique, MTRT. The obtained results are compared with several numerical and experimental results available in the specialized literature, presenting a good agreement. As a full wave analysis technique, practically there are no restrictions for patch dimensions or substrate height. The analysis of the resonance in each dimension of the patch allows a better understanding of the patch antenna resonance mechanisms what is especially interesting when effects as modal degeneration and polarization loss are analyzed.**

***Index Terms*—Patch antennas, resonant frequencies, MTRT.**

I. Introduction

In microwaves and millimeter waves frequencies patch antennas present some advantages, such as low profile, small dimensions and reduced cost. Basically, the patch antenna consists of a metallic patch placed above a ground plane. The patch and the ground plane are separated by a dielectric substrate, Fig. 1 [1-4]. 1. One of the principal limitations of the patch antenna is the small bandwidth, mainly determined by the patch dimensions and by the substrate height and dielectric constant. Another important aspect to be considered is the presence of higher order modes. If the antenna is projected to operate in a specific bandwidth, higher order modes can introduce undesirable effects as efficiency reduction, radiation diagram degradation and loss of the polarization characteristics. On the other hand, when multi-bandwidth antenna applications are desired, the presence of higher order mode can be interesting.

A higher order mode that can be present in a patch antenna is the substrate mode, also denominated surface wave mode. The antenna may couple power into substrate modes and as these modes do not contribute to primary radiation pattern, these modes are loss mechanisms [5]. Therefore, the knowledge of the higher order modes behavior, including the surface modes, is an important aspect to be considered in patch antennas project.

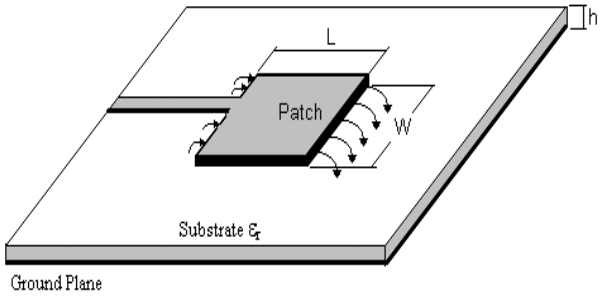

Fig. 1. Rectangular microstrip patch antenna

Actually, there are several theoretical methods of analysis of patch antennas. However, many of those methods are based on the quasi-static model of a microstrip transmission line in which the resonant frequency of antennas has been computed by placing a side magnetic wall extending from microstrip to the ground plan. Moreover, for high frequencies, or when thick substrates are used, the quasi-static analysis is not sufficiently accurate [6]. In these cases, full wave methods are commonly used.

In this article the Modified Transverse Resonance Technique, MTRT [7],[8] is applied to determine the behavior of the resonant modes in a patch antenna. As the MTRT is a full wave technique, higher order modes are clearly identified. The obtained results are compared with numerical and experimental results available in the literature, presenting a good agreement.

II. THEORY

In this work the rectangular patch antenna is analyzed as the superposition of two infinite microstrip lines (Fig. 2). The one dimension resonant frequencies, $f_{r(moo)}$, $f_{r(ono)}$ and $f_{r(oop)}$, where m, n and p are related to the W, L and h dimensions, respectively, are obtained separately, through the application of MTRT. The other resonant frequencies are obtained by (1).

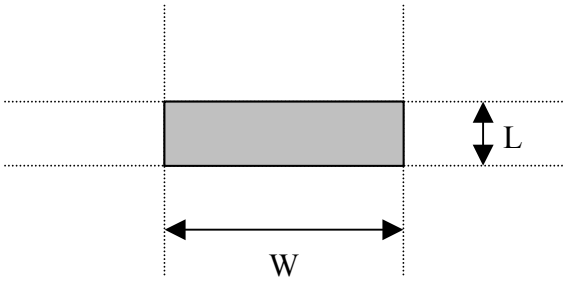

Fig. 2 – Superposition of two microstrip lines

$$f_{r(mnp)} = \sqrt{\left(f_{r(m00)}\right)^2 + \left(f_{r(0n0)}\right)^2 + \left(f_{r(00p)}\right)^2} \quad (1)$$

MODIFIED TRANVERSE RESONANCE TECHNIQUE, MTRT

In the conventional TRT formulation, an appropriate equivalent circuit is established, representing the discontinuity planes and the boundary conditions. By the calculation of the resonance frequencies of this equivalent circuit, the effective dielectric constant is obtained and other additional characteristics of the structure are determined [9]. The difference between TRT and MTRT is the adopted equivalent circuit. In TRT, the discontinuity planes are parallel to the strip, while in MTRT those planes are perpendicular. Fig. 3 and Fig. 4 present the equivalent networks and respective matrix admittances. Mode coupling that occurs at each discontinuity plane is represented by a generic voltage source. The different transmission line sections represent the different waveguide sections.

Observe that in TRT exist only homogeneous sections. Consequently, only TE and TM modes are considered. In MTRT there are two homogeneous sections and one inhomogeneous. Therefore, the solutions in MTRT include, besides the TE and TM modes, LSE and LSM modes, that are related to the surface modes. Furthermore, observe that the analyzed structure may be open sides, avoiding, in this manner, the presence of *boxed modes* in the numerical solutions. MTRT is described in [7],[8]. One of the obtained results is the effective dielectric constant, given by:

$$\varepsilon_{reff} = \left(\frac{\gamma_z}{k_0}\right)^2 \quad (2)$$

Positive values of ε_{reff} correspond to evanescent modes and negative values to propagating modes. The resonant frequency is given by ε_{reff}=0.

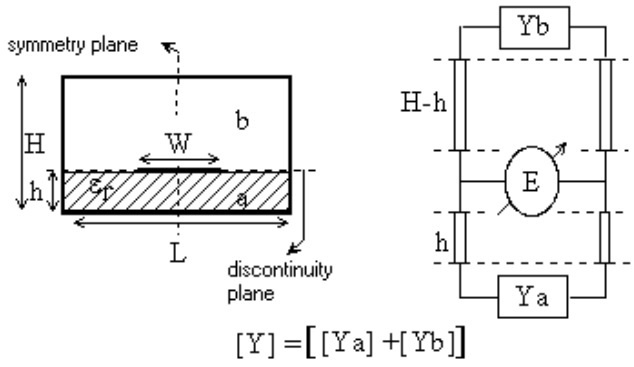

Fig. 3 - TRT – Equivalent network

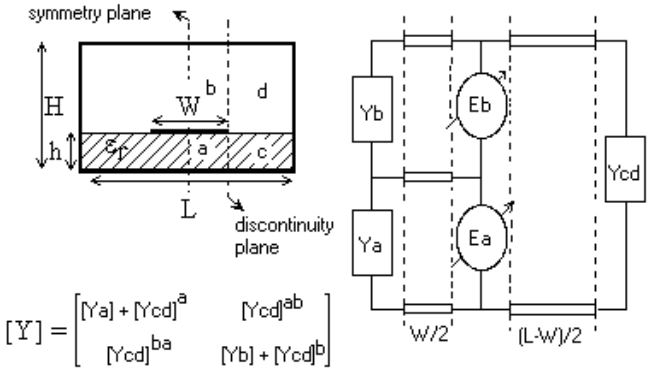

Fig. 4 - MTRT – Equivalent network

III. NUMERICAL RESULTS

Table I presents the patch dimensions, substrate height and dielectric constant for antennas with several configurations. The considered resonant frequency mode is the f_{r010}. Thus, MTRT is applied to a microstrip of width L, with an electric symmetry. The obtained results are compared to the results presented in [6], determined numerically by the spectral domain method (MDE), and experimentally. A good agreement is observed, with relative difference to the experimental results of a maximum of 2%.

In Fig. 5 are presented the curves of ε_{reff} *x frequency (GHz)* for the antennas 1, 4, 7 and 8. Even in the considered frequency bandwidth the microstrip has, in some cases, other modes, the curves for those were not exhibited. Analogous results are presented in Fig. 6, for the antennas 2, 3, 5 and 6.

Table II presents the patch dimensions, substrate height and dielectric constant for antennas with thick

substrate. The obtained results are compared to the experimental results presented in [10]. Again, the considered resonant frequency mode is the f_{r010} and a good agreement is observed.

TABLE I
MTRT – MDE - EXPERIMENTAL

Ant.	ε_r	h (mm)	W (mm)	L (mm)	fr(GHz) MTRT	fr(GHz) MDE [6]	fr(GHz) Exp. [6]
1	10,2	1,27	30,0	20,0	2,231	2,173	2,26
2	10,2	1,27	15,0	9,5	4,423	4,490	4,49
3	10,2	2,54	30,0	19,0	2,196	2,150	2,24
4	2,22	0,79	40,0	25,0	3,925	3,942	3,94
5	2,22	0,79	20,0	12,5	7,543	7,639	7,65
6	2,22	1,52	40,0	25,0	3,811	3,90	3,84
7	2,62	1,59	11,43	76,2	1,190	1,190	1,192
8	2,50	1,59	6,85	41,4	2,212	2,214	2,215

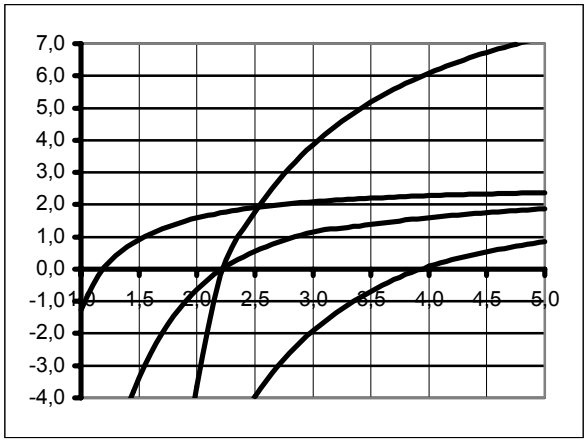

Fig. 5. ε_{reff} *x frequency (GHz)* – electrical symmetry ant. 1, 4, 7 and 8

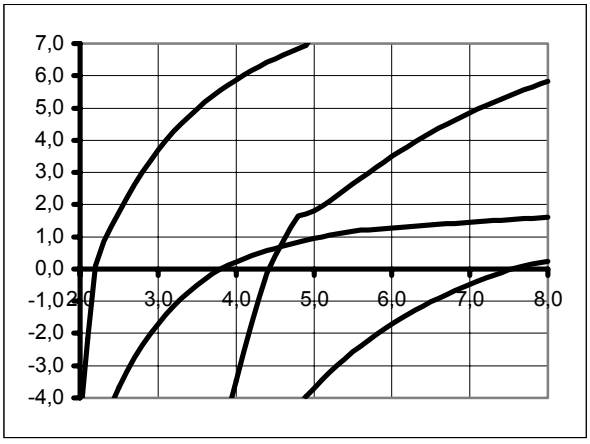

Fig. 6. ε_{reff} *x frequency (GHz)* – electrical symmetry ant. 2, 3, 5 and 6

Table III the obtained results for higher order modes are compared to the presented in [11]. Considering the *patch* dimensions and frequency bandwidth, only resonance in W and L are analyzed. For each considered mode adopted symmetry is indicated. For the modes f_{r02} and f_{r21}, it was not possible to measure the respective resonant frequencies [11]. The presented measured frequency, 5,535GHz, probably is resulted of the degeneration of the resonance frequencies of the modes f_{r02} (5,856GHz) and f_{r21} (5,741GHz). Certainly, the measurement process also influences this result. Evidence that the frequencies obtained with MTRT for those modes are correct is that the value of the resonance frequency for the mode f_{r12}, calculated from the theoretical value of f_{r02}, presents a very good agreement when compared with the experimental value.

TABLE II
MTRT – EXPERIMENTAL – THICK SUBSTRATE

Ant.	ε_r	h (mm)	W (mm)	L (mm)	fr(GHz) MTRT	fr(GHz) Exp. [10]
1	2,33	3,175	57,0	38,0	2,352	2,31
2	2,33	3,175	45,5	30,5	2,863	2,89
3	2,33	1,524	17,0	11,0	7,832	7,87
4	2,33	3,175	29,5	19,5	4,219	4,24
5	2,33	3,175	19,5	13,0	5,796	5,84
6	2,33	3,175	17,0	11,0	6,896	6,80
7	2,33	3,175	14,0	9,0	7,683	7,70
8	2,33	3,175	12,0	8,0	8,294	8,27
9	2,33	3,175	10,5	7,0	9,136	9,14
10	2,33	3,175	9,00	6,0	10,225	10,25
11	2,33	9,525	17,0	11,0	4,707	4,73

TABLE III
MTRT – EXERIMENTAL – HIGHER ORDER MODES

		W=38,0; L=31,8; h=1,568(mm); εr=2,34	
fr(mn).	Symmetry	fr(GHz) MTRT	fr(GHz) Exp. [11]
10	Electric	2,467	2,430
01	Electric	2,922	2,905
11	------	3,824	3,785
20	Magnetic	4,942	4,835
02	Magnetic	5,856	**5,535**
21	------	5,741	**5,535**
12	------	6,354	6,330
30	------	7,427	7,215

IV. CONCLUSIONS

In this article the determination of the resonant frequencies of a rectangular patch antenna, by the application of MTRT was presented. When compared to other results, numerical and experimental, the obtained results present a very good agreement, even considering higher order modes. As a full wave analysis technique, practically there is no restriction on patch dimensions or substrate height. One of the advantages of the proposed technique is the possibility of inclusion of the surface modes, what make MTRT interesting in project of structures type PBG. Finally, understand the resonance mechanism is one of the main advantages of the proposed methodology.

ACKNOWLEDGEMENT

The authors would like to thank to the Brazilian Research Agency CNPq and to VITAE for partial financial support.

REFERENCES

[1] I. J. Bahl and P. Bhartia, *Microstrip Antennas*, Artech House, Dedham, MA, 1980.

[2] J. R. James, P. S. Hall and C. Wood, *Microstrip Antenna – Theory and Design.* Peter Peregrinus LTD, London, UK, 1981.

[3] M. Pozar, "Microstrip Antennas," Proc. IEEE, vol. 80, No 1pp. 79–81, Jan. 1992.

[4] C. A. Balanis, *Antenna theory analysis and design*, 2nd edition, John Wiley & Sons Inc. 1997.

[5] Ramón Gonzalo, Peter de Maagt and Mario Sorolla, "Enhanced patch-antenna performance by suppressing surface waves using photonic-bandgap substrates", *IEEE Trans. on Microwave Theory and Techniques*, vol. 47, pp. 2131-2138, Nov. 1999.

[6] A. Kedar; K. Sharma; K. K. Gupta; G. P. Srivastava; M. Misra; and N. D. Kataria;. " Parametric study of microstrip patch antennas", *Microwave Conference, 2000 Asia-Pacific*, pp. 1403 - 1406 Dec. 2000

[7] Alfrêdo Gomes Neto, *An Alternative Formulation of the Transverse Resonance Technique (in Portuguese),* Dr. Thesis, UFPB, Campina Grande, Brazil, Dec., 1994

[8] Alfrêdo Gomes Neto, Creso S. da Rocha, Herve Aubert, D. Bajon, H. Baurdand, "MTRT – A modified transverse resonance technique", *ACES Journal*, vol. 12, pp. 19-25, Dec., 1997

[9] R. Sorrentino. *Transverse Resonance* Technique, in *Numerical techniques for Microwave and Millimeter- Waves Passive Structures*, T. Itoh, ed., John Wiley and Sons, Inc., New Yorkm New York, 1989

[10] E. Chang; S. A. Long; W. F. Richards: "An experimental investigation of electrically thick rectangular microstrip antennas", *IEEE Trans. On Antennas and Propagation*, vol. 34, pp. 767-772, June, 1986

[11] Russel W. Dearnley. Alain R. F. Barel: "A comparison of models to determine the resonant frequencies of a rectangular microstrip antenna, *IEEE Trans. On Antennas and Propagation*, vol. 37, pp. 114-118, Dec., 1989

A Study of Quality of Video Multicast in a Differentiated Services Domain with DSMCast

Karine Barbosa Carbonaro and Paulo Roberto Guardieiro

Faculty of Electrical Engineering, Federal University of Uberlândia
Av. João Naves de Ávila, 2121 - CEP 38400-902 - Uberlândia - MG - Brazil
karine@lrc.eletrica.ufu.br, prguardieiro@ufu.br

***Abstract*— Real time multicast video distribution is considered as one of the most important applications of the IP Multicast. This application presents difficulties in relation the heterogeneity and scalability of the receivers. The integration of the technologies multicast and DiffServ using DSMCast provides scalability to routing multicast and QoS guarantees. In this paper, we evaluate the performance of real-time video applications on the DSMCast architecture and, demonstrate the obtainment of heterogeneous QoS, scalability and conservation of bandwidth.**

***Index Terms*— DiffServ, Multicast, Video, Heterogeneous Quality of Service.**

I. Introdution

Given the rapid development and deployment of multimedia applications and the multi-receiver nature of video programs, real-time video distribution has emerged as one of the most important IP multicast applications [1]. It's also an essential component of many current and emerging Internet applications, such as videoconferencing and distance learning.

Because network conditions are dynamic and there is no quality of service (QoS) guarantee [2], [3] in the current best-effort Internet, bandwidth adaptability becomes an essential requirement for video distribution over the Internet [4]. The multicast model supports such applications in an efficient manner because rather than setting up separate unicast connections for each receiver in the group, a single group address is used to identify the entire group. In essence, the multiple unicast connections are reduced into a single multicast tree that transmits/replicates information only when necessary.

Generally, a non-adaptive stream suffers two deficiencies. First, it can either under-use the available bandwidth or cause congestion collapse, which eventually degrades the video playback quality. Second, it can potentially lead to unfair bandwidth allocation, as the dominant traffic in the Internet TCP (Transmission Control Protocol) is adaptive. A possible solution to these problems is to provide necessary QoS support via service differentiation. The Internet Engineering Task Forces (IETF) has proposed the technique to enhance QoS support in the Internet: Differentiated Services (DiffServ) [5].

The integration multicasting and DiffServ is advantageous because it will provide a method for conservation of network bandwidth and it will guarantee the attendance to the requirements of QoS with the differentiation service. The architecture DSMCast [6] can offer viable approach for DiffServ multicasting. DSMCast reduces the edge-to-edge transport problem across a single DiffServ domain. By migrating the per-group state information from the router to the packet, core routers are allowed to remove the complexity of multicast routing.

In this paper, by means of modelling and simulation, we evaluate the performance of the video applications on the DSMCast architecture and demonstrate the obtainment of heterogeneous QoS, scalability and conservation of bandwidth.

The remaining of this paper is organized as follows. In Section II, we describe the multicast and DiffServ integration problems. Section III presents the DSMCast architecture. Section IV presents the scenario and parameters of simulation. In Section V, the obtained results are presented. Finally, in Section VI, we make some concluding remarks.

II. Multicast and Diffserv Integration

DiffServ proposes a model for QoS while multicast proposes a model for group applications. Although both are complementary technologies, the integration of these technologies is a non-trivial task due to architectural conflicts between multicast and DiffServ.

A. IP Multicast

The proliferation of QoS-aware group applications associated with recent advancements in high-speed networks is driving the need for efficient multicast communication services satisfying the QoS requirements of such applications. There are two ways by which group communication can be achieved: multiple unicast connections and multicast. The difference between multicasting and separately unicasting data to several destinations is best captured by the host group model [7] definition. In the traditional unicast model, a group of n users requires that each piece of data be sent out n times from the source. This overhead is further compounded by the fact that such applications typically consume large amounts in the bandwidth due to their inherent rich multimedia nature. Thus, the multicasting model was proposed for supporting

such applications in an efficient manner because rather than setting up separate unicast connections for each receiver in the group, a single group address is used to identify the entire group. In essence, the multiple unicast connections are reduced into a single multicast tree that transmits/replicates information only when necessary.

B. DiffServ

In order to supply the QoS demand in the Internet, the IETF proposes the Differentiated Services (DiffServ or DS) model [5]. DiffServ offers a scalable model based on aggregated traffic flows where there isn't any need to maintain per-flow information. Through service classes, it offers a differentiated treatment to the several flows in Internet, according to the needs of bandwidth, delay, jitter and packet losses.

The networks that implement the DiffServ proposal are denominated DS domain. Routers in a DiffServ domain are divided into two categories: core routers and edge routers. Core routers do not have per-flow state and differentiate packets according to the marking DSCP (DiffServ Code Point) of the packet. In contrast, edge routers are statefull entities that are responsible for policing and/or marking all packets according to an SLA (Service Level Agreement) between the source and the domain, or between two domains.

The IP packets, when entering in a DS domain, they are classified based on header information. This classification defines the marking of the DSCP field [8], which determines the treatment received by the packets along the network in agreement with the established PHB (Per-Hop Behavior). Amongst the PHBs standardization proposal, there are PHB EF (Expedited Forwarding) and PHB AF (Assured Forwarding).

- *EF PHB:* The EF PHB is designed to implement a service with low delay, jitter, and loss in addition to an assured bandwidth, as specified in RFC 3246 [9]. EF is used for services that have strict requirements on delay and jitter such as time-critical and multimedia applications. This type of service is usually referred to as *virtual leased line* (VLL).
- *AF PHB:* The AF PHB is used for building services with controlled loss and assured bandwidth. Such services do not have any delay or jitter guarantees. The IETF DiffServ WG defined a PHB group for AF in [10]. The AF PHB group consists of three forwarding behaviors, AFx1, AFx2, and AFx3 in increasing order of drop precedence.

C. Multicast and DiffServ Conflicts

The primary conflicts between DiffServ and multicasting are summarized below:

i. *Scalability of per-group state:* The per-group state information of multicasting is not scalable to the high speeds of the core of the network. For instance, for each multicast group flowing across the domain, each router must store the state information as well as manage it.

ii. *Sender versus receiver-driven QoS:* In DiffServ, QoS is provided through a sender-driven QoS. As packets are sent from the sender, the sender and ingress router for the domain mark/shape the packet. In contrast, multicasting is built upon a receiver-driven QoS. It also implies that the marking should be based on the requirements and the capabilities of the receivers [11].

iii. *Resource management:* The conflict regarding resource management can be reduced to the problem of packet replication. Under unicast, one packet in yields one packet out. However with multicasting, this is may not be the case as one packet entering the domain may become multiple packets out. Group membership in multicast operation is dynamic. When a new host joins a multicast group, a new branch may be generated. The DSCP code is copied from existing branch, this may lead to SLA violations.

III. DSMCast Architecture

The DSMCast architecture is described in [12]. DSMCast can potentially satisfy the three conflicts between DiffServ and multicasting. This architecture proposes a method for DiffServ-based multicast that achieves the benefits of traditional IP multicast but does not require per-group state information in the core routers.

The DSMCast architecture can be subdivided into four main components: the transport mechanism, the extensions for heterogeneous QoS [13], the tree construction mechanism, and the egress join/leave protocol [14].

A. Tree Encapsulation Header

The Tree Encapsulation Header (TEH) [12] is the sequence of bits that are responsible for routing and replicating the packet across the core of the DiffServ domain. It consists of three fields, the *NumEntries* field, the *Options* field and the *Replication/Routing* Entries. Figure 1 presents the DSMCast TEH.

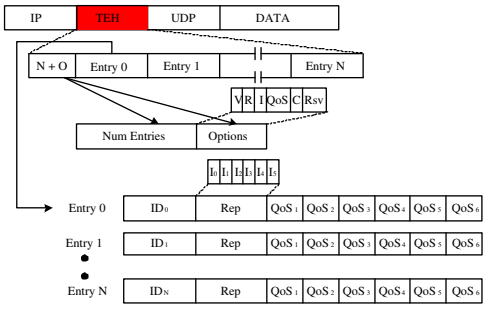

Fig. 1. DSMCast Tree Encapsulation Header [12].

The first field, the *NumEntries* field, is an 8 bit field that contains the number of entries present in the TEH itself. For each non-leaf node of the multicast

tree, an entry will be present. The second field, the *Options* field is used to convey the configuration of the TEH. The settings for this field are listed in Table I. The next portion of the TEH is the *replication/routing* information.

TABLE I
TREE ENCAPSULATION HEADER OPTIONS FIELD.

Bit(s)	Abrev	Field	Description
7	V	Variable QoS	0 - No variable QoS 1 - Variable QoS
6	R	Extended Replication Bits	0 - 24 bits 1 - 32 bits
5	I	Extended ID	0 - 8 bits 1 - 16 bits
4, 3	QoS	QoS Setting	Switch for QoS transformation methods
2	C	Clear Rep	0 - Leave 1 - Clear
1, 0	Rsv	Reserved	Unused

B. Tree Construction

The TEH is constructed and maintained by the ingress router of the multicast group. It is assumed that each edge router has complete topological knowledge of the entire DS domain, core and edge routers. As a result of its knowledge of the DS domain, the ingress router can appropriately construct a multicast distribution tree for a specific multicast group and update the tree as egress routers join and leave the multicast group.

C. Transport Mechanism

The DSMCast architecture provides a core stateless transport mechanism for multicast traffic across the domain. To accomplish this goal, all replication/routing for multicast packets is controlled by the DSMCast Tree Encapsulation Header. When a multicast packet arrives at the ingress router to the DS domain, the ingress router must insert the TEH into the multicast packet. The ingress router looks up the TEH for the specific multicast group (S, G) and inserts the TEH between the layer 3 (IP - Internet Protocol) and layer 4 (UDP - User Datagram Protocol). This location is chosen as it preserves the standard IP routing and DiffServ classification. The TEH may be inserted without modifying any of the remaining fields of the packet. Since the TEH is only added at the ingress of the domain and removed at the egress, the TEH simply appears as packet data to the IP routing mechanisms of core routers.

Upon receiving a multicast packet, the core router will give the packet to the hardware mechanism for DSMCast. The hardware mechanism will inspect the packet to determine which interfaces the packet should be replicated upon. Once replicated, the packet will be placed in the standard DiffServ unicast class queue and treated according to the PHB specified by the DSCP. If necessary, the DSCP of the packet may be modified to support heterogeneous QoS as specified in the TEH.

D. Join/Leave Protocol

The *join/leave* protocol for DSMCast [14] is optimized for an SSM (Source Specific Multicast) environment [15]. When a join request arrive at an edge router, the request will include a source/group identifier (S,G). The edge router must then forward the packet to the appropriate ingress node for multicast source. Due to the fact that IP routing provides only for the next hop to a given destination IP, ascertaining the ingress point for an arbitrary IP may be difficult if not impossible. The solution to this problem is to simply tunnel [16] the join request towards the source of the group. As a result, the egress router can rely on standard IP routing rather than a special routing mechanism. In the tunnel header, a special identifier will be recognized by the ingress router. Upon receiving the packet, the ingress router would intercept and process the packet rather than forwarding the packet.

DSMCast provides flexibility in how the egress router joins the multicast group. Rather than forcing a router to explicitly specify a PHB with the initial join, an egress router may first probe for sender-driven QoS and then select a PHB.

IV. SIMULATION MODEL

In this study based on modelling and simulation, we use a network simulation tool called Network Simulator, version 2 (*ns-2*) [17]. For enabling Multicast in the DiffServ domain capabilities to *ns-2* the GenMCast [18] module was added.

A. Scenario and Simulation Parameters

The network simulation model used in this study is presented in Figure 2 and we considered 4 core routers and 10 edge routers. The links operate at 10 Mbps and they are submitted to 5 ms latency. Each edge router was considered the source for 1 SSM multicast group.

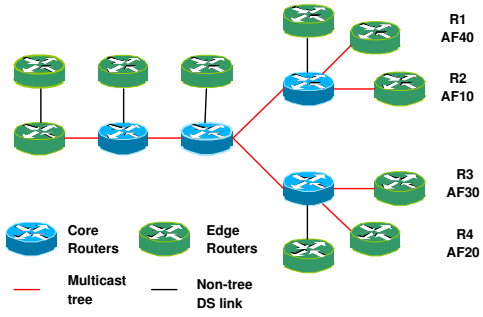

Fig. 2. Simulation model.

We configure video traffic with the traffic generator available in [19]. MPEG4 encoders generate video in three different frame types (I, P and B) that serve to encode different portions of the video signal in different levels of quality. The I, P and B frames were modelled using TES (Transform Expand Sample) models [20] and used multiplexing to generate the original sequence of frames for MPEG4. This generator was implemented in software and was integrated it into the network simulator *ns-2*.

In this study, we evaluate the video behavior when the receivers of multicast group have different requirements. Thus, we used the AF PHB group that consists of four independent AF classes with three drop precedences per class. We considered a single multicast group which is shaped by 4 receivers, each one with a different DSCP of AF10, AF20, AF30 and AF40. In this case, we have that R_1 joins first with a PHB of AF40 followed by R_3 with a PHB of AF30. Next, R_2 and R_4 join with PHBs of AF10 and AF20, respectively.

For each one of the edge nodes in the DiffServ domain, background traffic is sent to other edge nodes. The background traffic is modelled by FTP (File Transfer Protocol) and CBR (Constant Bit Rate) traffic sources.

TABLE II
BACKGROUND TRAFFIC PARAMETERS.

Background Traffic	Value(s)
Type	50% UDP and 50% TCP
Packet size	1000 bytes
Packet rate	10 ms
Session hold Time	15 s
Inter-Arrival Time	50 ms

In the simulator, we use a Weighted Round Robin (WRR) scheduling scheme [21] combined with Weighted Random Early Detection (WRED) buffer-management scheme [22] to configure the AF PHB group. The WRED is a variant of the RED algorithm that drops packets selectively based on IP precedence. The simulations were conducted for a single domain scenario of varying QoS distributions uniform and non-uniform. The values for the distributions and the weights to the WRR are listed in Table III. The simulation time was set to 100 seconds. The confidence intervals used in this simulations study are equal to 95%.

TABLE III
DIFFSERV PARAMETER.

Parameter	Value(s)
Scheduling	WRR, weights = (24, 18, 12, 6)
DSCPs	AFxy (x = 1..4, y = 1...3)
Uniform	x (25%, 25%, 25%, 25%) y (33%, 33%, 34%)
Non-Uniform	x (10%, 20%, 30%, 40%) y (15%, 30%, 55%)

V. RESULTS PRESENTATION AND ANALYSIS

In this section, we present an analysis of results obtained with the simulation based experiments. The throughput and delay were evaluated for all simulations.

A. PIM-SM

Figure 3 shows the throughput achieved by real-time video application when the background traffic is uniform. In the case of the traditional IP multicast, the PHB is not propagated "upstream". Hence, all downstream receivers suffer due to the fact that the AF40 codepoint dominates the multicast tree. Figure 4 shows the throughput achieved by real-time video application when the background traffic is non-uniform. Independent of the level of QoS requested for the member of the group, all present similar performance.

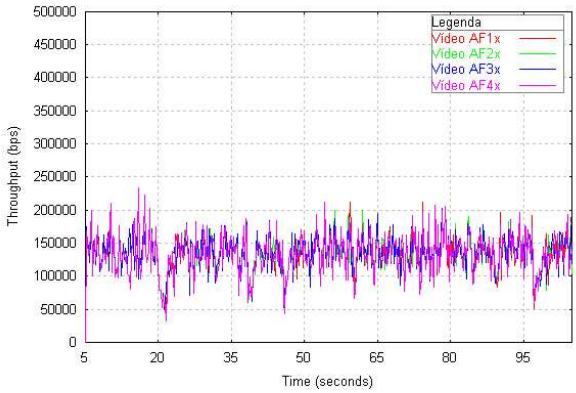

Fig. 3. Real-time video application throughput - Uniform distribution.

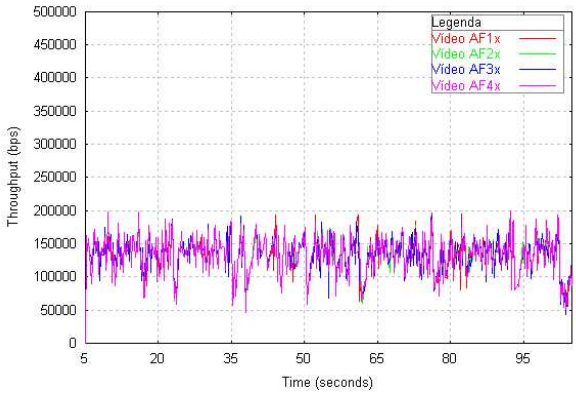

Fig. 4. Real-time video application throughput - Non-Uniform distribution.

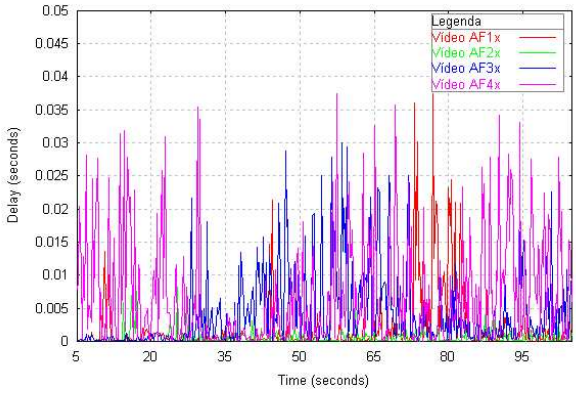

Fig. 5. Real-time video application delay - Uniform distribution.

Figures 5 and 6 show the delay to which the real-time video application were submitted when the background traffic is uniform and non-uniform. In the case of non-uniform background traffic we have the traffic is concentrated more heavily in the lower priority classes. As a result, less traffic exists with

higher priority and hence, the traffic receivers less queuing delay.

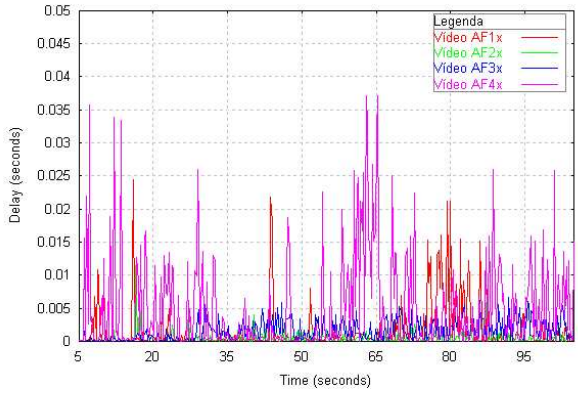

Fig. 6. Real-time video application delay - Non-Uniform distribution.

In this case, we observe that the receivers benefit as more of the background traffic is dropped before the multicast group traffic, real-time video applications.

B. DSMCast

In the DSMCast architecture, heterogeneous QoS is provided by means of dynamics PHBs. Figure 7 shows the throughput achieved by real-time video application when the background traffic is uniform. In this case, the real-time video application with AF20 PHB has more throughput than real-time video application with AF40 PHB, thus AF40 PHB doesn't dominate the multicast tree.

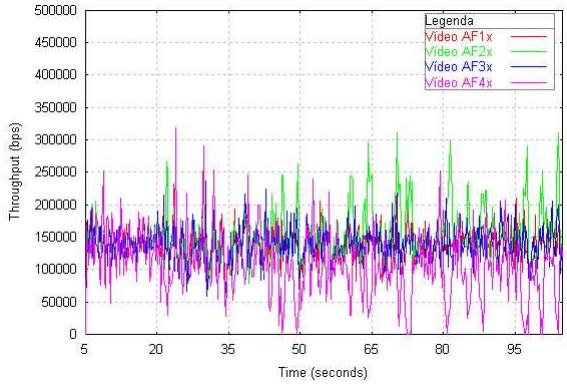

Fig. 7. Real-time video application throughput - Uniform distribution.

Figure 8 shows the throughput achieved by real-time video application when the background traffic is non-uniform. In this case, the real-time video application with lowest service class (AF40) performance similar to the highest service classes.

Figures 9 and 10 show the delay to which the real-time video application were submitted when the background traffic is uniform and non-uniform. In the case, all the classes have better performance than when we use IP Multicast traditional. When the non-uniform background traffic is used in the simulations, we observed that average delay values are inferiors. In this case, all the video applications, independent of its class of service, had been benefited. In the scenario of DSMCast architecture, we observed the *Good Neighbor* effect. This effect benefit the lowest service classes (AF30 and AF40) applications when they share links with the highest service classes (AF10 and AF20) applications.

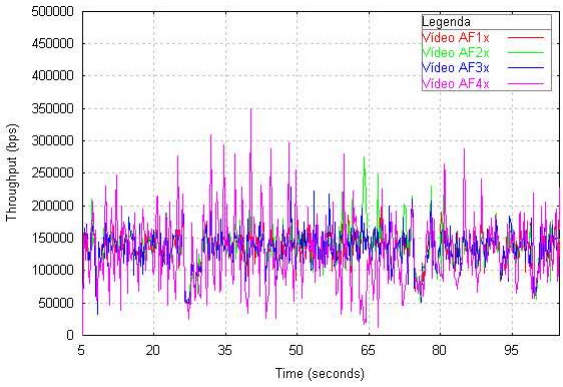

Fig. 8. Real-time video application throughput - Non-Uniform distribution.

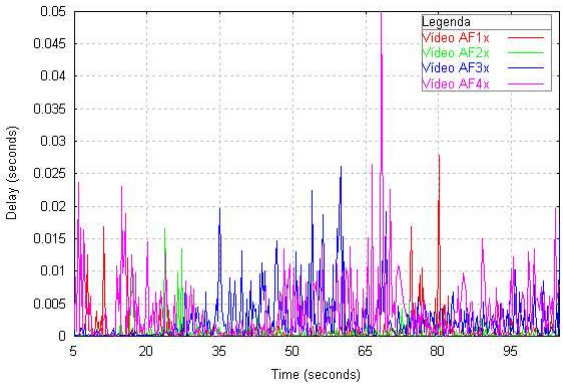

Fig. 9. Real-time video application delay - Uniform distribution.

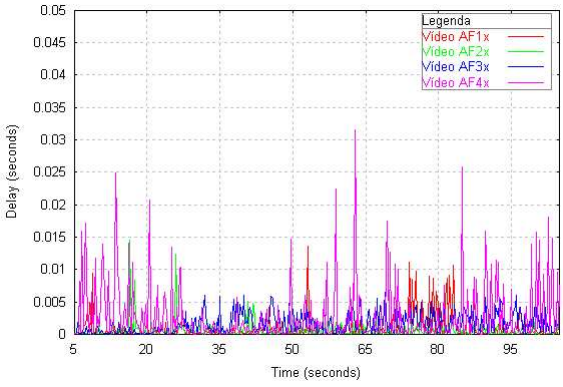

Fig. 10. Real-time video application delay - Non-Uniform distribution.

VI. Conclusion

Real-time video distribution is considered as one of the most important IP Multicast applications. Multicasting digital video over IP networks faces a number of challenges as the others IP Multicast applications. The major challenges in this area are the heterogeneity of

receivers' capabilities and maintaining the scalability when the number of receivers is unknown to the sender and may grow significantly.

In this paper, by means of modelling and simulation, we studied the performance of real-time video application in a scenario that integrate the diffserv and multicast technologies. The traditional IP Multicast, current model used in the Internet, shows scalability and differentiation services problems. In this study, we demonstrated that real-time video applications achieve the biggest throughput and suffer the lesser delays when the DSMCast architecture has been used. Thus, we conclude that DSMCast is an more efficient architecture to the development of multicast video applications.

VII. Acknowledgement

The authors gratefully acknowledge the financial support of FAPEMIG under Project TEC-1027/02.

References

[1] S. Paul, "Multicasting on the Internet and Its Applications", *Kluwer Academic Publishers*, pp. 456, 1998.
[2] X. Xiao e L. Ni, "Internet QoS: A Big Picture", *IEEE Network*, v. 13, pp.8-18, March 1999.
[3] S. Shenker, C. Partridge, R. Guerin, "Specification of guarantees quality of service", Internet RFC 2212, 1997.
[4] L. Jiangchuan, B. Li e Y.Q. Zhang, "Adaptive Video Multicast over the Internet", *IEEE Networks*, March 2003.
[5] S. Blake, "An Architecture for Differentiated Services", IETF RFC 2475, December 1998.
[6] A. Striegel e G. Manimaran, "A Scalable Approach for DiffServ Multicasting", *Proc. of IEEE ICC'2001,* pp. 2327-2331 Helsinki, Finland, June 2001.
[7] D. Cheriton e S. Deering, "Host Groups: A Multicast Extension for Datagram Internetworks", *ACM SIGCOMM Computer Communication Review*, v. 15, Setember 1985.
[8] K. Nichols, et al., "Definition of the Differentiated Services Field (DS Byte) in the IPv4 and IPv6 Headers", Internet RFC 2474, December 1998.
[9] B. Davie, et all., "An Expedited Forwarding PHB (Per-Hop Behavior)", IETF RFC 3246, March 2002.
[10] J. Heinanen, F. Baker, W. Weiss e J. Wroclawski, "Assured Forwarding PHB Group", IETF RFC 2597, June 1999.
[11] B. Yang and P. Mohapatra, "Multicasting in Differentiated Service domains", in Proc. of IEEE GLOBECOM, 2002.
[12] A. Striegel, "Scalable Approaches for DiffServ Multicasting", *Ph.D. Dissertation*, Iowa State University, December 2002.
[13] A. Striegel e G. Manimaran, "Dynamic DSCPs for Heterogeneous QoS in DiffServ Multicasting", *Proc. of IEEE Globeccom*, November 2002.
[14] A. Striegel e G. Manimaran, "A Scalable Protocol for Member Join/Leave in DiffServ Multicast", *Proc. of Local Computer Networks (LCN)*, November, Tampa, Florida, 2001.
[15] H. Holbrook e B. Cain, "Source-Specific Multicast for IP", *IETF RFC 3569*, July 2003.
[16] C. Perkins, "Minimal Encapsulation within IP", *IETF RFC 2004*, October 1996.
[17] UCB/LBNL/VINT Network Simulator - ns (version 2). Avaliable at: http://www.mash.cs.berkeley.edu/ns/.
[18] A. Striegel, "GenMCast: A Generic Multicast Extension for ns-2", *ND CSE Technical Report*, Avaliable at: http://www.cse.nd.edu/ striegel/GenMCast/GenMCast.html.
[19] A. Matrawy, I. Lambadaris e C. Huang, "MPEG4 Traffic Modeling using The Transform Expend Sample Methodology", *In Proc. of 4th IEEE International Workshop on Networked Appliances*, Janeiro 2002.
[20] B. Melamed, "An Overview of TES Processes and Modeling Methodology", *In Performance Evaluation of Computer and Communication Systems*, 1993.
[21] Bo-Kyoung Kim, "Simulation Study of Weighted Round-Robin Queuing Policy", Masters Thesis, University of Massachusetts Lowell, 1993.
[22] D. Lee, "Enhanced Ip Services for Cisco Networks", Cisco Press, Indianapolis, 1999.
[23] B. Fenner, H. Holbrook e I. Kouvelas, "Protocol Independent Multicast - Sparse Mode (PIM-SM) Protocol Specification (Revised)", *IETF Internet Draft* <draftietf- pim-sm-v2-new-08.txt>, October 2003.

A Comparison of MIRA and Residual MinHop Routing Algorithms for MPLS Networks

Lavoisier J.L.Farias
CPqD Foundation
P.O. Box 6070
13088-902 Campinas - SP - Brazil
lfarias@cpqd.com.br

Markus Frey
FEEC - UNICAMP
P.O. Box 6101
13083-970 Campinas - SP - Brazil
mfrey@df-elektronik.de

Ivanil S. Bonatti
FEEC - UNICAMP
P.O. Box 6101
13083-970 Campinas - SP - Brazil
ivanil@dt.fee.unicamp.br

***Abstract*— The performance of Minimum Interference Routing Algorithm (MIRA)[14] and Minimum Hop routing algorithm (Residual MinHop) to solve the offline traffic routing problem in Multiprotocol Label Switching (MPLS) networks are compared in this paper. This problem arises when the network operator needs to provision several LSPs in a MPLS network management tool, and he has to choose the best routes. The use of MIRA algorithm was motivated by its good performance, as described in several published works to solve the online routing problem and by the expectation to obtain the same good performance when all network connection requests are known in advance as in the offline routing problem. The performance criterion is the percentage of successful accepted connections and the study was carried out using networks with different topologies and demands.**

***Index Terms*— MPLS, MIRA, Residual MinHop, Routing Algorithms, offline.**

I. Introduction

Networks based on Internet Protocol (IP), which routing algorithms employ static information, do not allow the maximum network utilization since some links are overloaded and others are under-utilized. On the other side, connection-oriented networks such as ATM networks which routing algorithms take in account the current link load use efficiently the network resources and can provide better quality of service to the network users.

Multi-Protocol Label Switching (MPLS)[17] is a set of protocols, which have been standardized by IETF for several years, that allows IP networks to achieve better performance since MPLS is connection-oriented and allows to traffic-engineering IP networks. Traffic engineering aims the maximum network utilization avoiding the bottlenecks caused by the static routing algorithms.

MPLS uses the concept of virtual connection, called Label Switched Path (LSP), which permits the creation of paths using the mechanism of explicit route [7]. Explicit route is a path in which all hops of the path or part of them are defined during the path establishment and is implemented using the signalling protocols such as CR-LDP [4] or RSVP-TE [6]. Explicit routes are also referred as MPLS tunnels. Thus, many different dynamic routing strategies can be used in MPLS networks to find explicit routes. In MPLS networks, the dynamic information from the network, as for example, the reserved link bandwidth, is updated by using some existing routing protocol OSPF-TE [3]or ISIS-TE [18]. Therefore, once the path is defined, the signalling protocols are used to establish the tunnels and the routing protocols can be used to advertise the tunnels as new routes.

Several algorithms have been proposed to solve the problem of dynamic routing, such as [14], [25], [19], [3], [10], [27], [20], [26], [23] that provide solutions in which the network can admit more connections, or better distribution of the traffic throughout the network. All algorithms target the online routing problem, which considers that the requests arrive one-by-one and no knowledge about future requests is available.

In this paper, the offline routing problem is analyzed. Offline routing shows up during the provisioning of several simultaneously connection requests in the network by using a network management tool. Thus, the network provider has to calculate the best routes using some algorithm in order to implement those connections in the network. In general, the offline routing problems are formulated as multi-commodity flow problems and are solved by integer linear program approach. However, these problems are NP-hard and some heuristics based on particularities of the problems are applied with satisfactory results [21].

The main goal of this paper is to analyze the MIRA algorithm as a scheme for offline traffic routing, since MIRA is one of the best dynamic routing algorithms that has been published recently and there are several other works based on it, such as those ones describes in [5], [14], [25], [15], [11], [8], [9], [20], [26].

In the offline routing algorithm, the connection requests are known in advance and are treated simultaneously. The algorithm deals with the residual network, i.e., the network capacity is updated for each routed connection. This proposal also considers that the bandwidth is the only metric used to find the best route for each connection request, since delay and loss, for example, can be translated to bandwidth through an effective-bandwidth model as described in [13] and [12]. In order to evaluate the performance

MIRA algorithm in the offline context, a comparison of the Residual MinHop algorithm applying them to three different network topologies is carried out. The next sections are organized in the following way: the Section I describes the offline routing algorithm based on the online MIRA strategy and presents an illustrative example. The Section II-E describes the numerical results and discusses them. The Conclusions are presented in Section III.

II. Offline Routing Algorithm

The MIRA algorithm as used as a solution for offline routing problem to support the network provisioning of MPLS tunnels. This application is based on the recent algorithm MIRA [3] developed in the context of online routing. In the Kodialam and Lakshman proposal, hereafter named MIRA online algorithm, the connections arrive one-by-one and each request is routed based on its source and destination nodes, its bandwidth and the knowledge of residual capacity of the network. There is no knowledge about the future connection requests, only the set of ingress-egress pairs is known in advance. The main contribution of the authors of MIRA is finding a path to route the connection request based on link weights computed using the concept of critical links. The weight of the critical link is obtained by solving maximum flow problems to each ingress-egress node pairs. According to the authors of MIRA, this routing algorithm performs much better than the classical Residual MinHop algorithm, which corresponding "weight link" is equal to one.

In this paper, the MIRA algorithm is applied in the offline context to find the connections (explicit routes) in order to support the MPLS tunnel provisioning process. It is considered that all connection requests are known in advance and are simultaneously routed based in the shortest path algorithm considering the weights computed as in MIRA online algorithm. The connection paths are sequentially computed; the first one is obtained by computing the paths for all connection requests and choosing the path with the smallest weighted distance. The capacity of the links belonging to the path is updated by subtracting the bandwidth of the request associated to the selected path. The next paths are chosen in the same manner until there is no connection to be considered or the network residual capacity is not enough to admit more connections. This proposal chooses the request and its path that produces the minimum interference as defined by Kodialam and Lakshman. The MIRA offline algorithm is compared with Residual MinHop offline algorithm that chooses a path based in the minimum number of links belonging to the path in order to evaluate the performance of the proposed algorithm. In the next paragraphs, the online MIRA algorithm is firstly described in order to present the offline MIRA algorithm.

A. Online MIRA Algorithm

The authors of MIRA defined interference of the ingress-egress pair (s, d) over the ingress-egress pair (a, b), as the reduction in maximum flow value for the ingress-egress pair (a, b) due to the routing of a connection of the pair (s, d). They have also defined the critical link concept in order to calculate if a chosen path interferes more than any other one. A link is critical for an ingress-egress pair if it belongs to any minimal cut associated with that pair. Thus, a demand should be routed through a path which reduction of max-flow [1] is minimal. This path is the shortest path computed using the Dijkstra algorithm [1], on which the distance metric is the link weight obtained from the max-flow problem resolution.

The online MIRA algorithm is described in [14] as follows:

For each connection request between the ingress nodes a and the egress node b:

1.Compute the maximum flow values for all $(s, d)P\backslash(a, b)$

2.Compute the critical links sets for all C_{sd} ingress-egress pairs excluding the pair (a, b).

3.Compute the weights

$$w(l) = \sum_{(s,d):l \in C_{sd}} \alpha_{sd} \quad \forall l \in L \tag{1}$$

4.Remove all links, which have residual bandwidth smaller than the connection request bandwidth and form the reduced network.

5.Compute the shortest path using Dijkstra's algorithm for the reduced network considering as distance metric the weights computed $w(l)$ in the step 1.

6.If a path is found in the step 5, route the demand from node a to node b along this shortest path, i.e., update the residual link capacities of the network.

Important to note that α_{sd} was set equal to 1 in [14]. Our implementation of this algorithm had also used the same approach, i.e., the value equals to 1 of this parameter. The idea of this parameter is to prioritize some ingress-egress pair s and d.

B. Offline MIRA Routing Algorithm

The offline routing algorithm takes into account the bandwidth of the connections and considers all connection requests simultaneously as described right below. A Connection Request List containing all the requests is initially created. This list is updated as long as connections are accepted or blocked.

While the Connection Requests List is not empty do

1.Find a shortest path, using Dijkstra, for each pair of the Connection Request List using the weights of the links as computed by MIRA for all ingress-egress pair having requests in the Connection Request List.

2.Choose the path with the smallest weight (the weight of path is the sum of the weight of all links belonging to the path).

3.Route the demand (update the residual link capacities of the network) if a path

```
is found in step 1, otherwise increment the
number of blocked requests.
  4.Remove this request from the Connection
Request List
  End While
```

C. Residual MinHop Algorithm

The residual network is the network having its link capacities updated after a connection establishment. The shortest-path algorithm Dijkstra [1] is applied on the network considering the updated bandwidth of the links.

In order to evaluate the performance of this algorithm, an offline Residual MinHop algorithm has been implemented which consists of replacing the MIRA weight computation by using weights equals to one for the steps 1 and 2 in the offline MIRA algorithm.

D. An illustrative example

The Fig. 1 shows a six-nodes network with the link capacities. The label in the circle identifies the node and the label at the link represents the link capacity. All links are unidirectional and the link capacities are the same in both directions. The numbers beside the arrows indicate the number of connection requests originating at the node. The requests are uniformly distributed for the other five destination-nodes. For example, two of the ten requests entering the node c has destination to node a, two to node b, two to node d, two to node e and two to node f. All connection request bandwidths are equal to one.

The residual network after the establishment of 36 connections (all using one hop) routed by the Residual MinHop algorithm and the corresponding remaining requests are shown in the Fig. 2. The Fig. 3 shows the residual network after the establishment of 36 connections routed by the MIRA and the corresponding remaining requests. The MIRA has preserved the links between the nodes b-c and between the nodes d-e because they are critical links for several pairs of nodes, while the Residual MinHop has completely used these links to establish the one-hop connections, as it was expected to happen.

The Fig. 4 results after the routing of 44 connections (all using two hops) using the offline Residual MinHop algorithm and the Fig. 5 results using MIRA. These figures show the final results for both offline algorithms having surprisingly the same number of blocked connections, i.e., 16 connections, even though the residual network and the distribution of the remaining requests are different. It was expected that MIRA would produce a better performance than Residual MinHop. This result could be explained by the fact that the network is small and the requests are uniformly distributed in the network, which is not an usual situation. However, as shown in the next Section, this behavior is held for different topologies and network demands.

III. Numerical Results and Discussions

The percentage of accepted connections of MIRA and Residual MinHop algorithms have been numeri-

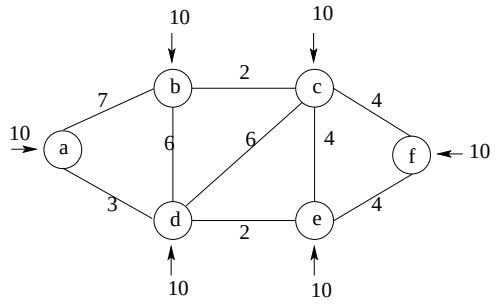

Fig. 1. Six-nodes network with uniform connection requests

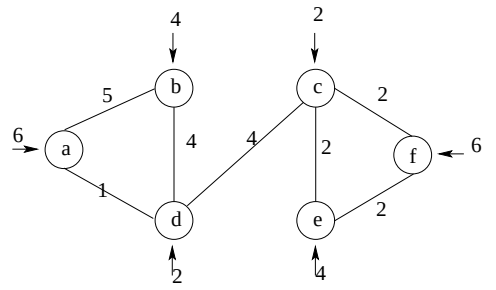

Fig. 2. Residual network after routing 36 connections by Residual MinHop

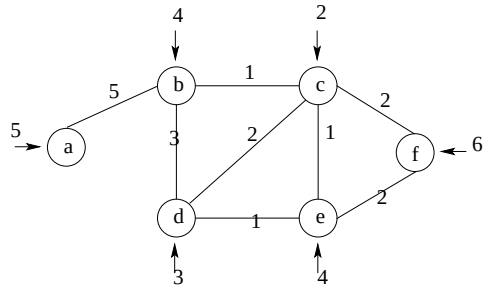

Fig. 3. Residual network after routing 36 connections by MIRA

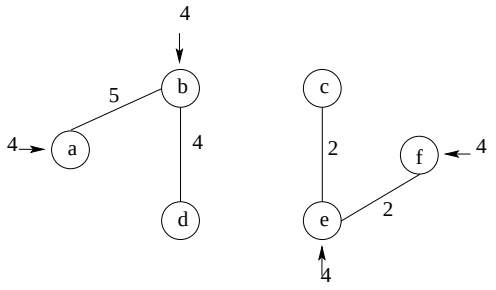

Fig. 4. Final residual network and blocked connection requests resulting from Residual MinHop application

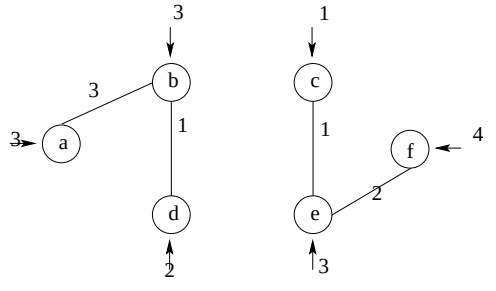

Fig. 5. Final residual network and blocked connection requests resulting from MIRA application

cally compared for three different network configurations: COST, NSF and MIRA (the network presented by the authors of the MIRA [14]) as shown in the Fig. 9.

The topologies and connection requests for each network are as follow: The COST network topology [9] is shown in Fig. 6. The acronyms represent the following city node names: Copenhagen (CO), Berlin (BE), Vienna (VN), Milan (ML), Paris (PR), London (LD), Amsterdam (AM), Prague (PG), Zurich (ZQ), Luxembourg (LU) and Brussels (BX). All links in the network are unidirectional and have capacities equal to 4. Note that the traffic, in the Fig. 9, varies from 33.33% to 100% corresponding to 150, 300 and 450 requests, respectively. The distribution of the connection requests corresponding to 33.33% of the maximum traffic load offered to the network is shown in Table I.

The NSF network topology [16] is shown in Fig. 7. The acronyms represent the following state node names: Washington (WA), California/Palo Alto (CA1), California/San Diego (CA2), Utah (UT), Colorado (CO), Texas (TX), Nebraska (NE), Illinois (IL), Pennsylvania (PA), Georgia (GA), Michigan (MI), New York (NY), New Jersey (NJ), Maryland (MD). The nodes AB and XY are not in the United States of America. All links in the network are unidirectional and have capacities equal to 15. Note that the traffic, in the Fig. 9, varies from 10% to 100% corresponding to 64, 128, 192, 256, 320, 384, 448, 512, 576 and 640 requests, respectively. The neighbor's nodes having one connection request between them are shown in Table II and these requests correspond to 10% of the maximum traffic load offered to the network.

The MIRA network topology [14] is shown in Fig. 8 . The link capacities are 12 and 48. Note that the traffic, in the Fig. 9, varies from 50% to 100% corresponding to 80, 100, 120, 140 and 160 requests, respectively, which are equally distributed between the nodes (1, 13), (4,2), (5,9) and (5,15).

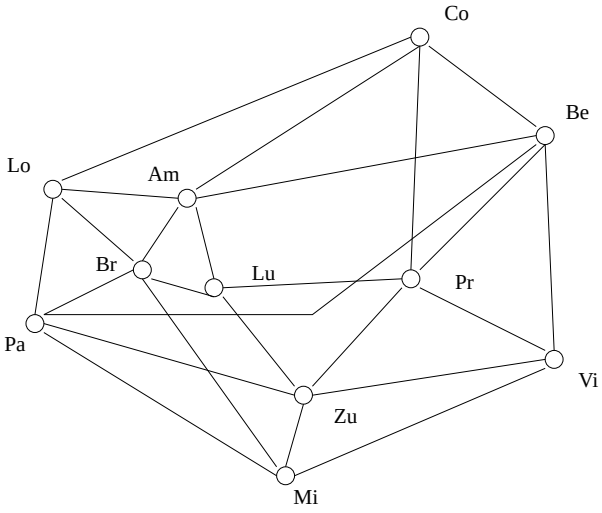

Fig. 6. COSTnet (*European Optical Network*) [22].

Even though MIRA's authors have claimed that MIRA performs better than Residual MinHop algorithm by Monte Carlo's simulations, the Fig. 9 clearly shows that both algorithms provides almost the same number of accepted connections for the three networks analyzed in the offline routing context considered in this paper. All three networks are partially meshed, each node having between two and five neighbors and the connection request distribution is very different for each network. All node pairs have connection requests between them in the COST network, while in the NSF network all nodes have requests to four neighbors. The MIRA network has only four pairs having connection requests between them. Both algorithms have the same performance independent of the connection requests distribution. Even for the MIRA network, which has a very small number of ingress-egress nodes, the

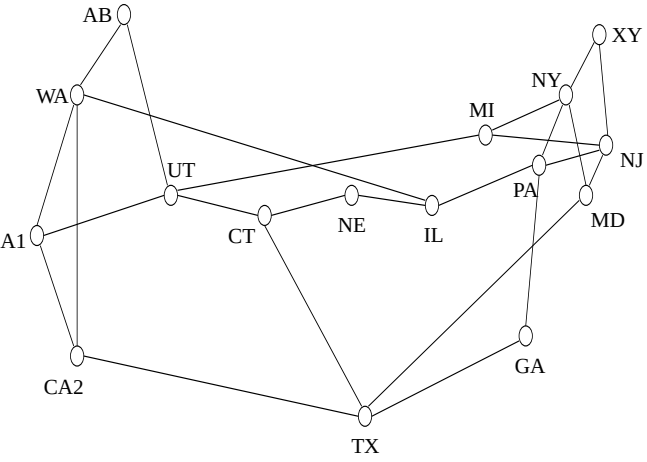

Fig. 7. NSFnet [16]

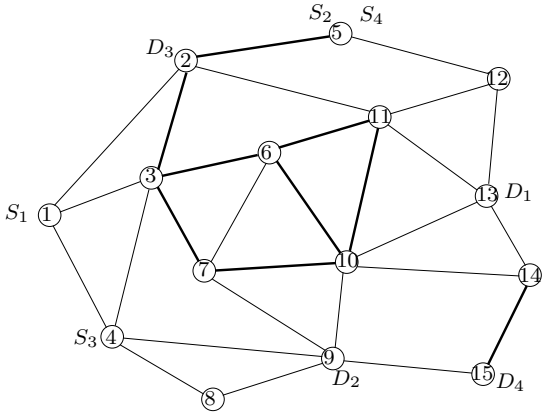

Fig. 8. MIRAnet [14].

TABLE I
CONNECTION REQUESTS FOR COSTNET.

	Co	Be	Vi	Mi	Pa	Lo	Am	Pr	Zu	Lu	Br
Co	–	1	1	1	1	1	1	1	1	1	1
Be	1	–	3	3	4	2	2	1	3	1	2
Vi	1	3	–	1	1	1	1	1	1	1	1
Mi	1	3	1	–	2	1	1	1	2	1	1
Pa	1	4	1	2	–	3	2	1	2	1	2
Lo	1	2	1	1	3	–	2	1	1	1	1
Am	1	2	1	1	2	2	–	1	1	1	1
Pr	1	1	1	1	1	1	1	–	1	1	1
Zu	1	3	1	2	2	1	1	1	–	1	1
Lu	1	1	1	1	1	1	1	1	1	–	1
Br	1	2	1	1	2	1	1	1	1	1	–

TABLE II
CONNECTION REQUESTS FOR NSFNET

	WA	CA1	CA2	UT	CO	TX	NE	IL
WA	–	1	0	0	0	1	0	1
CA1	1	–	1	1	0	0	1	0
CA2	0	1	–	0	0	0	0	0
UT	0	1	0	–	1	1	0	0
CO	0	0	0	1	–	0	1	0
TX	1	0	0	1	0	–	0	0
NE	0	1	0	0	1	0	–	1
IL	1	0	0	0	0	0	1	–
PA	0	0	0	0	0	0	0	1
GA	0	0	1	0	0	0	1	0
MI	0	0	0	0	1	0	0	0
NY	1	0	1	0	0	0	0	0
NJ	0	0	0	0	0	0	0	0
MD	0	0	0	0	1	1	0	1
AB	0	0	0	0	0	1	0	0
XY	0	0	1	1	0	0	0	0

TABLE III
CONNECTION REQUESTS FOR NSFNET (SECOND PART).

	PA	GA	MI	NY	NJ	MD	AB	XY
WA	0	0	0	1	0	0	0	0
CA1	0	0	0	0	0	0	0	0
CA2	0	1	0	1	0	0	0	1
UT	0	0	0	0	0	0	0	1
CO	0	0	1	0	0	1	0	0
TX	0	0	0	0	0	1	1	0
NE	0	1	0	0	0	0	0	0
IL	1	0	0	0	0	1	0	0
PA	–	1	0	1	1	0	0	0
GA	1	–	1	0	0	0	0	0
MI	0	1	–	0	1	0	0	1
NY	1	0	0	–	0	0	1	0
NJ	1	0	1	0	–	1	1	0
MD	0	0	0	0	1	–	0	0
AB	0	0	0	1	1	0	–	1
XY	0	0	1	0	0	0	1	–

performance of both algorithms is similar.

In addition to the results shown in the 9, the network capacities and the demands were multiplied by 10, the same results had remained.

In our opinion, these results can be explained if we realize that the offline Residual MinHop algorithm routes the connections using the minimal quantity of the network resources since it uses the minimum number of links to establish the connections. Therefore, both algorithms deal with the same goal that is to preserve link capacities for the other requests.

The Offline Residual MinHop algorithm has been compared with the optimal solution of the multicommodity minimal cost flow problem solved by Integer Linear Programming technique (ILP) [21] to establish the sub-optimality of the Residual MinHop. The Table IV shows the number of blocked connection requests for the COST network for link capacities varying from $n = 1$ to $n = 6$. The total number of connection requests is 160 and the number of blocked connection requests resulting from the ILP problem is very similar of the number resulting of the Residual MinHop algorithm. It is worthwhile to note that the ILP is much more hard to compute than the Residual MinHop.

TABLE IV
COMPARISON OF RESIDUAL MINHOP AND ILP

n	1	2	3	4	5	6
ILP	100	66	40	18	2	0
Residual MinHop	100	69	43	21	2	0

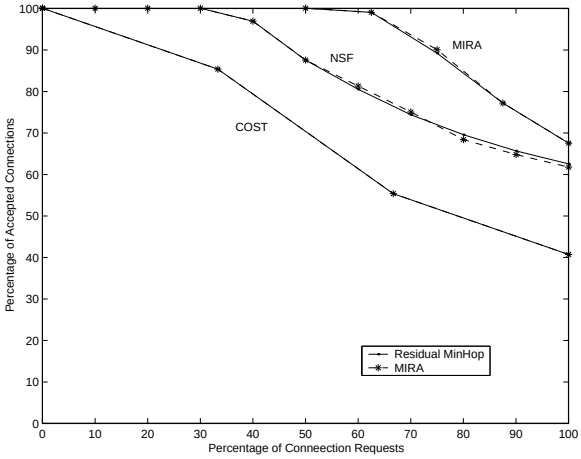

Fig. 9. Percentage of accepted connections for the three networks. Residual MinHop algorithm (continuous) and MIRA(dashed)

IV. CONCLUSION

MIRA and Residual MinHop have produced similar results when applied to typical networks with connection requests for all pairs of routers or with small number of ingress-egress nodes. However, MIRA solves several max-flow problems for each connection request in order to compute the criticality of the links. This intensive computational task is not worthwhile, since the number of blocked connections is roughly the same produced by Residual MinHop algorithm, which has much less iterations. The similar performance of both algorithms can be understood by realizing that the Residual MinHop algorithm also routes the connections using the minimal quantity of the network resources (minimum number of links). Therefore, both algorithms deal with the same goal: to preserve link capacities for the other requests. The main contribution of this paper is to show that the Residual MinHop algorithm remains a good choice for MPLS routing problem, since it is simple and provides the same results as the more complex MIRA.

Acknowledgments: The authors wish to thank the financial support of Conselho Nacional de Desenvolvimento Científico e Tecnológico-CNPq and the Fundação Centro de Pesquisa e Desenvolvimento Tecnológico - CPqD.

REFERENCES

[1] R. K. Ahuja, T. L. Magnanti, and J. B. Orlin. *Networks Flows: Theory, Algorithms, and Applications*. Prentice-Hall, Inc., New Jersey, 1993.

[2] R. K. Ahuja, T. L. Magnanti, and J. B. Orlin. *Networks Flows: Theory, Algorithms, and Applications*. Prentice-Hall, Inc., New Jersey, 1993.

[3] G. Apostolopoulos, S. Kama, D. Williams, R. Guerin, A. Orda, and T. Przygienda. QoS routing mechanisms and OSPF extensions. *RFC 2676 IETF*, 1999.

[4] J. Ash, Y. Lee, P. Ashwood-Smith, B. Jamoussi, D. Fedyk, D. Skalecki, and L. Li. LSP modification using CR-LDP. *RFC 3214*, January 2002.

[5] P. Aukia, M. Kodialam, P. V. N. Koppol, T. V. Lakshman, H. Sarin, and B. Suter. RATES: a server for MPLS traffic engineering. *Network, IEEE*, 14(2):34 – 41, March - April 2000.

[6] D. Awduche, L. Berger, D. Gan, T. Li, V. Srinivasan, and G. Swallow. RSVP-TE: Extensions to RSVP for LSP tunnels. RFC 3209, IETF, December 2001.

[7] D. Awduche, J. Malcolm, J. Agogbua, M. O'Dell, and J. McManus. Requirements for traffic engineering over MPLS. RFC 2702, IETF, September 1999.

[8] D. Bauer. Minimum-interference routing based on flow maximisation. *Electronics Letters*, 38(8):364 –365, April 2002.

[9] C.T. Chou. Traffic engineering for MPLS-based virtual private networks. *Computer Networks*, November 2003.

[10] R.A. Guerin, A. Orda, and D. Williams. QoS routing mechanisms and OSPF extensions. In *IEEE Global Telecommunications Conference GLOBECOM'97*, volume 3, pages 1903 – 1908, 3-8 November 1997.

[11] K. Kar, M. Kodialam, and T. V. Lakshman. Minimum interference routing of bandwidth guaranteed tunnels with MPLS traffic engineering applications. *IEEE Journal on Selected Areas in Communications*, 18(12):2566 – 2579, December 2000.

[12] F. P. Kelly. Notes on effective bandwidths. In F. P. Kelly, S. Zachary, and I. B. Ziedins, editors, *Stochastic Networks: Theory and Applications*, pages 141–168. Oxford University Press, 1996.

[13] G. Kesidis, J. Walrand, and C.-S. Chang. Effective bandwidths for multiclass Markov fluids and other ATM sources. *IEEE Transactions on Networking*, 1(4):424–428, August 1993.

[14] M. Kodialam and T. V. Lakshman. Minimum interference routing with applications to MPLS traffic engineering. In *INFOCOM 2000, Nineteenth Annual Joint Conference of the IEEE Computer and Communications Societies*, volume 2, pages 884 – 893, 26-30 March 2000.

[15] M. Kodialam, T.V. Lakshman, and S. Sengupta. Online multicast routing with bandwidth guarantees: a new approach using multicast network flow. *IEEE/ACM Transactions on Networking*, Volume: 11(Issue: 4):pp. 676– 686, August 2003.

[16] B. Mukherjee, D. Banerjee, and S. Ramamurthy. Some principles for designing a wide-area wdm optical network. *IEEE/ACM Transactions on Networking*, 1996.

[17] E. Rosen, A. Viswanathanand, and R. Callon. Multiprotocol label switching architecture. *RFC 3031*, January 2001.

[18] H. Smit and T. Li. IS-IS extensions for traffic engineering. *Internet Draft, IETF*, August 2003.

[19] S. Suri, M. Waldvodel, and P.R. Warkhede. Profile-based routing: A new framework for MPLS traffic engineering. In *Proceedings of the Second International Workshop on Quality of future Internet Services*, 2001.

[20] S. Suria, M. Waldvogel, D. Bauer, and P.R. Warkhede. Profile-based routing and traffic engineering. *Computer Networks*, September 2002.

[21] M.T. Takahashi, A. Yamakami, and E. Moschim. An algorithm to solve the static rwa problem with wavelength conversion using multicommodity optimization technique. In *Proceedings of the 2002 International Telecommunication Symposium*, pages 1244–1247, 2002.

[22] L. G. Tan and M. C. Sinclair. Wavelength Assignment between the Central Nodes of the COST 239 European Optical Network. In *Proceedings of the 11th UK Performance Engineering Workshop, Liverpool, September, pp. 235-247*, 1995.

[23] S.W. Tan, S.W. Lee, and B. Vaillaint. Non-greedy minimum interference routing algorithm for bandwidth-guaranteed flows. *Computer Netowrks*, March 2002.

[24] David Vose. *Quantitative Risk Analysis: A Guide to Monte Carlo Simulation Modelling*. John Wiley and Sons Ltd., 1996. 328pp.

[25] B. Wang, X. Su, and C.L.P Chen. A new bandwidth guaranteed routing algorithm for MPLS traffic engineering. *IEEE International Conference on Communications*, Volume: 2(ICC 2002):pp. 1001 –1005, 28 April-2 May 2002.

[26] B. Yang and P. Mohapatra. Multicasting in MPLS domains. *Computer Networks*, July 2003.

[27] Y. Yang, L. Zhang, J.K. Muppala, and S.T. Chanson. Bandwidth-delay constrained routing algorithms. *Computer Networks*, 42(4):503–520, July 2003.

[28] A. M. Zoubir and B. Boashash. The bootstrap and its application in signal processing. *IEEE Signal Processing Magazine*, 15(1):56 – 76, January 1998.

The Impact of the Lyapunov Number on the Cramér-Rao Lower Bound for the Estimation of Chaotic Signals

Marcio Eisencraft [1]
Mackenzie Presbyterian University
Rua da Consolação, 930. 01302-090.
São Paulo - SP - Brazil
marcioft@mackenzie.com.br

Luiz Antonio Baccalá
Escola Politécnica of the University of São Paulo
Av. Prof. Luciano Gualberto, Travessa 3, 158. 05508-900.
São Paulo - SP - Brazil
baccala@lcs.poli.usp.br

***Abstract*— This paper examines the problem of estimating initial conditions of noise-embedded chaotic signals generated by one-dimensional maps. A general expression for the Cramér-Rao lower bound is derived. When a large number of samples are used in the estimation, a relationship of this bound and the Lyapunov number of the attractor of the map is shown. These results can be used to choose the chaotic generator more suitable for applications on chaotic digital communication systems.**

***Index Terms*— Chaos, chaotic communications, spread spectrum communication, noise performance bounds.**

I. Introduction

OVER the last ten years a large number of papers involving the application of chaotic signals in digital communications has appeared, e.g. [1] - [6]. In chaotic digital communications, the digital information is mapped directly to a wide-band chaotic signal. The principal difference between a chaotic carrier and a conventional periodic carrier is that the sample function for a given symbol is nonperiodic and is different from one symbol interval to the next.

Chaotic digital communication systems are spread spectrum systems. Thus, the interest in this systems lies in many desirable properties such as mitigation of multipath effects and the reducing of the transmitted power spectral density in order to minimize interference with other radio communications in the same frequency band [7].

As each chaotic system generates signals with different characteristics, a natural question is how to choose the most desirable chaotic signal for use in communication systems. While the answer still remains largely open [1], the important class of systems using piece-wise linear maps [8] is the most used to generate chaotic signals because of its simplicity. In its use, however, there is very little concern about the existence of an optimum chaos generating map that can improve performance.

In digital communication systems employing one-dimensional chaotic maps, often, the identification of the transmitted bit requires determining the initial condition s_0 of the chaotic dynamics associated with an observed information bit. Thus, in this paper we address the question of comparing generic one-dimensional chaos generating maps. We use the statistical criterium known as the Cramér-Rao lower bound (CRLB). We relate this performance bound to a known descriptor of the chaoticness of a map: the Lyapunov number. The CRLB sets a theoretical limit on the attainable precision in the estimation of s_0.

Indeed, as there are many well-known numerical techniques for estimating the Lyapunov number of a map [9], once established, this relationship may be the key in predicting the optimum noise performance of a communication system using this map as chaotic generator.

In Section II we formulate the estimation problem and review the concepts of Lyapunov number and Cramér-Rao lower bound. The main theoretical results are stated in Section III and they are exemplified in Section IV. Section V contains a summary of our conclusions.

II. Problem Formulation

The problem of estimating the initial condition of a chaotic signal can be formulated as follows.

Consider the one-dimensional chaotic dynamical system

$$s_{n+1} = f(s_n) \tag{1}$$

where $\{s_0, s_1, \ldots, s_n, \ldots\}$ is the orbit generated by $f(.)$ with an initial condition s_0. This signal is corrupted by zero mean white gaussian noise w_n with variance σ_w^2:

$$x_n = s_n + w_n \tag{2}$$

and its observed samples x_n are available for $0 \leq n \leq N-1$.

Our goal is to compute the optimum performance bound that an unbiased estimator of the initial condition s_0 can attain by knowing the generating map $f(\cdot)$ and the observed sequence $\{x_0, x_1, \ldots, x_{N-1}\}$. In this paper, our optimality criterion is represented by the Cramér-Rao lower bound which we show to be

[1]Marcio Eisencraft is enrolled in a PhD program at Escola Politécnica of the University of Sao Paulo under the supervision of Dr. Luiz Antonio Baccalá.

a function of the Lyapunov number of the orbit traced from the initial condition s_0.

A. Lyapunov number for one-dimensional maps

Consider the one-dimensional map $s_{n+1} = f(s_n)$. If $f(\cdot)$ is differentiable at the orbit points starting with initial condition s_0, we define this ***orbit's Lyapunov number*** $L(s_0)$ as:

$$L(s_0) = \lim_{i\to\infty} \left(\left| \frac{\partial f(s)}{\partial s}|_{s_0} \cdot \ldots \cdot \frac{\partial f(s)}{\partial s}|_{s_i} \right| \right)^{\frac{1}{i}} \quad (3)$$

if the limit in (3) exists.

The larger the Lyapunov number of an orbit, the faster is its split from other neighboring orbits [10]. This intuitively suggests that the larger the Lyapunov number, the easier should our estimates of the initial condition be. This result is confirmed rigorously in Section III.

B. Cramér-Rao lower bound

The Cramér-Rao lower bound (CRLB) determines the smallest variance that an unbiased estimator can attain. Its knowledge in a certain problem allows answering whether a given unbiased estimator is efficient [11]. At the same time, it puts a cap on the least physically attainable variance by an unbiased estimator.

In the case of a signal depending on a single scalar parameter θ, $s_n(\theta)$, corrupted by white gaussian noise w_n with variance σ_w^2:

$$x_n = s_n(\theta) + w_n \qquad 0 \le n \le N-1, \quad (4)$$

the CRLB for θ is given by [11]

$$var(\hat{\theta}) \ge \frac{\sigma_w^2}{\sum_{n=0}^{N-1} \left(\frac{\partial s_n(\theta)}{\partial \theta} \right)^2}. \quad (5)$$

At this point, it is worth bearing in mind for latter comparison that a constant signal, $s_n = A$, in zero mean white gaussian noise with variance σ_w^2, has an associated CRLB in estimating A given by

$$var(\hat{A}) \ge \frac{\sigma_w^2}{N} \quad (6)$$

when using N observations as readily deducible from (5). This corresponds to a slow $O(1/N)$ decrease as $N \to \infty$.

III. CRLB FOR ESTIMATING THE INITIAL CONDITION OF ONE-DIMENSIONAL CHAOTIC MAPS

To estimate s_0 from $\{x_0, x_1, \ldots, x_{N-1}\}$ as defined by (2), one can compute the CRLB using (5) as:

$$var(\hat{s_0}) \ge \frac{\sigma_w^2}{\sum_{n=0}^{N-1} \left(\frac{\partial s_n}{\partial s_0} \right)^2}. \quad (7)$$

Using the chain rule and (1) leads to

$$\frac{\partial s_n}{\partial s_0} = \left. \frac{\partial f(s)}{\partial s} \right|_{s_0} \cdot \left. \frac{\partial f(s)}{\partial s} \right|_{s_1} \cdot \ldots \cdot \left. \frac{\partial f(s)}{\partial s} \right|_{s_{n-1}}. \quad (8)$$

Hence,

$$var(\hat{s_0}) \ge \frac{\sigma_w^2}{\sum_{n=0}^{N-1} \left(\left. \frac{\partial f(s)}{\partial s} \right|_{s_0} \cdot \ldots \cdot \left. \frac{\partial f(s)}{\partial s} \right|_{s_{n-1}} \right)^2}, \quad (9)$$

which shows how to find the CRLB numerically when estimating s_0 from N consecutive orbit samples under additive noise perturbation.

In general, $var(\hat{s_0})$ depends on s_0, the initial condition being estimated, i. e. the initial conditions do not enjoy uniform efficiency in their estimation. In the case of chaotic orbits, however, this nonuniformity becomes less pronounced as N grows. This occurs do to the $f(\cdot)$'s topological transitiveness, or equivalently as orbits roam all over the attractor [12].

For a sufficiently large n, we can use (3) to approximately compute

$$\left(\left. \frac{\partial f(s)}{\partial s} \right|_{s_0} \cdot \ldots \cdot \left. \frac{\partial f(s)}{\partial s} \right|_{s_{n-1}} \right)^2 \approx L^{2n}(s_0), \quad (10)$$

which leads to

$$\sum_{n=0}^{N-1} \left(\frac{\partial s_n}{\partial s_0} \right)^2 \approx \sum_{n=0}^{N-1} L^{2n}(s_0) = \frac{L^{2N}(s_0) - 1}{L^2(s_0) - 1}. \quad (11)$$

by substitution into the denominator of (7) for a sufficient large N.

Hence, considering an orbit that converges to a chaotic attractor, we conclude that the CRLB of its initial condition estimation using $N \to \infty$ samples of this orbit corrupted by white gaussian noise is given by

$$var(\hat{s_0}) \ge \sigma_w^2 \frac{L^2 - 1}{L^{2N} - 1}, \quad (12)$$

where L is the Lyapunov number of the attractor and σ_w^2 is the variance of the noise w_n. Similar asymptotic exponential CRLB decay in a more particular case was reported in [13].

Equation (12) shows that the estimation error decreases exponentially with N as a direct consequence of the information generation characteristic of chaotic systems. This result shows quantitatively how the Lyapunov number of the attractor influences the error limits on the initial condition estimation when N is sufficiently large. The larger L, the smaller the minimal variance of this estimator as heuristically argued in Section II.A.

The exponential decay of the CRLB with N is much faster than that involving the estimation of a constant signal which decreases only as $1/N$, as shown by (6). Theoretically, therefore, if unbiased estimators are available it should be possible to construct very accurate initial condition estimators.

The sensitive dependence on the initial condition is characteristic of the chaotic orbits. Thus, to obtain the initial condition with a relatively high precision does

not imply the precise reconstruction of the orbit generated by s_0. If the initial condition's estimation error is ϵ, then the error in computing s_N using the estimated value $\hat{s_0}$ and $f(\cdot)$ will be $O\left(\max\left(s_N, \epsilon L^N\right)\right)$.

Larger Lyapunov numbers imply greater precision in s_0 estimates. However, this advantage is offset by the large error amplification when calculating subsequent orbit points. Thus, if our aim is to encode and recover information solely by our choice of s_0, then we should choose maps and initial conditions with large Lyapunov numbers but should not expect good recovery of the full orbit.

IV. Examples

A. Bernoulli shift map

Consider the Bernoulli shift map [7]:

$$s_{n+1} = f_B\left(s_n\right) = 2s_n \bmod 1, \tag{13}$$

defined on the interval $I = [0, 1]$.

This piecewise linear map, shown in Figure 1, has chaotic orbits with Lyapunov number $L_B = 2$. As the derivative of $f_B(.)$ is constant with respect to s_n, we can compute the CRLB directly from (12) for every $N > 0$:

$$var(\hat{s_0}) \geq \sigma_w^2 \frac{3}{4^N - 1}. \tag{14}$$

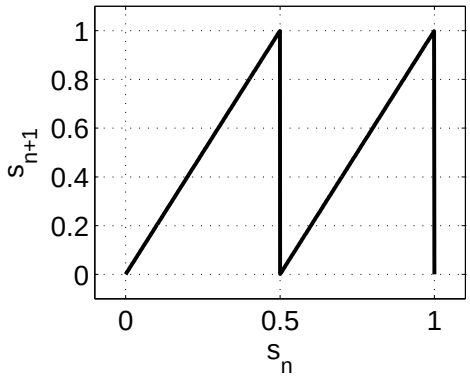

Fig. 1. Bernoulli shift map (13)

.

Figure 2 shows the allied CRLB for initial condition estimation of (13) as N grows ($\sigma_w^2 = 1$). For comparison, it shows the CRLB associated with estimating a constant (DC) value in noise according to (6).

B. Logistic map

A popular one-dimensional chaotic map is

$$s_{n+1} = f_\ell\left(s_n\right) = 4s_n(1 - s_n), \tag{15}$$

the logistic map, one of whose orbits is exemplified in Figure 3.

In this case, the derivative of f_ℓ with respect to s_n is not constant and (12) is valid only for $N \to \infty$. Hence, when N is small, (9) must be used. The associated CRLB bound for various s_0 values is portrayed in Figure 4 using $N = 3$ samples and $\sigma_w^2 = 1$ showing the strong dependence of CRLB on the choice of the

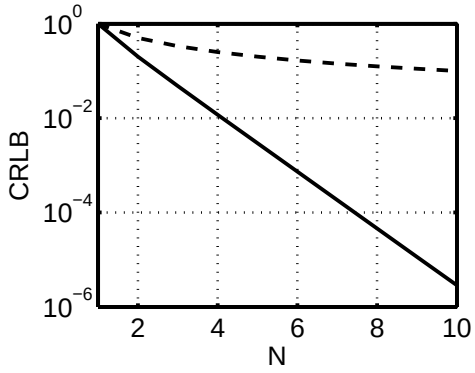

Fig. 2. CRLB for the estimation of the initial condition of the Bernoulli map (solid curve) and for a constant value (dashed curve) in additive white gaussian noise with $\sigma_w^2 = 1$

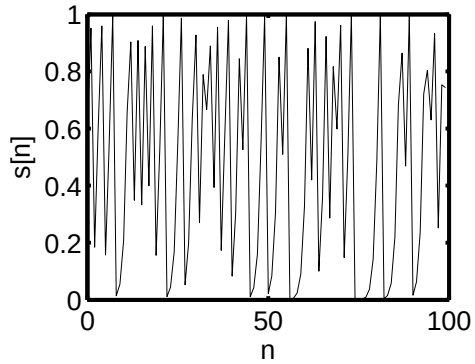

Fig. 3. Signal generated by the logistic map (15) with initial condition $s_0 = 0.61$.

initial condition and that the value $s_0 = 0.5$ is the least favorable choice in this case. This happens due to the nullity of the derivative of $f_\ell(\cdot)$ at this point. Thus, the orbits starting close to $s_0 = 0.5$ split more slowly from other close orbits hindering clear distinction of their initial conditions. The opposite occurs for s_0 close to the extremities of the interval $[0, 1]$ where the absolute value of the derivative of $f_\ell(.)$ is maximum.

Figure 5 portrays CRLB dependence on s_0 for different values of N and illustrates our theoretical discussion concerning the decreased dependence on s_0 when observation times are longer.

The Lyapunov number of an orbit of the logistic

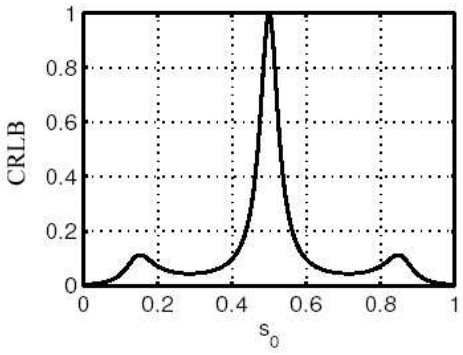

Fig. 4. CRLB for the estimation of s_0 for $N = 3$ samples.

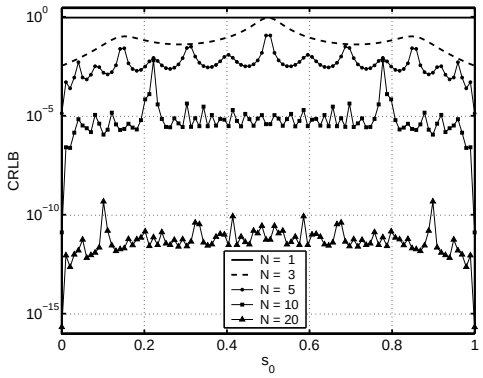

Fig. 5. CRLB for the estimation of s_0 for the map f_ℓ and various values of N.

map with initial condition on the interval $[0, 1]$, excluding a null measure set, is $L_\ell = 2$ [10]. Therefore, using (12), the same numerical result as for the Bernoulli map (14) is obtained for $N \to \infty$.

As a numerical illustration, using (14) when $N = 10$ and $\sigma_w^2 = 1$, leads to $var(\hat{s_0}) \approx 10^{-6}$ in accord with Figure 5, thereby validating the asymptotic approximation even for relatively small N.

V. Conclusions

Equation (12) shows the intimate relationship between the statistical properties of the chaotic attractor (Lyapunov number) and the performance of a would be efficient initial condition estimator of noise-embedded chaotic signals given by the CRLB when sufficiently many samples are used.

This result, in principle, provides a criterion for choosing the best one-dimensional map to be used to generate a chaotic signal from which to recover the initial condition under additive noise. Hence, if it is possible to find unbiased estimators, the larger the Lyapunov number of a map, the smaller the CRLB of its efficient initial condition estimator and hence, the better its estimates.

Another interesting conclusion from Equation (12) is that semi-conjugative maps [10] have the same CRLB performance for initial conditions for large N because they share the same Lyapunov number. For instance, $f_B(\cdot)$ and $f_\ell(\cdot)$ perform identically for large N under this criterion as $L = 2$ for both. When N is small, however, performance depends on the initial condition s_0.

References

[1] F. C. M. Lau and C. K. Tse, *Chaos-based digital communication systems*, 1st ed. Berlin: Springer Verlag, 2003.

[2] M. P. Kennedy, R. Rovatti and G. Setti, *Chaotic Electronics in Telecommunications*, 1st ed. New York: CRC Press, 2000.

[3] A. S. Dmitriev, G. Kassian and A. Khilinsky, "Limit effi ciency of chaotic signal cleaning off noise", *Proc. NDES'99*, Bornholm, Dennark, pp. 187-190, July 1999.

[4] M. P. Kennedy and G. Kolumbán "Digital communications using chaos", *Signal Processing*, vol. 80, pp. 1307-1320, 2000.

[5] G. Kolumbán and M. P. Kennedy, "The role of synchronization in digital communications using chaos - part II: chaotic modulation and chaotic synchronization", *IEEE Transactions on Circuits and Systems - I*, vol. 45, no. 11, 1998.

[6] G. Kolumbán and M. P. Kennedy, "The role of synchronization in digital communications using chaos - part III: performace bounds for correlation receivers", *IEEE Transactions on Circuits and Systems - I*, vol. 47, no. 12, pp. 1673-1683, 2000.

[7] M. P. Kennedy, G. Kolumbán, G. Kis and Z. Jakó, "Performance evaluation of FM-DCSK modulation in multipath environments", *IEEE Transactions on Circuits and Systems - I*, vol. 47, no. 12, pp. 1702-1711, 2000.

[8] T. Schimming, M. Götz and W. Scwarz, "Signal Modeling using piecewise linear chaotic generators", *Proc. EUSIPCO-98*, Rhodes, Greece, pp. 1377-1380, 1998.

[9] D. I. Abarbanel, M. E. Gilpin, and M. Rotenberg, *Analysis of observed chaotic data*, 1st ed. New York: Springer Verlag, 1997.

[10] K. T. Alligood, T. D. Sauer and J. A. Yorke, *Chaos - an introduction to dynamical systems*, 1st ed. New York: Springer Verlag, 1997.

[11] S. M. Kay, *Fundamentals of statistical signal processing*, 1st ed. New Jersey: Prentice Hall PTR, 1993.

[12] R. L. Devaney, *An Introduction to Chaotic Dynamical Systems*, 2nd ed. New York: Westview Press, 2003.

[13] S. Kay, "Asymptotic maximum likelihood estimator performance for chaotic signals in noise," *IEEE Transactions on Signal Processing*, vol. 43, no. 4, pp. 1009-1012, 1995.

Using JINI Technology for Network Management Purposes

Helcio Wagner da Silva and Luis Geraldo Pedroso Meloni
Departament of Communications - DECOM
School of Electrical and Computer Engineering. - FEEC
State University of Campinas - UNICAMP
P.O. Box 6101 - 13081-970
Campinas - SP - Brazil
[helcio,meloni]@decom.fee.unicamp.br

***Abstract*— The current systems for management of TCP/IP-based networks, although they are based on the strict definition of a protocol and a sintax for data formatting, have many open points, mainly on configuration and maintenance areas. This paper performs general considerations about utilization of JINI technology on building of those systems and points out application examples of applications of these considerations under form of two Network Management Systems, being one them designed with base on the Policy-based Network Management framework. These Systems, besides allow the utilization of multiple protocols, take advantage of features present in JINI technology for provision of automation on their configuration and maintenance procedures.**

***Index Terms*— Network Management, Distributed Systems, JINI.**

I. Introduction

The most of the network management systems currently developed are based on framework defined by IETF, which is composed by specification of a protocol and a sintax for data formatting.

Over the time, new functionalities have been incorporated to that framework, mainly flexibility and security enhancements. However, some points remain open, mainly those related to configuration and maintenance of those systems.

In this paper, we expose our ideas about how management systems can be designed with base on JINI technology, allowing flexible utilization of not only one but many protocols and taking advantage of features provided by that technology to automate the configuration and maintenance procedures of those systems.

In order to do that, the paper is structured in the following way: the section II provides an overview of evolution observed on traditional network management. After, the section III presents the basic features of JINI technology. The section IV presents general considerations that, in our vision, must be taken into account on design of Network Management Systems. The section V presents two examples of Network Management Systems designed with base on those general considerations. The section VI finalizes the paper.

II. Recent Advances on Management of TCP/IP-based Networks

The standardized management of TCP/IP-based networks was initially performed from the first version of the Simple Network Management Protocol (SNMP) [1]. The set of SNMPv1 specifications defined more than one protocol. It defined also a model for formatting and storaging of management information on Management Information Bases (MIBs), as well a lot of general purpose Managed Objects (MOs) named MIB-II.

Although it has raised a good market acceptance, the management framework defined from SNMPv1 specifications was considered inflexible, too few scalable and lacked efficient security mechanisms. An effort to supply those requirements was carried out through the sprouting of the second version of protocol [2]. However, although SNMPv2c provided new PDU types that made possible Manager-to-Manager communications and bulk data transfer, the lack of efficient security mechanisms was still a problem. Moreover, as commented in [3], the bulk data transfer requirement was just partially supplied.

Those security mechanisms only appeared on third and current version of protocol [4]. The SNMPv3 not only incorporate the functionalities appeared in the SNMPv2c design, but also provide support for using authentication and privacy, besides to introduce a sophisticated security mechanism for control access to the management informations.

Some other initiatives had been given in order to bring more flexibility to the management activity. However, they were not based on protocol changes, but on the design of specific MIBs. Some of most recent initiatives on that area were the Scheduling and Scripting MIBs, specified on [5] and [6], respectively. Those MIBs define mechanisms for scheduling and execution of scripts in remote platforms by an SNMP Agent. Those initiatives were strongly inspired on Management by Delegation (MbD) concept, introduced in [7].

One of the most recent frameworks designed by IETF for network management is named Policy-based Management, which has its basic concepts specified in [8]. Although being created in a context related

to the admission control on network resources, that framework can be certainly applied in other network management contexts.

As commented in [9], that specifies the terminology used on Policy-based Management framework, a Policy can be defined from two perspectives: a definite goal, course or method of action to guide and determine present and future decisions, or a set of rules to administer, manage, and control access to network resources.

A Policy can be defined on different leves, raising from business goals to configuration parameters. Thus, there are High-Level Policies, specified in a format that is intuitive to network administrators, and Low-Level Policies, specifically and consistently defined for each network device.

Policies are represented by means of the Policy Core Information Model (PCIM), specified in [10]. The PCIM is an extension of the Commom Information Model (CIM), which provides semantically rich definitions of management informations for systems, network, applications and services, and allows vendor extensions. CIM specifications can be found in [11].

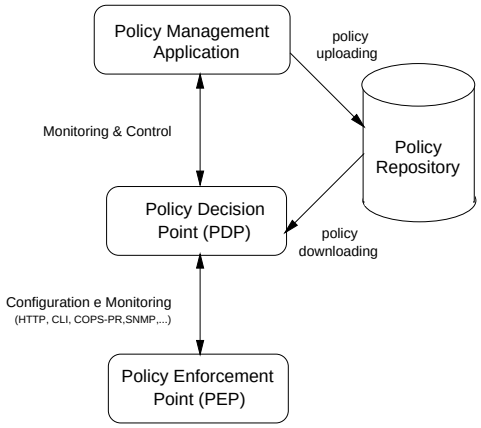

Fig. 1. Components defined for the Policy-based Management framework.

The Figure 1 shows the components defined by IETF for the Policy-based Management framework.

The Policy Management Application provides an interface for network administrators to create and deploy Policies, storing them in a Policy Repository, besides to monitor the state of environment managed with aid of those Policies.

The Policy Decision Point (PDP) is the logical entity that retrieves Policies from Repository and performs decisions on its behalf, or on behalf of network elements that request such decisions.

The Policy Enforcement Point is the logical entity that enforce Policies on the network elements.

The IETF suggests LDAP [12] as the protocol to be used for access to the Policy Repository, and COPS/COPS-PR [13] as the protocol to be used for Policy decisions transfer. However, other protocols, such as HTTP, FTP or SNMP, can be used as well in order to perform this latter function.

An important open point is that there is no any protocol suggested to be used on communications between the Policy Management Application and PDPs, or between cooperative PDPs. Additionally, there is no any specific implementation rule related to distribution, platform or language issues.

III. JINI Technology Overview

JINI is a technology developed by Sun Microsystems for building of self-healing distributed systems, that is, systems that require the minimum possible of human intervention in order to work, mainly on occurence of partial failures.

Described architecturally in [14], JINI is strongly based on utilization of Java technology and, in practical terms, it can be seen as an infrastructure and a programming model that address the fundamental requirements about how Clients and Services discover and connect one another.

In JINI, Services carry themselves proxies that provide all the code required in order that Clients can to interact with them. Those proxies are obtained dinamically by Clients when they want to use the Service, by means of communication with a meta Service named Lookup Service (LUS).

The Lookup Service is responsible for a grouping of JINI Services, named Community. Communities can be grouped together in a Federation. The communications between JINI Clients and Services and the Lookup Service can be performed with aid of multicast or unicast mechanisms.

The registration of JINI Services with the Lookup Service is maintained by means of a leasing discipline. This issue minimizes the effect of partial failures and provides the self-healing of the Community. Indeed, when the execution of a Service is suddenly or smoothly stopped the lease associated to its registration will not be renewed, and therefore that Service will not available anymore to any Client in potential. This issue makes unnecessary the requirement of human intervention in order to delete older registers.

One of the most important aspects of JINI technology is its protocol neutrality. Indeed, there is no any strict definition of protocol to be used on communications between JINI Clients and Services. Thus, although the default protocol used is the native implementation of Remote Method Invocation (RMI), named Java Remote Method Protocol (JRMP), virtually any protocol can be used, providing better flexibility to involved applications.

This is an important issue because, as commented in [15], the protocol design is often a trade-off between efficiency and generality. And, in systems that are designed around a one-size-fits-all protocol, such decisions need to favor generality. Therefore, although a protocol be designed to handle all currently conceived scenarios, this protocol is still susceptible on having an inferior performance when compared to another protocol specifically designed for a specific scenario, or even for a future scenario.

Mechanisms for generation and handling of remote events are also provided by JINI technology. From definition of a specific remote event, applications can

be designed for generating events of that type and/or be notified about firing of those events. The Lookup Service, for example, allows to interested applications be notified about events such as insertion and/or remotion of a Service which satisfies some requirement.

The mechanisms for generation and handling of remote events are performed by means of registration of event listeners on applications which generate them. And, in order to avoid wastefulness of resources by registering event listeners for applications which have their execution stopped in a suddenly or smoothly way, those mechanisms are ruled out by means of a lease discipline as well.

JINI also provides support for use of transactions, promoting the ACID properties on communications between Clients and Services.

The version 2.0 of JINI defines a security model that can be deployed on interactions between Clients and Services. Indeed, Services can to inject constraints on their proxies, requiring for example authentication on Client-side. The set of constraints that can be imposed is so extensible that security requirements for long time inexistents or even neglected can be considered.

Additionally, HTTPMD URLs can be deployed in order to provide guarantees about the integrity of transfered proxies's code. That security model provides also a new implementation of RMI, named JINI Extended Remote Invocation (JERI).

The fact regarding differents security mechanisms for interactions between Clients and Services can be deployed on exportation time of Services (i.e., those mechanisms are pluggable), enhances the produtivity on building of those Service when are foreseen many operation scenarios. In other way, those Services had to be rewritten at each changing of their operation scenarios.

Comparisions between JINI and other technologies are performed in [16] and [17], both pointing out JINI as preferential choice on building distributed applications.

In [16], JINI is compared to technologies such as Microsoft's Millennium and Universal Plug and Play, Lucent's Inferno and IBM's T-Spaces, taking into account aspects such as services, configuration, maintenance, scalability and portability. Although the aspect of cost had not been taken into account, JINI was pointed out as the most promissing technology for building of distributed systems.

In [17], JINI is compared to technologies such as CORBA and Mobile Agents for provisioning of the network service configuration, it has been also pointed out as the most suitable choice in comparision to those technologies.

IV. General Considerations About Utilization of JINI on Building of Network Management Systems

The following subsections expose, in a general way, our ideas about how to deploy the JINI technology features on building of applications destined to network management.

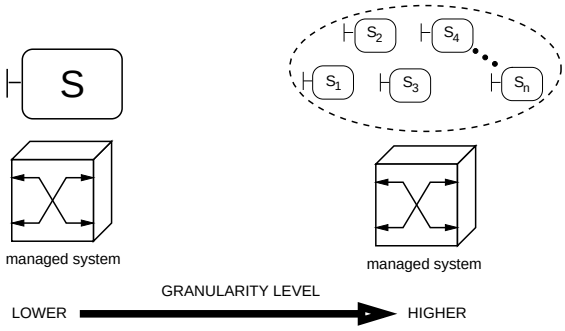

Fig. 2. Variation of granularity level on design of JINI Services associated to managed systems.

A. Associating JINI Services to Managed Systems

When it is considered the utilization of JINI on development of network management systems, the immediate idea is the utilization of JINI Services associated to managed systems. Indeed, differents granularity levels can be used in the design of JINI Services for managed systems, as shown by Figure 2.

As shown by Figure 2, it can be associated to a managed system as many JINI Services as desired.

The higher granularity level is that in which each JINI Service is equivalent to a Managed Object. Thus, the Figure 2 shows, at its right side, a system managed by JINI Services $S_1, S_2, ..., S_n$, which are equivalents, in terms of modelling, to the various Managed Objects that would be defined for management of that system using traditional techniques.

This correspondence between JINI Services and Managed Objects in terms of modelling was initially conceived in [18], that took into account the considerations performed in [19], about the utilization of CORBA Objects on building of network management systems.

Modelling JINI Services on granularity of Managed Objects can brings about a more smooth maintenance on the operations of a management system. That is occurs because each one of those Services is independent of any other, being the design issues performed basically at interface implemented and in the attributes that each Service Object carries.

However, a special care must be taken when that granularity level is adopted on modelling, because it can lead about a large number of JINI Service associated with only one managed system. In addition, because each one of those Services is executed by a different instance of the Java Virtual Machine (JVM), it is better to build them using the activation resource at most.

Nevertheless, it must be taken into account that simultaneous operation of all Services consume more computacional resources than only one equivalent Service in terms of modelling.

The lower granularity level is that in which the system is managed with aid of only one JINI Service. This level is shown by the left-side of Figure 2.

When a system is managed by means of only one JINI Service, there is a loss of maintenance because

functional changes in Service affect in a direct way the design of its interfaces and/or its attributes.

Additionally, it can be loaded into the memory much more than it is used usually, because there can be management aspects in a system that are rarely used, although they are foreseen and supported.

However, the utilization of only one JINI Service for management of a system can be advantageous compared to the fragmentation of that Service in many others when those Services are frequently used. That occurs because, as cited before, each one of those Services is executed by a different instance of JVM and the cumulative consumption of computacional resources in this case is higher than that observed by only one equivalent JINI Service.

B. Grouping JINI Services in Managed Domains

As has been seen in section III, JINI Services are grouped in Communities. By our proposition on to monitoring and controlling managed systems with aid of JINI Services, it is natural to group them in Communities.

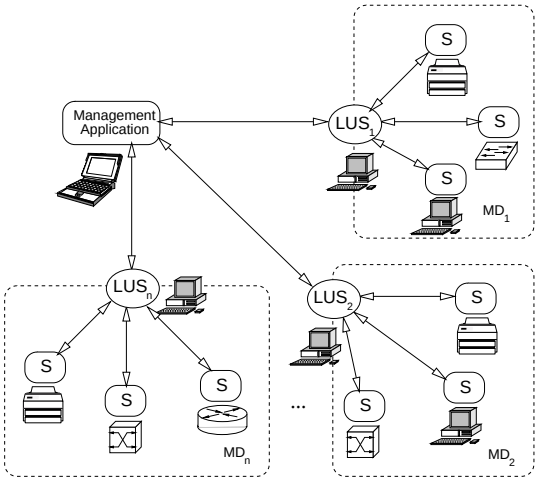

Fig. 3. JINI Services grouped in federated Managed Domains.

The Figure 3 shows a network infrastructure where there is a JINI Service associated to each managed system, therefore being deployed the lower granularity level on design of those Services.

Each one of those Services belongs to a Community and, for management purposes, each Community is named a Managed Domain. The Figure 3 shows the Managed Domains $MD_1, MD_2, ..., MD_n$, each one of them under responsibility of a Lookup Service. JINI Services are grouped in those Managed Domains by means of administrative and/or geographical principles.

The Figure 4 shows the interactions observed in a Managed Domain. Each one of JINI Services associated with a managed system initially registers its proxy on a Lookup Service, becoming part of the Managed Domain (a). As cited in section III, that registration is performed and maintained by means of a lease renewal procedure.

The Management Application communicates with the Lookup Service for the acquisition of a proxy to

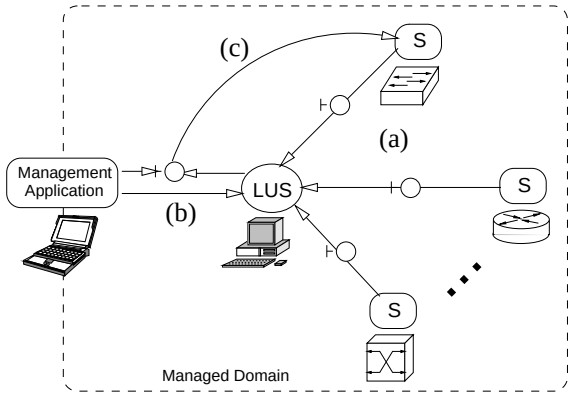

Fig. 4. Interactions observed in a Managed Domain.

one of Services belonging to that Domain (b). This search has usually as parameters the interface exported by Service and/or some of its attributes, such as the location or administrative name of the managed system to which that Service is associated, for example.

After having obtained one or more proxies on the Lookup Service, the Management Application can to invoke remote operations on those proxies, thus performing the monitoring and control of the managed system (c).

Although the Figure 4 shows a common communication between the Management Application and the JINI Services associated to managed systems, there are some additional points to be commented. The first of them is that, as cited in section III, virtually any protocol can be used on communications between those applications. It can be used any version of SNMP, for example.

The second remarkable point is related to ways of communication between the Management Application and the JINI Services destined to management of systems. Indeed, the registration of event listeners on those Services allows that remote events be transmitted to Management Applications. This issue provides the deployment of the notification strategy, in addtion to the polling strategy, in JINI-based Network Management Systems.

Finally, the combination of leasing and remote events mechanisms allows the guarantee of self-resilience for those systems as a whole. Thus, if the Management Application register specific event listeners on the Lookup Service responsible for a Managed Domain, this Application will be aware of insertion and/or remotion of Services in that Managed Domain, having an updated vision of its operation scenario.

C. Embedding Flexible User Interfaces into JINI Services

In traditional design of network management software, the MIB is considered as a result of the thought of specialists about what are the most remarkable points for monitoring and control of a whole system, or parts of that system, as commented in [20].

Those points many times address specific features of the vendors, usually those features that make the

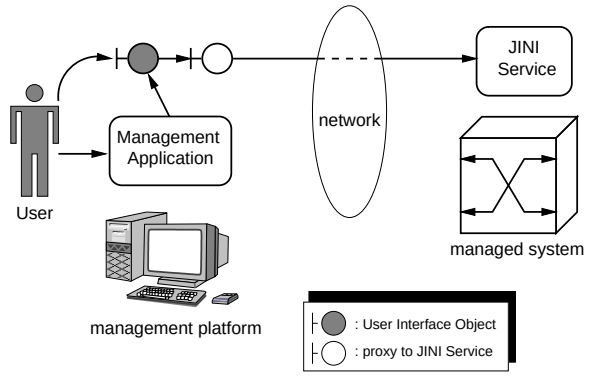

Fig. 5. Incorporation of ServiceUI Project.

system different of similar systems produced by other vendors.

The problem emerged from this fact is that, at most of time, Management Applications of general purpose are not aware of those points, and thus can not address them by means of SNMP PDUs.

Therefore, there is an undesirable scenario where the management of systems is performed locally or remotelly by means of the TELNET protocol. Many times, a palliative solution is provided by means of MIB browsers, but without expressive results.

In [21] is suggested an approach based on utilization of HTTP servers embedded in managed systems. Those HTTP servers exported HTML pages containing management information for Web browsers.

The principal advantage provided by that approach is that managed systems can export semantically rich Graphical User Interfaces (GUIs) for their monitoring and control, thus no more requiring customized management tools.

In spite of the enormous advantages provided by that approach, There is must be taken into account that, like the SNMP-based traditional approach, it is based on strict definition of a protocol and a data model. In this approach, management informations are codified in HTML and transfered using HTTP.

Inspired by approach exposed in [21], we take advantage of the API provided by ServiceUI Project [22] of JINI Community to make possible the dynamic importation of semantically rich User Interfaces from JINI Services associated to managed systems.

The idea behind the ServiceUI Project is to embed User Interface Objects in proxies to JINI Services, more specifically in their attributes. The incorporation of ServiceUI Project on design of JINI-based Network Management Systems is shown by Figure 5.

The incorporation of the ServiceUI Project allows the same functionality provided by approach exposed in [21], besides to offer advantages in comparision with that approach.

The first of those advantages is related to the utilization of JINI technology itself, more specifically to the fact that there is no strict definition of the protocol to be used on communications between proxies and their correspondent Services.

Thus, in contrast to the approach exposed in [21], JINI-based Network Management Systems allow that any protocol, not only HTTP, be used for transmission of management data. Moreover, for scenarios with security constraints, the simplified version of HTTP can not be used.

The second advantage provided by incorporation of ServiceUI Project in comparision to approach exposed in [21] is related to the ServiceUI Project itself, that does not impose any requirement on the type of User Interface provided by correspondent Object.

Therefore, the incorporation of the ServiceUI Project in JINI-based Network Management Systems allows users of those systems to use a graphical interface, a text interface, a combination of text and graphics or even a virtual reality environment. Indeed, as commented in [23], the Object is said to be simply an User Interface Object, instead of a Graphical User Interface Object.

Although the comments above are limited to comparision to the approach exposed in [21], there are other important considerations about utilization of User Interface Objects.

In [24], [25] and [26] are exposed the merits and demerits about utilization, in a global way, of proxies and User Interface Objects in contrast to traditional Client/Server communications consisting of HTML pages transfered by means of the HTTP protocol.

D. Providing Secure Interactions Between Management Applications and JINI Services

In section III, it was cited that JINI technology has a protocol neutrality, i.e., virtually any protocol can be used on communications between Clients and Services.

It was cited also that JINI has security mechanisms that allows the injection of constraints in proxies to Services and the guarantees of integrity of downloaded code.

There are two parameters to be considered on verification of the necessity of use of those security mechanisms on JINI Services associated with managed systems.

The first of those parameters is the security level of the environment on which the interactions between Management Application and JINI Services occurs. Secure environments do not demand the use of security mechanisms between Management Application and JINI Services. On other hand, insecure environments demand the use of those mechanisms to guarantee of secure communications.

When secure environments are considered, and therefore there is a demand for application of security mechanisms, the second parameter is considered for verification of necessity of application of security mechanisms provided by JINI. In effect, there must be investigated if the protocol to be used on communications between Management Application and JINI Services already supplies the security requirements imposed by the environment. If it does not, the application of security mechanisms provided by JINI technology is mandatory.

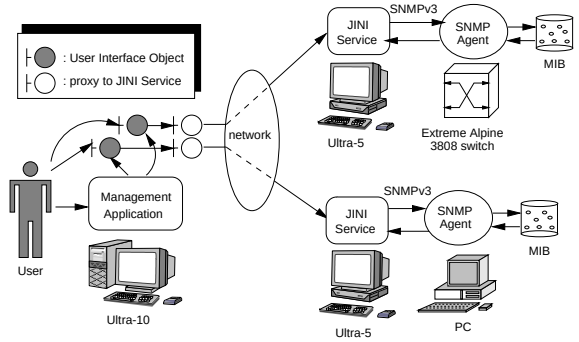

Fig. 6. The Bay of Devices.

V. Examples of Use

In this section, the general considerations performed in section IV are used in the design of two JINI-based Network Management Systems. The first them is a relativelly simple system for management of a little-medium-sized network infrastructure, being known as the Bay of Devices. The second System is more suitable for management of a more large-sized network infrastructure, being based on the Policy-based Network Management framework.

A. The First Example of Use: The Development of a Bay of Devices

An imediate example of deployment of considerations performed in the previous section is the Bay of Devices, ilustred by Figure 6.

The Bay of Devices is an experiment that consists on utilization of JINI Services for monitoring and control of some devices in a network infrastructure. For its development were used the 1.4.2 release of Java 2 Platform, Standard Edition (J2SE) [27] and the 2.0_002 release of JINI Technology Starter Kit (JTSK) [28].

Taking into account the Figure 6 and the considerations performed on subsection IV-A, it can be seen that was used the lower granularity level on design of JINI Services by associating only one Service with each one of managed systems. Those systems are composed currently by a PC and an Extreme Alpine 3808 switch.

Both devices support SNMP-based management. In PC, that runs the Mandrake 9 distribution of the Linux operational system, it was used the 4.2.3 release of daemon (Agent) SNMP developed in context of the NET-SNMP Project [29]. In switch, it was used the SNMP Agent embedded on that device. Both Agents support the v1/v2c/v3 versions of SNMP.

The Services developed communicated with the Agents installed on devices by means of the SNMPv3 protocol, being used the 3.3 release of SNMPv3 API provided by AdventNet [30] for their building. Those Services were grouped in a Community, which in subsection IV-B was named Managed Domain for network management purposes.

Those Services, along with the Lookup Service responsible by Domain, are deployed in Ultra-5 Sun workstations running Solaris 9. Those workstations are part of a same Ethernet LAN segment, thus JINI Services are inserted in Managed Domain using the multicast join mechanisms provided by JINI.

The Management Application is deployed in an Ultra-10 Sun workstation, also running Solaris 9. That workstation also is part of the same Ethernet LAN segment of Lookup Service, thus it also communicates with that Service by means of multicast mechanisms. However, unicast mechanisms were provided in order to run that Application from a platform located out of the Lookup Service's Ethernet LAN segment.

Applying the considerations performed in subsection IV-B, the Management Application has registered an event listener on Lookup Service in order to be notified about future insertions, or even eventual remotions, of Services in Managed Domain. Applying that design issue, the Management Application always maintains a consistent vision of Services currently present on Domain in question, which are represented by icons in its main panel.

As shown by Figure 6, for a more flexible management of a device, it was applied the considerations performed in subsection IV-C, being embedded User Interface Objects in proxies to developed JINI Services. Therefore, when the user point and fire one of icons present on the Management Application's main panel, the User Interface Object's code is downloaded and instantiated. The management of device is performed from that dynamically obtained Interface.

The communication environment of Applications that compose the Bay of Devices is very secure. However, by application of considerations performed in subsection IV-D, we are currently working on implementations that use protocols such as Secure Socket Layer (SSL) or Kerberos for guarantees of secure communications when the Management Application is executed from a platform outside the Lookup Service's Ethernet LAN segment.

Additionally, we are using the 2.1 release of the Java 2 Platform, Micro Edition (J2ME) Wireless Toolkit [31] for building a new version of the Bay of Device that can be executed from a mobile platform, such as a PDA or even a celular telephone. Naturally, besides of currently available User Interfaces, are been developed new Interfaces suitable to operation in those platforms.

B. Second Example of Use: Design of a Policy-based Network Management System

As cited in section II, there is no strictly defined protocol for communications between the Policy Management Application and PDPs in the Policy-based Management framework.

Moreover, it was cited in section III that distributed systems built with base on JINI do not require to be bound to any specific protocol.

It was cited also in section IV that those systems take advantage of key features provided by technology in order to maximize the flexibility and automation of their operations, minimizing the possibility of human intervention on occurence of partial failures.

The combination of those factors is the motivation for a study about what are the observable effects when JINI is used on building of Policy-based Network Management Systems.

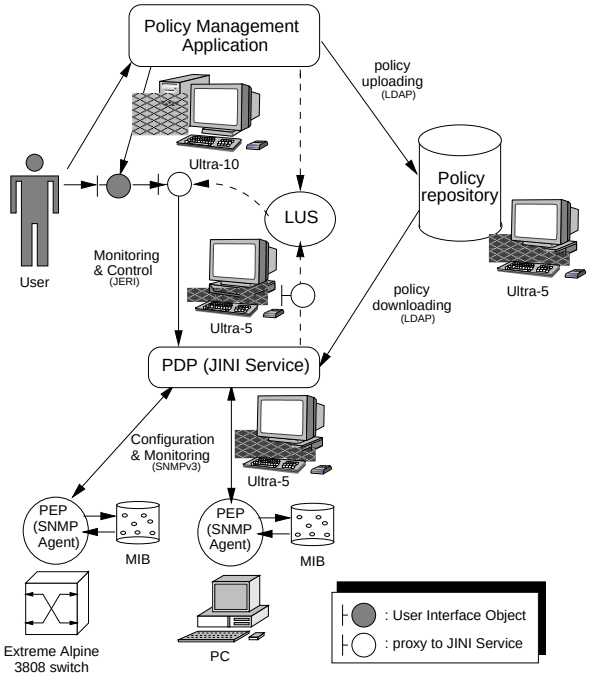

Fig. 7. Utilization of JINI in a Policy-based Network Management System.

The Figure 7 shows an example of application of JINI technology on building of Policy-based Network Management Systems. Applying the considerations performed in subsection IV-A, the PDP is modelled as a JINI Service that communicates with the Policy Management Application by means of its correspondent proxy.

There are remarkable advantages on modelling the PDP as a JINI Service. One of those advantages is the flexibility related to the several possibilities of implementation of the protocol to be used on communications between the Policy Management Application and PDP, being JERI or JRMP the most probable options. There must be considered that other options can be deployed, such as IIOP or SNMP, for example.

Another advantage on modelling the PDP as a JINI Service is related to the self-healing capability of that System. Indeed, applying the considerations performed in subsection IV-B, the System can be composed by various federated Managed Domains, each one of them under responsibility of a Lookup Service and being composed by one or more PDPs responsible by one or more PEPs.

Additionally, applying the considerations performed in subsection IV-C, it can be deployed User Interface Objects referenced in proxies to JINI Services, in order to allow that Policy Management Application can monitor and control PDPs by means of User Interface Objecs suitable to the hardware capabilities and specific features of each PDP in the System.

Finally, applying the considerations performed in subsection IV-D, constraints can be imposed in dynamically downloaded proxies in order to provide security mechanisms on communications between the Policy Management Applications and the PDP, specially when that application executes from a insecure environment.

For implementation of that Policy-based Network Management System using the JINI technology, it will be also used the release 1.4.2 of J2SE and the 2.0_002 release of JTSK. Additionally, will be used the 2.2.14 release of OpenLDAP [32] (an open source implementation of the LDAP protocol) for Policies transfer and the 3.3 release of SNMPv3 API provided by AdventNet for communications between PDPs and their subordinated PEPs.

At the completion of its development, this Policy-based Network Management System will be much more scalable than the Bay of Devices, because its user will have, on its main panel, icons that represent not devices but PDPs responsible by management of those devices. Moreover, that user will have mechanism for building, changing and removing Policies to be deployed in the System.

VI. Conclusions

This paper provided some ideas about the utilization of JINI technology on building of network management systems. It presented initially an overview of the traditional network management framework, exposing some advances occured over the time related to flexibility and security on operations of systems build with base on that traditional paradigm.

After that, it presented an overview of the key features of JINI Technology, after adjusting them for use in network management activities. It exposed that JINI Services can be associated to managed systems, grouped in Managed Domains, and also contain User Interface Objects suitable to several types of management platform. Moreover, it enforced that communications between Management Applications and JINI Services can take advantage of security mechanisms provided by the most recent release of JINI technology in order to assure a more secure communications in scenarios where that issue is mandatory.

After being presented those general considerations, the paper described two Network Management Systems that apply them. The first of them is the Bay of Devices, which is already in operation and is dedicated to management of few devices. The second of them, to be implemented, is the design of a Policy-based Network Management System that uses JINI on design of the Policy Management Application and PDPs. By using the Policy-based Management framework, this last system will be much more scalable than the Bay of Devices.

References

[1] J. Case, M. Fedor, M. Schoffstall, and J. Davin. *A Simple Network Management Protocol (SNMP) - rfc 1157*, May 1990. Available at http://www.ietf.org.

[2] J. Case, K. McCloghrie, M. Rose, and S. Waldbusser. *Introduction to Community-based SNMPv2 - rfc 1901*, January 1996. Available at http://www.ietf.org.

[3] Ron Sprenkels and Jean-Philippe Martin-Flatin. Bulk transfers of mib data. *The Simple Times - The Quarterly Newsletter of SNMP Technology, Comment, and Events*, 7(1):1–7, March 1999. Available at http://www.simple-times.org.

[4] D. Levi, P. Meyer, and B. Stewart. *SNMPv3 Applications - rfc 2273*, January 1998. Available at http://www.ietf.org.

[5] D. Levi and J. Schoenwaelder. *Definition of Managed Objects for Scheduling Management Operations - rfc2591*, May 1999. Available at http://www.ietf.org.

[6] D. Levi and J. Schoenwaelder. *Definition of Managed Objects for the Delegation of Management Scripts - rfc2592*, May 1999. Available at http://www.ietf.org.

[7] G. Goldszmidt and Y. Yemini. Distributed management by delegation. In *Proceedings of The 15th International Conference on Distributed Computing Systems*, June 1995. Available at http://citeseer.nj.nec.com.

[8] R. Yavatkar, D Pendarakis, and R Guerin. *A Framework for Policy-based Admission Control*, January 2000. Available at http://www.ietf.org.

[9] A. Westerinen, J. Schnizlein, J. Strassner, M. Scherling, B. Quinn, S. Herzog, A. Huynh, M. Carlson, J. Perry, and S. Waldbusser. *Terminology for Policy-Based Management*, November 2001. Available at http://www.ietf.org.

[10] B. Moore, E. Ellesson, J Strassner, and A. Westerinen. *Policy Core Information Model – Version 1 Specification*, February 2001. Available at http://www.ietf.org.

[11] Distributed Management Task Force (DMTF) Inc. Dmtf - common information model (cim). http://www.dmtf.org/standards/cim/.

[12] M. Wahl, T. Howes, and S. Kille. *Lightweight Directory Access Protocol (v3)*, December 1997. Available at http://www.ietf.org.

[13] D. Durham, J. Boyle, R. Cohen, S. Herzog, R. Rajan, and A. Sastry. *The COPS (Common Open Policy Service) Protocol*, January 2000. Available at http://www.ietf.org.

[14] $Jini^{tm}$ *Architecture Specification - Version 2.0*, June 2003.

[15] Jim Waldo. The end of protocols. Available at http://developer.java.sun.com/developer/technicalArticles/jini/protocols.html.

[16] Lai Olstad, Javier Ramirez, Clint Brady, and Bruce McHollan. Jini technology: Impromptu networking and its impact on telecommunications. Available at http://citeseer.nj.nec.com, 1999.

[17] S. Raza, B. Pagurek, and T. White. Distributed computing for plug-and-play network service configuration. In *Proceedings of the 2000 IEEE/IFIP Network Operations and Management Symposium (NOMS'2000), Honolulu, Hawaii, EUA*, 10-14 April 2000.

[18] H. Silva and L. Meloni. Using jini technology for building of network management systems. In *Proceedings of the IADIS International Conference Applied Computing 2004, Lisbon, Portugal*, March 2004.

[19] Juan Pavon. Building telecommunications management application with corba. *IEEE Communications Surveys*, pages 2–16, 2nd. Quarter 1999.

[20] C. Wellens and K Auerbach. Towards useful management. *The Simple Times - The Quarterly Newsletter of SNMP Technology, Comment, and Events*, 4(3):1–7, July 1996. Available at http://www.simple-times.org.

[21] Barry Bruins. Some experiences with emerging management technologies. *The Simple Times - The Quarterly Newsletter of SNMP Technology, Comment, and Events*, 4(3), July 1996. Available at http://www.simple-times.org.

[22] Bill Venners. Serviceui project. http://serviceui.jini.org/.

[23] Bill Venners. How to attach a user interface to a jini service - an in-depth look at the serviceui project from the jini community. *JavaWorld*, October 1999. Available at http://www.javaworld.com.

[24] Bill Venners. Objects versus documents for server-client interaction, part 1 - comparing two ways that software can interact with software. *JavaWorld*, May 2000. Available at http://www.javaworld.com.

[25] Bill Venners. Objects versus documents for server-client interaction, part 2 - determining the best approach when there is no client-server user. *JavaWorld*, July 2000. Available at http://www.javaworld.com.

[26] Bill Venners. Using objects in place of documents for server-client interaction, part 3 - why objects are for people, not for computers. *JavaWorld*, November 2000. Available at http://www.javaworld.com.

[27] Sun Microsystems. Java 2 platform, standard edition (j2se). http://java.sun.com/j2se/index.jsp.

[28] Sun Microsystems. Jini network technology. http://wwws.sun.com/software/jini/.

[29] NET-SNMP. The net-snmp project home page. http://net-snmp.sourceforge.net/.

[30] AdventNet Inc. Adventnet snmp api: Java snmp api/snmp stack/snmp library for snmp management. http://snmp.adventnet.com/.

[31] Sun Microsystems. Java 2 platform, micro edition (j2me). http://java.sun.com/j2me/index.jsp.

[32] OpenLDAP Foundation. Openldap. http://www.openldap.org/.

Feature Identification Techniques for HRTF Individualization

Sergio Gilberto Rodríguez Soria
EPUSP, Electronic Systems Departament
Av. Prof. Luciano Gualberto, tr. 3, 158
CEP 05508-900, São Paulo, SP, Brasil
sergio@lps.usp.br

Miguel Arjona Ramírez
EPUSP, Electronic Systems Departament
Av. Prof. Luciano Gualberto, tr. 3, 158
CEP 05508-900, São Paulo, SP, Brasil
miguel@lps.usp.br

***Abstract.* — This article contains information about spatial hearing and the localization process of the human hearing system. The analysis of head-related transfer functions (HRTF's), which are of central importance for 3D audio systems, is geared to its adaptation to the listener's features. We work with Linear Prediction analysis to decompose the median plane measured HRTF, in order to extract meaningful features related to specific parts of the body such as pinnae and head-torso combination. The LPC response tracks the resonances caused by the pinnae, while for the notches we use a simple thresholding procedure in the image processing domain. Thus, the frequency response associated with the pinnae transfer function (PTF) is extracted. Guidelines are established for obtaining the head-torso (HAT) response. The next stage is to model the obtained responses, aiming at low order representations. The final goal is the customization of the HRTF for a particular individual allowing a fast adaptation to his features, while obviating the tedious measurement process and attaining better performance than generalized HRTF's do.**

***Index Terms*— 3D sound, spatial hearing, head-related transfer function, HRTF, sound localization.**

I. INTRODUCTION

With the fast growing interest in interactive distance communication, from the traditional circuit switched telephony to the most recent real time video conference over packet switched networks, it is essential to take full advantage of perceptual characteristics of the auditory system, both for preserving the communication environment and for increasing the perceptual dimensions in order to improve the immersion effect. On this respect, the development of spatial audio systems capable of giving the user a high-quality virtual audio scene rendering is a major issue.

The aim of spatial sound reproduction is to create an impression of a sound environment, which will surround the listener in the 3D space. The level of perceptual accuracy of this environment will depend on the spatial audio application, which can range from sophisticated simulators to the simplest consumer products [1]. Apart from the qualitative measure of perceptual accuracy, spatial audio reproduction systems employ methods that can be divided into soundfield-related [2] and head-related methods [3]. The former were conceived for giving a natural spatial impression over a certain listening area. This is attained by using loudspeaker arrays to generate wavefronts. The number and distribution of loudspeakers will determine the size of the reproduction area (i.e. Cinema applications). Examples of soundfield-related methods are Ambisonics [4], Wave Field Synthesis [2] and others. On the other hand, head-related audio systems, also called binaural or 3D-audio systems, are based on special pre-filtering of recorded or artificial sound signals. This filtering process imitates mainly the outer ear's (pinna) work and is based on pre-measured head-related transfer functions (HRTF's). 3D-audio systems have been designed for creating a spatial audio impression for a single listener and can be reproduced by loudspeakers [5] or headphones [6]. Thus, they are more suited to consumer-oriented products for communication applications.

The HRTF captures sound localization cues created by the scattering of sound waves incident on the body. Specifically, it characterizes the transformation of the sound signal when taken from an arbitrary point in space to the eardrum of a listener. This single-input/double-output system is often obtained via direct measurements in a relatively tedious process that requires access to specialized experimental facilities. Measurement process details are given in [7]. The idea is to collect a set of impulse responses (head related impulse response, HRIR), one for each direction in a spherical grid. When the 3D audio system requires synthesizing a sound source in a way that its sound appears to arrive from a given direction, the sound source signal is convolved with the corresponding impulse response of the stored set. In practice, the measurement point could be any point in the listener's ear canal [8].

From heuristics, HRTF's depend explicitly on frequency and the spatial locations of the source relative to the listener, and implicitly on the size and shape of the listener's body. Hence, the HRTF varies significantly between individuals according to their ear-shapes and to a smaller extent in relation to their head and body size as well. The use of generalized HRTF's results in poor localization performance, elevation perception errors, front-back confusion, in-head localization and others [9] [10]. Applications in the creation of virtual auditory displays unfailingly require individual HRTF's for perceptual fidelity. Until now, the greater amount of effort has been dedicated to either the reduction of the data in order to reduce processing time (i.e. HRTF modeling) [11] or the development of spatial interpolation techniques that reduce the set of measured HRTF's [12]. As we can see in the literature, previous research on the field has already obtained fairly good results on these two tasks; right now, the biggest and still-open problem is the customization of the HRTF's for a particular individual. This task hasn't been much explored, although some approaches that include numerical modeling [13], frequency scaling [14] and database matching [15] have been already presented with varying degree of success. On the other hand, the customization task leads to another kind of important studies, like quality assesment of HRTF's [16], repeatability analysis [7] and others, all geared to establish

quantitative representations of the variability of HRTF measurements. The final goal is to get a general set of HRTF's that function reasonably well for every human.

It's presumed that each person learns her own HRTF given visual feedback about the source position but the HRTF's of different people look very different when plotted and are not interchangeable. The challenge is to get a customized HRTF model allowing a fast adaptation to an individual's features while obviating the tedious measurement process and attaining better performance than generalized HRTF's do.

We must point out that different anatomical parts such as the pinnae, head, torso and shoulders contribute to different temporal and spectral features in the HRTF, as it has been already studied in previous works [17]. Then, we can indentify two main goals which are: i) to obtain a reliable technique to decompose the HRTF in meaningful features related to specific parts of the body, and specific ranges of frequencies; and ii) to study the quantitative relationship between these extracted features and anthropometric correlates. It may be possible to synthesize, from anthropometric measurements, a response which incorporates the perceptually significant features for any person and for any source location. These measurements could be obtained, for example, via simple image processing of a person's picture.

Our purpose in this paper is to decompose the HRTF in meaningful features in the frequency domain: the pinnae transfer function (PTF) and the head-torso (HAT) response. Besides, one contribution of this work is to introduce simple image processing (IP) techniques used for isolating the notches caused by the pinnae in the HRTF, presented as a 2D artificial grayscale image. In Section II, we discuss some issues about localization cues. In Section III, we present some background about HRTF mathematics and the data we used for this study. In Section IV we specify the techniques used in decomposing the HRTF's. Finally, in Section V we give a summary of the results and future work.

II. LOCALIZATION CUES

We can define monoaural as those facts or attributes related to one ear; binaural, as those related to the two ears and interaural as those related to the differences between the two ears. Besides of that, we define "localization" as the relation between corresponding positions in the sound space (real physical space), and in the auditory space ("imaginary" listener space) [18].

During the localization process, the hearing system simultaneously evaluates a multitude of cues which have to be sorted for relevance to the localization task. Recently, a new classification scheme has been introduced, which divides the cues into three main groups: sound source cues, environmental cues, and subject-dependent cues [19].

Belonging to the last group, the HRTF is our subject matter. From Lord Rayleigh with his classical model of a head as a rigid sphere [20] to Duda and his work modeling the interaural time difference (ITD) and the interaural level difference (ILD) [21], we can roughly say that horizontal localization, and part of the vertical one, is well understood. The ILD exists in the whole frequency range but its importance rises at frequencies above 2 kHz, when ITD detection becomes ambiguous. These are the interaural cues, which are recognized like the most important providers of subject-dependent localization cues. Anyway, a monoaural spectral modification of the input signal, which is performed mainly by the pinna, exists. In particular, it becomes important in the median plane; where there are no interaural cues (azimuth angle is equal to 0°).

Acoustically, each pinna acts as a linear filter whose transfer function depends on the direction and distance of the sound source. By distorting incident sound signals linearly, the pinna codes spatial attributes of the sound field into temporal and spectral attributes. The acoustical phenomena are various such as reflection, shadowing, dispersion, diffraction, interference and resonance. Most researches accept the conclusion that monoaural attributes of the ear input signals provide the most significant cues in forming the distance and elevation angle of the auditory event and the front-back discrimination as well. Here is one reason for the great variance between inter-individual HRTF's; the great difference between pinnae shapes and sizes. Besides, at frequencies below 3 kHz, the pinnae are unable to filter the input signals due to their great wavelengths. Then, the reflection caused by the HAT becomes important. It's proved that in this frequency range it is the HAT that provides the best elevation localization cues [22].

From these facts, we can draw preliminary conclusions:

- Every particular combination of spectral resonances and notches (i.e. poles and zeros) in the frequency response associated with the PTF is a fundamental issue in the elevation localization process above 3 kHz.
- The HAT reflection is the principal provider of localization elevation cues below 3 kHz. Due to the more standard shape of the frequency response associated with the HAT, when compared with the one associated with the PTF, the customization task is not so critical, but anyhow important.

The exact location of the pinnae resonances has been studied by Shaw and Teranishi, having found the six eigenfrequencies in the HRTF [23].

The fact that the HRTF is essentially a minimum-phase function leads us to use just the magnitude of the HRTF. Further, the HRTF is taken along the median plane where there are no great binaural differences.

III. HRTF DATA

A. HRTF Basics

The HRTF relates the time-varing free-field sound pressure $x(n)$ of a sound source to the sound-pressures $x_L(n)$ and $x_R(n)$ at the left and right eardrum. The time domain convolution of the source signal with the head-related impulse responses $h_L(n)$ and $h_R(n)$ for the left and right ear, respectively, becomes in the frequency domain the product of their Fourier transforms:

$$X_L(e^{jw}) = H_L(e^{jw}) \cdot X(e^{jw}) \quad (1)$$

$$X_R(e^{jw}) = H_R(e^{jw}) \cdot X(e^{jw}) \quad (2)$$

If the source location is specified with a head-centered spherical coordinate system, H_L and H_R vary with frequency, and with azimuth Φ, elevation θ, and range r.

Thus, the HRTF can be expressed as $H_L(e^{jw}, \Phi, \theta, r)$ and $H_R(e^{jw}, \Phi, \theta, r)$ or simply $H(e^{jw}, \Phi, \theta, r)$.

B. *Public Database*

The HRTF's used for analysis were taken from the CIPIC database [24]. This is a public domain database of high spatial resolution HRTF measurements for 45 different subjects at 25 different azimuths and 50 different elevations (1250 directions) at aproximately 5° angular increments. The distance *r* was set and fixed at 1m. In addition, the database contains anthropometric measurements for each subject. The azimuth is sampled from –80° to 80° and the elevation from –45° to +230.625°. For each azimuth we display a 2D artificial image, where each column is the HRTF for a given elevation, and the magnitude of the frequency response is expressed in grayscale levels. Then, if we have a frequency response of 100 points (up to half sampling frequency), for each ear and azimuth, we have a 100x50 pixel image. This method of visualization helps to identify different features and their variation with elevation. Peaks are the brighter regions and nulls are the darker ones.

C. *Structural Approach*

In figure 1, the HRTF image (right and left ear) of a subject in the database, with azimuth at 0° is shown and some structural features are marked.

According to previous researches [17] we can recognize the arch-shaped notches structure below 3 kHz, as the effect of the HAT reflection. We also mark the first Shaw's eigenfrequency at approximately 4 kHz (the other ones are at 6 kHz, 9 kHz, 11 kHz, etc., see [23]). The pinnae notches appear from 6~7 kHz. They are mixed with the notches produced by the head diffraction. Anyway, we can heuristically deduce that the most important notches are the diagonal ones due to their explicit variation with elevation.

At this point it's important to highlight the assumption made by Algalzi and Duda. They hypothesize, according to their experimental results, that it's possible to approximate the effects of the pinna and the HAT like two independent filters in cascade. Details are given in [17].

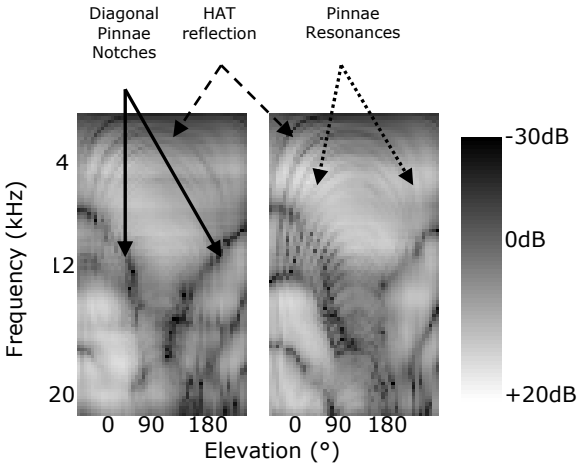

Fig.1 Left and right ear HRTF for azimuth 0°, subject 10. Some structural features are marked.

IV. Feature Identification and HRTF Decomposition Techiques

In order to model the elevation localization effect in the median plane, we focus the efforts on separating the pinna response from the HAT one in the frequency domain.

Basically, we reproduce a method based on LP analysis [25] for tracking the pinna eigenfrequencies and develop a simple thresholding procedure in the IP domain for extracting the notches caused by the pinna. The HAT response is partially obtained by IP too, but it's not working for all the subjects yet. For obtaining the HAT response we prefer to rely on the HAT model proposed in [26].

A. *Linear Prediction Analysis*

We summarize the procedure of [25] in table 1.

TABLE 1
LP PROCEDURE TO EXTRACT PINNA RESONANCES

Step	Goal	Algorithm basis
1	HRIR time aligment	Maximun peak
2	DC remove if any	Pre – emphasis operation
3	Pinnae resonances	LPC analysis , p = 20 , Levinson Durbin
4	Spectral notches	LP residual
5	First approximation to the pinnae notches	Emphasize LP residual

The emphasized LP residual signal in the z-transform domain is given by:

$$R_{EM}(z) = R_E(z/r) \qquad (3)$$

Where r is the emphasis factor, also called bandwidth expansion coefficient, which ranges from 0.9 to 1.0; and $R_E(z)$ is the residual signal in the z-transform domain, given by:

$$R_E(z) = A(z) \cdot H^d(z) \qquad (4)$$

Where $A(z)$ is the LPC analysis filter and $H^d(z)$ is the pre-emphasized HRTF. They are, respectively:

$$A(z) = 1 + \sum_{K=1}^{P} a_K \cdot z^{-K} \qquad (5)$$

and,

$$H^d(z) = H(z).(1 - z^{-1}) \qquad (6)$$

Some results are displayed in figure 2, where we show the images corresponding to the LPC and LP residual frequency responses. Figure 3 shows the images corresponding to the emphasized LP residual frequency responses, for $r = 0.91$, $r = 93$ and $r = 0.95$. The attained goals here are: i) determination of pinnae resonances tracks from the LPC frequency responses and ii) a first approximation to the pinna notches location with the emphasized LP residual frequency responses.

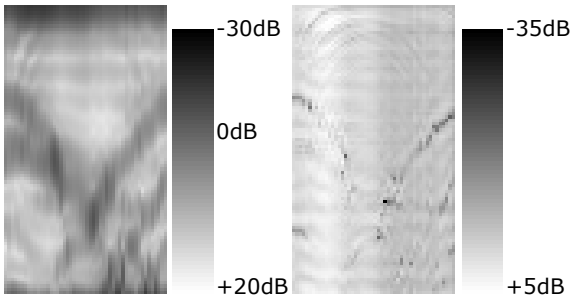

Fig. 2 LPC and LP residual frequency responses of the left ear HRTF for azimuth 0°, subject 10.

B. *Image Processing*

The quantization error introduced by the grayscale conversion and processing is much lower than other degradations introduced by the measurements process (see [8] and [16]). For the grayscale used here (256 levels) and the dinamic range of the signal (50dB at the most), the maximum error would be 0.195dB. For giving an idea: in [27] the variation between measurements in different days, in the same measurement system, with the same individual is within ± 0.5dB. Therefore, the image processing is viable.

Observing the resulting images of the previous section we conclude:

- Figure 3 shows two well differenciated "zones" in the images corresponding to the emphasized LP residual frequency responses. In zone 1 the background is brighter, while in zone 2 the background is darker. This can also be appreciated with more dificulty in the original HRTF image in figure 1. The reason is probably the antisymmetric shape of the pinnae in relation with the elevation angle of 90°. There are some subjects where the differenciated zones are more than two.
- Figure 3 shows that the location of the notches is almost the same for all the emphasis factors up to approximately 0.95 (this value varies between individuals), when the notches caused by the HAT become more evident. The difference is the darker section positoned along the notches. We can conclude that the notches are the same (the pinna ones) but at different elevations they acquire more depth depending on the path emphasized by r (the direct path towards the pinna or the head-diffraction path towards the pinna). Therefore, differentiating the notches from the backgroun like binary images and adding all of them result in the complete location of the pinna notches and head diffraction effect. Afterwards, we reconstruct the depth of the notches looking at the original HRTF.

In table 2 we summarize the thresholding procedure which has the aim of binarizing the emphasized LP residual images up to $r = 0.95$ and adding all the resulting images. In table 3 we show the results of the thresholding process for the subject 10 left ear. The threshold values are given in grayscale levels (0~255). Figure 4 shows the resulting binary images for the input images of the figure 3.

Thus, the binarization process serves the purpose of obtaining not only the exact location of the pinna notches, but also the width of the notch in every frequency response along the elevation. The next step is to pass the binary image to the frequency response domain, converting the binary level to the corresponding level in dB as follows: When the point is white the corresponding magnitude is 0dB, when the point is black the corresponding magnitude is the HRTF original magnitude. Thus we obtain a flat response in 0dB with the correct notches's width and depth.

Now, we can reconstruct the frequency response associated with the PTF from the "pole-part" obtained earlier, and the "zero-part" obtained here. Preliminary MA modeling was performed for the "zero part" but the results are not the optimal yet. Figure 5 shows the resulting image of the thresholding process and the reconstructed pinna frequency response image. As we can see, the arch-shaped response of the HAT is absent. Figure 6 shows some isolated HRTF's, and the corresponding LPC and pinna frequency responses.

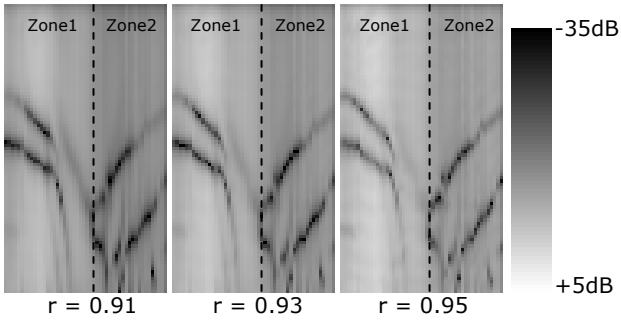

Fig. 3 Emphasized LP residual frequency responses of the left ear HRTF for azimuth 0°, subject 10. Two background – differenciated zones are marked.

TABLE 2
THRESHOLDING PROCEDURE
TO EXTRACT PINNA NOTCHES

Step	Goal	Algorithm basis
1	Locate the "zones"	Inspection
2	Divide the image in "zones"	Simple MATLAB function
3	Increase the constrast	Sharpness function
4	Binarization	Histogram inspection Thresholding function
5	Noise elimination	Conectivity Algorithm
6	"Zones" re-unification	Simple MATLAB function
7	Add all the binary images	Simple MATLAB funcion

TABLE 3
THRESHOLDING PROCESS RESULTS
FOR SUBJECT10, LEFT EAR

r	Sharp	zone1 threshold	zone2 threshold	% Black Pixels
0.90	Yes	130	100	10.56
0.91	Yes	130	112	10.69
0.92	Yes	140	120	11.48
0.93	Yes	150	125	11.79
0.94	Yes	160	130	12.24
0.95	Yes	167	130	10.94

C. *HAT Response*

One of the last objectives of this work was to separate the frequency response associated with the PTF from the one associated with the HAT in the median plane magnitude HRTF. Once we get the PTF image with the procedures described above, it's possible to think that some kind of "subtraction" from the original HRTF image would lead to the HAT image. This was attempted in the IP domain. The results were relatively satisfactory for some subjects, but not so good for others. Anyway, not all the images can be worked out from a "connected" point of view; therefore, segmentation processes may not work. The problem can be appreciated in figure 1. When comparing the left and right ear images, from simple inspection, we can see in the former case that the low frequency HAT response is not so "connected" with the pinna notches in higher frequencies, then it's easier to perform the

"subtraction", while in the later case, at least the first notches are greatly mixed with the arch-shaped response of the HAT. This verifies once again that the responses differ substantially even when they refer to the two ears of the same individual. Nevertheless, the HAT model developed in [26] works very well representing the response at low frequencies. Several works use this model and it's possible to customize it from anthropometric measurements.

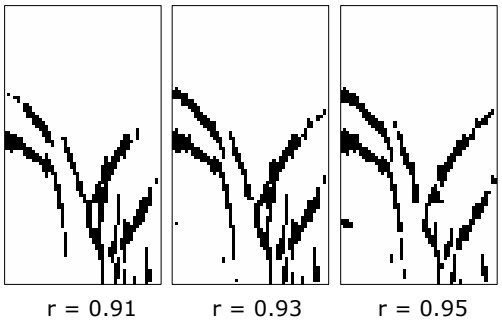

Fig. 4 Binary images corresponding to emphasized LP residual frequency responses of the left ear HRTF, subject 10.

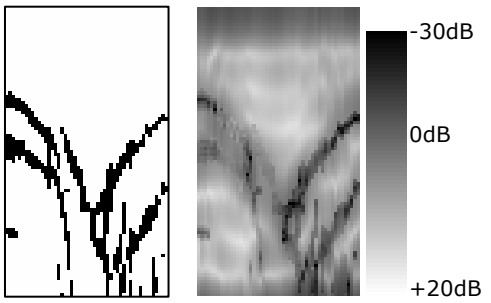

Fig. 5 Resulting image of the thresholding process and resulting PTF image (poles and zeros), left ear, subject 10.

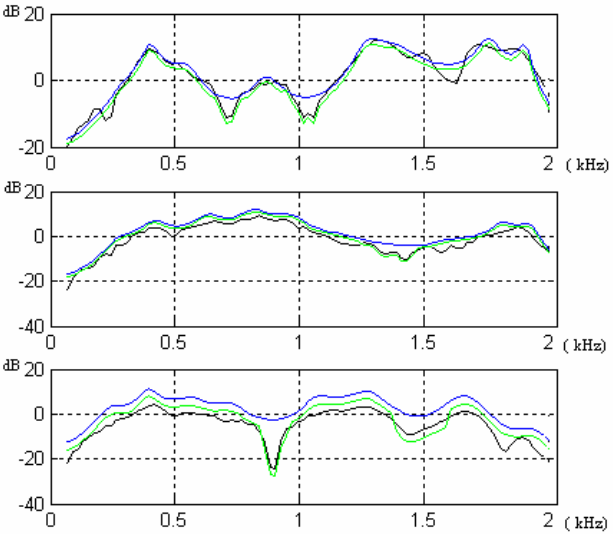

Fig. 6 Black line: Original HRTF, Blue Line: LPC frequency response (resonances), Green Line: Frequency response associated with the PTF (LPC frequency response + Pinna Notches).

V. Results and Future Work

A method has been presented for obtaining the magnitude frequency response associated with the PTF, based upon LP analysis and a thresholding procedure in the IP domain. The automation of the thresholding procedure remains to be done. Auto-regressive modeling for the poles and preliminary moving-average modeling for the zeros was performed. Other ARMA modeling techniques can be used aiming at low order representations. About the IP domain, more advanced techniques could be performed in order to separate the PTF image from the HAT one in the median plane magnitude HRTF image. Finally, the more important response for elevation localization is already obtained.

Acknowledgments

The authors thank Conselho Nacional de Desenvolvimento Cientifico e Tecnologico (CNPQ) for supporting this work, by grant No. 830612/1999-8.

References

[1] A. Valjamae, "A feasibility study regarding implementation of holographic audio rendering techniques over broadcast networks", Master of Science Dissertation, Chalmers University of Technology, 2003

[2] D. De Vries, "Sound reinforcement by wave field synthesis: adaptation of the synthesis operator to the loudspeaker directivity characteristics", Journal of the Audio Engineering Society, Vol. 44, pp. 1120-1131, December 1996.

[3] D. R. Begault, "3-D Sound for Virtual Reality and Multimedia". Boston, MA, Academic Press, 1994.

[4] A. Farina, E. Ugolotti, "Software Implementation Of B-Format Encoding And Decoding", Preprints of the 104rd Audio Engineering Society Convention, Amsterdam, Netherland, May 15 - 20, 1998.

[5] W.G. Gardner, "3D Audio using loudspeakers", Philosophy Doctor Thesis, MIT, 1997.

[6] H. Møller, D. Hammershøi, C. B. Jensen, and M. F. Sørensen, "Transfer characteristics of headphones measured on human ears", Journal of the Audio Engineering Society, Vol. 43, pp. 203–217, April 1995.

[7] K.J.A.Riederer, "Head related transfer functions measurements", Master of Science Dissertation, Helsinki University of Tecnhology, 1998.

[8] K.J.A. Riederer, "Repeatability analysis of HRTF measurements", Preprints of the 105th Audio Engineering Society Convention, San Francisco, CA, USA, October 26-29, 1998.

[9] V. R. Algazi, C. Avendano, D. Thompson, "Dependence of Subject and Measurement Position in Binaural Signal Acquisition," Journal of the Audio Engineering Society, Vol. 47, pp. 937-947, 1999.

[10] G. Theile, "On Localization in a superimposed sound field", Philosophy Doctor Thesis, Technische Universtit¨at Berlin, 1980.

[11] M. A. Blommer, G. H. Wakefield, "Pole-Zero Approximations for HRTF Using a Logarithmic Error Criterion", IEEE Transactions on speech and audio processing, Vol. 5, No. 3, pp. 278-287, 1997

[12] P. R. Runkle, M. A. Blommer, G. H. Wakefield "A comparison of head related transfer function interpolation methods," IEEE Workshop on Applications of Signal Processing to Audio and Acoustics, New Paltz, NY, pp. 88-91, October 15-18, 1995.

[13] Y. Kahana,"Numerical modelling of the headrelated transfer function", Philosophy Doctor Thesis, University of Southampton, 2000.

[14] J. C. Middlebrooks, "Individual differences in external-ear transfer functions reduced by scaling in frequency", Journal of Acoustical Society of America., Vol. 106, No. 3, pp. 1480-1492, 1999.

[15] D. N. Zotkin, R. Duraiswami, L. Davis, A. Mohan, V. Raykar, "Virtual audio system customization using visual matching of ear parameters," 16th International Conference on Pattern Recognition, Vol. 3, pp. 1003-1006, August 11-15, 2002.

[16] K.J.A. Riederer, "Computational Quality Assessment of HRTFs", European Signal Processing Conference, Tampere, Finland, October 5-8, 2000.

[17] V. R. Algazi, R. O. Duda, R. P. Morrison, D. M. Thompson "Structural composition and decomposition of HRTF's", IEEE WASSP Workshop on Applications of Signal Processing to Audio and Acoustics, New Paltz, NY, pp. 103-106, October 21-24 , 2001.

[18] J. Blauert, "Spatial Hearing. The Psychophysics of the Human Sound Localization", MIT Press, Cambridge, USA, 1997.

[19] P. Mackensen, "Auditive Localization. Head movements, an additional cue in Localization", Philosophy Doctor Thesis, Technische Universtit¨at Berlin, 2004.

[20] J. W. Strutt (Lord Rayleigh), "On the acoustic shadow of a sphere," Philosophy Transactions Real Society of London, Vol. 203A, pp. 87–97, 1904.

[21] R. O. Duda, "Modeling head related transfer functions," Procedingsof the 27th Annual Asilomar Conference on Signals, Systems and Computers, Asilomar, CA, November 1993.

[22] V. R. Algazi, C. Avendano R. O. Duda, "Elevation localization and head-related transfer function analysis at low frequencies ", Journal of the Acoustical Society of America., Vol. 109, No. 3, pp. 1110 – 1122, March 2001.

[23] E. A. G. Shaw, R. Teranishi, "Sound Pressure generated in an external-ear replica and real human ears by a nearby sound source", Journal of the Acoustical Society of America, Vol. 44, pp. 240 – 249, 1968.

[24] V. R. Algazi, R. O. Duda , D. M. Thompson, C. Avendano, "THE CIPIC HRTF DATABASE", IEEE WASSP Workshop on Applications of Signal Processing to Audio and Acoustics New Paltz, NY, pp. 99-102, October 21-24 , 2001.

[25] V. C. Raykar, R. Duraiswami, L. Davis, B. Yegnanarayana, "Extracting significant features from the HRTF", Proceedings of the 2003 International Conference on Auditory Display, Boston MA, July 6-9, pp. 115 – 118, 2003.

[26] V. R. Algazi, R. O. Duda, D. M. Thompson, "The use of head-and-torso models for improved spatial sound synthesis", Procedings of the 113th Audio Engineering Society Convention, preprint No. 5712, Los Angeles, CA, 2002.

[27] H. Møller, D. Hammershøi, C. B. Jensen, "Head-related transfer functions of the human subjects", Journal of the Audio Engineering Society, Vol. 43, No. 5, pp. 300 – 321, 1995.

Determining the Number of Gaussians per State in HMM-based Speech Recognition System

Glauco Ferreira Gazel Yared
State University of Campinas - Unicamp
P.O. Box 6101 - CEP 13083-852
Campinas - SP - Brazil
glauco@decom.fee.unicamp.br

Fábio Violaro
State University of Campinas - Unicamp
P.O. Box 6101 - CEP 13083-852
Campinas - SP - Brazil
fabio@decom.fee.unicamp.br

***Abstract*— Nowadays, HMM-based speech recognition systems are used in many real time processing applications, from cell phones to automobile automation. In this context, one important aspect to be considered is the HMM model size, which directly determines the computational load. So, in order to make the system practical, it is interesting to optimize the HMM model size constrained to a minimum acceptable recognition performance. This work presents a new approach for determining the more suitable number of Gaussian components per state, which is based on a discriminative criterion. We also compare our results with an entropy-based Gaussian selection method.**

***Index Terms*— Discriminative Gaussian selection, speech recognition, entropy, model size.**

I. Introduction

In the last years, applications requiring speech recognition techniques have grown considerably, varying from speaker independent to speaker adapted systems in low and high noise environments. Moreover, the speech recognition systems have been designed to achieve both higher processing performance and accuracy. In order to achieve such aims, the model size is an important aspect to be analyzed as it is directly related to the processing load and to the model classification capability. As we use three state continuous density HMM (CDHMM) to model acoustic units (context independent phones) of a small vocabulary continuous speech recognition system [1], [2], the model size is related to the number of Gaussian components used in each mixture. So, this work discusses two approaches used to determine the number of Gaussian components of each state in each phone model: the first one is based on entropy criterion [3] and the second one is based on discriminant measures [4], [5], [6].

II. Background

The statistical modeling problem has some points that do not depend on the specific task for which the model was designed. One classical problem that must be overcome is the over-parameterization [7] which may occur with large models, that is, models with an excessive number of parameters. In general, such models present low training error rate, due to the high flexibility, but the performance, with a test database, is almost always unsatisfactory. On the other hand, models with insufficient number of parameters can not even be trained. At this point there is a trade-off between robustness and trainability, which must be accomplished in order to obtain a high performance model. In the speech recognition context, we use word error rate as a performance measure and the total number of Gaussian components as the model size.

Another important issue to be considered is that the estimation of Gaussian parameters is consistent only when enough data is available, otherwise they are poorly estimated. As we have different number of data samples of each phone in our database, it is reasonable to expected that the number of data samples is also a limiting factor for increasing the number of clusters in a given phone model. In addition, some phones may have short duration, and thus there may be just a few or a lack of data to cluster some states.

There are also some practical arguments to support the idea of determining a varying number of Gaussian components per state. The computational cost is directly related to the number of Gaussian components during training and during recognition. As a consequence, the number of operations and the memory requirements increase with the number of components.

The theoretical and practical reasons presented above are the main concepts which support the idea to obtain acoustic models with varying number of Gaussian components per state.

In the last decade, many approaches have been proposed in order to determine the best model complexity. Briefly, these techniques are based on pruning or growing procedures according to specific criteria. There are methods that start from large-sized well trained HMM models and then reduces the number of parameters following some criteria [8], [9], while other methods start from small-sized models and then grow it up by means of splitting procedure. There also exist hybrid methods, which combine pruning and growing procedures [9].

The merging procedure, in which two Gaussians are replaced by a new one, is used to reduce the model size and to solve the problem of poorly estimated Gaussians due to the insufficiency of data that commonly occurs in context-dependent phone models. On the other hand,

splitting procedure, in which one Gaussian is replace by two new Gaussians, is used to increase the model size and the acoustic precision of the model, when there is enough data available. There also exist tree-based techniques [10], [11], [12], in which Gaussians are selected from lists (one list for each codeword) and then used to calculate the likelihood.

In previous works in this area, there is no quantitative mention about how much data is necessary for a reliable estimation of acoustic models. So, the initial model size used in splitting and merging procedures are usually arbitrary and the algorithms are supposed to discover the more suitable model size from training data, based on some criteria, for instance the state entropy. In addition, when distributions data are overlapped, it seems to be difficult to know a priori if a Gaussian component belongs to one or various distributions in tree-based algorithms.

In the initial experiments, we implemented a splitting algorithm based on state entropy criterion that tries to determine which states may have more Gaussian components in an iterative manner. So, the model grows until the maximum size defined a priori is reached. In the sequence, we developed a new method based on a discriminative criterion, which starts from a large well trained model and then decreases the model size in order to eliminate Gaussians responsibe for wrong classification.

Briefly, section III will describe the speech recognition system implemented and the database used in the experiments. Then in section IV we will present two methods for determining the more suitable model size. Finally, sections V and VI will show the discussion and conclusions of this work respectively.

III. Speech Recognition System and Database

It is important to describe a little bit the database and the speech recognition system used, which were developed in the LPDF laboratory [2].

A. Database

A small vocabulary database (700 different words), with a set of 200 different sentences [13], spoken by 40 speakers (20 male and 20 female) was used in our simulations. In the experiments, 1200 utterances were used for training and 400 for testing.

B. Speech Recognition System

A basic maximum likelihood (ML) training system was implemented in order to obtain continuous HMM models. The output model for each phone is a three state left-right HMM.

As we work with 36 context-independent phones (including silence), we obtain 108 multidimensional Gaussian mixtures, with a variable or fixed number of components in each mixture. In addition, each Gaussian component is represented in a 39-dimensional space, corresponding to the acoustic parameters extracted from the speech signal (12 mel cepstral coefficients, 1 log-energy coefficient, first and second derivatives of mel cepstral and log-energy parameters), and uses diagonal covariance matrix.

The recognizer [2] is based on the One Step algorithm, and uses a word-pair grammatic based on the set of 200 sentences.

IV. Experiments

In this work we present 2 methods for determining the number of Gaussian components to be used in each HMM state in order to obtain the more suitable compromise between model size and performance. Briefly, the first is a growing method while the second is a pruning method. The resulting models will be compared to those with fixed number of Gaussians per state.

Initialy, we determined models with fixed number of Gaussian components per mixture, varying from 5 to 10, resulting in 540 to 1080 Gaussians (considering all phone models). The word recognition rates obtained using these models are shown in Table I.

After that, we will discuss a method which starts with unit size mixtures and then increases the number of Gaussians according to entropy measures. Finally, we propose a new method based on a discriminative criterion which starts with large well trained models and then tries to eliminate guassians associated with wrong classification.

TABLE I
System performance using models with fixed number of Gaussians per state.

Number of Gaussians per State	Total Number of Gaussians	Word Recognition Rate (%)
5	540	91.75
6	648	92.66
7	756	92.47
8	864	91.75
9	972	93.08
10	1080	93.69

A. Entropy-based method

The method we are going to explain now is based on the entropy measure and uses growing procedures to determine the appropriate model size. Basically, all acoustic models starts with unit-sized Gaussian mixture per state, and the entropy information of each Gaussian is calculated by Equation 1

$$H_{si} = \sum_{d=1}^{D} \frac{1}{2} \log_{10}\left(2\pi e \sigma_{sd}^2\right), \tag{1}$$

where "*s*" is the state number, "*i*" is the Gaussian number, "**D**" is the Gaussian dimensionality and "σ^2" is the variance of the *i*-th mixture component in state "*s*".

After that, we can calculate the entropy of each state (H_s) as shown in Equation 2

$$H_s = \sum_{i=1}^{M_S} N_{si} H_{si}, \tag{2}$$

where $\mathbf{M}_S$ is the number of Gaussian components in state "*s*" and N_{si} the number of data samples associated to the *i*-th mixture component in state "*s*".

Then segmental K-means algorithm is applied in order to split all Gaussian components in such a way that, after splitting, the model will have twice the number of components. The entropy for this new configuration ($\hat{H}_s$) is then calculated and now it is possible to obtain the entropy variation (Equation 3)

$$d_s = H_s - \hat{H}_s. \tag{3}$$

The idea is to arrange the states in a decreasing order of the entropy variation, retain the first **N** states with the new configuration and then decrease the others by one Gaussian component (previous configuration). This process is repeated until the desired model size is reached. The algorithm is summarized below.

- Start with one Gaussian per state and calculate H_s.
- Split all clusters so that the model will have twice the number of Gaussians.
- Apply one step of segmental K-means algorithm.
- Calculate $\hat{H}_s$.
- Calculate the entropy variation d_s and arrange it in decreasing order.
- Retain the current size of the first **N** states arranged in decreasing order of d_s while returning the others to the previous configuration.
- Repeat the steps above util the expected model size is reached.

As a inital test, we tried to determine a model with varying number of Gaussians per state using the procedure described above, in order to compare the performance of the resulting model with that of a model containing fixed number of Gaussians per state. So, we tried to find models with 540 Gaussians using **N** equal to 20, 40, 60, 80 and 100. The only model with varying number of Gaussians that outperformed the 5-Gaussians per state model was found for **N** equal to 80, giving a recognition rate of 93.38%. Thus, if we compare these two models containing 540 Gaussians, we increased the model performance in 1.63%. Moreover, if we want to obtain a similar performance with models containing fixed number of Gaussians per state, it would be necessary to choose a model with at least 9 Gaussians per state, what corresponds to an increase of 80% in the model size.

The result confirms the hypothesis that it is possible to find the more appropriate model size for obtaining a better system performance. The model configuration obtained using the entropy-based method is shown in Figure 1.

The results showed that, in general, the third state tends to concentrate the greatest number of Gaussians while the intermediate state tends to concentrate the smallest number of Gaussians, as we can observe in Table II. In addition, the intermediate state of the consonants concentrated less Gaussians than the intermediate state of vowels.

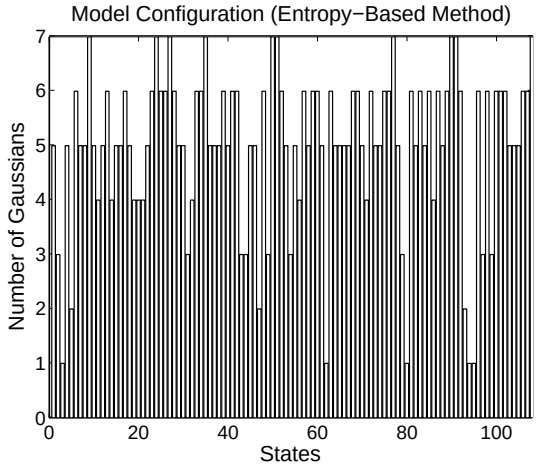

Fig. 1. HMM model configuration. States 1-3 are associated to silence. States 4-42 are associated to vocalic phones. States 43-108 are associated to consonantal phones.

It is important to note that although the mean number of Gaussians per state is around 5, that is, the same as the model with fixed number of Gaussians per state, there may be small variantions in the number of Gaussians per state in some classes of vowels and/or in some classes of consonants that explain the increase in recognition performance.

TABLE II
MEAN NUMBER OF GAUSSIANS IN THE FIRST, SECOND AND THIRD STATE. THE CONFIDENCE LEVEL IS 90%.

Phonemes	1^{st} State	2^{nd} State	3^{rd} State
Silence	5	3	1
Vowels	5.08 $\pm$10%	4.92 $\pm$15%	5.69 $\pm$10%
Consonants	4.77 $\pm$15%	4.64 $\pm$22%	5.45 $\pm$12%

B. Discriminative-based method

We propose in this work a new discriminative method for determining the more suitable number of Gaussians per state, which differs from previous works in this area [4], [5], [6] in the sense that we indicate which Gaussians should be eliminated in order to achieve a better compromise between size and performance. Those works only indicate if there are too many Gaussians or there is a lack of them in the model. No mention about which Gaussians should be eliminated or included was made before.

The main idea is that when we modify the model size including or eliminating Gaussians, the result will affect directly the model capacity of classification. So, first suppose for simplicity that there are two clusters (states) we intend to classify: "**A**" and "**B**". The model associated with cluster "**A**" must give high likelihood for patterns that really belong to this cluster and must give small likelihood for patterns that belong to cluster "**B**". The opposite can be said about the model of cluster "**B**". So, our goal is maximize the difference between these two likelihoods for every HMM model, by eliminating Gaussians from the model.

As we discussed previously, excessive parameters in the model may also be responsible for modeling noise

in data and thus should be avoided. Morevoer, there may be a minimum size below which the model could not even be trained.

So, consider the probability function below, which we call the Winner Gaussian Probability (WGP).It consists on the probability of a Gaussian to give the highest likelihood for a specific state as defined by Equation 4

$$P_{wg}^{(i;j;s)} = \frac{\begin{array}{c}Number\ of\ times\ the\ Gaussian\ \text{“}i\text{”},\\ that\ belongs\ to\ state\ \text{“}j\text{”},\\ presents\ the\ highest\ likelihood\\ for\ frames\ of\ state\ \text{“}s\text{”}\end{array}}{\begin{array}{c}Number\ of\ frames\ analysed\\ that\ are\ associated\ to\ state\ \text{“}s\text{”}\end{array}}. \quad (4)$$

In order to calculate the WGP of each Gaussian, it is required a segmented database, since Equation 4 uses labelled frames in the calculation. Thus we have to associate each frame to a specific state. As our database is not segmented, we used an HMM model, which gives a recognition rate of 94.1%, and the Viterbi algorithm to segment our training database and to label each frame. Although this segmentation is not ideal, it seems to be reasonable to adopt this procedure, and afterwards to perform an accurate database segmentation.

Consider again, for instance, only two clusters (“**A**” and “**B**”) and that models “M_1” and “M_2” are used to represent these clusters respectively. We can determine the WGP of each Gaussian that belongs to model “M_1” for cluster “**A**” and for cluster “**B**”, so that idealy the most important Gaussians of model “M_1” will give a WGP close to 1 for cluster “**A**” and low or null for cluster “**B**”.

In the context of phone classification, we can calculate the WGP of each Gaussian in every state. Then, we can verify the WGP values for frames that are associated with the state in which the Gaussian is included (correct states) and for frames associated with any other state (wrong states). Ideally, we should obtain WGP close to 1 for the correct state and WGP close to zero for wrong states. Unfortunately, in pratice we obtain many times the opposite, that is, low WGP for the correct state and high WGP for the wrong states, what must be avoided in order to prevent from misclassification.

As we discussed previously, the purpose of the discriminative method is to maximize the difference or the relation between the WGP of the correct state and the WGP of the wrong states. This can be done by the maximization of Equation 5 below

$$DC^{(j)} = \frac{\left[\sum_{i=1}^{M_j} P_{wg}^{(i;j;j)}\right]^K}{\sum_{s\neq j}^{N}\sum_{i=1}^{M_j} P_{wg}^{(i;j;s)}}, \quad (5)$$

where **K** is the rigour exponent, M_j is the number of Gaussians in state “j” and N is the total number of states.

The Discriminative Constant (DC) given above may increase or decrease depending on the relevance of the Gaussian eliminated from the model. When the Gaussian eliminated causes the numerator to decrease much more than the denominator, DC will decrease, what suggests that the Gaussian should be kept in the model. In the other hand, when the Gaussian eliminated causes the numerator to decrease less than the denominator, DC will increase, what suggests that the Gaussian eliminated was more important for wrong states than for the correct state, and in this case, the Gaussian must be taken out of the model in order to avoid misclassification errors.

So, Equation 5 describes the behaviour of each state and the rigour exponent plays an important role in the Gaussian selection, since it makes the discriminative criterion DC more restrictive, that is, the greater the exponent the more rigorous the criterion is and therefore less Gaussians are eliminated.

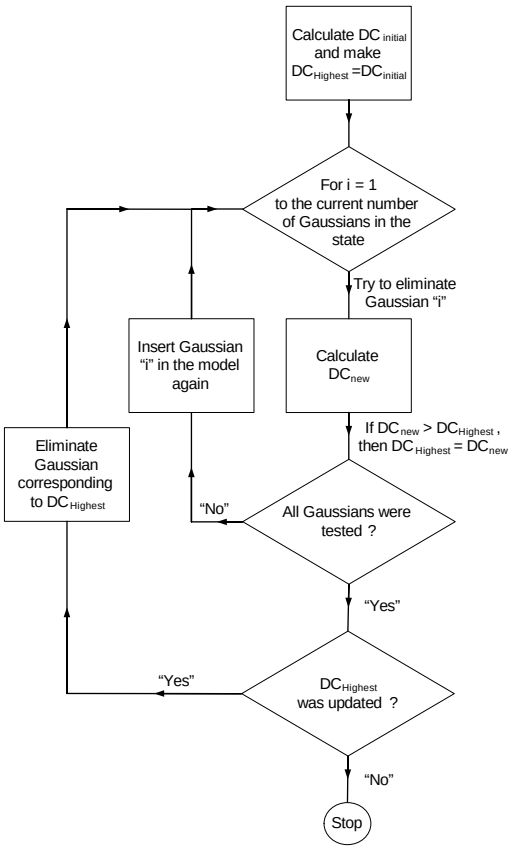

Fig. 2. Discriminative Gaussian selection algorithm.

Once the concepts related to the discriminative criterion are presented and understood, it is possible to explain the algorithm through which the Gaussian selection is performed (Figure 2). Firstly, a well trained large model with fixed number of Gaussians per state is used as a start point. Then, the WGP of each Gaussian with respect to each state (considering all phones) is calculated. So, we choose the first state, calculate the initial DC values, start eliminating Gaussians from the HMM model one by one, and observe what happens with the discriminative constant DC. If only one DC value increases after eliminating a specific Gaussian,

it suggests that we have to keep this component out of the model. If more than one DC value increases, choose the Gaussian associated to the higher increase in DC value. This process is repeated until the DC value does not increase anymore.

The procedure above is applied for each state of every HMM model. Once the discriminative Gaussian selection is finished, we train the resulting model by means of the Baum-Wech algorithm. Our tests showed that depending on the number of Gaussians eliminated, in general it was necessary from 2 to 5 epochs of training to obtain the final model parameters.

We used models containing from 6 to 10 Gaussians per state as the start points for the algorithm proposed, and for each of them, we tried different values of rigour exponent (from 2 to 14). So, we obtained models with different sizes according to the rigour exponent used.

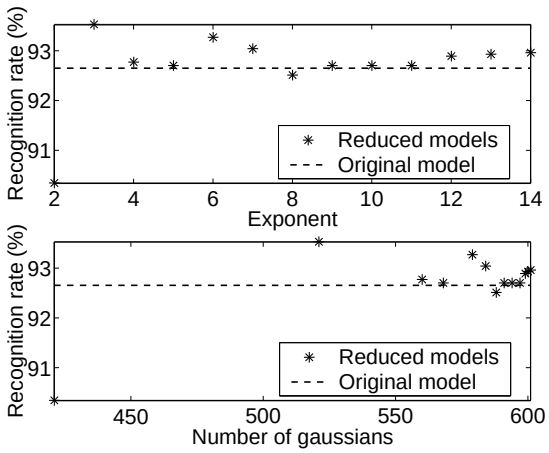

Fig. 3. Performance of models obtained from a 648-Gaussians HMM (6 Gaussians per state).

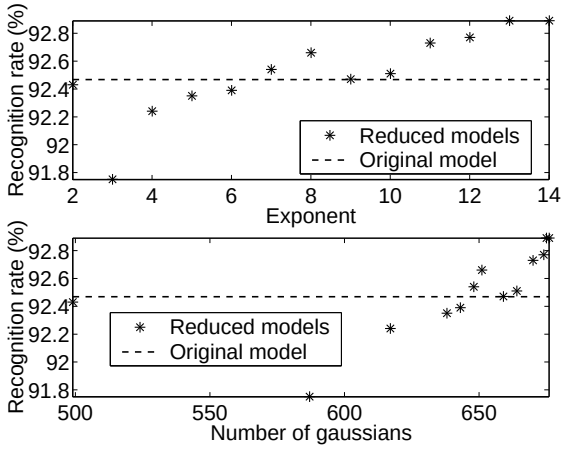

Fig. 4. Performance of models obtained from a 756-Gaussians HMM (7 Gaussians per state).

At this point, we would like to verify how many Gaussians can be eliminated while maintaining the same system performance. Moreover, it would be interesting to verify if it is also possible to increase the system performance even when less Gaussians are eliminated. So, Figures 3 to 7 ilustrates that when the rigour exponent assumes increasing **K** values, less

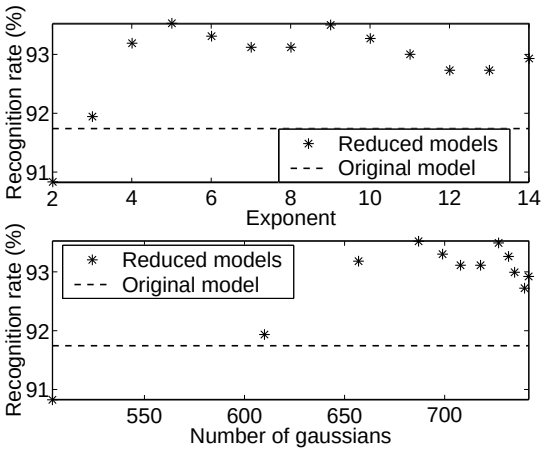

Fig. 5. Performance of models obtained from a 864-Gaussians HMM (8 Gaussians per state).

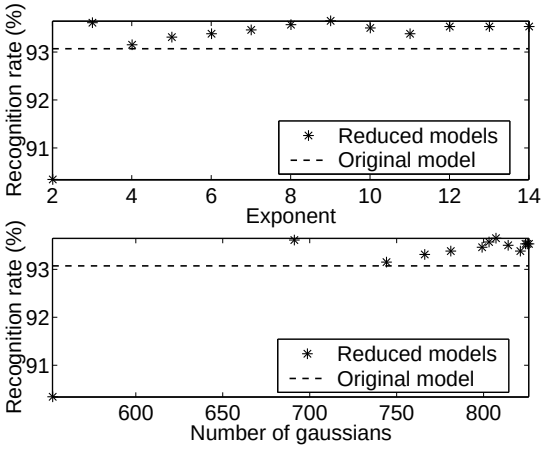

Fig. 6. Performance of models obtained from a 972-Gaussians HMM (9 Gaussians per state).

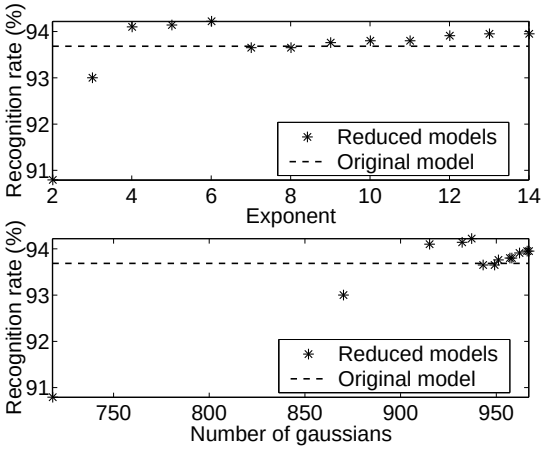

Fig. 7. Performance of models obtained from a 1080-Gaussians HMM (10 Gaussians per state).

Gaussians are eliminated and the system tends to have better performance.

We can observe from the results above that there is more than one model configuration that gives the same or better system performance compared to the original model with fixed number of Gaussians per state. So, it is possible to choose the configuration that best fits our low complexity objective.

We are going to find first what is the minimum model size that gives approximately the same performance as the original model, in order to obtain the maximum economy.

TABLE III
ECONOMY OF GAUSSIANS USING THE DISCRIMINATIVE ALGORITHM. THE LAST COLLUMN SHOWS THE PERFORMANCE DIFFERENCE BETWEEN THE ORIGINAL MODEL AND THE REDUCED MODEL IN TERMS OF WORD RECOGNITION RATE.

Initial model size	Reduced model size	Economy of Gaussians (%)	Recog. rate (%)	Difference in performance (%)
648	521	19.6	93.53	+0.87
756	499	34.0	92.43	-0.04
864	610	29.4	91.94	+0.19
972	691	28.9	93.61	+0.53
1080	915	15.3	94.1	+0.41

Table III shows that we have an economy of 15% to 34% in the number of Gaussian. We would like to highlight the model with 521 Gaussians, which was obtained from an inital model containing 6 Gaussians per state (first line of Table III), since its recognition rate is close to that given by the model with 1080 Gaussians (10 per state). Moreover, if we compare this model with that containing 540 Gaussians (5 per state), which has approximately the same size, we observe an increase of 1.78% in the recognition rate. This result suggests that for a specific model size, obtaining models by means of a Gaussian selection method is better than using models with a fixed number of Gaussians per state.

At this point, it is important to compare the model obtained from the discriminative Gaussian selection method (521 Gaussians) with that obtained from the entropy-based method (540 Gaussians), since they have almost the same size. The first gave a recognition rate of 93.53% while the second gave a recognition rate of 93.38%. The first method was a little better. But if we had tried to find a model with exactly 521 Gaussians using the entropy-based method, the result could be even better. The only problem is that it is not possible to know a priori what should be the more suitable final model size, and this information is required to start the entropy-based method.

Now we are going to find the models that give the highest system performances with no concern about the economy of Gaussians. Table IV shows the best performances obtained.

As we can observe from the the results above, it is always possible to find a reduced model that outperforms the original model with fixed number of Gaussians per state. Moreover, it is important to remark that if we compare models containing fixed number of Gaussians per state and models containing varying number of Gaussians per state, but with approximately the same size, the gain in performance is even higher (around 1%).

We have noted that for **K** values close to 14, the number of Gaussians eliminated is almost the same and so is the system performance. Although the rigour

TABLE IV
INCREASE IN SYSTEM PERFORMANCE DUE TO DISCRIMINATIVE GAUSSIAN SELECTION ALGORITHM. THE LAST COLLUMN SHOWS THE PERFORMANCE DIFFERENCE BETWEEN THE ORIGINAL MODEL AND THE REDUCED MODEL IN TERMS OF WORD RECOGNITION RATE.

Initial model size	Reduced model size	Economy of Gaussians (%)	Recog. rate (%)	Difference in performance (%)
648	521	19.6	93.53	+0.87
756	675	10.7	92.89	+0.42
864	687	20.5	93.53	+1.78
972	807	17.0	93.65	+0.57
1080	937	13.2	94.22	+0.53

increases with **K** values, the number of Gaussians given by the discriminative criterion seems to saturate, what suggests the existence of an excessive number of Gaussians in the model.

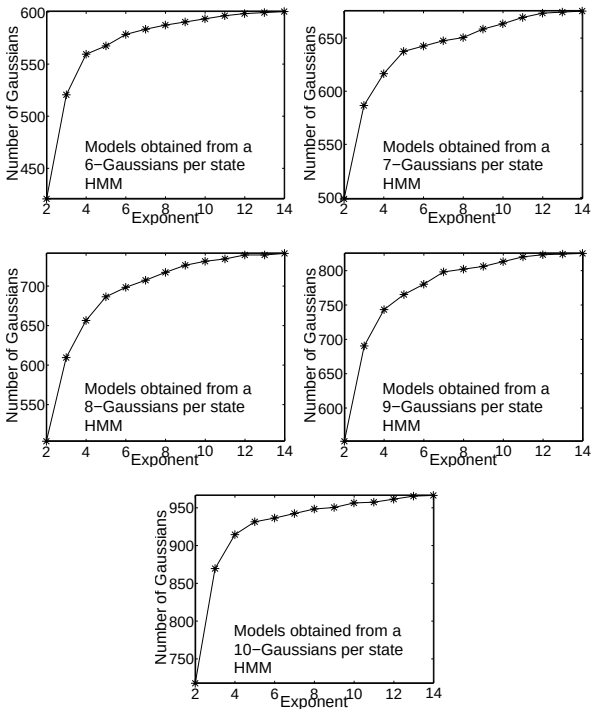

Fig. 8. Number of remaining Gaussians in the model as the rigour exponent increases.

In addition, it seems that the relation between the number of Gaussians in the model and the rigour exponent is exponential, as displayed in Figure 8.

Now we are going to analyse the influence of different initial models on the final configuration. We selected two models for the analysis: the first containing 521 Gaussians, obtained from a 6-Gaussians per state model, and the second containing 937 Gaussians, obtained from a 10-Gaussians per state model. Figures 9 and 10 show the configurations corresponding to the models described above.

It is important to observe the Gaussians' distributions (mean number of Gaussians per state) among vowels and consonants and to verify if these configurations are simililar to that obtained from the entropy-based method. The results are displayed in Tables V

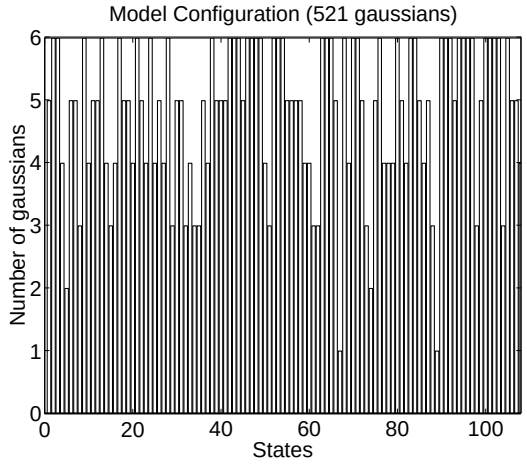

Fig. 9. Model configuration, with varying number of Gaussians per state, obtained from the discriminative method (521 Gaussians). States 1-3 correspond to the silence phone. States 4-42 correspond to vocalic phones. States 43-108 correspond to consonantal phones.

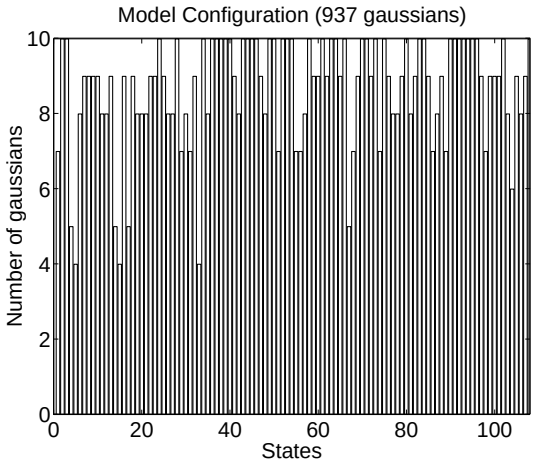

Fig. 10. Model configuration, with varying number of Gaussians per state, obtained from the discriminative method (937 Gaussians). States 1-3 correspond to the silence phone. States 4-42 correspond to vocalic phones. States 43-108 correspond to consonantal phones.

and VI.

TABLE V

MEAN NUMBER OF GAUSSIANS IN THE FIRST, SECOND AND THIRD STATE FOR A 521 GAUSSIANS MODEL (OBTAINED FROM A 6-GAUSSIANS PER STATE MODEL). THE CONFIDENCE LEVEL IS 90%.

Phonemes	1^{st} State	2^{nd} State	3^{rd} State
Silence	5	6	6
Vowels	4.62 $\pm$10%	4.08 $\pm$17%	5 $\pm$10%
Consonants	5 $\pm$15%	4.73 $\pm$18%	5.09 $\pm$10%

TABLE VI

MEAN NUMBER OF GAUSSIANS IN THE FIRST, SECOND AND THIRD STATE FOR A 937 GAUSSIANS MODEL (OBTAINED FROM A 10-GAUSSIANS PER STATE MODEL). THE CONFIDENCE LEVEL IS 90%.

Phonemes	1^{st} State	2^{nd} State	3^{rd} State
Silence	7	10	10
Vowels	8.77 $\pm$10%	7.62 $\pm$13%	8 $\pm$13%
Consonants	9.14 $\pm$10%	8.64 $\pm$10%	9.18 $\pm$10%

As we can note, the mean number of Gaussians per state in the consonant models is higher than in the vowel models, when we compare the same state. In fact we noted the same tendency in the models obtained from the entropy-based method and in the models obtained from the discriminative method, in terms of Gaussians distribution among vowels and consonants. Moreover, there is also a tendency of the third state to concentrate the majority of Gaussians while the intermediate concentrates less than the others. The only exception was in the model with 937 Gaussians, in which we observe more Gaussian concentration in the first state instead of the third.

The silence model configurations are similar when we compare the two models obtained from the second method, but is very different when models from the first and the second method are compared.

V. DISCUSSION

In the entropy-based method, the final model size (540 Gaussians) and the incremental number of Guassians (**N**) per iteration were defined a priori. The resulting configuration outperformed the model with 5-Gaussians per state, but there was no information if the choice for the final model size was the more appropriate. The only reason for choosing such size was to compare with the system containing fixed number of 5 Gaussian components per state.

On the other hand, the discriminative method does not defines a final model size, but it starts from a well trained model with fixed number of Gaussians per state. The results showed that it is always possible to reduce model size while at least maintaining the same original system performance. In general, the maximum size reduction obtained was of 37.48$\pm$10% and the minimum reduction was of 11.49$\pm$10% (confidence level of 95%).

Thus, the first method should be used when it is really necessary to fix a final model size, despite of the more suitable compromise between size and system performance. The second method may find the more appropriate relation between size and performance, but do not allow to fix a priori the exact final model size. In addition, both methods indicates that consonants concentrate the greatest mean number of Gaussians per state, when compared to vowels. This fact may be due to the higher variability of consonants phonemes.

VI. CONCLUSION

In this work we implemented two methods for determining the more suitable HMM model size for a small vocabulary continuous speech recognition system. The first, based on entropy measures, seems to be more interesting when it is necessary to fix the final model size. The second uses a discriminative approach and seems to give the more appropriate compromise between size and performance, since we do not fix a priori the final model size. Moreover, both methods present an increase in system performance (around 1%) when we compare the fixed number of Gaussian per state model and the varying number of Gaussian

per state model for the same total number of Gaussian components. The methods are supposed to give HMMs that have a better compromise between reliability and robustness for modeling speech data, despite of the amount of data available.

The methods presented use growing and pruning procedures respectively. As a next step, we intend to implemented the well known tied-state methods [14], which also reduces the model size, in order to compare with the discriminative method proposed here.

In addition, we also would like to perform a more accurate study of the Gaussian distribution among vowels and consonants in order to understand where a more detailed acoustic resolution is really necessary.

VII. Acknowledgement

We would like to thank the CNPq (Conselho Nacional de Desenvolvimento Científico e Tecnológico) for the financial support to this work. We also thank Edmilson Morais and Lívio Carvalho for the important discussions during this work.

References

[1] L. Rabiner and B.-H. Juang, *Fundamentals of Speech Recognition*. Prentice Hall, 1993.

[2] C. A. Ynoguti, *Continuous Speech Recognition Using Hidden Markov Models (in portuguese)*. PhD thesis, State University of Campinas, 1999.

[3] Y. J. Chung and C. K. Un, "Use of different number of mixtures in continuous density hidden markov models," *Electronics Letters*, vol. 29, no. 9, pp. 824–825, 1993.

[4] L. R. Bahl and M. Padmanabhan, "A discriminant measure for model complexity adaptation," in *IEEE International Conference on Acoustic, Speech and Signal Processing*, 1998.

[5] Y. Gao, E.-E. Jan, M. Padmanabhan, and M. Picheny, "Hmm training based on quality measurement," in *IEEE International Conference on Acoustic, Speech and Signal Processing*, 1999.

[6] M. Padmanabhan and L. R. Bahl, "Model complexity adaptation using a discriminant measure," *IEEE Transactions on Speech and Audio Processing*, vol. 8, no. 2, pp. 205–208, 2000.

[7] L. A. Aguirre, *An Introduction to Systems Identification - Linear and Non-linear Techniques Applied to Real Systems (in portuguese)*. Editora UFMG, 2000.

[8] M.-Y. Hwang and X. Huang, "Dinamically configurable acoustic models for speech recognition," in *IEEE International Conference on Acoustic, Speech and Signal Processing*, 1998.

[9] J. Simonin, S. Bodin, D. Jouvet, and K. Bartkova, "Parameter tying for flexible speech recognition," in *4th International Conference on Spoken Language*, 1996.

[10] M. J. F. Gales, K. M. Knill, and S. J. Young, "State-based gaussian selection in large vocabulary continuous speech recognition using hmms," *IEEE Transactions on Speech and Audio Processing*, vol. 7, no. 2, pp. 152–161, 1999.

[11] J. Duchateau, KrisDemuynck, and P. Wambacq, "Discriminative resolution enhancement in acoustic modelling," in *IEEE International Conference on Acoustic, Speech and Signal Processing*, 2000.

[12] K. Shinoda and K. ichi Iso, "Efficient reduction of gaussian components using mdl criterion for hmm-based speech recognition," in *IEEE International Conference on Acoustic, Speech and Signal Processing*, 2002.

[13] A. Alcaim, J. A. Solewicz, and J. A. Moraes, "Frequência de ocorrência dos fones e lista de frases foneticamente balanceadas no português falado no rio de janeiro.," *Revista da Sociedade Brasileira de Telecomunicações.*, vol. 7, no. 1, pp. 23–41, 1992.

[14] L. R. Bahl, F. Jelinek, and R. L. Mercer, "A maximum likelyhood approach to continuous speech recognition," *IEEE Transactions on Pattern Anal. Machine Intell.*, vol. 5, pp. 179–190, 1983.

An Improvement for STC Vocoder Amplitudes Estimation

Fabio A. R. Nascimento
National Institute of Telecommunications - Inatel
P.O. Box 05 - 37540-000
Santa Rita do Sapucaí, MG - Brazil
fabio.nascimento@inatel.br

Francisco J. Fraga da Silva
National Institute of Telecommunications - Inatel
P.O. Box 05 - 37540-000
Santa Rita do Sapucaí, MG – Brazil
fraga@inatel.br

Abstract **- An improvement for a Sinusoidal Transform Vocoder operating at 2.4 or 4.8 kbps is presented. A more efficient procedure for estimation of the set of coefficients that represents the spectral envelope is proposed. This procedure exploits the subjective loudness psychoacoustic characteristic of the human hearing system and causes the envelope to be smoother, allowing for a reduction in the number of necessary coefficients and keeping the speech quality. Experimental results indicate that the use of this method enhances the performance of a Sinusoidal Transform Vocoder operating at 2.4 or 4.8 kbps, improving its perceptual quality.**

Index Terms **– Sinusoidal Coding, STC vocoder, Sine-wave parameters, Objective quality, Subjective loudness.**

I. INTRODUCTION

In the sinusoidal representation of the speech production model [1], the focus is to model the excitation of the vocal tract filter as a combination of sinusoidal components with their particular amplitudes, frequencies and phases. The motivation for this sine-wave representation is that voiced excitation, when perfectly periodic, can be represented by a Fourier series decomposition, in which each harmonic component corresponds to a single sine-wave. More generally, the sine-wave in the model won't be harmonic when periodicity is not exact and when the excitation is unvoiced. Then, by defining a criterion that is able to correctly extract the information of sine-wave amplitudes, frequencies and phases, we would be, at the same time, defining a new set of parameters, which would be ready for a specific coding.

It is demonstrated in the literature how a simplified set of parameters is obtained through the sinusoidal representation and how they can be efficiently coded. This kind of speech coding is known as Sinusoidal Transform Coding. The basis of this work was built using the concepts of Sinusoidal Coding, described by MacAulay and Quatieri, involving the basic sinusoidal analysis/synthesis system [2]: a model for the sine-wave frequencies, the minimum phase harmonic sine-wave speech model and the sine-wave amplitude coding, using an all-pole model. Although many efficient analysis-synthesis methods have been developed there is still a demand for improvement in the performance of the envelope parameters estimation.

This work assumes that the sine-wave frequencies and phases coding processes are already defined and that the techniques used for them were the harmonic model for the sine-wave frequencies and a minimum phase model for the sine-wave phases. This means that not only one specific frequency is coded for each sinusoidal component, but, instead, it is used a harmonic set of them, constructed through the fundamental frequency of the speech, in this specific case treated simply as Pitch. The sine-wave original phases are not coded as well, and a proper model for them is developed at the decoder. In this case the parameter of the model for the sine-wave frequencies is only the pitch and a concept used for the harmonic reconstruction, known as Voicing Probability. There are no parameters to be transmitted for the minimum phase harmonic sine-wave speech model.

The contribution of this work is just on the sine-wave amplitudes coding. One may know that the amplitudes are not coded one by one as well. Instead, a set of coefficients is coded, which is able to represent the spectral envelope, which is obtained by a spline interpolation of the sine-wave amplitudes. This is possible, considering proper sine-wave frequency estimation, because the envelope sample at certain sine-wave frequency has the same value of the referred sine-wave amplitude. The contribution itself occurs with the exploration of a psychoacoustic characteristic of the human hearing system, known as subjective loudness.

In the next section, we present the benefits of considering the subjective loudness concept, so that the envelope estimation performance is improved, with no loss in the perceptual quality.

Finally, we present our results. They indicate that the use of this method in combination with the basic sinusoidal analysis/synthesis system enhances the performance of a Sinusoidal Transform Vocoder operating at 2.4 and 4.8 kbps and classify it as comparable to the correspondent US Federal Standards MELP (2.4 kbps) and CELP (4.8 kbps).

II. SPECTRAL ENVELOPE ESTIMATION

The basic sinusoidal vocoder uses an all-pole model such that the magnitude of its transfer function is a best fit to the spline approximation of the sine-wave envelope. The computation of the parameters of the all-pole model demands the calculation of the autocorrelation coefficients:

$$R_k = \frac{1}{2\pi}\int_{-\pi}^{\pi} \left|H_s(\omega)\right|^2 e^{jk\,w} d\omega \qquad (5)$$

where $H_s(\omega)$ represents the sine-wave amplitudes envelope. However, the experimental results of this work indicate that the quality of the synthetic speech was good provided the all-pole model order is above 22. This means that very few bits would be available to the quantization of each coefficient on 2.4 or even 4.8 kbps bit rates. This implies that some additional properties of the human hearing system must be exploited. McAulay and Quatieri [2] suggest that the linear frequency scale should be warped, following a conversion function which considers the non linearity of the human hearing system for the perception of different frequencies. In other words, it demands a conversion of the linear frequency scale ω to a perceptual frequency scale b. The known Bark scale can efficiently represent this perceptual scale. This procedure exploits the assumption that the shape of the auditory filters is approximately constant over the Bark scale [9]. This way, instead of $H_s(\omega)$, we would have $H_s(b)$. Our proposal is that the sine wave amplitude envelope, represented by the system function $H_s(\omega)$, besides warped through the bark scale, $H_s(b)$, should be cubic-root compressed

$$\Phi_s(b) = \sqrt[3]{H_s(b)} \qquad (6)$$

It is an approximation to the power law of hearing [10] and simulates the nonlinear relation between the intensity of sound and its perceived loudness [11] [12]. The human hear emphasizes low amplitude sounds and becomes less sensitive to details as the amplitudes increase. The cubic root compression simulates the human hearing behavior and, as consequence, produces an envelope of the speech signal which is smoother than the original one. This yields in an all-pole model of lower order, which demands fewer bits in the quantization process. Figure 1 shows the smoothness caused to a spectral envelope when cubic-root compression is applied.

Once the sine-wave amplitudes envelope $H_s(\omega)$ is properly estimated in the warped scale, the inverse DFT (Discrete Fourier Transform) is applied to yield in the autocorrelation function, dual to $\Phi_s(b)$, as in (5). After that, as we may know, the first $M+1$ autocorrelation values are used to solve the Yule-Walker equations [5] leading to the autoregressive coefficients of the M^{th}-order all-pole model, as desired.

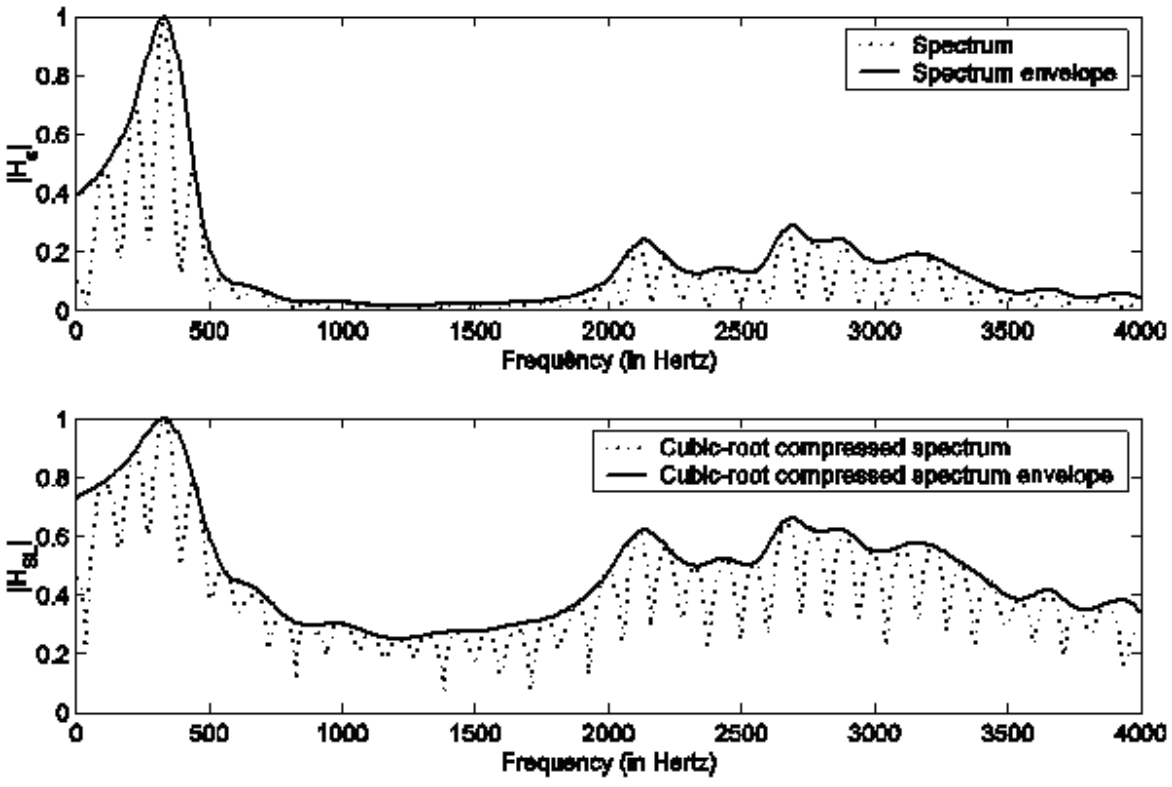

Fig. 1 – Spectral smoothness caused by the use of the subjective loudness concept

The autoregressive coefficients could be further transformed into some other set of parameters of interest, such as Line Spectral Frequencies (LSF). The transformation involved, whatever is chosen, has the objective of facilitate the quantization process. This topic is not in the scope of this work.

III. EXPERIMENTAL RESULTS

The Matlab® program was used to implement several modifications of the STC Vocoder, involving different increments between consecutive frames (from now on, referred just as "increment"), all-pole model orders and the utilization of the subjective loudness concept or not. The increments used were 10ms and 15ms, while the all-pole model order used were 14 and 18. In all the possible combinations above 168 utterances of the TIMIT Acoustic-Phonetic Speech Database were randomly chosen as the speech input.

The developed vocoders are classified as low bit-rate vocoders and can operate at 2400 bps or 4800 bps, depending on the quantization scheme that is used. It is necessary to mention that the quantization of the all-pole coefficients was not performed in this work. For this reason, the comparative data showed below requires the consideration that a small degradation of the speech quality at 2400 bps and an almost insignificant one at 4800 b/s are expected. This way, considering that quantization was applied only to the parameters Gain (4 bits), Pitch (8 bits) and Voicing Probability (2 bits), the entire system was evaluated in comparison to the MELP (Mixed Excitation Linear Prediction) algorithm, which is currently the US Federal Standard vocoder at 2400 bps. It was also evaluated in comparison to the US Federal Standard vocoder at 4800 bps, CELP (Coded Excited Linear Prediction). The PESQ (Perceptual Evaluation of Speech Quality) algorithm, ITU P.862 recommendation, was the tool used for measuring the performance of the vocoder.

Table 1 shows the average objective results obtained for the various modifications (in terms of increment, all-pole model order and the use or not of the subjective loudness concept) of the STC vocoder mentioned above.

TABLE 1 - AVERAGE PESQ FOR DIFFERENT MODIFICATIONS OF THE STC VOCODER

Model order	Increment (ms)	Identifier	PESQ S.L.	PESQ Std.
14	10	p14q10	3.172	3.102
14	15	p14q15	3.094	3.026
18	10	p18q10	3.220	3.114
18	15	p18q15	3.132	3.103

PESQ S.L. means the PESQ result for the STC vocoder using the Subjective Loudness technique. PESQ Std. means the PESQ result for the Standard STC vocoder. The identifier column is used to refer to the correspondent model order and increment in Figure 2. Figure 2 shows the graphical results of Table 1.

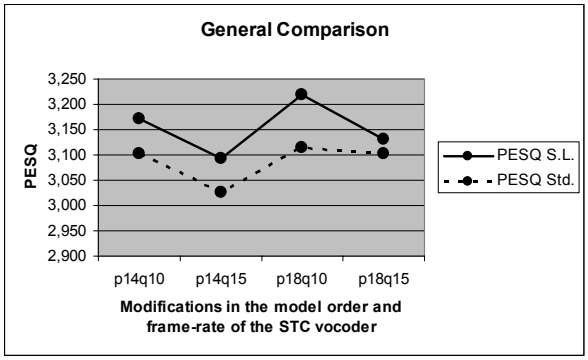

Fig. 1 – Graphical comparison between different modifications of the STC vocoder

For comparison purposes we measured the PESQ objective quality results for the US Federal Standards CELP and MELP, considering the same 168 TIMIT utterances. The PESQ results for these two algorithms along with the result of a 14th order all-pole model and 10 ms increment STC vocoder, developed with the subjective loudness concept, are showed in Table 2.

TABLE 2 – COMPARISON OF THE PESQ RESULTS FOR MELP CELP AND STC VOCODERS

-	MELP	CELP	STC
PESQ	2.988	3.071	3.172

IV. CONCLUSIONS

Firstly, we must compare the STC vocoder to itself, taking in consideration the combination of the factors increment, all-pole model order and the utilization or not of the Subjective Loudness technique. Based on Table 1 data, we can calculate that the modification in the increment factor from 15ms to 10ms caused the PESQ to increase 0.063 points, in average. The modification in the filter order from 14 to 18 caused the PESQ to increase 0.044 points, in average. In average, the most significant modification to the STC vocoder was exactly the utilization of the Subjective Loudness concept, which raised the PESQ of 0.068 points. This is a very important result, since, in opposition to the modification of the increment and the filter order, the utilization of the Subjective Loudness technique doesn't require the bit-rate to be increased. The decision about which increment and filter order to

use is related to the bit-rate that will be chosen for the STC vocoder (in our case 2400 or 4800 bps).

Secondly, we must compare the STC vocoder to its competitors MELP and CELP, operating at 2400 and 4800 bps, respectively.

A STC vocoder at 2400 bps seems to be reachable only if the increment factor is set to 15ms and the filter order is set to 14, because, considering the quantization scheme used for Pitch (8 bits), Voicing probability (2 bits) and Gain (4 bits), it would remain only 22 bits for the quantization of the 14 or more filter coefficients. Notice that for 2400 bps and an increment of 15ms there would be an availability of only 36 bits per frame. In this case, comparing the STC vocoder at 2400 bps to the MELP vocoder we notice that it is justifiable only if the quantization scheme for the filter coefficients decreases its PESQ of 0.106 points (which is the difference between the STC vocoder p14q15 and the MELP vocoder). This might be a big challenge, but not unreachable.

The development of a STC vocoder operating at 4800 bps is an easier task, because it allows for an exploration of an increment of 10ms and a filter order of 18. In this case we would have a frame-rate equal to 100 and the amount of available bits per frame would be 48. Separating, as mentioned, 8 bits for the Pitch, 4 bits for the Gain and 2 bits for the Voice Probability parameters it would remain 34 bits for the quantization of 18 all-pole parameters. In this case the performance comparison would be between the STC and the CELP vocoders. This way, use of the STC vocoder operating at 4800 bps is justifiable only is the quantization scheme for the filter coefficients decreases its PESQ of 0.149 points (which is the difference between the STC vocoder p18q10 and the CELP vocoder). As we can notice, considering the availability of more bits in the quantization of each parameter of the all-pole model, this seems to be an easier task than in the case of the STC vocoder at 2400 bps.

Although the algorithm is not completely implemented, since the quantization of the filter parameters are not ready, by applying the basic concepts described by McAulay and Quatieri [2] and the technique described in this work it was obtained results which are superior to the ones obtained for the US Federal Standards MELP and CELP. In addition, the estimation of the spectral envelope using the Subjective Loudness concept increased the objective quality of the STC vocoder, as we can see in Table 1.

V. REFERENCES

[1] R. J. McAulay and T. F. Quatieri, *Speech Analysis/Synthesis Based on a Sinusoidal Representation*, in *IEEE Trans. Acoust., Speech and Signal Proc.,* vol. 34, (4), pp. 744-754, August 1986.

[2] R. J. McAulay and T. F. Quatieri, *Sinusoidal Coding*, in *Speech Coding and Synthesis* (W B Kleijn and K K Paliwal, eds.) ch. 4, Elsevier Science B V, pp 121 – 173, 1995.

[3] R. J. McAulay and T. F. Quatieri, *Pitch Estimation and Voicing Detection Based on a Sinusoidal Model*, in Proc. IEEE Int. Conf. Acoust., Speech and Signal Proc., Albuquerque, NM, pp. 249-252, April 1990.

[4] L. Rabiner and R. Schafer, *Digital Processing of Speech*, Prentice Hall, Inc., Englewood Cliffs, NJ, 1978.

[5] J. R. Deller, Jr., J. H. L. Hansen, J. G. Proakis, *Discrete-Time Processing of Speech Signals*, Wiley-IEEE Press, September 1999.

[6] W. B. Kleijn, P. Kroon, L. Celario and D. Sereno, *A 5.85 kb/s CELP Algorithm for Cellular Applications*, in *Proc. IEEE Int. Conf. Acoust. Speech and Signal Proc.,* Minneapolis, MN, pp II596-599, 1993.

[7] W. W. Chang and D. Y. Wang, *Quality enhancement of sinusoidal transform vocoders*, *IEE Proc.-Vis. Image Signal Process.,* vol. 145, (6), pp 379-383, December 1998.

[8] R. J. McAulay and T. F. Quatieri, "*Phase Modelling and its application to Sinusoidal Transform Coding*", in *Proc. IEEE Int. Conf. Acoust., Speech and Signal Proc.,* Tokyo, Japan, pp. 207-209, 1986.

[9] J. W. Picone, *Signal Modeling Techniques in Speech Recognition*, in Proc. IEEE, vol. 8 (9), pp. 1215-1247, Sept. 1993.

[10] S. S. Stevens, *On the psychophysical law*. Psychol. Rev. 64, pp. 153-181, 1957.

[11] S. Wang, A. Sekey and A. Gersho, *An objective measure for predicting subjective quality of speech coders*, *IEEE J. Select. Areas Commun*., vol. 10 (5), pp 819-829, June 1992.

[12] H. Hermansky, *Perceptual linear predictive (PLP) analysis of speech*, *J. Accoust. Soc. Am.*, vol. 87 (4), pp 1738-1752, April 1990.

[13] K. K. Paliwal and B. S. Atal, *Efficient Vector Quantization of LPC Parameters at 24 bits/frame*, *IEEE Transactions on Speech and Audio Processing,* Vol. 1 (1), pp 3-14, January 1993.

[14] B. H. Juang, D. Y. Gray and A. H. Gray, Jr., "*Distortion Performance of Vector Quantization for LPC Voice Coding*", in *IEEE Trans. Acoust., Speech and Signal Proc.,* vol. ASSP-30, pp 294-303, April 1982.

[15] F. Itakura, *Line spectrum representation of linear predictive coefficients of speech signals*, *J. Accoust. Soc. Am.*, vol. 57, p S35, April 1975.

[16] F. K. Soong and B. H. Juang, *Line spectrum pair (LSP) and speech data compression*, in *Proc. IEEE Int. Conf. Acoust., Speech and Signal Proc.,* San Diego, CA, pp 1.10.1-1.10.4, March 1984.

LPC Parameter Interpolation to Enhance Speech Quality in VoIP Netwoks Using the GSM-AMR Speech Codec

Paulo Henrique Marques Santos
State University of Campinas - Unicamp
P.O. Box 6101
Campinas - SP - Brazil
psantos@cpqd.com.br

Luís Geraldo Pedroso Meloni
State University of Campinas - Unicamp
P.O. Box 6101
Campinas - SP - Brazil
meloni@decom.fee.unicamp.br

***Abstract*—One feature of current IP networks is that packet transmission without loss cannot be guaranteed. Among parameters transmitted by voice coders, LPC are considered to be the highest weight to speech quality. Therefore, an interpolation scheme has been proposed to estimate these parameters in occurrence of frame loss. The scheme uses correctly received parameters extracted from frames adjacent to the lost one(s). Simulations were performed using the GSM-AMR codec at a 7.95 kbps rate. The proposed interpolation scheme achieves average spectral distortions 0.09 – 0.31 dB smaller than that caused by the existing GSM-AMR scheme.**

***Index Terms*—Parameter Interpolation, Speech Coding, Voice over IP.**

I. INTRODUCTION

With microelectronic development, faster circuits, and increase in machine processing capacity, it is becoming common to use the Internet structure to transmit continuous signals such as voice and video. However, one using IP networks to send out this kind of signal has to cope with serious problems related to packet loss.

When using codecs in speech communication, only a few parameters have to be transmitted instead of the whole signal. An important feature of parameters such as LPC and pitch period is a good smoothness observed between frames [1]. As LPCs play an important role in quality of coded speech, a recovery scheme based on LPC interpolation was proposed to improve quality in packet loss presence.

This work shows the frame recovery system used by GSM-AMR ACELP coder [2] at a 7.95 kbps rate. It will also be shown the interpolation scheme proposed to recover lost frames. Comparative results will be analyzed and discussed based on average spectral distortion values computed by the use of the synthesized speech signal.

II. GSM-AMR OVERVIEW

The GSM-AMR codec consists of eight source codecs with bit-rates of 12.2, 10.2, 7.95, 7.40, 6.70, 5.90, 5.15 and 4.75 kbit/s. The codec is based on the ACELP (*Algebraic Code-Excited Linear Predictive*) coding model. Fig.1 shows ACELP speech synthesis model.

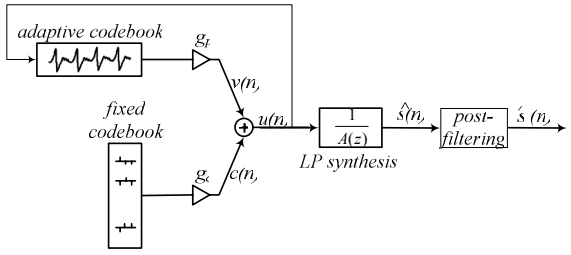

Fig. 1. Simplified block diagram of the ACELP synthesis model

A 10^{th} order linear prediction (LP), or short-term, synthesis filter is used which is given by

$$H(z) = \frac{1}{A(z)} = \frac{1}{1 + \sum_{i=1}^{m} a_i z^{-i}}, \qquad (1)$$

where a_i, $i = 1, \ldots, m$, are the linear prediction (LP) parameters, and $m = 10$ is the predictor order. The long-term, or pitch, synthesis filter is given by

$$\frac{1}{B(z)} = \frac{1}{1 - g_p z^{-T}} \qquad (2)$$

where T is the pitch delay and g_p is the pitch gain.

At ACELP model, the excitation signal at the input of the short-term LP synthesis filter is constructed by adding two excitation vectors from adaptive and fixed (innovative) codebooks. The speech is synthesized by feeding the two properly chosen vectors from these codebooks through the short-term synthesis filter. The optimum excitation sequence in a codebook is chosen using an analysis-by-synthesis search procedure in which the error between the original and synthesized speech is minimized according to a perceptually weighted distortion measure.

The coder operates on speech frames of 20 ms corresponding to 160 samples at the sampling frequency of 8000 sample/s. At each 160 speech samples, the speech signal is analyzed to extract the parameters of the ACELP model (LP filter coefficients, adaptive and fixed codebooks' indices and gains). Part of the signal processing is performed in subframes, i.e., the speech frame is divided into 4

subframes of 5 ms each (40 samples). The parameters are encoded and transmitted. At the decoder, these parameters are decoded and speech is synthesized by filtering the reconstructed excitation signal through the LP synthesis filter.

III. SUBSTITUTION AND MUTING OF LOST FRAMES FOR THE ADAPTIVE MULTI RATE SPEECH CODEC

This section defines a frame substitution and muting procedure when the indication of one or more lost speech frames is received in GSM-AMR decoder. The purpose of frame substitution is to conceal the effect of lost frames. The purpose of muting the output in the case of several lost frames is to indicate the breakdown of the channel to the user and to avoid generating possible annoying sounds as a result from the frame substitution procedure.

Normal decoding of lost speech frames would result in very unpleasant noise effects. In order to improve the subjective quality, lost speech frames shall be substituted with either a repetition or an extrapolation of the previous good speech frame(s). This substitution is done so that it gradually will decrease the output level, resulting in silence at the output.

A. State Machine

Solution for substitution and muting is based on a state machine with seven states (Fig. 2). The system starts in state 0. Each time a bad frame is detected, the state counter is incremented by one and is saturated when it reaches 6. Each time a good speech frame is detected, the state counter is reset to zero, except when the system is in state 6, where it is set to 5. The state indicates the quality of the channel: the larger the value of the state counter, the worse the channel quality is. The control flow of the state machine can be described by the following C code (**BFI** = bad frame indicator, **State** = state variable):

```
if (BFI != 0 )
  State = State + 1;
else if(State == 6)
  State = 5;
else
  State = 0;

if(State > 6 )
  State = 6;
```

In addition to this state machine, the **Bad Frame Flag** from the previous frame is checked (**prevBFI**). The processing depends on the value of the **State**-variable. In states 0 and 5, the processing depends also on the two flags **BFI** and **prevBFI**.

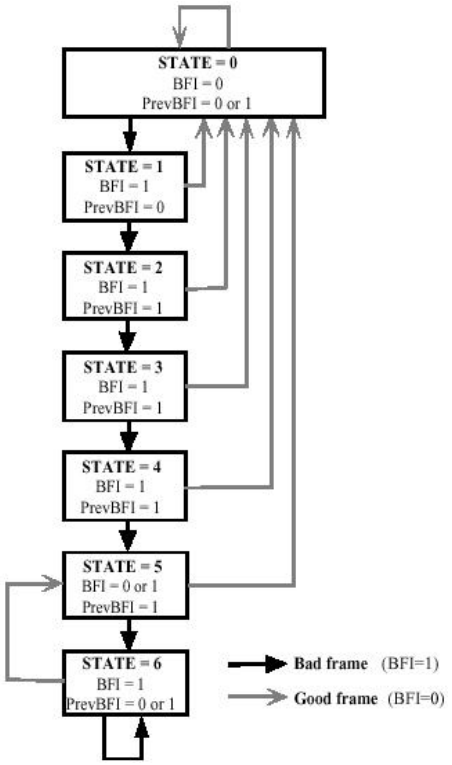

Fig. 2. State machine for controlling the bad frame substitution

The procedure can be described as follows:

B. Assumed Active Speech Frame Error Concealment Unit Actions

1) BFI = 0, prevBFI = 0, State = 0:

No error is detected in the received or in the previous received speech frame. The received speech parameters are used in the normal way in the speech synthesis. The current frame of speech parameters is saved.

2) BFI = 0, prevBFI = 1, State = 0 or 5:

No error is detected in the received speech frame, but the previous received speech frame was bad. The pitch gain and fixed codebook gain are limited below the values used for the last received good subframe:

$$g^p = \begin{cases} g^p, & g^p \le g^p(-1) \\ g^p(-1), & g^p > g^p(-1) \end{cases} \quad (3)$$

where g^p = current decoded pitch gain, $g^p(-1)$ = pitch gain used for the last good subframe (BFI = 0), and

$$g^c = \begin{cases} g^c, & g^c \le g^c(-1) \\ g^c(-1), & g^c > g^c(-1) \end{cases} \quad (4)$$

where g^c = current decoded fixed codebook gain and $g^c(-1)$ = fixed codebook gain used for the last good subframe (BFI = 0).

The rest of the received speech parameters are used normally in the speech synthesis. The current frame of speech parameters is saved.

3) BFI = 1, prevBFI = 0 or 1, State = 1 ... 6:

An error is detected in the received speech frame and the substitution and muting procedure is started. The pitch gain and fixed codebook gain are replaced

by attenuated values from the previous subframes:

$$g^p = \begin{cases} P(state)\, g^p(-1), & g^p(-1) \le m_p \\ P(state)\, m_p, & g^p(-1) > m_p \end{cases} \quad (5)$$

where g^p = current decoded pitch gain, m_p = *median5*(g^p*(-1),…,*g^p*(-5))*, where $g^p(-1),\ldots,g^p(-n)$ = pitch gains used for the last *n* subframes and *median5()* = 5-point median operation, *P(state)* = attenuation factor (*P(1)* = 0.98, *P(2)* = 0.98, *P(3)* = 0.8, *P(4)* = 0.3, *P(5)* = 0.2, *P(6)* = 0.2), *state* = state number, and

$$g^c = \begin{cases} C(state)\, g^c(-1), & g^c(-1) \le m_c \\ C(state)\, m_c, & g^c(-1) > m_c \end{cases} \quad (6)$$

where g^c = current decoded fixed codebook gain, m_c = *median5*(g^c*(-1),…,*g^c*(-5))*, where $g^c(-1),\ldots,g^c(-n)$ = fixed codebook gains used for the last *n* subframes and *median5()* = 5-point median operation, *C(state)* = attenuation factor (*C(1)* = 0.98, *C(2)* = 0.98, *C(3)* = 0.98, *C(4)* = 0.98, *C(5)* = 0.98, *C(6)* = 0.7), and *state* = state number.

The higher the state value is, the more the gains are attenuated. Also the memory of the predictive fixed codebook gain is updated by using the average value of the past four values in the memory:

$$ener(0) = \frac{1}{4}\sum_{i=1}^{4} ener(-i) \quad (7)$$

The past LSFs (LPCs are converted to LSP parameters and LSFs are the LSPs in the frequency domain [3]) are shifted towards their mean:

$$lsf\_q(i) = \alpha.past\_lsf\_q(i) + (1-\alpha).mean\_lsf(i),\ i = 0\ldots9 \quad (8)$$

where α = 0.90, lsf_q is a set of LSF-vectors for current frame, *past_lsf_q* is *lsf_q* from the previous frame, and *mean_lsf* is the average LSF-vector.

IV. INTERPOLATION OF LPC FOR RECOVERING OF LOST FRAMES

This section relates the interpolation scheme proposed to substitute lost frames. The interpolation is limited to a maximum of three consecutive losses, due to the non stationary nature of speech. After this number, the recovery GSM-AMR scheme is applied. Another restriction applied to the simulation model is that the first frame has to be a good frame. And if the last frame is a bad one, the algorithm will use parameters recovered by GSM-AMR decoder.

The applied scheme is a simple linear interpolation among LSP parameter vectors extracted from the nearest good received frames. GSM-AMR vocoder already performs some computation in this representation. As the vocoder linear prediction filter is 10^{th} order, ten element vectors are used in interpolation computation.

A huge problem inherent to interframe coding occurs when LPC parameters are decoded in an environment of lost frames [4]. Fig. 3 shows the error propagation problem. If a previous frame receives incorrect parameters or none, it will generate wrong updated states. In the current frame, even if correct parameters are received, the bad states from the previous frame will cause bad LPCs. It has a direct effect in the interpolation scheme, given that the frame following the lost one will provide inaccurate parameters to the computation.

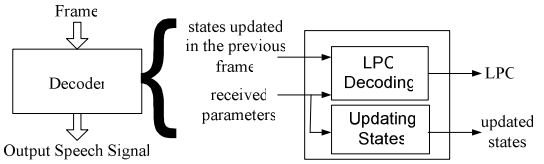

Fig. 3. Block Diagram to Error Propagation

The simulations were conducted using or not the transmission of the LPC coding states. This extra information would increase transmission rate in 8 kbps, what should not be interesting in terms of bandwidth. Researches have been developed in an attempt to reduce degradation in speech quality due to error propagation. In [1], good results have been achieved through employment of different quantization schemes. This has generated an increase of just 0.4 kbps in transmission rate.

During simulations, the voice over packet network was set with each packet containing one frame. Packet loss is approximated by a Markov random process, which emphasizes the "bursty" nature of Internet packet loss. Fig. 4 shows the implemented Markov random process.

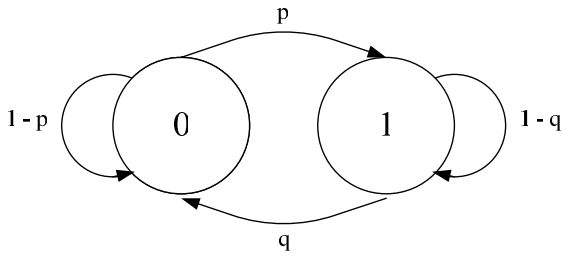

Fig. 4. Packet Loss Modeled by a Markov Random Process

Let state "0" stands for a packet being correctly received while state "1" is achieved when a lost packet is detected. Let the *p* be the transition probability from "0" to "1" and *q* be the probability from "1" to "0". Four different loss rates are simulated as listed in Table I [1].

TABLE I
SIMULATED LOSS RATES.

Rate(%)	p	q
0	0	0
10	.1	.85
20	.2	.70
30	.3	.65

The speech signals used in simulation are from the "Telephone Network Acoustic-Phonetic Continuous

Speech Corpus" – NTIMIT [5]. This database is composed by a set of 2680 voice signal files. It is split in eight groups (DR1 – DR8), each group corresponding to a different recording region [6]. Aiming better results, ten phrases have been used to get an average end result: five male voices and five female voices. Table II presents the speech signals used during simulations.

TABLE II
SPEECH SIGNALS USED DURIING SIMULATIONS.

Region	Phrase	Duration (s)
DR1	"To many experts, this trend was inevitable"	2.961
DR1	"A muscular abdomen is good for your back"	3.327
DR2	"December and January are nice months to spend in Miami"	3.084
DR2	"Steve wore a bright red cashmere sweater"	2.957
DR2	"Iguanas and alligators are tropical reptiles"	2.930
DR1	"My father ran him off here six years ago"	2.943
DR1	"Jane may earn more money by working hard"	3.014
DR2	"The emblem depicts the Acropolis all aglow"	2.962
DR2	"Catastrophic economic cutbacks neglect the poor"	3.102
DR2	"Jeff thought you argued in favor of a centrifuge purchase"	3.257

All NTIMIT recorded files are sampled with a sample rate of 16 kHz, and quantized with 16 bits/sample. As GSM-AMR has input signals sampled at 8 kHz, the signals were filtered and decimated to this sample frequency by the following low-pass FIR filter, designed in MATLAB^{TM}:

```
f = [0 0.425 0.5 1];
m = [1 1 0 0];
b = remez(96, f, m);
```

This filter has 97 taps, a cutoff frequency of about 3400 Hz and offers 64 dB of attenuation at 4000 Hz. The SNR of the original and filtered signals is at minimum 30 dB, showing that actually almost all energy of the signal is inside the frequency band of the telephone channel [7].

V. SIMULATION RESULTS

To analyze the quality of the decoded speech signals, an objective distortion measure was used observing LSP parameters. Spectral distortion is defined as the root mean square difference between the original LPC log power spectrum and the interpolated LPC log power spectrum [8]. The mathematical definition of the spectral distortion for frame *i* is as follows

$$SD_i = \sqrt{\frac{1}{F_s}\int_0^{F_s}\left[10\log_{10}\frac{S_i(f)}{\hat{S}_i(f)}\right]^2 df} \quad (dB) \quad (9)$$

where, F_s is the sample frequency, $S_i(f)$ and $\hat{S}_i(f)$ are the LPC power spectra of the ith frame given by,

$$S_i(f) = \frac{1}{\left|A_i(e^{j2\pi f}/F_s)\right|^2} \quad (10)$$

and

$$\hat{S}_i(f) = \frac{1}{\left|\hat{A}_i(e^{j2\pi f}/F_s)\right|^2}, \quad (11)$$

where $A_i(z)$ and $\hat{A}_i(z)$ are respectively the original and interpolated LPC polynomials, defined in (1), for the ith frame.

It was used a discrete version of this distortion measure. The computation of the power spectrum uses a FFT of 512 points. The lower and upper frequencies are 125Hz and 3400Hz respectively. The SD_i is calculated as a summation over uniformly spaced points between the previously referred frequencies. This can be expressed as [9]

$$SD_i = \sqrt{\frac{1}{n_1 - n_0}\sum_{n=n_0}^{n_1-1}\left[10\log_{10}\frac{S(e^{\frac{j2\pi n}{N}})}{\hat{S}(e^{\frac{j2\pi n}{N}})}\right]^2} \quad (dB) \quad (12)$$

Also, it has been observed the percentage of occurrence of outlier frames (frames with large spectral distortion), which also affect the speech signal quality. There are two types of outlier frames:

- The frames having SD in 2-4 dB range (outlier type 1).
- The frames having SD greater than 4 dB (outlier type 2).

The following outcomes are divided in interpolation results using or not the coding states. In both cases, there is always a comparison among the proposed interpolation scheme and the GSM-AMR recovery scheme.

Fig. 5 shows the performance of both schemes in relation to packet loss rate and average spectral distortion. The interpolation scheme is not using states originated during coding.

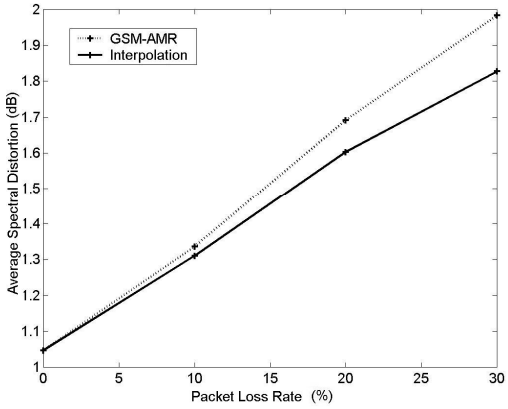

Fig. 5. Average LPC spectral distortion with frame erasure. Coding States are not used in Interpolation Scheme.

Outliers are important parameters affecting the perceptual quality of the decoded speech. Table III shows the average outlier values, achieved when parameters are being interpolated without coding states. The interpolation scheme achieves an average spectral distortion 0.03 – 0.16 dB smaller. The percentage of outliers is also smaller, which yields perceptual quality improvement when frame erasures occur.

TABLE III
OUTLIERS OF LPC SPECTRAL DISTORTION WITH PACKET LOSS.

Loss Rate (%)	GSM			Interpolation		
	Av. SD (dB)	Outliers (%) 2-4dB	>4dB	Av. SD (dB)	Outliers (%) 2-4dB	>4dB
0	1.05	1.19	0.00	1.05	1.19	0.00
10	1.34	9.56	2.10	1.31	10.28	1.45
20	1.69	19.41	5.45	1.60	19.06	4.09
30	1.98	22.92	9.77	1.83	23.48	7.34

Fig. 6 also shows the performance of both schemes in relation to packet loss rate and average spectral distortion. In this simulation, the interpolation scheme uses states originated during coding.

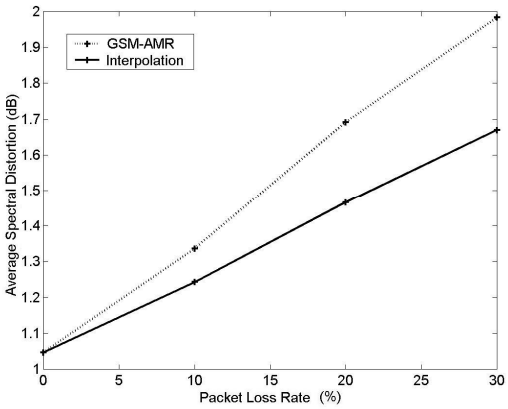

Fig. 6. Average LPC spectral distortion with frame erasure. Coding States are used in Interpolation Scheme.

Table IV shows the average outlier values, achieved when parameters are being interpolated with coding states. The interpolation scheme achieves an average spectral distortion 0.09 – 0.31 dB smaller. Here, the percentage of outliers is also smaller.

TABLE IV
OUTLIERS OF LPC SPECTRAL DISTORTION WITH PACKET LOSS.

Loss Rate (%)	GSM			Interpolation		
	Av. SD (dB)	Outliers (%) 2-4dB	>4dB	Av. SD (dB)	Outliers (%) 2-4dB	>4dB
0	1.05	1.19	0.00	1.05	1.19	0.00
10	1.34	9.56	2.10	1.24	8.34	0.73
20	1.69	19.41	5.45	1.47	14.98	2.60
30	1.98	22.92	9.77	1.67	20.45	4.78

VI. CONCLUSIONS

The proposed interpolation scheme achieved an improvement in speech quality in relation to GSM-AMR scheme. Without using LPC coding states, an average spectral distortion 0.03 – 0.16 dB smaller than that caused by GSM-AMR scheme was reached. Using LPC coding states, an average spectral distortion 0.09 – 0.31 dB smaller was achieved. A scheme involving interpolation of all ACELP parameters is been developed.

REFERENCES

[1] Jian Wang and Jerry D. Gibson, "*Parameter Interpolation to Enhance the Frame Erasure Robustness of CELP Coders in Packet Networks*". *IEEE*, 2001.

[2] TS 26.090: "*AMR Speech Codec; Speech Transcoding Functions*". 1999.

[3] Kondoz, A.M.; *Digital Speech. Coding for Low Bit Rate Communication Systems*. John Wiley & Sons, Ltd. Chichester. UK. 1999.

[4] Jian Wang and Jerry D. Gibson, "*Performance Comparison of Intraframe and Interframe LSF Quantization in Packet Networks*". *Proc. 2000 IEEE Workshop on Speech Coding*, Delavan, WI, USA, September 2000.

[5] C. Jankowski, A. Kalyanswamy, S. Basson and J. Spitz, *"NTIMIT: a phonetically balanced, continuous speech, telephone bandwidth speech database", Proc. ICASSP*, Albuquerque, Apr. 1990.

[6] Barbosa, L. M. J. *"Algoritmos de Busca em Codificadores ACELP,"*. Master's Thesis. State University of Campinas – UNICAMP. Brazil. November 2002.

[7] Bertan H. C., Meloni L. G. P., *"LSP Transcoding between G.729ª and GSM-AMR"*. International Telecommunication Symposium – ITS2002, Natal, Brazil.

[8] Tamanna Islam, "*Interpolation of Linear Prediction Coefficients for Speech Coding*". McGill University, Montreal, Canada, April 2000.

[9] J. H. Y. Loo, *"Intraframe and interframe coding of speech spectral parameters,"* Master's thesis, Department of Electrical and Computer Engineering, McGill University, Montreal, Canada, Sept. 1996.

Token-based Admission Control for DiffServ Networks

Eduardo Garnier
Pontifícia Universidade Católica - PUC-Rio
P.O. Box 38097 - 22453-900
Rio de Janeiro - RJ - Brazil
garnier@cetuc.puc-rio.br

João Célio Brandão
Pontifícia Universidade Católica - PUC-Rio
P.O. Box 38097 - 22453-900
Rio de Janeiro - RJ - Brazil
jcelio@cetuc.puc-rio.br

***Abstract*— In this paper, we evaluate the performance of an admission control technique to be used in a DiffServ environment, based on a token-passing mechanism. This kind of solution has been proposed in [2] for core-stateless networks, in wich the core nodes don't store state information about individual flows and the edge nodes perform per-flow management. Per-flow management, however, is not allowed in the Diffserv architecture and for this reason some modifications are necessary to adapt this algorithm to the DiffServ paradigm. The Token Based Admission Control (TBAC) is described and simulated in a simple network topology for three different traffic patterns using ns-2 simulation package. Packet loss, link utilization and the number of admitted flows are estimated for different configuration of TBAC parameters.**

***Index Terms*— Admission Control, DiffServ, QoS.**

I. Introduction

Recently, strategies to implement Quality of Service in the Internet have been an important research topic [13], [1]. Integrated Services (Intserv [7], [10], [11]) and Differentiated Services (Diffserv [9], [5], [8]) are frameworks currently proposed at IETF aiming to this objective. DiffServ has been considered a more realistic approach once it has scalability properties but some problems are still not properly solved. That is the case of the admission control mechanism. This is a major component of a communication network with QoS and it is not included in the IETF documents related to DiffServ. So, in order to make DiffServ a fully functional QoS framework, it is necessary to develop admission control techniques that are compatible with Diffserv paradigm.

The difficulty in implementing admission control on a DiffServ environment relies on the fact that this architecture deals with aggregated flows and statistical guarantees, without resource reservation. Traditional admission control schemes, on the other hand, deal with individual flow control. So, it's clearly necessary to search other ways to regulate the entrance of new flows into the domain, avoiding, thus, QoS degradation. Some recent contributions have have addressed this subject [6], [3], [4].

In this paper, we propose an admission control method which complies with the Diffserv paradigm and uses a token-passing mechanism to carry signaling information to be used in admission decisions. We call it Token Based Admission Control (TBAC). The technique has been proposed in [2] for core-stateless networks i.e, networks where the core nodes don´t store state information about individual flows and the edge nodes perform per flow management. Since per-flow management is not allowed in Diffserv networks, the technique had to be modified to be used in a Diffserv environment. TBAC uses DiffServ's class differentiation principle and a token packet to perform implicit signaling among the network nodes and allowing effective admission control without per-flow management.

Using ns-2 simulation software we have simulated a simple network with 3 edge nodes and 1 core node operating the TBAC technique. Traffic flows of different types and with high arrival rate have been input to the network. The effectiveness of the mechanism in blocking the entrance of new flows in order to prevent QoS degradation has been assessed. As QoS parameters, we have considered packet loss and link utilization.

The paper is organized as follows. Section II, presents a detailed description of the TBAC mechanism. In Section III, the simulation model, the system parameters and the obtained results are presented. Concluding remarks are presented in in Section IV.

II. TBAC

TBAC is a distributed measurement-based admission control technique, in wich signaling information is obtained by the circulation of a single packet - the token packet - among the network nodes. It has been designed to operate in a Diffserv framework, where different service classes are identified by the Diffserv Code Point in the DS field of the IP header. The token packet is marked with an specific code and it is classified as an ordinary Diffserv service class. TBAC uses the information carried by this packet to take admission decisions. It's an implicit signalling mechanism fully based on the Per-Hop Behaviour (PHB) of each class, accordingly to the DiffServ paradigm. The token packet circulates around the domain, among all nodes, following a predefined order contained in it's class PHB. Thus, the token reaches every node of the domain.

The token packet contains a table relating each link of the domain to it's occupied bandwidth. Each node that receives the token, updates the value of the

occupied bandwidth of it's links and in this way, the token collects information about all the links. As an illustrative example of the token packet, see Table I.

Link	Occupied BW	Total BW
$E1 \longrightarrow C1$	1 kbps	5 kbps
$E2 \longrightarrow C1$	3 kbps	5 kbps
$C1 \longrightarrow E3$	4 kbps	10 kbps

TABLE I
THE TOKEN PACKET

In Token Ring networks (IEEE 802.5), a node is allowed to transmit only when it has the token. Likewise, in TBAC mechanism, an edge node admits new flows only when the token arrives. At that time, the edge node, aware of the route required by the arriving flow and the bandwidth that should be "reserved" for it in that route, can take the admission decision based on the occupied bandwidth information in the token. Ideally, the new flow should be accepted only if there is enough bandwidth available in all the links of the requested route. The available bandwidth is continuously evaluated by comparing a time window rate estimator with the total bandwidth for each link. A time window estimator is a device that simply measures the number of bits that arrives during a given time interval (the time window) and determine the average bit rate by dividing that number by interval length. The measurement time window is an important parameter that has to be carefully designed. Its effect of the admission control performance is considered in Section III.

When the token arrives at a node, a new measurement interval begins. During this interval, the outputs of time window rate estimators are fed into the "Occupied BW" field of the token and subtracted from the "Total BW" parameter. If "Occupied BW" is greater then or equal to "Total BW", new flows that intend to use that link are rejected. Otherwise a certain number of flows are admitted. This number u may be calculated as

$$u = \frac{BW_T - BW_O}{R} \quad (1)$$

where BW_T is the total bandwidth, BW_O is the Occupied Bandwidth and R is the mean rate of the flow. The "Total BW" parameter may be used as a tuning knob for the mechanism which sets the maximum number of admitted flows M through the following expression

$$M = \frac{BW_T}{R} \quad (2)$$

As we raise the value of M, more flows will be admitted, resulting in higher utilization and higher loss rate. Note that in this approach, each traffic source

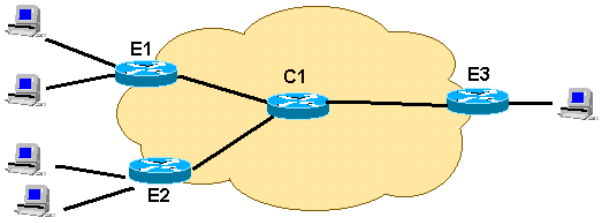

Fig. 1. Topology used in simulations

is just represented by its average rate. More detailed representation may be used as in [6], [3], [4].

Considering that in DiffServ environments, we don?t have any kind of information regarding individual flows, the described technique seems to be adequate to operate in DiffServ networks. It provides to the edge nodes the amount of information needed to take the admission decision, without any transgressions on the DiffServ paradigm. On the other hand, we believe that the signaling load due to the token circulation doesn't have impact on the architecture scalability.

III. PERFORMANCE EVALUATION

We considered the topology ilustrated in Figure 1. Traffic sources are created and connected to nodes E1 and E2, and traffic flows to node E3. The connection between nodes are all 2 Mbps links, and the buffer size at all nodes corresponds to 10 packets.

Since we have two entrance nodes in our topology (E1 and E2), and all the links and buffers are equal, it's clear that the critical point of this topology is node C1. The link C1-E3 will be shared by all flows originated in E1 and E2. Thus, the results presented here refer to these node (C1) and link (C1-E3).

As performance parameters we considered the link utilization and the loss rate. The link utilization is defined as the the average rate achieved, i.e., the number of bits successfully transmitted during the period, divided by the link capacity. The loss rate corresponds to the percentage of packets lost in transmission.

A large number of cases corresponding to different sets of parameters have been simulated. Each simulated run has been repeated 10 times with different random number initialization. The simulation time in each run was 2000 seconds. For comparison purposes, we considered also the case where no admission control is available.

Traffic Sources

Simulations were ran with three kinds of traffic sources: periodic *on-off*, exponential *on-off* and MPEG. The source models are described as follows.

Periodic ON-OFF and Exponential ON-OFF

Using ns simulator terminology, periodic on-off and exponential on-off traffic sources are labeled, respectively, CBR and EXP. Actually, the periodic on-off source is not really a CBR (constant bit rate) source,

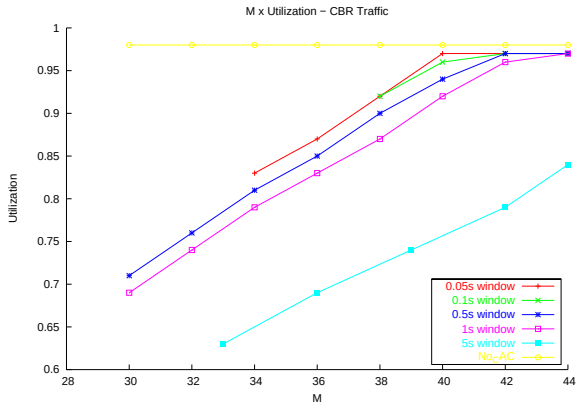

Fig. 2. Link utilization - CBR traffic

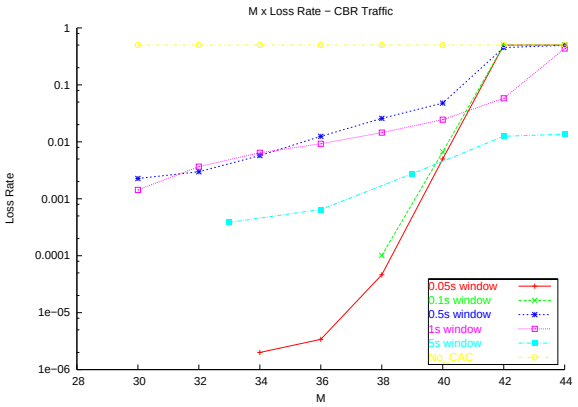

Fig. 3. Loss rate - CBR traffic

but we kept this label to provide a clear reference to ns users.

The EXP sources can be seen as a packet model for voice traffic with activity detection. The activity and inactivity periods are exponential random variables with mean values 1.004 second and 1.587 second respectively. These values are specified in [14] as representative values of a real conversation.

For both CBR and EXP sources, we configured an average rate of 50 kbps and the packet size was 120 bytes. The flow inter-arrival times and duration are exponentially distributed with an average of 0.2 second and 30 seconds, respectively.

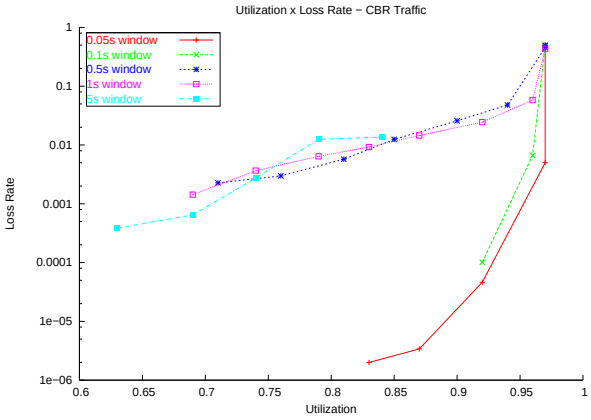

Fig. 4. Loss-load curve - CBR traffic

MPEG

To simulate MPEG traffic, we used a 10 seconds *trace* of the *Star Wars* movie ([12]) that transmits at an average rate of 320 kbps, and uses 200 bytes packets. Each arriving flow is represented by a single *trace* and the flow interarrival times are exponentially distributed with an average of 1 second.

A. Simulation results

Figures 2 to 7 show a set of graphs relating network performance parameters and TBAC configuration parameters. Figures 2 and 3 relate link utilization and loss rate to the parameter M for CBR traffic and several values of the time window size. The graphs of figure 4 are called loss-load curves since they relate loss rate to link utilization (load). Figure 5 shows the number of admitted flows compared to the number of requests that arrived to the edge nodes. This figure illustrates the ability of TBAC to keep the number of admitted flows sufficiently small to guarantee the performance level, regardless the high number of solicitations. Figures 6 and 7 show the loss-load curves for EXP and MPEG traffic. Note that, in each figure, a curve corresponding to no admission control is included. Obviously, in that case, the network will be fully utilized but at a cost of a huge loss rate.

As explained before, M is the maximum number of admitted flows. The range of M was chosen high enough to make the sum of the average rates of the flows to exceed the link capacity.

The measurement window size ΔT is a configuration parameter that may affect directly the efficiency of the admission control mechanism. Longer measurement periods lead to more precision in traffic long range characterization, but, on the other hand, may result in low updating rate, and consequently, in a slow admission control mechanism. We should also observe that small windows could lead to low accuracy, considering the high burstiness of the traffic sources. In our simulations, we have considered several

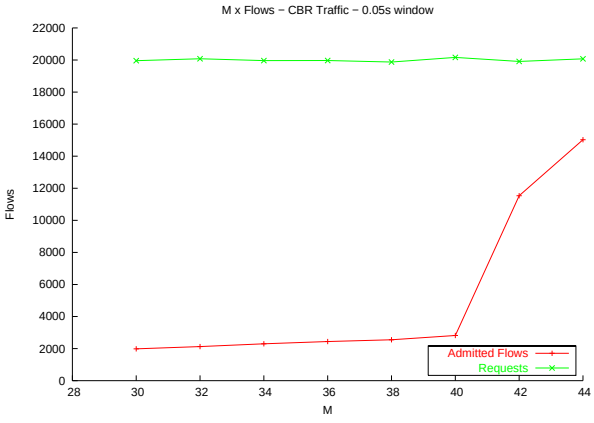

Fig. 5. Admitted flows - CBR traffic

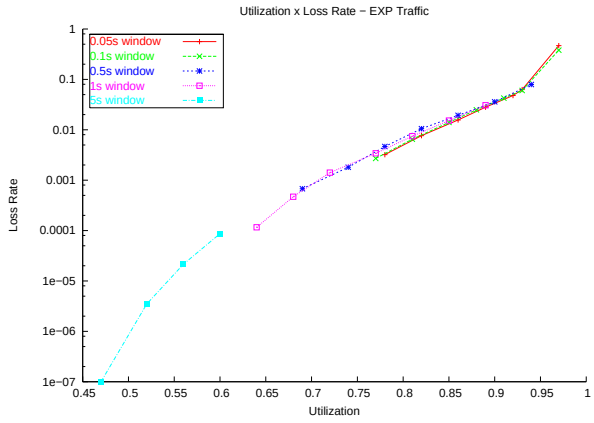

Fig. 6. Loss-load curve - EXP traffic

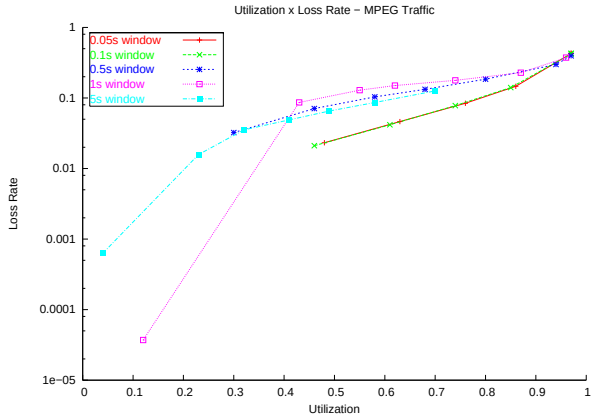

Fig. 7. Loss-load curve - MPEG traffic

measurement window sizes and observed it's impact on the performance of TBAC.

As we can see in those figures, there is a significant variation in the performance level, as we change the window size. Note the comparison of the several confgurations of TBAC and the performance level of the system without any admission control policy. As depicted in Figure 4, the 0.05 and 0.1 second window configuration offer an excellent performance level, even under high traffic load, for CBR traffic.

The other traffic patterns show different results. The simulations with EXP sources show pratically no difference among the examined measurement windows. Under MPEG traffic, like in the CBR case, the smaller windows (0.05 and 0.1 second) offer the best results.

IV. Conclusion

In this paper, we have proposed an admission control technique for DiffServ networks, based on a token packet which carries information on network occupation. This information is continuously updated in the edge nodes through a time window rate estimator and compared to the total bandwidth occupation. TBAC performance has been evaluated under 3 different traffic patterns, in a simple network topology. Link utilization and loss-load have been obtained by simulation and the results confirm the proper operation of the technique in a Diffserv environment. In addition they provide basic and preliminary information that could be used in the mechanism design. We think that TBAC may be an interesting solution to the admission control in DiffServ, and deserve more extensive studies.

References

[1] Aquila Project - www.ist-aquila.org/.
[2] Sudeept Bhatnagar and Brett Vickers, *Providing quality of service guarantees using only edge routers*, IEEE Globecom, 2001.
[3] G. Bianchi and N. Blefari-Melazzi, *Admission control over assured forwarding phbs: a way to provide service accuracy in a diffserv framework*, IEEE Globecom 2001, 2001.
[4] G. Bianchi, N. Blefari-Melazzi, and M. Femminella, *Per-flow qos support over a stateless differentiated services ip domain*, Computer Networks: The International Journal of Computer and Telecommunications Networking (2002).
[5] S. Blake, D. Black, M. Carlson, E. Davies, Z. Wang, and W. Weiss, *Rfc 2475: An architecture for differentiated services*, Tech. report, IETF - Network Working Group, 1998.
[6] N. Blefari-Melazzi, M. Feminella, and F. Pugini, *Definition and performance evaluation of a distributed and stateless algorithm for qos support in ip domains with heterogeneous traffic*, SSGRR (2001).
[7] R. Braden, D. Clark, and S. Shenker, *Rfc 1633: Integrated services in the internet architecture*, Tech. report, IETF - Network Working Group, 1994.
[8] D. Grossman, *Rfc 3260: New terminology and clarifications for diffserv*, Tech. report, IETF - Network Working Group, 2002.
[9] K. Nichols, S. Blake, F. Baker, and D. Black, *Rfc 2474: Definition of the differentiated services field (ds field) in the ipv4 and ipv6 headers*, Tech. report, IETF - Network Working Group, 1998.
[10] S. Shenker, C. Partridge, and R. Guerin, *Rfc 2212: Specification of guaranteed quality of service*, Tech. report, IETF - Network Working Group, 1997.
[11] S. Shenker and J. Wroclawski, *Rfc 2215: General characterization parameters for integrated service network elements*, Tech. report, IETF - Network Working Group, 1997.
[12] Example traffic trace for ns - http://www.research.att.com/ breslau/vint/trace.html.
[13] Tequila Project - http://www.ist-tequila.org.
[14] *Telephone transmission quality objective measuring apparatus: Artificial conversation speech*, Rec. P.59 ITU-T, 1993.

A Switched Multicast Protocol for Intranets

Edison de Qeiroz Albuquerque
albuquerque@ieee.org
Hugo E. Hernandez-Figueroa
hugo@dmo.fee.unicamp.br
DMO – FEEC – UNICAMP

Shusaburo Motoyama
motoyama@dt.fee.unicamp.br
DT – FEEC – UNICAMP
Campinas, São Paulo, Brasil

***Abstract* — In this work a bi-directional multicast protocol for corporate networks (Intranets) called XMP (Switched Multicast Protocol) is proposed. In this protocol the concept of focal point router (FP) in which all participants of a given multicast session point to the same IP address. The use of such a router simplifies the transmission direction switching allowing, for example, multicast connections sender-receiver and vice-versa, during a multimedia conversation. XMP has been validated by means of a simulator developed using the software package ns-2. The simulation is carried out using a real corporate network that belongs to a large Brazilian telecommunications company with nationwide presence. The traffic that is carried by the simulated network is the regular traffic that has been measured in the real network.**

***Index Terms* — Bi-directional, Performance, Multicast Protocol.**

I. INTRODUCTION

The multicast protocols in use nowadays, such as DVMRP (Distance Vector Multicast Routing Protocol), MOSPF (Multicast Open Shortest Path First), PIM-SM (Protocol Independent Multicast – Sparse Mode) e PIM-DM (Protocol Independent Multicast – Dense Mode) [1]-[3], do not allow audio/video bi-directionality that is necessary for an enhanced interaction among participants of a multicast session.

A bi-directional multicast protocol, called BI-DIR PIM is being currently standardized by IETF [5]. This new protocol has been designed to add bi-directionality to the PIM and it can operate in a large network.

For corporate training in an Intranet environment, a simpler bi-directional multicast protocol could be proposed. In this environment, it is possible to eliminate the need to discover the neighbor routers by providing multicast capabilities for all routers. This provisioning can provide a lighter code to be processed at the routers and small routing tables.

In this paper a bi-directional multicast protocol for Intranets named Switched Multicast Protocol (XMP) is proposed. In the proposed protocol a focal point router (FP) concept is used. In this concept all the machines involved in multicast connections always point to the same IP address. The presence of a FP router facilitates the transmission direction switching allowing, for instance, multicast connections in the teacher-student direction and vice-versa in a distance-learning multimedia conversation. By using DHCP protocol the teacher and students could be anywhere in the Intranet moving with their notebooks.

The organization of paper is as follows. In section II the XMP is described in detail. The validation methodology, the software package used and some cases of protocol validation using a real network are presented in section III. Finally, in section IV the main conclusions are presented.

II. XMP DESCRIPTION

Since XMP is based on the concept of focal point (FP) router it does not optimize path but its operational advantage is that it allows to teacher and students to connect themselves wherever they are.

XMP is composed of 5 phases:

Phase 1 – Registration of each participant, including the teacher, in the FP router and also in the intermediate routers in the path to FP.

Phase 2 – Sending audio/video (A/V) signal by teacher to remote hosts (students).

Phase 3 – Switching receiver to become a transmitter.

Phase 4 – Recovering transmission by teacher.

Phase 5 – Ending session.

Phase 1 – Registration of each participant.

Each participant sends a START(G) message to FP. The sender sends this packet with the field "Who I Am" set to S and the receivers send it with this field set to R. Every router in the path from the participant to FP builds an XMP routing table (XRT), including FP. Fig. 2.1 illustrates message format and Fig. 2.2 shows XRT table format.

Group number	Who I Am	Message Type
Pay-Load		

Group number: a number designated by the network administrator
Who I Am: Sender (S) or Receiver (R)

Message type: START, STOP or A/V (audio/video)
Payload: exists for A/V packets only

Figure 2.1. XMP packet format.

Interface	Who I Am
1	Sender (S)
2	Receiver (R)

Figure 2.2. XRT table format.

The START(G) message is unicast and is forwarded by conventional means, i.e., consulting the regular routing table. The IP address of the FP router is placed in the destination address field of the IP packet that transports the START message.

To recognize if an incoming packet is an XMP message, each router examines the HEADER LENGTH FIELD of the IP packet overhead, and in case it indicates the presence of the OPTIONS FIELD, the router examines the options field [1][3]. If this field indicates that the packet is an XMP then the table XRT is read and forwarding the packet in the appropriate interface toward FP.

Phase 2 – Sending audio/video signal by teacher to remote hosts (students).

The sender, after registration, starts sending audio/video samples in IP packets. When a router receives this packet looks up the XRT and forwards it to the all interfaces labeled R.

Phase 3 – Switching receiver to become a transmitter.

The receiver sends a START(G) message setting S in the field "Who I Am" (see Fig. 2.1 above). This message travels toward FP and every router in its path updates the label of the interface that received it to sender in the XRT table. Now the A/V packets have their origins at the new sender and travels toward all participants. This is the only case when the control message travels through FP and reaches the teacher host and plays the role of an acknowledgement, so the teacher host will cease to send A/V.

Phase 4 – Recovering transmission by teacher.

When the teacher, the former sender, understands the student finished its intervention, he sends a START(G) with the field "Who I Am" set to S which will updates each XRT in its path to FP. The new A/V packets, originated at the teacher host will restart flowing toward all participants.

Phase 5 – Ending session.

When a receiver wants to leave the group it sends a STOP(G) message with R in the field "Who I Am". When a router receives such a message the counter for that interface is decremented. This counter has been incremented when START(G) was received. When the counter reaches zero, that interface is removed from XRT. When a router receives a STOP(G) message with S the XMP routing table for that group is removed.

III. XMP VALIDATION

The methodology used to validate the XMP Protocol is the exhaustive test criteria. In this method the proposed protocol is implemented in a simulator (software package) and several situations are tested to verify the correct functioning. The adoption of this methodology is due to the fact that besides of the functioning verification it is possible to study the impact of the protocol on the corporate network related to the link utilization and packet delay.

The simulator has been implemented in the ns-2 software package [4]. The ns-2 incorporates some basic functions of an IP network like UDP, TCP, MPLS, wireless, and satellite and can be easily used. Ns-2 uses C++ in the core functions and Otcl (Object Tools Command Language) to implement less critical functions. Furthermore Otcl is used to write the script describing the topology, traffic load and type and time events. After the simulation run a file is generated which contains all the operations performed during simulation (trace file) and is used to compute several parameters such as packet delay (W), utilization (U), queue size (n) and throughput (X). Ns-2 components are *nodes, links* and *agents*. With these basic components it is possible to build a variety of networks with many combinations of topology, traffic load, type of traffic and protocols. The nodes represent the hosts and routers. Nodes are interconnected to each other using links, building the desired topology. Agents generate and/or consume packets and may perform control functions inside routers.

XMP is validated by means of a simulation using a real Corporate Network. The network is shown in Fig. 3.1. The XMP has been written in C++ and Otcl and incorporated to the Ns-2. Each one of the 5 phases of proposed protocol is tested. As ns-2 offers an animation package (NAM) the correct functioning of XMP was easily seen graphically, observing the packet flow along the links and passing through the nodes.

The A/V traffic model used is CBR and all other traffic models are EXPO On-Off. The transmission rate of CBR traffic is 384 kbps and each packet is 200 bytes long.

The FP router is placed at São Paulo and the teacher is transmitting from Rio de Janeiro. To validate the proposed protocol many situations are tested assuming that the network is working with regular traffic that was previously measured.

The phases 1 and 2 are tested assuming that the teacher started transmission of CBR packets, after the registration, and students in PAE, SDR, CPE, CAS, VTA, BHE and RCE join to the group in different instants of time.

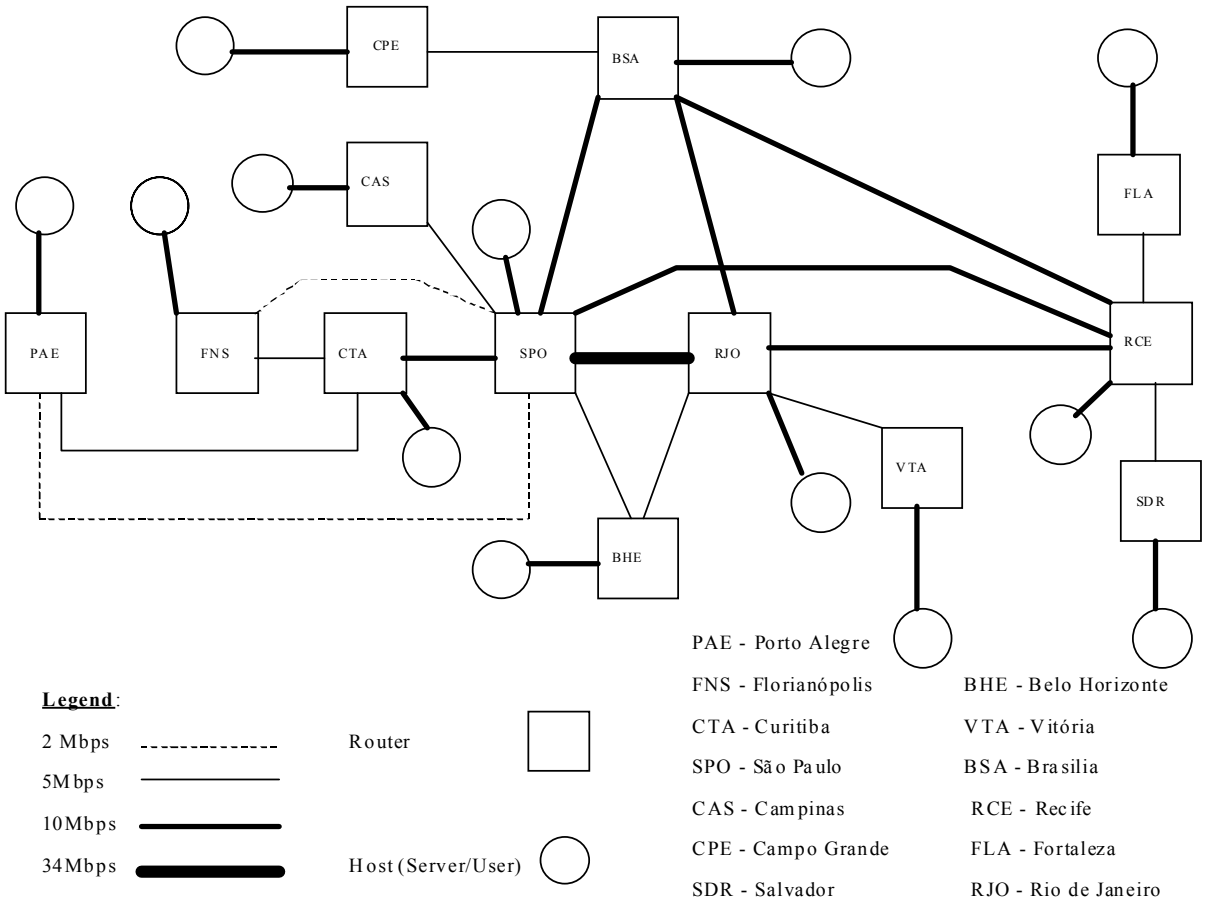

Figure 3.1 – Example of network used for validation of proposed protocol.

The phases 3 and 4 are tested assuming that the student in PAE becomes sender and starts to send A/V packets. It is also tested when the teacher recovers the transmission and the student becomes receiver again. Many other situations are tested to validate these phases.

The phase 5 is tested assuming that a receiver leaves the group at any time.

The XMP simulator developed is capable to measure many performance parameters to verify the impact of new application on the existing network.

The AWK language has been used to process the trace file generated after the simulation run. Writing appropriate programs several parameters have been computed such as utilization of each link (in each direction), packet delay (latency) of each link and overall packet loss. The computation of throughput can be obtained using the relationship between utilization and bandwidth (BW), while the number of packets in queue is obtained using Little's Law. Table 3.1 presents the results of computations made on each direction of each link.

To evaluate the impact of XMP on the network running regular traffic two measurements are carried out: one with EXPO traffic only and later adding XMP traffic using CBR (Constant Bit Rate to simulate A/V traffic).

The corporate network used as an example has its servers in Rio de Janeiro (Database Servers) and São Paulo (Web Servers). The applications are mostly client to server and also the remote hosts generating traffic toward the servers. The difference is that this traffic is less intense than in the server to client direction.

At each locality several users are connected to the local router via LAN. These LANs operate at 100Mbps in Rio de Janeiro and São Paulo and at 10Mbps at the other cities. The traffic generated by all servers has been simulated using EXPO ON-OFF ns-2 traffic generator. All users are represented by a single node (circle in Fig. 3.1) at each locality generating an equivalent traffic.

The EXPO (on-off) traffic generator has been configured as follows:

- burst time = 500 ms for servers and users
- idle time = 500 ms for servers and 100 ms for users
- packet size = 210 (constant)
- variable rate per locality and configured at the Otcl script which builds the network

The CBR traffic generator is configured as follows:

- CBR packets 200 bytes size (included the RTP, UDP e IP overhead) at a rate of 384 kbps.

Under the regular traffic load, simulated by the EXPO ON-OFF and CBR traffics, the utilization of each link is measured in the network. Next it is removed the CBR traffic keeping the XMP control messages, i.e., START and STOP messages. The

utilization in each link is measured again for this new scenario. In Tab. 3.2 are shown most representative time intervals and the link utilizations where CBR traffics have been flowing.

Table 3.1
UTILIZATION IN EACH LINK.

Link	Utilization
PAE – CTA	0,48
CTA – PAE	9,68
PAE – SPO	3,50
SPO – PAE	7,29
FNS – CTA	0,38
CTA – FNS	7,21
FNS – SPO	2,38
SPO – FNS	3,84
CTA – SPO	0,62
SPO – CTA	12,94
CAS – SPO	1,69
SPO – CAS	12,13
SPO – BSA	4,93
BSA – SPO	2,35
SPO – BHE	10,96
BHE – SPO	0,80
SPO – RJO	1,45
RJO – SPO	1,86
SPO – RCE	6,68
RCE – SPO	1,75
BSA – CPE	9,02
CPE – BSA	1,49
RJO – BSA	7,98
BSA – RJO	0,97
RJO - RCE	5,70
RCE - RJO	1,34
RJO – VTA	8,07
VTA – RJO	1,55
RCE – SDR	5,34
SDR – RCE	1,73
RCE – FLA	11,86
FLA - RCE	1,40

TABLE 3.2
UTILIZATION VARIATION DUE TO WITHDRAWAL OF CBR LOAD.

Link	time interval	Earlier Utilization	Current Utilization
SPO – PAE	2 – 3	15,68	6,7
SPO – CAS	3 – 4	19,38	10,5
BSA – CPE	3 – 4	13,90	4,9
RJO – VTA	4 - 5	14.30	5,3
RCE – SDR	4 – 5	10,06	3,6
RCE – FLA	2 – 3	18,85	11,0

As expected the removal of CBR traffic resulted in a smaller value for link utilization. The load due to the audio/video (CBR) traffic does not depend on the multicast protocol used but depends solely on the chosen image quality (128kbps, 256 kbps, 384 kbps or higher).

The next step is the removal of the XMP control messages, from senders as well as the receivers. The new link utilizations for this case are identical to the previous values, i.e., the Current Utilization values in the Tab. 3.2. As expected, the load imposed on the network by the control messages of the XMP protocol is negligible, as it was designed for.

The time interval between the instant the sender stops sending A/V signal and starts receiving it from the new sender was measured to be 21 ms. Although this time depends on the number of routers involved it has been considered acceptable.

I. CONCLUSIONS

In this work it has been proposed a multicast protocol to be used in corporate networks (Intranets) in order to impose a light load on existing routers and links. It has also been designed to a fast switching of audio/video transmission from teacher to students and student to teacher and the other students attending the same class, so increasing interaction between participants. This is a key feature to make Distance Learning more effective. This proposed protocol makes use of a Focal Point Router which simplifies the network operation taking into account that teacher and students can be anywhere and even move from place to place during the period a class is been given.

A simulator developed in Ns-2 software package validated the proposed protocol. In many situations tested the protocol worked very well.

The developed simulator also allowed the study of the performance of real network used for protocol validation. The main characteristic studied was link utilization when the traffic multicast was superimposed to the normal network traffic. It was concluded that the control traffic of proposed protocol had negligible effect but the audio/video traffic had considerable influence in link utilization.

REFERENCES

[1] Martin W. Murhammer, et al., “TCP/IP Tutorial and Technical Overview”, MAKRON Books, 2000.
[2] Estrin D., et al, Request for Comments: RFC 2117 – Protocol Independent Multicast – Sparse Mode (PIM – SM): Protocol Specification.
[3] Stevens, W. Richard, “TCP/IP ILLUSTRATED – vol 1 – THE PROTOCOLS”, Addison Wesley, 1994.
[4] Fall K., Varadhan K., “The ns Manual”, The VINT Project, http://www.isi.edu/nsnam/ns-documentation.html.
[5] Handley, M., et al, Bi-directional Protocol Independent Multicast (BIDIR-PIM), http://www.ietf.org/internet-drafts/draft-ietf-pim-bidir-05.txt (Expires December, 2004).

Mbox - An efficient and secure connectivity solution

R. B. Drago, W. Polonini, A. S. Garcia
Federal University of Espirito Santo – LPRM
Fernando Ferrari, Avenue – Campus de Goiabeiras – CT VII – Vitória – ES – Brazil – CEP 29060-970.
{bonfa,anilton}@inf.ufes.br; wpolonini@ig.com.br

A. P. Carmo, R.S.Villaça
Unitera Technology Ltd.
Leitão da Silva 141, Avenue – Room 601 – Praia do Suá – Vitória – ES – Brazil – CEP 29052-110.
{alexandre, rodolfo}@unitera.com.br

***Abstract* - This paper proposes a new connectivity solution called Mbox that allows companies exchange data and resources from their local networks to remote sites, such as branch, retail and partner sites, in a low cost, safe, efficient and flexible way. In order to implement such connectivity, Mbox was developed based on free software, using the Internet for connecting LANs and using ADSL to access the Internet.**

I. INTRODUCTION

Private networks provide important business data communication between companies, their clients and partners that are usually spread over a larger geographic area. Such networks should allow all the users to access net data and resources as they were in a LAN (Local Area Network), providing a reliable connectivity for all the users and protecting the companies' data and resources. Integrity, authenticity and privacy on data exchange can be achieved by using a VPN (Virtual Private Network) while a secure net access can be provided through firewalls and proxies.

This work proposes a new connectivity solution called Mbox (Management box) that allows companies exchange data and resources from their local networks to remote sites, such as branch, retail and partner sites, in a low cost, safe, efficient and flexible way. In order to implement such connectivity, Mbox was developed based on free software, using the Internet for connecting LANs and using ADSL (Asymmetric Digital Subscriber Line) to access the Internet.

II. HOW PRIVATE NETWORKS ARE IMPLEMENTED

Earlier, private networks were only implemented by service providers through point-to-point and circuit-switched links. Although both cases provide high availability, security and reliability are not guaranteed. Besides that they represent a high cost solution, once companies must pay for expensive links [1].

Nowadays, companies can use VPNs to transfer private data between remote sites through the Internet [1]. Service providers offer a fast Internet access by ADSL technology [2], using IP (Internet Protocol) addresses and telephone lines. These facilities allow data transmission through VPN gateways that encapsulate data packets in order to keep their privacy, authenticity and integrity during transmission. Once VPN gateways use the Internet and work as firewall, it is possible to implement an efficient private network more safe and cheaper than networks based on dedicated links. Fig. 1 illustrates a system using VPNs.

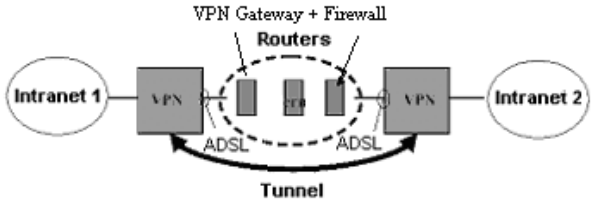

Fig. 1. A virtual private network illustration. [1]

There are already hardware and software solutions that implement the system shown in Fig. 1. However, these solutions only work in two ways: with fixed IP addresses for Internet access, which rise implementation costs; or with dynamic IP address and manual reconfiguration of the VPNs whenever the service provider changes the VPN gateway IP address, which reduces system availability and usability.

The solution proposed in this work implements the system in Fig. 1 using dynamic IP address and automatic VPNs reconfiguration. Net reconfigurations occur in a transparent way without users noticing the changes made by the service providers. Also a firewall is added to each VPN gateway implementation, in order to avoid attacks from the Internet.

III. MBOX – A CONNECTIVITY SOLUTION

A simplified architecture using Mbox solution is shown in Fig. 2. The system is composed by some Mboxes linked through VPNs. Each Mbox is a VPN gateway of the companies LANs.

In Fig. 2, Mbox2 and Mbox3 are the VPN gateways for the nets being linked. Internet access is done through ADSL using dynamic IP address. Considering Mbox2 and Mbox3 as two remote sites of the same company, the VPN between these sites should always be online, which means that reconfiguration must be done automatically whenever needed. The NOC Mbox – Zeus allows a manual connection with any other Mbox for remote support on clients' networks. The Mbox1 is an essential equipment for the system works, having a fixed IP address and a dedicated link to connect to the Internet. It works as a dynamic security DNS server that must map all the others Mbox names to their IP addresses. Whenever the IP addresses are changed by the ADSL connection, each Mbox detects its new IP address and informs the

Mbox1 using the DNSSEC (DNS security) protocol [3]. The VPNs will be reconfigured automatically between any pair of Mboxes whenever one of the VPN gateways has its IP address changed.

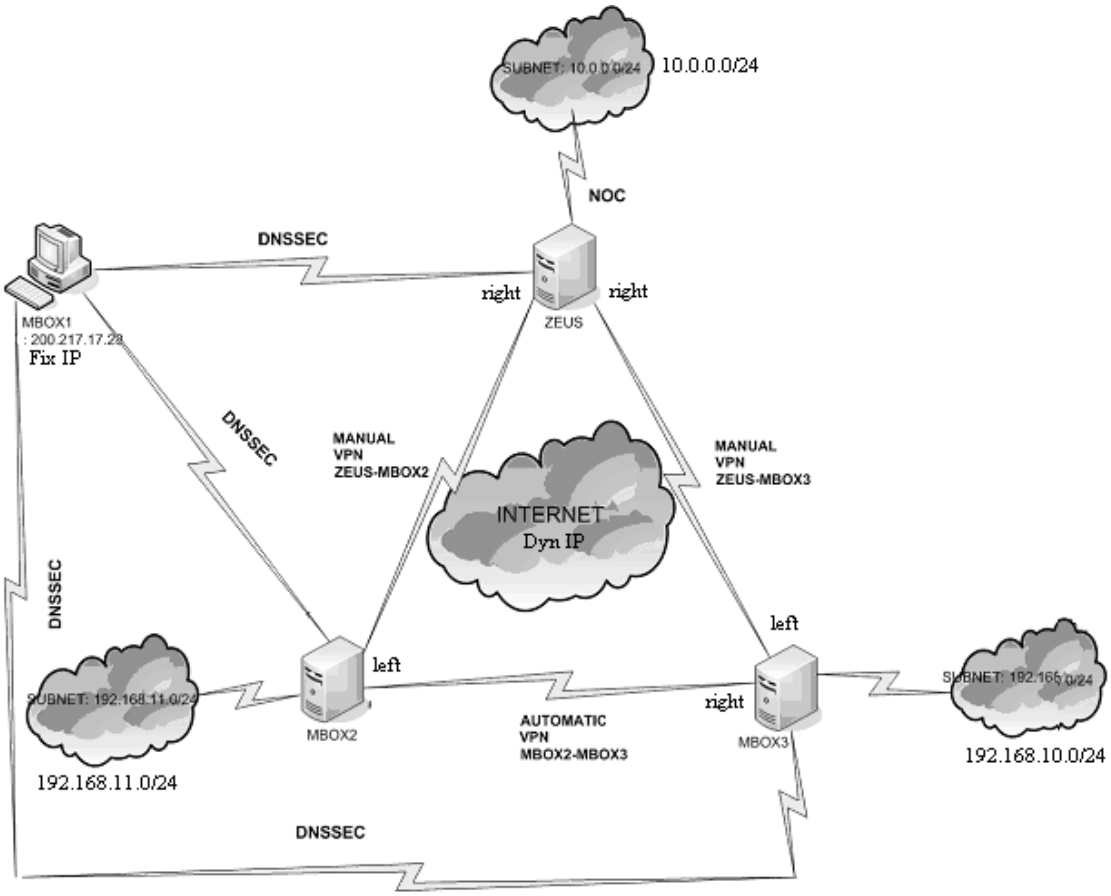

Fig. 2. A simplified architecture based on Mbox.

The algorithm used to solve the dynamic IP problem and automatic reconnection, when link fail, folow this steps: check if ADSL is internet connected with a valid IP address; check if ADSL is authenticated by Internet Service Provider; check if Mbox1 is available; check the new IP address and compares it with the old one; if they are different, the new IP address is sent to Mbox1; check IP addresses of the Mboxes having VPNs to restore; finding differences, reconfigure IPSec files at Linux (the Mbox operating system) and restart sessions. Fig. 3 shows this algorithm in a flowchart style.

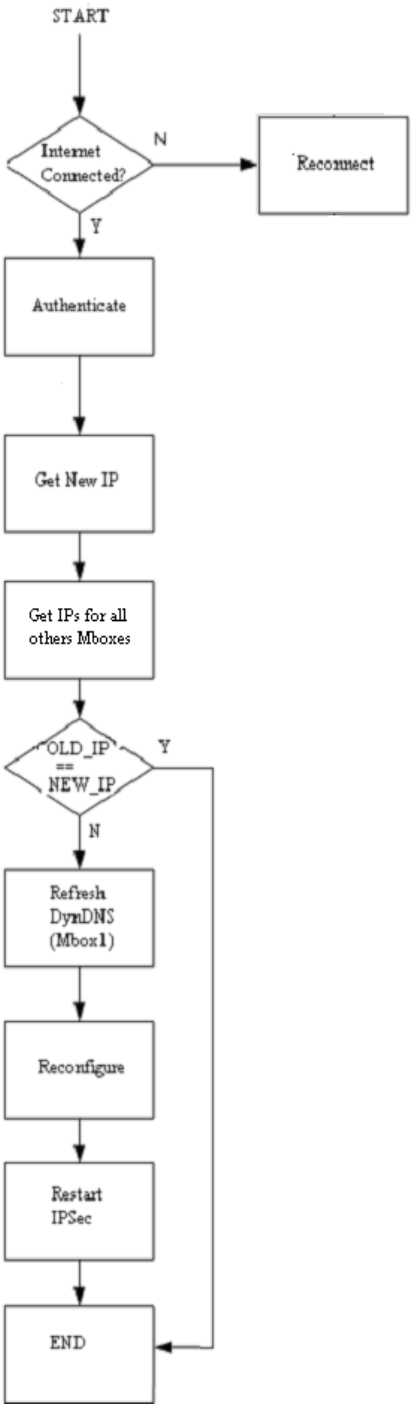

.Fig. 3 – Mbox reconfigure and reconnect algorithm

IV. Components of the Mbox solution

The Mbox is a PC running an operational system based on Linux Red Hat 8. The basic components and their usage can be seen in Table I.

TABLE I
COMPONENTS OF THE MBOX

Component	Usage
Linux FreeS/WAN	VPNs using the IP Security Protocol (IPSec) [4]
BIND 9.2	DYNDNS and DNSSEC
Velox Telemar	ADSL connection
Bastille	Operational system security
Tripwire	File system integrity
IPTables	Packet filter [5]
Squid	Webproxy
PSAD	Port Scanner Attack Detector
Logcheck	Log analyzer
Sendmail	Mail server
Servelets and JSP	Graphic interface for Mbox configuration

V. Tests and Advantages

Mbox is already running in some companies such as metallurgical industries, tourism and educational institutions, located in the metropolitan region of Vitória – ES – Brazil.

All the Mboxes are monitored 24x7, running at the NOC (Network Operations Center) installed at the company that developed and provides the Mbox service. During a five months period of measurements, the system has been out 25 times/month, in the average. For all the times, the system did the reconfiguration automatically. The reconfiguration timing for IP changing done by the service provider usually takes about 2 to 4 minutes.

Mboxes are a good solution for connectivity, once it is safe, flexible and represents a low cost system, becoming also a good choice for small companies. Besides that, it allows remote monitoring and support, reducing costs for keeping data communication between companies, their clients and partners even if they are located over a larger geographic area.

Measurements of this solution were made using Nagios[6] software and, as a mean result, the system (VPN using ADSL with dynamic IP and Mbox) presents 95% of availability. Fig. 4. shows a 8 (eight) day monitoring result on April, 2004.

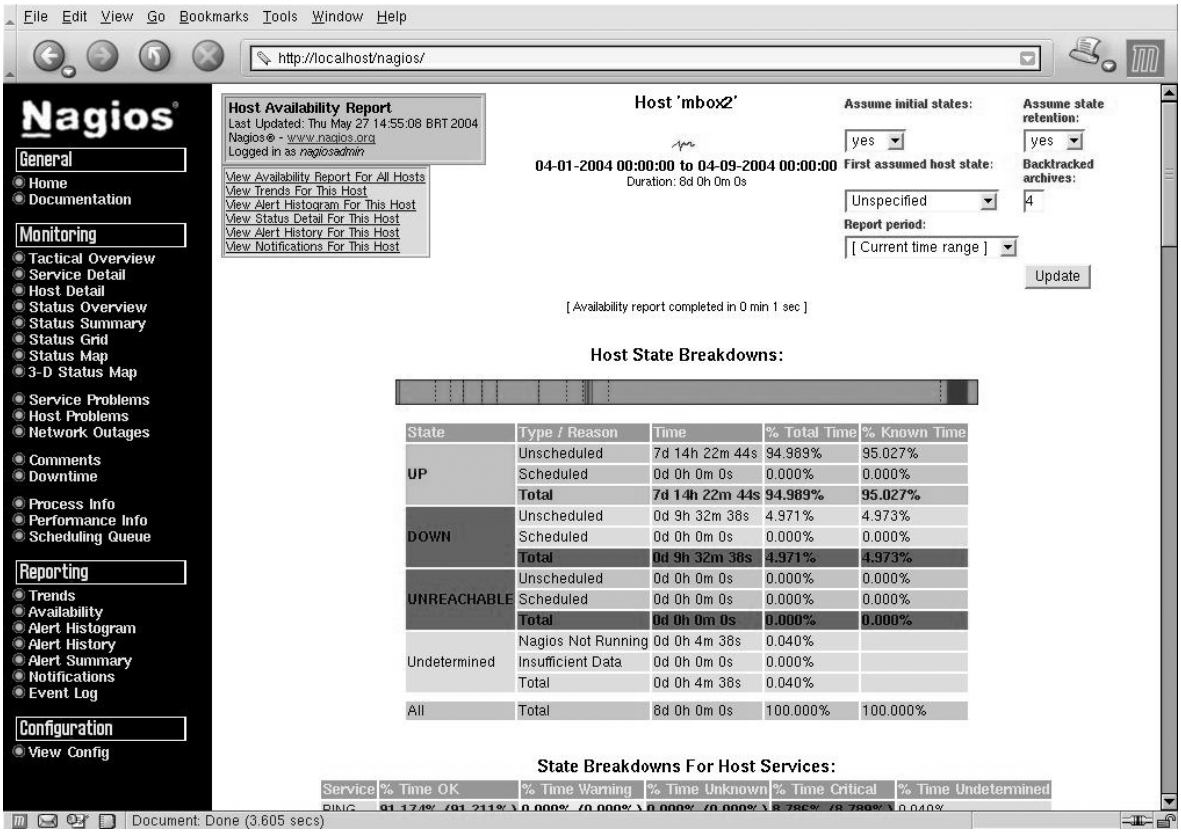

Fig. 5 – 8 (eight) day availability of an Mbox using Nagios

To make easy the Mbox software and hardware components configuration, a graphical inteface was developed using Java and web-interface. This interface lets the user of Mbox configure all the features actually available: IPSec and VPN connections, HTTP (Hyper Text Transfer protocol) and FTP (File Transfer Protocol) Proxy, TCP and UDP PortScan detector, IDS (Intrusion Detection System), email addresses to send reports, Firewall Rules, System Name and DNS clients.

In this interface LAN adapters can also be configured, and, if the network card is presented on the hardware compatibility list of Mbox it will be automatically detected and installed on Linux system. Fig. 6 shows an example of this interface.

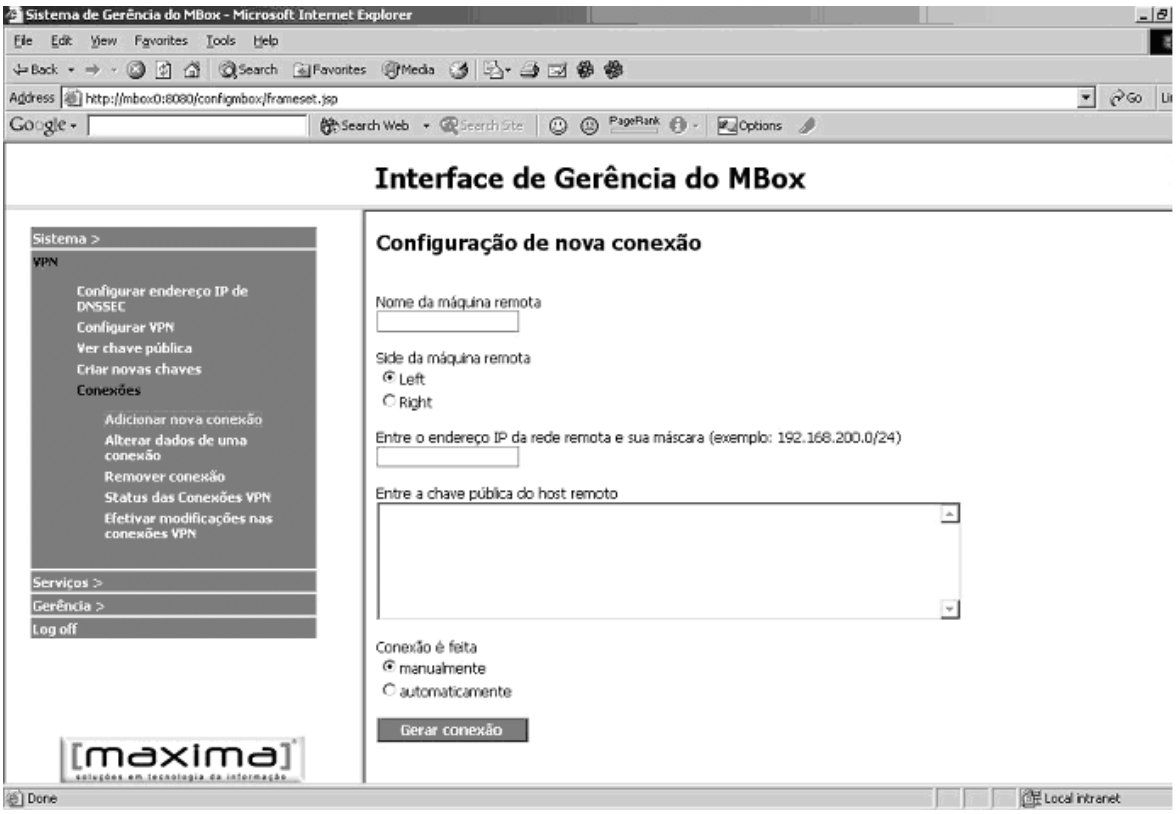

Fig. 6 – New VPN connection (Mbox interface configuration).

VI. NOC

Looking forward the integration of all management activities in a unique environment which is able to produce cost reductions and to be as flexible as possible, Mbox can be used as a tool to help IT (Information Technology) management integrated in a remote NOC.

The NOC can be composed of a central network management server and a database that keeps historical statistics about the networks managed. It can be web-accessed safely, based on the concept of virtual private networks (VPN). The other elements involved in NOC are an event and information database containing fault and performance data collected through SNMP (Simple Network Management Protocol) and a management server, located in each network monitored by NOC.

Mbox can be used on NOC as a low cost connectivity hardware and software platform to connects NOC to the managed networks. MBOX monitors managed objects, stores data information collected at its Local Database, generates events (traps) for the NOC operators, communicates with NOC to store data at the historical database and relates the events generated in order to try to find and anticipate fault and performance problems;

This work is already in progress as presented in [7]. and has presented encouraging results..

VI. CONCLUSIONS

The main advantages of using the Mbox solution instead of using other alternatives are:

1. Customized scalability, since the user can choose which features he wants, removing the others or, implement new services;
2. Free-software based, giving the product a zero-cost software solution;
3. Low hardware requirements;
4. Brazillian support and development, for Brazillian users

The availability obtained in this 6 (six) months of experience is satisfactory for non-critical applications, ideal for low and medium size offices such as medical clinics, tourism agencies, chemical laboratories, and others.

The Linux Operational System gives to the system the ability to be applied in a very large set of solutions in network management, such as remote monitoring of hardware elements, SNMP Proxy gateways and a Remote NOC.

As the next step, a low cost hardware solution is going to be tested to place Mbox into an inexpensive, robust and little dimensions hardware appliance.

REFERENCES

1 A White Paper by NetScreen Technologies, Inc., “Deploying Scalable, Secure, Dynamic Virtual Private Networks”, May 2003.

2 Mark Peden, Gavin Young, “From voice-band modems to DSL technologies”, International Journal of Network Management,2001,11:265-276.

3 Giuseppe Ateniese, Stefan Mangard, “A New Approach to DNS Security (DNSSEC)”.

4 Eli Herscovitz, “Secure Virtual Private Networks: The Future of Data Communications”, International Journal of Network Management,1999,9:213-220.

5 Khalid Al-Tawil, Ibrahim Al-Kaltham, “Evaluation and Testing of Internet Firewalls”, International Journal of Network Management, 1999.

6 Galstad, Ethan. Nagios. Available at http://www.nagios.org/. Acessed at June 20, 2004.

7 Villaça, Rodolfo. Et al. A Web-Based Pro-Active Fault and Performance Network Management Architecture. 11th International Conference on Telecommunications. August, 2004. Fortaleza:CE, Brazil.

TDMoIP over Ethernet Backbones

Tarcisio Bruneli Pilati
Universidade Presbiteriana Mackenzie
Tarcisio.pilati@siemens.com - 11 81195530

Wagner Luiz Zucchi
Universidade Presbiteriana Mackenzie
wzucchi@mackenzie.com.br - 11 32368711

Abstract – **This article analyses the transport of TDM channels over packet switching networks in a transparent way. Schemes for Circuit Emulation Services over IP Networks are studied and a practical experiment was built in order to show that is possible to obtain proper QoS levels to TDM traffic with fine-tuning of the network and suitable prioritization methods.**

Index Terms – **Circuit Emulation Service, Quality of Service, Metro Ethernet, TDMoIP.**

I. INTRODUCTION

As an alternative to deploy NGN (Next Generation Networks), mainly aiming to use legacy networks, new technologies and network architectures have been developed to transport, in a transparent way, the traffic from TDM (Time Division Multiplex) circuits throughout a packet switching network. These new technologies provide services convergence easier to deploy than the typical NGN solution, transporting in a transparent way any flow of bits and any kind of signaling, assuring all the capacities of the native network. One of the main methods to deploy this kind of service is the **TDMoIP** (TDM over IP) [1], based on the **PWE3** (Pseudo Wire Emulation Edge to Edge) recommendations and requirements [2] [3].

The proposal of this work is to analyze the **QoS** (Quality of Service) parameters regarding TDM circuit emulation services over IP in backbones deployed through Ethernet links. It was analyzed:

- The trade-off between packetization delay and overhead;
- The QoS parameters [4] regarding TDMoIP in Ethernet backbones;
  - End-to-end delay
  - Throughput
  - Jitter
  - Packet Loss
- The necessity and performance of the QoS mechanism;
- A model in order to estimate the end-to-end delay;
- The impact of the strict priority scheduling mechanism upon the applications using the network

To do such analyses it has been proposed a method in order to simulate the TDMoIP traffic, based on benchmark softwares: Netperf [5] and Iperf [6], configured to faithfully represent the TDMoIP encapsulation premises. These softwares enable the network performance analyses by measuring the QoS parameters. The payload size effect was analyzed in order to find the better compromise between bandwidth and encapsulation delay.

A specific scenario was proposed based on **MAN** (Metropolitan Area Network) backbones [7], where the frames were switched by real Ethernet switches based on the MAC Address. The simulated TDMoIP traffic crosses the network competing for bandwidth with traffic from other applications. TDMoIP and competing traffics were simulated and rigorously controlled by data protocol analyzers (Acterna DA-320)[8]. A traffic prioritization scheme, acting at the link layer, was set up in order to prioritize the TDM circuit emulation service. The QoS parameters were evaluated with the presence and absence of a QoS mechanism, and in the presence and absence of traffic congestion, allowing the performance study of the QoS mechanism method. The proposed method, based on DiffServ Architecture [9] and IEEE 802.1P priority tags, established a strict priority queuing mechanism [10]. It was also analyzed the possibility to provide QoS over-dimensioning the backbone links.

II. SIMULATION AND TEST PLATFORM

Figure 1 shows the basic lab scenario adopted during the experimental tests, including the devices used to generate (emulate) and analyze the TDMoIP traffic. This simulation and test platform aimed to verify the performance analyses of the QoS mechanism acting at the link layer (Ethernet).

The Ethernet Switches (Cisco Catalyst 2900XL) were directly connected via an Ethernet trunk set up to IEEE 802.1Q standard (VLAN Tagging); representing a Metro Ethernet link carrying data through dedicated optical fiber link between the switches. In a Metro Ethernet network it would be possible to deploy high-speed links of 100Mbps, 1Gbps or 10Gbps [7]. The Ethernet Switches used for the present work can have their trunk speed set to 10Mbps or 100Mbps. They also allow classification and strict priority queuing (*Priority Queuing*) [11]. Initially the trunk was set up to 10Mbps and the access ports to 100Mbps, aiming to reproduce a bottleneck condition and verify the QoS mechanism performance. The ports receiving TDMoIP traffic was classified as high priority, so its traffic was forwarded to the high priority output queue of the trunk. Afterwards, the trunk was also set up to 100Mbps and

all the tests were repeated in order to analyze the over-dimensioning condition.

The devices illustrated as A, B, E and F at figure 1, are PCs (Personal Computers) running benchmark softwares. The software HP NETPERF (Network Performance Benchmark) [5], developed by *Information Networks Division* of *Hewlett Packard*, was used in its release 2.2 for OPEN BSD operational system. The software IPERF [6], developed by National Laboratory for Applied Network Research (NLARN), was used in its release 1.7.0 for MS Windows 2000.

The device **A - HP Netperf 1 or Iperf 1 (Client)**, simulates (emulates) the TDMoIP traffic. The device **E - HP Netperf 2 or Iperf 2 (Server)** receives and analyses the QoS Parameters of the simulated traffic. Devices **A** and **E** works in a client to server model, in a way that **A** (client) generates the data to be analyzed at **E** (server). The benchmark software at the PC client is able to generate traffic in a configurable and controlled way, with throughput and stack of protocols equivalent to the TDMoIP adaptors (TDMoIP PE – Provider Edge) [1]. It was used IPERF to analyze jitter, packet loss and throughput and the HP NETPERF to analyze the End-to-end delay. The Iperf running in the server mode provides one statistic per second of the effective throughput received at the destination, packet loss (absolute and percentage) and jitter. The HP Netperf in the client mode provides, when running the UDP_RR (UDP *Request Response*) test type, the statistics of the number of command-response transactions (round-trip transactions) per second, allowing to calculate the mean end-to-end delay. Both benchmark applications have the mandatory characteristics to simulate a faithful TDMoIP traffic:

- Generation of traffic in a constant and configurable rate (in Kbps);
- Option of choosing the transport layer protocol (UDP or TCP) - just UDP is used for TDMoIP;
- Configuration of the buffer size (segment size) between the application and transport layers, allowing the simulation of different TDMoIP payload sizes;
- IP protocol at the network layer, allowing the configuration of the destination IP Address;
- Ethernet protocol at the link layer;
- Configuration of the UDP or TCP port number, allowing many test simultaneously, each one with its own settings, generating independent and different flows;
- Configuration of the test duration;
- Generation of an output log, recording each tests statistics;

The devices **B** (Iperf 3) and **F** (Iperf 4) have the function of simulating (emulating) a background traffic that competes with the TDMoIP one. This competing traffic (non TDMoIP), classified at the respective switches access ports as best effort (non prioritary), represents the remaining applications using the same backbone, as Internet, e-mail, file transfer etc. This way of simulating the background traffic is configurable, flexible, with predictable characteristics and easy to be monitored. It was important to guarantee that the prioritary TDMoIP traffic really competed with the background traffic load considered for each test.

The device **C** (DominoLAN DA-320) [8] is a data protocol analyzer. It is able to monitor, capture, analyze (including protocol decoding) or generate LAN traffic in real time. Its main function was the monitoration of the traffic generated by the benchmark softwares Iperf and HP Netperf, aiming to validate the TDMoIP traffic premises. It was also used to consolidate some statistics collected during the tests.

Different combinations of interest traffic load (TDMoIP) versus background traffic load with or without prioritization of the interest one, and with or without over-dimensioning, were simulated and had their respective QoS parameters measured at the destination after being transported by the Ethernet switches. Each load and prioritization scenario was repeated six times to analyze the results collected for the six different payload sizes considered in this work. For each different traffic and backbone scenario, a 2 minutes long test was done, collecting one statistic per second (120 values per test)

The TDMoIP encapsulation mechanism cannot guarantee by itself the quality of the TDM over IP circuit emulation services. It clearly depends on the QoS provided by the PSN [3].

III. ANALYSES AND RESULTS

- **Trade-off between packetization delay and overhead**

A suitable choice of the TDMoIP Payload size can lead to an optimum trade-off between packetization delay and overhead. Such payload, based on N payloads with the AAL1 format [12], is a multiple of 48 octets, varying among 1 and 30 sub-frames of 48 octets [1]. Each sub-frame uses at least one octet as AAL1 overhead (AAL1 non pointer format), resulting in 47 octets really useful to transport the original TDM data.

Table 2 – *Overhead* versus Packeting delay for different TDMoIP payload sizes considering the transport of an entire E1 link (2Mbps TDM stream)

N (Nº of AAL1 payloads)	Nº of octets with original TDM information	Total Nº of octets in the headers	Total Nº of octets in the Ethernet Frames	Overhead	Packetization Delay (ms) considering one entire E1 link (2Mbps)
1	47	63	110	134,04%	0,18
4	188	66	254	33,51%	0,73
8	376	70	446	16,76%	1,47
16	752	78	830	8,38%	2,94
24	1128	86	1214	5,59%	4,41
30	1410	92	1502	4,47%	5,51

Table 1 – Headers involved in the TDMoIP stack of protocols. N is the number of sub-frame with 48 octets that compose the configurable TDMoIP Payload.

AAL1 Header (inside each sub-frame of 48 octets of the payload)	N x 1 octet
TDMoIP Control Word	4 octets
RTP	12 octets
UDP	8 octets
IP	20 octets
Ethernet	18 octets

Table 1 shows the headers involved in the complete stack of protocols used during the experiments. If a large payload size directly increases the packetization delay it also drastically optimize the network bandwidth, with a very lower overhead. This choice, as in the CESoATM (Circuit Emulation Services over ATM), depends on the desired performance to be offered to the application to be transported [13]. The table 2 shows the maximum and minimum overhead and delay and also some interesting values between these two boundaries.

For N > 8 the overhead starts to become acceptable, lower than 17%, while the packetization delay remains acceptable, under 6 ms (i.e. the packetization delay for VoATM). These numbers are interesting even if compared with packetization delay and overhead numbers for VoIP (Voice over IP) [19].

- **Throughput and Packet loss**

TDMoIP uses UDP at the Transport layer. As UDP does not provide any flow control, the application layer is able to send data at the rate it wishes even if the data is being discarded. So, it is important to consider as throughput only the data rate effectively received by the destination device [14].

The proposed QoS mechanism, based on IEEE 802.1P, establishing a strict priority queuing, demonstrated to be efficient and easy to deploy. It was experimentally pointed, as showed by the results in figures 1 and 2, that the prioritization method has assured the convenient transport of all the TDMoIP frames offered to the network, assuring the necessary throughput and the zero packet loss, even with the links permanently congested. In figure 1, the losses plotted are due to the high overhead caused by the short TDMoIP payload sizes that generates bandwidth saturation, even with no competing traffic. The results for the experiments considering no competing traffic (only TDMoIP traffic in the backbone) and without QoS mechanism are the same illustrated by figure 1. Here, both figures consider the mean losses.

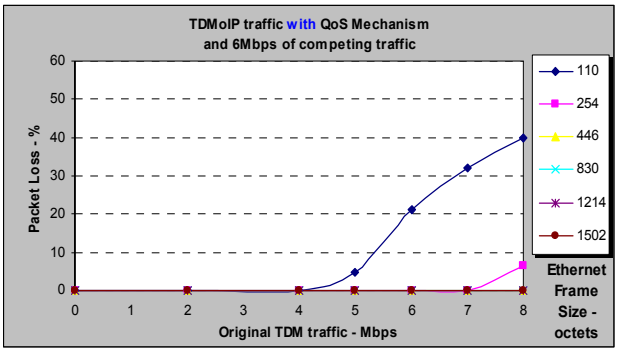

Figure 2 – Pack Loss and original offered TDM Traffic, with priority queuing and competing traffic scenarios of a 1Mbps, 2Mbps, 4Mbps or 6Mbps. The lines are shown with the same top-down order of the legend.

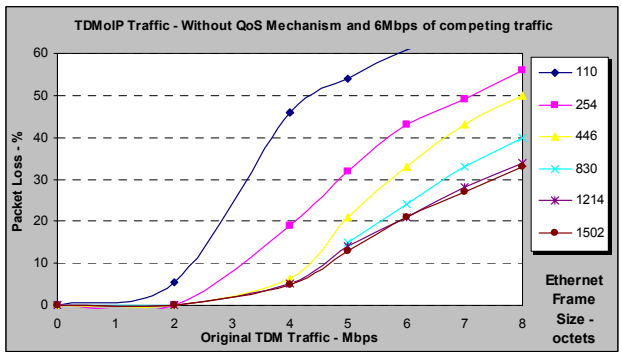

Figure 3 – Packet loss versus original offered TDM traffic, without QoS mechanism and with 6Mbps of competing traffic. The lines are shown with the same top-down order of the legend.

- **Jitter**

The worst jitter peaks collected during the experiments showed values lower than 10ms when deploying the QoS mechanism, and such values do not compromise most of the potential TDMoIP applications [15] [16]. Figures 3 and 4 compares jitter with and without QoS mechanism, for the heaviest traffic load condition tested.

Each plotted value represents the worst value in a 120 seconds long test with one jitter statistic result provided per second. So, it was considered the worst jitter result (and not the mean value) among the 120 ones.

Here, one more time the QoS mechanism was important to guarantee the QoS parameters of the TDM circuit emulation services over IP.

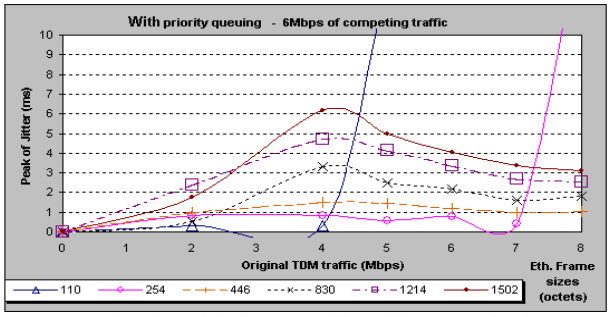

Figure 4 – Jitter for original TDM traffic, with QoS mechanism and with 6Mbps of competing traffic.

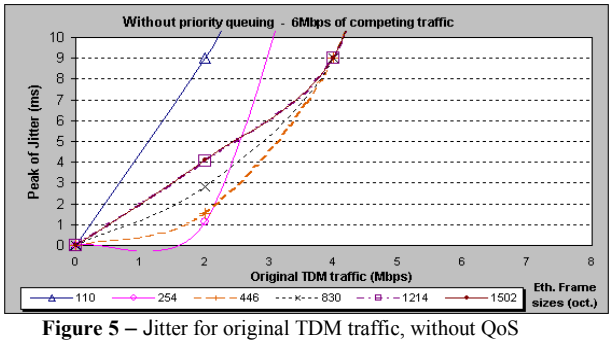

Figure 5 – Jitter for original TDM traffic, without QoS mechanism and with 6Mbps of competing traffic.

- **End-to-end Delay**

The proposed model, that aims to estimate the end-to-end delay (D_{ee}) in the adopted backbone. When submitted to experimental tests, using HP Netperf to generate the traffic and analyze the end-to-end delay of the proposed backbone (figure 1), demonstrated a low error percentage (around 0,5 %), showing to be reliable.

$$D_{ee} = \Sigma D_{serial.} + \Sigma D_{process.} + \Sigma D_{comut.} + [(\beta x \Sigma D_{queuing}) + D_{packet.}] \quad (1)$$

The estimated D_{ee}, considering different backbone configurations and the previously studied payload sizes, are summarized in figure 6, where it was considered packetization (Dpacket) and queuing delays ($D_{queuing}$), both transformed into fixed delays due to the implementation of the de-jitter buffer [17] [16].

When the queuing delay ($D_{queuing}$) is known for each switch (or queuing point in the backbone) but not for the overall backbone, its necessary to adopt a coefficient (β) that best represents the probability of one packet experiments all the queuing delays considered. In VoIP networks it is adopted a value of β between 1 and 2 (usually 1,5) [18]. The study of β was not the purpose of this paper and for figure 6 it was adopted β=1 as the overall jitter of the lab backbone was experimentally measured and showed to be always lower than 10ms.

For the small frames (up to 254 octets), the speed of the Ethernet trunks did not influence significantly the end-to-end delay, resulting in values with differences around 0,5ms. The packetization and serialization delays are relevant mainly for large frame sizes and trunks with lower speeds. Even for a TDMoIP adaptor with traffic demand lower than 10Mbps, it would be interesting to consider access ports of 100Mbps in such device, as it would not significantly increase the costs of the local access to the switch and the serialization delays would decrease (i.e. 2ms for the 1502 octets frames).

IV. CONCLUSIONS

The QoS mechanism proposed, based on IEEE 802.1P, deploying a strict prioritization of the interest traffic (TDMoIP) showed to be efficient and easy to deploy (what is a premise for TDMoIP). The tests showed the necessity of the QoS mechanism when the critical traffic experiments congestion. However, when the over-dimensioning was deployed and there was no competition for bandwidth, the QoS mechanism was not necessary. It can be an alternative in order to achieve the desired QoS. With over-dimensioning the cost of the trunks would be higher but some interesting advantages would follow this solution: the remaining traffic (non prioritary) would experiment a better service and serialization delay would be lower.

The best choice of the TDMoIP payload size will be application dependent. The references [15] and [17] can provide a helpful guidance regarding such choice, as they provide boundaries for the QoS parameters related to different kind of traffic and services.

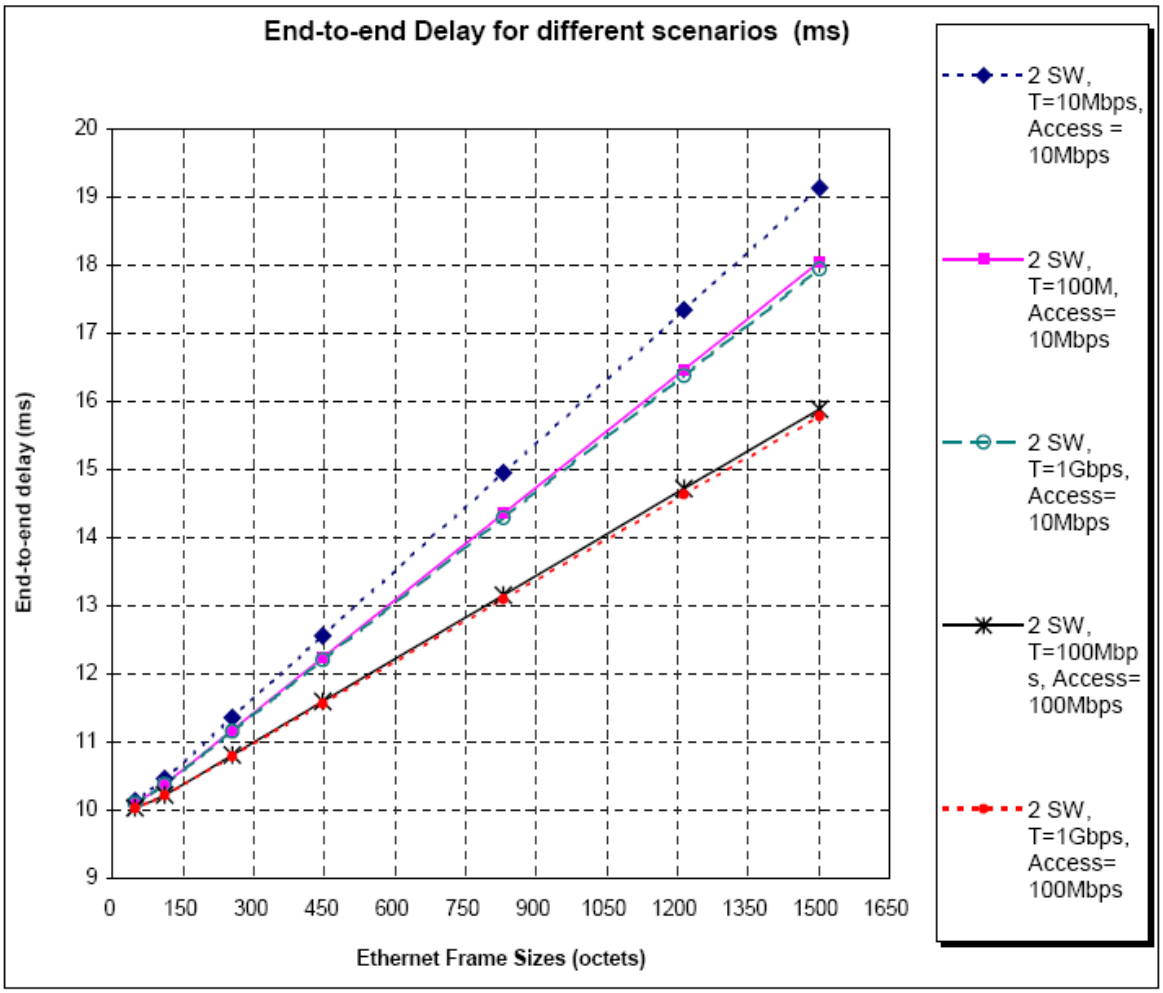

Figure 6. End-to-end delay parallel considering different payload sizes and scenarios. The lines are shown with the same top-down order of the legend.

REFERENCES

[1] Y. Stein et al., "*TDM over IP*" (draft-anavi-tdmoip-03.txt), work in progress, IETF *Internet-Draft*, PWE3 Working Group, February 2002.

[2] P. Pate et al., "*Framework for Pseudo Wire Emulation Edge to Edge* (PWE3)" (draft-ietf-pwe3-framework-00.txt), work in progress, IETF *Internet-Draft*, PWE3 Working Group, February 2002.

[3] XiPeng Xiao et al., "*Requirements for Pseudo Wire Emulation Edge to Edge (PWE3)*" (draft-ietf-pwe3-requirements-00.txt), work in progress, IETF *Internet-Draft*, PWE3 Working Group, February 2002.

[4] J. Gozdecki, A. Jajszczyk, R. Stankiewicz, "*Quality of Service Terminology in IP Networks*", IEEE Communications Magazine, pp. 153 to 159, March 2003.

[5] Hewlett-Packard, "*Netperf: A Network Performance Benchmark v2.0*", Information Network Division, Hewlett-Packard Company, February 1995. Available at: http://www.netperf.org/netperf/training/Netperf.html .

[6] M. Gates, A. Tirumala, "*Iperf User Docs*", National Laboratory for Applied Network Research, May 2002. Available at: http://issola.ncsa.uiuc.edu/Projects/Iperf/iperfdocs_1.6.html

[7] M. Whalley, D. Mohan, T. Madsen, L. Anderson, "Metro Ethernet Networks – A Technical Overview", white paper, Metro Ethernet Forum, May 2002.

[8] Wandel & Goltermann, "*DominoLAN Getting Started*", handbook, Wandel & Goltermann Inc (Acterna), February de 1996.

[9] S. Blake, "*An Architecture for Differentiated Services*", RFC 2475, IETF, December 1998.

[10] Cisco Systems,"*Catalyst 2950 Desktop Switch Software ConfigurationGuide*", chapter 13 – *Configuring QoS*. Cisco Systems, August 2002.

Available at: http://www.cisco.com/univercd/cc/td/doc/product/lan/cat2950/12111ea1/scg/scg2950.pdf

[11] Cisco Systems, "*Catalyst 2900 series XL Software Configuration Guide*", chapter 7 – *Configuring the Switch Ports*. Cisco Systems, Abril de 2001. Available at: http://www.cisco.com/univercd/cc/td/doc/product/lan/cat2900

[12] ITU-T Recommendation I.363.1 "*B-ISDN ATM Adaptation Layer specification: Type 1 AAL*", ITU-T, 1996.

[13] ATM Forum Technical Committee, "*Circuit Emulation Service Interoperability Specification*", af-vtoa-0078.000, ATM Forum, January 1997.

[14] J. F. Kurose, K. W. Ross, "Redes de Computadores e a Internet – Uma Nova Abordagem", chapter 6, Ed. Addison Wesley, 2003

[15] ETSI *Technical Report*, *"Telecommunication and Internet Protocol Harmonization over Networks (TIPHON); General Aspects of Quality of Service (QoS)*", TR 101329 v2.1.1 ETSI (*European Telecommunication Standardization Institute*), chapter 5 e 6, June 1999.

[16] R. Noro, "*Synchronization over Packet-Switching Networks: Theory and Applications*", Doctor Tesis, chapter 4 "Circuit Emulation over IP Networks", *Ecolé Polytechnique Federale de Lausanne*, Switzerland, 2000.

[17] [ETSI99] ETSI *Technical Report*, *"Telecommunication and Internet Protocol Harmonization over Networks (TIPHON); General Aspects of Quality of Service (QoS)*", TR 101329 v2.1.1 ETSI (*European Telecommunication Standardization Institute*), chapters 5 e 6, June 1999.

[18] Cisco Systems, "*Understanding Delay in Packet Voice Networks*", Cisco Systems, white paper, May 2003. Available at: http://www.cisco.com/

[19] D. Minoli, "Delivering Voice over IP Networks", Ed. Wiley, 2nd edition, 2002.

Implementation issues on HMM discriminative training for isolated word recognition

Amarildo Martins de Mattos
National Institute of Telecommunications - Inatel
P.O. Box 05 - 37540-000
Santa Rita do Sapucaí - MG - Brazil
amartins@inatel.br

Carlos Alberto Ynoguti
National Institute of Telecommunications - Inatel
P.O. Box 05 - 37540-000
Santa Rita do Sapucaí - MG - Brazil
ynoguti@inatel.br

***Abstract*— Traditionally, the Baum-Welch algorithm is used to train Hidden Markov Models (HMMs) for the task of speech recognition. It uses the Maximum Likelihood (ML) criterion that tries to maximize the probability of the correct model generate the training utterances. As an alternative one can use the Segmental GPD algorithm, which is based on the Minimum Classification Error criterion, that tries to directly minimize the recognition error. In this work, some implementation issues are investigated when using the Segmental GPD algorithm to train a small vocabulary, isolated word speech recognizer, based on continuous HMMs.**

***Index Terms*— Hidden Markov Models, isolated word recognition, discriminative training.**

I. INTRODUCTION

For the HMMs, the training algorithm is usually the Baum-Welch, which is based on the Maximum Likelihood criterion that maximizes the likelihood of a model, given a observation sequence.

As an alternative method, the Maximum Mutual Information (MMI) criterion can be used to train the models [1]. The main feature of the MMI criterion is that it enhances the difference between the competing models, therefore using the available training information in an optimized fashion. In other words, for a given sequence of acoustic observations X, the MMI criterion maximizes the likelihood of the model M_i (associated to X) and minimizes the likelihood of the concurrent models (M_j), therefore enhancing the discriminability between the models.

An algorithm that implements this method, and the one chosen for this work, is the Segmental Generalized Probabilistic Descent Algorithm (Segmental GPD) [2], [3]. This algorithm has a great similarity with the Back-Propagation algorithm, that is used to train a multilayer perceptron neural network [11].

The main goals of this work is to investigate the enhancement in word error rate when using the discriminative training and to investigate some implementation issues when this algorithm is used to train a continuous HMM for the task of isolated word recognition. Because of the great similarity of this algorithm with the Back-propagation algorithm, some issues like over-training, order of presentation of the training pairs are also investigated.

The results show that it possible to achieve a little improvement in the error rate when using the discriminative training.

II. THE SEGMENTAL GPD ALGORITHM

The main features of this algorithm are:

- It uses the Minimum Classification Error (MCE) criterion [3], [4], [5], in which the parameters re-estimation process is based on the minimization of the system's error rate. It is achieved by raising the probability of the correct model to generate the training utterance, and simultaneously lowering the probability of the concurrent models to generate the training utterance.
- The algorithm uses both the wrong and right answers to adjust the HMM parameters.
- The initialization can be done from a pre-trained HMM (for example using the Baum-Welch algorithm).

A. Implementation Steps

The basis of the Segmental GPD algorithm is the *classification cost function* [2], [6], [7], [8], [9], that represents a distance measure among the correct model and the concurrent ones. To calculate this function, a four step procedure is performed:

1) Define the discriminant function;
2) Define the classification error function for each training epoch;
3) Define the cost function that depends on the error function;
4) Define a new cost function based on the indicator function.

1) First step: Definition of the discriminant function: The discriminant function (DF) measures the probability of each model to generate the observation sequence X. In this work, the following form will be used for the DF:

$$g_k(X|\lambda_k) = \max_q g_k(X, q|\lambda_k) \tag{1}$$

where:

- q is a generic state sequence,
- λ_k is the HMM that models the kth word of the vocabulary,

- $g_k(X, q|\lambda_k) = \ln\{(P(X, q \mid \lambda_k))\}$,
- $P(X, q \mid \lambda_k)$ is the probability of generating the observation sequence X and the occurrence of the state sequence q, given the model λ_k.

These definitions are adequate for the HMMs, since the acoustic decoding process is based on the likelihood values, obtained from the state sequences q. Therefore, it's possible to define the probability of generating the observation sequence X given the model λ_k as:

$$P_k(X|\lambda_k) = \max_q P_k(X, q|\lambda_k) \tag{2}$$

For a HMM, the probability of generating the observation sequence X and the occurrence of the state sequence q, given the model λ_k can be calculated as:

$$P_k(X, q|\lambda_k) = \pi^k_{q_0} \prod_{t=1}^{T} a^k_{q_{t-1}q_t} b^k_{q_t}(x_t) \tag{3}$$

where:

- $\pi^k_{q_0}$ is the probability of the process to begin in state q_0,
- $a^k_{q_{t-1}q_t}$ is the probability of the occurrence of a transition from state q_{t-1} to q_t of the model λ_k,
- $b^k_{q_t}(x_t)$ is the probability of emission of symbol x_t in state q_t of the kth model.

Substituting (2) in (1) and taking the logarithm, the following definition for the discriminant function can be derived:

$$\begin{aligned} g_k(X|\lambda_k) &= \ln\{\max_q P_k(X, q|\lambda_k)\} \\ &= \ln\{P_k(X, \bar{q}|\lambda_k)\} \end{aligned} \tag{4}$$

where $\bar{q}$ is the optimal state sequence (maximum likelihood path), obtained from the Viterbi algorithm.

Using (3) it possible to rewrite (4) as:

$$g_k(X|\lambda_k) = \ln\{\pi^k_{\bar{q}_0}\} + \sum_{t=1}^{T} \ln\{a^k_{\bar{q}_{t-1}\bar{q}_t}\} + \sum_{t=1}^{T} \ln\{b^k_{\bar{q}_t}(x_t)\} \tag{5}$$

In other words, the discriminant function can be viewed as the log-probability of each HMM to generate the observation sequence X, passing through the optimum state sequence, given by the Viterbi algorithm.

2) Second step: Definition of the classification error function of each training epoch: This function is a measure of the difference among the probabilities of the correct model and the concurrent models to generate the observation sequence X. Now considering the discriminative function $g_j(X|\lambda_j)$ as the log-likelihood of the observation sequence X given the model λ_j of the jth word of the vocabulary, the classification error function of the word i is defined as [2], [3], [4], [5], [6]:

$$d_i(X|\Lambda) = \underbrace{-g_i(X|\lambda_i)}_{1} + \underbrace{\ln\left[\frac{1}{W-1}\sum_{j\neq i} e^{g_j(X|\lambda_j)\eta}\right]^{\frac{1}{\eta}}}_{2} \tag{6}$$

where:

- 1 is the probability of the correct model to generate the observation sequence X;
- 2 is the mean if the probabilities of the concurrent models to generate the observation sequence X;
- η is a normalization constant;
- W is the number of the words in the vocabulary.

It's interesting to note that if X corresponds to an utterance of the word i, the correct model will generate a discriminant function $g_i(X|\lambda_i)$, and the concurrent models will generate the concurrent discriminant functions $g_j(X|\lambda_j)$. The contribution of the concurrent models is introduced in the $d_i(X|\Lambda)$ measure in (6) with an opposite signal compared to the discriminant function $g_i(X|\lambda_i)$ of the correct model.

Observation: For an observation sequence X of the ith class:

- $d_i(X|\Lambda) < 0$ means that there was no classification error, that is, the probability of the correct model was greater than the mean of the probabilities of the concurrent models,
- but $d_i(X|\Lambda) > 0$ doesn't necessarily mean that there was a classification error.

3) Third step: Definition of the cost function that depends on the error function: In practice, the error function $d_i(X|\Lambda))$ spreads over a wide range of values. These extreme values can lead to numerical problems in the subsequent algorithm steps, so it becomes necessary to represent the error function within a more parsimonious interval. With these things in mind, one can define the cost function as:

$$l_i(X|\Lambda) = l_i(d_i(X|\Lambda)) = \frac{1}{1 + e^{-\gamma d_i(X|\Lambda)}} \tag{7}$$

As shown in Figure 1, the cost function allows a mapping of the error function (that has a very large dynamic range) over the $(0, 1)$ interval.

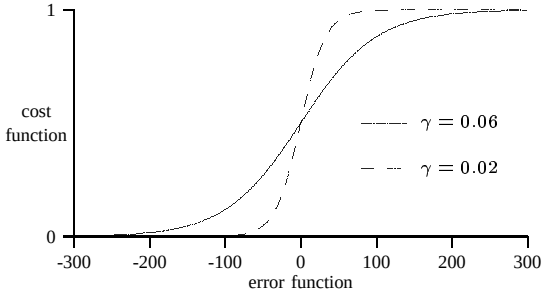

Fig. 1. Error function vs cost function.

The parameter γ is a constant that is used to avoid numerical problems when calculating the cost function.

4) Forth step: Definition of a new cost function based on the indicator function: This step is not necessary for isolated word speech recognition systems

In large vocabulary systems the word models are usually built from sub-word subunits such as phones or allophones. In these systems not all the words in the training set will be in the final vocabulary. Thats because in these cases the training is made for the sub-word models and not for the whole words.

However, as the discriminative training goal is to directly minimize the system's error rate, only the utterances corresponding to some word in the final vocabulary should be used. The indicator function, shown below is the responsible to verify whether some utterance corresponds or not to a word in the vocabulary:

$$I(X;W_k) = \begin{cases} 1, & X \in W_k \\ 0, & c.c. \end{cases} \quad (8)$$

where W_k is the portion of the training set that corresponds to the kth word of the vocabulary.

Therefore, it possible to generalize the cost function for the whole training set using both the function $l_i(X|\Lambda)$ and the indicator function $I(X;W_k)$, using the following expression:

$$l_i(X|\Lambda) = \sum_{k=1}^{W} l_k(X|\Lambda) I(X;W_k) \quad (9)$$

B. Parameters reestimation

In this algorithm, the HMMs parameters reestimation problem is mapped into an optimization problem based on cost minimization that, in this case, can be translated into the problem of directly minimizing the word error rate.

This minimization can be carried out using traditional optimization methods, such as the Descent Gradient Method, that adjusts the model parameters Λ in a recursive way, described as follows:

$$\Lambda_{n+1} = \Lambda_n - \varepsilon \nabla l(X_n|\Lambda_n) \quad (10)$$

where:

- Λ_n is the HMM set at iteration n;
- ε is the learning rate;
- $\nabla l(X_n|\Lambda_n)$ is the gradient of the cost function.

C. Application to the HMMs parameters reestimation task

The discriminative training algorithm for continuous HMMs and word models is based on Equation (10), and can be summarized in the following steps:

1) Initialization: The initial values of HMM parameters are in general obtained by the use of the Forward-Backward algorithm.

2) HMM parameters reestimation: The first step is to segment the training utterance using the Viterbi algorithm and calculate the cost function (7). After this, each of the HMM parameters is updated as follows:

Transition probabilities (a_{ij})

- For the model corresponding to the observation sequence:

$$\overline{a}_{kj}^i(n+1) = a_{kj}^i(n) + \varepsilon\gamma l_i(X;\Lambda)\{1 - l_i(X;\Lambda)\} \sum_{t=2}^{T} \delta(q_{t-1},k)\delta(q_t,j)\frac{1}{a_{kj}^i} \quad (11)$$

- For the concurrent models:

$$\overline{a}_{kj}^i(n+1) = a_{kj}^i(n) - \varepsilon\gamma l_i(X|\Lambda)\{1 - l_i(X|\Lambda)\} \frac{e^{g_p(X|\lambda_p)\eta}}{\sum_{j\neq i} e^{g_j(X|\lambda_j)\eta}} \sum_{t=2}^{T} \delta(q_{t-1},k)\delta(q_t,j)\frac{1}{a_{kj}^i} \quad (12)$$

Mixture coefficients c_{jm}^i

- For the model corresponding to the observation sequence:

$$\overline{c}_{jm}^i(n+1) = c_{jm}^i(n) + \varepsilon\gamma l_i(X;\Lambda)\{1 - l_i(X;\Lambda)\} \sum_{t=1}^{T} \delta(q_t,j)\frac{1}{b_j^i(x_t)} N(x_t;\mu_{jm}^i,W_{jm}^i) \quad (13)$$

- For the concurrent models:

$$\overline{c}_{jm}^i(n+1) = c_{jm}^i(n) - \varepsilon\gamma l_i(X;\Lambda) \{1 - l_i(X;\Lambda)\}\frac{e^{g_p(X|\lambda_p)\eta}}{\sum_{j\neq i} e^{g_j(X|\lambda_j)\eta}} \sum_{t=1}^{T} \delta(q_t,j)\frac{1}{b_j^i(x_t)} N(x_t;\mu_{jm}^i,W_{jm}^i) \quad (14)$$

Gaussians means μ_{jm}^i

- For the model corresponding to the observation sequence:

$$\overline{\mu}_{jml}^i(n+1) = \mu_{jml}^i(n) + \varepsilon\gamma l_i(X;\Lambda) \{1 - l_i(X;\Lambda)\} \sum_{t=1}^{T} \delta(q_t,j)\frac{1}{b_j^i(x_t)} N(x_t;\mu_{jm}^i,W_{jm}^i)\, c_{jm}^i \frac{(x_{tl} - \mu_{jml})}{\sigma_{jml}^2} \quad (15)$$

- For the concurrent models:

$$\overline{\mu}_{jml}^i(n+1) = \mu_{jml}^i(n) - \varepsilon\gamma l_i(X;\Lambda) \{1 - l_i(X;\Lambda)\}\frac{e^{g_p(X|\lambda_p)\eta}}{\sum_{j\neq i} e^{g_j(X|\lambda_j)\eta}} \sum_{t=1}^{T} \delta(q_t,j) \frac{1}{b_j^i(x_t)} N(x_t;\mu_{jm}^i,W_{jm}^i) c_{jm}^i \frac{(x_{tl} - \mu_{jml})}{\sigma_{jml}^2} \quad (16)$$

Gaussians standard deviations σ^i_{jm}

- For the model corresponding to the observation sequence:

$$\overline{\sigma}^i_{jml}(n+1) = \sigma^i_{jml}(n) + \varepsilon\gamma l_i(X;\Lambda) \{1 - l_i(X;\Lambda)\} \sum_{t=1}^{T} \delta(q_t, j) \frac{1}{b^i_j(x_t)} N(x_t; \mu^i_{jm}, W^i_{jm}) c^i_{jm} \frac{1}{\sigma_{jml}} \left\{ -1 + \left(\frac{x_{tl} - \mu_{jml}}{\sigma_{jml}} \right)^2 \right\} \quad (17)$$

- For the concurrent models:

$$\overline{\sigma}^i_{jml}(n+1) = \sigma^i_{jml}(n) - \varepsilon\gamma l_i(X;\Lambda) \{1 - l_i(X;\Lambda)\} \frac{e^{g_p(X|\lambda_p)\eta}}{\sum_{j \neq i} e^{g_j(X|\lambda_j)\eta}} \sum_{t=1}^{T} \delta(q_t, j) \frac{1}{b^i_j(x_t)} N(x_t; \mu^i_{jm}, W^i_{jm}) c^i_{jm} \frac{1}{\sigma_{jml}} \left\{ -1 + \left(\frac{x_{tl} - \mu_{jml}}{\sigma_{jml}} \right)^2 \right\} \quad (18)$$

Parameter normalization

The Segmental GPD algorithm does not guarantee that the reestimated parameters obey the total probability law (sum of probabilities equals to one). Therefore, after the parameters reestimation process, it's necessary normalize the transition probabilities and Gaussian mixture coefficients.

For the Gaussian variances there not such limitation, but there exists a numerical problem: when the values of these variances are too low, the system experiments numerical problems when the observation sequence vector is far from the mean. Therefore, it's important to limit the lower value of the Gaussian variances.

- Transition probabilities (a_{ij})

$$a^i_{kj} = \frac{\overline{a}^i_{kj}}{\sum_{k=1}^{Q} \overline{a}^i_{kj}}, \qquad k, j = 1, \ldots, Q \quad (19)$$

- Gaussians mixture coefficients (c^i_{jm})

$$c^i_{jm} = \frac{\overline{c}^i_{jm}}{\sum_{j=1}^{Q} \overline{c}^i_{jm}}, j = 1, \ldots, Q; m = 1, \ldots, M \quad (20)$$

- Gaussian variances (σ^2_{jmd})

$$\sigma^2_{jmd} \geq \varepsilon_2, d = 1, \ldots, D; m = 1, \ldots, M \quad (21)$$

where ε_2 is a small positive number.

3) End of training: Differently from the Baum-Welch algorithm, the Segmental GDP algorithm does not guarantee that the log-likelihood of the observation sequence X given the model λ_i always increase. There are two reasons for this fact: first, a large value of the learning rate ε can lead to divergence in the training process; secondly, as observed in neural networks training process, after a number of training epochs, the system becomes "addicted" to the training samples, and the word error rate for the validation set starts growing.

With this things in mind, the strategy used to determine the end of training was as follows:

- the system was trained during a number of epochs (say 100 epochs);
- after each epoch, a recognition test was performed in the validation set: if the word error rate is better than that obtained in the previous epochs, then that set of parameters is recorded as the final one.

In practice, this procedure saves the set of parameters values that achieved the best performance for the validation set, through the 100 training epochs.

Formally, the database should be broken in three parts: training, validation and testing subsets. However, due to the database's size, the test set was used as the validation set. Although it's not a correct procedure, the conclusions still hold.

III. Experimental Setup

In this section, the experimental setup used in the tests is described.

A. Databases

The system was evaluated using two distinct databases, both containing only utterances of isolated words. In this work they'll be referenced as *Small Database* and *Large Database*, and will be described below:

1) Small Database: This database contains 10 distinct words, corresponding to the name of some common Windows applications, as shown in Table I:

TABLE I
WORDS OF THE FIRST VOCABULARY (WINDOWS APPLICATIONS).

calculadora	excel
explorer	freecell
internet	matlab
notepad	paint
powerpoint	word

The words were spoken by 12 speakers (10 male and 2 female), and each speaker pronounced all the 10 words three times. Therefore, there is a total of 36 utterances for each word, and the database has a total of 360 utterances. The utterances of 9 male and 1 female speakers were selected for training, and the utterances of the two remaining speakers were used for the tests.

The recordings were performed in an office environment, with low noise level, using a good quality directional microphone (SHURE SM-58), and a Sound Blaster AWE 64 sound card, at a 11025 Hz sampling rate and quantized using 16 bits. The data were stored in Windows PCM file format.

2) Large Database: This database was developed by José Antônio Martins, [10], who kindly allowed its use in this work. It consists of 50 words, organized in six groups, as follows:

- **Digits**: zero, um, dois, três, quatro, cinco, seis, sete, oito, nove, meia;

- **Commands**: sim, não, terminar, repetir, continuar, voltar, avançar, certo, errado, opções, ajuda;
- **Regions**: norte,nordeste, sul, sudeste, centro-oeste;
- **Signs**: áries, touro, câncer, leão, gêmeos, virgem, libra, escorpião, capricórnio, sagitário, aquário, peixes;
- **Options**: horóscopo, dólar, real, tempo, esportes;
- **Organizations**: departamento, divisão, seção, coordenação, imagem, voz.

For each word, three utterances were recorded for each of the 43 male and 26 female speakers. Therefore, there is a total of $50 \times 69 \times 3 = 10350$ utterances in this database. The utterances of 22 male and 13 female speakers were used to train the system, while the remaining ones were used for the tests.

The recordings were also made in an office environment, but with a different setup: an Ariel DSP-16 *Data Acquisition Processor* sound card was used, and the recordings were made at a sampling rate of 8 kHz and quantized at 16 bits per sample. Prior to sampling, the analog signal was pre-filtered in the range of 100 Hz to 3400 Hz.

B. Training and recognition systems

As mentioned above, a locally developed, continuous density, HMM system was used. It uses whole words as recognition units, and was initially trained using the Forward Backward algorithm. Recognition was performed using the Viterbi algorithm. Next, more details about the system will be presented.

1) HMM model for the vocabulary words: A straight (*left-right*) model, with number of states equal to the number of phones plus 3 states was used for each word, as shown in Figure 2. For each state, a 3 Gaussian mixture was considered.

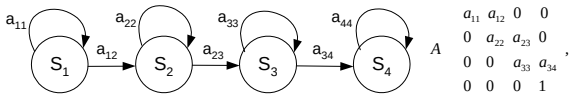

Fig. 2. straight left-to-right model used in the system.

2) Acoustic parameters: As acoustic vectors, 12 mel-cepstrum parameters were used. They were calculated using 20ms windows, with 50% overlap. Prior to parameterization, the voice signal was submitted to a pre-emphasis filter $H(z) = 1 - 0,95z^{-1}$, and windowed by a Hamming window.

3) Training module: The training is performed in two steps:

1) Initial training using the Forward-Backward algorithm;
2) discriminative training using the Segmental GPD algorithm.

For each of the steps a C++ routine was implemented.

4) Recognition module: For the recognition module, the Viterbi algorithm was implemented instead of the exact Forward algorithm, because of its better efficiency in computing time.

IV. Implementation issues for the Segmental GPD algorithm

Numerical problems are common when dealing with continuous densities HMMs. Discriminative training of these structures add more numerical problems to be solved. In fact, it was very difficult to find a combination of training parameters that lead to good results: after fixing all the bugs in the programs, several days were spent looking for more bugs when the problem was with the parameters values.

Also, due to the high similarity between the Segmental GPD algorithm and the Backpropagation algorithm, it seems reasonable to investigate some problems that are commonly associate with the last one, namely the choice of the learning rate, overtraining effect, and the need to randomize the sequence of training pairs presentation.

A. Numerical problems due to the normalization constants

Tests showed that the Segmental GPD is numerically unstable. The use of exponential functions in some equations makes the variables assume extremely high (or extremely low) values, making them exceed the representation range, even using double precision variables.

The problematic equations are the one that defines the classification error function (6), and the one that defines the cost function (7). An adequate choice of the normalization constants is critical in both cases:

- The equation that defines the classification error function is

$$d_i(X|\Lambda) = -g_i(X|\lambda_i) + \ln\left[\frac{1}{W-1}\sum_{j\neq i} e^{g_j(X|\lambda_j)\eta}\right]^{\frac{1}{\eta}}$$

  The term $g_j(X|\lambda_j)$ is the log-likelihood of the observation sequence X given the word model j, and therefore has a negative value. In practice, for this specific case, observed values of this variable fall into the range (-1000,-5000), making the exponential assume a constant value of zero. The problem arises when calculating the natural logarithm of this value: $\ln(0) = -\infty$. A proper choice of the normalization constant η is obviously $0 < \eta < 1$, in order to lower down the dynamic range of these values. In this work, a value of $\eta = 0.001$ was used.
- The cost function is given by

$$l_i(X|\Lambda) = l_i(d_i(X|\Lambda)) = \frac{1}{1+e^{-\gamma d_i(X|\Lambda)}}$$

  In practice, $d_i(X|\Lambda)$ assume values in the range (-750,+750). For $d_i(X|\Lambda) = -750$ we have $e^{-(-750)} = \infty$, and for $d_i(X|\Lambda) = 750$ we have $e^{-750} = 0$. As the previous case, this problem can be solved by choosing the normalization constant

γ in the interval $(0, 1)$. After several tests, a value $\gamma = 0.001$ was chosen.

B. Choice of the learning rate

After defining the normalization constants γ and η, the next step is the determination of the learning rate ε. As mentioned above, the parameters reestimation formula for the Segmental GPD algorithm is given by:

$$\Lambda_{n+1} = \Lambda_n - \varepsilon \nabla l(X_n|\Lambda n)$$

One thing that must be noted is that in all of the reestimation formulas ((11) to (18)), the learning rate is always multiplied by the normalization constant γ. Therefore it's value is totally dependent on the value of the parameter γ.

To find the optimum value of the learning rate, the values of the normalization constants were fixed to $\gamma = \eta = 0.001$, and a sweeping was performed for values of the learning rate ranging from 0.1 to 10. The best performance was achieved when using $\varepsilon = 1.0$.

C. Training samples presentation order

As the Segmental GPD algorithm is very similar to the Backpropagation algorithm, it's natural to investigate if the issues related to the last one appears on the former. One of these issues is the presentation order of the training samples: the Backpropagation algorithm becomes "addicted" not only to the training samples, but also in the *order* in which they are presented to the system.

Two tests were performed to verify this point: in the first test, the training pairs were always presented following the same order, while in the second test, the training pairs were shuffled before presentation. The results were the same for both tests, showing that, for the Segmental GPD algorithm, the order of presentation of the training pair is not important.

V. Tests and result analysis

In this section the experimental results regarding the evaluation of the discriminative training are presented.

A. Initial tests

An initial test was performed, with the system trained only with the Baum-Welch algorithm. The goal of this test is to establish a standard performance, to which all the subsequent results will be compared. The results of this initial tests are shown in Table II.

TABLE II
INITIAL TESTS RESULTS (ONLY BAUM-WELCH FOR TRAINING).

Database	Recognition rate
Small	$91,6667\%$
Large	$90,177\%$

TABLE III
RECOGNITION RATES FOR SYSTEMS TRAINED WITH THE BAUM-WELCH AND DISCRIMINATIVE ALGORITHMS.

Database	Baum-Welch	Discriminative
Small	91.667%	93.333%
Large	90.177%	90.471%

B. Tests with discriminative training

The next tests were performed to determine the performance improvement when using the discriminative training. For these tests, all of the issues of the previous section were implemented, in order to achieve the best possible results. The results of these tests are shown in Table III

These results show a little improvement in the recognition performance when using the discriminative training.

C. Is it possible to perform discriminative training using a subset of the training pairs?

A final test was conducted to investigate the following issue: discriminative training of HMMs is a very time consuming task because each training utterance updates the parameters of all vocabulary words models. Therefore, the higher are the vocabulary size and the number of training pairs, the longer will be the training process. An alternative to this procedure would be the use of a subset of the training utterances for the discriminative training. Defined the strategy, the next problem is to choose an adequate training subset. A choice that seems reasonable is to select only those (training) utterances that the system misrecognized. These would be the *problematic* sentences and should be better "re-teached" to the system.

To test this idea, two discriminative training were performed: the first one (TD1) with the whole training set, and the second one (TD2) using only the *problematic* utterances. These tests were performed only for the *Large Database*, and the results are shown in Table IV.

TABLE IV
TRAINING SUBSET VERIFICATION TESTS RESULTS.

Baum-Welch	TD1	TD2
$90,177\,\%$	$90,471\,\%$	$90,255\,\%$

The analysis of Table IV shows that the use of a subset of the training samples leads to an improved performance, but the use of the whole training set is better. This results confirms the theoretical claim that the algorithm maximizes the likelihood of the correct model to generate the observation sequence and minimizes the likelihood of the concurrent models. Therefore, the larger is the information amount, the better is the performance.

VI. Conclusions

The Baum-Welch algorithm, which is the most used one to train HMMs for the task of speech recognition, is based on the Maximum Likelihood Criterion, that

maximizes the likelihood of a given model to generate the observation sequence.

The Segmental GPD algorithm is a discriminative training algorithm that both maximizes the likelihood of the correct model to generate the observation sequence and minimizes the likelihood of the concurrent models to generate the same observation sequence. This procedure would lead to better recognition rates, because it enhances the discriminability between the competing models.

Two issues were addressed in this work: the establishment of the performance improvement when using the Segmental GPD algorithm to train HMMs in the task of isolated word recognition, and the discussion of some implementation issues related to this algorithm.

With the use of discriminative training, a little improvement in the recognition rate was observed: for the *Small Database*, the recognition rate raised from 91.667% to 93.333%, and for the *Large Database*, from 90.177% to 90.471%. These results are similar to those found in the literature [1] [2] [3].

Some implementation issues were also studied:

- The choice of the learning rate is difficult, because it depends on the value of the normalization parameter γ. Therefore it's necessary to test values over a wide range to determine the optimum value for this parameter.
- The algorithm does not guarantee that the likelihood of the observation sequence given the model always increase with the training epochs. In fact, the recognition rate begins to decline after a number of training epochs, indicating the overtraining effect.
- Because of the high computational costs of this algorithm, a test was made to verify if it's possible to perform the discriminative training using only a subset of the training utterances. The results showed that it possible, but the use of a subset of the training utterances instead of the whole set, lead to lower improvement in the recognition rate.

VII. Future work

In order to achieve better results with the discriminative training, the following alternatives worth a test:

- Alteration of calculation of the error function: instead of using the difference between the likelihood of the correct model and the mean of the likelihood of the concurrent models, one could use the difference between the likelihood of the correct model and the likelihood of the concurrent model with the largest likelihood. Maybe the use of the worst case instead if the mean could lead to better results.
- Use of adaptive learning rates and momentum in the reestimation equations.

A natural expansion of this work is the adaptation of this algorithm to train subword units in large vocabulary speech recognition systems.

Acknowledgements

To Ericsson for partial funding of this research.

References

[1] Juang, B. H., Fellow, W. C. and Chin-Hui, L., "Minimum Classifi cation Error Rate Methods for Speech Recognition", *IEEE Transactions on Speech and Audio Processing*, vol. 5, no. 3, pp. 257-265, May 1997.

[2] McDermott, E., "Discriminative Training for Speech Recognition", PhD Thesis, Waseda University, 1997.

[3] Shigeru, K., Chin, H. L., and Biing H. J. , "New Discriminative Training Algorithms Based on the Generalized Probabilistic Descent Method", *Proceedings of the IEEE Workshop on Neural Networks for Signal Processing*, pp. 298-308, Princeton, New Jersey, USA, October 1991.

[4] Chi L.S., Chin H. L., Bing, H. J. and Aoron, E. R., "Speaker Recognition Based on Minimum Error Discriminative Training", *Proceedings of the International Conference on Acoustics, Speech and Signal Processing*, pp. 325-328, Adelaide, Australia, April 1994.

[5] Jung, K. C. and Frank, K. S., "An N-Best Candidates-Based Discriminative Training for Speech Recognition Applications", *IEEE Transactions on Speech and Audio Processing*, vol. 2, no. 1 Part II, pp. 206-216, January 1994.

[6] Chou W., Juang, B. H. and Lee, C. H., "Segmental GPD Training of HMM Based Speech Recognizer", *Proceedings of the International Conference on Acoustics, Speech and Signal Processing*, pp. 473-476, San Francisco, March 1992.

[7] Qiang, H. and Chorkin, C., "The Gradient Projection Method for the Training of Hidden Markov Models", *Speech Communication*, vol. 13, pp. 307-313, December 1993.

[8] Chou W., Lee, C.H. and Juang, B. H. , "Minimum Error Rate Training Based on N-Best String Models", *Proceedings of the International Conference on Acoustics, Speech and Signal Processing*, vol. 2, pp. 652-655, Minneapolis, April 1993.

[9] Schluter, R., Macherey, W., Kanthak, S., Ney, H. and Welling, L., Comparison of Optimization Methods for Discriminative Training Criteria, *Proceedings of the 1997 European Conference on Speech Communication and Technology*, Rhodes, Greece, Vol. 1, pp. 15-18, September 1997.

[10] Martins, J. A. "Avaliaç ˜ao de Diferentes T´ecnicas Para Reconhecimento de Fala", PhD Thesis, Universidade de Campinas, Campinas, Brazil, 1997.

[11] Haykin, Simon. *Neural Networks: a comprehensive foundation*. Prentice Hall. 1999.

Excitation models for speech interpolation coding

Miguel Arjona Ramírez
University of São Paulo - EP - PSI
Av. Prof. Luciano Gualberto, trav. 3, 158
05508-900 São Paulo - SP - Brazil
miguel@lps.usp.br

Alexandre Bezerra de Melo
University of São Paulo - EP - PSI
Av. Prof. Luciano Gualberto, trav. 3, 158
05508-900 São Paulo - SP - Brazil
alexandre.melo@poli.usp.br

***Abstract*— Line spectra appear in sinusoidal coders such as the sinusoidal transform coder (STC) and the multiband excitation (MBE) coder and also in waveform interpolation (WI) coders. For WI coding, the excitation waveform surface is decomposed into a rapidly evolving waveform (REW) and a slowly evolving waveform (SEW). Especially for modeling the SEWs, autoregressive (AR) and autoregressive moving average (ARMA) spectral models are proposed to fit Fourier series line spectra. Autoregressive modeling for WI coding is more natural because the inherent cycle length normalization may be used to enhance the model estimation accuracy. Autoregressive moving average (ARMA) models are fitted to the SEW spectrum by using only AR spectral estimation algorithms so that the ARMA model is represented as a couple made of an intrinsic AR model and an approximation AR model for the intrinsic MA part. For SEW coding at lower bit rates, the zinc pulse model is tested as well. Log spectral distortions show that AR modeling suits WI coding, turning out to be just as good as it is for modeling sinusoidal amplitudes. The single pulse zinc model when used for fine spectral modeling causes significantly larger spectral distortion while retaining its good results for low-bit-rate coding.**

***Index Terms*— Signal processing, speech coding, waveform interpolation, WI, spectral modeling.**

I. INTRODUCTION

Compact and accurate representations of the periodicity in a speech signal are important for speech coders and particularly so for low-bit-rate coders due to the high perceptual sensitivity attached to periodicity. Explicit parameterization of periodicity is used in sinusoidal coders such as the sinusoidal transform coder (STC) and the multiband excitation (MBE) coder and also in waveform interpolation (WI) coders. Therefore, for all of these coder types, harmonic spectra emerge somewhere along the signal processing chain. In particular for waveform interpolation coders, the speech signal is first segmented in cycle waveforms when speech is periodic or arbitrary length segments when speech is more random. After length normalization, these finite length waveforms are known as characteristic waveforms (CWs) [1]. Actually, most often a linear prediction model is estimated in the first place for the speech signal, whose residual signal is segmented instead. Length normalization effectively removes the periodicity from the residual signal, and the collective arrangement of CWs retains the evolution of waveshape information [2]. The periodic and aperiodic components of the waveshape may be continuously decomposed from the CW surface by lowpass and highpass filtering along the time evolution, yielding the slowly evolving waveform (SEW) and the rapidly evolving waveform (REW), respectively. Both surfaces are sampled at different rates, being the SEW sampling rate around 1/20 that of the REW sampling rate typically [3]. On the other hand, the frequency and amplitude resolutions for SEW spectra have to be larger, usually represented by a Fourier series whose components below 800 Hz are primarily coded by means of variable dimensional vector quantization (VDVQ), while for the REW a uniform power spectral density model is sufficient for lower rates. Especially for modeling the SEWs, autoregressive (AR) and autoregressive moving average (ARMA) spectral models are proposed to fit Fourier series line spectra. Previously, AR models have been fitted to line spectra for sinusoidal coding [4] but their use has not been reported for WI coders. In these cases, a continuous intermediate spectrum is obtained by interpolating the line spectrum prior to AR model estimation. The main reason why AR models are interesting lies in the efficient vector quantizers available for coding their parameters, mostly developed for code-excited linear predictive (CELP) coders along about two decades of research and development. For SEW coding at lower bit rates, the zinc pulse model [5] is tested as well.

This work is supported by Fundaç˜ao de Amparo à Pesquisa do Estado de S˜ao Paulo (FAPESP) under Grant no. 03/04506-4.

II. WAVEFORM ANALYSIS FRAMEWORK

A waveform analysis system has been set up which preserves perfect reconstruction capability when the CWs are represented by Fourier series coefficients or are interpolated by using sinc functions [6]. Since the pitch period of speech is variable, cycle waveform length is time-varying or, what amounts to the same thing, the natural CW rate is irregular. In this framework, CWs are acquired at their natural irregular rate and then are uniformly upsampled to the signal sampling rate, which is 8 kHz in our case. In order to reach a regular perceptually transparent rate for the CWs, the target for natural sampling rate must be at least 1/20 the signal rate [3]. Consistent with this bound, a downsampling factor of 16 is conveniently applied along the CW evolution axis by means of four

stages of halfband filtering and downsampling using a dyadic wavelet or filterbank. An evolving waveform $e_m(n)$ at the signal sampling rate is shown as it is downsampled to a 500 Hz sampling rate in Fig. 1, resulting in the evolving waveform $e_{m_p}(n_p)$.

A symmetric 11-sample FIR truncated sinc filter is used as lowpass halfband prototype

$$\begin{aligned} h_0(n) &= 2f_c \frac{\sin(\omega_c n)}{\omega_c n} \\ &= 2f_c \mathrm{sinc}(2f_c n), \end{aligned} \tag{1}$$

for $n = -D, -(D-1), \cdots, D$, where $f_c = \frac{1}{4}$ cycle/sample is the lowpass cutoff frequency and $D = 5$.

The highpass filter $H_1(z)$ is defined through the conjugate quadrature relation

$$H_1(z) = H_0(-1/z) \tag{2}$$

with respect to $H_0(z)$.

The SEWs are obtained using four additional lowpass filtering stages by means of the dyadic filterbank in Fig. 2, reaching a sampling rate of 31.25 Hz as the evolving waveform $e_{m_p}(n_p)$ is decomposed into the SEW $s_{m_4}(n_4)$ and the REWs $r_{m_i}(n_i)$ for $i = 1, 2, \cdots, 4$. The D-sample delay is compensated for at each filtering stage.

III. Autoregressive modeling

Alternatively, in a more natural procedure for WI spectral modeling, by representing the SEWs in the time domain, standard LP analysis algorithms may be used for estimating the parameters for the AR models. Coupled with this, the time normalization process inherent in WI analysis for generating the SEW surface is used for positioning the spectral lines throughout the base band frequency range instead of the uniform or variable interpolations and extrapolations of harmonic amplitudes which are usually used for fitting AR [7] or ARMA [8] models to line spectra. The periodicity of the SEWs is used to advantage by employing rectangular windows for the determination of autocorrelation coefficients, thereby increasing their accuracy.

IV. ARMA modeling

An autoregressive moving average (ARMA) spectral model is associated to the transfer function

$$H_{ARMA}(z) = \frac{1 + \sum_{l=1}^{q} b_l z^{-l}}{1 + \sum_{l=1}^{p} a_l z^{-l}}, \tag{3}$$

which may be decomposed into a cascade association of an AR model transfer function

$$H_{AR}(z) = \frac{1}{1 + \sum_{l=1}^{p} a_l z^{-l}} \tag{4}$$

and an MA model transfer function

$$H_{MA}(z) = 1 + \sum_{l=1}^{q} b_l z^{-l}. \tag{5}$$

In order to use just AR spectral estimation algorithms for fitting the ARMA model to the SEW spectrum, its representation as a couple made of an intrinsic AR model and an approximation AR model for the intrinsic MA part of the ARMA model is proposed. First, the undelying AR model $H_{AR}(z)$ is estimated, which may be used to determine the AR residual $u(n)$ by its Fourier series

$$U\left(e^{j\omega_k}\right) = \frac{S\left(e^{j\omega_k}\right)}{H\left(e^{j\omega_k}\right)} \tag{6}$$

for $k = 1, 2, \ldots, K$, where K is the number of harmonics. Then an rth-order approximation AR model

$$H_{AAR}(z) = \frac{1}{1 + \sum_{l=1}^{r} c_l z^{-l}} \tag{7}$$

is estimated, where the condition

$$r \gg q \tag{8}$$

should hold because any finite order MA model may be exactly represented by an infinite order AR model [8]. The ARMA models used in the Section VI deliberately neglect Condition (8) in order not to cause the coding rate to increase inordinately.

At last, the underlying MA model parameters may be determined by

$$b_m = -c_m + \sum_{l=1}^{m-1} b_l c_{m-l} \tag{9}$$

for $m = 1, 2, \ldots, q$. It is suggested that usual AR parameters such as LSPs be used for coding MA parameters as well.

V. Zinc pulse model

The zinc pulse model [5] is defined by

$$z(n) = A\mathrm{sinc}(n) + B\mathrm{cosc}(n) \tag{10}$$

where

$$\mathrm{sinc}(n) = \frac{\sin(2\pi f_c n)}{2\pi f_c n} \tag{11}$$

and

$$\mathrm{cosc}(n) = \frac{1 - \cos(2\pi f_c n)}{2\pi f_c n} \tag{12}$$

for the signal bandwidth f_c. Usually the whole Nyquist bandwidth, $f_c = 1/2$ cycle/sample, is taken.

In this case, a time domain projection method is used for estimating the amplitude values A and B for the underlying sinc and cosc functions. Being $\mathbf{s}$ the SEW P-dimensional column vector and $\mathbf{s}_P$ the first P-sample vector of the sinc series, then the sinc amplitude is estimated as

$$A = \frac{\mathbf{s}_P^T \mathbf{s}}{\mathbf{s}_P^T \mathbf{s}_P}. \tag{13}$$

Similarly, the cosc function amplitude B is determined by using a P-sample vector $\mathbf{c}_P$ from the cosc series as

$$B = \frac{\mathbf{c}_P^T \mathbf{s}}{\mathbf{c}_P^T \mathbf{c}_P}. \tag{14}$$

The zinc pulse is constrained to be at the midpoint of the CW, which is consistent with the CW alignment usually carried out for WI coding.

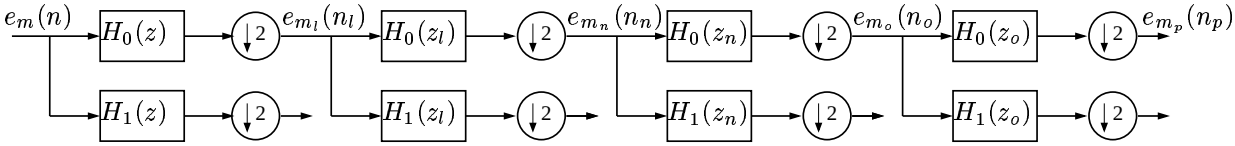

Fig. 1. Four-stage dyadic analysis filterbank for an evolving waveform on the oversampled CW surface, extracting an evolving waveform on the CW surface sampled at a lower perceptually transparent rate.

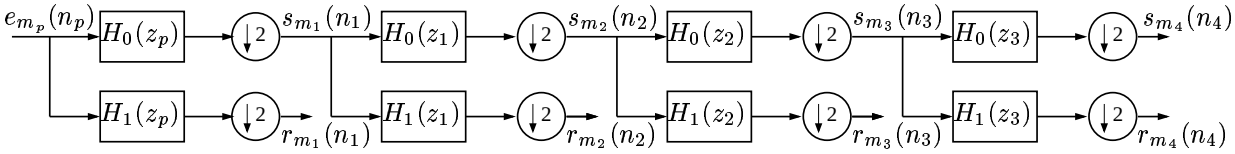

Fig. 2. Four-stage dyadic analysis filterbank for an evolving waveform on the CW surface, extracting an evolving waveform on the SEW surface and evolving waveforms on four different scale REW surfaces.

VI. Excitation Modeling Tests

As test signals, sixteen sentences from the TIMIT speech database have been used, equally distributed between male and female speakers, for a total recording time of 29.0 s of female speech and 20.6 s of male speech. The log spectral distortion (SD) measure has been used for comparing modeled line spectral values to their original counterparts while all spectra have been normalized to $P/2 = 128$ one-sided lines. A typical AR(14) model fit to a SEW amplitude spectrum is shown in Fig. 3, where the high-frequency tail of the model poorly fits the higher null harmonic amplitudes. Therefore, the model spectrum floor is properly adjusted by considering a high-frequency cutoff calculated as a function of the SEW pitch frequency, resulting in the spectral fit shown in Fig. 4. Besides, a comparison of AR(14) to ARMA(2,12) spectral fits can be seen in Fig. 5. The ARMA model order is the sum of its numbers of poles and zeros and it is constrained to be equal to the AR model order used for AR modeling for comparison purposes.

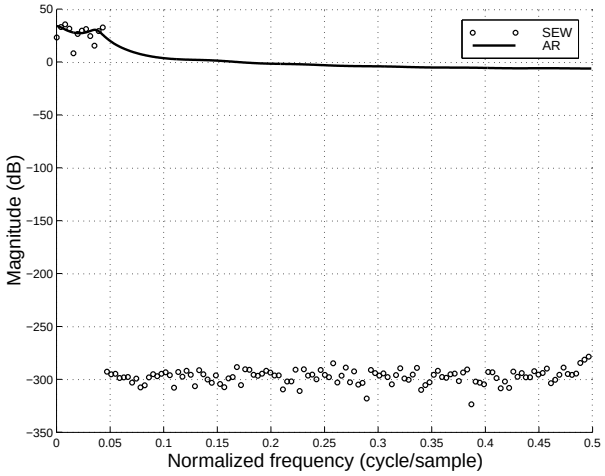

Fig. 3. Natural AR(14) model spectral fit to SEW spectral amplitudes.

The resulting log spectral distortions are presented in Table I, where it can be seen that AR modeling for WI coding is comparable to AR modeling for sinusoidal amplitudes [7], while there is still room

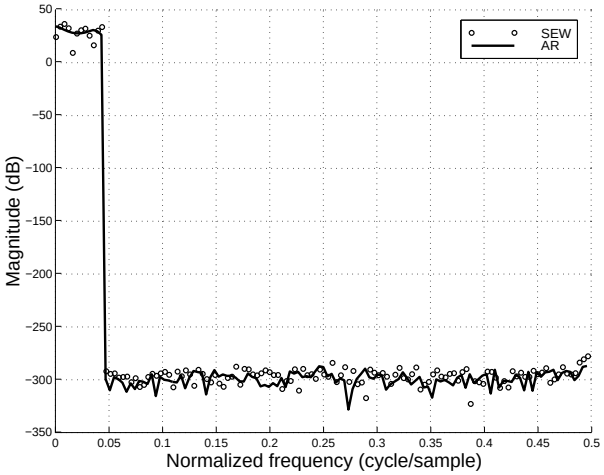

Fig. 4. AR(14) model spectrum with noise floor fit to SEW spectral amplitudes.

left for sophisticating the model estimation algorithm because normal WI coding constraints may be eventually relieved if more complexity could be tolerated. The proposed ARMA modeling is only slightly better than simpler AR modeling for the same total order. However, when comparing ARMA(2,12) against AR(14) a substantial improvement is noticed for female speech. Improved MA modeling for the ARMA estimation could be considered [9] provided additional complexity could be accomodated. In this fine spectral modeling context, the single pulse zinc model causes significantly larger spectral distortion while displaying a good performance when used for low-bit-rate coding [10].

VII. Conclusion

Autoregressive modeling for WI excitation has been found to perform just as well as it does for sinusoidal amplitudes. Therefore, efficient LSP vector quantization algorithms may be used for coding SEW spectra in WI coding. Simple ARMA estimation methods have been found not to be worthwile when considering the slight modeling improvement against the additional estimation complexity. Further, compact excitation models such as the zinc pulse, while efficient for low bit rate coding, have been found to be rather inaccurate

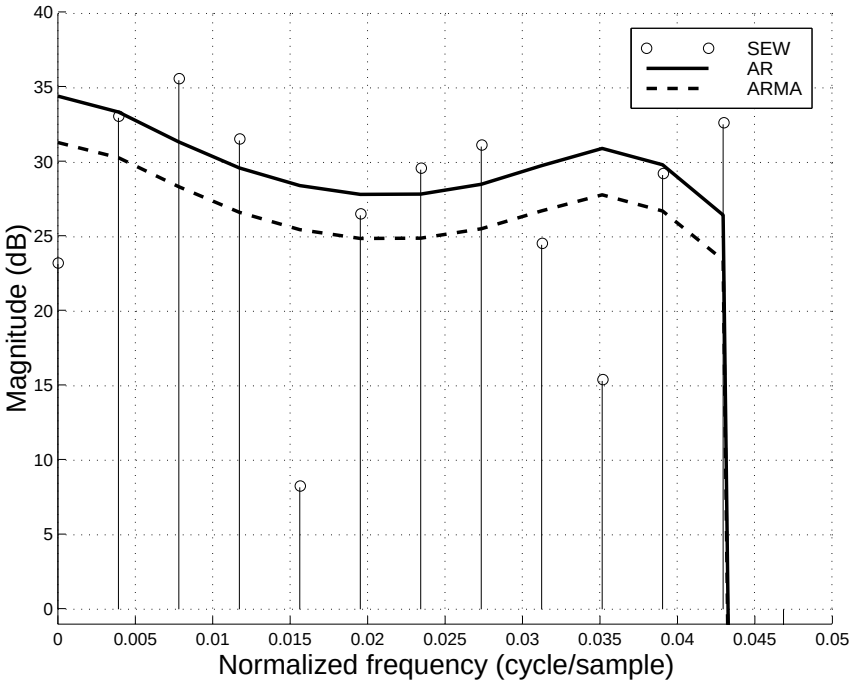

Fig. 5. AR(14) and ARMA(2,12) model spectra fit to SEW spectral amplitudes.

TABLE I
SPECTRAL DISTORTION FOR AR, ARMA AND ZINC EXCITATION MODELS FOR THE SET OF SPEECH TEST SIGNALS.

Model	Spectral distortion (dB)	
	Female	Male
AR(10)	2.91	3.07
AR(14)	2.84	2.93
AR(18)	2.78	2.98
ARMA(2,8)	2.88	3.01
ARMA(2,12)	2.74	2.89
ARMA(4,14)	2.70	2.84
Zinc(1,1)	4.25	4.46

at higher resolution.

REFERENCES

[1] W. B. Kleijn and J. Haagen, "Waveform interpolation for coding and synthesis," in *Speech Coding and Synthesis*, W. B. Kleijn and K. K. Paliwal, Eds. Amsterdam: Elsevier Science, 1995, pp. 175–207.

[2] M. Arjona Ramírez, "A waveform extractor for scalable speech coding," in *Proc. of IEEE Int. Conf. Acoust., Speech, Signal Processing*, vol. 2, Hong Kong, 2003, pp. 169–172.

[3] W. Bastiaan Kleijn and J. Haagen, "A speech coder based on decomposition of characteristic waveforms," in *Proc. IEEE Int. Conf. Acoust., Speech, Signal Processing*, vol. 1, Detroit, 1995, pp. 508–511.

[4] T. G. Champion, R. G. McAulay, and T. F. Quatieri, "High-order allpole modelling of the spectral envelope," in *Proc. IEEE Int. Conf. Acoust., Speech, Signal Processing*, vol. 1, Adelaide, 1994, pp. 529–532.

[5] R. A. Sukkar, J. L. LoCicero, and J. W. Picone, "Decomposition of the LPC excitation using the zinc basis functions," *IEEE Trans. Acoust., Speech, Signal Processing*, vol. 37, no. 9, pp. 1329–1341, Sept. 1989.

[6] M. Arjona Ramírez, "Cycle extraction for perfect reconstruction and rate scalability," in *Proc. of EUROSPEECH, European Conference on Speech Communication and Technology*, vol. 4, Geneva, 2003, pp. 2945–2948.

[7] T. Ramabadran, A. Smith, and M. Jasiuk, "An iterative interpolative transform method for modeling harmonic magnitudes," in *2002 IEEE Speech Coding Workshop Proc.*, Tsukuba, 2002, pp. 38–40.

[8] S. M. Kay, *Modern spectral estimation.* Englewood Cliffs: Prentice-Hall, 1987.

[9] N. Malik and W. H. Holmes, "Encoding sinusoidal amplitudes with a minimum phase rational model," in *Proc. of IEEE Int. Conf. Acoust., Speech, Signal Processing*, vol. 3, Istanbul, 2000, pp. 1463–1466.

[10] J. Lukasiak and I. S. Burnett, "Low rate WI SEW representation using a REW-implicit pulse model," *IEEE Signal Processing Lett.*, vol. 8, no. 8, pp. 228–230, Sept. 2001.

Speaker Adaptation Using Eigenvoices in a Continuous Speech Recognition System

Lívio Carvalho Sousa
State University of Campinas - UNICAMP
P.O. Box 6101 - 13083-852
Campinas - SP - Brazil
livio@decom.fee.unicamp.br

Fábio Violaro
State University of Campinas - UNICAMP
P.O. Box 6101 - 13083-852
Campinas - SP - Brazil
fabio@decom.fee.unicamp.br

***Abstract*— The intention of this work is to present the result of some experiments carried on speaker adaptation using eigenvoices [1, 2, 3] and applied over a continuous speech recognition system (SRS) under development at the Digital Speech Processing Laboratory of the School of Electrical and Computer Engineering (FEEC), University of Campinas (UNICAMP), Brazil. Although not yet fully conclusive, the results of some simulations show the potential of the eigenvoice technique in improving the word recognition rate with only a few sentences of adaptation. Improvements of up to 5% in word recognition rate were obtained. Sometimes just one adaptation sentence showed to be more effective than 10 adaptation sentences. The question remaining is what set of sentences to choose in order to get a better adaptation.**

***Index Terms*—eigenvoices, speaker adaptation, continuous speech recognition system.**

I. INTRODUCTION

Nowadays, speech recognition systems (SRS) are being used in many applications like user identification systems, call centers, embedded devices, voice control systems and other applications. In all these applications the system must present an user independent minimum acceptable performance. Sometimes, to achieve this minimum acceptable performance, a real time fast adaptation is required for each new user.

In SRS the speech subunits are stochastically modeled by Hidden Markov Models (HMM). In continuous SRS these subunits are normally context independent or context dependent phones. The models can be either speaker dependent (SD) or speaker independent (SI). The SD models are trained with the speech data from a single speaker, the one that is supposed to be the SRS user. The SI models are trained with the speech data from many speakers and can be used by any speaker, but at the expense of a higher error rate (typically 2 or 3 times higher) [2,4].

The first step to train the models is to get a large speech database. As more speech material is available, better-trained models will be obtained with a consequent lower word error rate. In many applications where the users change frequently, it is not feasible to retrain the system for each new user with a long lasting training session. Therefore, many studies are been made in order to adapt models, that is, transform a SI model into a SD model, using much less speech data than would be necessary to directly train a SD model. One of the most promising techniques is the one based on eigenvoices.

II. SPEAKER ADAPTATION

The main objective of speaker adaptation is to get a specific model for a new speaker when this speaker is not well represented by the SI model. The generation of this new model demands a lot of training time and a large SD database, what is not feasible in many applications where the user just wants to access a service for a few minutes. Because of that there is a lot of effort in developing adaptation algorithms requiring only a few sentences of adaptation and demanding a low adaptation time, what is a main requirement for SRS accessed by many different people for short periods of use. Normally not all the CDHMMs (Continuous Density Hidden Markov Models) parameters must be adapted, just the gaussian means. The remaining parameters (variances, weighting coefficients and transition probabilities) are inherited from the previous SI system [9,21].

At the present time many speaker adaptation techniques are available for speaker adaptation in SRS [9]:

- MAP (Maximum a Posteriory) [10,11,12,13,14, 15];
- MLLR (Maximum Likelihood Linear Regression) [16,17,18,19];
- CAT (Cluster Adaptive Training) [20].

A disadvantage of the MAP technique is that it has a slow adaptation. Furthermore speech data related to all speech sub-units must be present in the adaptation database. MLLR on the other hand can re-estimate parameters whose data were not observed in the adaptation database, but also requires a large adaptation database. In the CAT technique, different models are generated and associated to clusters of speakers and a new SD model is represented as a linear combination of cluster models.

III. EIGENVOICE TECHNIQUE

The eigenvoice technique [1,2,3,4,5] represents a new speaker as a linear combination of previously trained SD models, resembling in some aspects the ideas of the CAT technique.

Consider that a SI model is available. Consider also that L speaker databases are available and that a SD model is created for each one of these L speakers. As we are considering in this paper only the adaptation of the gaussian means, from each SD model all the gaussian means are stored into one vector called supervector. In the simulations reported in this paper, a continuous SRS is considered using 36 context independent phones, with each phone represented by a 3 state HMM. The emission density of each state is modeled as a mixture of 5 gaussians of dimension 25 (the dimension of a grouped set of acoustic parameters after dimension reduction by using principal component analysis - PCA). The dimension of each supervector is then 36x3x5x25=13500 and L supervectors with dimension 13500 are then created.

By using dimension reduction techniques, the eigenvalues and eigenvectors of the covariance or correlation matrix associated to the L supervectors are then calculated. As the covariance or correlation matrix has dimension [13500 x 13500], the computational load to calculate the eigenvalues and eigenvectors would be very expensive. So, as an alternative, the SVD (Singular Value Decomposition) was chosen for calculating the eigenvalues and eigenvectors from XX^T, where X is the supervector matrix [13500 x L]. The L eigenvectors [13500 x 1] obtained using SVD are then ordered in a decreasing order of their corresponding eigenvalues. The higher order eigenvectors (lower eigenvalues) can then be discarded, resulting K eigenvectors ($K<L$). These K eigenvectors ($e(j)$, j=1,...,K) are called eigenvoices and the mean value of the supervectors is called eigenvoice $e(0)$. The eigenvoices constitute an orthogonal base of the eigenspace where each new speaker will be represented.

The eigenvoice technique estimates the supervector of the new speaker as $e(0)$ plus a linear combination of the K eigenvectors that point to the directions of maximum variability of the speaker space:

$$\hat{\mu} = e(0) + \sum_{j=1}^{K} w_j e(j) \tag{1}$$

To get the adapted model for the new speaker it is just necessary to calculate the eigenvoice coefficients w_j. Remember that, as we are adapting only the gaussian means, the variances, weighting coefficients and transition probabilities are kept the same as in the SI model.

The Maximum Likelihood Eigen Decomposition Algorithm (MLED) was proposed by Kuhn [1,3,5] as the iterative algorithm to estimate the w_j coefficients based on a maximum likelihood criterion.

Each eigenvoice can be considered as the association of 36x3x5=540 concatenated sub-eigenvoices, with each sub-eigenvoice having dimension 25 and corresponding to the mean of each gaussian of the 5 gaussians per state, 3 state, 36 CDHMMs:

$$e(j) = \begin{bmatrix} e_1^{(1)}(j) \\ e_2^{(1)}(j) \\ \vdots \\ e_m^{(s)}(j) \\ \vdots \\ e_M^{(S)}(j) \end{bmatrix}, \tag{2}$$

where $e_m^{(s)}(j)$ is the j^{th} sub-eigenvoice corresponding to gaussian m (m=1,...,M, M=5) in state s (s=1,...,S, S=36x3=108).

The re-estimation equations of the MLED algorithm are obtained from the Baum equation [1,3,22]

$$Q(\lambda,\lambda') = -\tfrac{1}{2} P(O/\lambda) \sum_s \sum_m \sum_t \gamma_m^{(s)}(t) f(o_t,s,m), \tag{3}$$

where

$$f(o_t,s,m) = [-D.\log(2\pi) - \log\left|C_m^s\right| + h(o_t,s,m)], \tag{4}$$

$$h(o_t,s,m) = \left(\mu_m^{(s)} - o_t\right)^T C_m^{(s)^{-1}} \left(\mu_m^{(s)} - o_t\right) \tag{5}$$

and

- $P(O/\lambda)$ is the probability of the observation sequence O, given the model λ;
- D is the dimension of the acoustic parameters o_t;
- $C_m^{(s)^{-1}}$ is the inverse covariance matrix of gaussian m in state s;
- $\mu_m^{(s)}$ is the mean of gaussian m in state s.
- $\gamma_m^{(s)}(t)$ is the emission probability of parameter o_t produced by gaussian m in state s.

Consider the representation of the adapted gaussian means by equation

$$\hat{\mu} = \sum_{j=1}^{K} w_j e(j), \tag{6}$$

where K is the chosen number of eigenvoices. Substituting equation (6) in (5), deriving equation (3) with respect to w_j and making the derivative equal to zero, we obtain the re-estimation equation

$$\begin{aligned} &\sum_s \sum_m \sum_t [\gamma_m^{(s)}(t) \left(e_m^{(s)}(j)\right)^T C_m^{(s)^{-1}} o_t] = \\ &= \sum_s \sum_m \sum_t \left\{ \gamma_m^{(s)}(t) \left[\sum_{k=1}^{K} \left(w_k \left(e_m^{(s)}(k)\right)^T C_m^{(s)^{-1}} e_m^{(s)}(j) \right) \right] \right\} \end{aligned} \tag{7}$$

Notice that equation (7) is based on equation (6) and not on equation (1). To compensate this difference, a normalization is provided in the acoustic

parameters by subtracting the corresponding sub-eigenvoice $e_m^{(s)}(0)$ [3].

Equation (7) can then be rewritten as

$$d(1,j)w_1 + \cdots + d(K,j)w_K = D(j), \qquad (8)$$

where

$$d(k,j) = \sum_s \sum_m \left[\sum_{n=1}^{N} \left(\frac{e_{mn}^{(s)}(k) e_{mn}^{(s)}(j)}{\sigma_{mn}^{2\ (s)}} \right) \sum_t \gamma_m^{(s)}(t) \right] \qquad (9)$$

and

$$D(j) = \sum_s \sum_m \sum_t \left[\sum_{n=1}^{N} \left(\frac{e_{mn}^{(s)}(j) o_{tn}}{\sigma_{mn}^{2\ (s)}} \right) \gamma_m^{(s)}(t) \right]. \qquad (10)$$

The term $e_{mn}^{(s)}(j)$ is the n^{th} component of sub-eigenvoice $e_m^{(s)}(j)$, o_{tn} is the n^{th} component of the parameters vector o_t, and $\sigma^2_{mn}{}^{(s)}$ is the n^{th} component of the variance of gaussian m in state s.

Making J=1,2,...,K in equation (8), we get a K equations system with K unknown variables that can be solved by using the gaussian elimination method. After calculating the eigenvoice coefficients, new means are re-estimated using equation (5) and a new model is obtained. From this new model, new values of $\gamma_m^{(s)}(t)$ are calculated and a new iteration is done, resulting a new set of coefficients w's. The procedure continues until some stopping criterion is reached.

The reported works about isolated word applications indicate 2 iterations for MLED algorithm [3,5], while [2] applied 3 iterations for his continuous speech application. An objective of this work is also to verify the influence of the number of iterations in the performance of the adapted system.

IV. Acoustic Parameters and Speech Databases

The acoustic parameters used in the CDHMMs are extracted at each 10 ms from a pre-emphasized speech signal ($1-0.95z^{-1}$) using a 20 ms Hamming window. The employed parameters are: 12 Mel-cepstral coefficients; 12 associated delta-Mel-cepstral coefficients; 12 associated delta-delta-Mel-cepstral coefficients; 1 normalized log-energy-coefficient; 1 associated delta-log-energy coefficient; 1 associated delta-delta-log-energy coefficient [6,7]. In calculating the delta coefficients, only one frame was considered to the left and right of the considered frame. All these 6 parameters were joined into a single vector with dimension 39 and, after a PCA analysis [8], this dimension was reduced to 25.

The speech database for the SI system was created using a sampling frequency of 11.025 kHz, a set of 200 phonetically balanced sentences and 40 speakers, 20 male and 20 female [22]. The training set consisted of 1200 phrases spoken by 30 speakers and the testing set consisted of 400 phrases spoken by other 10 speakers. The phonetic transcription of the speech files was made manually, speaker dependent, file by file, considering 36 context-independent phones for the Brazilian Portuguese language.

For the eigenvoices based adaptation algorithm, 18 SD databases were generated, over the same set of 200 phonetically balanced sentences, with 400 sentences per speaker. Just male speakers were considered. In the SD databases, to reduce the time spent with the preparation of the simulations, a standard phonetic transcription was employed (not speaker dependent).

The whole vocabulary consisted of 700 words. In the recognition section a word-pair grammar was employed. This grammar was created over the set of 200 sentences used in the database.

V. Adaptation Process

From the SD models, 18 supervectors were created and the SVD was applied on this set of supervectors resulting 18 eigenvalues and 18 eigenvectors, the eigenvoices. Because the number of base speakers used in our simulations was very low, the number of eigenvoices was made equal to the number of base speakers (K=L).

The adaptation data consisted of a set of up to 10 sentences with their associated phonetic transcriptions.

The Viterbi algorithm was used to calculate $\gamma_m^{(s)}(t)$, although, as reported in [2], the Forward-Backward algorithm could also be used.

When using just one adaptation sentence, the parameters o_t are extracted and the parameters $\gamma_m^{(s)}(t)$ are calculated using the means of the SI model. The eigenvoices coefficients are estimated by K equations (8) and new means are re-estimated. After that new parameters $\gamma_m^{(s)}(t)$ are calculated using the means obtained in the previous iteration. The iterative procedure continues until a certain number of iterations or a stopping criterion is reached.

For more than one adaptation sentence, equations (9) and (10) require one more summation in the number of sentences. After all sentences are processed, the eigenvoices coefficients are estimated and the new means are re-estimated.

The adaptation was applied for 10 speakers belonging to the SI speech database. The number of adaptation sentences was varied from 1 to 10 for each speaker and the number of iterations was made to vary from 1 to 5.

VI. Results and Comments

At first the speaker adaptation was tested over 10 speakers with a variable number of iterations and adaptation sentences. One set of 10 adaptation sentences was applied for speakers (M01, M07); other different sets were applied for speakers (M03, M06, M11), speakers (M04, M15) and speakers (M05, M17). The results are summarized in Tables I to X. On the top of the tables is presented the average word recognition rate of the considered speaker when using the SI system. The remaining values refer to the adapted system for the specific speaker under different number of adaptation sentences and

algorithm iterations. The resulting improved average word recognition rates are presented in bold style.

TABLE I

Speaker M01					SI Model: 87,57%
Nºof sentences	Nº of Iterations				
	1	2	3	4	5
1	**88,17%**	**92,90%**	**91,72%**	**92,90%**	**92,90%**
2	**87,57%**	**91,72%**	**92,90%**	**92,90%**	**93,49%**
3	**87,57%**	**92,31%**	**91,72%**	**88,76%**	**88,76%**
4	**88,17%**	**88,76%**	**91,12%**	**88,17%**	85,80%
5	85,21%	**91,12%**	**91,12%**	**91,72%**	**91,72%**
6	85,21%	**89,94%**	**91,12%**	**91,12%**	**91,72%**
7	86,98%	**90,53%**	**91,12%**	**91,12%**	**91,12%**
8	**88,17%**	**88,76%**	**90,53%**	**91,12%**	**91,12%**
9	86,39%	**88,76%**	**90,53%**	**90,53%**	**91,12%**
10	86,98%	**89,35%**	**91,12%**	**91,12%**	**91,72%**

TABLE II

Speaker M03					SI Model: 82,18%
Nºof sentences	Nº of Iterations				
	1	2	3	4	5
1	62,38%	69,80%	68,32%	66,34%	64,36%
2	58,42%	69,31%	73,27%	75,25%	76,24%
3	64,85%	67,82%	74,26%	73,27%	72,77%
4	64,85%	76,24%	74,26%	73,76%	73,76%
5	62,38%	78,22%	79,21%	77,72%	80,20%
6	66,34%	76,73%	79,70%	79,21%	79,21%
7	64,36%	76,73%	79,21%	79,21%	75,74%
8	64,85%	71,78%	75,74%	76,73%	75,74%
9	65,35%	72,77%	77,72%	78,22%	75,74%
10	65,35%	79,70%	79,21%	79,70%	78,71%

TABLE III

Speaker M04					SI Model: 81,41%
Nºof sentences	Nº of Iterations				
	1	2	3	4	5
1	76,38%	78,89%	71,36%	76,38%	71,86%
2	78,39%	79,40%	74,87%	75,88%	74,87%
3	76,88%	80,40%	75,38%	75,38%	75,88%
4	77,39%	78,89%	**81,91%**	79,40%	80,40%
5	74,87%	77,39%	80,90%	**81,91%**	79,40%
6	77,39%	**81,41%**	**81,91%**	**82,91%**	79,90%
7	77,39%	80,90%	**82,91%**	**82,91%**	79,90%
8	78,39%	79,90%	80,90%	**81,41%**	80,40%
9	78,89%	**81,91%**	79,90%	**83,42%**	**82,41%**
10	78,89%	78,89%	80,90%	**83,42%**	80,90%

TABLE IV

Speaker M05					SI Model: 92,09%
Nºof sentences	Nº of Iterations				
	1	2	3	4	5
1	84,65%	80,93%	81,40%	82,79%	81,40%
2	87,44%	85,05%	85,12%	85,12%	84,19%
3	82,79%	83,72%	85,12%	83,26%	79,07%
4	83,72%	80,93%	80,93%	81,86%	82,79%
5	80,93%	81,86%	80,47%	80,93%	82,33%
6	83,26%	81,86%	80,93%	80,93%	82,33%
7	84,19%	81,86%	82,33%	82,33%	83,26%
8	84,19%	81,86%	80,47%	79,53%	81,86%
9	83,72%	83,26%	81,86%	81,86%	80,00%
10	82,33%	84,19%	81,86%	82,33%	82,79%

TABLE V

Speaker M06					SI Model: 69,80%
Nºof sentences	Nº of Iterations				
	1	2	3	4	5
1	69,31%	68,32%	65,84%	64,85%	60,40%
2	66,83%	65,84%	63,37%	63,37%	63,86%
3	69,31%	67,33%	**69,80%**	67,82%	68,32%
4	68,32%	69,31%	**71,29%**	**70,79%**	**70,79%**
5	**74,26%**	68,81%	**71,29%**	**72,28%**	68,32%
6	**73,27%**	68,81%	**71,29%**	**71,29%**	68,32%
7	**75,74%**	**70,79%**	**71,29%**	**70,30%**	**73,76%**
8	**75,74%**	**69,80%**	**70,79%**	**73,27%**	**74,26%**
9	**73,27%**	**72,77%**	**72,77%**	**70,79%**	**72,28%**
10	**72,77%**	**71,78%**	**69,80%**	**72,77%**	**73,27%**

TABLE VI

Speaker M07					SI Model: 93,49%
Nºof sentences	Nº of Iterations				
	1	2	3	4	5
1	74,56%	85,21%	85,21%	84,02%	83,43%
2	85,80%	83,43%	84,02%	86,98%	84,02%
3	82,84%	78,70%	77,51%	79,88%	81,66%
4	82,25%	82,84%	85,21%	88,17%	87,57%
5	82,84%	82,84%	82,84%	89,35%	89,35%
6	83,43%	79,88%	85,80%	84,02%	86,98%
7	84,02%	81,66%	87,57%	86,39%	85,80%
8	83,43%	83,43%	85,80%	86,39%	84,02%
9	82,25%	81,07%	87,57%	88,17%	88,17%
10	83,43%	82,84%	86,39%	88,17%	88,17%

TABLEI VII

Speaker M11					SI Model: 94,55%
Nºof sentences	Nº of Iterations				
	1	2	3	4	5
1	93,07%	**95,54%**	**94,55%**	94,06%	93,56%
2	94,06%	94,06%	92,08%	91,58%	91,58%
3	**95,05%**	**95,54%**	**95,54%**	**95,05%**	**95,05%**
4	94,06%	**95,54%**	**96,04%**	**94,55%**	**94,55%**
5	**95,05%**	**96,04%**	**96,04%**	**96,04%**	**95,05%**
6	**96,53%**	**96,04%**	**96,04%**	**95,05%**	**95,05%**
7	94,06%	**95,54%**	**95,05%**	**95,05%**	**95,05%**
8	**94,55%**	**95,54%**	**95,54%**	**95,05%**	**95,05%**
9	**94,55%**	**95,54%**	**94,55%**	**95,05%**	**95,05%**
10	**94,55%**	**94,55%**	**94,55%**	**94,55%**	**94,55%**

TABLE X

Speaker M23					SI Model: 89,10%
Nºof sentences	Nº of Iterations				
	1	2	3	4	5
1	88,15%	**89,10%**	86,73%	86,73%	87,68%
2	86,73%	**89,57%**	**91,00%**	**89,10%**	**89,10%**
3	87,68%	**91,94%**	**91,00%**	**90,05%**	**91,47%**
4	**91,00%**	**94,31%**	**92,89%**	**92,89%**	**92,89%**
5	**89,57%**	**92,42%**	**92,42%**	**91,47%**	**92,89%**
6	**89,57%**	**92,89%**	**92,89%**	**92,42%**	**92,42%**
7	**89,10%**	**94,31%**	**92,89%**	**92,89%**	**91,94%**
8	87,68%	**94,31%**	**92,42%**	**92,42%**	**92,42%**
9	**89,57%**	**92,42%**	**90,52%**	**90,52%**	**90,05%**
10	87,68%	**93,84%**	**91,00%**	**91,47%**	**91,47%**

TABLE VIII

Speaker M15					SI Model: 93,97%
Nºof sentences	Nº of Iterations				
	1	2	3	4	5
1	88,44%	85,93%	85,43%	83,92%	82,91%
2	92,46%	90,45%	86,43%	86,43%	88,44%
3	90,50%	89,95%	88,94%	88,94%	88,94%
4	91,46%	93,47%	91,46%	92,46%	92,46%
5	89,45%	92,46%	91,46%	90,45%	91,46%
6	90,45%	92,46%	90,45%	91,46%	91,46%
7	89,95%	92,46%	91,96%	90,95%	90,45%
8	90,45%	92,46%	90,95%	90,95%	91,46%
9	90,45%	90,95%	91,96%	90,95%	90,95%
10	90,45%	90,95%	91,96%	90,95%	90,95%

TABLE IX

Speaker M17					SI Model: 92,56%
Nºof sentences	Nº of Iterations				
	1	2	3	4	5
1	87,47%	87,91%	90,70%	88,84%	86,98%
2	83,26%	86,05%	89,77%	90,70%	89,77%
3	86,05%	86,98%	87,44%	87,91%	89,77%
4	87,44%	85,12%	88,84%	91,16%	91,63%
5	85,58%	87,91%	89,30%	89,77%	90,70%
6	85,12%	87,44%	89,77%	89,30%	89,77%
7	84,65%	87,91%	88,84%	88,84%	88,84%
8	84,19%	86,51%	89,77%	89,77%	90,23%
9	83,26%	87,91%	87,91%	89,30%	89,77%
10	83,72%	88,84%	89,77%	89,77%	89,77%

The general conclusions that can be inferred from the tables above are:

- For some speakers (M01, M04, M06, M11, M23) the adaptation resulted an increase in the word recognition rate (results in bold style), while for others (M03, M05, M07, M15, M17) it resulted a decrease in the recognition rate;
- The maximum improvement was 5.92%, obtained for speaker M01 with 2 adaptation sentences and 5 iterations;
- For some speakers some degradation resulted after using the adaptation algorithm. With speaker M07 the reduction in the average recognition word rate exceeded 18% when using 1 adaptation sentence and 1 iteration;
- Not always increasing the number of iterations is worthwhile. A good compromise value for the number of iterations can be set equal to 3;
- Not always increasing the number of adaptation sentences results an increase in the average word recognition rate;
- Examining the 10 tables, the results may appear disappointing. The improvement was observed just over 5 of the 10 test speakers.

For two speakers to whom the adaptation procedures were not worthwhile, a new test was made, using a single adaptation sentence and trying each one of the 10 adaptation sentences available. In this case it was observed that just one specific adaptation sentence could result a gain over the SI result. These results are summarized in Figs. 1 and 2. In Fig. 1, related to speaker M15, only 2 iterations were employed and with the 7th adaptation sentence the performance exceeded the SI performance by 1%. In Fig. 2, related to speaker M17, 3 iterations were employed and with the 2nd adaptation sentence the performance exceeded the SI performance by 1.5%. It should be reminded that in the previous simulations, with the adaptation being made with up to 10 sentences, speaker M15 was in the best case 0.51% below the SI result and speaker M17 was 0.92%

below the SI result. It must be also emphasized that the good adaptation sentences in these two situations are different from the first sentences used in the adaptations shown in Tables VIII and IX. The test with one sentence and 2 iterations in Table VIII (85.93%) corresponds to individual sentence 1 in Fig. 1. The test with one sentence and 3 iterations in Table IX (90.7%) corresponds to individual sentence 1 in Fig. 2.

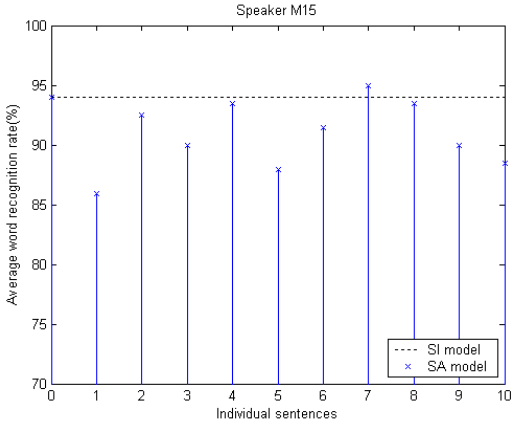

Fig. 1. Adaptation of speaker M15 using a single sentence

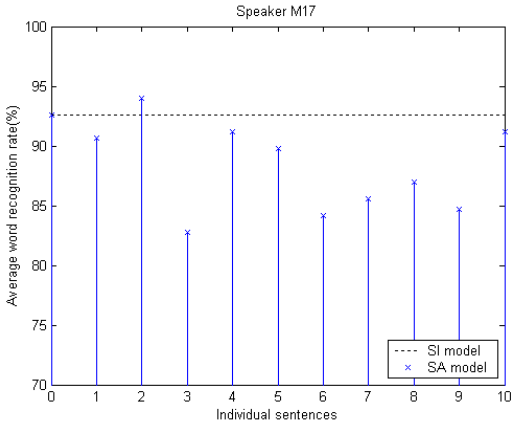

Fig. 2. Adaptation of speaker M17 using a single sentence

In others simulations the number of eigenvoices was reduced ($K<L$) but the performance decreased. This suggests that the number of SD base models used in our simulations was not enough to take into account the acoustic variability of the new speaker. In order to fulfill this deficiency in our simulations, additional SD databases are being recorded in order to result a higher value of base vectors (L around 50) and allow a dimension reduction of the speaker space ($K<L$).

The majority of tests on speaker adaptation using the eigenvoice technique and reported in the literature were made on isolated words SRS. Additionally, not all details are well explained. So, more simulations are necessary in order to understand how to conduct the adaptation so that a gain is always produced in the recognition rate. One point that has to be fully investigated is the high sensitivity of the adaptation process with the number of adaptation sentences and also with the specific sentences used, as shown in Figs. 1 and 2.

Although the results of our simulations are not yet fully conclusive, we hope to have given a little contribution to the research activities in this area.

ACKNOWLEDGEMENTS

The authors would like to express their acknowledgements to FAPESP Agency (Fundação de Amparo à Pesquisa do Estado de São Paulo) for supporting this research under grant 02/05206-1.

REFERENCES

[1] Nguyen, P. “Fast Speaker Adaptation”. *Technical report*, Institut Eurécom, July 1998;

[2] Westwood R.J. “Speaker Adaptation Using Eigenvoices”. Mphil Thesys, University of Cambridge, August 1999;

[3] Kuhn, R.; Junqua, J.-C.; Nguyen, P. and Niedzielski, N. “Rapid Speaker Adaptation in Eigenvoice Space”. *Speech and Audio Processing, IEEE Transactions on*, vol. 8, Edição 6, pp. 695-707, November 2000;

[4] Kuhn, R.; Nguyen, P.; Junqua, J.C. and Goldwasser, L. “Eigenfaces and Eigenvoices: Dimensionality Reduction for Specialized Pattern Recognition”, in *Proc. 2nd IEEE Workshop Multimedia Signal Processing*, Redondo Beach, CA, pp. 71-76, December 1998;

[5] Kuhn, R.; Nguyen, P.; Junqua, J.C.; Goldwasser, L.; Niedzielski, N.; Fincke, S.; Field, K. and Contolini, M. “Eigenvoices for Speaker Adaptation”, in *Int. Conf. Speech Language Processing `98*, Sydney Austrália, vol. 5, pp. 1771-1774, November 30 – December 04 1998;

[6] Ynoguti, C.A. and Violaro, F. “Desenvolvimento de um Conjunto de Ferramentas para Pesquisas em Reconhecimento de Fala”, *Telecomunicações, Revista do Instituto Nacional de Telecomunicações - INATEL*, ISSN 1516-2338, vol. 04, nº 02, pp. 36-43, December 2001;

[7] Davis S. B. and Mermelstein P. “Comparison of Parametric Representations for Monosyllabic Word Recognition in Continuously Spoken Sentences”, *IEEE Transactions on Acustic, Speech, and Signal Processing,* ASSP-28, nº 04, August 1980;

[8] Richard J.A. and Dean W.W. “*Applied Multivariate Statistical Analysis*”, Prentice Hall 1992;

[9] Woodland P.C. “Speaker Adaptation: Techniques and Challenges”, in *Proc IEEE Workshop on Automatic Speech Recognition and Understanding*, pp. 85-90, 2000;

[10] Gauvain J.-L. and Lee C.-H. “Bayesian Learning for HMM with Gaussian Mixture State Observation Densities”, *Speech Comm.* vol 11, pp. 205-213 1992;

[11] Gauvain J.-L. and Lee C.-H. “Maximum a Posteriori Estimation for Multivariate Gaussian Mixture Observations of Markov Chains”, *IEEE Transactions on Speech and Audio Processing*, vol 02, pp. 291-298, april 1994;

[12] Zavagliakos G., Schwartz R. and McDonough J. “Maximum *a Posteriori* Adaptation for Large Scale HMM Recognizers”, in *Int. Conf. Acoustics, Speech, Signal Processing '96*, Atlanta GA, pp. 725-728, 1996.

[13] Lee C.-H. and Gauvain J.-H. “Speaker Adaptation Based on MAP Estimation of HMM Parameters”, *IEEE ICASSP-93*, pp. 558-561, 1993;

[14] Shinoda K. and Lee C.-H. “Structural MAP Speaker Adaptation Using Hierarchical Priors”, *Proc. IEEE Workshop on Automatic Speech Recognition and Undestanding*, pp. 381-387, 1997;

[15] Ahadi S.M. and Woodland P.C. “Combined Bayesian and Predictive Techniques for Rapid Speaker Adaptation of Continuous Density Hidden Markov Models”, *Computer Speech and Language*, vol 11, pp.187-206, 1997;

[16] Leggetter C.J. and Woodland P.C. “Speaker Adaptation of Continuous Density HMM`s Using Linear Regression”, in *Int. Conf. Speech Language Processing '94*, Yokohama Japan, vol 02, pp. 451-454, 1994;

[17] Leggetter C.J. and Woodland P.C. “Maximum Likelihood Linear Regression for Speaker Adaptation of Continuous Density Markov Models”, *Computer Speech and Language*, vol 09, nº 02, pp. 171-185, april 1995;

[18] Gales M. and Woodland P.C. “Mean and Variance Adaptation within the MLLR Framework”, *Computer Speech and Language*, vol 10, pp. 250-264, october 1996;

[19] Digilakis V., Ritchev D. and Neumeyer L. “Fast Speaker Adaptation Using Constrained Estimation of Gaussian Mixtures”, *IEEE Transactions on Speech and Audio Processing*, vol 03, nº 05, pp. 357-366, september 1995;

[20] Gales M. J. F. “Cluster Adaptive Training for Speech Recognition”, in Proc. International Conf. on Spoken Language Processing '98, Sydney Australia, pp. 1783-1786, 1998;

[21] Lee C.-H., Lin C.-H. and Juang B.H. “A Study on Speaker Adaptation of the Parameters of Continuous Density Hidden Markov Models”, *IEEE Transactions on Signal Processing*, vol 39, nº 04, pp. 806-814, 1991;

[22] Ynoguti C.A. “*Reconhecimento de Fala Contínua Usando Modelos Ocultos de Markov*”, PhD thesys, Universidade Estadual de Campinas, maio 1999.

Speech Enhancement Based on Masking Properties Using a Nonlinear Short-Time Spectral Attenuation

Lidiane Krebsky da Silveira Abranches
National Institute of Telecommunications - Inatel
P.O. Box 05 - 37540-000
Santa Rita do Sapucaí - MG - Brazil
lidiane@inatel.br

Francisco José Fraga da Silva
National Institute of Telecommunications - Inatel
P.O. Box 05 - 37540-000
Santa Rita do Sapucaí - MG - Brazil
fraga@inatel.br

***Abstract*—This paper presents a speech enhancement system based on the Ephraim and Malah noise suppression rule. Using a noise masking threshold in a frame-by-frame basis, some important modifications were done in the original algorithm in order to increase the amount of noise reduction and simultaneously provide a more efficient elimination of the musical noise phenomenon. Evaluation results have shown that an improvement on the overall speech quality was achieved for all types of nearly stationary noise considered in the experiment, in a very wide signal–to–noise ratio range of the original noisy signal.**

Index Terms—**Speech enhancement, Ephraim and Malah suppression rule, masking threshold.**

I. INTRODUCTION

Over the years researchers have developed a variety of theoretical and relatively effective techniques to combat the presence of background noise in speech signals.

Noise reduction or speech enhancement algorithms are used to suppress such background noise and improve the perceptual quality and intelligibility of the speech.

Even though speech is easily perceptible in a moderate noisy environment, many applications like mobile communications drive the effort to build more effective noise reduction algorithms. However, the problem of perfect cleaning of noisy speech still poses a challenge to the area of signal processing. Removing various types of noise is difficult due to the random nature of the noise and the inherent complexity of speech signals. Noise reduction techniques usually face a tradeoff between the amount of noise removal and speech distortion.

The basic idea of this work is to present a single channel speech enhancement algorithm. In this class of algorithms there is no reference channel available for noise estimation, which is realized only during speech pauses. Usually, single channel speech enhancement systems are based on short–time spectral attenuation, which is the working principle of the so called subtractive–type algorithms. These subtractive–type algorithms are often used because they are easy to implement and offer several possibilities of varying the subtraction parameters according to the intended application. However, the major drawback of these methods is the appearing of the “musical residual noise” in the enhanced speech, which presents a very unnatural disturbing quality [1]. It occurs because the magnitude of the short–time spectrum exhibits strong variations in noisy speech [2]. After performing the spectral subtraction, the short–time magnitude spectrum in the frequency bands that contained only noise, now presents a succession of randomly spaced spectral peaks, corresponding to the points of the current spectral frame where the local magnitude exceeds the average noise estimation.

Various modifications of the basic suppression rules have been proposed to reduce this effect: magnitude averaging [3], oversubtraction of noise and use of a spectral floor [4], nonlinear spectral subtraction [5], etc. But these techniques only reduce the musical noise without completely eliminating it. Its complete elimination is generally only obtained by a crude overestimation of the noise average spectrum. An undesired consequence of this technique is that the short–time noisy speech spectrum is attenuated much more than would be necessary, leading to audible distortions in the audio signal [6].

The noise suppression rule proposed by Ephraim and Malah [7], [8] became possible to obtain a moderate noise reduction while avoiding completely the musical noise phenomenon. On the other hand, at very low signal–to–noise ratios (SNR < 5 dB), the Ephraim and Malah noise suppression rule did not offer a strong attenuation of the unwanted noise, i.e., there is a considerable amount of the original noise that is kept in the enhanced signal.

Based on this reasons, we proposed a new speech enhancement scheme, which kernel is based on Ephraim and Malah’s rule, but with some modifications added in order to deal with noisy speech presenting very low signal–to–noise ratios (SNR < 5 dB). This is done by introducing the concept of noise masking threshold, which is a well–know property of the human auditory system, already widely used in

wideband audio coding [9]. A human listener tolerates additive noise as long as it remains below this threshold. The basic gain function proposed by Ephraim and Malah were modified by adapting its parameters based on the calculation of this noise masking threshold. This allows us to find the best tradeoff between the amount of noise reduction and the speech distortion in a perceptual sense.

II. Short-Time Spectral Attenuation Algorithms

If we assume that $y(n)$, the discrete noisy input signal, is composed of the clean speech signal $s(n)$ and the uncorrelated additive noise signal $d(n)$, then we can represent it as:

$$y(n) = s(n) + d(n) \tag{1}$$

In this class of algorithms, the processing is done on a frame-by-frame basis in the frequency domain. In the Power Spectral Subtraction (PSS) algorithm, the magnitude of the short-time Fast Fourier Transform (FFT) is estimated as:

$$\left|\hat{S}(\omega)\right|^2 = \begin{cases} |Y(\omega)|^2 - \left|\hat{D}(\omega)\right|^2 & , \text{ if } |Y(\omega)|^2 > \left|\hat{D}(\omega)\right|^2 \\ 0 & , \text{ otherwise} \end{cases} \tag{2}$$

where $\left|\hat{D}(\omega)\right|^2$ is the average noise power spectrum estimated during speech pauses. The phase of the noisy speech is used in order to resynthesize the enhanced speech signal. The best result achievable by any kind of *subtractive-type* algorithms is given by the combination of the clean speech spectral magnitude with the noisy spectral phase. Following N. Virag [9], this situation is called in this paper the *theoretical limit.*

The noise suppression can also be implemented as a time-varying filtering process and viewed as *short-time spectral attenuation.* The PSS process is equivalent to a multiplication of the short-time FFT magnitude of the noisy speech by a gain function :

$$\left|\hat{S}(\omega)\right| = G(\omega)\cdot|Y(\omega)| \quad \text{with} \quad 0 \le G(\omega) \le 1 \tag{3}$$

where:

$$G(\omega) = \begin{cases} \sqrt{1 - \dfrac{\left|\hat{D}(\omega)\right|^2}{|Y(\omega)|^2}} & , \text{ if } |Y(\omega)|^2 > \left|\hat{D}(\omega)\right|^2 \\ 0 & , \text{ otherwise} \end{cases} \tag{4}$$

This new way of presentation permits a better understanding of the *short–time spectral attenuation* process: subtractive–type algorithms attempt to emphasize the spectral components as a function of the amount by which they exceed the noise estimation. The consequence is that the spectrum sections where the speech is strong compared with the noise are unmodified, while sections containing only noise are suppressed. Between these two cases, the gain function takes a value depending on the inverse of the SNR of each spectral component.

Berouti et al. [4] proposed a very flexible form of subtractive-type algorithm. It is one of the most famous algorithms for residual noise reduction where the tuning some parameters allows the variation of the tradeoff between noise reduction, residual noise and speech distortion :

$$G(\omega) = \begin{cases} \left[1 - \alpha.\left(\dfrac{\left|\hat{D}(\omega)\right|}{|Y(\omega)|}\right)^{\gamma}\right]^{1/\gamma} & , \text{ if } \left(\dfrac{\left|\hat{D}(\omega)\right|}{|Y(\omega)|}\right)^{\gamma} < \dfrac{1}{\alpha+\beta} \\ \left[\beta\cdot\left(\dfrac{\left|\hat{D}(\omega)\right|}{|Y(\omega)|}\right)^{\gamma}\right]^{1/\gamma} & , \text{ otherwise} \end{cases} \tag{5}$$

where α is the O*versubtraction factor* ($\alpha > 1$), β is the *Spectral Flooring factor* ($0 \le \beta << 1$) and the *Exponent* γ determines the shapness of the transition from the $G(\omega) = 1$ to the $G(\omega) = 0$. The choice of these three parameters allows great flexibility, but at low SNR's, it is impossible to minimize speech distortion and residual noise, simultaneously. But, if we consider the SNR of each spectral component from previous frames, it is possible to minimize the effect of the residual noise while keeping the speech distortion as low as possible. This is the topic of the section IV.

III. Using masking properties in spectral subtraction Algorithms

The idea of exploiting the masking properties of human auditory system were taken from a successful speech enhancement system proposed by Nathalie Virag [9]. In her paper, she adapted the classical subtraction parameters in (5) using the noise masking threshold, obtaining an improvement of the speech quality if compared with the basic spectral subtraction algorithm. She used a perceptual model that was developed by Johnston for audio coding [10]. This model, with some adaptations, presents some steps for the masking threshold calculation:

- Critical band analysis of the signal: The first step calculates the energy present in each critical band, assuming discrete non-overlapping critical bands.

$$B_i = \sum_{\omega=bl_i}^{bh_i} P(\omega) \tag{6}$$

where bl_i and bh_i are the lower and upper boundaries of the i[th] critical band and $P(\omega)$ is the power spectrum.

- Applying of a spreading function to the critical band spectrum: The spreading function B_i is then convolved with the bark spectrum B_i :

$$C_i = S_i * B_i \tag{7}$$

where S_i is given by [11], in decibels :

$$S_i = 15{,}81 + 7{,}5(i + 0{,}4) - 17{,}5\sqrt{1 + (i + 0{,}474)^2} \tag{8}$$

The spreading function S_i has lower and upper skirts of $+25$ dB/Critical band and -10 dB/Critical band, respectively.

- Calculation of the noise masking threshold by subtraction of a relative threshold offset $O(k)$ depending on the noise-like or tone-like nature of the masker and the maskee signals. A simple method were proposed by Sinha and Tewfik [12], $O(k)$ is given by a simple estimation, based on the fact that often the speech signal has a tonelike nature in lower critical bands and a noiselike nature in higher bands, as showed in Fig. 1.

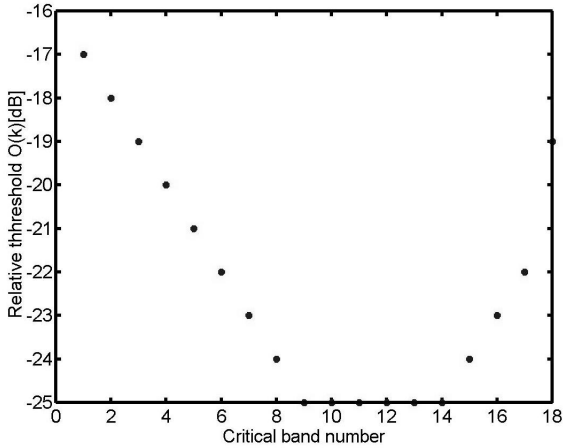

Fig. 1: Relative threshold offset (after Sinha and Tewfik[12])

$$T_i = 10^{\log_{10}(C_i) - (O_i/10)} \tag{9}$$

- Relating the spread masking threshold to the critical band masking threshold. The convolution of the spreading function with B_i must be undone, i.e., the threshold calculated as B_i should be deconvolved. As this process is very unstable, in place of the deconvolution, renormalization is used multiplying each T_i by the inverse of the energy gain obtained by the convolution in (7).
- Accounting for absolute thresholds: Any critical band that has a calculated noise threshold lower than the absolute threshold of hearing is replaced by the to the absolute threshold in that critical band.

In the method presented for noise masking threshold calculation described above, the noise masking threshold must be calculated from the power spectrum of the clean speech. However, in practice only the original noisy signal is available. Then a rough estimate of the clean speech signal is computed using a simple power spectral subtraction scheme (see block diagram in Fig. 5).

Virag uses the masking threshold (obtained using power spectrum subtraction) to adjust the spectral subtraction parameters α and β of (5), for each frequency ω of a given speech frame q.

The adaptation of the subtraction parameters is performed by:

$$\begin{aligned} \alpha(q,\omega) &= F_\alpha[\alpha_{\min}, \alpha_{\max}, T(\omega)] \\ \beta(q,\omega) &= F_\beta[\beta_{\min}, \beta_{\max}, T(\omega)] \end{aligned} \tag{10}$$

where $\alpha_{\min}$, $\alpha_{\max}$ and $\beta_{\min}$, $\beta_{\max}$ are the minimal and maximal values of the oversubtraction and spectral flooring parameters, respectively.

The functions F_α and F_β perform a linear interpolation according to the following boundaries:

$$\begin{aligned} F_\alpha &= \alpha_{\max} \text{ if } \quad T(\omega) = T(\omega)_{\min} \\ F_\beta &= \alpha_{\min} \text{ if } \quad T(\omega) = T(\omega)_{\max} \\ F_\beta &= \beta_{\max} \quad \text{if } \quad T(\omega) = T(\omega)_{\min} \\ F_\beta &= \beta_{\min} \quad \text{if } \quad T(\omega) = T(\omega)_{\max} \end{aligned}$$

where $T(\omega)_{\min}$ and $T(\omega)_{\max}$ are the minimal and maximal values of the masking threshold in the current frame.

N.Virag [9] found out that the choices of $\alpha_{\min} = 1$, $\alpha_{\max} = 6$, $\beta_{\min} = 0$ and $\beta_{\max} = 0{,}02$ gave a good tradeoff between residual noise and speech distortion. The parameter γ is fixed: $\gamma = 2$.

But we have found out that with this scheme it was not possible to completely eliminate the musical noise phenomenon. In our work, the information given by the noise masking threshold were used to adapt the Ephraim and Malah noise suppression rule, which by itself completely eliminates the musical noise, in order to increase its performance regarding the amount of noise reduction when the noisy speech signal presents a very low signal–to–noise ratio (SNR < 5 dB).

In the following section, we will present the basic Ephraim and Malah noise suppresion rule and the mechanisms that counter the musical noise phenomenon.

IV. The Ephraim and Malah Suppression rule

In this paper we will focus in the original algorithm proposed by Ephraim and Malah in [7] and developed in [8]. The Ephraim and Malah Suppression Rule (EMSR) is a special type of *short–time spectral attenuation* algorithm were the spectral gain $G(q,\omega)$ that is applied to each short–time spectral component $|Y(q,\omega)|$ of the current speech frame is given by:

$$G = \frac{\sqrt{\pi}}{2}\sqrt{\left(\frac{1}{1+R_{post}}\right)\cdot\left(\frac{R_{prio}}{1+R_{prio}}\right)}\cdot M[\theta]$$

where

$$\theta = \left(1+R_{post}\right)\cdot\left(\frac{R_{prio}}{1+R_{prio}}\right) \quad \textit{and} \qquad (11)$$

$$\mathrm{M}[\theta] = \exp\left(-\frac{\theta}{2}\right)\cdot\left[(1+\theta)\cdot I_0\left(\frac{\theta}{2}\right)+\theta\cdot I_1\cdot\left(\frac{\theta}{2}\right)\right]$$

and where I_0 and I_1 are the modified Bessel functions of zero and first order, respectively [8].

In (11), the frame index q and the frequency index ω have been omitted for reasons of compactness. The spectral gain depends on two parameters:

$$R_{post}(q,\omega) = \begin{cases} \dfrac{|Y(q,\omega)|^2}{\left|\hat{D}(\omega)\right|^2} - 1 & , \text{ if } \dfrac{|Y(q,\omega)|^2}{\left|\hat{D}(\omega)\right|^2} > 1 \\ 0 & , \text{ otherwise} \end{cases} \qquad (12)$$

$$R_{prio}(q,\omega) = (1-\mu)\cdot R_{post}(q,\omega) + \mu\cdot G^2(q-1,\omega)\cdot\frac{|Y(q-1,\omega)|^2}{\left|\hat{D}(\omega)\right|^2} \qquad (13)$$

where $G(q–1, \omega)$ stands for the gain function (11) estimated in the previous frame. A detailed explanation about the effect of each parameter of (12) and (13) in the gain function expressed by (11) can be found in [13]. Here we will only report that the parameter μ was experimentally set to 0.98 in [13] and explain the fundamental mechanism that counters the musical noise effect.

The a priori SNR $Rprio(q,\omega)$ is evaluated by the nonlinear recursive relation of (13) and is the dominant parameter in (11), as we can see in Fig. 2. Strong attenuations are obtained only if $Rprio(q,\omega)$ is low and low attenuations are obtained only if $Rprio(q,\omega)$ is high. When $Rprio(q,\omega)$ is low, $Rpost(q,\omega)$ acts as a correction parameter (left–hand part of Fig. 2).

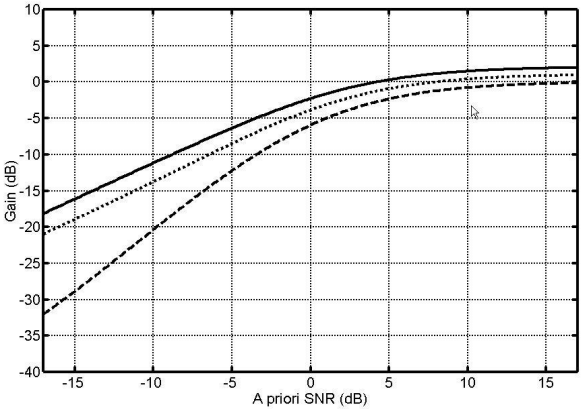

Fig. 2: EMSR gain versus a priori SNR for different values of Rpost; top curve: Rpost = –17 dB; middle curve: Rpost = 0 dB; bottom curve: Rpost = 17 dB

Surprisingly, the effect is opposite of what is intuitively expected: when $Rprio(q,\omega)$ is low and $Rpost(q,\omega)$ is high, there is a very strong attenuation. This behavior is a consequence of the disagreement between the a priori and the a posteriori SNR's and it is actually useful in the elimination of the musical noise, as we will explain later.

An experimental study of (13) indicates two different behaviors for the a priori SNR:

1. When the a posteriori SNR $Rpost(q,\omega)$ stays below or near to 0 dB, the a priori SNR corresponds to a highly smoothed version of the a posteriori SNR over successive short–time frames. Consequently, the variance of $Rprio(q,\omega)$ for a given frequency along successive frames is much smaller than that of $Rpost(q,\omega)$.
2. Just the opposite, when $Rpost(q,\omega)$ is much larger than 0 dB, the a priori SNR follows the a posteriori SNR along successive frames, with a

delay of one short–time frame. To see that behavior, note that when *Rprio(q,ω)* is high, $G(q,\omega) \cong 1$ (right–hand part of Fig. 2). Then, because $\mu \cong 1$ and $Rpost(q,\omega) >> 1$, (13) can be approximated by

$$R_{prio}(q,\omega) = \mu \cdot R_{post}(q-1,\omega) \tag{13}$$

These two different behaviors of *Rprio(q,ω)* are quite visible on Fig. 3. Observe how in the left–hand part of the figure, the curve of *Rprio(q,ω)* is much more smooth than that of *Rpost(q,ω)*, whereas on the right–hand part (last 20 frames), *Rprio(q,ω)* follows *Rpost(q,ω)* with just one frame delay.

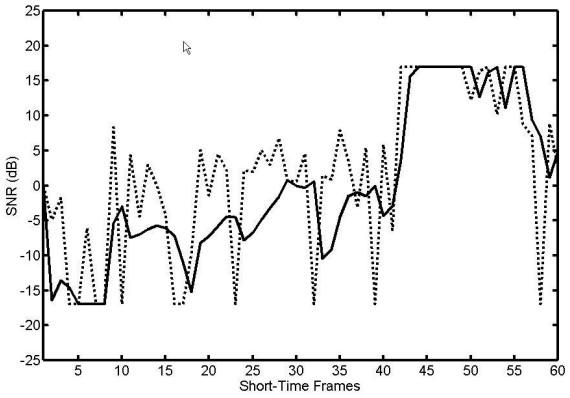

Fig. 3: SNR's in successive short–time frames; dashed curve: A posteriori SNR; solid curve: A priori SNR. For the first 40 frames, the signal contains only noise at the chosen frequency; for the next 20 frames, a component with more than 15 dB SNR emerges at the displayed frequency.

In the original paper by Ephraim and Malah, the gain function of (11) was tabulated for values of both SNR's Rprio and Rpost between –15 and 15 dB. In our work, we limited the range of Rprio and Rpost between –17 and 17 dB. The smoothness of the a priori SNR is a key factor in the elimination of the musical noise effect. In that parts of the short–time spectrum corresponding to noise only, the a posteriori SNR is –17 dB in average, which corresponds to the first case: Due to the smoothing behavior, the a priori SNR has a significantly reduced variance. Because the gain function of the EMSR depends mainly on the value of the a priori SNR, the attenuation itself does not exhibit large variations over successive frames. As a consequence, the musical noise phenomenon, which consists in discrete tones at random frequencies appearing and disappearing rapidly over successive frames, is completely eliminated. When the signal level is well above the noise level, *Rprio* follows *Rpost* with a one–frame delay, which is important in the nonstationary parts of the speech signal.

V. Proposed Speech Enhancement System

In our algorithm, the gain function is also calculated by (11), but the a priori and the a posteriori SNR's are derived by means of the following relations:

$$R_{post}(q,\omega) = \frac{|Y(q,\omega)|^2}{\alpha(q,\omega)\cdot|\hat{D}(\omega)|^2} - 1 \tag{14}$$

$$\begin{aligned} R_{prio}(q,\omega) &= (1-\mu)\cdot R_{post}(q,\omega) + \\ &+ \mu\cdot\nu\cdot G^2(q-1,\omega)\cdot\frac{|Y(q-1,\omega)|^2}{\alpha(q,\omega)\cdot|\hat{D}(\omega)|^2} + \\ &+ \mu\cdot(1-\nu)\cdot G^2(q-2,\omega)\cdot\frac{|Y(q-2,\omega)|^2}{\alpha(q,\omega)\cdot|\hat{D}(\omega)|^2} \end{aligned} \tag{15}$$

where μ and ν were experimentally set to 0.96 and 0.75, respectively. The perceptual overattenuation factor $\alpha(q,\omega)$ operates in a way similar to parameter α in (5). This function $\alpha(q,\omega)$ depends directly on the noise masking threshold $T(q,\omega)$, which is calculated for each frame q as explained in the previous section. When $T(q,\omega)$ is high, it means that the noise level at that frequency can be also high because it will be masked by the speech. Therefore, $\alpha(q,\omega)$ can be set to a low level in order to prevent audible distortions. At the contrary, when $T(q,\omega)$ is low, even a low–level noise at frequency ω will be perceptually annoying, which means that $\alpha(q,\omega)$ must be set to a high level with the aim of reducing at most the residual noise.

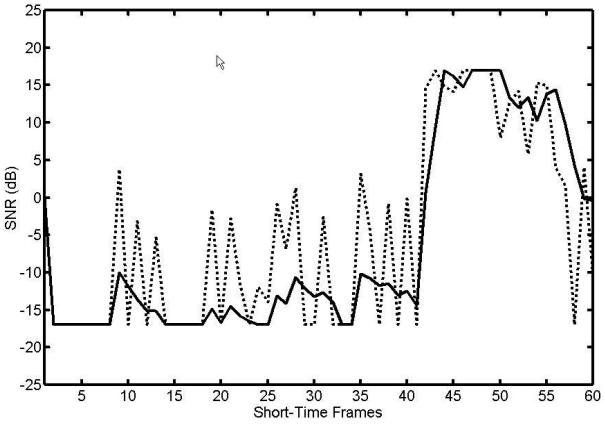

Fig. 4: SNR's in successive short–time frames calculated by (14) and (15); dashed curve: A posteriori SNR; solid curve: A priori SNR. The noisy signal and the displayed frequency were the same of those used to generate the curves of Fig. 2.

Other important difference between our algorithm and the standard EMSR is the presence of a third term in (15), which was empirically proved to be efficient in increasing the smoothness of *Rprio* over successive frames.

The effect of both modifications of the EMSR can be clearly visualized comparing Fig. 3 to Fig. 4. In the

first 40 frames of Fig. 3, *Rprio* has a mean value much lower than the mean value that can be observed in Fig. 3, which means that our algorithm performs a stronger attenuation of the noisy signal at those frequencies containing only noise, if compared with the standard EMSR. We can also observe that the smoothing effect on *Rprio* was increased, which has the consequence of improving the reduction of the musical noise phenomenon, as had been explained before. On the other hand, in the last 20 frames of Fig. 4, *Rprio* does not follow *Rpost* as well as it does in Fig. 3. But the following effect still occurs and, despite being less strong than that of EMSR, the results presented in next section proved that the overall effect of the introduced modifications was beneficial to the perceptual evaluation of the enhanced speech quality.

The complete proposed enhancement scheme can be visualized in Fig. 5:

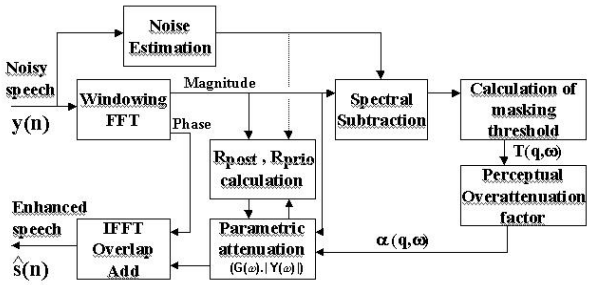

Fig. 5 – The proposed speech enhancement system

VI. RESULTS

In order to compare the performance of our algorithm to the performance of both standard PSS and EMSR algorithms, we performed an objective evaluation of the enhanced speech quality using the PESQ–MOS score (PESQ – Perceptual Evaluation of Speech Quality, ITU recommendation P.862). The PESQ–MOS scores presents a correlation of more than 95% with the subjective MOS (Mean Opinion Score) with the advantage or being far easier to obtain [14].

TABLE I
AVERAGE PESQ–MOS MEASURES FOR ENHANCED SPEECH SIGNALS USING DIFFERENT METHODS WITH ORIGINAL NOISY SIGNALS AT SNR BETWEEN 0 AND 5 dB

NOISE TYPE → (Average SNR dB)	WHITE (3,22dB)	PINK (2,78dB)	F16 (2,65dB)	FACTORY (3,49dB)
No processing	1,980	1,917	2,094	2,414
PSS ($\alpha = 2$)	2,272	2,157	2,271	2,582
EMSR ($\mu = 0.96$)	2,487	2,386	2,484	2,756
Proposed algorithm	**2,601**	**2,512**	**2,591**	**2,854**
Theoretical limit	3,879	3,728	3,801	3,877

TABLE II
AVERAGE PESQ–MOS MEASURES FOR ENHANCED SPEECH SIGNALS USING DIFFERENT METHODS WITH ORIGINAL NOISY SIGNALS AT SNR BETWEEN 5 AND 10 dB

NOISE TYPE → (Average SNR dB)	PINK (6,97dB)	F16 (6,21dB)	CAR (7,89dB)	FACTORY (5,17dB)
No processing	1,878	2,194	3,183	2,213
PSS ($\alpha = 2$)	2,243	2,493	3,489	2,489
EMSR ($\mu = 0.96$)	2,489	2,749	3,667	2,622
Proposed algorithm	**2,663**	**2,883**	**3,695**	**2,744**
Theoretical limit	3,620	3,910	4,143	3,747

TABLE III
AVERAGE PESQ–MOS MEASURES FOR ENHANCED SPEECH SIGNALS USING DIFFERENT METHODS WITH ORIGINAL NOISY SIGNALS AT SNR BETWEEN 10 AND 15 dB

NOISE TYPE → (Average SNR dB)	PINK (14,85dB)	F16 (12,13dB)
No processing	2,499	2,647
PSS ($\alpha = 2$)	2,971	2,995
EMSR ($\mu = 0.96$)	3,254	3,257
Proposed algorithm	**3,410**	**3,298**
Theoretical limit	3,957	4,064

Tables I, II and III presents the results of the evaluation of the three above mentioned enhancement methods plus the PESQ–MOS scores of the noisy signal itself and that corresponding to the theoretical limit (see section II). The noisy signals and the reference clean signals were got from the SpEAR database [15].

The following noise types were considered:

- WHITE noise
- PINK noise
- FACTORY noise: This noise is from a car production hall.
- F16 noise: The noise from the co-pilot's seat in a two-seat F-16, traveling at a speed of 500 knots, and an altitude of 300-600 feet.
- CAR noise: The noise from the interior of a Volvo car at 120 km/h, in 4th gear, on an asphalt road, in rainy conditions.

In this database, the noisy signals were obtained by acoustically adding the clean signal and the noise in a controlled environment. The clean signals were taken from the TIMIT database but they were re–recorded using the same room used to generate the noisy signals. Several types of noise were combined with clean speech at different SNR's, and the results were presented in the form of averages (of both SNR's and PESQ scores) got from a total of 33 WAVE files.

VII. Conclusion

The proposed speech enhancement system is very efficient in the reduction of background noise. The results presented in the last section showed that our speech enhancement system outperforms the standard EMSR algorithm for all types of nearly stationary noise considered in the experiment, in a very wide SNR range of the original noisy signal. The improvement in performance can be explained by the effect of introducing a perceptual–dependent overattenuation factor in the derivation of both the *a priori* and *a posteriori* SNR's, which is responsible by an increased amount of noise reduction without increasing the speech distortion. Furthermore, the consideration of two previous frames in (15) allows a better smoothing effect over the a priori SNR, which is directly related with an efficient elimination of the musical noise phenomenon.

REFERENCES

[1] J. A. Moorer and M. Berger, *Linear–phase bandsplitting: Theory and applications*, Journal of Audio Eng. Soc. , vol 34, no. 3, pp. 143–152, 1986.

[2] D. R. Brilinger, *Time Series Data Analysis and Theory*. San Francisco: Holden–Day, 1981.

[3] S. F. Boll, *Suppression of acoustic noise in speech using spectral subtraction*, IEEE Trans. Acoust., Speech, Signal Processing, vol. ASSP–27, pp. 113–120, Apr. 1979.

[4] M. Berouti, R. Schwartz, and J. Makhoul, *Enhancement of speech corrupted by acoustic noise*, in Proc. IEEE ICASSP, Washington, DC, pp. 208–211, Apr. 1979.

[5] P. Lockwood and J. Boudy, *Experiments with a nonlinear spectral subtractor (NSS), hidden Markov models and projection, for robust recognition in cars*, Speech Communication, vol 11, pp. 215–228, June 1992.

[6] O. Cappé and J. Laroche, *Evaluation of short–time spectral attenuation techniques for the restoration of musical recordings*, IEEE Trans. Speech Audio Processing, vol. 3, no. 1, pp. 84–93, January 1995.

[7] Y. Ephraim and D. Malah, *Speech enhancement using optimal nonlinear spectral amplitude estimation*, in Proc. IEEE ICASSP, pp. 1118–1121, Boston, 1983.

[8] Y. Ephraim and D. Malah, *Speech enhancement using a minimum mean–square error short-time spectral amplitude estimator*, IEEE Trans. Acoust., Speech, Signal Processing, vol. ASSP–32, no. 6, pp. 1109-1121, 1984

[9] N. Virag, *Single Channel Speech Enhancement Based on Masking Properties of the Human Auditory System*, IEEE Trans. Speech Audio Processing, vol. 7, no. 2, pp. 126–137, March 1999.

[10] J. D. Johnston, *Transform coding of audio signals using perceptual noise criteria*, IEEE J. Select. Areas Commun., vol. 6, pp. 314–323, Feb. 1988.

[11] M. R. Schroeder, B.S. Atal and J.L. Hall, *Optimizing Digital Speech Coders by Exploiting Masking Properties of the Human Ear*, in Journal of Acoustical Soc. of America, pp. 1647-1652, 1979.

[12] D. Sinha and A.H. TEWFIK, *Low bit rate transparent audio compression using adaptad wavelets*, Trans. Signal Processing, vol.41, pp. 3463-3479, December 1993.

[13] O. Cappé, *Elimination of the Musical Noise Phenomenon with the Ephraim and Malah Noise Suppressor*, IEEE Trans. Speech Audio Processing, vol. 2, no. 2, pp. 345–349, April 1994.

[14] Antony W.Rix et. al., *Perceptual Evaluation of Speech Quality (PESQ). The New ITU Standard for End–to–End Speech Quality Assessment*, Journal of Audio Eng. Soc., vol. 50, no. 10, pp. 755–778, October 2002.

[15] E. Wan, A. Nelson, and Rick Peterson. *SpeechEnhancement Assessment Resource (SpEAR)database*. < http://cslu.ece.ogi.edu/nsel/data/SpEAR_database.html. > Beta Release v1.0. CSLU, Oregon Graduate Institute of Science and Technology..